Sensorless Position Control of Induction Machines using High Frequency Signal Injection

by **Dipl.-Ing. N. Teske**

Thesis submitted to the University of Nottingham for the degree of Doctor of Philosophy, July 2001

To my parents for their encouragement to go abroad

and

to my girlfriend Lourdes for her support

Acknowledgements

This thesis is the result of my work as a research assistant with the Power Electronics, Machines and Control Group (PEMC) at the University of Nottingham.

I would like to express my sincere gratitude to my supervisors Prof. G.M. Asher, Dr. K.J. Bradley and Dr. M. Sumner for their guidance, support and constructive comments over the course of this research.

The accomplishment of the research became possible through the financial support by the members of the Nottingham Drives Consortium, in particular Brook Hansen Ltd. and Eurotherm Drives Ltd. who provided the necessary hardware for the experimental part of the research. The project was funded by the EPSRC Award GR/K84172.

Thanks also to Dipl.-Ing. M. Bienert for his assistance in designing PCBs and his help in constructing the rig.

I like to thank all my friends and collegues in the laboratory of the Power Electronics, Control and Machines Group for the support, valuable discussions and motivating atmosphere. Special thanks to Cesar Silva for the valuable suggestions about deadtime effects in inverters and the modelling of saturation in machines, to Cedric Mifsud for the discussions about Vector Control and *hf* injection, to Lee Empringham for his valuable tips concerning hardware design and to James Campbell and the prementioned for proofreading.

Finally I would like to thank Prof. Paul P. Acarnley from the Department of Electrical and Electronic Engineering at the University of Newcastle upon Tyne for taking over as the external examiner and for his interest in the work. I would also like to thank Dr. Jon Clare for acting as internal examiner.

Contents

Abstract

The aim of this research project was to develop a position controlled induction machine vector drive operating without a speed or position sensor but having a dynamic performance comparable to that of a sensored position vector drive. The methodology relies on the detection of a rotor saliency in the machine by persistent high-frequency voltage injection. The rotor position is then estimated from the resulting stator current harmonics that are modulated by the spatial rotor saliency. This can be a built-in rotor saliency (a designed asymmetry) or the natural saliency due to rotor slotting. This project investigates the demodulation of the extracted high-frequency current spectrum and different topologies for the estimation of rotor position.

The tracking of rotor position through rotor saliencies helps to overcome the limitations of model-based approaches that are restricted to speeds above 30rpm on a 4-pole machine and are sensitive to parameter mismatches.

The project addresses the difficult problem of separating the modulation effects due to the rotor saliency from distorting modulations due to the saturation saliency and inverter effects. In previous research it had been found that the saturation saliency causes a deterioration of the position estimate that can result in a loss of position and eventually causes the drive to fail. The application of filters to remove the interfering saturation harmonics is not possible. In this research a new approach was developed that compensates online for the saturation effect using pre-commissioned information about the machine.

This harmonic compensation scheme was utilized for a $30kW$, 4-pole induction machine with asymmetric rotor and enabled the operation from zero to full load and from standstill up to about $\pm$150rpm ($\pm$5Hz). The steady-state performance and accuracy of the resulting sensorless drive has been found to operate similarly to a sensored drive fitted with a medium resolution encoder of 600ppr.

The project involved studies of the inverter switching deadtime and its distorting effect on the position estimation. A second compensation strategy was therefore de-

veloped that is better suited if a large interfering modulation due to the inverter deadtime is present in the machine.

The new compensation method was implemented for a second $30kW$ machine that utilizes the rotor slotting saliency. Good tracking results were obtained with a mean error of less than $\pm 0.5°$ mechanical under steady-state. The derivation of the position signal for higher speeds introduces an additional speed-dependent error of about 4° mechanical at 170rpm. Sensorless position control was realized for operation from zero to full load for the fully fluxed machine. The performance allowed low and zero speed operation including position transients reaching a speed of 50rpm.

The high-frequency modulation introduced by the fundamental currents during transient operation was examined and identified as the main factor limiting the dynamics of the sensorless drive.

Two rigs were used for the research. The first rig is build around a network of Transputers, the second rig uses state-of-the-art TMS320C40 and TMS320F240 digital signal processors for the control and was designed and constructed as part of the research.

Chapter 1:

Introduction

The induction machine was invented by Nikola Tesla in early 1888, just before Prof. Ferraris published his independent discovery in Italy. This invention gave a strong impulse for the widespread use of polyphase generation, transmission and distribution of electrical energy [1]. The main advantage of the induction machine over the popular DC drive was its simple and robust structure that does not require brushes for its operation, resulting in less maintenance costs and higher power density per volume [2]. Nowadays about 70% of all the electrical energy used in the industrial sector in the EU and Japan is consumed by motor systems [3, 4]. The figure for the commercial sector in the EU is 36% of the electricity [3]. The largest amount of the motor systems are cage induction machines. Alone in Japan, about 10 million induction motors are produced each year [4].

The majority of induction machines are connected directly to the mains (star-delta) in fixed-speed applications. Only due to the progress in power electronics it has become possible to build variable-speed drives using induction machines at an acceptable cost. Originally, thyristor controlled three-phase bridges were used, now IGBTs or transistors with faster switching times, shorter dead-time, and higher power levels are being developed [5]. Induction machines are popularly applied with open-loop control that does not require an encoder or the knowledge of machine parameters.

The development of Field Oriented Control in Germany in the early seventies [6–8] has meant that induction machine drives are slowly substituting DC machines in the field of variable speed or high dynamic drive applications. The dynamic control of induction machines is more complicated when compared to DC machines. It is however superior to the popular DC drives powered by a 6-pulse thyristor bridge. An area

where costs of the drive can be reduced is that of the sensors. In particular the position or speed encoder required for a field oriented dynamic system can considerably contribute to the overall system costs. For small machines, the cost of the encoder can be similar to that of the machine. On large machines it can still be around $20-30\%$. With the aim to reduce costs, size and maintenance, control techniques have been developed for the induction machine that operate without an encoder, termed *sensorless*. Sensorless techniques can also improve the drive robustness and reliability when operated on a sensored drive. Typically, a numerical model of the machine is used to estimate the rotor speed.

All modern induction machine drives require some parameter identification. This can be relatively simple for the sensored drive. It is however essential for the quality of the sensorless drive. Parameter identification may be realized in the form of self-commissioning when setting up the drive [9, 10]. With the *a priori* knowledge of the machine's electrical parameters that are given on the name-plate, the drive may perform a number of tests at standstill to tune the current controllers and determine further electrical parameters. Key parameters for sensorless drives are the stator resistance R_s or the rotor time constant T_r that may need permanent adaptation by using online identification [11]. Run-up or down tests may then determine the inertia and speed characteristic of the drive. Self-commissioning can reduce the set-up time and is for the convenience of the customer. However, it is also essential to adjust parameters to changing operating conditions to get most out of the machine. In particular, sensorless drives require the correct adaption of parameters because they are model-based and thus more sensitive to the machine parameters than a sensored drive.

Another pacemaker in the drives field is the constantly falling price and the increased complexity and integration of digital processors [12]. They easily perform the complex vector transformations required for field oriented control that wasn't accurately possible by using analogue circuits. New powerful processors come with fast multipliers, large internal memory and integration of modules to interface peripherals such as encoders, inverters, transducers and other drives [13, 14]. Typical integrated modules are fast A/D converters, internal timers for the generation of pulse-width modulation (PWM), serial interfaces, the controller area network (CAN) or other field bus systems to connect the drive to supervisory networks. Better module integration simplifies system design and increases flexibility whilst reducing costs.

Sensorless drives are typically limited to operation above 1Hz. Especially at low speeds, the speed estimation and torque and flux control of model-based approaches is poor or fail [15]. Parameter tuning and online parameter identification has only yielded a partial improvement [16]. This is why attention has turned to tracking

saliencies within an induction machine through the use of high-frequency (*hf*) signal injection [17]. This can yield either the rotor position or an orientation flux angle without recourse to a machine model and thereby promises to overcome the zero- and low-speed problems. These methods fall into two categories. The first tracks the natural saturation saliency to yield an orientation flux angle which is applicable to a torque-controlled drive [18–20]. The second category tracks a rotor saliency arising from rotor slotting [21] or an engineered saliency involving circumferential variation of surface rotor resistance [22] or leakage inductance [23]. This methods are called *self-sensing*, *auto-sensing* or *eigensensing* control since the position sensor is an inherent part of the machine ('the machine is the encoder').

This category yields a rotor position estimate from the rotor saliency which can be used both for sensorless position control and field orientation via standard vector control techniques. Unfortunately, for a fully fluxed machine, or a machine under load, the saturation saliency becomes significant and its modulation of the *hf* stator currents interferes with (or even dominates over) the rotor saliency modulation. Under such conditions, the rotor estimate and position control is lost [24].

The objectives for this research project are to improve the controllability and robustness of a sensorless drive in the zero and low speed region using *hf* signal injection. The aim is on improving the rotor position estimate for machines with either circumferential or rotor slotting saliencies and to operate the sensorless machine under all operating conditions. This work discusses the problem of saturation saliency interference. A solution is presented in which the modulated *hf* currents are compensated so as to substantially reduce or eliminate the saturation saliency harmonic. For the sensorless drive based on the rotor slotting saliency it was discovered that the inverter deadtime causes a modulation similar to that due to saturation. This work examines the modulation due to inverter clamping and presents a compensation method. Also the *hf* modulation due to transient fundamental currents is investigated that results in a distortion of the *hf* position signals during fast transient machine operation.

The developed methodologies have been implemented on an experimental $30k$W induction machine drive. This work shows that the resulting sensorless position control using an induction machine with a designed rotor saliency is effective under all static loads, for dynamic load conditions and for transient position changes.

Sensorless position control is also demonstrated experimentally for an induction machine using rotor slot harmonics. The rotor position can be reliably estimated at standstill and low speeds by using a technique to suppress the clamping and saturation saliency modulation.

Chapter 2:

Field Oriented Control and Review of Sensorless Techniques

This chapter covers the mathematical background that is required for the control of 3-phase induction machines. The machine is described by using the standard two-axis model based on the *Space Phasor Theory* that provides an approximation that is sufficient for control purposes. Iron saturation is neglected in the model as only operation under constant flux is considered. Since single and double cage rotors are used for the sensorless position control, the differences in the machine model will be examined. An analysis of saliency models for sensorless control is covered later in Chapter 5. These can be added to the fundamental machine models described in this chapter to combine fundamental and *hf* characteristics [25].

The two-axis machine model provides the basis for so-called flux models that estimate the flux vector from terminal quantities such as voltages and currents. A flux model is required to realize field-oriented control. The strategy for Vector Control is described that allows the high-dynamic control of induction machines and an overview of sensorless control is given. The controller layout is covered separately in Chapter 3.

A simple model for the inverter is also introduced in this chapter and the modulation strategy that is presented is the *Space Vector Theory*. The importance of modulation strategies and their use in a vector-controlled drive are discussed. The basics are given to understand its use and effects on a position-sensorless drive using machine saliencies. These are the so-called *transient injection*, described in Chapter 5 and the *inverter modulation* that is covered in Chapter 6.1.

2.1 Basics of the Induction Machine and Vector Control

The induction machine is the most widely used electrical drive motor. In 1995 the drives market worldwide was estimated to be worth 906.6 million US$ for AC drives, expected to double within a couple of years in contrast to 473.1 million US$ for DC drives with a declining tendency [26].
The name of the induction machine originates from its operation principle: When the flux density wave produced by the stator magnetizing currents sweeps past the shorted rotor conductors, a voltage is induced in them due to the relative movement between field and rotor. The resulting rotor currents interact with the air-gap flux and produce a torque. The rotor frequency f_r will therefore in motoring mode be lower than the excitation frequency f_e of the rotating stator field. The difference is called the slip frequency f_{sl}. Most induction machines are designed to operate from a 3-phase source of alternating voltage. For variable-speed drives an inverter is used to produce approximately sinusoidal stator voltages or currents of controllable magnitude and frequency.

The main advantage of the induction machine compared to other types of electrical machines is its rugged and robust structure that allows for a high overload capability. The induction machine can withstand overcurrents up to 10 times the rated current for short periods and it does not suffer from the danger of demagnetization like permanent magnet (PM) machines. Due to its simple structure, the induction machine has low manufacturing costs [27]. This advantage is mainly due to the construction of the rotor that is made of thin rotor laminations that are stacked onto the main shaft where the rotor bars are made of aluminium that is cast axially into slots in the outer periphery of the rotor and shorted together at both ends. The fact that the induction machine does not need slip rings or commutators allows for the operation in explosive or extremely dirty environments and guarantees low maintenance costs. The induction machine is also suitable for operation above rated speed in the field-weakening region.
Vector Control provides the key to rapid control for operating an induction machine highly dynamically and in the same way as a separately excited DC machine [7, 8]. This is physically possible because stator and rotor windings are magnetically tightly coupled. Rapid changes in the secondary current can be obtained by making rapid changes in the stator currents. The inductance under transient conditions as seen from the stator side is low because of the short-circuited cage bars. This means that only a modest volt-second product is needed to affect rapid changes in the stator currents [28]. The condition necessary for the rotor current wave to adjust immediately to a new steady state is that the rotor flux linkage ψ_r must remain

constant. Due to the natural tendency of a closed inductive circuit to oppose changes in the stored energy and to maintain the flux linkage constant, it cannot be changed instantaneously. The rotor flux linkage must not be changed if oscillations in ψ_r and transients in rotor currents and torque shall be avoided.

Under Vector Control, the magnitude and position of the flux linkage are controlled both in steady state and transient operations by adjusting the instantaneous amplitude, frequency and phase of the stator current. This makes rapid changes in the torque possible and achieves high dynamic position, speed or torque control.

The differential equations of the induction machine that have time-dependent coefficients are converted via transformations to a simple set of equations with constant coefficients in the field-oriented coordinate system. Transformed stator currents are used as control variables in a closed loop system to indirectly control and decouple rotor flux and torque. The three possibilities for field orientation are *stator flux oriented control* (SFOC), *air-gap flux oriented control* (AFOC that is not very popular) and *rotor flux oriented control* (RFOC) that provides a natural decoupled control over the rotor flux linkage and torque (see Section 2.2.3).

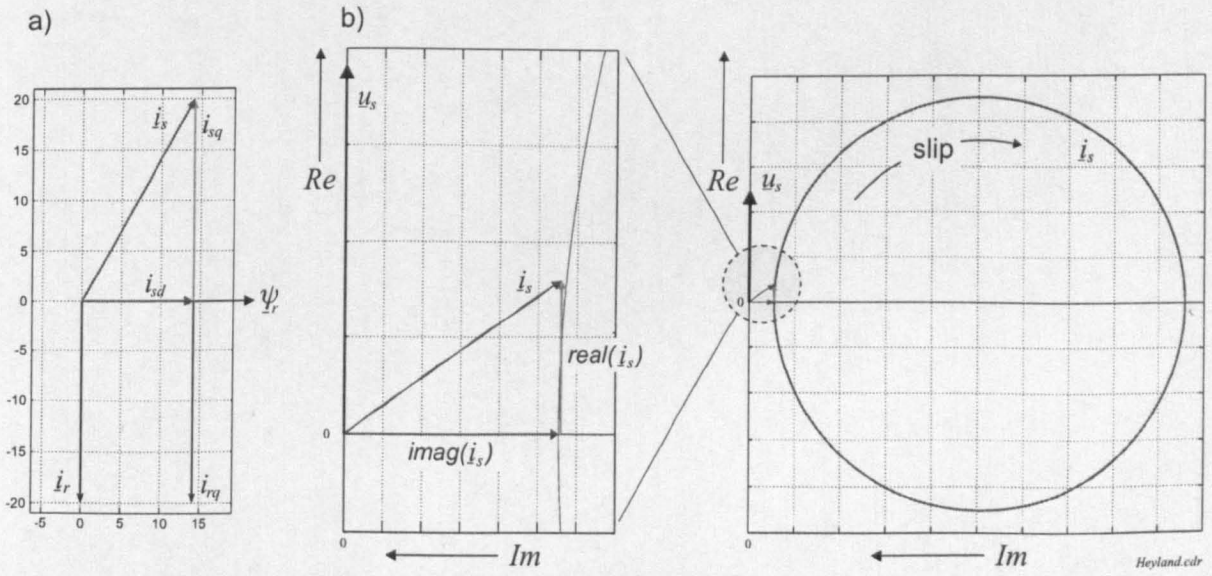

Figure 2.1: *Current phasors under Vector Control and locus of stator current*

By mapping the magnetic operating point with a current component i_{sd} in parallel to the rotor flux $\underline{\psi}_r$ and by adjusting the required electrical torque T_{el} by the orthogonal (quadrature) component i_{sq}, the rotor flux and the torque can be controlled:

$$T_r \frac{d\psi_r}{dt} + \psi_r = k_1 \cdot i_{sd} \tag{2.1}$$

$$T_{el} = k_2 \cdot \psi_r \cdot i_{sq} \tag{2.2}$$

Up to the base speed, the flux is kept constant which simplifies (2.1) and reduces the differential equation with the rotor time constant T_r to that of a proportional relation with the factor k_1 between rotor flux and i_{sd}. The torque is determined by the product of rotor flux and stator q-current component with coefficient k_2, and can be rewritten:

$$T_{el} = 3 \cdot pp \cdot \frac{L_o^2}{L_r} \cdot i_{mR} \cdot i_{sq} \tag{2.3}$$

where $k_2 = 3 \cdot pp \cdot L_o/L_r$, the ratio of mutual inductance L_o to rotor inductance L_r with the number of pole pairs pp. Under field orientation, the flux is aligned to the d-axis and with $\underline{\psi}_r = \psi_{rd} = L_o i_{mR}$, the q-component of the rotor flux is zero ($\psi_{rq} = 0$), where i_{mR} is the current component in direction of the rotor flux ψ_r. For the q rotor current $i_{rq} = -\frac{L_o}{L_r} i_{sq}$ where i_{sq} is proportional to load and speed, shown in Fig. 2.1-*a*. The stator voltages adjust under steady-state similar to the conditions for V/f control. For a small leakage coefficient σ and constant i_{sd}, the voltage $v_{sd} \approx R_s i_{sd}$ and $v_{sq} \approx R_s i_{sq} + \sigma L_s \frac{di_{sq}}{dt} + \omega_e L_s i_{sd}$. The q voltage component v_{sq} is adjusted proportional to the i_{sq} current and its derivative and is also linearly dependent on the rotor speed. The q component of the rotor current $\underline{i}_r$ has approximately the amplitude of i_{sq} and is in phase opposition. Only if i_{sd} is kept constant, $i_{rd} = -\frac{pL_o}{pL_r + R_r} \cdot i_{sd} = 0$. Otherwise oscillations in the rotor currents are the result. The vector diagram is shown in Fig. 2.1 on the left (subplot *a*). Adjusting $\underline{i}_s$ in amplitude, frequency and phase dynamically, allows to maintain the situation shown in the vector diagram. This is similar to the Heyland circle on the right of Fig. 2.1. It shows the current circle as a function of slip under steady-state conditions for an induction machine and assumes that the stator resistance $R_s = 0$. The vector diagram is shown for low slip, where flux and torque-producing current components are perpendicular and torque is proportional to the slip. With Vector Control these ideal conditions can also be maintained during dynamic operation.

Critical for Vector Control is the need for an encoder and the knowledge of the correct machine parameters. The latter is tackled by parameter identification schemes (e.g. [11, 16, 29, 30]) and self-commissioning [9, 10, 31] prior to starting the machine. The encoder is not required when using sensorless control schemes.

2.2 Modelling and Theory

To approximate the behaviour of the induction machine both under steady-state and transient conditions, a dynamic model of the machine is used. This model can be conveniently described using the *Space Phasor Theory.*

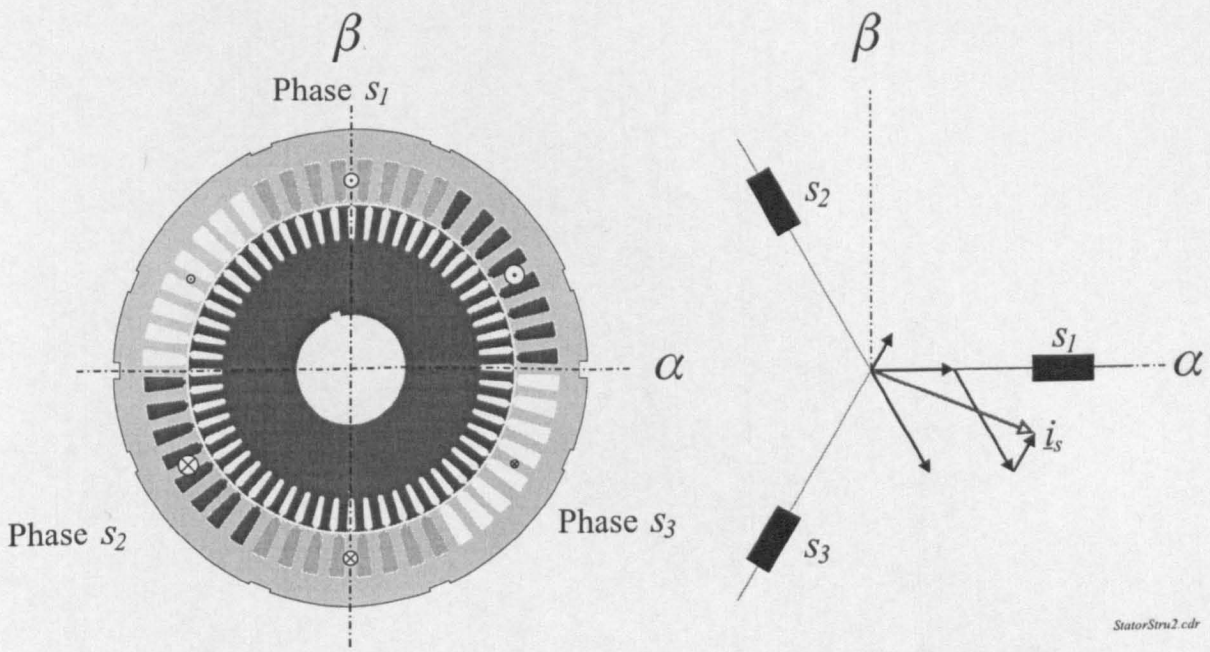

Figure 2.2: *Cross-section of two-pole squirrel cage induction machine*

2.2.1 Space Phasor Theory

The Space Phasor Theory had been developed in Hungary for multi-phase AC machines and was published at the end of the 1950s [32–34]. This theory made it possible to easily combine phase quantities into a single vector variable rotating in any reference frame in the complex two-dimensional plane. It will be used throughout this thesis wherever possible. The following limitations hold:

- the air gap is uniform
- the stator windings are sinusoidally distributed (no space harmonics)
- saturation in the magnetic circuits is neglected

A typical cross-section of a three-phase squirrel-cage induction machine is shown in Fig. 2.2. The stator has the three phase windings s_1, s_2 and s_3 where the current through winding s_1 is aligned to the α-axis. The rotor is a cage with the rotor bars short-circuited at the endrings. Each winding has a resistance and a self-inductance. Stator and rotor are magnetically coupled via the air-gap.
For the time-dependent space phasor of the three-phase stator currents:

$$\underline{i}_s = i_{s_1}(t)e^{j0^\circ} + i_{s_2}(t)e^{j120^\circ} + i_{s_3}(t)e^{j240^\circ} = |\underline{i}_s(t)|e^{j\phi(t)} \tag{2.4}$$

The instantaneous values of the stator currents are $i_{s_1}(t)$, $i_{s_2}(t)$ and $i_{s_3}(t)$. In general, the magnitude and phase of the current vectors vary with time and can be of any

shape. The exponential factor represents mathematically the displacement of the windings by 120° in space. For the instantaneous currents in a machine with an isolated neutral, the following restriction holds:

$$i_{s_1}(t) + i_{s_2}(t) + i_{s_3}(t) = 0 \tag{2.5}$$

Under steady-state, thus for a symmetrical three-phase system of sinusoidal currents, the expression of (2.4) for the current space phasor simplifies:

$$\underline{i}_s = \underline{I}_s e^{j\omega_e t} \tag{2.6}$$

Now, the space phasor is a complex current phasor $\underline{I}_s$ with fixed amplitude I_s and an arbitrary phase angle ϕ_e, that rotates with the fixed stator angular velocity ω_e.

The space phasors of other machine variables, such as stator voltage $\underline{v}_s$ or rotor flux $\underline{\psi}_r$ can be obtained similarly to that of the stator current shown above [32,34].

2.2.2 Transforms

In a balanced system, 3-phase signals can be converted to an equivalent orthogonal set of signals. This simplifies handling and is common practice [7]. For the transformation into a phase-equivalent circuit it can be important to determine if the machine is connected in delta ($\mathbf{\Delta}$) as most machines above $5kW$ are, or in star ($\mathbf{Y}$). In this thesis, the machines used are connected in $\mathbf{\Delta}$ (see also Section 4.6). The measured line-to-line *voltages* are then equal to the phase voltage of the equivalent circuit. No transformation is required. The measured line *currents* i_A, i_B and i_C however have to be explicitly converted to phase currents.

$$i_{s_1} = i_{AB} = (i_A - i_B)/3 \tag{2.7}$$

The result of the transformation is that the *rms* value of the phase current i_{AB} is lower than the *rms* value of the line current i_A and is lagging it by 30°:

$$rms(i_{AB}) = rms(i_A)/\sqrt{3} \qquad \text{where } rms(x) = \sqrt{\frac{1}{T}\int_0^T x^2 d\tau} \tag{2.8}$$

$$\angle i_{AB} = \angle i_A - 30° \qquad i_A \text{ is leading!} \tag{2.9}$$

The inverse conversion from phase to line currents is useful when comparing reference currents with real line currents. These reference currents will be transformed according to:

$$i_A = i_{AB} - i_{CA} \tag{2.10}$$

For the signal conversion into an orthogonal coordinate system, the so-called *RMS transformation* is used throughout this work (see Appendix A.1).

$$i_\alpha = i_{AB}/\sqrt{2} \tag{2.11}$$

$$i_\beta = \frac{\sqrt{3}}{2} \cdot \frac{2}{3}(i_{BC}/\sqrt{2} - i_{CA}/\sqrt{2}) = (i_{BC} - i_{CA})/\sqrt{6} \tag{2.12}$$

For the use in field-oriented control, the machine model is simplified by transforming the measured stator quantities into a rotating frame. Well known is the rotor frame [6]. This frame is aligned to the rotor flux at angle ρ and rotating with the angular frequency $\omega_e = \frac{d\rho}{dt}$. Multiplying a space phasor $\underline{i}_{s_{\alpha\beta}} = (i_{s\alpha} + j i_{s\beta})$ by $e^{-j\rho}$ will cause a rotation in the mathematical negative direction (clockwise rotation):

$$\underline{i}_{s_{dq}} = \underline{i}_{s_{\alpha\beta}} e^{-j\rho} \tag{2.13}$$

$$(i_{sd} + j i_{sq}) = (i_{s\alpha} + j i_{s\beta}) \cdot [\cos(\rho) - j \sin(\rho)] \tag{2.14}$$

2.2.3 Mathematical Model of the Induction Machine

The modelling of the electrical characteristic is done on the basis of additional assumptions:

- the structure of the machine is assumed to be symmetric
- saturation effects in the iron are neglected
- skin effect, stray losses and iron losses are not considered
- the machine parameters are assumed to be initially constant

For the general induction machine, described in an arbitrary reference frame rotating at arbitrary speed ω_a, the general stator and rotor voltage equations are [7, 34]:

$$\underline{v}_s = R_s \underline{i}_s + \frac{d\underline{\psi}_s}{dt} + j\omega_a \underline{\psi}_s \tag{2.15}$$

$$\underline{v}_r = R_r \underline{i}_r + \frac{d\underline{\psi}_r}{dt} + j(\omega_a - \omega_r)\underline{\psi}_r \tag{2.16}$$

The rotor quantities have been transformed to the stator side. Simplifying for the squirrel-cage type ($\underline{v}_r = 0$) and the electrical equations in stator coordinates (with $\omega_a = 0$):

$$\underline{v}_s = R_s \underline{i}_s + \frac{d\underline{\psi}_s}{dt} \tag{2.17}$$

$$0 = R_r \underline{i}_r + \frac{d\underline{\psi}_r}{dt} - j\omega_r \underline{\psi}_r \tag{2.18}$$

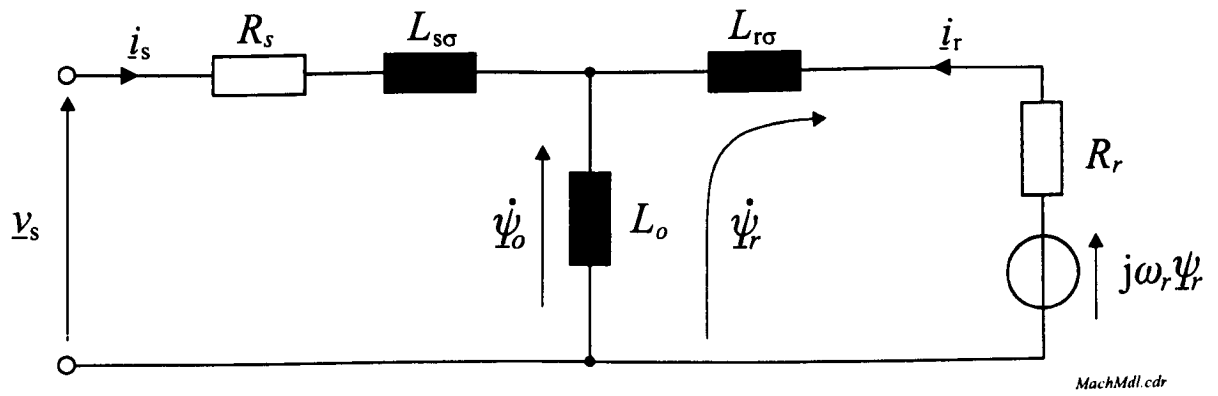

Figure 2.3: *Linear equivalent circuit of squirrel-cage induction machine*

Fig. 2.3 is a graphical representation of (2.17) and (2.18). The speed-proportional voltage that is induced in the rotor winding is shown on the right of Fig. 2.3 and is equivalent to the induced voltage or back-*emf* in a DC machine. The flux linkage equations below are valid in any coordinate frame, assuming linear conditions:

$$\underline{\psi}_s = L_s\underline{i}_s + L_o\underline{i}_r \tag{2.19}$$
$$\underline{\psi}_r = L_r\underline{i}_r + L_o\underline{i}_s \tag{2.20}$$
$$\underline{\psi}_o = L_o(\underline{i}_s + \underline{i}_r) \tag{2.21}$$

For the stator self-inductance L_s and rotor inductance L_r and the mutual inductance L_o with the leakage inductances $L_{s\sigma}$ and $L_{r\sigma}$ on stator and rotor side respectively as shown in Fig. 2.3:

$$L_s = L_{s\sigma} + L_o = (1+\sigma_s)L_o \tag{2.22}$$
$$L_r = L_{r\sigma} + L_o = (1+\sigma_r)L_o \tag{2.23}$$

and the machine leakage coefficient:

$$\sigma = 1 - \frac{L_o^2}{L_sL_r} \tag{2.24}$$
$$= 1 - \frac{1}{(1+\sigma_s)(1+\sigma_r)} \tag{2.25}$$

The mechanical output power of the machine is three times (for 3 phases) the product of the back-*emf* $j\omega_r\underline{\psi}_r$ and the conjugate complex (denoted by the superscript *) of the rotor current:

$$P_{3\sim} = 3 \cdot j\omega_r\underline{\psi}_r \cdot \underline{i}_r^\star \tag{2.26}$$

The torque produced by the machine is:

$$\begin{aligned} T_{el} &= \frac{P_{3\sim}}{\Omega_r} = 3 \cdot pp \cdot j(\underline{\psi}_r \cdot \underline{i}_r^*) \\ &= 3 \cdot pp \cdot j(L_o \underline{i}_s + L_r \underline{i}_r) \cdot \underline{i}_r^* \\ &= 3 \cdot pp \cdot L_o \cdot \Im\{\underline{i}_s \cdot \underline{i}_r^*\} = 3 \cdot pp \cdot \frac{L_o}{1+\sigma_r} \cdot i_{mR} \cdot i_{sq} \end{aligned} \tag{2.27}$$

$$T_{el} = -3 \cdot pp \cdot \frac{1}{L_\sigma} \cdot \psi_s \cdot \psi_{r_{(D)}} \cdot \sin(\theta_\psi) \tag{2.28}$$

where $\theta_\psi = \angle(\underline{\psi}_s, \underline{\psi}_r)$ is the angle between stator and rotor flux and $\Im\{\ldots\}$ is the imaginary component. Equation (2.27) is the basis for Vector Control. The description of (2.28) is popular for Direct-Torque Control (DTC) [35, 36] or DSC [37]. The substitutions $\psi_{r_{(D)}} = \psi_r \cdot L_s/L_o$ and $i_{mR} = \psi_r/L_o$ are used which will be derived in the following sections.

The relation between electrical and mechanical quantities is given by the mechanical differential equation:

$$J \frac{d\Omega_r}{dt} = T_{el} - T_L(\Theta_r, \Omega_r, t) \tag{2.29}$$

T_L is the load torque which is not further specified here and can include stiction, friction and nonlinearities depending on Θ_r and Ω_r, the mechanical rotor position and angular velocity respectively. The lumped inertia of the whole drive is given with J in [kg m^2] or [Nm s^2].

Electrical and mechanical angular quantities differ when the number of pole pairs pp is larger than 1. For the electrical and mechanical angular velocity of the rotor:

$$\omega_r = pp \cdot \Omega_r \tag{2.30}$$

Ω_r is the mechanical angular velocity of the rotor in [rad/s] and $\omega_r = d\theta_r/dt$ is the instantaneous electrical angular velocity of the rotor in [rad/s]. The relation for the mechanical and electrical angles is:

$$\theta_r = pp \cdot \Theta_r \tag{2.31}$$

where pp is the number of pole pairs, Θ_r is the mechanical rotor angle in [rad] with reference to an arbitrary starting position and measured in the stator frame of coordinates. The electrical rotor angle is θ_r that is also given in [rad].

The induction machines with double cage rotors used in the research (see Section 4.6.1) can be approximately described by applying the theory of a single cage rotor above.

This approximation is valid since under Vector Control the slip is controlled and does not exceed its rated value. For a more precise transient analysis, the additional leakage paths and resistance due to the outer cage (or starting cage) have to be considered that play a role for higher slip frequencies. These are described in Section 4.6.1. The full dynamic machine model and the design of Vector Control strategies for direct and indirect common rotor flux orientations are described in e.g. [22, 25, 38].

Model Orientations

The voltage equations (2.17) and (2.18) are the basis for the mathematical model and derived from the stator and rotor meshes of the machine. For this the rotor cage is substituted by a three wire AC circuit. The equations are represented by the circuits of Fig. 2.3 that are similar to the single-phase equivalent circuits of the induction machine in steady-state.

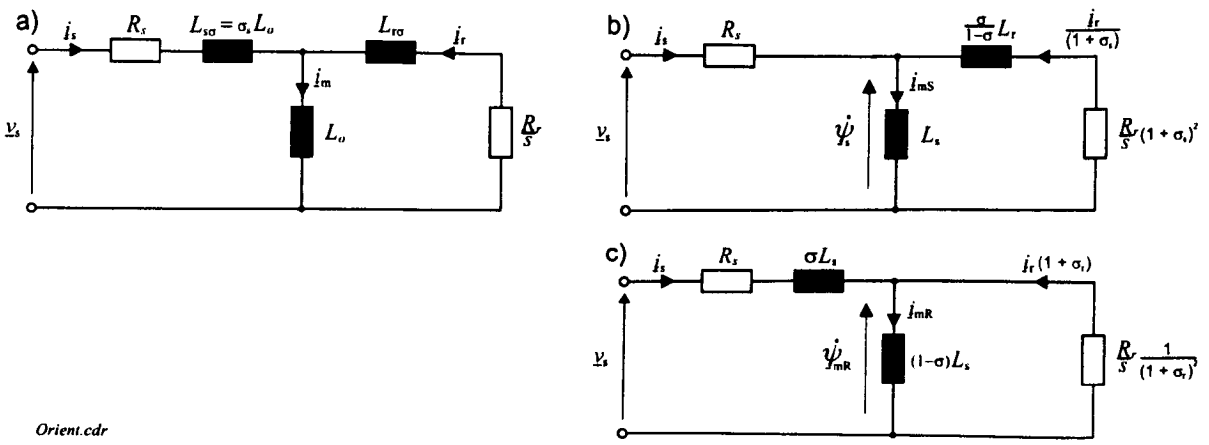

Figure 2.4: *Steady-state equivalent circuits used for Vector Control based on a) air-gap flux, b) stator flux, and c) rotor flux orientation*

Using a simple conversion, the equivalent circuit can be simplified. This is because of $\underline{i}_m = \underline{i}_s + \underline{i}_r$, the three inductances L_s, L_r and L_o do not represent independent energy storages [7]. Hence the equations can be rearranged with only two inductances. The modified steady-state equivalent circuits derived from Fig. 2.4-*a* are shown in Figs. 2.4-*b* and *c*.

The first model (Fig. 2.4-*b*) concentrates all leakage inductances in the rotor mesh. This is convenient when using a **stator flux** oriented control (SFOC), like DTC or the control of doubly-fed induction machines [7]. The stator flux linkage is chosen as orientation reference so the control behaves similar to V/f control (see Section A.2.2) where $\psi_{sd} \approx v_{sd}/\omega_e$, simplifying (2.40). This orientation is popular for simple sensor-

less schemes but does not achieve a full decoupling of stator flux linkage and rotor current. This coupling effect is similar to the armature reaction of a DC machine [7]. If the load is increased, the flux component i_{sd} also has to be increased to maintain the stator flux at a constant level [7].

- The stator voltage equation is written with the stator flux represented by the stator inductance L_s and the current derivative:

$$R_s\underline{i}_s + L_s\frac{d}{dt}\left[\underline{i}_s + \frac{\underline{i}_r}{1+\sigma_s}\right] = \underline{v}_s$$

- The rotor equation (2.18) is extended by the term $\underline{i}_r/(1+\sigma_s)$ to get the same current derivative through L_s as in the stator voltage equation above:

$$L_s\frac{d}{dt}\left[\underline{i}_s + \frac{\underline{i}_r}{1+\sigma_s}\right] + \frac{\underline{i}_r}{1+\sigma_s}\left[(1+\sigma_r)(1+\sigma_s)^2 L_o\frac{d}{dt} + R_r(1+\sigma_s)^2\right] = j\omega_r\underline{\psi}_r(1+\sigma_s)$$

The following substitutions can be introduced:

$$\begin{aligned}
\underline{i}_{r(D)} &= \frac{\underline{i}_r}{(1+\sigma_s)} \\
R_{r(D)} &= R_r(1+\sigma_s)^2 = R_r(\tfrac{L_s}{L_o})^2 \\
\underline{\psi}_{r(D)} &= \underline{\psi}_r(1+\sigma_s) = \underline{\psi}_r\tfrac{L_s}{L_o} \\
L_\sigma &= \tfrac{\sigma L_s}{1-\sigma}
\end{aligned}$$

The subscript $_{(D)}$ indicates the transformed quantity of the stator flux oriented model. The final equations are:

- stator equation:

$$R_s\underline{i}_s + L_s\frac{d}{dt}\left[\underline{i}_s + \underline{i}_{r(D)}\right] = \underline{v}_s \tag{2.32}$$

- rotor equation:

$$L_s\frac{d}{dt}\left[\underline{i}_s + \underline{i}_{r(D)}\right] + \left[R_{r(D)} + L_\sigma\frac{d}{dt}\right]\underline{i}_{r(D)} = j\omega_r\underline{\psi}_{r(D)} \tag{2.33}$$

The steady-state stator oriented model is shown in Fig. 2.4-*b* where all the leakage is referred to the rotor side.

The second model is **rotor flux** oriented and shown in Fig. 2.4-*c*. This equivalent circuit is suitable when working with Vector Control. Only the rotor flux orientation allows true and full decoupling of rotor flux and machine torque.

- The stator equation (2.17) is rearranged by concentrating all the leakage on the stator side:

$$\left[R_s + \sigma L_s \frac{d}{dt}\right]\underline{i}_s + (1-\sigma)L_s \frac{d}{dt}\left[\underline{i}_s + (1+\sigma_r)\underline{i}_r\right] = \underline{v}_s$$

- For the rotor equation, only the rotor resistance remains in the rotor branch:

$$(1-\sigma)L_s \frac{d}{dt}\left[\underline{i}_s + (1+\sigma_r)\underline{i}_r\right] + \frac{R_r}{(1+\sigma_r)^2}(1+\sigma_r)\underline{i}_r = j\omega_r \frac{\underline{\psi}_r}{1+\sigma_r}$$

The following substitutions simplify the equations:

$$\begin{aligned} \underline{i}_{r(V)} &= (1+\sigma_r)\underline{i}_r \\ R_{r(V)} &= \tfrac{R_r}{(1+\sigma_r)^2} \\ \underline{\psi}_{r(V)} &= \tfrac{\underline{\psi}_r}{1+\sigma_r} = \underline{\psi}_{mR} \end{aligned}$$

Therefore with the subscript $_{(V)}$ for the substituted quantities:

- stator:

$$\left[R_s + \sigma L_s \frac{d}{dt}\right]\underline{i}_s + (1-\sigma)L_s \frac{d}{dt}\left[\underline{i}_s + \underline{i}_{r(V)}\right] = \underline{v}_s \tag{2.34}$$

- rotor:

$$(1-\sigma)L_s \frac{d}{dt}\Big[\underbrace{\underline{i}_s + \underline{i}_{r(V)}}_{\underline{i}_{mR}}\Big] + R_{r(V)}\underline{i}_{r(V)} = j\omega_r \underline{\psi}_{r(V)} \tag{2.35}$$

The new synthetic magnetizing current $\underline{i}_{mR} = \underline{\psi}_r / L_o$ is aligned and proportional to the rotor flux $\underline{\psi}_{mR} = \underline{\psi}_r/(1+\sigma_r)$ [7]. This current can also be directly derived from the flux equations (2.19) and (2.20). The equivalent rotor orientated circuit is shown in Fig. 2.4-*c* that clearly visualizes that the stator current is split into two components that are perpendicular. The rotor branch is purely resistive whereas the magnetizing branch is only inductive.

For the stator side, the inductance σL_s is the so-called stator transient inductance. This parameter plays a role for the high-frequency model of the induction machine when using *hf* signal injection.

2.2.4 Flux Model

The instantaneous values of the angular position and magnitude of the flux are essential for the correct field orientation and dynamic control of the induction machine. Two categories exist to determine the flux:

The direct method uses Hall-effect sensors or search-coils built into the machine to directly measure the flux. In practice, this has not been accepted much due to the requirements of mounting sensors into the machine and partially due to inferior results compared to other methods.
Of significant importance are the indirect methods. Here, the flux is estimated via suitable numerical machine models that are based on measurable terminal electrical and shaft mechanical quantities. There are basically two groups of flux models: the current- or i,n-model is based on measuring the stator currents and the rotor position or speed via encoders or resolvers. The voltage- or u,i-model measures voltages and currents to derive the flux.

Current Model

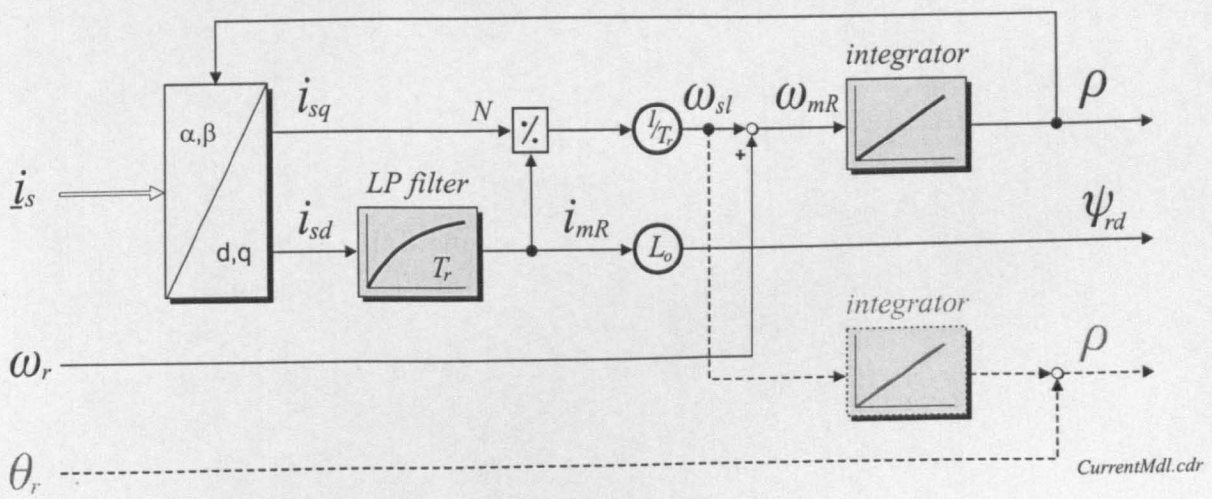

Figure 2.5: *Current Model (N: numerator)*

The current model that is shown in Fig. 2.5 can be derived from the rotor mesh in the synchronous reference frame ($\omega_a = \omega_e$) or from (2.35) multiplied by $e^{-j\rho}$:

$$i_{sd} = i_{mR} + T_r \frac{di_{mR}}{dt} \tag{2.36}$$

$$i_{sq} = \omega_{sl} T_r \cdot i_{mR} \tag{2.37}$$

where $i_{mR} = \underline{i}_{mR}$ is the magnetizing current as shown in Section 2.2.3 and derived from the rotor flux oriented equivalent circuit in Fig. 2.4. This current component is directly proportional to the rotor flux:

$$\psi_{mR} = \frac{L_o}{1+\sigma_r} i_{mR} \qquad = (1-\sigma) L_s i_{mR}$$

In steady-state, the magnetizing current i_{mR} is equal to the d-component stator current. Dynamically however, they are linked via the rotor time constant T_r that usually is in the range of a few hundred milliseconds. During machine startup, the flux is built-up once and then kept constant for machine operation.
From equation (2.37), the rotor flux angle can be derived via integration of the flux angular velocity which is derived from adding the rotor angular velocity and the slip frequency:

$$\rho = \rho_0 + \int_{t_0}^{t} \left(\omega_r + \frac{i_{sq}}{T_r i_{mR}} \right) dt = \underbrace{pp \cdot \Theta_r}_{\theta_r} + \int_{t_0}^{t} \frac{i_{sq}}{T_r i_{mR}} dt + \theta_{sl_0} \tag{2.38}$$

Normally, the measured rotor position can be used directly and only the slip frequency is integrated as on the right of (2.38) where θ_{sl_0} is the initial slip angle. The following structure for the calculation of the rotor flux angle can be preferable if the saturation characteristic of the rotor inductance L_r is included:

$$\begin{aligned}
\psi_r' &= \int U_{Hd}\, dt = (1+\sigma_r)^2 \cdot \psi_{mR} \quad \text{and} \quad U_{Hd} = R_r(i_{sd} - i_{mR}) \\
i_{mR} &= \psi_r'/L_r \quad \text{where} \quad L_r = f(\psi_r') \\
\omega_{mR} &= \underbrace{pp \cdot \Omega_r}_{\omega_r} + \frac{R_r i_{sq}}{\psi_r'} = \omega_e \\
\rho_{k+1} &= \rho_k + T_a \cdot \omega_{mR} \quad \text{with the sampling period } T_a
\end{aligned} \tag{2.39}$$

Characteristics for the current model are:

- The model allows for operation over the whole operating range.
- A problem with this model is that it is sensitive to changes in the rotor time constant T_r which can vary considerably during operation (temperature, saturation). Accurate orientation depends on the precise knowledge of this parameter and the calculation of slip that is normally small compared to the angular rotor speed. A parameter mismatch between model and machine affects the flux linkage identification/reconstruction and determination of the flux angle and thus the control performance. The wrong T_r can cause a derating of the drive since the rated torque cannot be produced.
- Therefore, T_r should be adapted in real time (on-line parameter adaption). Often, a non-linear table is implemented with $L_r = f(\psi_r')$ [39] according to the alternative model implementation above.
- The model requires the measurement of the rotor angle or rotor speed. Operation without a position/speed encoder is not directly possible.

Voltage Model

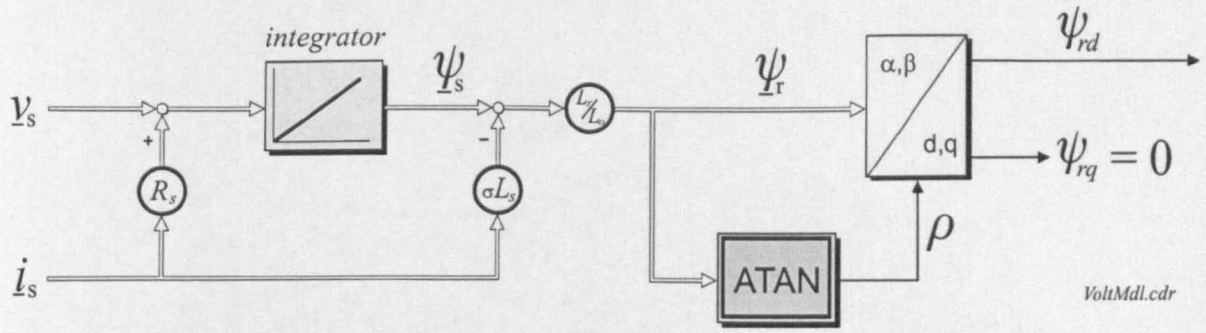

Figure 2.6: *Voltage Model*

The voltage model shown in Fig. 2.6 is based on the integration of the stator voltage equations in the stationary reference frame:

$$\underline{\psi}_s = \underline{\psi}_{s0} + \int_{t_0}^{t} (\underline{v}_s - R_s \underline{i}_s) dt \tag{2.40}$$

The rotor flux linkage $\underline{\psi}_r$ can then be derived from the stator flux linkage $\underline{\psi}_s$:

$$\underline{\psi}_r = (\underline{\psi}_s - \sigma L_s \underline{i}_s) \frac{L_r}{L_o} = \underline{\psi}_{mR} \frac{L_r}{L_o} \tag{2.41}$$

Finally, the rotor flux angle can be extracted by applying the arctan function on the ratio of the flux components:

$$\rho = \arctan(\psi_{r\beta} / \psi_{r\alpha}) \tag{2.42}$$

Characteristics of the voltage model are:

- The model only requires the feedback of stator terminal quantities (stator voltages, stator currents) that can easily be obtained via measurements.
- An advantage over the current model is that it does not require speed or position information for the determination of the field angle.
- The field angle ρ is only dependent on two parameters: the stator resistance R_s and the leakage inductance σL_s.
- The leakage inductance is a relatively constant value over the speed range.

- The resistive part is relatively small for high speeds and can then easily be neglected. The model is therefore very robust for high speeds. A problem however can be the correct and undelayed measurement of the stator voltages. Usually, the reference voltages can be used instead (see Section 4.5.2).
- For low speeds (low ω_e), the open integration and the temperature dependency of the stator resistance cause considerable problems:
  - The voltage drop across the resistor becomes an important part of the stator voltage.
  - The induced voltage decreases proportionally with a decrease in the stator frequency. This can result in problems of getting sufficient signal resolution.
- A small DC input to the integrator can cause a failure of the model, especially when approaching zero speed. As the estimated flux linkage drifts from the real flux linkage of the machine, an increasing difference and estimation error certainly causes instability. A common way to avoid the problem, is to use a bandpass filter (BP) or lowpass filter (LP) with a low centre or cutoff frequency in place of the pure integrator [40,41]. The low-pass filter acts as an integrator for higher frequencies, the high-pass filter blocks and removes the DC offset. Other methods make use of drift correction, max-min evaluation or use a moving averager [42,43]. Mathematically it can be shown that for zero stator frequency, the magnetic coupling of the stator and rotor circuit vanishes, the voltage model is 'blind' [15]. Practically, no induction exists.

In the work for this thesis, the current model is used because an encoder is available for the experimental drive. For sensorless control, the estimated rotor position replaces the encoder signal.

2.2.5 Inverter Model

Placed between the controller and the machine is the inverter. For the design of the current controllers, a suitable model of the inverter is required. For Vector Control, the operation of the inverter (see Section 2.2.6) can be linearized and simplified. For the control design, the inverter is then approximated by an equivalent first order lag. More accurately, it can be modelled by the transfer function e^{-jT_d} where T_d is the delay time. Although the new reference values for the inverter switching times are written into their respective timer registers as soon as they have been calculated by the current controllers, they are not updated immediately but with the start of the new PWM period. In symmetrical PWM that is used here, this update will be at the timer underflow only, resulting in a delay $T_d = 2T_p$ or it can be additionally at the timer overflow [14], giving a delay $T_d = T_p$ where $2T_p$ is the PWM period.

Two rigs are used for the research, the older rig based on a network of transputers, called *TRANSPUTER rig* (see Section 4.1) and a new platform described in Section 4.2 using a digital signal processor (DSP) and therefore named *DSP rig*. For the *DSP rig*, the PWM period is $2T_p = 200\mu s$ which is equal to the A/D sampling time and the period for the current loop. The old *TRANSPUTER rig* has a PWM period of $2T_p = 168\mu s$ where the main control loop is at $504\mu s$. Currents were sampled and processed every $T_p = 84\mu s$.

The presence of deadtime is responsible for a PWM voltage error in the voltage-source inverter. This error voltage is proportional to the deadtime and the switching frequency of the inverter and can be regarded in the control design as a disturbance in the current loop of the control system [44] and will be examined in more detail in Section 6.1.
The inverter can be modelled more accurately by considering the voltage drop across the switching devices or the freewheeling diodes [45]. The voltage drop is responsible for a difference between reference and applied voltage across the machine terminals and can be included in the inverter model as a disturbance. This disturbance depends on threshold voltages and the on-state resistances of active switch and diode and the current through the devices. This model requires the line currents as feedback parameters.

2.2.6 PWM Strategies

For the control design, it is sufficient to describe the characteristic of the inverter by a linearized and simplified model as described in the previous section. This section provides a more detailed description of the discrete operation of a voltage source inverter. An understanding of the discrete and nonlinear inverter characteristic is essential to evaluate its modulation effects on the *hf* signal injection as discussed in Section 6.1. The discrete PWM switching characteristic can be applied to generate PWM test pulses that can be used for the estimation of the flux or rotor angle in machines.

Vector Control adjusts the inverter reference voltages to control the machine currents. Pure sinusoidal currents are required for the induction machine in steady-state. Higher current harmonics result in torque ripple and additional losses. Practically the sinusoidal currents can only be approximated. For the inverter of the experimental rig this approximation can be regarded as accurate enough due to the high inverter switching frequency. The basic idea behind variable-speed drives is that the voltage amplitude and frequency can be adjusted rapidly and independently to control the currents. The classical method is to use a 3-phase rectifier and an inverter that are

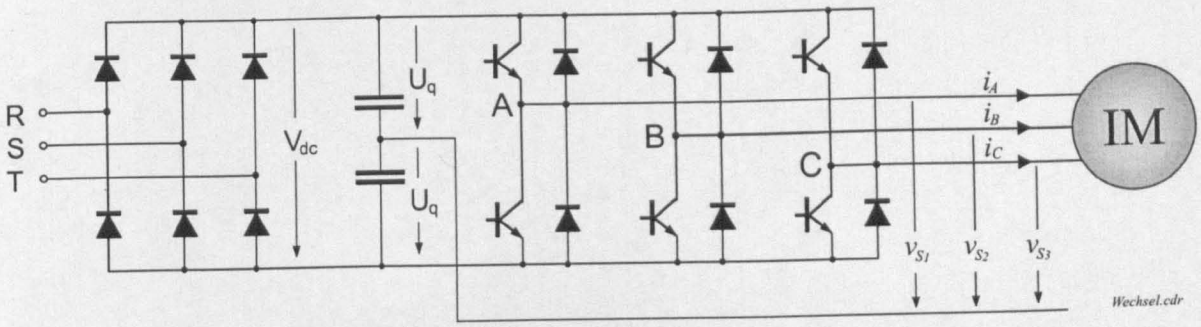

Figure 2.7: *Rectifier, Inverter and Induction Machine*

coupled via the DC-link and a capacitor bank as shown in Fig. 2.7. With fast switching of the devices in the inverter stage and techniques like pulse width modulation (PWM) it is possible to create 3-phase voltages with variable fundamental amplitude and frequency. In PWM, the width of the discrete voltage pulses follows the magnitude of the reference signal. For a long time, PWM strategies have been investigated to reduce torque ripples, optimize the switching sequence and increase the amplitude of the output fundamental voltage [46].
The first stage is the rectification. The DC link decouples the second stage – the inverter – from the mains so that the output frequency can be independent of the mains frequency. If using a diode rectifier, energy cannot be fed back into the mains and has to be dissipated by e.g. using a chopper in the DC link. If the DC link voltage is not constant, it can be measured and included in the PWM switching time calculation to improve the output voltage.

The ideal stator voltage vector $\underline{v}_s$ describes a circle in the complex plane, as shown in Fig. 2.8 and is formed by the voltages in the three phases:

$$\underline{v}_s(t) = v_{s_1}(t)e^{j0^\circ} + v_{s_2}(t)e^{j120^\circ} + v_{s_3}(t)e^{j240^\circ} \overset{\text{steady state}}{=} \frac{3}{2}\sqrt{2}\underline{V}_s\, e^{j\gamma} \tag{2.43}$$

This shape of a circle can only be approximated by inverters with switching devices. Two quantizising effects occur:

- Quantization of amplitude
- Quantization in direction

The inverter is usually simplified by a switching model, where semiconducters are substituted by ideal switches. In an inverter leg the switches are operated complementary. The states of the possible voltages are represented by the number triple $[S_A,S_B,S_C]$ that indicates the selected control signal. By permutation, this results in $2^3 = 8$ possible states for $\underline{v}_s$.

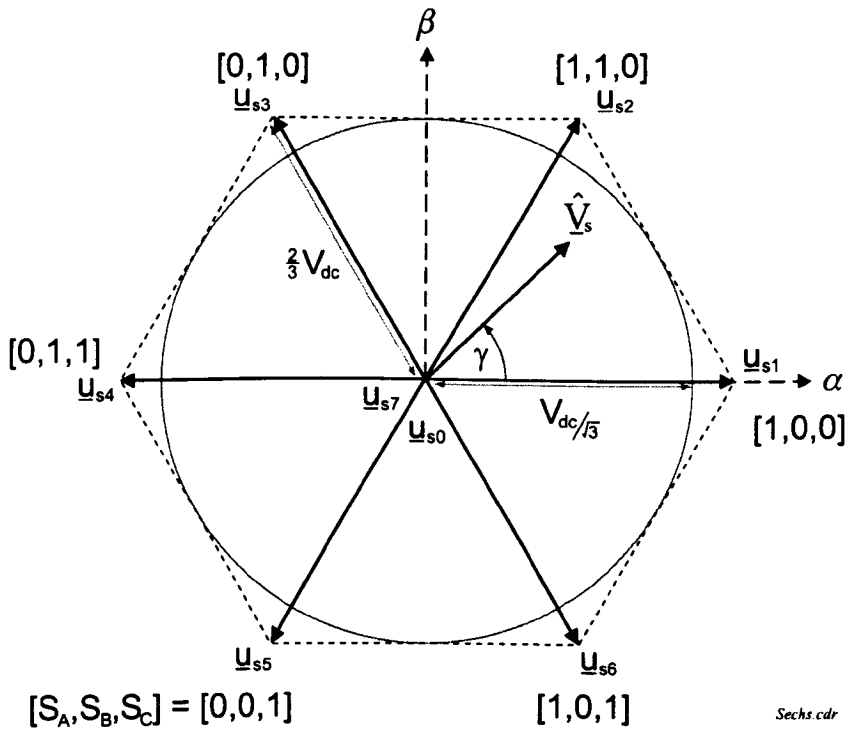

Figure 2.8: *Inverter-Hexagon*

Six of these discrete voltage vectors (1 – 6) form the edges of an equilateral triangle of border length $2V_{dc}/3$. The voltage vectors 0 and 7 are zero vectors ($[1,1,1]$ and $[0,0,0]$). They can be achieved by connecting the load terminals (A,B,C) either to the positive or negative pole of the DC link voltage.

$$\begin{aligned} \underline{u}_{s_k} &= \tfrac{2}{3}V_{dc}e^{j(k-1)60°} \qquad k = 1\ldots6 \\ \underline{u}_{s0} &= \underline{u}_{s7} = 0 \end{aligned} \tag{2.44}$$

Space Vector Modulation

The difference between the discrete voltage vector $\underline{u}_{s_k}$ and the voltage vector $\underline{v}_s$ causes current harmonics. It is $\underline{v}_s$ which determines the behaviour of the machine. A criterion for the quality of a PWM strategy is the deviation of the machine currents from their fundamental. The aim is to switch the phase voltages in such a manner that the desired current shape is achieved with a minimum of distortion and that a mean voltage vector corresponding to $\underline{v}_s$ is created. The current ripples due to PWM switching is shown in Fig. 4.4. An optimal PWM can be expected when [47]:

- the maximum difference of the current vector from the ideal is as small as possible for different switching states and
- the switching or pulse frequency f_p of the inverter is as low as possible. Note that an optimal compromise for the frequencies has to be found as the harmonics are shifted to higher frequencies by increasing f_p whereas however the losses of the semiconducters also increase.

Space Vector Modulation (SVM) is such an optimal PWM strategy [47]. The switching time calculation for SVM can be either performed in polar coordinates or in 3-phase coordinates. Both methods lead to the same voltage demand and allow an effective increase of the applied voltage of 15% compared to sinusoidal PWM. The absolute value of $\underline{\hat{V}}_s$ can reach a maximum of $\frac{2}{3}V_{dc} \cdot \cos(30°) = V_{dc}/\sqrt{3}$, shown in Fig. 2.8. This is equivalent that the tip of $\underline{\hat{V}}_s$ cannot leave the circle imprinted in the hexagon.

Switching Times in Polar Coordinates

The calculation of switching times depends on the coordinate system in which $\underline{v}_s(t)$ is described. For the voltage vector in polar coordinates (described by amplitude and angle), the calculation for the first sector is:

$$\int_0^{T_p} \underline{v}_s(t)dt = \sum_{k=1}^{2} T_k \underline{u}_{s_k} \tag{2.45}$$

where $1/T_p = f_p$ is the pulse or switching frequency of the inverter. The basis of the shown relation is the demand for equality of voltage-time areas (VTA). In case of a Δ connected machine, the following equations hold:

$$\vartheta = \phi - 30° \tag{2.46}$$

$$\gamma = \mathrm{rem}(\vartheta, 60°) \tag{2.47}$$

$$m_x = m \cdot \frac{\sqrt{3}\sqrt{2}V_s}{V_{dc}} = \sqrt{2} \cdot \sqrt{v_\alpha^2 + v_\beta^2}\Big/V_{dc} \tag{2.48}$$

$$T_1 = m_x \cdot T_p \sin(60° - \gamma) \tag{2.49}$$

$$T_2 = m_x \cdot T_p \sin(\gamma) \tag{2.50}$$

$$T_0 = (T_p - T_2 - T_1)/2 \tag{2.51}$$

where $2T_p$ is the PWM period and for $\phi = \arctan(v_\beta/v_\alpha)$ the angle of the voltage vector. The 30° phase shift in (2.46) is a result of the conversion from line-to-line to phase voltages. The zero state calculated in (2.51) is symmetrically split into $\underline{u}_{s_0}$ and $\underline{u}_{s_7}$ as shown in Appendix A.3. The peak of the $\alpha\beta$ voltages are scaled to represent the **rms** phase voltage. This is 415V for the Δ connected machine. For every sector,

the PWM timings T_{s1}, T_{s2} T_{s3} have to be calculated separately from the switching times T_1, T_2 and T_0 as shown in Table 2.1. There can be a difference for the *low-to-high* and the *high-to-low* switching time calculation, if the PWM counter only makes use of a count-up **or** a count-down mode. Appendix A.3.1 and [48] give more details about the practical implementation of Space Vector Modulation.

sector	T_{s1}	T_{s2}	T_{s3}
0	$T_0 + T_1 + T_2$	$T_0 + T_2$	T_0
1	$T_0 + T_1$	$T_0 + T_1 + T_2$	T_0
2	T_0	$T_0 + T_1 + T_2$	$T_0 + T_2$
3	T_0	$T_0 + T_1$	$T_0 + T_1 + T_2$
4	$T_0 + T_2$	T_0	$T_0 + T_1 + T_2$
5	$T_0 + T_1 + T_2$	T_0	$T_0 + T_1$

Table 2.1: *Low-to-high PWM switching times*

Switching Times in Three-Phase Coordinates

If phase voltages are already available, the switching times can be derived directly by calculating a mean value. The calculation then is much easier than the polar approach in the previous section. The results are mathematically exactly the same [48].

According to Fig. 2.7, the phase voltages can only have the two discrete values U_q and $-U_q$ (quantization in amplitude). U_q is equivalent to high-level, when the upper switch is closed (device conducting) and the lower switch is open. The low-level state $-U_q$ results from the inverse switching state. The mean value of a phase voltage $\overline{U}_n$ in a switching interval T_p is determined by the ratio of high-level to low-level at a load terminal connection n that can be $s1$, $s2$ or $s3$. From this results with the PWM switching time T_n for the mean phase voltage:

$$\begin{aligned}
\overline{U}_n &= \frac{1}{T_p}\left(-U_q T_n + U_q(T_p - T_n)\right), \qquad V_{dc} = 2U_q \\
&= -\frac{U_q T_n}{T_p} - \frac{U_q T_n}{T_p} + U_q \\
&= V_{dc}\left(\frac{1}{2} - \frac{T_n}{T_p}\right) \qquad \text{for} \quad n = s1, s2, s3
\end{aligned}$$

By rearranging, the switching time per phase follows as

$$T_n = \left(\frac{1}{2} - \frac{\overline{U}_n}{V_{dc}}\right) T_p \qquad \text{for} \quad n = s1, s2, s3 \tag{2.52}$$

for the PWM timings T_{s1}, T_{s2} and T_{s3} where $0 \leq T_n \leq T_p$ and with the phase voltages according to $\overline{U}_{s1} = v_A$.

Introducing a third harmonic voltage component, added to the desired mean voltage $\overline{U}_n$, can result in the same Space Vector Modulation as shown in the polar approach. For the modulation with three switches, the third harmonic provides a centering of the vector threepod between the rectifier limits (Appendix A.3.2). The condition that the distance on the real axis between vector tips and DC link limit for upper and lower bounds have to be equal, leads to the calculation of the third harmonic:

$$|U_q - (U_{max} + U_{harm3})| \stackrel{!}{=} |-U_q - (U_{min} + U_{harm3})| \tag{2.53}$$

rearranging of (2.53) for U_{harm3} gives with $U_{max} = \max(v_A, v_B, v_C)$ and $U_{min} = \min(v_A, v_B, v_C)$

$$U_{harm3} = -\frac{U_{max} + U_{min}}{2} \tag{2.54}$$

The switching times, based on 2.52, including the third harmonic are:

$$T_n = \left(\frac{1}{2} - \frac{\overline{U}_n + U_{harm3}}{V_{dc}}\right) T_p \tag{2.55}$$

The phase voltages can now be increased without the switch-on time exceeding the length of the switching interval T_p. The presented method, based on voltages in the three-phase coordinate system has the advantage that the sector in the hexagon does not have to be known as in Table 2.1. The processing requirements are lower since neither the magnitude (typically using the square root *sqrt*) nor the angle (*arcus tangens*) are needed. For the modulation with three switches, a triangular shape results with a frequency that is three times that of the fundamental. The third harmonic has no influence on the line-to-line voltages, as it cancels when subtracting two phase voltages.

2.3 Sensorless Control

The operation without a position sensor or encoder removes a number of disadvantages from the drive. Cost reduction is a very important aim of drives manufacturers. In particular for small machines, the encoder significantly increases the cost. The expense of installation is increased and cables need space to be mounted securely. Cabling and connectors introduce unwanted complexity to the drive that requires longer installation and more maintenance. The latter is due to the mean time between failures that is reduced as connectors are often the cause for failures. Noise can

couple in via the cables or dirt can cause contact problems and reduces the reliability and robustness of the drive. Even for sensored drives, the robustness can be increased by adding redundancy with a sensorless algorithm running in the background. In case the encoder or a cable breaks the drive can still be operated. Another disadvantage of the encoder is that the volume of the drive is increased. Only special models are designed not to block one end of the rotor shaft. The encoder size is in opposition to the trend for miniaturization. Encoders however allow high dynamic control and provide an accurate feedback to the speed controller. This quality is the benchmark for sensorless drives.

Soon after the field oriented control of induction machines became possible, research for sensorless techniques started. First, speed sensorless techniques were developed and have been in the centre of research interest [49]. At low speed however, the estimate for flux, torque and speed is generally poor and eventually breaks down. This is called the '*low speed problem*' that afflicts all model-based estimation. Until now, it has not been possible to realize sensorless control at zero speed under all loads. This has changed with new non-model based approaches [17, 18] that allow a dynamic and sensorless position control also for changing loads [50, 51].

2.3.1 Sensorless Speed Control

Most speed sensorless control techniques use a numerical model of the machine to estimate at least the speed and flux. Sometimes machine parameters or additional machine states are also estimated. Sensorless speed control can also be realized using frequency-dependent nonlinearities of the machine. These allow the estimation of rotor speed, flux angular velocity or machine parameters directly without the need for a machine model. These techniques are termed non-model based estimators.

Model-Based Rotor Speed Estimators

There are many different machine models known with different complexity that try to approximate the real machine. The quality achieved depends on the accurate knowledge of the machine parameters for every operating condition. The parameters can vary with temperature, saturation level, operation frequency or load.

Sensorless control methods have been evaluated as low, medium or high performance according to the dynamic of their torque response [15]. The performance in the low speed region and the accuracy of the speed estimation are other important criteria. It is the rotor time constant T_r that reduces the speed error when properly tuned and therefore should be estimated online. The stator resistance R_s has to be known accurately for operation at low speed [52].

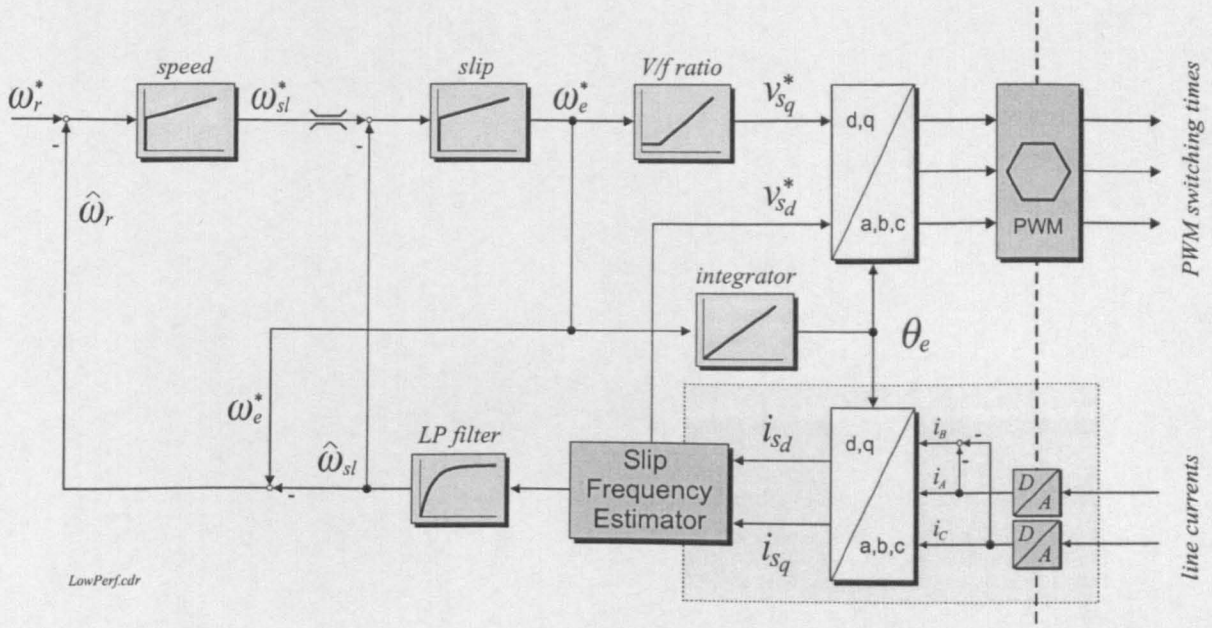

Figure 2.9: *Stator-flux oriented speed-sensorless drive using slip estimator based on stator currents only*

A simple and **low performance** speed sensorless implementation is *open loop speed control.* The synchronous frequency is regulated while the estimated slip frequency is only used to compensate for load changes. This is similar to closed loop V/f control (Appendix A.2.2) or to the structure shown in Fig. 2.9 without the outer speed loop. The slip frequency estimator is based on a steady state model of the induction machine or can be calculated from the rotor back-*emf* that requires the knowledge of stator currents and voltages. The state equations can additionally be used to separate slip and speed estimation [49].

In *sensorless closed loop speed control* [53], the rotor frequency is estimated by subtracting the estimated slip frequency from the known and imposed excitation frequency as shown in Fig. 2.9. The estimated rotor speed is then used as a feedback signal for closed loop speed regulation. The speed controller provides the reference for the slip controller that outputs the demanded excitation frequency for the V/f frontend. A filter for the slip estimate is usually required that will reduce the achievable dynamic of the torque response. Low speed operation is specifically sensitive to R_s because of the V/f voltage boost. There is no decoupling in estimating the flux angle and the rotor speed. For the slip frequency estimator including the grey area in Fig. 2.9, a model based on stator currents and voltages can also be used.

An alternative approach, and one termed "**Medium Performance**" is that in Fig. 2.10 and uses the field-oriented stator equations to impose the reference voltages $v_{sd_{comp}}$

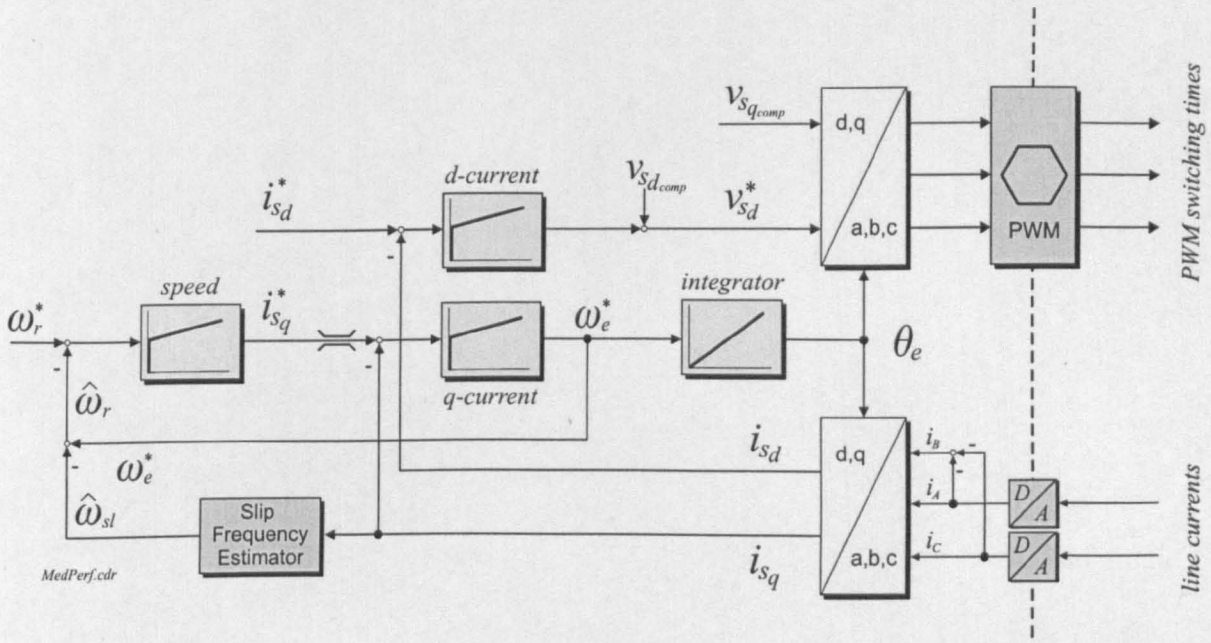

Figure 2.10: *Stator-flux oriented speed-sensorless drive with slip estimator using voltage feedforward based on stator equations*

and $v_{sq_{comp}}$ onto the machine. This forces field orientation where the stator flux orientation is generally preferred. The machine model is then independent of variations in the stator leakage inductance and is only based on stator quantities. Again, the stator resistance R_s has to be known precisely for operation at lower speeds. The field-oriented rotor equations can be used to estimate the slip frequency. The rotor frequency is then derived from the known and imposed synchronous frequency. The speed controller uses the estimated speed to produce the i_{sq} demand. A q-current controller then produces the excitation frequency demand [53]. The demand voltages are derived in two ways. The v_{sd} demand voltage is the output of the d-current controller. The v_{sq} demand however has to be imposed using the q stator voltage equation because i_{sq} is already used to generate the excitation frequency. The structure is likely to suffer from fast transients due to unavoidable parameter uncertainties in the imposed q-voltage equation [52].

High performance speed-sensorless drives are based on a structure where the flux-angle estimate needed to obtain field orientation is independent of the speed estimate. A common solution is to use the voltage model that does not require the rotor speed, to estimate the flux. Operation above 1 or 2Hz ensures good field orientation. The speed estimator can be based on a model reference adaptive structure (MRAS) [54,55]. The estimated rotor flux from the current model that is speed dependent is compared in an MRAS to the estimate of the voltage model. The latter model serves as the

reference and adjusts the speed estimate by driving the cross-product between the two flux estimates to zero [52]. The speed estimator can also drive the error between the estimated and measured i_{sq} to zero by adjusting the estimated speed [56]. The adaptive rotor flux observer in [57] adjusts the rotor speed via a PI controller to drive an estimate of the torque error to zero. This error is based on the difference between observed and measured stator currents. The rotor flux is an additional output of the observer. In [11] a *hf* injection is proposed to decouple and simultaneously estimate speed and rotor resistance.

Typical observers that are model-based are the Luenberger Observer, Kalman Filter or the Extended Kalman Filter (EKF). The latter two incorporate the disturbance and measurement noise, thus combining a stochastic model with the numeric model. The EKF is based on the nonlinear model of the induction machine that is linearized for particular operating points. These structures may require the inversion of the system matrix, that can be based on a 5^{th} order machine model. This demands powerful and expensive processors.

Estimators using artificial intelligence such as neural networks can be used in parallel to other models e.g. for the online-adaptation of the stator resistance R_s that changes with temperature [30].

The problem of all speed sensorless techniques is the reliable operation for a synchronous frequency below about 2Hz. It can be shown mathematically [15] that the mechanical speed of the rotor is not observable at $\omega_e = 0$. Stator and rotor equations are magnetically decoupled. From $\omega_e = \omega_r + \omega_{sl} \stackrel{!}{=} 0$, the line of instability along $\omega_r = -\omega_{sl}$, that is in the generating region, can be derived. In practice, this line will expand to a wider region. Reasons are that the induced stator voltages are low for a low stator frequency while unavoidable model and measurement errors remain about constant [15]. States of the induction machine and estimated values will then drift away from the real values to larger differences which cannot accurately be determined. The changes in the machine parameters and the resulting accuracy of the estimation depends on the operating point.

Often, sensorless drives remain stable during a quick reverse through the zero speed region [15]. For longer operation in the *low speed region* however, sensorless techniques need to apply some type of open-loop V/f, constant current [58] or slip management [59,60]. The performance of the drive is generally very low with limited speed holding capability and significantly reduced torque dynamics.

Performance criteria for speed sensorless algorithms are [61]:

- dynamic behaviour: the quality of disturbance rejection, torque response and the transient rise time.
- parameter sensitivity: the resistances R_r and R_s detune with temperature and the rotor leakage inductance $l_r = L_{r\sigma}$ changes due to saturation. The latter

with the change in R_r causes a change in the rotor time constant T_r. This can result in the derating of the drive since the rated torque cannot be produced.

- low speed robustness and operation: minimum speed at which the drive can be operated reliably. It is also interesting if the algorithm can recover once orientation is lost.
- steady-state speed error: the error is parameter dependent and is usually worst at low speed.
- noise sensitivity: has an effect on the low speed performance and speed accuracy. Noise results in a degradation of the measured signals. It has a large effect on the sensorless algorithms at low speed and might require filtering which reduces the system dynamics.
- complexity and computation time: most models are based on the linear 2-axis model of the induction machine. This assumes a sinusoidal distribution of the windings. In reality, the windings are discrete in the stator (slots in stator and rotor). This characteristic is difficult to include in the machine model, as is saturation in the machine. For the implementation on a cheap fixed-point processor, a matrix inversion might be too complex to realize for a given sampling period.

Model-Independent Speed Estimators

Estimators that are not based on the machine model can be used to gain more information about the real machine that could be obtained by evaluating the fundamental currents and voltages only. These estimators can then be used to correct machine models [62, 63] and to eliminate parameter uncertainties. When extracting rotor slot harmonics, speed sensorless control can be realized [40]. It also allows the decoupling of the speed estimation from the derivation of the flux vector. Rotor slot harmonics originate from an inductance variation due to the geometrical design of the machine. Stator and rotor slots produce slot harmonics in the air-gap flux when the rotor moves. The harmonics are induced in stator voltage or current from where they can be extracted for speed estimation [64, 65]. The largest slot harmonic will exist at a slot-harmonic frequency $f_{sh} = \frac{N_r}{pp} f_r \pm f_e$ where N_r is the number of rotor slots, pp are the number of pole pairs. The corresponding slot harmonic f_{sh} will not exist if $(N_r/pp + 1)$ or $(N_r/pp - 1)$ is even or a multiple of 3. In many machines only one harmonic will exist and the estimated rotor speed is $n_r = \frac{60 \cdot pp}{N_r}(f_{sh} \diamond f_e)$, with $\diamond = +$, $-$ or $\pm$.

A back-*emf* method is shown in [66] that uses virtual short circuits. At lower speeds, the inverter zero states ('000' or '111') can be used since they occur sufficiently often.

During these states, the current is only driven by the back-*emf*. For higher speeds, inverter zero states need to be constructed to cause virtual short-circuit conditions for the voltage. The current change due to the back-*emf* can be directly used to model the flux linkage and estimate the angle to obtain field orientation. This technique does not require the knowledge of stator voltages and does not depend on machine parameters. It also does not suffer from difficulties related to integration but loses orientation similar to other *emf*-models in the low-speed region and at standstill. This is because the stator resistance is neglected in this technique. Also, due to the smaller *emf*, the current changes are smaller and more difficult to measure. The technique works well for speeds above a quarter of the base speed. Below, the required processing increases significantly. A Kalman Filter interpolates and provides flux estimates in between the discrete measurements for the rotor flux angle calculations.

Zinger *et al.* [67] propose a phase-locked loop (PLL) to extract the rotor speed from the frequency of the rotor slot harmonics. The field orientation is decoupled from the speed estimation by measuring the induced voltages in specifically tapped stator windings. This allows the estimation of the airgap-flux and to cancel the resistive voltage drop that usually is a problem in the low speed range. Still, operation becomes worse below 5Hz and full torque cannot be achieved in the operating range.

For star-connected machines, the 3^{rd} harmonic of the stator voltage, that is due to stator and rotor teeth saturation, can be used for the estimation of the flux angle [68]. Only the neutral point of the stator windings has to be accessible. The problem is that the amplitude of the third harmonic voltage v_3 decreases for reduced flux and low speed. An interpolation that is based on the mechanical model is used to estimate the position between the zero crossings of v_3 that only occur after a time $T = 1/(6 \cdot f_e)$. This allows the realization of sensorless torque control for operation that is claimed to be stable above 1.2Hz. The stator and rotor slot harmonics are proposed to estimate the speed. This however is not demonstrated and the measured encoder position is used instead.

It can be summarized that the estimators that are not based on the linearized machine equations also fail in the zero speed range. This is because either the voltage is too small to provide reliable information or the measurement interval increases inversely to the frequency and all dynamics are lost. The 3^{rd} harmonic, induced harmonics or rotor slot harmonics get very close or overlap with the fundamental signals at low speeds and cannot be separated. All model-based and model-independent techniques have in common that they track a speed dependent phenomenon instead of a position phenomenon that does not vanish at zero speed [69].

2.3.2 Sensorless Position Control

For sensorless position control, the robust operation in the low speed region is mandatory. Since model-based approaches do not operate reliably in this region, other methods are required to obtain the flux or rotor angle. Tracking the position of a saliency provides a solution to the *low speed problem*. Saliencies are practically present in any machine and can provide an absolute information about the position of the machine rotor or flux. For synchronous reluctance and switched reluctance (SR) machines, salient pole and buried permanent magnet machines, magnetic saliency is an inherent part of the rotor design due to their geometry [18, 70–76]. For induction machines and surface PMSMs, saliencies are secondary or parasitic effects that are not covered by the ideal and linear model [18, 77, 78]. Sensorless control of the induction machine exploits magnetic asymmetries due to main flux saturation [18, 79–81], rotor slotting [21, 82, 83] or engineered rotor saliencies [23, 24, 50]. Typically, a high-frequency (*hf*) signal is injected [17] or an inverter transient [84] is used to excite the saliency. This allows the separation of *hf* modulation from the large fundamentals and hence the measurement of the response of the machine that contains the information about the saliency position.

Historically, the first sensorless control based on saliencies for induction machines to be investigated was sensorless torque control. This is because of the similarity to sensorless position estimation in PMSMs and SR machines, the lower requirements on signal processing and the pronounced type of saliency. Lately, sensorless position control, that is the subject of this thesis, has become a focus for research [17, 24, 51, 85]. Rotor position estimation poses higher demands to the complexity of the position estimator than flux estimation.

INFORM

The first method to extract the spacial saliency information from a machine for sensorless control was developed by Schrödl [18]. The indirect flux detection by on-line reactance measurement (INFORM) had its origin in the detection of the initial position of the rotor in synchronous machines [70]. The knowledge of the correct rotor orientation and position of the permanent magnets is essential for starting PMSMs, especially when using speed sensorless techniques. Magnetic saturation due to the permanent magnets causes an anisotropy in the inductance around the machine perimeter that can be measured. Voltage test vectors are then applied in one or more of the discrete PWM directions (Section 2.2.6). A sufficiently large armature current shifts the magnetic set point in the machine. This will change the inductance nonlinearly due to increased or decreased saturation and helps to identify the magnetic polarity

of the permanent magnets and hence the orientation of the rotor.
Introducing a regular injection of the test vectors, it becomes possible to continuously monitor the saliency and to use this information for a sensorless control scheme. In [18], the measurement to determine the saturation saliency is developed. This allows sensorless position and speed control for synchronous machines [86] but only torque control or crude speed control for induction machines [87]. This is because rotor frequency and flux frequency differ by the slip frequency in induction machines. The knowledge of the saturation saliency helps to obtain field orientation. The slip can be estimated, and therefore the rotor frequency, that allows sensorless speed control. Since saliencies are a position-dependent phenomenon, the derived speed-estimate will be very noisy [18]. For position control, the estimation of the rotor position via slip is not accurate enough.
Applying a voltage $\underline{u}_s$ at an angle α_u that is referred to the $\alpha\beta$ plane, a current change $\Delta\underline{i}_s/\Delta\tau$ is measured. The ratio of applied voltage to current change is the complex differential 'inductance' $\underline{X}(2\beta_u)$ [18]. The angle α_u of the voltage phasor can be split into the two components β_u and θ_e (see Section 5.3.1) where the latter is the orientation of the magnet axis (d-axis) referred to the $\alpha\beta$ plane and β_u is the angle between d-axis and the voltage phasor. It can be shown that $\underline{X}$ contains the saliency information due to saturation and depends on β_u [18] as by (2.56). Extracting this angle allows the determination of the direction of the applied voltage phasor within the dq reference frame. From the knowledge of its position within the stationary $\alpha\beta$ reference frame, the estimate of the flux angle θ_e can be derived using (2.57).
From (5.33) for a *stationary* rotor:

$$\frac{d\underline{i}_s}{dt} = \underline{v}_s \cdot \underbrace{(\overline{Y} + \Delta Y e^{-j2\beta_u})}_{\underline{Y}} \tag{2.56}$$

$$\hat{\theta}_e = \alpha_u - \beta_u \tag{2.57}$$

it can be shown that two measurements are needed to estimate β_u without knowing the differential inductance $\underline{X}$ [18] or its *inverse* $\underline{Y}$ (see Section 5.3.1). The inverter allows 3 independent and different measurements. This is because there are only 6 discrete directions possible for the voltage phasor as shown in (2.44). Only three of them provide new information, the other three voltage phasors are in the opposite direction [18]. Using the information from all three possible directions, the measurements can be combined to form a complex variable $\underline{c}$. This can be formed by using the amplitude information of the current change $\Delta\underline{i}$ only, or by using the phase information of $\underline{Y} = \frac{d\underline{i}_s}{dt \cdot \underline{v}_s}$. The argument of $\underline{c}$, that is $\underline{c} = \Delta\underline{i}_{s_1} + \Delta\underline{i}_{s_2}e^{j2\pi/3} + \Delta\underline{i}_{s_3}e^{j4\pi/3}$ when using the amplitude information or $\underline{c} = \underline{Y}_1 + \underline{Y}_2 e^{j2\pi/3} + \underline{Y}_3 e^{j4\pi/3}$ when directly using the phase information, contains the desired flux vector θ_e. Estimating the flux angle from the phase information is reported to give more accurate results [18].

For the *rotating* machine, the influence of the back-*emf* has to be eliminated. In [18], two INFORM cycles are combined. The two INFORM measurements have to take place within a short time so that the back-*emf* does not change too much. Ideally, the test vectors replace a voltage zero state since their mean stator voltage is zero. The deviation from the normal PWM generation is hence minimized [88]. Subtracting the two cycles results in

$$\underline{u}_{s_I} - \underline{u}_{s_{II}} = \underline{X}(2\beta_u) \cdot \left\{ \left.\frac{d\underline{i}_s}{dt}\right|_I - \left.\frac{d\underline{i}_s}{dt}\right|_{II} \right\} \tag{2.58}$$

which is independent of ω_r. The angle β_u is now the argument of the difference of the two voltage phasors $\underline{u}_{s_I}$ and $\underline{u}_{s_{II}}$ [18].

The problem due to changing saturation in the machine and its effect on the estimation of the saliency position is also addressed in [18]. The identified angle differed by 30° under full load compared to no-load and the angular difference between the real flux angle and position of the saliency depended linearly on the load and i_{sq}. Subtracting a correction term $\Delta\rho$, that is determined by a commissioning procedure from the estimated saliency angle, solves the problem. A similar approach is shown in [72,73] for a PM synchronous machine. A correction function is proposed by Lorenz and Corley in [73] to compensate for filter delays, saturation and inverter deadtime. The estimation errors due to the filter delay and saturation are approximately linear with speed and stator current respectively. The correction for the inverter deadtime is not shown.

For a position control system of sufficient quality, the rotor position and rotor speed are required. For the PMSM in [18], the rotor position is determined by the INFORM estimator. Deriving the speed by differentiating the estimated position "yields practically useless results because of the disturbed position signal" (quoted from [18]). A Kalman Filter is suggested to improve the position estimate and to obtain a speed estimate. The use of a Kalman Filter requires the knowledge of the electrical and mechanical machine parameters. Therefore the use of a PLL is proposed to simplify the estimation of the flux angular velocity.

Applying the INFORM method to induction machines, a sensorless torque-controlled drive can be realized. Crude speed control is also possible as shown in [18].

Rotor Position Estimation for Interior PMSMs

Ogasawara *et al.* show, in [89] and earlier publications such as [71], a possible implementation of the Schrödl method for a PMSM at zero and low speed that is extended to high-speeds in [90]. The motor current is varied by applying redundant voltage vectors. Ideally, all 6 voltage directions (see Section 2.2.6) are used to excite the currents

and obtain the linear independent current samples needed for the signal processing. The average voltage vector hereby has to remain unchanged from the fundamental voltage vector, not to change the machine flux and torque. In contrast to Schrödl, test vectors are permanently applied. The current deviations $\Delta \underline{i}_{k\alpha\beta}$ from the mean current $\underline{i}_{k\alpha\beta}$ are measured at the end of each voltage switching interval k. With the relation $\underline{v} = R\underline{i} + L\frac{d\underline{i}}{dt} + \underline{e}$ for the fundamental signals of the PMSM, the transient relation due to a voltage test vector is:

$$\underline{L}_k \cdot \Delta \underline{i}_{k\alpha\beta} = \underline{v}_k t_k \tag{2.59}$$

where the machine resistance and back-*emf* $\underline{e}$ are neglected. The inductance matrix is given as

$$L = \begin{bmatrix} \overline{L} + \Delta L \cos(2\theta_r) & \Delta L \sin(2\theta_r) \\ \overline{L} + \Delta L \sin(2\theta_r) & \overline{L} - \Delta L \cos(2\theta_r) \end{bmatrix} \tag{2.60}$$

with $\overline{L} = (L_d + L_q)/2$ and $\Delta L = (L_d - L_q)/2$ and θ_r the rotor angle of the PMSM. The parameters of L and most important, the rotor angle θ_r can be obtained according to [71] via processing α-β cross coupling terms of voltages and current differences in a least-squares approach to minimize the estimation error. It is not mentioned if the back-*emf* needs to be eliminated for operation at higher speeds.

The technique relies on the precise sampling of ADCs that are synchronized to the PWM switching to measure the current change Δi_k. At low speed, all 6 non-zero voltage vectors are applied within one modulation period $T_a = \sum t_k$ where $T_a = T_p$ is half the PWM period. The switching time t_k for each vector is determined so that the mean voltage vector equals the demanded stator voltage. From above half-rated speed and for high-speed operation, one zero-state vector is selected plus the three voltage vectors spanning two of the sectors that are within $\pm 30°$ of the demanded stator voltage vector to excite current transients. The switching times t_k are again calculated so that the mean vector is equal to the demanded stator voltage.

Blaschke Flux Angle Detection

Blaschke *et al.* [79] use the nonlinear effect caused by the mutual inductance when injecting a pulsating *hf* current onto the *d*-current axis. Saturation is responsible for differences in the resulting *hf* rotor currents that are a function of the flux angle. Ideally, these rotor currents have to be measured. With no access to the rotor, they can be approximated and estimated from the stator voltages. A misalignment in the field orientation can be derived from the *hf* rotor currents or stator voltages and used as a feedback to correct the voltage model. This allows field orientation at zero and low speeds and different loads. This technique is suitable for current source inverters

(CSI), using a hysteresis current regulated PWM inverter. Sensorless torque control is presented in [79] with the relatively low carrier frequency of 20Hz for the *hf* current injection. No technique to realize sensorless speed or position control at zero speed is presented. As will be shown later, it can be a disadvantage to have a low injection frequency. An increased carrier frequency for current injection however is more difficult to realize than voltage injection due to the limited bandwidth of the current controllers [91].

Sul Flux Angle Detection

Sul [20] proposes a technique, very similar to that in [79]. The main difference is that a VSI and *hf* voltage injection are used. Therefore, the saliency information is derived from the *hf* stator currents. Again, a pulsating injection in the *d*-axis is applied. The resulting *hf* currents are measured and transformed into a measurement frame that is aligned to the flux axis by a balancing controller. Ideally, the measurement axes are symmetrically aligned to the flux axis so that the modulation effect of the saturation saliency on both measurement axes is the same. The two measuring axes are both ideally 45° apart from the flux axis which they enclose. Differences in the *hf* currents will result in an error signal that serves as input to the balancing controller that will adjust the frame orientation of the measurement axes and the field orientation. A correction controller is needed to compensate for the difference between the direction of the saturation saliency and the rotor flux alignment. The difference is a function of loading and therefore i_{s_q}. This makes torque control possible. The estimated flux angle is also differentiated and filtered. Adding a slip estimate, the rotor speed can be estimated and basic speed control is possible. The primary problem is the differentiation that can be very noisy. Filtering will improve the signal but reduce the dynamics. The secondary problem is that the slip estimator is parameter-dependent and also requires accurate field orientation. From the experimental results given in [92], it is obvious that zero-current clamping (see Section 6.1.3) causes problems in the flux estimation. This results in torque ripples and large errors between real and estimated speed. None of the experimental results proves the claimed quality of the *d*-axis injection to reduce torque pulsations. The proposed technique depends on the level of saturation in the machine. Not all machines generate sufficient difference in saturation for the balancing controller. This is especially true for semi-open or open-slot machines.

Consoli Flux Angle Detection

Another method to estimate the saturation saliency of induction machines is published by Consoli, *et al.* [81]. This method is based on earlier work, using the 3rd harmonic of the stator voltage due to saturation that can be measured between the machine star-point and the inverter midpoint [68]. This third harmonic technique providing field orientation however fails for low speeds. To overcome this limitation, a *hf* voltage is now injected onto the stator reference voltages [81]. The common mode voltage is measured as before but the *hf* voltage component $v_{0_{hf}}$ is extracted. This signal contains information about the saturation saliency position in the machine. In [74], the technique was applied to PM synchronous machines. For the induction machine, only sensorless torque control or crude sensorless speed control can theoretically be realized. Until now, only tracking results for the airgap flux position have been published [81]. Sensorless control of induction machines has not yet been shown.

An alternative approach to determine the saturation saliency angle is published in [93], where the common mode current component $i_{0_{hf}}$ instead of the voltage is measured. Practically, all three line currents are measured and added, then sent through a bandpass filter. The resulting *hf* common mode current component $i_{0_{hf}}$ contains the saliency information. This current signal is lagging $v_{0_{hf}}$ by about 90°. The *hf* model of the machine assumes a neutral-to-ground stray capacitance between the stator windings and the grounded frame for the common-mode current to flow. This parasitic capacitance has a value in the order of nF [93] that determines the common-mode path admittance that is higher for *hf* currents than for fundamental currents. From the publication [93] it is not clear if the method is restricted to star-connected machines. Experimental tests performed by the author using a delta-connected machine resulted only in a small DC signal without any *hf* component. All three line currents were measured and sent through three separate analogue bandpass filters before sampled by three A/D converters. The signal addition was performed in the digital processor. The DC offset resulted from small offsets in the A/D converters and the analogue filters. It is assumed that there is no *hf* common mode current in a delta connected induction machine.

Lorenz Flux and Rotor Angle Detection

Jansen and Lorenz [17] were the first to suggest a continuous *hf* injection to allow a sustained excitation of the saliency. This can be a continuous *hf* voltage or current injection, the voltage injection however is preferred. This approach has been adopted by many researchers. Possible implementations are suggested for sensorless torque control using saturation saliencies [19] or sensorless position control using engineered variations in the leakage inductance of the rotor [77] or the natural inductance variation due to rotor slotting [82].

All three types of sensorless strategies use a so-called *heterodyning tracking observer.* For the rotor position estimator, this is appended by a model of the mechanical system. The flux angle estimator only uses an integrator to derive the flux angle from the angular frequency. These structures are effectively phase-locked loops (PLL) that derive the position information contained in the saliency-modulated signal. The structure works as follows: The *hf* currents containing the low-frequency modulation are fed into a phase detector. Here the cross-product is formed with a virtual *hf* current phasor containing the estimated saliency angle. The low-frequency components of this error signal are a measure for the phase difference between real and estimated saliency angle. This error is the input to the loop-filter that outputs a phase change reference. Integration then results in the estimated saliency angle and thus closing the loop to the phase detector. The disadvantage is that the PLL or tracking observer require a sinusoidally distributed saliency and only allow the tracking of a single saliency. If more saliencies are present in the machine, the tracking fails, resulting in a loss of the position signal.

Early publications covering flux estimation [19,94] only present experimental results that show the change of the *hf* impedance with stator or magnetizing current for two induction machines. No tracking results for the flux or saliency angle are shown. Loading causes an angle difference between the saliency angle and the flux angle that is analyzed quantitatively. This phenomenon is further investigated in [50,92,95].

The use of rotor saliencies is investigated in [17,77]. Experimental results are presented for a $3.7kW$ (5hp) induction machine under 33% flux and 10% rated torque. Real and estimated rotor position are shown where the rotor saliency is due to a modulation of the rotor leakage inductance. This inductance varies sinusoidally due to the different slot openings with widths of 1.6mm and 0.15mm for 6 or 5 successive rotor slots respectively. The distortion of the *hf* modulation due to inverter deadtime is claimed to prevent higher loading of the machine. Problems in the rotor position estimation due to the increased saturation saliency under heavy loading are discussed. The distorting effect of saturation is reduced by opening all rotor slots.

Results presented in later publications [85,96] show the tracking of rotor position where the distorting effect of saturation is originally neglected which means that the machine is operated without fundamental currents. One result is shown where the test machine produces a constant torque of 5% rated. It is believed that the drive is operated under sensored IRFO with the rotor position tracking running in parallel.

In [96], the *direct homodyne* transformation is developed to separate positive and negative sequence harmonics. This does not solve the basic problem of separating single saliencies since rotor saliency and saturation saliency are both negative sequence harmonics. The reliable operation of the PLL or tracking observer cannot be obtained in this way. This technique however allows the elegant removal of the carrier from the *hf* signals by signal processing.

Most tests in [69] showing the estimated rotor position are without any fundamental excitation present in the machine. The machine then simply acts as a big resolver (see Section 8.2.1). In [82], rotor slot harmonics provide a rotor position estimate for a torque-controlled induction machine that is controlled to produce a constant torque of 31% rated while a dynamometer enforces speed changes. The position error is within about $\pm 4°$ electrical. No information is given if the machine is operating under rated flux. Still, no sensorless position control at full flux or full load has yet been presented.

Cilia Rotor Angle Detection

Cilia *et al.* [24] were the first to demonstrate true sensorless position control of an induction machine. To get a position dependent modulation, an asymmetric rotor is used. This means that an engineered circumferential variation in the resistance of a high-resistance outer-section cage of the induction machine rotor is introduced. This design provides incremental rotor position tracking with good dynamics where the rotor position dependent signals are robust to changes in load. The sensorless position control was implemented for a $30kW$ machine. An $\alpha\beta$ rotating *hf* voltage is used for injection. The resulting *hf* currents are extracted from the large fundamental stator currents using an analogue bandpass filter. The *hf* currents contain the modulation due to the engineered rotor saliency. This can be tracked using the PLL of [17]. The estimated rotor position is fed into the flux model to obtain field orientation and is used as feedback for the position controller. Sensorless position control is shown for a number of different conditions. A good transient response to a 360° position change is achieved for 60% rated flux and no load. For the same reduced flux, a load transient from 0 to 30% rated load is shown. Under stationary conditions, 50% load is demonstrated for 60% flux. The error on the estimated angle has increased to $\pm 15°$ for this condition. For full flux and higher load, additional interference harmonics arising from slot saturation cause problems for rotor position tracking. The PLL then partially tracks the saturation saliency, causing instabilities for the position control and a loss of orientation.

Saturation Saliency Elimination

The problem of saturation for position-sensorless control is addressed in [97]. A periodic burst injection is used that is a symbiosis of discrete and continuous *hf* injection. For very low speeds, the saturation terms in the *hf* currents can then be eliminated mathematically. The obtained position estimate is independent of load and flux level. The publication shows the quality of the estimated rotor position even for severe saturation. The position estimate is tracked only and not used as feedback

for sensorless position control. The disadvantage of this method is that the achievable dynamics and speed are low. It however would allow tuning of model-based observers.

Holtz Rotor Angle Detection

Building upon the approach of [18], a technique for the estimation of the rotor angle is presented by Holtz, *et al.* [98]. The aim is to obtain sensorless position control using a rotor with a particular number of rotor slots by applying a transient injection. A specific PWM switching cycle is introduced, causing a short current 'distortion' that can be picked up by measuring the star point voltage of the machine. Hence this technique is limited to machines that are connected in star and also have the star point accessible. The dual of this method for sensorless torque control is published in [81] using continuous *hf* voltage injection and measuring the voltage at the star point of the machine. An advantage of [98] might be that measuring a voltage can be easier than measuring a current change as in [18]. Still, the measurement requires synchronization with the applied fundamental voltage space phasor. Initial analysis in [99, 100], applying this technique, neglect the distorting effects of saturation and rotor speed. The influence of rotor speed is eliminated by the measurement technique presented by Schrödl in [18]. The problem of saturation effects is not considered, since the machine is used similar to a resolver without any fundamental excitation. Only two graphics are presented in [99] showing position signals for the drive running under sensorless position control. No information is given about the flux level or load applied. A magnitude error of 5% in the two perpendicular position signals is analyzed that is attributed to saturation. Problems in the position estimation due to saturation are finally shown in [100] but are not solved.
The idea behind the technique of [98] is that the star point-voltage is zero if the stray inductances $l_{\sigma a}$, $l_{\sigma b}$ and $l_{\sigma c}$ are the same. If however there are non-linearities in the machine such as those due to rotor slotting, the inductances become functions of this saliency angle. The stray inductivity of line a can then be expressed by the approximation

$$l_{\sigma a}(\delta_N) = l_{\sigma a0} + \Delta l_{\sigma a} \cos \delta_N \tag{2.61}$$

Here, $l_{\sigma a0}$ is the component that is independent of the rotor position and $\Delta l_{\sigma a}$ is the amplitude of the stray inductivity that is dependent on the rotor position. The spacial dependency is given by the angle $\delta_N = N_r \omega_r t$. N_r is the number of rotor slots, ω_r the rotor angular velocity and δ_N the slot angle. With the inductances changing with position due to slotting, the zero voltage also becomes a function of the rotor position that can be measured and used to then estimate the rotor position.

By combining two voltage measurements with opposite inverter states as proposed by [18], the influence of the back-*emf* and therefore the speed-dependency can be

cancelled. The normal PWM switching cycle has to be interrupted by a specific voltage phase test phasor for the duration of the measurement cycle. In [99], the two inverse switching states are within the same switching period with $\Delta t = 6\mu s$. None of the publications specifies the precise measurement setup or discusses possible problems with switching oscillations or measurement synchronization. The signal from combining e.g. states *(1)* and *(4)* (see Section 2.2.6) is

$$\begin{aligned} p_a(\delta_N) &= u_\sigma^{(1)} - u_\sigma^{(4)} \\ &= 2V_{dc}\frac{l_{\sigma a}l_{\sigma b} + l_{\sigma a}l_{\sigma c} - 2l_{\sigma b}l_{\sigma c}}{l_{\sigma a}l_{\sigma b} + l_{\sigma a}l_{\sigma c} + l_{\sigma c}l_{\sigma a}} \\ &\approx 2V_{dc}\frac{\Delta l_\sigma \cos(N_r\omega_r t)}{L_{\sigma 0}} = 2V_{dc}k_{1\sigma}\cos(N_r\omega_r t) \end{aligned} \tag{2.62}$$

where $u_\sigma^{(k)} = v_{An} + v_{Bn} + v_{Cn}$ is the sum of the three line-to-neutral voltages for a test vector in direction k. The measured difference in the voltages $u_\sigma^{(1)}$ and $u_\sigma^{(4)}$ results in the position-dependent term $p_a(\delta_N)$, where typically $k_{1\sigma} < 0.1$ and V_{dc} as the DC-link voltage. The phase shift between the measured signals can be assumed to be zero. Two similar position-dependent terms are found for the two remaining directions $p_b(\delta_N)$ and $p_c(\delta_N)$, that have a phase shift of $120°/N_r$ and $240°/N_r$ to $p_a(\delta_N)$ respectively. Different possible solutions on how to obtain the rotor position signal are mentioned in [21], such as zero-crossing detection (see Section 5.5). The most robust solution is to combine the three position signals p_a, p_b and p_c to form a complex position vector $\underline{c}$. Extracting the phase of $\underline{c}$ (e.g. using the ARCTAN function [21]) will give the estimated rotor position.

The analysis in (2.62) neglects saturation in the machine and also assumes an ideal slotting saliency. The inductivity parameters will however in practice also depend on saturation. This will cause a spacial modulation of the position signals p_a to p_c. The resulting saturation saliency will then degrade the quality of the rotor position tracking or cause a loss of the estimated position.

Chapter 3:

Control Structure and Design

One important aspect of this research is naturally the use of the estimated rotor position as a variable in the control system. For the field-oriented control, the rotor position directly influences the stability of the position-controlled drive. The position signal is required to obtain field orientation and also to provide the feedback for the position controller. The control structure for the experimental drive and the layout and design of the controllers is covered in this chapter. This gives an insight into the performance of the experimental drive. Typically a cascaded control structure based upon proportional and integral (PI) controllers is used for the field-oriented control of induction machines. A subset of this structure is used for the sensorless position control.

3.1 Cascade Control

Cascade or nested control is the most common structure for the control of field-oriented induction machine drives and is the basis for the control in this work. Usually, PI controllers are chosen that can be designed using root locus, pole placement or quality criteria. The integral part ensures stationary accuracy while the proportional part determines the dynamics. The controller design is based on the linear and time-invariant model of the induction machine (Section 2.2.3). Cascade control is very suitable for the decoupled control of speed and torque under field orientation. Speed and the torque component i_{sq} of the current are in one branch and field weakening, flux and i_{sd} control are in the second branch as shown in Fig. 3.1. Cascade control is relatively easy to set up because it allows a commissioning step-by-step from the fast inner current controllers to the outer superimposed control loops. Outer control loops must have a lower bandwidth than the inner loops. Outer extensions for field

weakening or position control are easily possible. The cascade system also provides more protection of the drive by limiting internal quantities like current, torque and speed and it allows fast rejection of inner disturbances. The dynamic response can be improved by adding feedforward reference signals acting on the individual loops [7].

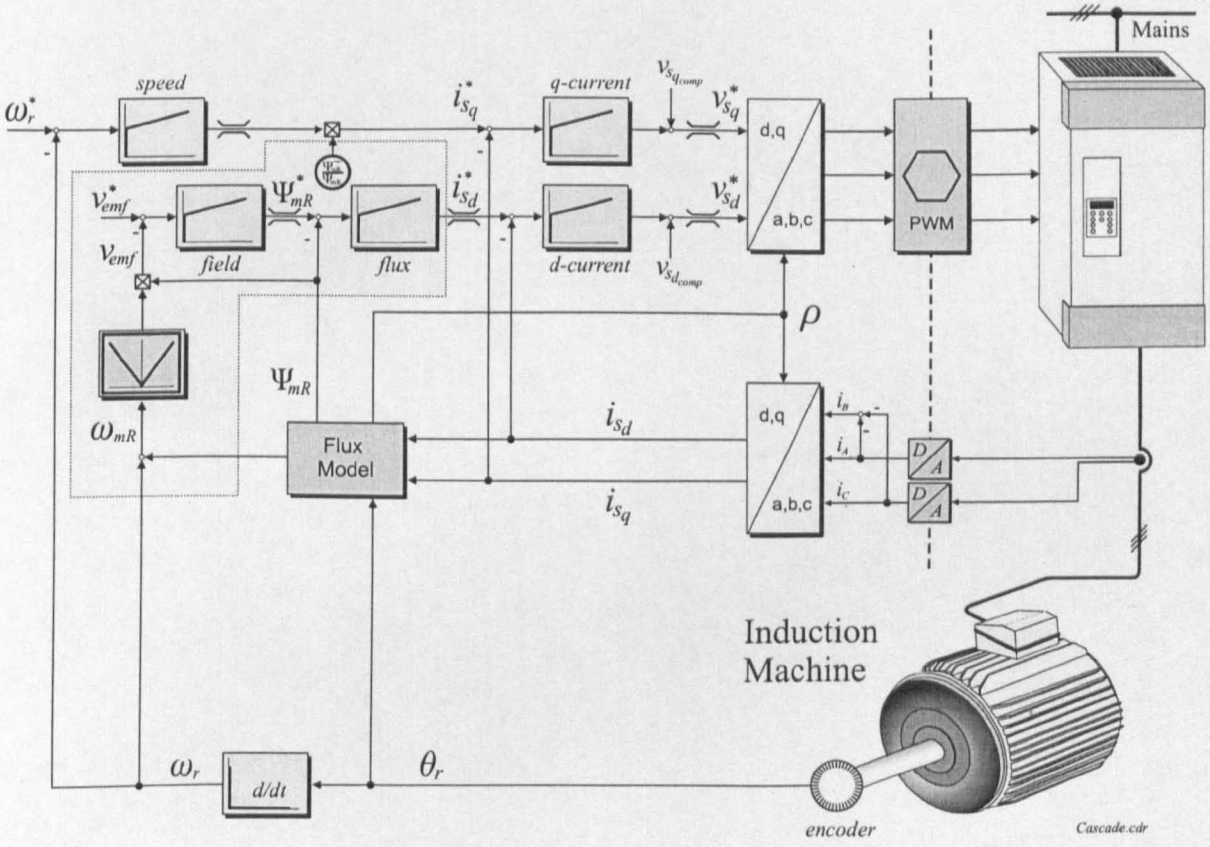

Figure 3.1: *Full cascaded control of induction machine used in the research programme [7, 101]*

Fig. 3.1 shows the structure for speed control of the induction machine as used for the research. The d and q current controllers in the inner loop generate the voltage demand that is transformed into the 3-phase stator frame. Then the PWM switching times are calculated. The speed feedback is obtained by differentiation of the encoder position. Field and flux controllers feed the inner d-current loop. Above the base speed range, the flux is reduced inversely with speed. The lack of a torque controller makes it necessary to adapt the i_{sq} reference by multiplication with the ratio $\frac{\psi_{mR}^{max}}{\psi_{mR}}$ in field-weakening. A flux model provides the transformation angle for field orientation and a flux estimate. With the focus on low-speed operation and sensorless control in

this work, the structure of Fig. 3.1 can be simplified. Then, the structure marked by the dashed area including field and flux controllers is not required.
Note that the linear function blocks of Fig. 3.1 are characterized by their step response [7]. All of the linear function blocks are PI controllers. A derivative block with d/dt converts the encoder position into a speed signal. Nonlinear functions are represented by a block with a double frame.

3.2 PI Controller and Anti-Windup

PI controllers are used for most of the control in this work. The Laplace transfer function of the PI controller is

$$G_c(s) = k_c \frac{T_c s + 1}{T_c s} = k_c \frac{(s + a_c)}{s}$$

where k_c is the controller gain and T_c is the controller time constant. The zero is at $s_o = -1/T_c = -a_c$. Conversion to the discrete transfer function with sampling time T gives

$$G_c(z) = \frac{z-1}{z} \mathcal{Z}\left\{\frac{1}{s} k_c \frac{s + a_c}{s}\right\} \tag{3.1}$$

$$= P + \frac{I \cdot z}{z - 1} \tag{3.2}$$

$$= \frac{z \cdot a_1 - a_o}{z - 1} \tag{3.3}$$

where $P = k_c$ and $I = k_c a_c T$ for (3.2) of the discrete controller and $a_1 = k_c(1 + a_c T)$ and $a_o = k_c$ for (3.3). In real control systems, the outputs of the controller usually have to be limited because the actuators saturate or their range is limited. Also operating conditions may be limited by electrical or mechanical design. This can be a speed that must not be exceeded or a maximum current that is allowed for the switching devices in an inverter. In this case, the controller output must be limited. When the controller output reaches the set limit, the integrating part of the controller may cause a deterioration of the control performance due to a substantial overshoot. This is because the integrator will keep accumulating the controller error even when the output is limited, which is called *windup*.
There are a number of techniques how to avoid the integrator windup [102, 103]. A dynamic anti-windup controller is shown in Fig. 3.2. It is derived from the discrete controller of (3.2) and used in this work for the speed control. The structure can be seen to consist of the proportional and the integral branch that are in parallel. Both branches have limiters, where the proportional path always has preference over the integral path. This means that the integral action will be disabled first if the

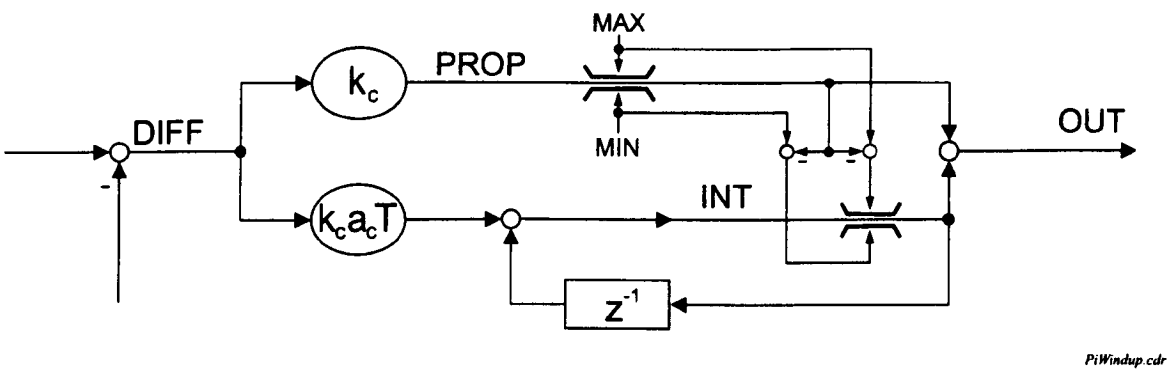

Figure 3.2: *PI Controller with Dynamic Anti-Windup*

output reaches the given limits. This ensures a fast settling time due to the strong proportional term and guarantees steady-state accuracy when the input error becomes small since the integrator is active.

3.3 Current Control

Both inner current loops consist of identical PI controllers. Under rotor flux orientation, the control loops for the torque and the flux currents are decoupled and the currents are constant DC-values under steady-state. The model of the plant for the d and q current loop, shown in Fig. 3.3 is $G_p(s) = 1/(\sigma L_s s + R_s)$.
The characteristic of the transducer is represented by $G_T(s)$ and can also contain the transfer function of a lowpass filter for anti-aliasing before the A/D converter. Since the dynamic performance of the current transducers allow tracking a current change of more than 50A per microsecond, the time lag due to the current transducers can be neglected here. For the old rig, the currents are sampled at $2k$Hz and the anti-aliasing filter is a second order Butterworth with a cutoff frequency of 600Hz [22]. In the new rig, the currents are sampled every 200μs that is a frequency of $5k$Hz. The current sampling is synchronized with the PWM generation so that no anti-aliasing filter is required here (see Section 4.5.1). Reading out the sampled and digitized currents occurs in each control cycle before the control code is started. The current controllers then determine the new reference voltages that are sent down to the PWM generator at the start of the new cycle.
The basis for the design of the current controllers $G_c(s)$ in Fig. 3.3 are the voltage

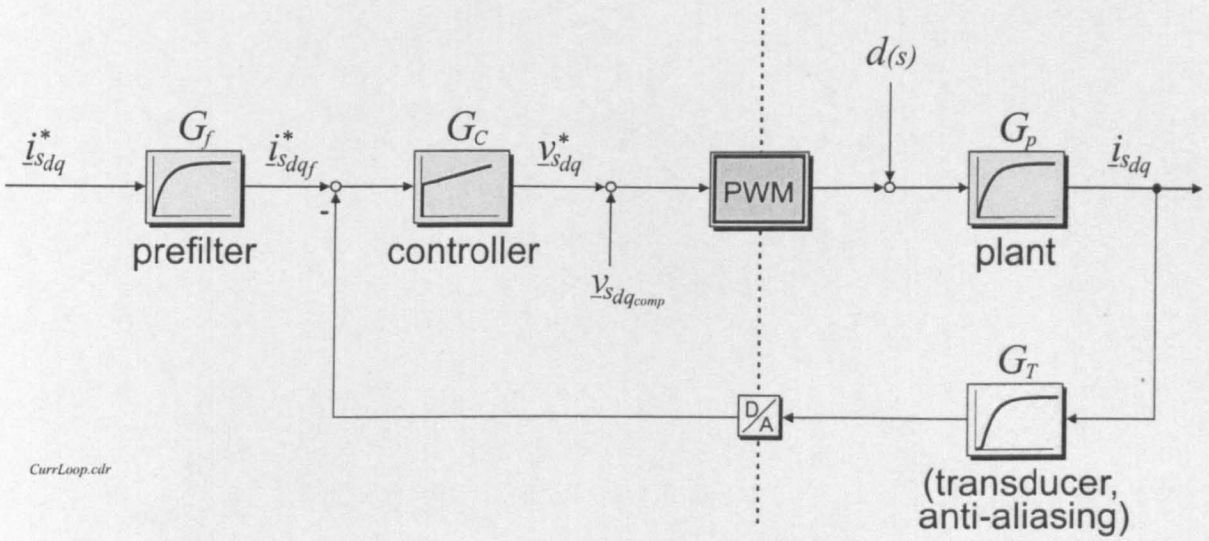

Figure 3.3: *Schematic diagram showing the $i_{s_{dq}}$ current control loop*

equations that can be derived from (2.17) for rotor flux orientation:

$$v_{sd} = \underbrace{\sigma L_s \frac{di_{sd}}{dt} + R_s i_{sd}}_{linear} \underbrace{-\sigma L_s \omega_e i_{sq} + (1-\sigma) L_s \frac{di_{mR}}{dt}}_{coupling} \tag{3.4}$$

$$v_{sq} = \underbrace{\sigma L_s \frac{di_{sq}}{dt} + R_s i_{sq}}_{linear} \underbrace{+\sigma L_s \omega_e i_{sd} + (1-\sigma) L_s \omega_e i_{mR}}_{coupling} \tag{3.5}$$

It is obvious that the current controllers are dealing with a non-linear multivariable system and it is advantageous to compensate the voltage coupling terms in (3.4) and (3.5) using a feedforward voltage $\underline{v}_{s_{dq_{comp}}}$, if the machine parameters are known. The decoupling network then allows for a better drive utilization under dynamic conditions. In particular the q controller is freed from having to contribute the large voltage component that is proportional to ω_e during acceleration. The coupling terms above can be simplified for constant-flux operation:

$$v_{sd_{comp}} = -\sigma L_s \omega_e i_{sq} \tag{3.6}$$

$$v_{sq_{comp}} = L_s \cdot \omega_e i_{sd} \tag{3.7}$$

The steady-state $R_s i_{sd}$ and $R_s i_{sq}$ terms can also be included to the respective feedforward voltage.

To additionally improve the current controller bandwidth, the current controllers were designed in the z-plane and a prefilter $G_f(z)$ was used to process the reference

input [104]. This enables a decoupling of the design for the disturbance response from that of the command tracking.

A possible choice for designing the prefilter is to compensate the controller zero. For plants of the n^{th}-order lag type as that of Fig. 3.3, the numerator of the closed loop transfer function of the reference response is determined by the controller zero. This derivative characteristic due to the PI controller can be easily compensated by the prefilter. A reference step will then be smoothed. Also, for the prefilter, the DC gain should be unity. This can be verified mathematically by replacing z by 1 in the transfer function $G_f(z)$ which should be equal to 1. The prefilter allowed the increase of the PI gain by a factor of 4 and the bandwidth of the current loop could be doubled. This is because the prefilter reduces the current overshoot as shown in Fig. 3.6.

The voltage source inverter using PWM is a non-linear amplifier. For simplicity, the real transfer function can be approximated by a delay $z^{-1} = e^{-sT}$, where $T = 200\mu s$ is the sampling period of the control system. For larger sampling times T, the gains of the PI controller have to be decreased to maintain stability (see [44]). The shown distortion $d(s)$ covers noise and the inverter non-linearities due to the dead-time effect.

In [44], the control scheme of Fig. 3.3 is presented as *Two-Degree-of-Freedom Controller* (2DOFC), claiming to significantly reduce the flattening of the line currents during zero crossing. This is known as *current clamping effect* and is the result of the inverter deadtime (see Section 6.1.2). Experimental tests by the author do not support the claimed level of improvement. Feedforward compensation and the prefilter allow only a slight reduction of the flattening of the currents. The major improvement concerning current clamping could be achieved by using the reference $\underline{i}^*_{s_{dq}}$ currents for the flux model instead of the actual measured ones.

The current controller bandwidth for the new rig was tested experimentally by superimposing a variable *hf* voltage signal (e.g. at $\underline{v}_{s_{dqcomp}}$) onto the voltage reference. Due to the closed loop nature, the resulting *hf* currents are fed back into the current controllers that cause a *hf* voltage demand to remove the injection. It was found that the current loop resonated (i.e. amplified the *hf* signal) at an injection frequency of 594Hz and 650Hz for the machines with symmetric and asymmetric rotor respectively. The loop bandwidths are slightly higher than the measured resonant frequencies. The value of $G_c(z)$ in the new rig are $P = 14$, $I = 0.85$ and $T = 200\mu s$. The transfer function of the prefilter therefore is $G_f(z) = \frac{0.15 \cdot z}{z - 0.85}$. The current controllers $G_c(s)$ in the old rig are set to the parameters $k_c = 4.5$ and $a_c = 140$ rad/s ($T = 504\mu s$), resulting in a natural closed loop frequency of 120Hz. The reason for the lower resonance frequency for the symmetric rotor is that the gain was minimally reduced since a higher amplification interacted with current ripples that originate from rotor slot harmonics.

The experimental step response for the i_{sq} current is shown in Fig. 3.4. The actual

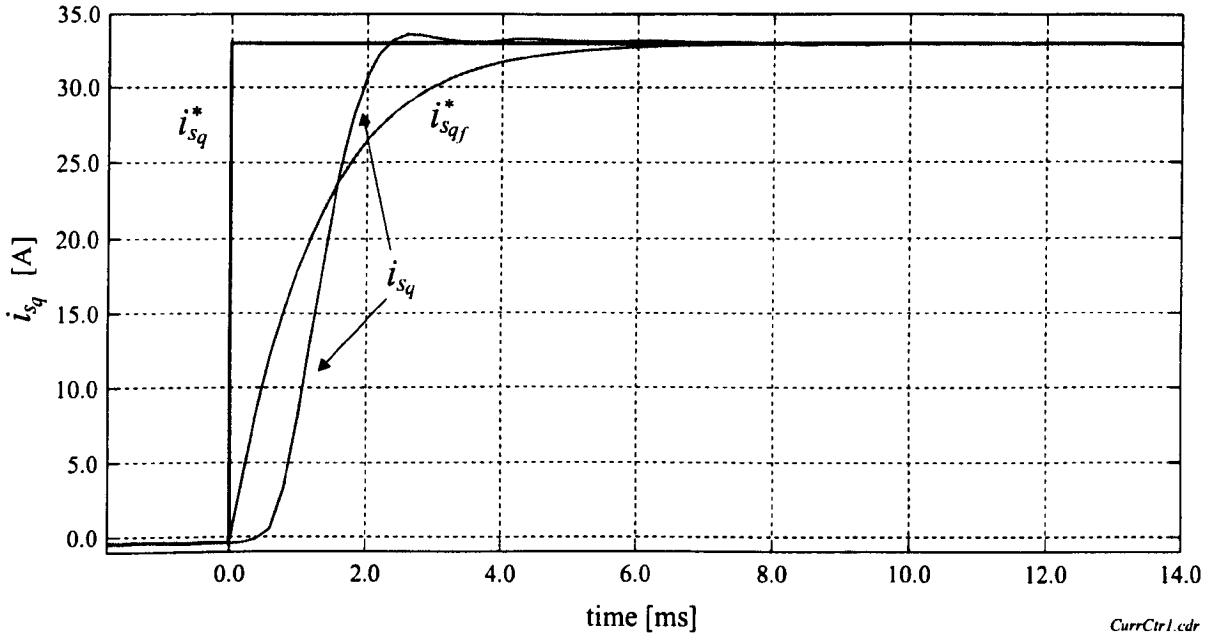

Figure 3.4: i_{sq} *step response for machine with symmetric rotor*

current follows the demand i^*_{sq} for 33A within about 3ms. The overshoot is minimized since not i^*_{sq} but $i^*_{sq_f}$ after the prefilter serves as the reference. The *control area*, that is the signed area between $i^*_{sq_f}$ and i_{sq} is zero. A controller design for a faster response is not easily obtainable due to the inverter delay of z^{-1} in the closed loop transfer function that is visible in Fig. 3.4.

A sequence of current step responses is shown in Fig. 3.6. During the speed change, the i_{sq} demand is set to the limit of $\pm$33A, that is 118% of rated i_{sq}.

For higher speeds, a distortion can be seen on the currents. This oscillation is due to the rotor slot harmonics. These are at frequency $\frac{N_r}{pp} f_r + f_e$ where $N_r = 56$ is the number of rotor slots, $pp = 2$ is the number of pole pairs and f_r and f_e are the electrical rotor and excitation frequency respectively. The amplitude of the rotor slot harmonics also depends on speed.

3.4 Speed Control

For the speed loop it is essential that the PI controller comes with anti-windup implemented. The speed controller directly acts upon the inner i_{sq} loop and its reference output is usually in the limits. This is because the mechanical time constant can be in the range of several hundred milliseconds whereas the i_{sq} response is in the range of a few milliseconds. The current limit will then be reached nearly instantaneously while the speed error does not decrease quickly. The operation of the speed-controlled drive

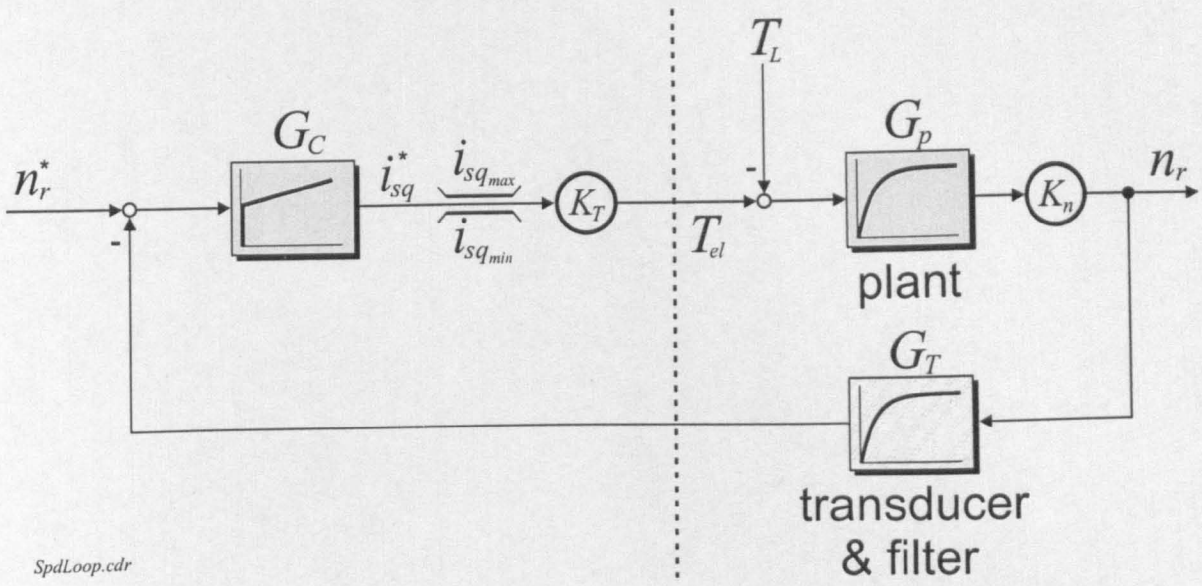

Figure 3.5: *Structure of speed loop*

is shown in Fig. 3.6. The $30k$W machine changes speed under unloaded conditions by 1000rpm in less than $300ms$. For most of the time during the speed change, the i_{sq} current is at its limit. The i_{sd} current is controlled to remain constant whereas i_{sq} changes step-like until the reference speed is reached. The i_{sq}-overshoot is the result of a small overshoot in the speed.

Because the electrical time constants are much smaller than the mechanical time constants, the inner i_{sq} loop and inverter can be substituted by a first order lag. The parameters of the transfer function are the torque gain K_T and the equivalent time constant T_c of the current loop. Since T_c is only about 1.7 milliseconds it can easily be neglected, leaving only the torque gain K_T as shown in Fig. 3.5. This gain can be derived from (2.3) and is $3 \cdot pp \cdot L_o^2/L_r \cdot i_{mR}$. The transfer function of the mechanical plant is $G_p(s) = \frac{1}{Js+b_F}$. J is the lumped inertia of the total drive system and b_F is the friction coefficient. The speed factor $K_n = n_{max}/\omega_{r_{max}}$ serves the conversion from angular velocity to speed in [rpm]. The feedback path shows the block '*transducer & filter*' that consists in the real system of a 3000-line incremental encoder (multiplied to 12000 ppr using the quadrature signal) and a filter of time constant $14ms$. With a sampling frequency of $0.6ms$, a standard deviation of 0.44rpm was obtained for low speeds and 0.25rpm for higher speeds above 100rpm. A filter with less phaseshift would be desirable for higher speeds. The emphasis in this work is however on the low-speed operation.

The nonlinear structure of the speed controller makes it difficult to determine the bandwidth mathematically. This can be done in simulation or experimentally by

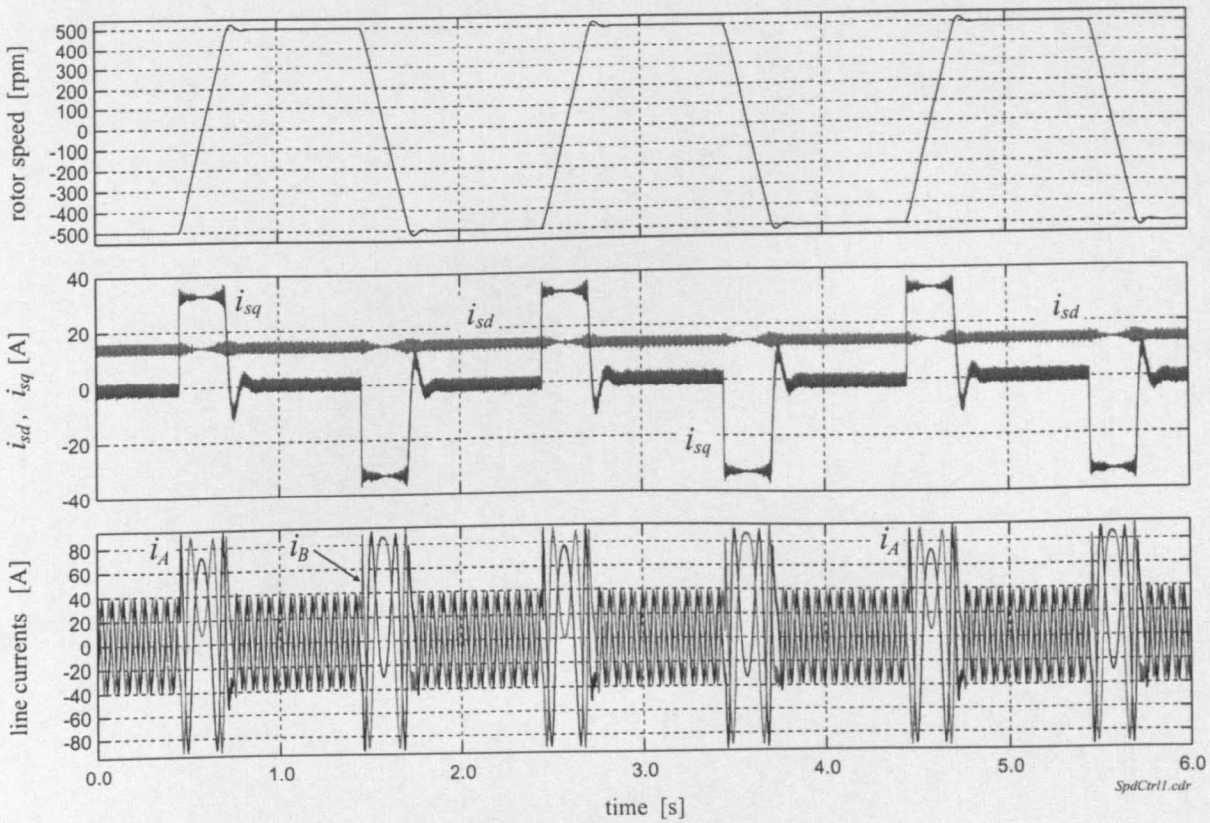

Figure 3.6: *Sequence of speed changes from* $+500$ *to* -500 *rpm for drive under Vector Control (symmetric rotor)*

using a sinusoidal reference speed such that the speed controller is not driven into saturation. The frequency at which the real speed reduced to $1/\sqrt{2}$ of the reference (the phase shift is close to 45°), is the cut-off frequency. This has been found to be about 8.5Hz or 53rad/s. The sampling frequency could have been reduced without affecting the speed loop bandwidth but for practical reasons the sampling rate was not changed. The *TRANSPUTER rig* had a speed bandwidth of 8.8Hz.

3.5 Flux Control

A flux controller can be implemented with an additional outer field controller as shown in the dashed box of Fig. 3.1. This structure is useful when extending the operation range into field-weakening. In this work, the focus is on the low-speed range. A simple i^*_{sd} demand is sufficient since the flux current i_{sd} will be kept constant. However, an approach is required to initially flux the machine.

The flux current demand i_{sd}^* is increased gradually via a first order lag with time constant T_d to the level of ψ_r^*/L_o. The current controllers will ensure that the real i_{sd} follows the reference and that i_{sq} is maintained at zero during start-up. The time constant T_d is chosen to be twice the rotor time constant T_r.

$$i_{sd}^* = \frac{1}{T_d s + 1} \cdot \frac{\psi_r^*}{L_o}$$

After about three time constants T_d, the reference i_{sd}^* is switched to its final value.

3.6 Position Control

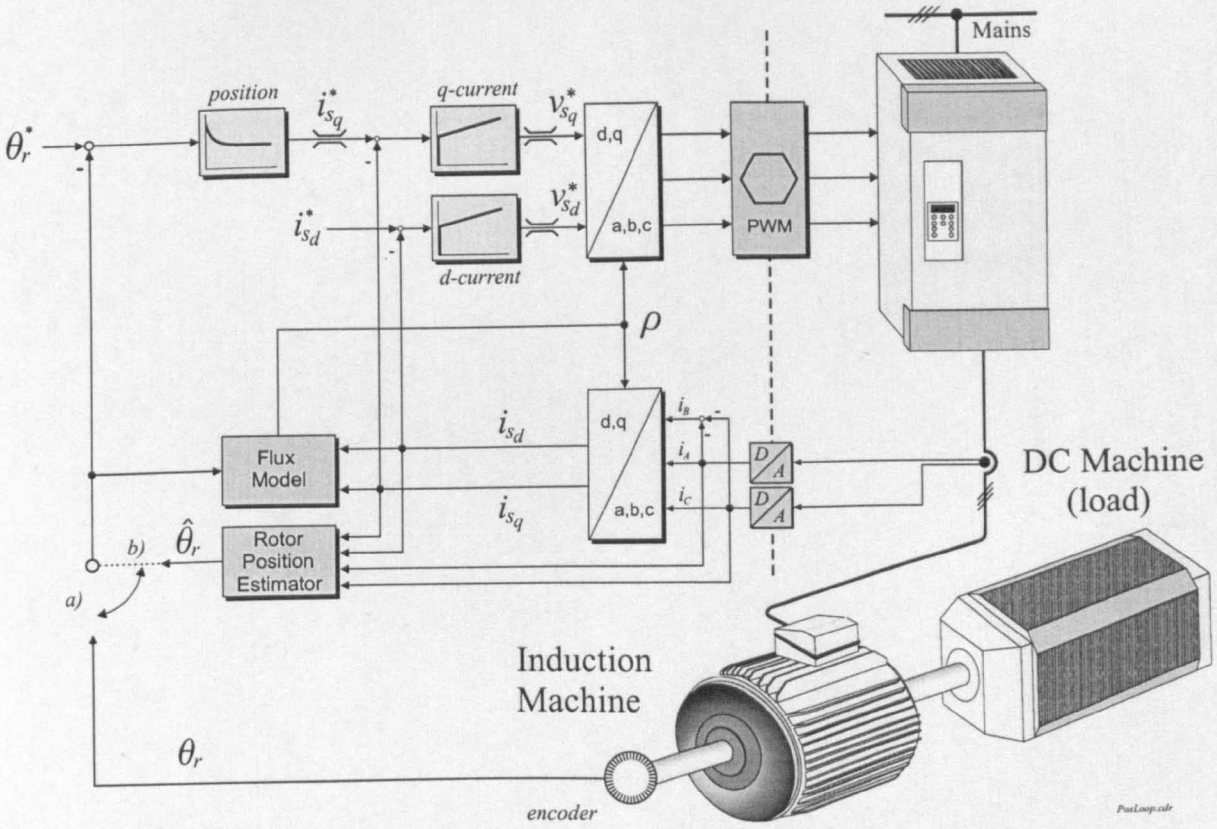

Figure 3.7: *Structure for sensored (a) or sensorless (b) field oriented position control*

The standard implementation for a position controller is to extend the speed control system of Fig. 3.1 by an outer position loop. A proportional controller is used if steady-state accuracy under a torque disturbance is not required. Otherwise, a PI

controller can be used that is often combined with an optimal path prediction [7]. This ensures position holding under load and minimum time for a demanded position change.

The implementation chosen in this work does not make use of an explicit internal speed loop because it is the position that is estimated and a speed estimate will usually be very noisy when derived from the estimated position. A lead controller is chosen that acts directly on the i_{sq}-loop as shown in Fig. 3.7. The lead controller can be split into separate speed and position loops. The equivalent nested controllers are a proportional speed controller of gain V_n and a proportional position controller of gain V_p.

$$\begin{aligned} i_{sq}^* &= V_n \cdot (n_r^* - n_r) + \underbrace{\frac{V_n \cdot k_n \cdot s}{T_f s + 1} \cdot \theta_r^*}_{feedforward} \\ n_r^* &= V_p \cdot (\theta_r^* - \theta_r) \\ & \text{where} \quad n_r = \frac{k_n s}{T_f s + 1} \cdot \theta_r \end{aligned}$$

The speed feedback n_r is obtained by differentiation of θ_r and by smoothing with the lowpass filter $\frac{1}{T_f s+1}$. This filter is mandatory since the differentiation will amplify the noise on the estimated position. The speed reference n_r^* from the position controller is complemented by the position reference, sent through the feedforward block $\frac{k_n s}{T_f s+1}$ that is identical to that used for the position feedback.

The Laplace transfer function of the combined lead controller $G(s)$ is

$$i_{sq}^* = V_i \cdot \frac{T_i s + 1}{T_{ic} s + 1} \cdot (\theta_r^* - \theta_r) \quad = \quad G(s) \cdot (\theta_r^* - \theta_r) \tag{3.8}$$

where $V_i = V_n \cdot V_p$, $T_i = (T_f + \frac{k_n}{V_p})$ and $T_{ic} = T_f$. Discretizing $G(s)$, one gets:

$$G(z) \quad = \quad k_p \cdot \frac{z - z_p}{z - z_z} \tag{3.9}$$

The parameters are:

$$\begin{aligned} z_p &= T_i/(T_i + T) && = 0.95 \\ z_z &= \exp(-T/T_{ic}) \approx (1 - T/T_{ic}) && = 0.997 \\ k_p &= V_i \cdot \tfrac{T_i+T}{T_{ic}} && = 300 \end{aligned}$$

To improve the controller performance the continuous control design was replaced by a discrete control using the implementation of (3.9). The control design was not

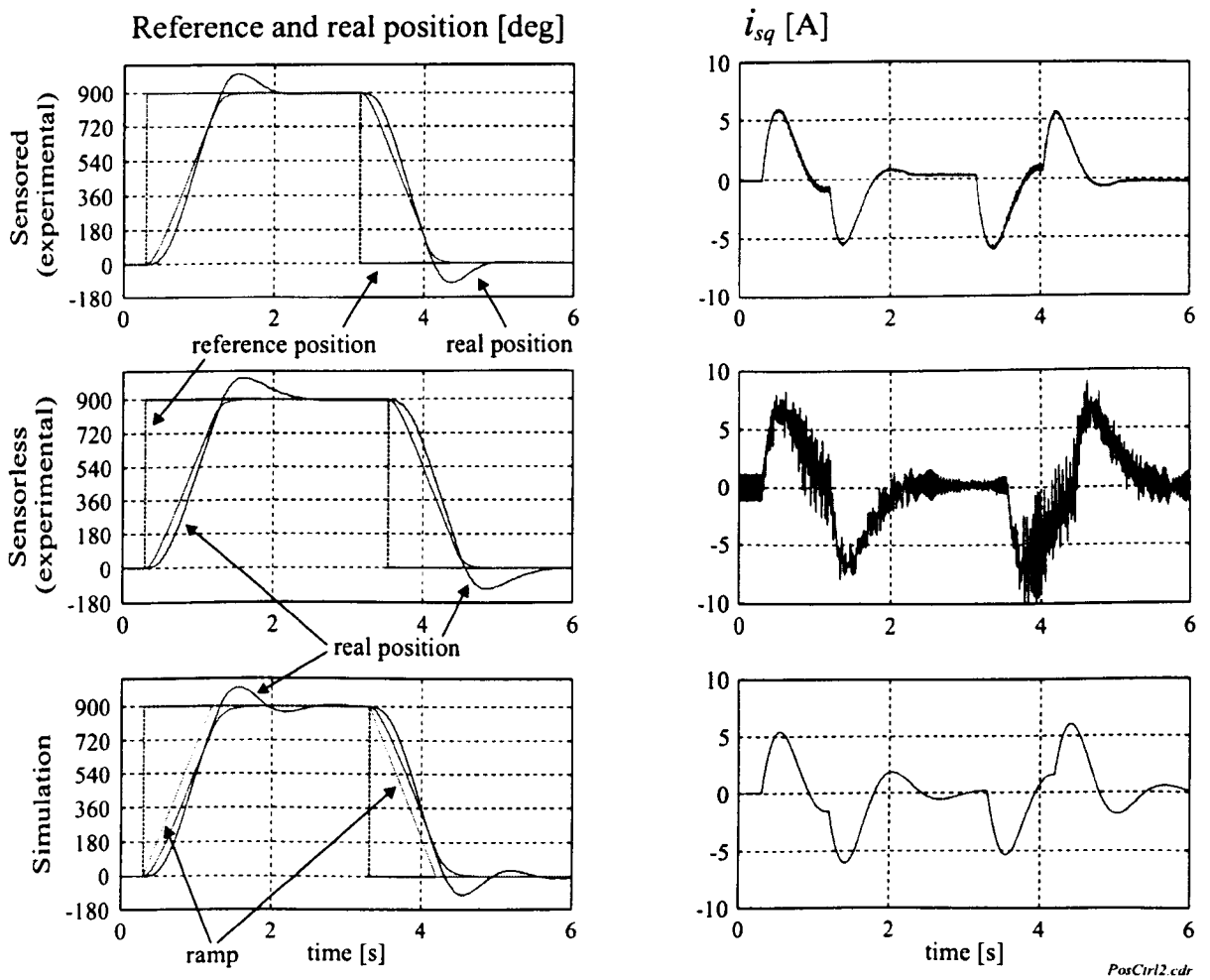

Figure 3.8: Position change by 2.5 revolutions (900°) under no load for sensored drive (upper), sensorless drive (centre) and simulated control using SIMULINK model (bottom)

optimized for maximum performance but a compromise was found so that sensorless operation using the noisier estimated position worked reliably. The same discrete controller was used for sensored and sensorless control as indicated by the switch in Fig. 3.7. The step demand θ_r^* was sent through a ramp function followed by a lowpass filter as shown in Fig. 3.8. This is to reduce the rate of change of position since it will be shown (Section 6.2) that high $d\theta_r^*/dt$ results in a high di_{sq}/dt that causes high frequency components of the fundamental current. These interfere with the *hf* signals that are used to estimate the rotor position. The reliability of the position estimation is then significantly reduced. The ramp function is that of a delayed integrator with a rate of change of 1000° per second. Some of the position transients using the machine

with symmetrical rotor were operated with a rate of change of 300° per second. The time constant for the lowpass ramp-filter is $95ms$. The parameters of the position controller for the tests of Fig. 3.8 differed slightly from that given above with $k_p = 420$, $z_z = 0.997$ and $z_p = 0.48$. The reason being a marginally better performance of the sensorless drive under no-load. For the position-controlled sensorless field-orientated drive under load, see Section 8.1.2.

The response to a 900° position change for the drive under no-load is shown on the left of Fig. 3.8. The upper two plots show experimental data from the sensored and the sensorless drive respectively. The sensorless drive uses the position estimator of Fig. 5.17 in Section 5.6. The lower plot is obtained from simulation using a SIMULINK model of the controller and the mechanical plant. The same code was used for the ramp and controller as used to control the real machine. The simulation results show the reference position, the real position and the ramp next to the smoothed position reference after the lowpass filter.

The torque current i_{sq} is shown on the right where the upper two plots are obtained experimentally from the sensored and sensorless drive respectively. The lower plot shows i_{sq} as obtained from simulation which is in good agreement with the experimental results.

Experimental tests using a sinusoidal reference input resulted in a bandwidth of 2.5Hz for the position control loop.

Chapter 4:

Experimental Rig

This chapter provides an overview of the experimental system including hardware and software. The research uses two $30kW$ experimental rigs. The first was constructed in a previous project and is fully documented in [22,25]. It consists of a $30kW$ induction machine driven by a $45kW$ IGBT inverter. The control is provided by an array of $T800$ Transputer processors, interfaced to the commercial $45kW$ inverter. The rig is referred to as *TRANSPUTER rig.*

A new rig has been constructed which has evolved from the old *TRANSPUTER rig.* This new rig with the function and operation of the different specific boards is described in this chapter and appropriate appendices. The new rig uses a state-of-the-art floating-point digital signal processor (DSP). A separate fixed-point DSP that is optimized for machine control serves as frontend and interface to a $45kW$ inverter. This new rig is called the *DSP rig.* A PC was used that serves as the host platform to develop code and analyze data. The PC host also provides the user interface to the control system. The structure of the safety box, control and power connections of the load drive and the *DSP rig* are also covered in this chapter.

In contrast to typical industrial systems, the processing power of the two experimental systems is much higher. Industrial solutions demand cost effectiveness and therefore use fixed-point processors with integrated peripherals that run highly optimized code. The experimental systems are oversized to allow modifications or changes and can also be easily extended in hardware and software.

Finally, the induction machines used for the research project are discussed. Three rotors were used for the testing of different algorithms for sensorless position control. Parameters are given and the modifications on the rotors are described.

4.1 Transputer Rig

The *TRANSPUTER rig* was taken over from previous research and is documented in [22] and [25]. It was modified to allow an analysis of the frequency spectrum of processed *hf* signals; a two-channel D/A converter being added to the system. Therefore a new transputer had to be included as the links of all other processors were already occupied and the available processing power was not sufficient. This modification increased the number of transputers to six. The structure of the transputer network and the links to peripheral components of the *TRANSPUTER rig* are shown in Appendix D.12. The extra processing power could however not fully be utilized but the additional processor allows for a simplification in the communication by buffering of transferred variables. The current configuration also shows that the system has reached a point where further extension only increases the complexity. Much time is spent on communication and inter-processor transfers via the serial links. Two-dimensional timing analysis is necessary to resolve communication deadlocks and to keep the system optimized. Small changes in code can delay the transfer of variables to up to $500\mu s$. The communication overhead and idle states cause a drastic degradation of the average processor utilization. A cause for the limitation is that each transputer only provides four links. Two of them are required to maintain the loop structure, that only leaves two links for the connection of external devices.

An advantage of the transputer system is that external hardware can be easily connected to a transputer link by means of a specific serial-to-parallel interface chip. This reduces development time considerably. The distributed processing power allows the calculation and generation of a PWM switching pulse every $84\mu s$. The distributed processing is also advantageous for the *hf* injection, since signal sampling and demodulation can run at $12k$Hz. This provides the possibility to inject higher carrier frequencies and still guarantees a fine resolution of the sampled signals. The main control, including communication with the user, updating the flux model or current control is only run every $504\mu s$.

The software on transputers and PC required structural changes from that of [22,25]. The monitoring of internal variables and sampled external signals on the transputers and the upload of data to the PC blocked all user communication with the transputer network. Therefore, monitoring was buffered and the communication was changed to be event-controlled. This allowed the arbitrary change of the reference signal during monitoring. The user interface was extended to allow more parameters to be sent to the control transputer online. Functions were implemented to download compensation tables and compensation parameters for the sensorless algorithm and control.

4.2 DSP Rig

From the experiences with the *TRANSPUTER rig*, a new rig was constructed, shown in Fig. 4.1. Instead of the transputer network, an established and powerful digital signal processor (DSP), the TMS320C40 was used. To reduce development time, a C40 motherboard was purchased from *Loughborough Sound Images Ltd.* (LSI). This comes in the form of a peripheral card that is placed in an ISA-slot of a PC and can be accessed by the user via software running on the PC. A set of analogue and digital I/O boards had to be constructed similar to that of the *TRANSPUTER rig*. An interface to the *Eurotherm* inverter of the *584 SV* series (type 7, 45kW) and the position encoder had to be built. Also a number of transducers for measuring currents and voltages and the respective A/D converters were needed. Bandpass filters were required for extracting the *hf* modulation of the stator currents for the sensorless algorithms and control.

From the experiences from the *TRANSPUTER rig*, a number of improvements for the new rig were achieved. The board layout was standardized, allowing more flexibility and possibility for future expansion. Boards were designed with ground planes allowing higher noise suppression and reliability. The efficiency of the expansion boards could be improved and the processing power of some boards was increased. Additional features were included like the analogue and digital output channels or the possibility to connect a SinCoder. The number of analogue signals that can be measured was doubled and more channels of analogue bandpass filters were made available. The control software and user interface were designed new from ground up, including new functionality, easier maintenance, ease of use combined with more powerful data acquisition and analysis. Any variable in the C40 control code can be sampled and this concurrent to the user control and debug activity. All the new design in software and hardware lead to a maximum of efficiency and flexibility for the research work.

4.2.1 C40 Motherboard

The *DPC/C40B* [105] is a C40 motherboard that occupies a single slot of the PC. It provides space for two C40 processors via specific module connectors. Only the primary module is populated that has direct access to a dual-port RAM and I/O ports to communicate with the PC. Both interfaces can be accessed autonomously. The I/O ports are primarily used from the PC side to configure the C40 motherboard. This includes access to a test-bus controller (JTAG) that simplifies code debugging. The dual-port RAM that is mapped into the physical address space of the PC is required for data exchange. The interface libraries provided by the manufacturer had been rewritten for the use under modern PC operating systems. Specific hardware

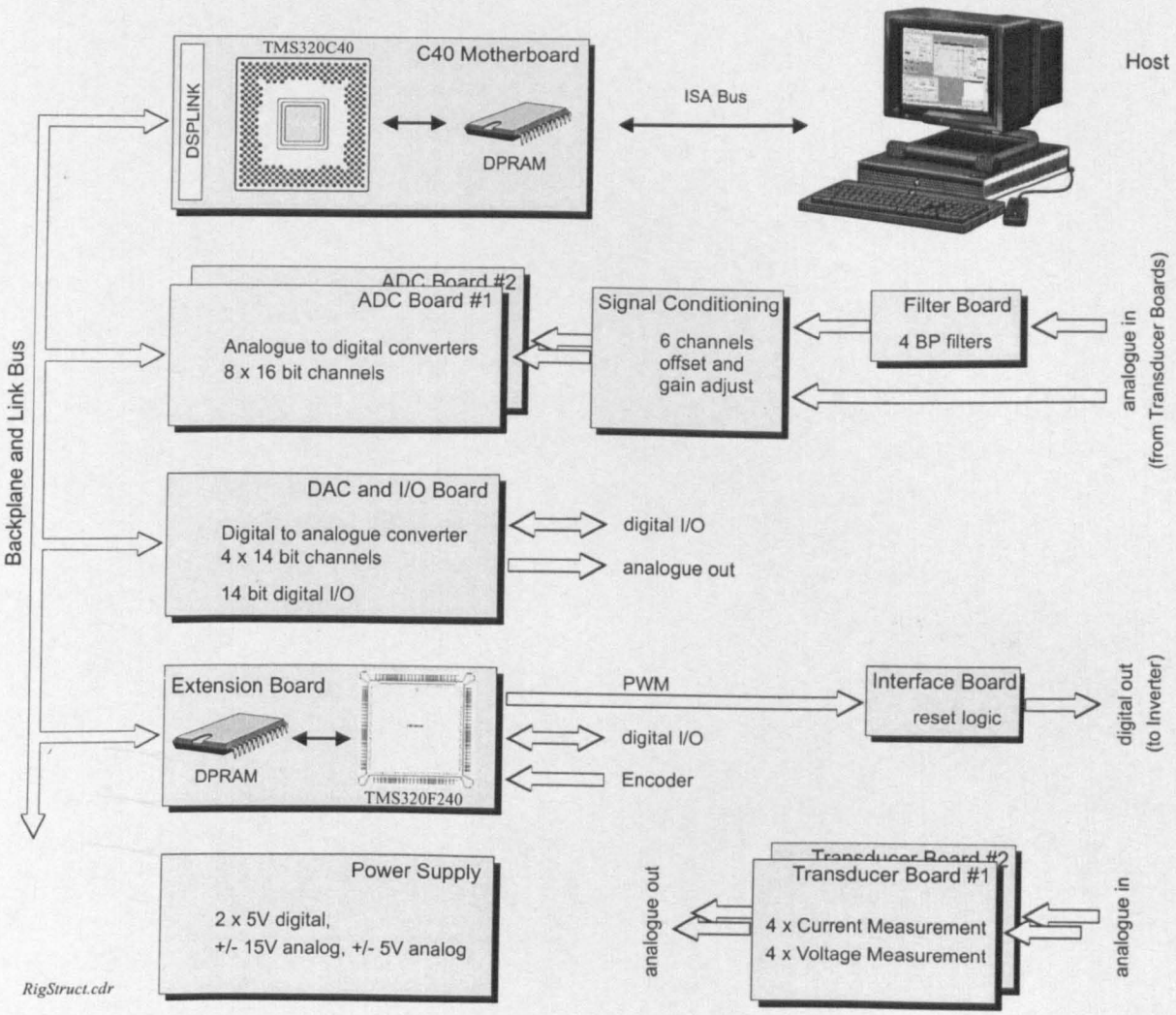

Figure 4.1: *Layout of the new DSP rig*

drivers were needed to provide access to the real memory.

The dual-port RAM allows a relatively fast data transfer between the PC and the DSP on the C40 motherboard. This type of communication interface exceeds the achievable transfer rate of serial ports or solutions based on the C40 CommPorts but is below that of a typical PCI transfer. However, the C40 motherboard was considered a good compromise as the usual communication is restricted to a small number of user actions and short data bursts when sampled data is transferred from the C40 to the host for further analysis. The code for field-oriented control of the induction machine is solely executed by the C40 and does not require any intervention from the host side. An instantaneous emergency shut-down is not only possible via software from the PC but also directly via hardware switches. This is why no

critical requirements for the communication speed with the PC exist. The typical 0.1 seconds response-time to process a user command are usually achieved and no operating system with real-time capabilities on the PC is needed. The C40 motherboard comes with a set of tools that run on the PC. A debugger is provided that allows the testing of code on the C40 and to change internal registers, data and code instantaneously, similar to a JTAG controller. Breakpoints can be set, step-over and trace-in are possible and the C40 can be operated in a free-run mode. A set of software libraries was provided with the board to load code to the C40 and access the dual-port RAM. These had to be rewritten for the use with a multitasking graphical operating system on the PC. A set of C40 tools like compiler, linker, archiver and libraries were available for writing code in the high-level language *C*. A precompiler and parser were written to allow easier documentation of the code and extraction of information for the debugger. An overview of the C40 code production tools can be found in [106]. This document lists important switches, settings, configuration files and summarizes additional useful tools. The C40 can access external boards either via the CommPorts or the external memory interface. The LSI motherboard only uses the CommPorts if a second C40 processor is mounted. The secondary DSP is then linked to the master DSP via the CommPorts. Access from the PC is only via the master DSP. A secondary DSP is currently not equipped. A small subset of the external memory interface of the primary C40 is provided via the DSPLINK interface on the LSI motherboard. This allows to write within about $300ns$ and an external read within $500ns$ and is therefore more than 10 times faster than the transputer interface using channels. The C40 provides a much faster external memory interface but is slowed down by the logic of the DSPLINK to allow the use of slow and cheap external hardware. The LSI motherboard comes with a number of memory modules of $256k$ words in total that adds to the $2k$ words internal RAM of the C40. The memory modules are used to store data from tables and signal monitoring and hold the program code. The variables are placed into the fast internal RAM to speed-up program execution.

The TMS320C40 is a 32 bit floating-point processor. The processor used is of the slowest version that is clocked with $40MHz$ and has a $50ns$ instruction cycle time. This can only be fully exploited if code from the internal RAM is executed, otherwise wait-states are inserted or the pipeline is not efficiently filled. The internal program cache can improve performance. The central processing unit (CPU) of the C40 integrates a numerical floating-point unit, a barrel shifter, arithmetic-logical unit (ALU), twelve 40-bit registers and eight auxiliary registers that can each be used like an accumulator. Multiplication, division and square-root operation are performed within an instruction cycle which is advantageous for the control code of the drive. Fast conversion from integer to float or vice versa is possible. Several modules can work in parallel. The

address decoder can update a new address and initiate the loading of code or data during numeric operations. The direct memory access (DMA) coprocessor allows to move large blocks of data without intervention of the CPU. This is very useful when transferring monitoring data from the external RAM via the dual-port RAM to the PC for further processing or inspection. Six CommPorts are available that work similarly to the links of a transputer. The difference is that the CommPorts are faster, work bidirectionally and are decoupled form the CPU via buffers. A pending transmission will therefore not stop the execution of code, the communication runs in parallel. The CommPorts are currently not used due to the lack of a simple interface chip to provide standard memory mapping. Two timers are integrated that can be used to run two interrupt service routines (ISRs) independently. Currently, only one timer is used for interrupt generation, the second serves as a watchdog timer. A small number of pins can be configured for digital I/O. This allows the C40 to communicate with the PWM generator chip. One external interrupt pin is used to trigger an ISR from the PWM generator. This allows to synchronize the C40 interrupt routine with the PWM. The internal bootloader is extended by that of the LSI motherboard for a faster downloading of code from the PC.

4.2.2 Backplane and Power Supply

The signals of the DSPLINK bus on the C40 motherboard are directly connected to the backplane of the rack that is shown in Appendix D.8. Some additional signals that are not available on the DSPLINK can be obtained by directly connecting to the DSP pins. The analogue and digital power lines are also a part of the backplane. They are connected to the respective power supplies that are integrated on a separate power board, shown in Appendix D.10. This board provides a regulated symmetrical $\pm 15V$ analogue voltage, used mainly for OpAmps, and stabilized analogue $\pm 5V$ supplies to power some special chips and OpAmps. Two voltage generators provide the $+5V$ supply for digital components. Separation of analogue and digital grounds is necessary to improve signal quality and reduce the digital switching noise for the analogue components. The power board consists of two transformers to deliver the different required digital and analogue voltages. The backplane separates analogue from digital signal lines and includes a number of ground lines to reduce cross-coupling. All boards get their signals from the backplane via a standard 3-row slot connector. This provides the flexibility to plug any board into any slot. The voltage and current transducers are currently powered by an external voltage supply to avoid problems with earth loops. This is also why the different analogue and digital grounds are only connected in one single point on the power supply board, near the transformers.

4.2.3 Transducers

The transducers are located outside the rack between the inverter and the induction machine, within a box for shielding. The board layout is shown in Appendix D.4. The three-phase power cables are connected via terminal blocks. Two boards exist with two current and two voltage transducers each. LEM modules *LTA100/SP1* are used for the non-intrusive measurement of the line currents. The modules are Hall-effect devices that provide a galvanic decoupling from the power circuit and have an output voltage that is proportional to the measured current. The voltage transducers are connected between the power cables to measure the line-to-line voltages. According to specification, their bandwidth is lower than that of the LEM modules. Their DC drift however is very low in practice whereas the LEM current modules require regular offset correction. All transducers are followed by lowpass filters and driver circuits to transfer the measured signals via coaxial cables to the rack.

4.2.4 Signal Conditioning Board

The gain board (see Appendix D.5) is used to provide an interface between the boards with the current and voltage transducers and the boards for A/D conversion. The gain board allows easy access to potentiometers to adjust gain and offset for each signal channel. Two of the input channels have two output stages. This is useful for the current signals. Two fundamental currents are needed for the vector control algorithm and the *hf* modulation of the line currents is required for the sensorless algorithm. One output stage per current channel is connected to the analogue bandpass filter respectively.

4.2.5 Analogue-Digital Converters

There are two ADC boards (described in Appendix D.6) in the system with four A/D channels each. Only the two channels measuring the line currents are essential for sensored Vector Control. For sensorless control, two *hf* currents from the analogue bandpass filters are converted and two line-to-line voltages are read. Two channels serve as a backup and can be used to measure additional currents or voltages. Each AD converter has a theoretical resolution of 16 bit and a conversion and acquisition time of about $10\mu s$. All channels are triggered synchronously and aligned to the PWM. This makes it possible to avoid sampling of current spikes at the instance of a PWM switching. The usual lowpass filters in the current path can then be omitted. These filters can reduce the bandwidth of the current controllers significantly. The trigger to start a conversion does not involve a software instruction and is provided in hardware by the PWM generator. This results in a deterministic timing event and also allows to take account of inverter deadtime and changes in the PWM period.

4.2.6 Digital-Analogue Board

The layout of the DAC board is explained in Appendix D.7. The board provides the analogue and optional digital output channels. Four analogue channels are available. The AD7835 DAC converts a 14 bit digital word within $10\mu s$ into an analogue voltage. Currently, the analogue output is only used to send internal variables to a digital oscilloscope. This can be useful to check or debug code, to display signals resulting from the processing of measured signals and to monitor signals over a long time with a high resolution. In this case, the large memory buffer of a digital oscilloscope can be used to store the data. In particular for FFTs, it can be very useful to obtain good spectral resolution over a large frequency range. The DACs could also be used to set reference values for the thyristor converter of the DC load machine. This however has not been realized because the analogue input channels are very noise sensitive. The settings of the DC converter are preferably changed via the digital interface.
A bank of 8 LEDs can be addressed to signal events or software states. They indicate if the control is running or if an error has occurred. Eight bits digital input can be set via a DIP switch. The digital position of the switches can be read by software. To allow more flexible digital I/O, 13 bits can be written or read via buffers. A header provides interface to the digital lines. This can be very useful to test the length of code sections. The rising or falling edges can be monitored by an oscilloscope that are set before and after the code to be timed. Additional digital devices can also be quickly connected and integrated into the control rig.

4.2.7 PWM and Encoder Board (Extension Board)

The PWM generation and the signals from the encoder are managed by a DSP that is specifically optimized for machine control. This is the TMS320F240 fixed-point processor. The F240 is a DSP that comes with a large number of integrated peripherals that are suitable and common in control applications. The DSP includes three 16-bit timers that are easily configured to generate pulse-width modulation (PWM). A watchdog timer module increases safety and can disable the PWM output lines to protect the inverter. A digital pulse encoder can directly be connected to the quadrature unit (QEP) that increases the pulse count and resolution by four via edge detection. Two of the integrated 10-bit ADCs can help to improve the resolution of the rotor position when employing a SinCoder as high-resolution position encoder. A large number of pins for digital I/O is available and a large FLASH memory that allows keeping program code permanently on the chip. The address, data and control lines of F240 and C40 are tightly coupled via the backplane and a dual-port RAM to guarantee a fast communication.
The instruction cycle of the F240 is $50ns$. The FLASH memory also runs at this speed without wait-states. Only the facilities to generate PWM and to read an encoder are

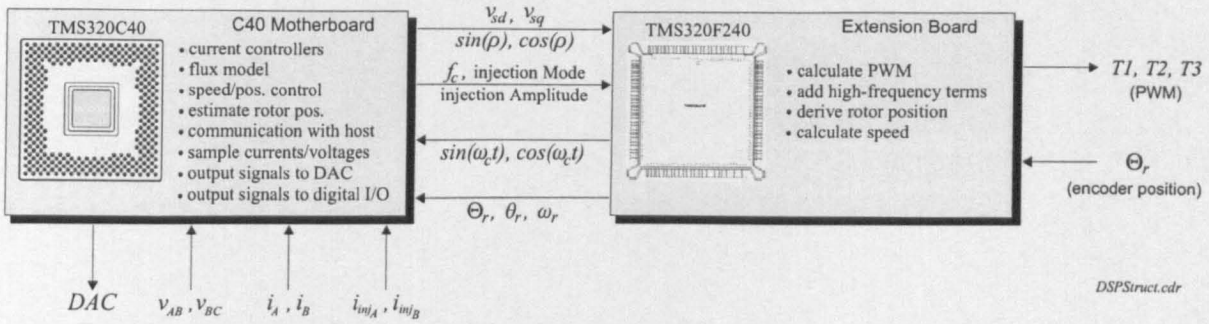

Figure 4.2: *Task allocation between C40 and F240 DSPs*

used on the F240 including some I/O lines for the hardware handshaking with the C40. The F240 code is permanently stored in FLASH memory and includes the following tasks that are also shown in Fig. 4.2:

- communication with the C40 via the dual-port RAM and additional hardware handshaking
- the switching time calculation and PWM generation from the *dq* reference voltages that are provided by the C40
- the injection of *hf* voltages needed for the sensorless control
- reading of the encoder signal to derive rotor position and speed for the C40

To reduce development time, an evaluation module for the TMS320F240 processor was embedded into the rack. This evaluation module comes with a debugger that works similar to that for the C40 but communicates via a serial port of the PC. Software to easily program the FLASH memory is provided and a simple cross-table compiler to generate a simple *common object file format* (COFF) file that can run on the F240. A description of the schematics is given in Appendix D.1. An older version of the PWM generation board using a 8254 timer chip is shown in Appendix D.2.

4.2.8 PWM Interface Board

The generated PWM pulses are sent as differential signals via a cable to an interface box in the inverter. This inverter interface provides the signals for the *Power Board* of the inverter. Optocouplers transfer the signals across an isolation barrier between the galvanically decoupled sides of DSP rack and inverter. A mechanical switch selects if the PWM reference signals are provided by the DSP rack or by the *Control Board* of the inverter. The latter option allows the inverter operation in the original V/f mode of the manufacturer. This can be useful when testing the inverter.

4.2.9 Analogue Bandpass Filters

For the sensorless control, good results were obtained by using analogue bandpass filters instead of digital software filters in the C40 code. This is because the *hf* signals are relatively small compared to the large fundamental signals amplitude. The analogue filtering allows to obtain the *hf* signals at a higher resolution. The input range of the A/D converters can be scaled to the magnitude of the *hf* current signal and does not have to cover the magnitude of the large fundamental. Two filter boards are available where each board comes with four independent channels. Each channel is divided into two sections that can be swapped in order or can be disabled individually. The footprint allows the realization of any type of filter, but only bandpass filters are currently required. The filter centre frequency for different injection frequencies can be adapted by changing a small number of resistors.

4.3 Load Drive

In order to load the sensorless induction machine, a load drive is used. This consists of a *Eurotherm* converter of the 590 series ($45kW$) controlling a DC machine. The converter is a 4-quadrant thyristor converter that consists of 12 thyristors to generate the torque-producing armature current i_a from the mains. The converter is used in torque control mode by setting the limit for the maximum armature current. An additional tacho generator is used for speed feedback, to keep the machine within the settings for maximum speed.
Originally it was planned to interface the PC to the thyristor converter via its digital bus connection. This would have made possible the synchronization of control events of the induction machine and the load drive. Monitoring of status information and data sampling on the converter could have been possible. The digital interface could not be made to work reliably. Therefore the DC load machine and thyristor converter were controlled via a simple analogue interface that limits the possibilities for parameter supervision. The interface signals and the control panel are shown in [107]. The converter is switched on, enabled and set to run via three switches on the control panel. Two potentiometers allow the setting of maximum armature current and speed. For torque-control mode, the maximum reference speed has to be set high enough to ensure the armature current demand remains at its maximum value. Further parameters have to be set or read via the LCD display of the converter. The specific parameters and settings that are required for the control of the DC load machine are also documented in [107].

A three-phase coil was placed between the mains side of inverter and thyristor converter to smooth the currents. A three-phase relay is placed near the converter that

disconnects the thyristor bridge from the mains supply. Since the DC load machine is usually operating in the generating region and feeding power directly into the inverter and induction machine, semiconductor fuses needed to be placed in the armature circuit to protect the converter. To monitor the armature current, a LEM current transducer *LT 100-S/SP90* is mounted to the power connection between thyristor converter and load machine as shown in the schematic in Appendix D.11.
Additional contactors are located in a safety box. This includes the main power switch and three circuit breakers that provide overcurrent and thermal protection of the machines and semiconductors switches. The circuit breakers can be used to manually disconnect the induction machine, load drive or the cooling fan from the mains. The fan is mounted onto the load machine and is driven by a three-phase $0.75kW$ induction machine.

4.4 Software

Software was written for three different platforms. The main control program is running on the C40. The F240 requires hardware-related software that is written in assembler and the graphical user interface on the PC is programmed in a visual object-oriented programming language.

4.4.1 Control Program

The control software for the C40 was written entirely in the high-level language *C*. It consists of the high-priority interrupt routine for the current control loops. The communication with the F240 takes place, currents and voltages are read from the A/D converters, data is sent to the D/A converters, the *hf* currents are demodulated, communication and monitoring takes place. The data and signal monitoring allows the inspection of internal variables that are first buffered in fast internal memory before sent to the host for graphical visualization and further analysis. Signals are sampled with the resolution of $200\mu s$ that is also the sampling period of the current loops. This main interrupt is started by an external interrupt request that is triggered by the PWM generator of the F240. The second interrupt routine that uses an internal timer has a lower priority and runs at $600\mu s$. The outer control loops such as the speed or position control, the flux model and the algorithms to estimate the rotor position are calculated.

The software for the F240 is written in assembler to achieve maximum performance. The disadvantage of the fixed-point architecture is that signals have to be scaled appropriately to efficiently make use of the available 16-bit integer resolution. This

consumes processing and development time. The exchange of data with the C40 is via a dual-port RAM. The communication protocol makes use of low-level routines to ensure fast user control over the C40 and F240 processors. A checksum and a number of status variables are transferred next to the reference voltage, voltage injection parameters and speed and rotor position data. The latter two are sent from the F240 to the C40. Semaphores are used to avoid clashes when accessing the data. Error counters make sure that the available data is valid and that both of the two processors are still working correctly. The F240 then transforms the voltage demands to three-phase voltages, adds the voltage injection and determines the PWM switching times. The rotor position is read. Depending on the type of encoder connected, a routine to enhance the rotor position resolution is executed. The rotor speed is then calculated.

4.4.2 User Interface

The user interface running on the PC is written using C++-Builder. It is a typical graphical user interface (GUI) and simplifies overview because the structure is clearer and more comfortable to use than a text-based interface. User action is possible via mouse or keyboard. Some of the important features that are part of the GUI are:

- *On-line debugger:* allows to change and inspect variables during run-time. All global variables on the C40 and F240 are accessible and can be monitored, checked or changed. The address of the variable is indicated in one column. Type and current value are shown in other columns and can both be changed. The resolution of the update in within 10 - 20Hz.

- *Monitor:* any global variable can be selected and sampled at different resolutions and for a selected length. The finest resolution allows to sample every 200μs. Monitoring can be triggered by different events such as a commanded speed or position change or a modification of a variable within the debug window. The monitor displays up to 16 variables simultaneously in a graphical window. The monitored variables are plotted over time that simplifies data visualization. Curves or traces can be scaled, shifted or disabled easily. Zooming into the plots or panning within the window are possible. A cursor function allows to determine absolute time and amplitude or the differences between two points or the frequency.

- *MATLAB interface* and output for various graphical formats and data file types: MATLAB can be linked into the GUI to receive data directly. This makes it possible to use the same names for the variables in the data-analysis as in the control software. MATLAB comes with a large library of functions that simplify the post-analysis of the monitored data. From the plot window, the user can

plot directly to a printer or into a graphical file format. Data can be saved as data file on disk in various ASCII or binary data formats.

- *Software oscilloscope:* is a graphical window that allows to monitor two slow changing signals on-line. The data comes from the two first variables in the debug window. Updating is limited to about 20Hz and can be adjusted. The signals can be scaled in amplitude and individually disabled.

- *DAC interface:* allows to select or scale signals at run-time for the output via the four channel digital-to-analogue converter to an external oscilloscope. The variable can be any global variable in the C40 code. Amplification is possible to adjust optimally for the given output range of the DAC.

- *Control panel* for easy access to the main control parameters: Reference speed, position and direction for the machine can be changed for example. A fixed value can be imposed or the reference value can be changed gradually. Important feedback values are displayed such as the measured speed, position, torque and currents.

- *Parameter panel:* for setting machine and control parameters. Machine constants such as the rotor time constant T_r can be set or the number of pole pairs and maximum allowable speed. The encoder pulse number can be specified. These panels are useful to check for correct drive initialization and to get quick access to standard parameters of the machine control algorithms.

- *ADC calibration:* can be performed on-line but with the control being switched-off. The averaged converter output is shown. Offset values can be typed in for correction.

- The GUI allows to change from speed control to position control or sensorless control.

- The switch from V/f to Vector Control mode has to be set via compiler switches in the C40 code. The GUI displays the current setting and adjusts menus and user interfaces.

- *High frequency injection:* parameters can be adjusted easily via a menu such as amplitude, frequency or mode (rotating, pulsating, dq or $\alpha\beta$).

- *Harmonic Compensation:* parameters can be updated via a database or loaded from a file. The table for *Space-Modulation Profiling* (SMP) can be loaded via a MATLAB interface.

- *Auto-Sequencing generator:* provides a synchronized arbitrary reference signal for running the machine. This is useful when a predefined sequence of reference changes in e.g. speed or position is required. The operation is possible in one-shot or continuous mode where the reference data is read cyclically.

The flexibility for data acquisition and machine control derives from the communication protocol between the PC and C40 that is documented in [108]. A synchronous and an asynchronous communication exist via the dual-port RAM. The speed of the communication is limited by the relatively slow ISA bus that does not have bus-mastering capabilities and by the software drivers that are required for the multitasking operating system.

4.5 Sensors

In practice, an inverter will always come with overvoltage and overcurrent protection that requires the measurement of voltages and currents. The required sensors for Vector Control always include two current sensors and depending on the flux model, either a position/speed encoder or two voltage transducers. The instantaneous, efficient and dynamic control of the induction machine demands that the sensors can measure the input signals with high resolution and accuracy.

4.5.1 Current Measurement

The conventional field-orientated control (FOC) requires the measurements of at least two phase currents. In practice this will be the line currents, measured at the output terminals of the inverter. There is no need to measure the third line current as in a balanced system this current can be derived from the negative sum of the other two currents (see equation (2.5)).

To protect the measurement and control circuits from the high machine currents, a galvanic decoupling within the current transducer is required. Often, LEM current transducers are used. Here the current is measured via a Hall-element and the output is a low voltage proportional to the current in the coil. A cheaper method is to measure the voltage drop across a shunt resistor. An isolation amplifier with a high common mode rejection (CMR) such as the HCPL-7800 provide an isolated voltage output proportional to the current through the shunt. Both methods have a sufficiently high bandwidth and are also accurate and precise. LEM current transducers are used in the experimental rig.

Alternatively to measuring the line currents near the terminals, the DC-link current can be measured. With the knowledge of the PWM switching state, the phase currents can be calculated [109, 110] with the advantage that only one current transducer

is needed. This method however can get problems when the PWM pulses are short. This is because the currents need time to settle down after a switching event. There might not be enough time to measure the steady-state current before the next switching event occurs.

In a practical inverter drive system, the currents are distorted due to the voltage switching. The resulting current spikes are relatively short but can be of a large amplitude. Machine control requires the measurement of the fundamental or 'mean' current as only this contributes to the useful torque production. Filtering the currents is one solution. Due to the spikes, the filter cutoff frequency needs to be relatively low. In practice, a compromise has to be found between smoothing the current signal and obtaining a measurement of the instantaneous current. A low cutoff frequency also means a high and unwanted signal propagation delay. A filter not only gives delay for the control loop, but additionally introduces a d and q-axis cross-coupling [7,111,112]. A good compromise for the cutoff frequency is $1/5^{th}$ of the PWM frequency but even a cutoff frequency of half the PWM frequency would still cause a significant time delay, comparable to the control period [39,101,113].

A solution is the synchronized current sampling, also called synchronized simultaneous sample and hold (S^3H) [39,101] that is used for the experimental rig. All currents are sampled at the same time, that is a suitable sampling point within the switching period. When using symmetric PWM, this will be the period centre point. No filter is required to perform the typical anti-aliasing. A lowpass filter can however still be useful, designed to suppress high frequency noise only. The cutoff frequency will then be a multiple of the PWM frequency.

Assume a rectangular PWM voltage signal $v_s(t)$ of amplitude U_s and period $2T_p$ that can be described by a Fourier-series.

$$v_s(t) = \frac{4}{\pi} \cdot U_s \sum_{k=1,3,5,\ldots}^{\infty} (-1)^{\frac{k-1}{2}} \cdot \frac{1}{k} \cdot \cos\left(\frac{2\pi k \cdot t}{2T_p}\right)$$

This series shall be symmetrical to the origin of the coordinate system (see Fig. 4.3). The transfer function $H(s)$ of the electrical circuit of the machine can be approximated by a first order lag with time constant T_f. The current output $i_s(t)$ will then be a mean current $i_m(t)$ with a superimposed high-frequency ripple $i_t(t)$ due to the PWM. Ideally, the PWM period $2T_p$ ($T_p = 1/f_p$ is the pulse period where f_p is the pulse or switching frequency) is much smaller than T_f. The first order lag will then cause a phase shift of 90° for all harmonic components of the ripple current $i_t(t)$ as shown in the right plot of Fig. 4.3. The figure shows the bode plot for the transfer function $G_p(s) = 1/(\sigma L_s s + R_s)$, for $R_s = 0.19\Omega$ and $\sigma L_s = 8.553mH$. The phase can be

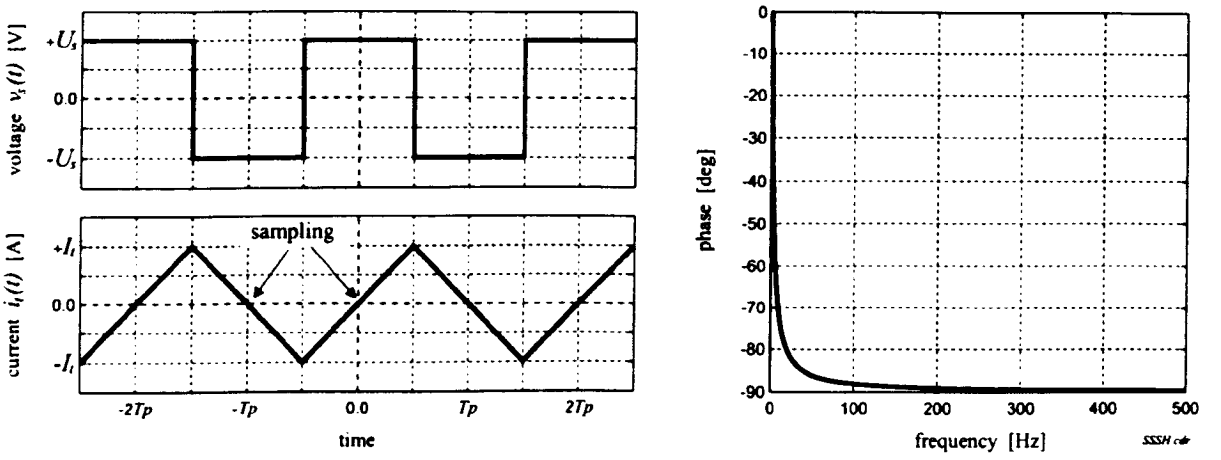

Figure 4.3: *Voltage PWM pulses and resulting current (left). Bode plot of first order lag (right)*

considered constant and at $-90°$ from frequencies above 500Hz. The current $i_t(t)$ then has a triangular shape. The current output written as a Fourier-series is:

$$
\begin{aligned}
i_s(t) &= i_m(t) + i_t(t) \\
i_s(t) &= i_m(t) + I_t \sum_{k=1,3,5,\ldots}^{\infty} \frac{1}{k} \cdot \cos\left(\frac{2\pi k \cdot t}{2T_p} + k \cdot \phi\right), \qquad \phi = -\pi/2 \\
&= i_m(t) + I_t \sum_{k=1,3,5,\ldots}^{\infty} (-1)^{\frac{k-1}{2}} \cdot \frac{1}{k} \cdot \sin\left(\frac{2\pi k \cdot t}{2T_p}\right)
\end{aligned}
$$

The function $i_t(t)$ is zero in the origin of the coordinate system with a rising slope. The 90° phase shift of the plant has converted the cos-terms of $v_s(t)$ to sin-terms in $i_t(t)$. The idea of S^{3}H is to select the sampling instance t_n so that all harmonics of $i_t(t)$ are zero with $i_t(t_n) \stackrel{!}{=} 0$. This can easily be achieved by sampling in the origin and multiples of the period $2T_p$ at $t_n = n \cdot T_p$ for $n = 0, 2, 4, \ldots$ or for $n = 0, 1, 2, \ldots$ if the zero crossing of the negative slope of $i_t(t)$ is to be included. This is the centre point of the PWM if deadtime is not considered.

The current sampling is shown in Fig. 4.4 for the symmetric machine. The real current has spikes during the voltage switching and a triangular shape due to the rectangular PWM waveform. The step-like signal is the sampled current and the smooth line is the mean or fundamental current that is obtained by post-process filtering. In the bottom left of Fig. 4.4, the v_{AB} and v_{BC} line-to-line voltages are printed with the PWM centre point indicated by an arrow.

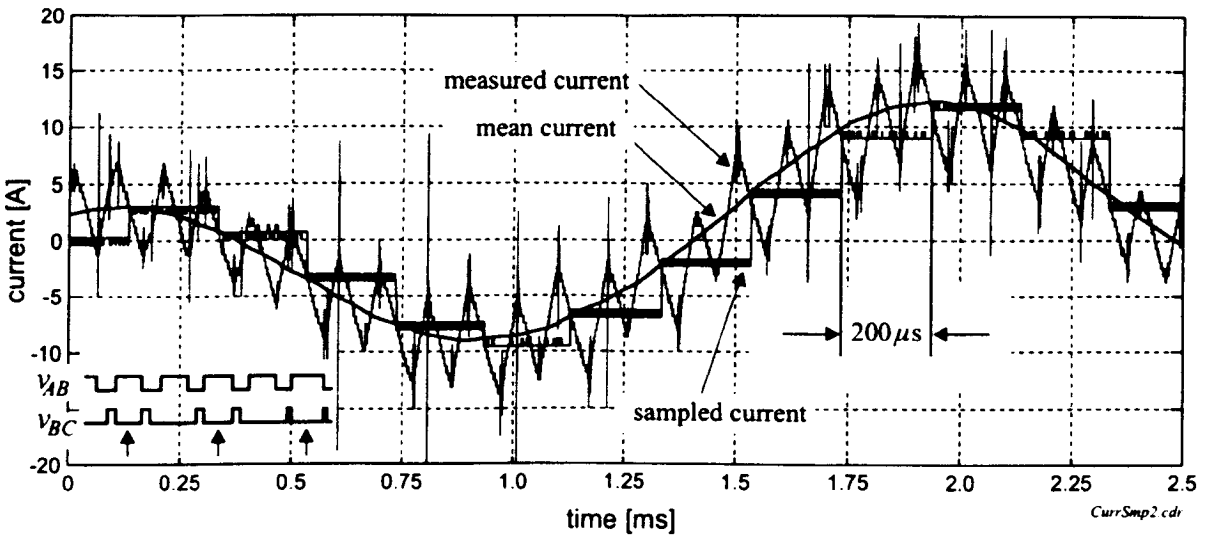

Figure 4.4: *Real and mean i_a line current with sampling points*

In the signal-conditioning path for the acquisition of line currents offsets in the measured currents cannot be avoided. These will be removed before starting the drive by observing the channels and forming an average. Ideally, this average should be zero, otherwise it will act as a constant offset for any further sampled value. Still, small errors can remain. It can easily be shown [114] that an offset error on the currents will cause a torque pulsation at the synchronous frequency f_e with $\Delta T_{el} = f(\omega_e)$. This is because an offset in the $\alpha\beta$ currents introduces Δi_{sd} and $\Delta i_{sq} = f(\rho)$ components in the dq frame where the latter directly has an impact on the torque.

A scaling error in the acquisition of currents will cause a torque ripple at twice the synchronous frequency [114] with $\Delta T_{el} = f(2\omega_e)$. A transformation from the stationary frame into the dq frame creates an additional component $\Delta i_{sq} = \Delta i_{s\beta} \cos(\rho)$ where $\Delta i_{s\beta}$ and ρ are a function of ω_e.

In practice, these errors will be small. Current scaling was no problem in the laboratory drive. Once calibrated, it could be verified by performing random checks, that the scaling had not changed. Offset can be a problem, as the LEM current transducers can keep a remanence, in particular for the case of a drive shut-down due to overcurrent. Offset correction at startup is used to reduce the error. The accuracy obtained is within the measurement uncertainty due to noise and can be less than 61 increments per million.

4.5.2 Voltage Measurement

Determining the instantaneous value of the line-to-line voltages is a difficult measurement problem due to the discrete nature of the voltage pulses. When using an

analogue lowpass filter, the cutoff frequency usually has to be quite low (around 300 to 650Hz) to remove the switching harmonics, that are multiples of $1/(2f_p) = 5k$Hz, from the fundamental voltage. Typically, a lowpass filter of order ≥ 2 is the preferred choice [22] where the cutoff frequency is between $1/8^{th}$ to $1/15^{th}$ of $1/(2f_p)$. When operating the drive at higher speeds, the inherent propagation delay might be unacceptably high such that care has to be taken when performing simultaneous calculations on measured voltages and measured currents. Device tolerance can also be the cause for unaccurate and unsymmetrical frequency characteristics of different acquisition channels. There are a number of alternative solutions:

- The reference voltage can be used instead of the measured voltage. This works well for higher speeds and avoids the difficulties with the filter delay. Difficulties arise in particular when operating in the low-speed range. As the absolute value of the stator voltages is small, the difference between reference and actual voltage becomes more dominant that is mainly caused by the inverter deadtime.

- The voltage can be determined by using a high frequency timer to measure the realistic pulse width [101]. This timer value is proportional to the mean voltage over one switching period. Variations in the DC link voltage are not considered and will cause an error if not measured separately.

- Direct integration of voltage pulses by determining the voltage-time areas can give a good measure of the real voltage applied to the machine. The voltage pulses are integrated using analogue components. The A/D conversion of the integrator output will be synchronized to the PWM. The integrator is then reset after each PWM period [101]. The maximum delay is only one PWM period an thus has a constant phase delay. Practically, this circuit is configured as a twin module with the modules used alternately. While one is being read or in reset, the other integrates.

The measurement of the DC-link voltage can be important for some of the methods above but also can be justified for optimizing the PWM switching times (Section 2.2.6). The knowledge about changes in the DC-link voltage V_{dc} can be used to adjust the modulation index m for the PWM. The result is an automatic and fast compensation without affecting the dynamics of the current controllers.
Currently, only a first order lowpass filter with a cutoff frequency of 340Hz is used for the two voltage channels since the fundamental voltages are not required for the control.

4.5.3 Measurement of the Rotor Position

To determine the rotor position, an incremental position encoder is used. Typical incremental encoders come with 100 - 5000 sector pairs or lines per revolution. The encoders for the *TRANSPUTER rig* and the *DSP rig* come with 2500 and 3000 lines per revolution, respectively.

The lines of the encoder are counted to determine the position angle. If the level ratio of the lines is symmetric, the pulse transitions can be detected to increase the resolution. This so-called quadrature encoding pulses (QEP) quadruples the original resolution. From the chronology of the two pulse streams, it is possible to determine the direction of rotation. The encoder interface with the QEP-unit is part of the integrated peripherals of the F240 processor. An extra code slot for the zero pulse is available. Once per revolution this signal line changes the logic level.

At the initial stage, the rotor requires half a revolution in average, until the zero marker pulse occurs and the absolute position is identified.

The resolution for an incremental encoder is $\Delta\theta_r = 2\pi/(4 \cdot N)$ [rad] where N is the number of sector pairs or lines of the encoder and the factor 4 is due to QEP. For the incremental encoder used in the experimental rig, this is 0.03° for $N = 3000$ lines. To avoid the installation of a separate speed sensor, the rotor speed is derived from the position signal. The position values are differentiated digitally in the processor.

The rotor speed is $n_r = \frac{\Delta n \cdot 60}{4 \cdot N \cdot T_s}$ [rpm], where Δn is the difference in increments between two samples and T_s is the sampling interval. A quantization error exists due to the discrete number of lines. The speed resolution decreases for low speeds where Δn becomes very low because the pulse quantization error remains constant whereas the number of pulses in the sampling interval decreases. The sampling time T_s can then be increased so that Δn becomes larger. Obviously, the speed will be updated less frequently which will reduce the dynamics of the drive because of the phase shift between the real, instantaneous and the measured speed.

In the experimental drive, the measured speed is calculated for an interval $T_s = 600\mu s$ and then smoothed using a lowpass filter. The measured speed is now an average over 14 milliseconds. The steady-state speed error therefore is $\Delta n_r = \pm\frac{60}{4 \cdot N \cdot T_s} = \pm 0.357$rpm that is suitable for low speed operation as needed for this research. A T_s of $5ms$ is used in the *TRANSPUTER rig* and results is a resolution of ± 1.2rpm that is a better compromise for more dynamic speed operation.

A popular approach to increase the speed resolution is to combine the previous method with pulse width measurements. For lower speeds, where the number of encoder pulses is low within the measurement interval, the time between two pulses is determined using a high frequency clock. The encoder pulse width measurement is practically limited to a low speed since the number of clock ticks between two encoder pulses decreases for higher speeds where the quantization error remains constant.

A similar approach is a merger of both ideas. The pulse difference Δn within the measurement T_s is determined and also the exact time between the first and last pulse, the pulse period T_n. For low speeds, T_n might be only half of T_s because only two pulses occurred. Since the ratio $\Delta n/T_n$ has been determined more accurately, the speed resolution is improved. The speed signal needs to be corrected if notch and bar of the encoder disk do not have the same width.
The *DSP rig* additionally allows the connection of a SinCoder to obtain the improvement of speed resolution at both high and low speeds and this with sampling times T_s of less than $1\mu s$ [39,115,116]. Two sinusoidal analogue signals with 1024 periods per revolution are transmitted via twisted wires from the encoder to the F240 controller. By combining the digital position information (QEP) with an analogue interpolation using two 10-bit ADCs of the F240, the position resolution can be equivalent to that of an incremental encoder with 262,136 lines. This position signal is therefore over 250 times more accurate than that of the used incremental encoders and the same improvement is valid for the derived speed signal. In addition, the SinCoder can be configured at start-up to act like a resolver with one pole pair to allow the detection of the initial position.

4.6 Electrical Machines

This section gives an overview of the different induction machines and the load DC machine that are part of the rig and used for the research. The three rotors were used to test different aspects of *hf* rotor position detection. Two of the rotors had an asymmetric design, the third is a symmetric rotor. The DC machine is a standard industrial model and acts as a load. It comes with its own converter and control.

4.6.1 Machine Rotors

All three rotors are of the same size with a radius of about 110mm and for $30kW$ induction machines. The same size enables the comparison of drive performance and results of the sensorless techniques. The control only required minimal changes for the different machines.

Rotor #1 – Asymmetric Double Cage

The first rotor used is based on a double-cage design and was built by Cilia [22]. Fig. 4.5 shows the first asymmetric rotor with an engineered circumferential resistance variation in the outer cage. Alternatively, it also can be the outer section of a deep bar cage type. The rotor had been assembled in the departmental's workshop, the laminations were those of a standard double cage machine and supplied by the

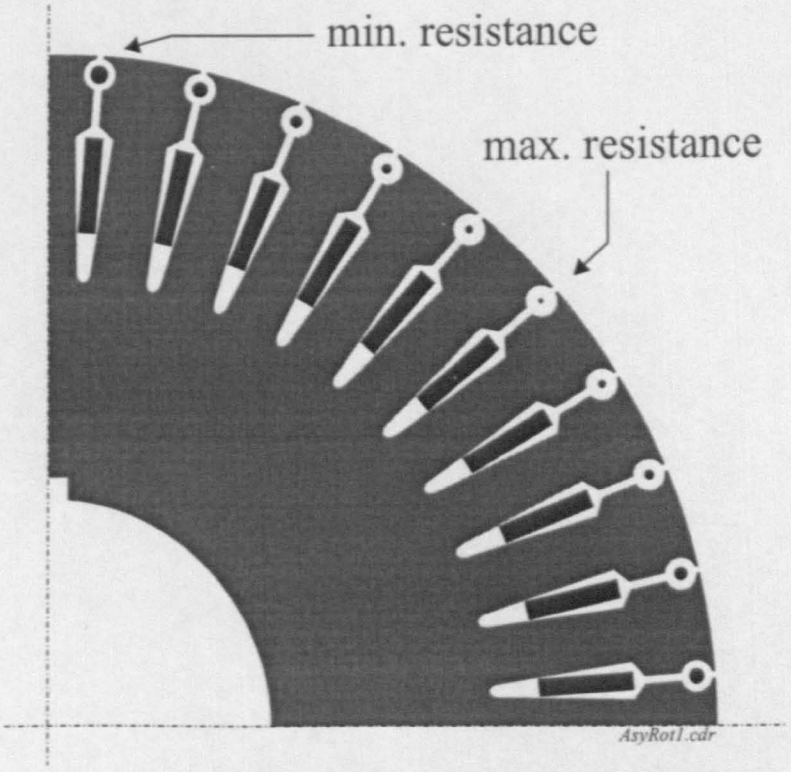

Figure 4.5: *Cross section of rotor lamination for Rotor#1*

manufacturer *Brook Crompton Ltd.* The design including the sinusoidal resistance variation over the circumference had been chosen so that standard manufacturing techniques such as lamination punching and aluminium casting could be used. For manufacturing simplicity, copper had been used for the inner and outer rotor bars. Due to the higher conductivity of copper compared to aluminium, the copper bars in the inner rotor slots required less cross-sectional area than the equivalent casted aluminium bars to yield the same rotor resistance. Fig. 4.6 shows the mechanical dimensions of the rotor slots. The self-inductances for the geometry in Fig. 4.6 are

$$\begin{aligned} L_s &= L_0 + l_s \qquad (l_s = L_{s\sigma}) \\ L_{r1} &= L_0 + l_{r12} + l_{r1} \\ L_{r2} &= L_0 + l_{r12} + l_{r2} \\ L_{r12} &= L_0 + l_{r12} \end{aligned}$$

The total fluxes are a function of the leakage fluxes or can be expressed as a function of the currents:

$$\underline{\psi}_s = \underline{\lambda}_s + \underline{\psi}_0 = l_s \underline{i}_s + L_0(\underline{i}_s + \underline{i}_r)$$

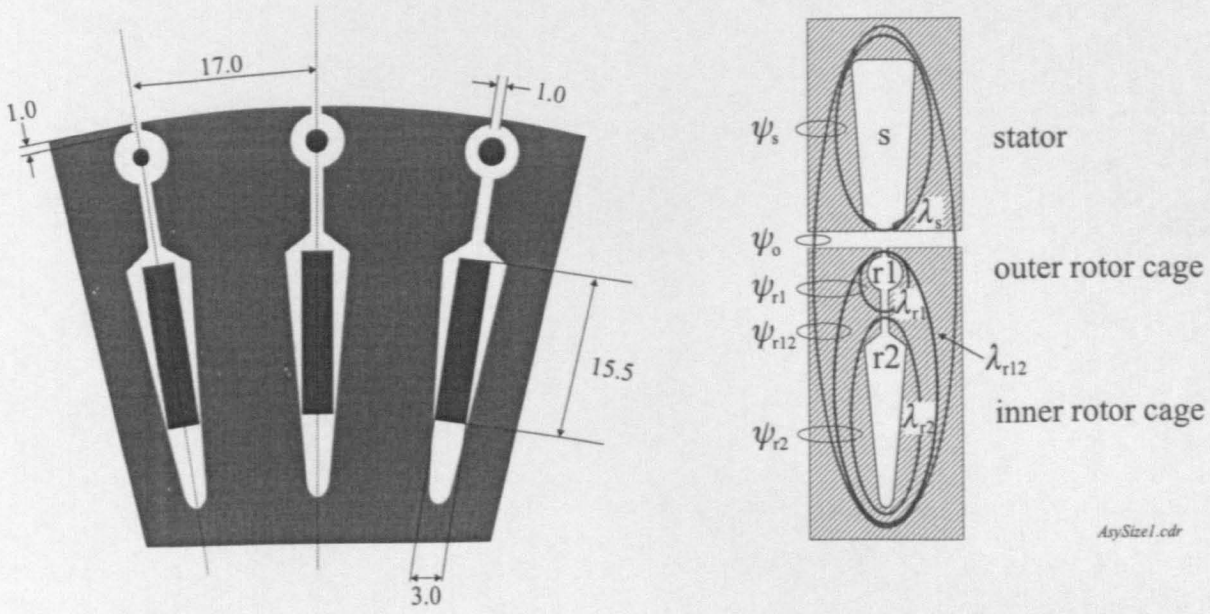

Figure 4.6: *Mechanical dimensions for the double cage rotor#1 (all dimensions in mm) and magnetic equivalent circuit with flux linkages [22]*

$$\begin{aligned}
\underline{\psi}_{r1} &= \underline{\lambda}_{r1} + \underline{\lambda}_{r12} + \underline{\psi}_0 = l_{r1}\underline{i}_{r1} + l_{r12}\underline{i}_r + L_0(\underline{i}_s + \underline{i}_r) \\
\underline{\psi}_{r2} &= \underline{\lambda}_{r2} + \underline{\lambda}_{r12} + \underline{\psi}_0 = l_{r2}\underline{i}_{r2} + l_{r12}\underline{i}_r + L_0(\underline{i}_s + \underline{i}_r) \\
\underline{\psi}_{r12} &= \underline{\lambda}_{r12} + \underline{\psi}_0 = l_{r12}\underline{i}_r + L_0(\underline{i}_s + \underline{i}_r)
\end{aligned}$$

A background to double-cage and deep-bar rotors and about advanced motor models can be found in [117–119]. The theory covering optimal control of a double-cage machine can be found in [22] termed *Common Rotor Flux Orientation* or in [38] termed *Pseudorotor Flux Orientation.*

The rotor has a total of 40 rotor slots and a skew of approximately 0.8 times the distance between two rotor slots over the rotor length. The length is about 225mm and the diameter around 220mm. The sinusoidal variation in resistance in the outer cage is achieved by changing the diameter of the copper wires. The following table lists the selected wire sizes:

Resistance value [Ω]	Crossectional Area [mm^2]	gauge of copper wire (standard wire gauge = s.w.g)
0.98	9.00	9
1.84	6.63	11
4.09	4.67	13
6.87	2.63	15
9.12	1.59	17
9.98	0.81	19

There are four sinusoidal variations over the whole 360 degrees mechanical . Practically, the resistance variation is not fully sinusoidal. This is due to the uneven distribution of the standard wire gauges that had to be used. No negative influence on the *hf* modulation due to this deviation from the sinusoidal shape could be discovered.

The design idea behind rotor #1 is that

- the outer cage is of a higher resistance than the inner cage and
- the leakage inductance of the outer cage is much lower than that of the inner section due to the magnetic geometry. The inner leakage inductance dominates therefore the combined bar leakage.

For a high frequency (*hf*) voltage signal, the inner section reactance is therefore large and *hf* currents are induced in the asymmetric outer cage. It is these currents that induce the position dependent stator currents.

For the fundamental voltages, the inner cage impedance is significantly lower than that of the outer section. Currents at the slip frequency flow therefore in the main inner bars in the normal manner. A small slip-dependent torque ripple will exist that stems from the slip frequency currents that flow in the outer cage. This has been further examined in [22].

Rotor #2 – Asymmetric Single Cage

There are two basic ideas behind the design of this asymmetric rotor. Firstly, rotor teeth saturation is reduced by opening the rotor slots. Secondly, a better decoupling between the single cage and the outer asymmetric cage is aimed at, when compared to rotor #1. This reduces the interaction of the fundamental frequency excitation with the outer asymmetric cage and also increases efficiency due to a reduction in copper losses induced in the outer cage by inverter harmonics. In the new design,

the asymmetric cage is embedded in the rotor surface between the main cage bars of the standard single cage rotor. The common-flux leakage between the two cages will therefore be reduced. The leakage of the asymmetric cage is also designed to be reduced when compared to the double-cage design.
The second rotor is a single cage rotor. The number of rotor slots is 58. Practically, no rotor slot harmonics will exist (see Section B and [120, 121]). For manufacturing

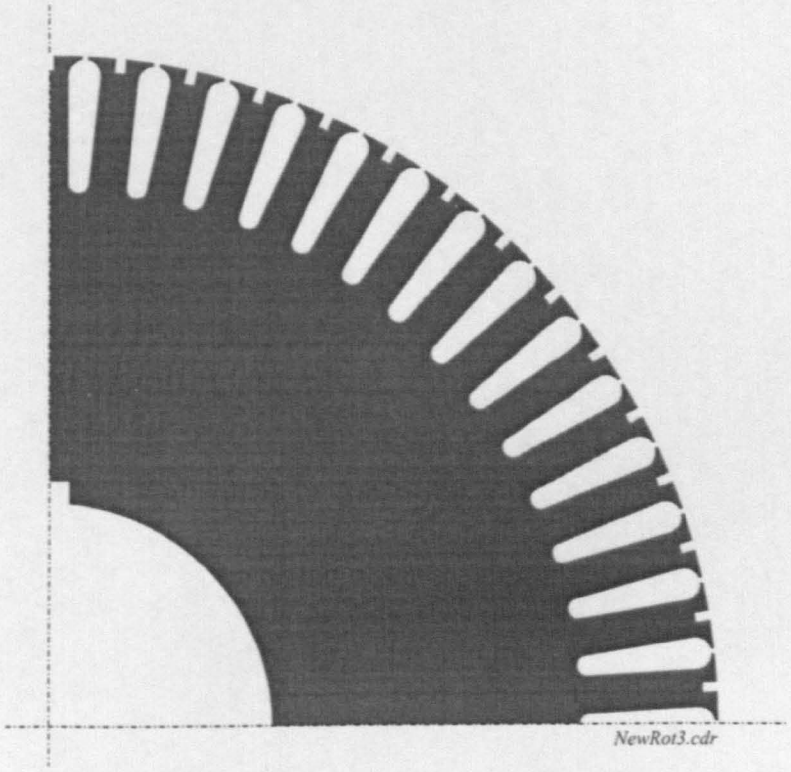

Figure 4.7: *Cross section of rotor lamination for Rotor#2*

reasons, an unskewed rotor was chosen. Similar to rotor #1, an additional outer cage with a resistance variation has been implemented. Fine slots were cut into the circumference that were filled by copper sheets. These are offset to the rotor bars by half a slot pitch.

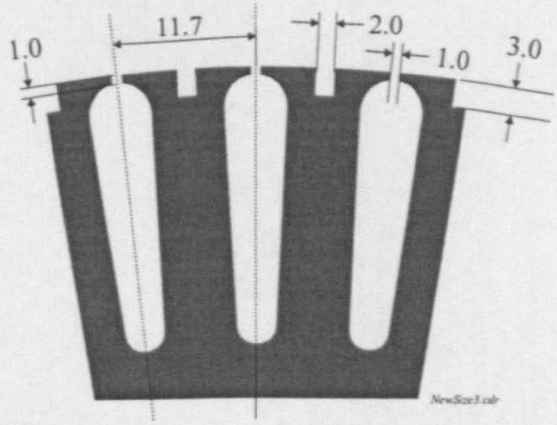

Figure 4.8: *Mechanical dimensions for modified single cage Rotor#2*

no.	times	resistance [Ω]	thickness [*mm*]	depth [*mm*]
1:	4	1.458	2.100	3.382 mm (1x 78, 1x 8)
2:	4	1.756	1.803	3.095 mm (1x 78)
3:	4	2.346	1.350	3.171 mm (1x 57)
4:	4	3.191	0.993	2.827 mm (1x 47)
5:	4	4.264	0.743	2.762 mm (1x 36)
6:	4	5.516	0.574	3.075 mm (1x 25)
7:	4	6.876	0.461	3.083 mm (1x 20)
8:	4	8.277	0.383	3.410 mm (1x 15)
9:	4	9.671	0.328	2.923 mm (1x 15)
10:	4	10.977	0.289	3.219 mm (1x 12)
11:	4	12.161	0.260	2.905 mm (1x 12)
12:	4	13.129	0.241	3.229 mm (1x 10)
13:	4	13.860	0.229	3.059 mm (1x 10)
14:	6	14.313	0.221	2.962 mm (1x 10)

The slots are 3mm deep to provide space for the copper bar fillings. All copper bars are about 3mm deep as can be seen from the table. A compromise had to be found, since standard copper laminations were to be used and the thickness could not be chosen arbitrarily. To change the resistance, ideally only the width is changed whereas the depth should be kept constant. This is because a variable depth would change the inductance. The copper bars are centered in the slot. Calculated depths $>$ 3mm were reduced to 3mm. With the designed four sinusoidal periods over the whole circumference, there are $58/4 = 14.5$ rotor slots per period. The distribution of the 14 different sizes over 180° mechanical of the rotor can be seen in Fig. 4.9. The first column in the table shows the bar number, the second column indicates the

quantity required of every bar number. Since there are four periods of rotor saliency implemented as can be seen on the right of Fig. 4.9, most bars are needed four times. The resistance distribution within one period is not fully symmetrical due to the odd number of slots per pole. This explains why bar no. 14 is needed more than four times. The resistance changes between $R_{min} > 0$ and R_{max}. This is $R_{min} = 1.458\Omega$ for bar no. 1 and $R_{max} = 14.313\Omega$ for bar no. 14 when referred to the stator. The resistance is calculated on the basis of [22].

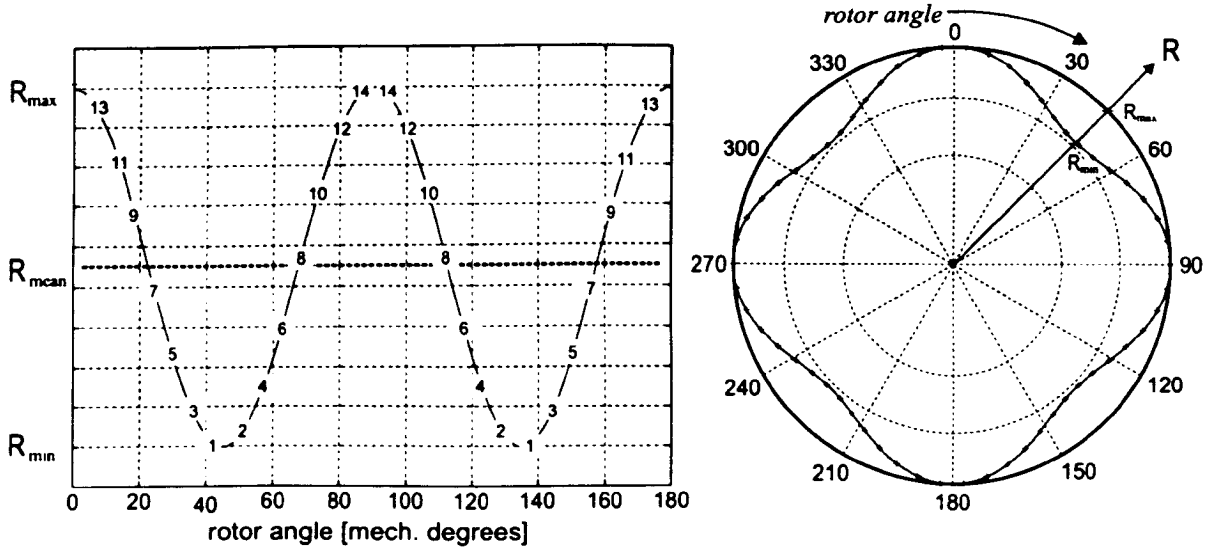

Figure 4.9: *Sinusoidal distribution of copper bars for Rotor#2 with bar number*

Rotor #3 – Symmetric Single Cage

The third rotor examined is a standard industrial single cage rotor with a total of 56 rotor slots. To reduce the effect of bridge saturation, the slots had been opened by cutting 1mm deep and 1.8mm wide as can be seen on the left of Fig. 4.10. This also ensured a consistent slot characteristic since the aluminium filling and alignment of the laminations was slightly uneven. The rotor itself is typical with a cast aluminium filling, pressed into the open areas of the laminations. The size is the same as that of rotor #1 with a length of 225mm and a radius of 110mm. The rotor is unskewed, to allow for easier cutting of the slot bridge and increased amplitude of the rotor slot harmonics [120, 121] (see Section B).

For a *hf* signal, the rotor slots act similar to a variation of the air-gap length. The variation in reactance causes a modulation in the induced *hf* currents. These can be extracted from the stator currents to derive the (incremental) rotor position.

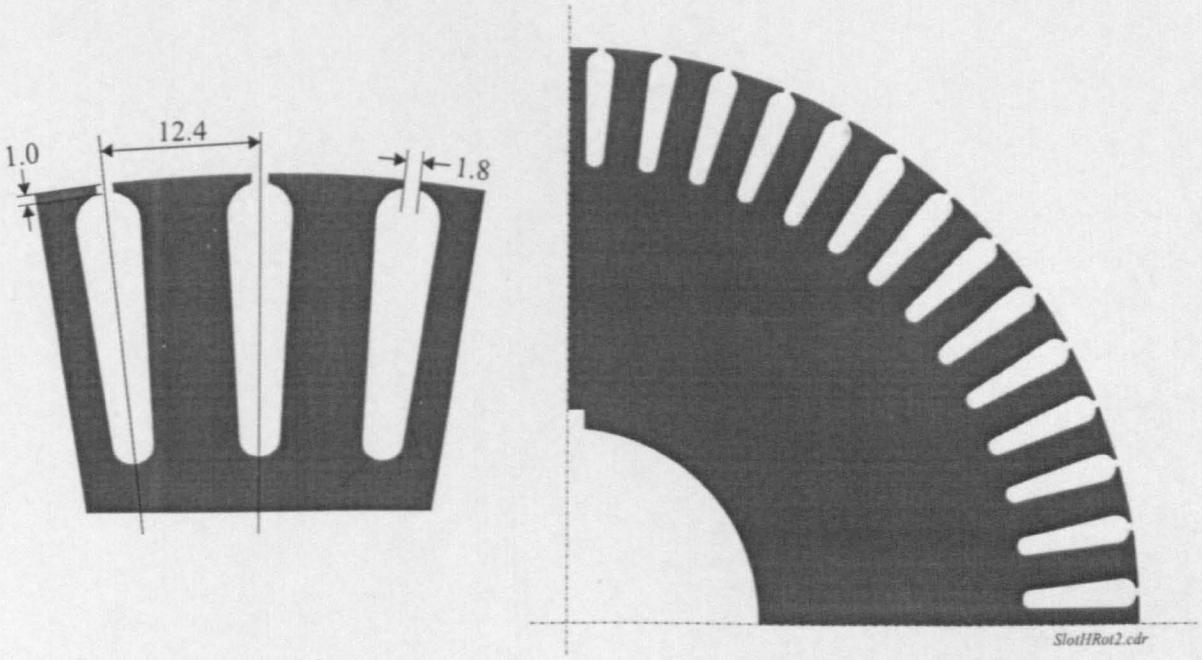

Figure 4.10: *Cross section of rotor lamination for Rotor#3 and mechanical dimensions (in mm)*

4.6.2 Machine Parameters

For Vector Control, the basic machine data provided by the manufacturer (see Appendix C.1.1) is not sufficient. The electrical parameters σL_s, R_s and time constant T_r are required. The mechanical parameters are needed for the layout of the speed loop. The parameters for rotor #1 (asymmetric double cage) have been determined in [22]:

- Double cage parameters:

stator:	L_s	=	0.1191H,	R_s	=	0.19Ω
mutual:	L_o	=	0.1171H,			
common rotor:	L_{r12}	=	0.1208H,			
outer rotor:	L_{r1}	=	0.1208H,	R_{r1}	=	9.98Ω
inner rotor:	L_{r2}	=	0.1272H,	R_{r2}	=	0.39Ω

The rotor is a double-cage design. The electrical parameters of the outer cage in relation to those of the inner cage are important for the response to the *hf* injection [22]. For field orientation, a control theory for double-cage machines is presented in [22]. For simplicity, the theory of a single-cage machine can be

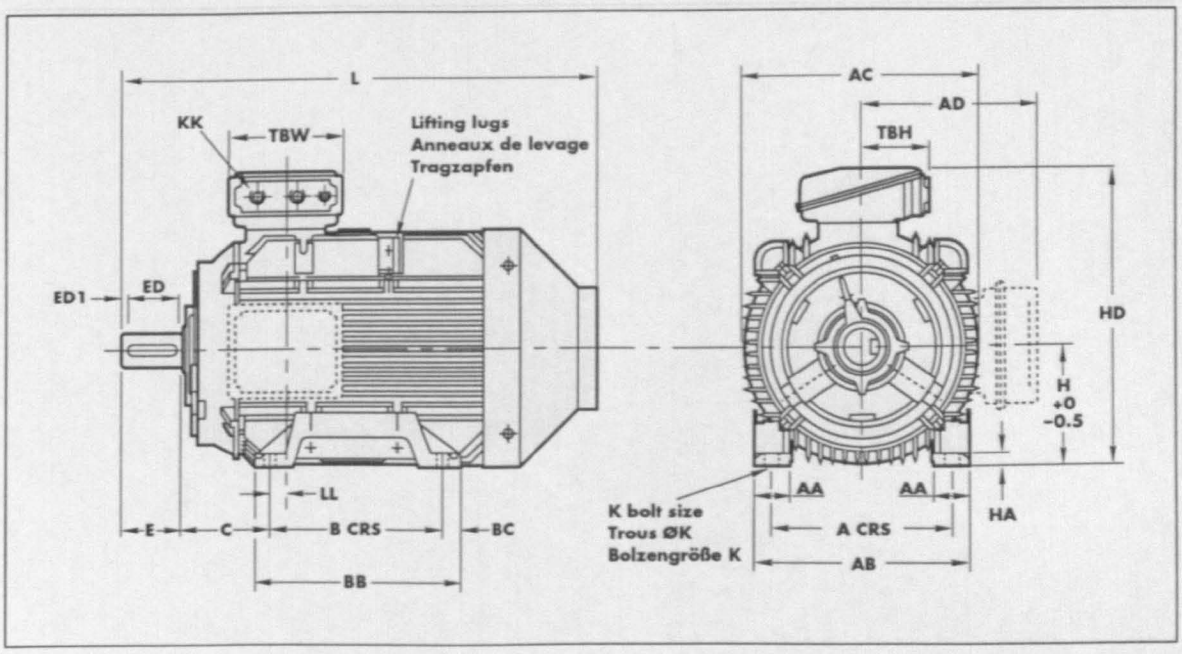

Figure 4.11: *Manufacturer's schematic for* $30kW$ *induction machine*

applied. This is possible, since the slip is usually small under Vector Control. The fundamental currents can then penetrate deep into the rotor and the inner cage then dominates the characteristic of the rotor.

- Equivalent single cage parameters:

stator:	l_s	=	$2.0mH$,	R_s	=	0.19Ω
mutual:	L_o	=	$117.1mH$,	R_o	=	355.18Ω
rotor:	l_r	=	$7.1mH$,	R_r	=	0.28Ω

- Resulting electrical parameters:

$T_r = L_r/R_r = 0.443\text{s}, \quad \sigma L_s \approx 8.553mH$

$\sigma \approx 0.0723 = 1 - \frac{L_o^2}{L_s L_r}$

- Mechanical parameters [22]:

mechanical power	P_{mech}	=	$30k$W	$\cos\phi$	=	0.85
number of stator slots	N_s	=	48	rated i_{sd}	=	14A
number of rotor slots	N_r	=	40	rated i_{sq}	=	29A
number of pole pairs	pp	=	2	rated speed	=	1465rpm
Inertia	J	$\approx$	0.69Nms^2	connection:	Δ	
friction coefficient	b_F	=	0.0223Nms			
windage coefficient	f_a	=	$57 \cdot 10^{-6}\text{Nms}^2$			
rated torque	$T_{el_{nom}}$	=	$195\text{Nm} \approx \frac{30kW}{2\pi \cdot 1465/60}$			

The parameters given above are mostly valid for the induction machine using rotors #2 and #3. A number of tests was performed for verification. The following differences were found for rotor #3:

rated speed	n_{rated}	=	1477rpm
power factor	$\cos\phi$	=	0.88
	rated i_{sd}	=	13.8A
	rated i_{sq}	=	28.0A
rotor time const.	T_r	=	0.414s
rated torque	$T_{3\sim max}$	=	192Nm
total drive inertia	J	=	0.61Nms^2

The differences are mostly within 5% that is the usual expected deviation.

4.6.3 DC Loading Machine

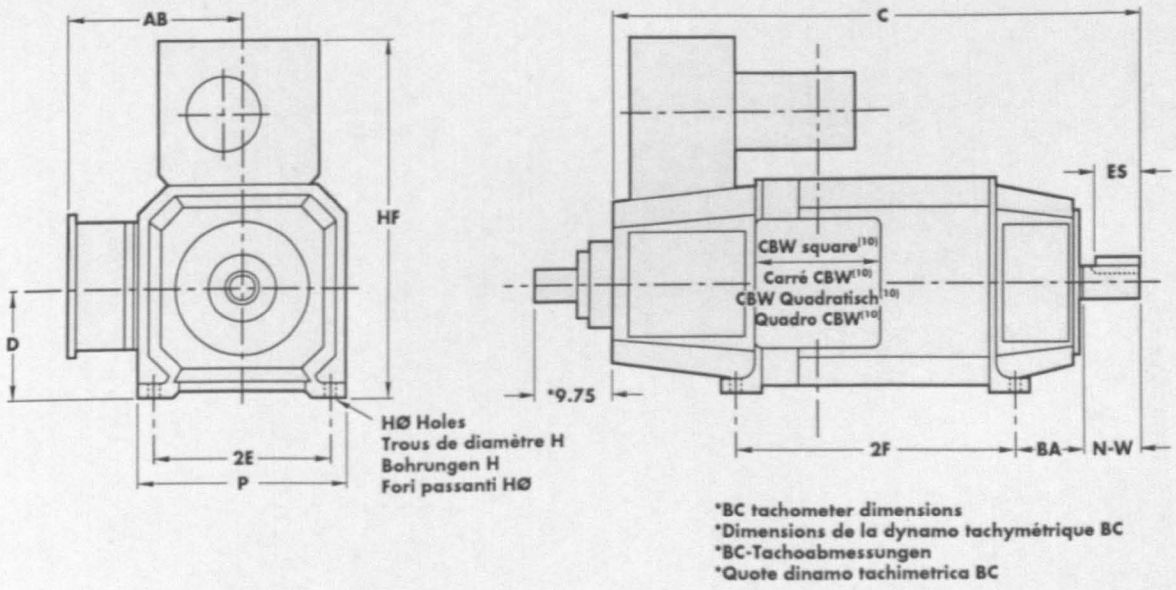

Figure 4.12: *Manufacturer's schematic for DC machine*

The load drive is a *Bull Electric Ltd.* 40kW separately excited DC machine that is controlled from a *Eurotherm 590* 4-quadrant DC thyristor converter. The 0.75kW blower fan mounted on top of the machine is provided for cooling and allows the DC machine to produce rated torque continuously also at low speeds and standstill as required for the research. The machine is aligned on the rig to the induction machine and connected to its shaft via a flexible coupling. The main purpose of the DC machine is to provide a load for the induction machine under test. The tachogenerator

is directly connected to the converter but is normally not used since the DC machine is torque controlled. The manufacturer's data of the DC machine is given in the table below.

Manufacturer's data (typical direct on line operation) as given on nameplate:			
model:	MK3	frame:	160L
output power:	40kW	armature voltage:	400V
rated speed:	1950rpm	rated full load torque	209Nm
rated full load I_a:	112A	Rotor inertia:	0.27 Nms^2
insulation class:	H	rating:	continuous
enclosure:	IP23	winding:	shunt
Excitation	300V, 2.89A	Year:	1998

In the table, I_a is the armature current. To better match the induction machine, the DC machine was not supplied with the rated parameters given on the nameplate but as a 30kW machine with reduced armature voltage. The torque is still about 209Nm since the rated speed is also reduced.

Machine data as used:	
output power:	30kW
armature voltage:	335V
rated speed:	1500rpm
excitation (field volts, series connect.):	370V
rated full load armature current I_a:	101A
armature resistance R_a:	0.117Ω (at 20°C) (0.163Ω, hot)
interpole resistance:	0.062Ω (at 20°C) (0.086Ω, hot)
shunt resistance R_f:	79.9Ω (at 20°C) (112.0Ω, hot)
armature inductance L_a:	2.64mH
shunt inductance L_f:	18.2H
shunt current (hot, base speed):	3.31A (note: 370V/3.31A = 112Ω)
shunt current (hot, top speed):	1.47A

The machine used for the *TRANSPUTER rig* is a 25kW *Leroy Somer* DC machine. This machine could only produce about 80% of the rated torque of the induction machine. An increase in armature current above rated value only caused a small increase in output torque due to armature reaction.

Chapter 5:

Theory of Saliency

This chapter reviews the techniques to estimate the flux or rotor position from machine saliencies. This can be either a

- saturation saliency
- saliency due to rotor eccentricity
- saliency due to magnetic anisotropy in the rotor lamination
- rotor saliency due to rotor resistance variation
- saliency due to rotor slotting
- rotor saliency due to inductance variation

These saliencies are analyzed theoretically and an overview is given, showing common saliency models. Most models describe the saturation saliency that is used to detect the flux angle for sensorless torque control. For the saturation saliency, the physical effect is examined. Rotor saliencies are utilized to obtain information about the rotor position. Sensorless techniques employ a transient injection or high frequency (hf) signal injection to excite the saliencies. An analysis of different solutions for the signal demodulation is given and the design of filters is discussed. Demodulation, often combined with a saliency estimator, is required to extract the saliency position information from the hf signals.

5.1 Introduction to Signal Injection

Two methods of *hf* signal injection can be used to extract the saliency information from the machine. The first which may be termed *Transient Injection* technique imposes a short distortion in the voltage. The resulting current deviation has to be measured. This process takes place in the time-domain and is based on the transient equivalent circuit of the induction machine. The measurement has to be precisely synchronized with the voltage distortion.

The second type of injection is termed continuous *hf* injection. A bandpass filter is needed to separate the resulting *hf* signal from the fundamental voltages or currents. The signal analysis is based on the steady state *hf* equivalent circuit of the induction machine and takes place in the frequency-domain. Transient effects do not play a role for the analysis or the signal measurement.
Transient injection was not used in the experimental rig in this thesis. An overview is given however to show advantages and disadvantages of this technique and reasons are given why *hf* injection was used instead.

5.1.1 Transient Injection through Modification of PWM

Transient injection uses a short deviation from the normal PWM voltage generation to excite the dynamics of the machine. The reaction can either be measured in the current change [84, 89] or in the voltage of the open star-point [21]. Care has to be taken when introducing the voltage deviation. The normal torque production of the machine should not be disturbed and the current controllers will also respond to the transient distortion. The deviation of the stator current is generally small since the distortion of the voltage vector is also small. The voltage applied is only a few percent of the rated voltage at low and zero speed. The INFORM method [18,88] exploits the zero PWM states that occur regularly when the demanded voltage is low. The mean test vector will be zero with one inactive and two inverse active switching states. This is an interruption of the normal PWM generation that works by selecting two active and one zero switching state of individual width, depending on the sector of the desired voltage phasor [88].

The hardware necessary for the precise sampling of a current transient during a controlled voltage deviation might be complex for the transient injection. An example of a hardware structure to estimate the current change is shown in [71]. Two separate current transducers are required and the currents are transformed into the $\alpha\beta$ frame. At low speeds all 6 different non-zero voltage vectors $\underline{u}_{s_k}$ are applied during one PWM period (see Section 2.2.6). Each new voltage vector triggers a sample & hold for the

α and for the β current. The sampling will be on the edge of a new PWM output just before a new switching instance. Fourteen sample & holds are needed to derive the 12 differential currents $\Delta i_{k\alpha}$ and $\Delta i_{k\beta}$. Using multiplexers, two AD converters are required to digitalize the signals. The resolution does not have to be too high because the current difference is calculated using analogue components.
PWM switching will cause large current spikes and oscillations on the cables and the precise trigger to start the current sampling is important. With larger inverters, deadtime is responsible for a difference between demanded switching edges and the actual one of the PWM. This makes it more difficult to align the current sampling with the PWM. The applied voltage vector also has to be known as accurately as possible which can be a problem.

Different techniques are used to excite the current dynamics in the machine. Schrödl [18,70] interrupts the normal PWM generation every $1 - 2ms$ to apply specific voltage test vectors. The mean value of the stator voltage during the application of the voltage test pulses is zero. This only causes a small voltage error since the reference stator voltage is small for operation at low speeds [88]. The active vectors $\underline{u}_{s_k}$ are relatively short compared to the duration of the zero vectors $\underline{u}_{s_0}$ and $\underline{u}_{s_7}$.
It is believed that Holtz and Jiang [122] use a similar technique to that of [18]. The switching duration of an active voltage vector is extended by a measurement time Δt. The inverse voltage vector is then applied within the same or directly in the next switching period for the same time Δt which ensures that the mean voltage remains unchanged. In [122], a measurement time of $\Delta t = 6\mu s$ is mentioned. The measurement of the sum of the three phase-to-neutral voltages has to be synchronized to the switching state of the test vectors.
Ogasawara *et al.* [71, 89, 90] extend the idea of [18] and use the generation of the normal PWM to excite the currents continuously. Below half rated speed, all six active voltage vectors $\underline{u}_{s_k}$ will be applied during one period $2T_p$.

$$\int_0^{2T_p} \underline{v}_s(t)dt = \sum_{k=1}^{6} (\underline{u}_{s_k} \cdot T_k)$$

The switching times T_k are calculated so that the mean voltage vector $\underline{v}_s$ remains unchanged. For higher speeds, only a maximum of three active voltage switches and one zero-state can be used during one period $2T_p$. The active switches are selected according to which discrete vectors are closest to the mean voltage vector $\underline{v}_s$.
When the machine is rotating, the dynamical behaviour of the current is influenced by the *emf* and becomes dependent on speed. The solution is to apply two voltage test vectors in opposite directions within a sufficiently short time [84] and perform two INFORM measurements. Mathematically, the speed-dependent terms cancel. The

requirement is only that the speed remains constant during the time between the two measurements.
It is believed that the transient injection interferes with the normal operation of the current controllers. These see the additional test signal like a distortion. There are attempts to include the test pulse generation into the current control that produces the normal PWM [88].

5.1.2 High Frequency Sinusoidal Injection

The high frequency (*hf*) signal injection is superimposed onto the voltage or current demand of the current or torque controllers. The injection is continuous and sinusoidal and easy to implement. The *hf* signal response of the machine is separated from the large fundamental signals by using a bandpass filter. The type of saliency tracked and the width of the bandpass filter determine the possible speed range. Usually, the *hf* signal is only applied at lower speeds and switched-off for higher speeds when one of the established speed-sensorless models is used. The measurement of the *hf* signals is usually uncritical because the injection is sinusoidal and continuous, unlike the transient injection. The continuous excitation is the reason why a simplified steady-state model of the induction machine can be used and the analysis is done in the frequency domain. The *hf* voltage injection also causes a response from the current controllers and care has to be taken with the control resonance frequency. The *hf* signal frequency is normally chosen to be above the current controller bandwidth. Most injection schemes use voltage injection that is added to the fundamental voltage demand and easy to produce on a VSI. High frequency current injection has also been tried [79,91], but requires a high bandwidth of the current controllers. The bandwidth will have to be several times that of the carrier signal frequency to regulate the *hf* carrier with neglectable error [91]. In [79] the reported injection frequency was 20Hz. Mostly, *hf* rotating injection is used, because no knowledge of the rotor flux orientation is required. But pulsating injection in the *d-q* frame has been reported [20, 79]. In this work only *hf* voltage injection is considered.

Classification of Methods

The *rotating* and the *pulsating hf* injection are the most common methods reported in literature. Injection methods that share some characteristics with the transient injection are the *periodic burst* injection and the use of inverter harmonics.

- High frequency $\alpha - \beta$ rotating injection:
  A rotating continuous *hf* voltage injection in the stationary $\alpha\beta$ frame is the most common method used [17, 24, 50, 74]. Two sinusoidal *hf* voltage signals

are added to the $\alpha\beta$ voltage demand $\underline{v}^*_{s_{\alpha\beta}}$:

$$\begin{aligned} \underline{v}'^*_{s_{\alpha\beta}} &= \underline{v}^*_{s_{\alpha\beta}} + \underline{v}_{\alpha\beta_c} = V^*_{s_{\alpha\beta}} e^{j\omega_e t} + V_c e^{j\omega_c t} \\ &\text{where} \quad v_{\alpha_c} = V_c \cos(\omega_c t), \\ &\text{and} \quad v_{\beta_c} = V_c \sin(\omega_c t) \end{aligned}$$

The result is a vector of constant magnitude, moving around the perimeter of the stator at the carrier frequency f_c. Advantage of this method is the simplicity. No frame transformations are required and the instantaneous position of the injected voltage can be easily predicted. The frequency is kept constant and therefore no transients complicate the extraction of the resulting saliency modulation.

- High frequency $\alpha - \beta$ burst injection:
  A special case of the $\alpha\beta$ rotating injection is the periodic burst injection method (PBI) [25,97]. The injection is for short time intervals and in bursts. This can be useful when eliminating the modulation due to the saturation saliency from the position signals. Transient conditions will occur so that sampling should only start after oscillations have settled down and the *hf* signals are in steady-state.

- High frequency *dq* pulsating injection:
  A pulsating injection can be implemented similarly to the rotating injection. Here however, the two sinusoidal *hf* voltage signals are in phase where $v_{d_c} = v_{q_c} = V_c \cos(\omega_c t)$ or $V_c \sin(\omega_c t)$. Injection is in two axes that are perpendicular in space, preferably those of the *dq* field oriented frame. This injection results in a *hf* vector that is fixed in space within the *dq* frame and has a changing amplitude. A possibility is also to inject a continuous and sinusoidal *hf* signal into only one axis. Seen from the stationary $\alpha\beta$ frame, two harmonics occur, rotating at frequency $f_c - f_e$ and $f_c + f_e$ where f_e is the frequency of the *dq* frame in respect to the stationary frame. This is because the *hf* voltages get modulated by the *dq* angle $\theta_e = \omega_e t$. Assuming the *hf*–*dq* injection as $\cos(\omega_c t)$, one gets

$$\cos(\omega_c t) \cdot \cos(\omega_e t) = 0.5 \cdot [\cos(\omega_c t - \omega_e t) + \cos(\omega_c t + \omega_e t)]$$

  From the *dq* frame, the injection is stationary and only one harmonic can be seen at frequency f_c. The advantage of the *dq* pulsating injection is that the torque pulsations can be minimized if the *hf* signal vector is aligned to the *d*-axis [20, 79]. This is because of the relatively large rotor time constant. The difficulty of the pulsating injection is that the saliency demodulation might be more complicated than for the rotating injection and that the reduction of torque pulsation cannot be guaranteed under all conditions in a sensorless drive.

A small misalignment in the estimation of the flux axis will directly cause torque pulsations.

Other types of injection, such as pulsating $\alpha\beta$ and rotating dq have not been reported in literature. The first would introduce additional complexity to the *hf* signal demodulation and the latter discards the advantage of reducing torque pulsations.

- Use of inverter harmonics as test signal:
  The idea here is to make use of the inevitable inverter harmonics. No separate *hf* injection would be required if any switching harmonics could show a sufficient perturbation of the machine saliencies. The inverter switching harmonic has a high magnitude and the switching frequency is accurately known. This should give any resulting modulation harmonics of an amplitude so that the demodulation of the saliency information is theoretically possible. In the stator current spectrum of the examined induction machines (asymmetric rotors), only harmonics that were $\pm\omega_e$, $\pm 2\omega_e$, $\pm 3\omega_e$ and $\pm 4\omega_e$ apart from the PWM carrier could be detected. No harmonics depending on ω_r could be found in the spectrum, although the machine had a suitable rotor saliency. The $\pm 2\omega_e$ harmonics were largest, next to the carrier. This could be used for detecting the flux position. The amplitudes are however more than 50 times smaller than the position harmonics due to a carrier in the range 300 – 1000Hz. A strategy might then be necessary to 'fold' all multiples of ω_e onto one frequency, because spectral separation using filters will not be possible. Otherwise, the saliency information contained in these harmonics will not be of much use.

  Spectral analysis of the stator currents of the symmetric machine (rotor #3) showed that modulation harmonics around the PWM frequency of $5k$Hz and its multiples exist that depend on f_e. The modulation harmonics at $10kHz \pm f_e$ were the largest with about $300mA$ under no-load and an increased amplitude of $450mA$ under full load. The size of the harmonic amplitude would make this harmonic attractive for the use in sensorless torque control, especially since it does not require an additional *hf* carrier injection.

  The current spectrum also included higher harmonics of the injection frequency. These were at $n \cdot 5kHz \pm f_c$, where n is an integer. The harmonics however had an amplitude of less than 20% of the carrier at frequency f_c. If a slotting modulation was present it will probably not be exploitable due to the small signal amplitude.

Practical Considerations for *hf* Injection

A number of problems and issues when using high frequency (*hf*) voltage injection to detect the saliency angle are important to be considered:

- Magnitude of injected signal:
  The optimal choice for the amplitude V_c of the injected *hf* voltage is a function of the carrier frequency f_c. If V_c is chosen too high, the audible noise increases or the injected signal causes additional unwanted saturation or losses [20, 92]. If V_c is too low, the signal-to-noise ratio is also low. A good compromise is a voltage magnitude of 20 to 35V line-to-line. To obtain optimum resolution of the *hf* signal amplitude and for the position estimation, the *hf* signal magnitude has to be scaled to match the full input range of the ADCs.

- Imbalance in α-β signals:
  In a practical drive it is possible that the amplitudes of the injected *hf* voltages are different in the three phases. This can be due to differences in the deadtime of the legs of the inverter. This imbalance can be modeled by using an $\alpha\beta$ voltage injection where the amplitudes in the α and β directions are different.

  The result is firstly a change in the magnitude of the extracted position harmonics $\underline{i}_{s_{dq\_c}}$ and secondly a DC offset. The first effect is simply due to the change in the *hf* voltage vector magnitude $\sqrt{v_{\alpha c}^2 + v_{\beta c}^2}$. If the α or β voltage component is increased, the resulting vector length is also increased and the amplitude of the *hf* currents is therefore larger. The second effect, the DC offset in the position harmonics $\underline{i}_{s_{dq\_c}}$, is more interesting. Generally, the more unbalanced the voltages are, the larger the DC offset in the position harmonics. This can be shown mathematically by observing that the unbalanced $\alpha\beta$ *hf* voltages cause unbalanced $\alpha\beta$ *hf* currents. The degree by which the *hf* currents differ in amplitude is determined by the machine saliency (see Section 5.2).

  The analysis can directly build upon the amplitude difference in the resulting $\alpha\beta$ *hf* currents. When applying the *Direct Homodyne Transformation* (see Section 5.4.4), the imbalance can be represented by introducing the term a that scales the β current component:

$$i_{s_{d\_c}} = i_{s_{\alpha\_c}} \cos(\omega_c t) + (1+a) \cdot i_{s_{\beta\_c}} \sin(\omega_c t) \tag{5.1}$$

$$i_{s_{q\_c}} = -i_{s_{\alpha\_c}} \sin(\omega_c t) + (1+a) \cdot i_{s_{\beta\_c}} \cos(\omega_c t) \tag{5.2}$$

  The transformation above is used to separate the saliency harmonics from the carrier harmonic. The terms $i_{s_{\alpha\_c}}$ and $i_{s_{\beta\_c}}$ are the *hf* currents that are separated from the stator currents via a bandpass filter. After the transformation, $i_{s_{d\_c}}$

and $i_{s_{q\_c}}$ have the saliency harmonics at DC. When assuming the modulated *hf* signals $\underline{i}_{s_{\alpha\beta\_c}}$ to be the result of a rotor resistance saliency (see Section 5.2.2):

$$i_{s_{\alpha\_c}} = I_1 \cos(\omega_c t + \phi_1) - I_2 \cos(2\theta_r - \omega_c t + \phi_2) \quad (5.3)$$

$$i_{s_{\beta\_c}} = I_1 \sin(\omega_c t + \phi_1) - I_2 \sin(2\theta_r - \omega_c t + \phi_2) \quad (5.4)$$

where I_1 is the amplitude of the carrier harmonic and I_2 the amplitude of the rotor saliency. With (5.1) and (5.2) into (5.3) and (5.4), resolving the trigonometric terms and using a lowpass filter to remove the $2\omega_c$ frequency components, one gets:

$$i_{s_{d\_c}} = \frac{a}{2} \cdot I_1 \cos\phi_1 - (1 + \frac{a}{2}) \cdot I_2 \cos(2\theta_r + \phi_2) \quad (5.5)$$

$$i_{s_{q\_c}} = -\frac{a}{2} \cdot I_1 \sin\phi_1 - (1 + \frac{a}{2}) \cdot I_2 \sin(2\theta_r + \phi_2) \quad (5.6)$$

Ideally, the terms containing I_1 should have cancelled and only the saliency harmonic should remain in $\underline{i}_{s_{dq\_c}}$. However, if $a \neq 0$, the $\cos\phi_1$ and $\sin\phi_1$ terms are not zero and thus cause a DC offset in the position signals. The amplitude of this offset depends on the phase shift ϕ_1 between the transformation terms $sin(\omega_c t)$ and $\cos(\omega_c t)$ and the resulting carrier harmonic on the stator currents. The transformation terms are generated by the digital processor and are used to generate the *hf* voltage injection demand. It can be assumed that the delay between voltage demand and actual *hf* voltages is constant. The same conclusion is valid for the phase shift between *hf* current and voltage carrier harmonics. As a result, the DC offset in the demodulated position signals can only be removed practically by avoiding an imbalance a. Care has to be taken therefore that the analogue circuitry for measuring the *hf* currents does not introduce unsymmetries in the acquisition channels. It has also been observed that differences in the deadtime of the three inverter legs of VSIs can be the cause for imbalances.

- Selection of injection frequency:
  Ideally, the higher the injection frequency the better the spectral separation of the modulation harmonics from the fundamental harmonics. The PWM frequency determines the maximum possible injection frequency that should be a number of factors smaller.

  For the first asymmetric machine (rotor #1), the injection frequency was 284Hz.

  For the symmetric machine (rotor #3), the injection frequency was set to 750Hz. This was considered a good compromise. A lower injection frequency would have been affected by the current controllers. For higher injection the usable position harmonic had been smaller. The voltage injection resulted in an rms *hf* current

of 4.8A on the line currents. The usable position modulation is about $365mA$ *rms* or 7.6% of the carrier harmonic.

- Effect of injection on machine control:
  For the current controllers, the *hf* signal injection causes a distortion on the measured currents. Depending on the bandwidth of the current controllers, this distortion will be more or less suppressed. The injection however can also be amplified if injected at the resonance frequency of the current loop. Only if the carrier frequency of the *hf* currents is above the loop bandwidth, the influences can be neglected. Another method is to use a notch filter that is designed to suppress the carrier frequency. This can also be a moving average (MA) filter that requires synchronized sampling of the fundamental currents. In this way, the *hf* current ripples are invisible to the controller. The difficulty here is that either the current sampling has to be low enough or the *hf* carrier frequency high enough to allow synchronization.

- Signal injection at higher frequencies:
  Hf signal injection at frequencies of $f_c > 1k$Hz are attractive as they are less audible and there will be no influence on the controllers of the current loop. For rotor #1 (first asymmetric rotor), injections with f_c up to $4k$Hz had been experimentally tried. The amplitude of the modulation harmonics due to saturation and rotor saliency were both very small for $f_c > 1k$Hz, when compared to $f_c = 300$Hz. For $4k$Hz, the amplitudes were about 300 times smaller which is a high burden when trying to achieve a sufficient amplitude resolution. The design of the analogue bandpass filters becomes more difficult since the large fundamental currents have to be removed.

- Sampling effects:
  For an increased injection frequency f_c, the carrier will become less of a smooth *sinus* function since less PWM periods are available. In the extreme case of $f_c = 1/(2T_p)$ with the PWM period $2T_p$, the injection will be a periodical rectangular function. It is not known if aliasing can cause problems for the *hf* demodulation. For voltage injections with f_c up to $6k$Hz, no problems could be found. Problems with current injection are reported in [91] in case that the *hf* carrier is not regulated with almost zero error. Unwanted harmonics (the negative sequence of the carrier, see Section 5.4.4) are the result, that make position estimation more difficult.

5.2 Modelling of Saliencies under *hf* Injection

This section gives an overview of the different saliencies in the induction machine that can be used to estimate flux or rotor position. The saturation saliency is covered more in detail and an approach is given to determine the physical effects behind this saliency. Most estimators assume a simplified and ideal saliency. A number of these simplified saliency models are presented and the technique to estimate flux or rotor position is shown.

A number of machine saliencies is known and some can be exploited to estimate the flux or rotor position for sensorless torque or position control respectively. Practically, there will always be a combination of several saliencies present in a machine. Ideally, only one saliency dominates. The others are then regarded as parasitic saliencies and can either be neglected or suppressed. They act as a disturbance to the main spacial saliency, that can be

1. *rotor saliencies* allow to estimate the rotor position directly. They can be either engineered or natural saliencies and

   (a) due to *rotor resistance variation*: a specially designed rotor is used with an embedded cage that has a circumferential variation of the rotor resistance. This can also be a double-cage design or based on deep-bar slots. There are typically two saliency periods per pole pair. Thus the saliency frequency is twice the rotor frequency with $f_{sal} = 2f_r$

   (b) due to *rotor slotting*: this rotor saliency is due to the geometry of the rotor slots and depends on the shape of the teeth and skewing. This saliency is inherent in most induction machines. For a limited number of rotor slots, the slotting effect is sufficient to provide a signal that can be used for sensorless control. The saliency frequency is a product of the number of rotor slots per pole pair $\frac{N_r}{pp}$ and the rotor frequency with $f_{sal} = \frac{N_r}{pp} \cdot f_r$

   (c) due to *inductance variation*: this saliency is engineered by changing the geometry of the rotor slots. Either width or depth is varied sinusoidally. There are typically two saliency periods per pole pair. Thus the saliency frequency is twice the rotor frequency with $f_{sal} = 2f_r$

   (d) due to *magnetic anisotropy* in the rotor lamination: this rotor saliency has not been investigated so far

2. *saturation saliency*: can be used to detect the flux position for sensorless torque control. This saliency can be found in all induction machines and is caused by the saturation of the stator and rotor teeth and bridges. The saturation saliency depends on the flux level and on the loading conditions. Since there is a positive

and a negative maximum of the flux wave per pole pair, the saliency frequency is twice that of the excitation frequency with $f_{sal} = 2f_e$

3. saliency due to *rotor eccentricity*: this saliency is generally very small and is unlikely to be exploitable for sensorless control

4. *clamping modulation* due to inverter deadtime: this is a discrete modulation that has the characteristics of a machine saliency but is caused by the deadtime of the inverter. It however has to be considered when using rotor or saturation saliencies for sensorless control. The modulation occurs during the zero crossing of the fundamental currents that occurs six times per electrical period. This results in an alternating frequency spectrum with $f_{sal} = -2f_e, +4f_e, -8f_e, +16f_e, \ldots$

5. *transient modulation*: this modulation has only been reported in conjunction with *hf* signal injection. During transient machine operation, the fundamental signals cause a short distortion in the extracted *hf* modulation.

For sensorless drives using saliencies, the saturation saliency is of particular interest. The flux angle detection for sensorless torque-controlled drives directly depends on this saliency. Drives for sensorless position control, using a rotor saliency however need to compensate for the saturation saliency. The better the saturation saliency can be predicted, the better the compensation and the higher the quality of the sensorless position control. Many researchers use a simplified fundamental machine model when applying a *hf* signal. The large magnetizing inductance and the iron-loss resistance can be neglected when deriving the transfer function between *hf* currents and voltages. This approach however is not fully justified. Machine parameters change for the *hf* injection due to skin effect, eddy-currents and saturation from the respective values at rated operating conditions. This section looks at the different physical effects to determine the parameters for the *hf* equivalent circuit [50]. The influence of saturation on the model is analyzed qualitatively [123,124]. The basic problem when designing a *hf* model is that leakage inductances in the fundamental model are small and cannot accurately be determined. For the *hf* model they play an even more important role than for the fundamental circuit. Thus for the *hf* model the parameter error can be relatively large. A final proof of the validity of the model can therefore not be given since measuring the effects on the real machine was out of the scope of this work.

5.2.1 Saliencies due to Geometry

A saliency commonly used for machine control is that due to the rotor geometry of a specifically designed machine. This machine is called resolver or synchro and is used as an encoder to provide the machine controller with information about rotor position and speed. The resolver is not the object of the research in this thesis but it provides an easy understanding and introduction to saliencies. There is one fundamental but important difference between the resolver and an induction machine drive that makes use of saliencies to estimate rotor position or flux angle. An induction machine is operated with fundamental voltages and currents. It will be shown later that these fundamental signals can be the cause for a number of saliencies and not only one as in a resolver. When operating the induction machine without fundamental signals and only with a *hf* signal injection to excite e.g. a rotor slotting saliency, the rotor position can easily be estimated (see Section 8.2.1).

The structure of the resolver resembles that of a rotating transformer or more accurately, that of a generator. The primary winding is in the rotor, the secondary in the stator. When the rotor moves, the mutual inductance between rotor and stator coil changes. Feeding alternating voltage of constant amplitude into the rotor winding (the primary), an alternating current is induced in the stator winding. Its amplitude is modulated by the angle φ between primary and secondary winding. The resolver has a single coil on the rotor side and a two-phase orthogonal secondary winding with a 90° mutual phase shift.

$$\begin{aligned} V_o &= A \cdot \sin(\omega_c t) \\ V_1 &= k_1 \cdot A \cdot \sin(\omega_c t + \gamma) \cdot \sin(\varphi) \\ V_2 &= k_2 \cdot A \cdot \sin(\omega_c t + \gamma) \cdot \cos(\varphi) \end{aligned} \tag{5.7}$$

where V_o is the rotor voltage of excitation amplitude A and carrier frequency ω_c. The factors k_1 and k_2 are the transformation ratios between primary and secondary windings and will usually be equal. Note that the synchro is essentially a resolver but with a three-phase secondary winding of 120° mutual phase shift between the stator windings.

The resolver can also work inversely from the secondary to the primary side. If current is fed into the stator winding, the induced (primary) voltage is

$$V_o = k \cdot A \cdot \sin(\omega_c t + \varphi)$$

where the phase shift is proportional to angle φ. Using a phase demodulation, the rotor position can be derived.

Resolvers usually come equipped with brushes. The signals from or to the rotor are sent via slip rings. This can cause unwanted noise when the brushes are worn-out and

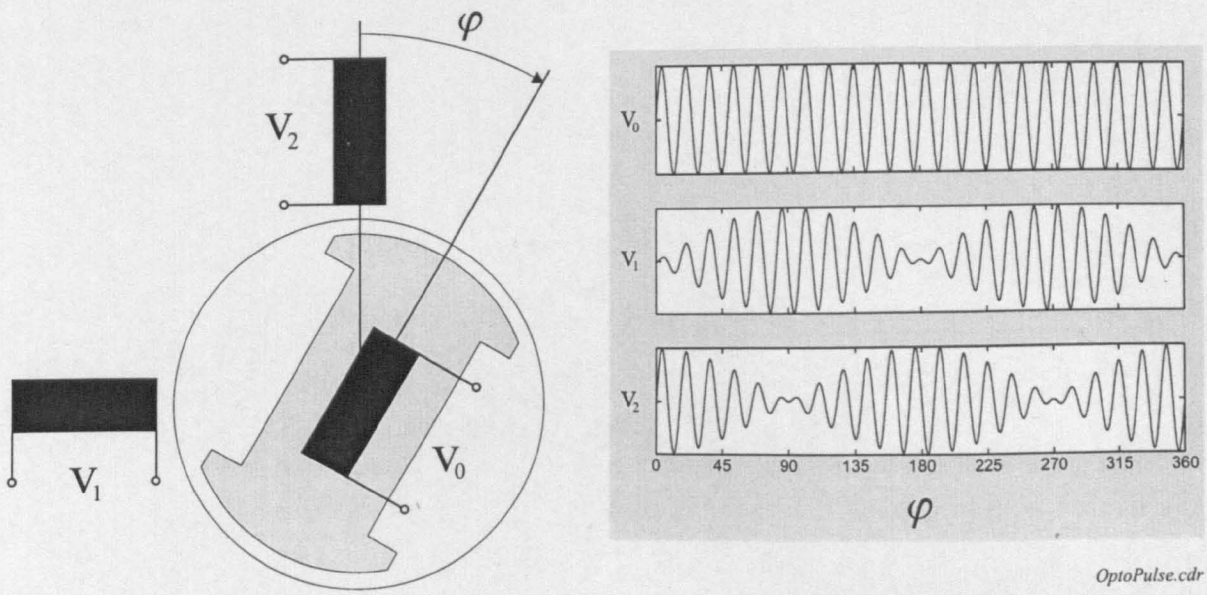

Figure 5.1: *Principle structure of resolver and resulting position modulated secondary signals. Left: geometry and coil position. Right: voltage injection and position-modulated secondary voltages*

the quality of the contacts has deteriorated. Thus, brushless resolvers can be used or a separate rotary transformer provides the power to the rotating primary winding, similar to an exciter found in synchronous machines.
The accuracy reached is about 0.1° mechanically per round. This can be improved by employing a gear transmission or a stack of several resolvers. Errors can be due to a bad primary voltage, the wrong impedance matching or a difference in the transformation ratio for the two orthogonal secondary windings.

5.2.2 Rotor Saliency

For estimating the rotor position, a saliency has to be fixed to the rotor. Different possible rotor saliencies have been suggested in literature for induction machines. A rotor saliency can be due to a specifically engineered "asymmetric" rotor, suggested by [77] and [24] or by employing rotor slot harmonics (termed "symmetric" rotor). The latter has been demonstrated by [98], using a star-connected induction machine with 28 rotor slots and by [83] demonstrating the tracking of rotor position.
The model for the rotor saliency assumes a difference in impedance Z that can be described in the rotor frame that is denoted by the subscript $_{(\alpha\beta)}$. Note that this frame is fixed to the rotor and is different from the dq frame [22]. Only saliencies with two distinct extrema, a maximum and a minimum in two perpendicular axes

can be described with this model.

In practice, conditions are not always that ideal with saliencies, in particular with the saturation saliency. Higher harmonics can exist that are generally not included in the model. For the case of the rotor saliency these higher harmonics do not exist or they are very small and can be neglected. With the asymmetric rotor (see Section 4.6.1), the deviation of the engineered saliency from the optimal sinusoidal shape is within a few percent. For the symmetric rotor (Section 4.6.1), the analysis of [100] can be used to estimate the effect of modulation due to the rotor saliency. The mutual inductance between stator and rotor is a function of the rotor position [100] and can be approximated by a triangular shape over the position (see m_{s1} in *Fig. 14* of [100]). The total leakage inductance is a function of the square of the mutual inductance ($l_{\sigma a} = l_s(1 - \frac{m_{s1}^2}{l_s l_1})$) and therefore has a parabolic shape [100] that is periodically repeated N_r times per mechanical revolution. The total leakage inductance is the rotor saliency that causes the position-dependent modulation in the *hf* stator currents. The spectrum of the total leakage inductance ($l_{\sigma a}$) contains a large spatial harmonic with (mechanical) period $2\pi/N_r$ and a small spatial harmonic with half the period. Its amplitude is less than 10% of the $2\pi/N_r$ harmonic. Higher harmonics can be neglected. No harmonics due to the π/N_r spatial modulation could be found in the spectrum of the *hf* stator currents (rotor #3).

Given the relation between the injected high frequency voltages and the resulting *hf* currents in the rotor frame (subscript is $_{(\alpha\beta)}$):

$$\begin{bmatrix} v_{s_{(\alpha)}} \\ v_{s_{(\beta)}} \end{bmatrix} = \begin{bmatrix} Z_{(\alpha)} & 0 \\ 0 & Z_{(\beta)} \end{bmatrix} \begin{bmatrix} i_{s_{(\alpha)}} \\ i_{s_{(\beta)}} \end{bmatrix}$$

$$[\underline{v}_{s_{(\alpha\beta)}}] = [Z_{(\alpha\beta)}][\underline{i}_{s_{(\alpha\beta)}}] \tag{5.8}$$

Note that the voltages and currents that are measured in the two perpendicular axes of the rotor frame are decoupled. Mathematically, this means that only the elements on the diagonal of the impedance matrix are not zero. The impedance in the (α) axis shall here be the larger value.

In practice, it is more convenient to work with the signals in the stationary or stator frame (subscript is $_{\alpha\beta}$). This is because the stator currents can directly be measured in this frame. The above matrix equation (5.8) therefore has to be transformed to the stator frame.

The transformation description for the voltages is:

$$[\underline{v}_{s_{\alpha\beta}}] = [e^{j\theta_r}][\underline{v}_{s_{(\alpha\beta)}}]$$

$$\begin{bmatrix} v_{s_\alpha} \\ v_{s_\beta} \end{bmatrix} = \begin{bmatrix} \cos\theta_r & -\sin\theta_r \\ \sin\theta_r & \cos\theta_r \end{bmatrix} \begin{bmatrix} v_{s_{(\alpha)}} \\ v_{s_{(\beta)}} \end{bmatrix}$$

For a symmetric system with a diagonal matrix with equal elements on the diagonal, the transformation matrix can be simplified:

$$\begin{aligned} \underline{v}_{s_{\alpha\beta}} &= e^{j\theta_r}\underline{v}_{s_{(\alpha\beta)}} \\ (v_{s_\alpha} + jv_{s_\beta}) &= (\cos\theta_r + j\sin\theta_r)(v_{s_{(\alpha)}} + jv_{s_{(\beta)}}) \end{aligned} \tag{5.9}$$

When transforming the impedance matrix, the elegant complex style shown in (5.9) cannot be used due to the different values on the main diagonal of the matrix. Finally, the complete matrix equation (5.8) can be transformed:

$$[e^{j\theta_r}][\underline{v}_{s_{(\alpha\beta)}}] = [e^{j\theta_r}][Z_{(\alpha\beta)}]\underbrace{[e^{-j\theta_r}][e^{j\theta_r}]}_{[1]}[\underline{i}_{s_{(\alpha\beta)}}] \tag{5.10}$$

$$[\underline{v}_{s_{\alpha\beta}}] = [e^{j\theta_r}][Z_{(\alpha\beta)}][e^{-j\theta_r}][\underline{i}_{s_{\alpha\beta}}]$$

In (5.10), both sides of the equation have been multiplied by $[e^{j\theta_r}]$. Note that matrix multiplication is not commutative, the multiplicand is on the left of either side. A unity matrix has been inserted on the right which can be split to give the matrix $[e^{j\theta_r}]$, required to transform the current matrix.

Performing a detailed transformation of the square matrix with different impedance values by using basic trigonometric theorems:

$$\begin{bmatrix} v_{s_\alpha} \\ v_{s_\beta} \end{bmatrix} = \begin{bmatrix} \cos\theta_r & -\sin\theta_r \\ \sin\theta_r & \cos\theta_r \end{bmatrix} \begin{bmatrix} Z_{(\alpha)} & 0 \\ 0 & Z_{(\beta)} \end{bmatrix} \begin{bmatrix} \cos\theta_r & \sin\theta_r \\ -\sin\theta_r & \cos\theta_r \end{bmatrix} \begin{bmatrix} i_{s_\alpha} \\ i_{s_\beta} \end{bmatrix}$$

$$\begin{bmatrix} v_{s_\alpha} \\ v_{s_\beta} \end{bmatrix} = \begin{bmatrix} Z_{(\alpha)}\cos^2\theta_r + Z_{(\beta)}\sin^2\theta_r & Z_{(\alpha)}\sin\theta_r\cos\theta_r - Z_{(\beta)}\sin\theta_r\cos\theta_r \\ Z_{(\alpha)}\sin\theta_r\cos\theta_r - Z_{(\beta)}\sin\theta_r\cos\theta_r & Z_{(\alpha)}\sin^2\theta_r + Z_{(\beta)}\cos^2\theta_r \end{bmatrix} \begin{bmatrix} i_{s_\alpha} \\ i_{s_\beta} \end{bmatrix}$$

$$\begin{bmatrix} v_{s_\alpha} \\ v_{s_\beta} \end{bmatrix} = \begin{bmatrix} \frac{Z_{(\alpha)}+Z_{(\beta)}}{2} + \frac{Z_{(\alpha)}-Z_{(\beta)}}{2}\cos(2\theta_r) & \frac{Z_{(\alpha)}-Z_{(\beta)}}{2}\sin(2\theta_r) \\ \frac{Z_{(\alpha)}-Z_{(\beta)}}{2}\sin(2\theta_r) & \frac{Z_{(\alpha)}+Z_{(\beta)}}{2} - \frac{Z_{(\alpha)}-Z_{(\beta)}}{2}\cos(2\theta_r) \end{bmatrix} \begin{bmatrix} i_{s_\alpha} \\ i_{s_\beta} \end{bmatrix}$$

$$\begin{bmatrix} v_{s_\alpha} \\ v_{s_\beta} \end{bmatrix} = \begin{bmatrix} \overline{Z} + \Delta Z\cos(2\theta_r) & \Delta Z\sin(2\theta_r) \\ \Delta Z\sin(2\theta_r) & \overline{Z} - \Delta Z\cos(2\theta_r) \end{bmatrix} \begin{bmatrix} i_{s_\alpha} \\ i_{s_\beta} \end{bmatrix} \tag{5.11}$$

The rotor saliency seen from the stator frame consists of a mean impedance $\overline{Z}$ and a variable term ΔZ that is modulated by twice the saliency angle θ_r.

The impedance terms are given as:

$$\begin{aligned} \overline{Z} + \Delta Z\cos(2\theta_r) &= Z_{(\alpha)}\cos^2\theta_r + Z_{(\beta)}\sin^2\theta_r \\ &= \overline{Z}(\sin^2\theta_r + \cos^2\theta_r) + \Delta Z(\cos^2\theta_r - \sin^2\theta_r) \end{aligned}$$

$$\Delta Z \sin(2\theta_r) = (Z_{(\alpha)} - Z_{(\beta)}) \sin\theta_r \cos\theta_r$$

$$\text{with} \quad \Delta Z = \frac{Z_{(\alpha)} - Z_{(\beta)}}{2} > 0$$

$$\text{and} \quad \overline{Z} = \frac{Z_{(\alpha)} + Z_{(\beta)}}{2}$$

For further analysis it is interesting to get an expression for the *hf* currents which requires the inversion of the impedance matrix:

$$\begin{bmatrix} i_{s_\alpha} \\ i_{s_\beta} \end{bmatrix} = \frac{1}{Z_{(\alpha)} \cdot Z_{(\beta)}} \begin{bmatrix} \overline{Z} - \Delta Z \cos(2\theta_r) & -\Delta Z \sin(2\theta_r) \\ -\Delta Z \sin(2\theta_r) & \overline{Z} + \Delta Z \cos(2\theta_r) \end{bmatrix} \begin{bmatrix} v_{s_\alpha} \\ v_{s_\beta} \end{bmatrix}$$

where the term $Det(Z) = Z_{(\alpha)} \cdot Z_{(\beta)} = (\overline{Z}^2 - \Delta Z^2)$ is the determinant. The currents can now be written as a function of the *hf* voltage and impedance:

$$i_{s_\alpha} = \frac{\overline{Z}}{Det(Z)} \cdot v_{s_\alpha} - \frac{\Delta Z}{Det(Z)} \cdot (v_{s_\alpha} \cos 2\theta_r + v_{s_\beta} \sin 2\theta_r)$$

$$i_{s_\beta} = \frac{\overline{Z}}{Det(Z)} \cdot v_{s_\beta} - \frac{\Delta Z}{Det(Z)} \cdot (v_{s_\alpha} \sin 2\theta_r - v_{s_\beta} \cos 2\theta_r)$$

Given a rotating $\alpha\beta$ voltage injection $\underline{v}_{s_{\alpha\beta}} = \underline{v}_c$ with amplitude V_c:

$$\underline{v}_c = V_c \begin{bmatrix} \cos(\omega_c t) \\ \sin(\omega_c t) \end{bmatrix} = V_c e^{j\omega_c t} = V_c [\cos(\omega_c t) + j \sin(\omega_c t)] \tag{5.12}$$

the resulting *hf* currents (subscript $_{\alpha\beta\_c}$) are

$$\underline{i}_{s_{\alpha\beta\_c}} = \frac{\overline{Z}}{Det(Z)} V_c \cdot \begin{bmatrix} \cos(\omega_c t) \\ \sin(\omega_c t) \end{bmatrix} - \frac{\Delta Z}{Det(Z)} V_c \cdot \begin{bmatrix} \cos(2\theta_r - \omega_c t) \\ \sin(2\theta_r - \omega_c t) \end{bmatrix}$$

$$\begin{aligned} \underline{i}_{s_{\alpha\beta\_c}} &= \underline{i}_{cp} e^{j\omega_c t} - \underline{i}_{cn} e^{j(2\theta_r - \omega_c t)} \\ &= I_{inj} + I_{pos} \end{aligned} \tag{5.13}$$

It can be seen that the first term of the current $\underline{i}_{cp}$ rotates in the direction of the injected voltage and the second term $\underline{i}_{cn}$ rotates in the inverse direction. The latter term is called the *negative sequence harmonic* [85]. Only this second term contains the interesting modulation due to the saliency, apparent from the θ_r in the argument of the trigonometric functions. The negative sequence harmonic has to be separated from the positive sequence harmonic that does not contain any saliency information if the rotor position θ_r is to be estimated.

When injecting a *hf* signal into the machine, it is of interest how large the signal containing the saliency information is in relation to the carrier signal. This is described by the following ratio:

$$\frac{I_{pos_{\max}}}{I_{inj_{\max}}} = \frac{|\Delta Z|}{|\overline{Z}|} \tag{5.14}$$

The higher ΔZ to $\overline{Z}$, the larger the useful position information in relation to the current ripple. ΔZ is directly a measure for the degree of saliency.
Equation (5.13) is the key relation between *hf* voltages, currents and the rotor saliency. The rotor position modulation is a function of the number of saliency periods per pole pair (*pp*). Generally, two periods are chosen, thus the factor 2 in $2\theta_r - \omega_c t$.

Inductance Variation

For a rotor with a modified inductance [77], the expressions in (5.13) can be simplified when analyzing the high frequency equivalent circuit of the induction machine. Under steady-state conditions the fundamental equations in the stator frame (2.17) and (2.18) can be simplified. For the *hf* signal, the derivatives can be replaced by $j\omega_c$ where $\underline{i}_s = \underline{I}_s e^{j\omega_c t}$, $\frac{d}{dt}\underline{i}_s = j\omega_c \underline{I}_s e^{j\omega_c t} = j\omega_c \underline{i}_s$:

$$\begin{aligned} \underline{u}_s &= R_s \underline{i}_s + j\omega_c L_s \underline{i}_s + j\omega_c L_o \underline{i}_r \\ 0 &= R_r \underline{i}_r + j\omega_c L_r \underline{i}_r + j\omega_c L_o \underline{i}_s - j\omega_r \underline{\psi}_r \end{aligned}$$

Note that the flux $\underline{\psi}_r$ is not due to the fundamental excitation but the *hf* signals. In the high frequency model, the resistances can be neglected ($R_s \approx 0$, $R_r \approx 0$) and for operation at low speeds where the injection is at a much higher frequency ω_c, the back-*emf* $j\omega_r \underline{\psi}_r \approx 0$. The remaining relations can be arranged

$$\begin{aligned} \underline{u}_s &\approx j\omega_c L_s \underline{i}_s + j\omega_c L_o \underline{i}_r \\ 0 &\approx j\omega_c L_r \underline{i}_r + j\omega_c L_o \underline{i}_s \quad \rightarrow \quad \underline{i}_r \approx -\frac{L_o}{L_r}\underline{i}_s \end{aligned}$$

$$\begin{aligned} \underline{u}_s &\approx j\omega_c L_s \underline{i}_s + j\omega_c L_o(-\frac{L_o}{L_r}\underline{i}_s) \approx j\omega_c \left(L_s - \frac{L_o^2}{L_r}\right)\underline{i}_s \\ &\approx j\omega_c \sigma L_s \underline{i}_s = j\omega_c L_{s_\sigma} \underline{i}_s \end{aligned}$$

The term $L_{s_\sigma} = L_s(1 - \frac{L_o^2}{L_s L_r})$ is called the stator transient inductance. An engineered inductance variation in the rotor can be achieved by e.g. opening the rotor slots with a sinusoidally changing width [19, 69, 125]. For such an asymmetric rotor where the stator transient inductance on the (α) and (β) axes differ, the saliency can be

described by a matrix:

$$\begin{bmatrix} v_{s_{(\alpha)}} \\ v_{s_{(\beta)}} \end{bmatrix} = j\omega_c \begin{bmatrix} L_{s_{\sigma(\alpha)}} & 0 \\ 0 & L_{s_{\sigma(\beta)}} \end{bmatrix} \begin{bmatrix} i_{s_{(\alpha)}} \\ i_{s_{(\beta)}} \end{bmatrix}$$

$$[\underline{v}_{s_{(\alpha\beta)}}] = j\omega_c \, [L_{s_{\sigma(\alpha\beta)}}][\underline{i}_{s_{(\alpha\beta)}}]$$

Generally, the number of saliency periods per pole pair are chosen to be two. This results in a modulation harmonic at $2\theta_r - \omega_c t$. After transformation into the stationary frame and matrix inversion, the *hf* currents can be described by

$$\underline{i}_{s_{\alpha\beta\_c}} = -j\left(\underline{i}_{cp} e^{j\omega_c t} + \underline{i}_{cn} e^{j(2\theta_r - \omega_c t)}\right)$$

where

$$i_{cp} = \frac{\overline{L}_{s_\sigma}}{\overline{L}_{s_\sigma}^2 - \Delta L_{s_\sigma}^2} \cdot \frac{V_c}{\omega_c}, \qquad \overline{L}_{s_\sigma} = \frac{L_{s_{\sigma(\alpha)}} + L_{s_{\sigma(\beta)}}}{2}$$

$$i_{cn} = \frac{\Delta L_{s_\sigma}}{\overline{L}_{s_\sigma}^2 - \Delta L_{s_\sigma}^2} \cdot \frac{V_c}{\omega_c}, \qquad \Delta L_{s_\sigma} = \frac{L_{s_{\sigma(\alpha)}} - L_{s_{\sigma(\beta)}}}{2}$$

Rotor Resistance Variation

The *hf* saliency model based on a spatial difference of the rotor resistance [22] is easily described in the rotor frame:

$$\begin{bmatrix} v_{s_{(\alpha)}} \\ v_{s_{(\beta)}} \end{bmatrix} = \begin{bmatrix} Z_{(\alpha)} & 0 \\ 0 & Z_{(\beta)} \end{bmatrix} \begin{bmatrix} i_{s_{(\alpha)}} \\ i_{s_{(\beta)}} \end{bmatrix}$$

where the impedance terms are given as

$$Z_{(\alpha)} = \left(R_s + j\omega_c (l_s + l_{r12}) + \frac{R_{r1_{(\alpha)}} \cdot (R_{r2} + j\omega_c l_{r2})}{(R_{r1_{(\alpha)}} + R_{r2}) + j\omega_c l_{r2}} \right)$$

$$Z_{(\beta)} = \left(R_s + j\omega_c (l_s + l_{r12}) + \frac{R_{r1_{(\beta)}} \cdot (R_{r2} + j\omega_c l_{r2})}{(R_{r1_{(\beta)}} + R_{r2}) + j\omega_c l_{r2}} \right)$$

The parameters for the *hf* impedances $Z_{(\alpha)}$ and $Z_{(\beta)}$ are derived from the fundamental machine model of a double-cage rotor (see Section 4.6.1). This can be a double-cage design (rotor #1) or a single cage rotor with additional asymmetric outer cage (rotor #2). Subscript $_{r1}$ is for the outer cage and $_{r2}$ for the inner cage parameters. The

leakage inductance l_{r12} stems from the common rotor leakage flux λ_{r12} that links both rotor cages but not the stator cage. From Alger's formula [22, 117] the leakage reactance in the outer cage is assumed to be zero, therefore $l_{r1} = 0$. The parameter values from the fundamental machine model can only give a crude estimation for the *hf* model. This is because of skin effect that has to be considered for high frequencies. Transformation into the stator frame and after the matrix inversion (see (5.11)) with a *hf* voltage $\underline{v}_{s_{\alpha\beta}} = \underline{v}_c$ results in:

$$\underline{i}_{s_{\alpha\beta\_c}} = \underline{i}_{cp} e^{j\omega_c t} - \underline{i}_{cn} e^{j(2\theta_r - \omega_c t)}$$

Again, two saliency periods per pole pair result in a modulation harmonic at frequency $f_c - 2f_r$. Note that this type of modulation is not a standard amplitude modulation (AM) but a single sideband AM that contains a carrier. Also, the signal is not of the scalar type but is a vector. This allows for some interesting signal processing (see Section 5.4 and following sections).

The circumferential resistance variation is easily realized by changing the diameter of the bars in the outer cage of an induction machine [24]. The *hf* signals penetrate only into the outer section of the rotor because of skin effect and the large reactance of the inner rotor section for the *hf* signals. Therefore the *hf* signals get influenced by a resistance variation in the outer perimeter. A copper bar with maximum diameter will have minimum resistance. The minimum resistance shall be $R_{r1_{(\beta)}}$ and the maximum resistance then $R_{r1_{(\alpha)}}$. Ideally, the resistance variation is sinusoidal. In practice, this is not easily achievable because of the standard sizes of copper bars and therefore limited number of different wire gauges. This is not really a problem since higher harmonics resulting from this non-ideal sinusoidal distribution will be small.

Rotor Slotting Saliency

For a range of motors, the inductance variation over the rotor slot pitch due to slotting can be used to estimate the rotor position. Injected *hf* voltages penetrate only into the outer perimeter of the rotor. The permeance and hence the *hf* inductance are modulated by the rotor slots that results in a modulation of the *hf* stator currents. In contrast to the previously described engineered rotor saliencies, this is a natural saliency, hence the term "symmetric" rotor. The saliency model is very similar to that of Section 5.2.2. The fundamental difference is that the number of saliency periods is generally larger than for the asymmetric rotors, that usually have one saliency period per pole pitch [24, 77]. The number of saliency periods due to rotor slotting is determined by the number of rotor slots N_r and the number of pole pairs *pp* as:

$$n = N_r/pp$$

The *hf* currents filtered from the stator currents then are

$$\underline{i}_{s_{\alpha\beta\_c}} = \underline{i}_{cp}e^{j\omega_c t} + \underline{i}_{cn}e^{j(n\theta_r - \omega_c t + \phi)} \tag{5.15}$$

where $\underline{i}_{cp}$ and $\underline{i}_{cn}$ are the positive and negative sequence *hf* currents respectively. The positive sequence is the unmodulated carrier that does not contain any information about the rotor position.

5.2.3 Saturation Saliency

A typical saliency that is naturally present in the machine is that due to saturation. The saturation saliency will be present for sufficiently high flux levels and will increase with load. Open or semi-open rotor slots will cause a reduction of the saturation modulation. The saturation saliency rotates at the flux angle θ_e (stator flux, air-gap flux or rotor flux) but can deviate considerably under load [18,50,95]. By neglecting higher harmonics and concentrating only on the fundamental, the saturation saliency seen by the *hf* currents can be described best in the *dq* frame. In this frame, the currents and voltages are decoupled. The *d*-axis shall be aligned in the direction of the maximum saturation (minimum impedance) with $Z_d < Z_q$. Similar to (5.8):

$$\begin{bmatrix} v_{s_d} \\ v_{s_q} \end{bmatrix} = \begin{bmatrix} Z_d & 0 \\ 0 & Z_q \end{bmatrix} \begin{bmatrix} i_{s_d} \\ i_{s_q} \end{bmatrix}$$

$$[\underline{v}_{s_{dq}}] = [Z_{dq}][\underline{i}_{s_{dq}}] \tag{5.16}$$

In practice, the *hf* currents are measured in the stationary $\alpha\beta$ frame, so that

$$\begin{bmatrix} i_{s_\alpha} \\ i_{s_\beta} \end{bmatrix} = \frac{1}{Z_d \cdot Z_q} \begin{bmatrix} \overline{Z} - \Delta Z\cos(2\theta_e) & -\Delta Z\sin(2\theta_e) \\ -\Delta Z\sin(2\theta_e) & \overline{Z} + \Delta Z\cos(2\theta_e) \end{bmatrix} \begin{bmatrix} v_{s_\alpha} \\ v_{s_\beta} \end{bmatrix} \tag{5.17}$$

where $\overline{Z} = 0.5(Z_d + Z_q)$ and $\Delta Z = 0.5(Z_q - Z_d) > 0$. For a given voltage $\underline{v}_{s_{\alpha\beta}} = \underline{v}_c$, the carrier signal as in (5.12):

$$\underline{i}_{s_{\alpha\beta\_c}} = \underline{i}_{cp}e^{j\omega_c t} - \underline{i}_{cn}e^{j(2\theta_e - \omega_c t)}$$

As in the situation with the rotor saliency, only the second term contains the useful information about the saliency position. Physically, there is one flux period per 360° electrical. There are two maxima of the flux per period, one positive, one negative. This causes two modulations of the *hf* signal per electrical period and results in a modulation harmonic at frequency $f_c - 2f_e$.

Physical Saliency Model

For the saturation saliency, physical models and approaches are given in [50, 92, 95, 126], explaining and deriving the relation between the saliency and machine fundamental saturation. This can be by *finite element methods* (FEM) or methods based on the two-axis model. This section will use an approximate *hf* model and discuss the variation in the leakage parameters which are the principle determinants of the saturation harmonics.

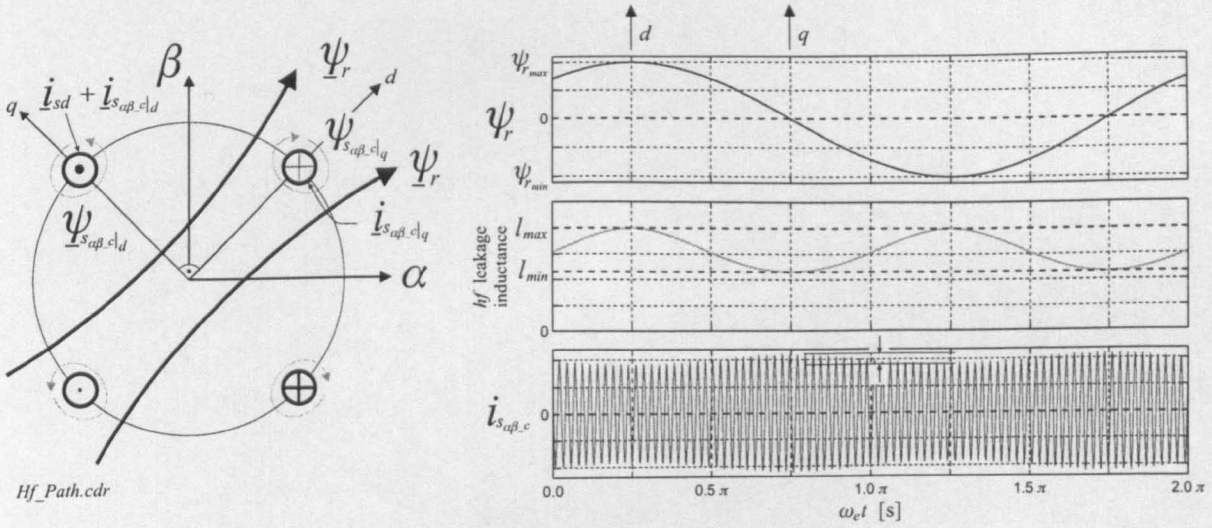

Figure 5.2: *Machine cross-section showing fundamental and hf current and flux vectors under no-load. Left: machine cross-section. Right: angular position of rotor flux magnitude, hf leakage inductance and hf current.*

In [92, 126], the relation between fundamental flux and *hf* modulation is examined in a graphical model of the machine cross-section, [92] additionally uses two-dimensional FEM. The left of Fig. 5.2 shows this simplistic model of the machine with the d and q current windings and the rotor flux vector ψ_r that determines the orientation of the d-axis. The rotor flux $\underline{\psi}_r$ is produced by the $\underline{i}_{sd}$ stator current component. Note that the rotor flux vector $\underline{\psi}_r$ and therefore the d-axes are in direction of the q-winding. The windings are additionally fed by a *hf* current $\underline{i}_{s_{\alpha\beta\_c}}$ that produces a *hf* flux $\underline{\psi}_{s_{\alpha\beta\_c}}$. The figure shows the components of the *hf* current and flux vectors in the d and q windings with subscripts $|_d$ and $|_q$ respectively.

The authors in [92] come to the conclusion that for no-load operation, the *hf* modulation does not cause the modulating envelope of $i_{s_{\alpha\beta\_c}}$ to be at a maximum in the d- or flux axis but in the q- or quadrature axis. The reason is that the rotor flux causes saturation in the d-axis, that reduces the *hf* leakage inductance where the

q-windings are located. The *hf* leakage inductance in the d-axis is not affected by the rotor flux and is therefore larger. Since the *hf* flux does not penetrate deeply into the machine, it is the q-component $\psi_{s_{\alpha\beta-c}|q}$ that gets affected by the saturation and reduced *hf* leakage inductance. Hence the envelope of the *hf* currents will be at a maximum in the q axis as shown in Fig. 5.2. A negative fundamental flux ψ_r will also cause a saturation of the leakage inductance with the result of an increased *hf* current. Since there are two extrema of the fundamental flux per electrical period, there are two maxima of the *hf* current. Hence, the angle of the saliency is twice that of the flux vector with $\theta_{sat} = 2 \cdot \theta_e$.

The *hf* currents are mainly influenced by the nonlinear behaviour of the *hf* leakage inductances. This behaviour is mainly determined by saturation of rotor slot bridges and teeth in stator and rotor [117,124]. For rotors with closed rotor slots, saturation of the slot bridges under rated conditions can reduce the leakage inductance by a factor of two from the unsaturated value [19]. The slot leakage on the stator side is not much influenced by a change of operating conditions because the stator slots are considerably wide by geometric design. If the injection frequency f_c is lower, the saturation of the main flux path will have an impact on the *hf* flux path as can be seen from the model of Fig. 5.2. The injection frequency f_c determines the degree of penetration of the *hf* signal into stator and rotor. The skin effect determines the *hf* resistance with $R \propto \sqrt{f_c}$ and the leakage impedance changes according to $\omega_c l \propto f_c$.

The graphical approach of Fig. 5.2 shows the limitation of the two-axis *hf* model from the sections before: Since the penetration of the *hf* flux $\underline{\psi}_{s_{\alpha\beta-c}}$ differs from that of the flux $\underline{\psi}_r$, there will be a displacement between the orientation of the *hf* flux vector to that of the fundamental flux. The displacement is a function of the injection frequency. Assuming no-load conditions and if the *hf* injection frequency is low, the *hf* flux shares paths with the fundamental flux and the displacement is small. A high injection frequency prevents deep penetration and the *hf* flux is orthogonal to the fundamental flux [126] as shown in Fig. 5.2 for no-load.

The effect of loading the induction machine is not discussed in [92] or [126]. A possible explanation for the induction machine is derived here from [127]. For the model shown on the left of Fig. 5.3, the load current i_{sq} will not be zero. Its magnetic field around the conductors will superimpose to that of the rotor flux ψ_r. The area of increased flux and therefore saturation is marked by a hatched oval. This is the area where the field due to i_{sq} adds to the rotor flux. The field will be weakened on the other side of the d-axis similar to the armature reaction in DC machines. This reduced flux decreases saturation; the saliency has moved in the mathematical positive direction. The angle φ_{C_k} that is obtained from the saturation saliency is marked in the figure. This angle is drawn between the d-axis and the saliency axis. Under load, the saliency axis will differ from that of the rotor flux and $\varphi_{C_k} \neq 0$ where the difference is also dependent on the flux level.

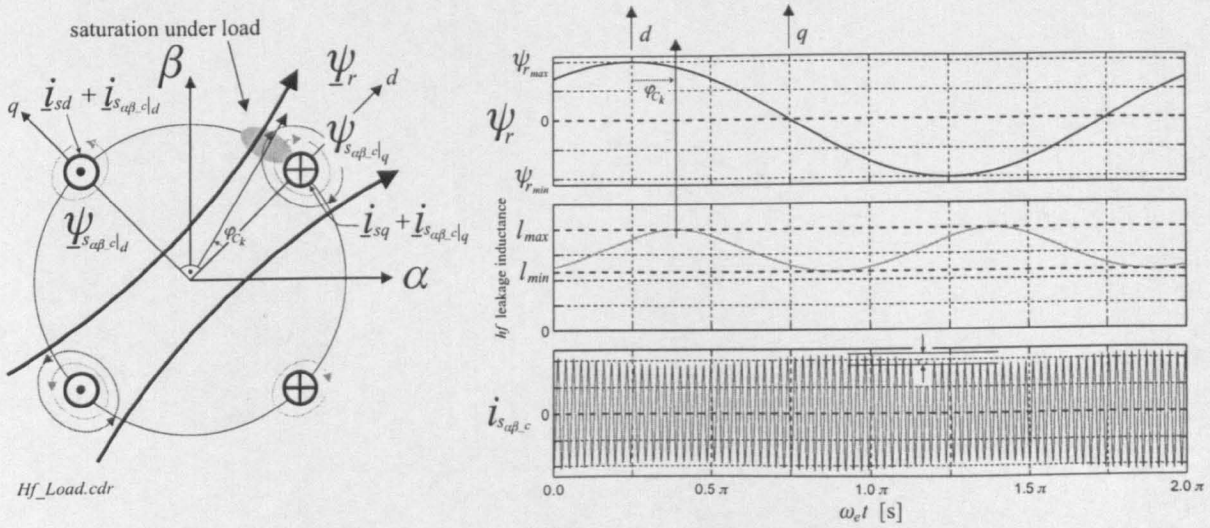

Figure 5.3: *Machine cross-section showing fundamental and hf current and flux vectors under loaded conditions. Left: machine cross-section. Right: angular position of rotor flux magnitude, leakage inductance and hf current envelope.*

In [128], the shift of the *hf* impedance and therefore that of the saliency axis is attributed to the shift of the saturation from the axis of the mutual flux to that of the rotor flux under load. Experiments by the author have shown that the angular shift of the saliency axis exceeds the values obtained in [128] when the machine is loaded or the flux level is changed. The experiments were conducted on three different machines and two rigs. The results are summarized in Sections 7.1.2 and 7.2.2 as part of the experimental commissioning results for the saturation saliency.

The following analysis derives the displacement angle between the vectors of the rotor flux linkage, mutual flux linkage and stator flux linkage. From the relation between rotor flux linkage and mutual flux linkage in Fig. 2.4 and relation (2.37):

$$\begin{aligned}
a) \qquad \underline{\psi}_m &= \underline{\psi}_r - L_{r\sigma}\underline{i}_r, \qquad L_{r\sigma} = (1+\sigma_r)L_o \\
b) \quad (1+\sigma_r)\cdot\underline{i}_r &= \underline{i}_{mR} - \underline{i}_s \\
c) \qquad i_{sq} &= \omega_{sl} T_r \cdot i_{mR}, \qquad T_r = L_r/R_r
\end{aligned}$$

Inserting $b)$ in $a)$ removes the rotor currents and gives:

$$\underline{\psi}_m = \underline{\psi}_r - \frac{L_{r\sigma}}{1+\sigma_r}\cdot(\underline{i}_{mR} - \underline{i}_s) \tag{5.18}$$

When resolving (5.18) in the dq-frame, where $\underline{i}_{mR} = i_{mR}$ and $\underline{\psi}_r = L_o i_{mR}$ and the respective q-components are zero, the angle θ_{rm} between the rotor flux linkage $\underline{\psi}_r$ and

the mutual flux linkage $\underline{\psi}_m$ can be obtained via the vectorial relations in (5.18):

$$\theta_{rm} = \arctan\left(\frac{L_{r\sigma} i_{sq}}{(1+\sigma_r) L_o i_{mR}}\right)$$

which can be simplified by substituting i_{sq} by using c):

$$\theta_{rm} = \arctan\left(\frac{\omega_{sl} L_{r\sigma}}{R_r}\right)$$

Clearly, the angular difference is only a few degrees under full load which does not explain the change of φ_{C_k} in Sections 7.1.2 and 7.2.2.
From equation (2.41), $\underline{\psi}_s = \underline{\psi}_r + \sigma L_s \underline{i}_s$, the displacement θ_{rs} between rotor flux linkage and stator flux linkage can be resolved in a similar way:

$$\begin{aligned} \theta_{rs} &= \arctan\left(\frac{\sigma L_s \cdot i_{sq}}{(L_o + \sigma L_s) i_{mR}}\right) \\ &= \arctan\left(\frac{\sigma L_s \cdot \omega_{sl} L_r}{(L_o + \sigma L_s) R_r}\right) \end{aligned}$$

The angular difference of the two flux linkage vectors will also reach only a few degrees under load. The experimental analysis in this thesis shows that the saliency angle φ_{C_k} differs from the angle of stator and airgap flux by more than θ_{rm} or θ_{rs} and can be better approximated by the load angle $\delta = \arctan(i_{sq}/i_{sd})$. The reason for this might be derived from Fig. 5.3 *quantitatively.* A conclusive theory is currently not available and cannot be based on the experience of only three machines. Since a qualitatively precise prediction of the change of the saturation saliency with load and/or flux is not possible, the commissioning strategies developed in this thesis are currently the only possibilities to obtain the displacement angle φ_{C_k}.

The analysis in this section has shown that the two-axis model does not include the shift of the saliency with load and flux level. A model is required that includes the precise geometry and saturation effects in order to predict the displacement between the saliency angle and the rotor flux vector.

5.2.4 Multiple Saliencies

In general there will be multiple saliencies in a machine. This can be the saturation saliency of Section 5.2.3 or a rotor saliency of Section 5.2.2. The latter can be due to an engineered inductance (Section 5.2.2) or resistance variation (Section 5.2.2) or due to the natural inductance variation due to the rotor slotting of Section 5.2.2.

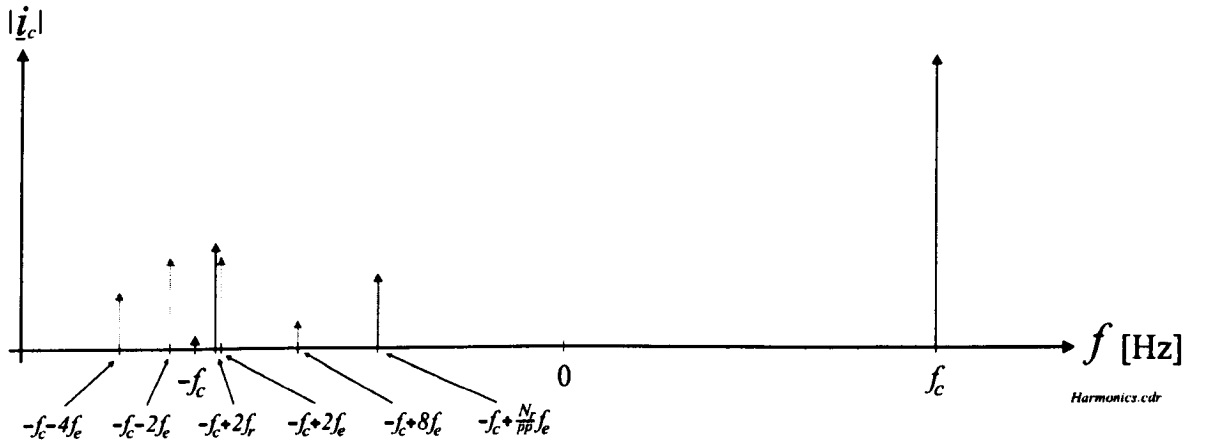

Figure 5.4: *Modulation harmonics in the hf current spectrum, excluding eccentricity harmonics and fundamental excitation*

Combining all saliencies into one model:

$$\underline{i}_{s_{\alpha\beta\_c}} = i_{cp}e^{j\omega_c t} + \sum_m \sum_k i_{cn_{mk}} e^{j(h_{mk}\theta_m - \omega_c t + \varphi_{mk})} \tag{5.19}$$

where $\underline{i}_{cp}$ and $\underline{i}_{cn_{mk}}$ are the positive and negative sequence *hf* currents respectively. The positive sequence currents $\underline{i}_{cp}$ are unmodulated. In (5.19) the various saliencies can be described with the different values of m:

$m = 0$, net $\alpha\beta$ imbalance:
$h_{0k} = 0$

$m = 1$, saturation saliency:
$h_{1k} = -2, +4, -8, \ldots, (-2)^k$ and $\theta_1 = 2\pi f_e t$

$m = 2$, rotor slotting saliency:
$h_{2k} = 2n, 4n, \ldots, 2nk$ and $\theta_2 = 2\pi f_r t$,
where $n = N_r/ps$ is the number of
rotor slots (N_r) per pole ($ps = 2pp$)

$m = 3$, engineered pitch saliency:
$h_{3k} = 2, 4, \ldots, 2k$ and $\theta_3 = 2\pi f_r t$

and k is the harmonic order. Rotor eccentricity effects have been neglected since these have not been found to be exploitable in commercial machines. For all saliencies, $k = +1$ denotes the fundamental modulation harmonic; higher values of k arise due to the non-sinusoidal spatial distribution of the respective saliency. The amplitude spectrum of $\underline{i}_{s_{\alpha\_c}}$ is shown in Fig. 5.4. The information about the phase difference from $\underline{i}_{s_{\beta\_c}}$ is used to expand the spectrum to negative frequencies. These can be physically

interpreted, since the *hf* signals are vectors. Positive frequencies are defined as a rotation in the direction of the injected voltage vector that serves as the reference. A harmonic with negative frequency represents a negative sequence harmonic that rotates in the opposite direction of the *hf* voltage vector.

In (5.19), the carrier component i_{cp} in $\underline{i}_{s\alpha\beta\_c}$ that is unmodulated can be separated from the negative sequence harmonics, leaving only the modulation harmonics due to the machine saliencies. In practical systems, a reflection of the carrier harmonic can be found as a negative sequence harmonic at frequency $-f_c$. This harmonic also contains no useful information for the sensorless control. In fact this harmonic is due to imbalances in the measured *hf* $\alpha\beta$ currents (see equations (5.5) and (5.6) for more information). The cause can be measurement errors or imbalances due to differences in the inverter deadtime of the three inverter legs.

For the sensorless control of induction machines, the rotor position or flux angle needs to be estimated. This estimation requires only one saliency present in the machine. It has not been possible so far to use two or more saliencies simultaneously for the estimation. Since it is very unlikely that there is only a single saliency in a real machine, the other saliency harmonics have to be removed.

It can be seen from (5.19) and Fig. 5.4 that all saliency harmonics are negative sequence harmonics. This means that the vectors of the saliency harmonics rotate in the opposite direction of the injected *hf* voltage vector. For the sensorless control, only the negative frequency spectrum is of interest. The reflection of the carrier frequency at $-f_c$ will be used as the reference for the further analysis. This is because for the demodulation of the saliency angle in sensorless control, the negative sequence harmonics will be transformed so that $-f_c$ will be at DC. It can be seen from Fig. 5.4 that the direction of rotation of the saliency harmonics with respect to $-f_c$ can differ. This means that some saliency harmonics are left of $-f_c$ in the spectrum of Fig. 5.4 and some are on the right. The direction of rotation with respect to $-f_c$ is e.g. different for the saturation saliency with $h_{21}\theta_2 = -2\theta_e$ compared to a slotting saliency of $h_{31}\theta_3 = +28\theta_r$ as observed for the machine with rotor #3. Both harmonics are negative sequence harmonics but of opposite direction. The spectral difference therefore is $h_{31} \cdot f_3 - h_{21} \cdot f_2 = 30f_r - 2f_{sl}$. Note that if the sequence information is not used, the spectral difference will only be $26f_r - 2f_{sl}$.

The direction of a negative sequence harmonic can be determined by a simple model: Two windings on the three-phase stator are mechanically apart by $360°/(3 \cdot pp)$. The three windings are called A, B and C and the saliency shall be initially aligned in direction of A. For rotation in a positive direction, the moving saliency has to be aligned in direction of winding B before it is aligned to C. Otherwise the saliency is rotating in the negative direction. The normalized distance function d_p can be used to determine if the period of the moving saliency will be aligned first to B (with

winding index $p = 1$) or C (index $p = 2$) when initially aligned to winding A ($p = 0$):

$$d_p = \frac{p \cdot \frac{360°}{3 \cdot pp} - \frac{360°}{N_{sal} \cdot pp} \cdot fix\,(p \cdot N_{sal}/3)}{\frac{360°}{N_{sal} \cdot pp}} \tag{5.20}$$

$$= p \cdot \frac{N_{sal}}{3} - fix\left(p \cdot \frac{N_{sal}}{3}\right) \tag{5.21}$$

where N_{sal} is the number of periods of the saliency harmonic over 360° mechanical, which means there are $360°/N_{sal}$ mechanical per sinusoidal variation. If the saliency is due to the slotting of the rotor, then $N_{sal} = N_r$, the total number of rotor slots. Typically, $N_{sal} = 4$ for an engineered rotor saliency or the main saturation saliency. The number of pole pairs are pp and p is the winding index. For $d_1(p = 1) < d_2(p = 2)$, the spacial distance of a saliency period to B is smaller than that to winding C. Therefore the saliency has a positive direction. For $d_1(p = 1) > d_2(p = 2)$, the saliency has a negative direction. The function $fix(\ldots)$ performs a conversion to the nearest integer less than or equal to its argument.

The normalized distance function d_p first determines the angle of winding p from A that is $p \cdot 360°/(3 \cdot pp)$ and is 60° for winding B in a four-pole machine. The angle covered by one saliency period is $360°/(N_{sal} \cdot pp)$ and there are $fix(p \cdot N_{sal}/3)$ full saliency periods between winding p and reference A. The product of full saliency periods and angle per saliency period is therefore the angle between windings p and A that is covered by full saliency periods. This angle subtracted from $p \cdot 360°/(3 \cdot pp)$ will therefore be within the interval $[0 \ldots \frac{360°}{N_{sal} \cdot pp}]$. Hence it is suitable to use the angle of one saliency period for normalization.

An overview of typical saliencies is given in the table below where the number of pole pairs $pp = 2$. The first row with $N_{sal} = 4$ is for a saturation saliency or an engineered saliency. The other entries are for slotting saliencies with $N_{sal} = N_r$.

N_{sal}	d_1	d_2	Sequence
4	$0.\overline{3}$	$0.\overline{6}$	ABC (positive direction)
40	$0.\overline{3}$	$0.\overline{6}$	ABC (positive direction)
56	$0.\overline{6}$	$0.\overline{3}$	ACB (negative direction)
58	$0.\overline{3}$	$0.\overline{6}$	ABC (positive direction)

The above discussion has shown that under some conditions the direction in which a saliency rotates, with respect to $-f_c$, can be positive or negative. After transforming the negative sequence harmonics to DC, the spectral separation of two saliencies rotating in different directions will be increased. This increased spectral distance can be useful when separating saliency harmonics. The spectral separation however can only be increased for saliencies rotating in different directions (with respect to $-f_c$) and is the sum of the absolute distance of each harmonic from $-f_c$.

At low speed, different harmonics, such as the rotor position harmonics at $h_{2k}f_r$ and the saturation harmonics at $h_{1k}f_e$ will be very close or will even overlap for $h_{2k}f_r = h_{1k}f_e$. It is therefore not possible to use a filter for the suppression of unwanted saliencies if the angle of the remaining saliency is to be estimated in real-time. The possibility of using adaptive filters as suggested in [100] to remove the saturation saliency from the slotting modulation is therefore very unlikely at low speeds and standstill. High speed results in an increased spectral distance of the harmonics in question so that adaptive filters might be applicable in steady-state operation. The difficulty of course is the origin of the qualifying signal that adapts the filter. This qualifier would require the knowledge of the rotor speed that also is in fact unknown and has to be estimated.

5.3 Alternative Saliency Models

This section describes three saliency models more in detail that were published first in [18,70], [79] and [20]. These saliency models differ in their presentation and explanation of the physical origin of the saliency from the two-axis saliency model of the previous section. The analysis of this section will show that the alternative saliency models can be described by the same mathematics as the model of [17, 24] in the previous section. A description of the signal processing and the techniques for the estimation of the saliency angle will also be given since the estimation strategies are closely related to the saliency models. The explanation of the saliency models and evaluation of limitations and performance of the estimation strategies are equally a result of practical experimentation and simulation by the author.

5.3.1 Schrödl Saliency Model

The INFORM method [18] requires the injection voltage test pulse vectors to obtain the saliency information in the machine. This can be a saliency due to saturation, rotor slotting (rotor geometry) or anisotropy [88]. For simplicity, this section only covers the modelling of the saturation saliency. The other saliencies can easily be derived from that model.

Assuming a simple LR circuit with a back-*emf* $\underline{e}$ and a voltage source of value $\underline{v}_s$, the differential equation is:

$$\underline{v}_s = L_s \frac{d\underline{i}_s}{dt} + R_s \underline{i}_s + e \tag{5.22}$$

The circuit parameters are L_s and R_s, the inductance and resistance respectively and $\underline{i}_s$ is the current. The time constant $T_s = L_s/R_s$. The solution in the time domain at

time t_1 for an initial current $\underline{i}_{s0}$ at $t = t_0$ is

$$\underline{i}_{s1} = \left(\frac{\underline{v}_s - \underline{e}}{R_s} - \underline{i}_{s0}\right) \cdot \left(1 - e^{-(t_1 - t_0)/T_s}\right) + \underline{i}_{s0} \tag{5.23}$$

$$\approx \left(\frac{\underline{v}_s - \underline{e}}{R_s} - \underline{i}_{s0}\right) \cdot \frac{\Delta t}{T_s} + \underline{i}_{s0} \tag{5.24}$$

where $\Delta t = t_1 - t_0$ and $\underline{v}_s = const$ and $\underline{e} = const$ during the period Δt. The solution of (5.23) can be approximated by (5.24) if $T_s \gg \Delta t$ which is valid for short voltage pulses. The exponential function can be approximated by a line of constant slope. Therefore, the current change $\Delta\underline{i}_{s_I}$ for the pulse length Δt can be described by the following equation:

$$\Delta\underline{i}_{s_I} = (\underline{i}_{s_1} - \underline{i}_{s0}) \approx \left(\frac{\underline{v}_{s_1} - \underline{e}_1}{R_s} - \underline{i}_{s0}\right) \cdot \frac{\Delta t_1}{T_s} \tag{5.25}$$

To eliminate $\underline{e}$ and $\underline{i}_{s0}$, a second voltage pulse is applied with $\underline{v}_{s_2} = -\underline{v}_{s_1}$ and same pulse width $\Delta t_2 = \Delta t_1 = \Delta t$. Since this second pulse is applied shortly after the first pulse $\underline{v}_{s_1}$, the back-*emf* can be assumed to remain unchanged, where $\underline{e}_2 = \underline{e}_1 = \underline{e}$:

$$\Delta\underline{i}_{s_{II}} = (\underline{i}_{s_2} - \underline{i}_{s_1}) = \left(\frac{\underline{v}_{s_2} - \underline{e}_2}{R_s} - \underline{i}_{s_1}\right) \cdot \frac{\Delta t_2}{T_s} \tag{5.26}$$

so that the difference of the current changes is

$$\Delta\underline{i}_{s_I} - \Delta\underline{i}_{s_{II}} = (2\underline{i}_{s_1} - \underline{i}_{s0} - \underline{i}_{s_2}) \stackrel{!}{=} \frac{2\underline{v}_{s_1}}{R_s} \cdot \frac{\Delta t}{T_s} + \underbrace{(\underline{i}_{s_1} - \underline{i}_{s0}) \cdot \frac{\Delta t}{T_s}}_{\approx 0} = \frac{2\underline{v}_{s_1} \cdot \Delta t}{L_s} \tag{5.27}$$

If the voltage pulses are kept constant in amplitude and duration (constant VTA), a changing inductance can be estimated with

$$L_s(\underline{i}_s) = \frac{c_s}{\Delta\underline{i}_{s_I} - \Delta\underline{i}_{s_{II}}} \tag{5.28}$$

where c_s is a constant factor and L_s is a function of the current.

Fig. 5.5 shows the stator current $\underline{i}_s$ from simulation with the machine rotating at constant speed of $n_r = 40$rpm, full flux and $1/3^{rd}$ of rated load. The pulse frequency of the PWM was $50\mu s$ with a short interruption of the normal PWM generation every $4ms$ to inject a test pulse. The resulting current transient can be seen in Fig. 5.5 with the three sampling points marked $\underline{i}_{s0}$, $\underline{i}_{s_1}$ and $\underline{i}_{s_2}$. The sampling of the currents has to be synchronized to the voltage test pulse generation. Inverter deadtime has been neglected in the simulation. From (5.27) it is obvious that the two current derivatives

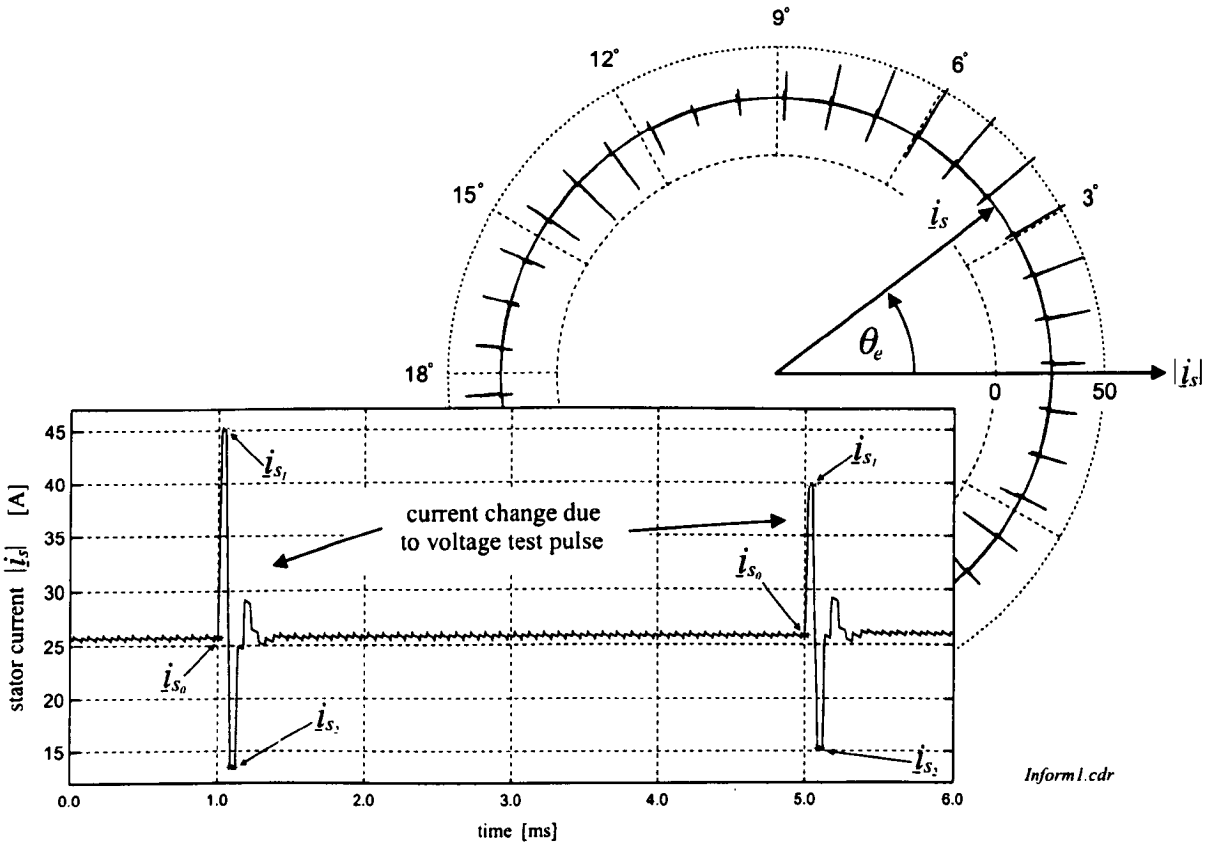

Figure 5.5: *Transient current response due to voltage test vectors, showing sampling points. Square: stator current magnitude over time. Circle: magnitude of stator current vector*

$\frac{di_s}{dt}|_I$ and $\frac{di_s}{dt}|_{II}$ can be determined by sampling the stator current at the specified three points. The knowledge of the current differences $\Delta\underline{i}_s$ allows the estimation of the inductance. The estimation of the inductance from the phase information $\underline{Y} = \frac{\Delta\underline{i}_s}{\Delta t \cdot \underline{v}_s}$ is claimed in [18] to give more accurate results. Inspecting (5.27) supports this claim since the actual pulse period Δt and voltage vector $\underline{v}_s$ can differ in practice from the reference values due to inverter deadtime.

Based on (5.27) and (5.28), a relation between applied voltage phasor and current derivative is given that describes the inductance that can be a function of the saturation in the machine. This saliency model is based on a difference in the inductance on the d and q axes, where the d-axis is aligned to the flux. Fig. 5.6 shows the elliptic path of the current derivative for the voltage phasor $\underline{v}_s$ describing a circular path. Note that without back-*emf* and negligible resistive term, only one current derivative i.e. $\frac{di_s}{dt}|_I$ has to be determined and not two as used in (5.27). This simplified condi-

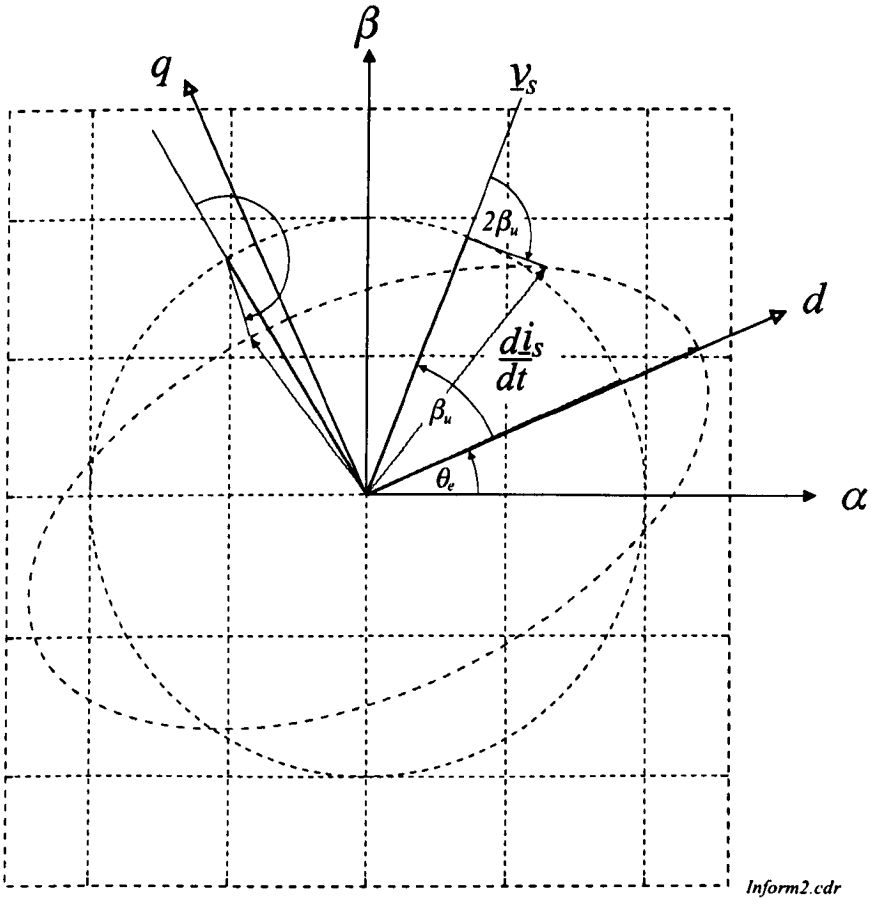

Figure 5.6: *Dependency of current change on the voltage vector and saturation saliency*

tion is used in Fig. 5.6 to display the relation between applied voltage vector, current derivative and inductance.

The longer axis of the ellipse is aligned in direction of the d or flux axis. For a particular applied voltage phasor, the current change is measured and the orientation of the d-axis can be derived. With the knowledge of the orientation of the voltage phasor in the $\alpha\beta$ frame and the angle β_u, the angle θ_e can be derived. The angle β_u describes the orientation of the voltage phasor in the dq frame.

Applying a test voltage vector, the relation between the voltages and the measured current transients in the dq frame can be described by the matrix of the inverse inductance:

$$\begin{bmatrix} di_{s_d}/dt \\ di_{s_q}/dt \end{bmatrix} = \begin{bmatrix} Y_d & 0 \\ 0 & Y_q \end{bmatrix} \begin{bmatrix} v_{s_d} \\ v_{s_q} \end{bmatrix}$$

$$\left[\frac{d\underline{i}_{s_{dq}}}{dt}\right] = \left[Y_{dq}\right]\left[\underline{v}_{s_{dq}}\right] \tag{5.29}$$

This model can easily be derived from (5.16) by matrix inversion. In the dq-frame only the elements on the main diagonal are non-zero. Saturation in the d-axis causes a decrease in the inductance. The inverse Y_d is therefore larger than Y_q. With the transformation from dq into the $\alpha\beta$ frame:

$$[\underline{v}_{s_{\alpha\beta}}] = [e^{j\theta_e}][\underline{v}_{s_{dq}}] \tag{5.30}$$

the voltages can be expressed in the general $\alpha\beta$ stator frame. Similar to (5.10), the matrix equation can be transformed into the $\alpha\beta$ frame using (5.30):

$$\left[e^{j\theta_e}\right]\left[\frac{d\underline{i}_{s_{dq}}}{dt}\right] = \left[e^{j\theta_e}\right]\left[Y_{dq}\right]\underbrace{\left[e^{-j\theta_e}\right]\left[e^{j\theta_e}\right]}_{[1]}\left[\underline{v}_{s_{dq}}\right]$$

$$\left[\frac{d\underline{i}_{s_{\alpha\beta}}}{dt}\right] = \left[e^{j\theta_e}\right]\left[Y_{dq}\right]\left[e^{-j\theta_e}\right]\left[\underline{v}_{s_{\alpha\beta}}\right] \tag{5.31}$$

resulting in an admittance matrix with $2\theta_e$ dependency.

$$\begin{bmatrix} di_{s_\alpha}/dt \\ di_{s_\beta}/dt \end{bmatrix} = \begin{bmatrix} \overline{Y} + \Delta Y\cos(2\theta_e) & \Delta Y\sin(2\theta_e) \\ \Delta Y\sin(2\theta_e) & \overline{Y} - \Delta Y\cos(2\theta_e) \end{bmatrix}\begin{bmatrix} v_{s_\alpha} \\ v_{s_\beta} \end{bmatrix} \tag{5.32}$$

where the mean inverse inductance is $\overline{Y} = 0.5 \cdot (Y_d + Y_q)$ and the differential term $\Delta Y = 0.5 \cdot (Y_d - Y_q)$. As $Y_d > Y_q$, $\Delta Y > 0$. This result is similar to the saturation saliency in (5.17) with sinusoidal signals. Here in (5.32), the currents and voltages are instantaneous.

Relation (5.32) can be further developed where the voltage phasor $\underline{v}_{s_{\alpha\beta}} = v_{s_\alpha} + jv_{s_\beta} = V_s e^{j(\beta_u+\theta_e)}$ is imposed and known in the $\alpha\beta$ frame. The conjugate complex vector is $\underline{v}^\star_{s_{\alpha\beta}} = v_{s_\alpha} - jv_{s_\beta}$. The measured current changes due to a voltage test pulse are:

$$\begin{aligned}
\frac{d\underline{i}_{s_{\alpha\beta}}}{dt} &= \overline{Y}\underline{v}_{s_{\alpha\beta}} + \Delta Y\underline{v}^\star_{s_{\alpha\beta}}\underbrace{\{\cos(2\theta_e) + j\sin(2\theta_e)\}}_{e^{j2\theta_e}} \\
&= \overline{Y}\underline{v}_{s_{\alpha\beta}} + \Delta Y\underline{v}^\star_{s_{\alpha\beta}}e^{j2\theta_e} \\
&= V_s\left(\overline{Y}e^{j(\beta_u+\theta_e)} + \Delta Y e^{j2\theta_e - j(\beta_u+\theta_e)}\right) \\
&= V_s e^{j(\beta_u+\theta_e)}\cdot\left(\overline{Y} + \Delta Y e^{-j2\beta_u}\right)
\end{aligned}$$

$$\frac{d\underline{i}_{s_{\alpha\beta}}}{dt} = \underline{v}_{s_{\alpha\beta}}\cdot\left(\overline{Y} + \Delta Y e^{-j2\beta_u}\right) \tag{5.33}$$

According to (5.33), the current change can be expressed as a component $\underline{v}_s \cdot \overline{Y}$ that is in the direction of the applied voltage phasor and a component $\underline{v}_s \cdot \Delta Y e^{-j2\beta_u}$ that changes with twice the angle β_u. It is only this latter term that contains the information about the saliency angle θ_e. This conclusion is not immediately obvious. Knowing β_u from analyzing the current change due to the applied voltage test vector $\underline{v}_{s_{\alpha\beta}}$, will provide the position of the voltage phasor with respect to the dq frame as shown in Fig. 5.6. Since the position of $\underline{v}_{s_{\alpha\beta}}$ is known in the $\alpha\beta$ frame, the saliency angle θ_e can easily be derived.

It can be shown that the solution of (5.33) is independent of the measurement frame. For a simplified analysis, the dq frame is used with the relation between currents and voltages from (5.29), where $Y_d = \overline{Y} + \Delta Y$ and $Y_q = \overline{Y} - \Delta Y$. Then with a voltage phasor $\underline{v}_{s_{dq}} = V_s e^{j\beta_u}$ in the dq frame:

$$\begin{bmatrix} di_{s_d}/dt \\ di_{s_q}/dt \end{bmatrix} = \begin{bmatrix} \overline{Y} + \Delta Y & 0 \\ 0 & \overline{Y} - \Delta Y \end{bmatrix} \begin{bmatrix} v_{s_d} \\ v_{s_q} \end{bmatrix} \tag{5.34}$$

$$\begin{aligned} \frac{d\underline{i}_{s_{dq}}}{dt} &= \overline{Y}\underline{v}_{s_{dq}} + \Delta Y v_{s_d} - j\Delta Y v_{s_q} \\ &= \overline{Y}\underline{v}_{s_{dq}} + \Delta Y \underline{v}^{\star}_{s_{dq}} \\ &= V_s(\overline{Y}e^{j\beta_u} + \Delta Y e^{-j\beta_u}) \\ &= V_s e^{j\beta_u} \cdot (\overline{Y} + \Delta Y e^{-j2\beta_u}) \end{aligned}$$

$$\frac{d\underline{i}_{s_{dq}}}{dt} = \underline{v}_{s_{dq}} \cdot (\overline{Y} + \Delta Y e^{-j2\beta_u}) \tag{5.35}$$

Note that the term in brackets in (5.35) is identical to that in the solution of (5.33). In fact, the relation between current changes and applied voltages is independent of the measurement frame.

In [18], (equation *(3.45)* on page *40*), the saliency is described by

$$\frac{d\underline{i}_s}{dt} = const_1 \cdot \underline{u}_s \cdot [\, \mu_{e\,0} - \frac{\mu_{e\,2}}{2} \cdot \exp(-j \cdot 2\beta_u)\,] \tag{5.36}$$

where $\mu_{e2} < 0$, $const_1 \cdot \mu_{e\,0} = \overline{Y}$ and $const_1 \cdot \mu_{e\,2}/2 = \Delta Y$ make relation (5.36) equal to that of (5.35). Equations (5.35) and (5.34) link the syntax given in [18] to that of [17] or [24]. This concludes that the saliency model of [18] can equally be described by a two-axis model in the dq frame as that in [17, 24].

For the general case that the difference between $\alpha\beta$ and dq frames is the (unknown) flux angle, the following relation is valid from Fig. 5.6:

$$\hat{\theta}_e = \angle(\underline{v}_s) - \beta_u \tag{5.37}$$

For simplicity, the voltage will be described in the stationary $\alpha\beta$-frame. The flux angle can then be estimated from the difference between the angle of the voltage test phasor and β_u, that can be derived from (5.33). Section 5.5 discusses techniques to obtain β_u from (5.33).

5.3.2 Blaschke Saliency Model

In [79] a technique to obtain field orientation under zero flux frequency conditions is proposed that allows the sensorless torque control. The basis of this method is the calculation of the resulting *hf* **rotor** currents in the induction machine that result from a *hf* stator current injection that is superposed onto the reference currents of the CSI-fed drive. Saturation in the machine helps to detect a misalignment of the estimated flux axis. The difficulty of this approach is that the *hf* rotor currents have to be determined. They are not easily accessible in a squirrel cage induction machine. A voltage model for the *hf* signals can be used to derive the required *hf* rotor currents. The saliency model used in [79] is obtained from the non-linear relation between rotor and stator currents.

The relation of rotor currents to stator currents can be derived from the machine equations under Vector Control (see Section 2.1). For the d component of the rotor current:

$$i_{r_d} \approx -\frac{pL_o}{pL_r + R_r} i_{s_d} \approx -\frac{L_o}{L_r} i_{s_d} \approx -\frac{1}{1 + \frac{l_r}{L_o}} i_{s_d} \tag{5.38}$$

where the rotor inductance is given as $L_r = l_r + L_o$ and the rotor resistance R_r is neglected. The approximation is valid for fast transients and/or small variations in the stator current, such as those arising from *hf* current injection.

Under rotor flux orientation, we have $\underline{\psi}_r = \psi_{r_d}$ and $\psi_{r_q} = 0$. Hence for the q component of the rotor current:

$$i_{r_q} \approx -\frac{L_o}{L_r} i_{s_q} \approx -\frac{1}{1 + \frac{l_r}{L_o}} i_{s_q} \tag{5.39}$$

For saturated conditions, the mutual inductance L_o differs in the d and q axis. In the d-axis, the airgap-flux is saturated and the mutual inductance is therefore small. This will be $L_{o_d} = \frac{d|\underline{\psi}_m|}{d|\underline{i}_m|}$ as shown in Fig. 5.7. The inductance is called the *dynamic inductance* and is the first derivative of the magnetization curve that is printed in Fig. 5.7. The dynamic inductance can also be expressed by the slope of the saturation curve as $L_{o_d} = \tan(\beta)$ with the angle β between horizontal and slope. In the q-axis, the flux is less saturated and the inductance is larger and can be approximated by $L_{o_q} = \frac{\underline{\psi}_m}{\underline{i}_m}$ that is called the *static inductance* [129]. The approximation is valid since the flux is in the linear part of the hysteresis curve. With the angle α determining the slope of the saturation curve, the inductance in the q-axis $L_{o_q} = \tan(\alpha)$.

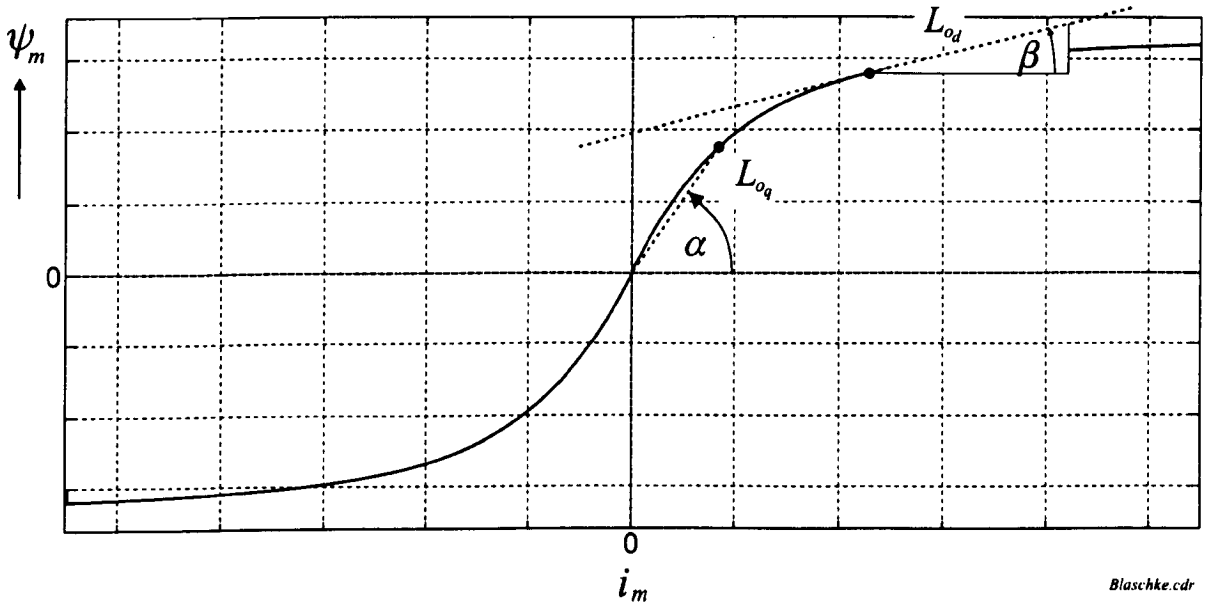

Figure 5.7: *Airgap flux saturation with differences in d and q inductances*

For a *hf* stator current signal or small signal variations in the stator current $\underline{i}_s$, the resulting rotor currents are given as

$$\Delta i_{r_d} = -\frac{1}{1 + l_r/\tan(\beta)} \cdot \Delta i_{s_d} = e_{11} \cdot \Delta i_{s_d} \tag{5.40}$$

$$\Delta i_{r_q} = -\frac{1}{1 + l_r/\tan(\alpha)} \cdot \Delta i_{s_q} = e_{22} \cdot \Delta i_{s_q} \tag{5.41}$$

or in matrix form:

$$\begin{bmatrix} \Delta i_{r_d} \\ \Delta i_{r_q} \end{bmatrix} = \begin{bmatrix} e_{11} & 0 \\ 0 & e_{22} \end{bmatrix} \begin{bmatrix} \Delta i_{s_d} \\ \Delta i_{s_q} \end{bmatrix} \tag{5.42}$$

where the factors e_{11} and e_{22} are different if one direction is more saturated in the machine. The absolute values of the two factors are not relevant for the approach given in [79].

The saturation saliency angle is obtained by injecting a *hf* current signal onto the reference stator currents. The *hf* signal is pulsating in parallel to the direction of the estimated flux axis to avoid *hf* torque pulsations. Thus, by measuring or estimating the *hf* rotor currents, the axis of the saturation saliency can be extracted and fed back for field orientation.

The technique of aligning the estimated to the real *d*-axis can be described as follows: A pulsating stator current $\Delta i_{s_d} = I_c \cos(\omega_c t)$ is injected. The rotor currents are measured and transformed into the *dq* frame. A highpass filter removes the fundamental

current component. This leaves Δi_{r_d} and Δi_{r_q} of (5.42). Assuming the estimated d-axis is not aligned to the real d-axis and the angle difference is γ, the rotor currents can be expressed as:

$$e^{j\gamma} \cdot \begin{bmatrix} \Delta i_{r_d} \\ \Delta i_{r_q} \end{bmatrix} = \begin{bmatrix} \cos\gamma & -\sin\gamma \\ \sin\gamma & \cos\gamma \end{bmatrix} \begin{bmatrix} e_{11} & 0 \\ 0 & e_{22} \end{bmatrix} \begin{bmatrix} \cos\gamma & \sin\gamma \\ -\sin\gamma & \cos\gamma \end{bmatrix} \cdot e^{j\gamma} \cdot \begin{bmatrix} \Delta i_{s_d} \\ \Delta i_{s_q} \end{bmatrix}$$

$$\begin{bmatrix} \Delta i'_{r_d} \\ \Delta i'_{r_q} \end{bmatrix} = I_c \cos(\omega_c t) \cdot \begin{bmatrix} \overline{Z} + \Delta Z \cos(2\gamma) & \Delta Z \sin(2\gamma) \\ \Delta Z \sin(2\gamma) & \overline{Z} - \Delta Z \cos(2\gamma) \end{bmatrix} \begin{bmatrix} \cos\gamma \\ \sin\gamma \end{bmatrix}$$

$$\begin{bmatrix} \Delta i'_{r_d} \\ \Delta i'_{r_q} \end{bmatrix} = I_c \cos(\omega_c t) \cdot \left(\overline{Z} + \Delta Z\right) \cdot \begin{bmatrix} \cos\gamma \\ \sin\gamma \end{bmatrix} \tag{5.43}$$

where

$$\begin{aligned} \overline{Z} &= 0.5 \cdot (e_{11} + e_{22}) \\ \Delta Z &= 0.5 \cdot (e_{11} - e_{22}) \\ Det(Z) &= e_{11} \cdot e_{22} \end{aligned}$$

From equation (5.43), $\Delta i'_{r_d} = \Delta i_{r_d}$ for $\gamma = 0$ and $\Delta i'_{r_q} = 0$ (since $\sin\gamma = 0$). The pulsating vector $\underline{i}'_{r_{dq}}$ can be split into two vectors of different sequence. A final multiplication by $e^{j\omega_c t}$ transforms the negative sequence of $\underline{i}'_{r_{dq}}$ to DC. A lowpass filter then removes the positive sequence that is now at frequency $2f_c$:

$$\underline{d}^a = \begin{bmatrix} d^{a_1} \\ d^{a_2} \end{bmatrix} = \underbrace{\begin{bmatrix} \cos(\omega_c t) & -\sin(\omega_c t) \\ \sin(\omega_c t) & \cos(\omega_c t) \end{bmatrix}}_{e^{j\omega_c t}} \cdot I_c \cos(\omega_c t) \cdot \left(\overline{Z} + \Delta Z\right) \cdot \begin{bmatrix} \cos\gamma \\ \sin\gamma \end{bmatrix}$$

$$\stackrel{LP}{=} \underbrace{0.5 \cdot I_c \cdot \left(\overline{Z} + \Delta Z\right)}_{\hat{d}} \cdot \begin{bmatrix} \cos\gamma \\ \sin\gamma \end{bmatrix} \tag{5.44}$$

Clearly, the vector $\underline{d}^a$ is a function of the alignment error γ. The imaginary part $d^{a_2} = \hat{d} \cdot \sin\gamma$ serves as feedback and directly adjusts the estimated d-axis. This error term is zero for $\gamma = 0$. The structure is that of a PLL where γ is the phase error for the PLL (see Section 5.5.2).

In practice, the stator voltage is measured instead of the rotor currents. This means that the relation of (5.42) can only be approximated.

5.3.3 Sul Saliency Model

The analysis in this section extends the short overview given in Section 2.3.2 by a more detailed description of the saliency model and signal processing of [20,78,80,92,

130,131]. This closer look seems to be justified, especially since the authors emphasize the robustness of the technique and the superiority to other sensorless strategies and announce its use in industrial drives for the near future. The estimation technique is based on a saturation saliency in the machine that is large enough to be used for the derivation of the flux angle and to obtain field orientation. Practically, this only allows for sensorless torque control or crude sensorless speed control.

The saliency model is based on a difference in the *hf* impedance in *d* (flux) and *q* axis of the field-oriented machine.
Assume the dynamic stator equation of the induction machine under field orientation of (2.34) with $\underline{i}_{mR} = i_{mR} = \frac{R_r \cdot i_{sd}}{pL_r + R_r}$ from (2.36) where p is the differential operator:

$$\underline{u}_s = (R_s + p\sigma L_s)\,\underline{i}_s + p(1-\sigma)L_s\underline{i}_{mR} \tag{5.45}$$

For the *hf* model under steady-state conditions with an injection frequency of f_c, the differential operator p can be substituted by $j\omega_c$. Equation (5.45) can be split into the *d* and *q* equations:

$$\begin{aligned} u_{sd} &= (R_s + j\omega_c\sigma L_s)i_{sd} + j\omega_c(1-\sigma)L_s R_r \frac{i_{sd}}{j\omega_c L_r + R_r} \\ &= (R_s + j\omega_c\sigma L_s + j\omega_c \frac{L_o^2}{L_r^2} \cdot R_r)i_{sd} = Z_d i_{sd} \end{aligned} \tag{5.46}$$

$$u_{sq} = (R_s + j\omega_c\sigma L_s)i_{sq} \qquad = Z_q i_{sq} \tag{5.47}$$

The simplification in (5.46) is valid for $\omega_c L_r \gg R_r$. The difference between Z_d and Z_q is in the term $j\omega_c \frac{R_r}{(1+\sigma_r)^2}$. In [20], skin effect at high frequency is claimed to cause an increase in the value of R_r that is much higher than at fundamental frequency. Similarly, σL_s is claimed to decrease for a *hf* injection, further increasing the difference between Z_d and Z_q. In spite of the different derivation of the saliency model, it still can be represented by a two-axis model in the *dq* frame as that of Section 5.2.3.

Sul, *et al.* [20] propose a pulsating *d* injection. The idea of injecting a high frequency signal in the flux axis and thus avoiding torque pulsations has been suggested earlier in [79]. Neither [20] nor [79] however have demonstrated the quality of the orientation and proven the functionality and reduction of torque pulsations due to the *d* injection. The basis for [20] is the saturation saliency in the *dq* frame as described by (5.16).
Fig. 5.8 shows part of the processing of the extracted *hf* currents to derive the flux angle. The currents $i_{s_d}^m$ and $i_{s_q}^m$ will not be measured in the *dq* frame but in a measuring frame that is aligned to the *dq* frame and rotated at the same angular velocity. The angle offset between measuring and *dq* frames is the constant measurement angle ϕ_m.

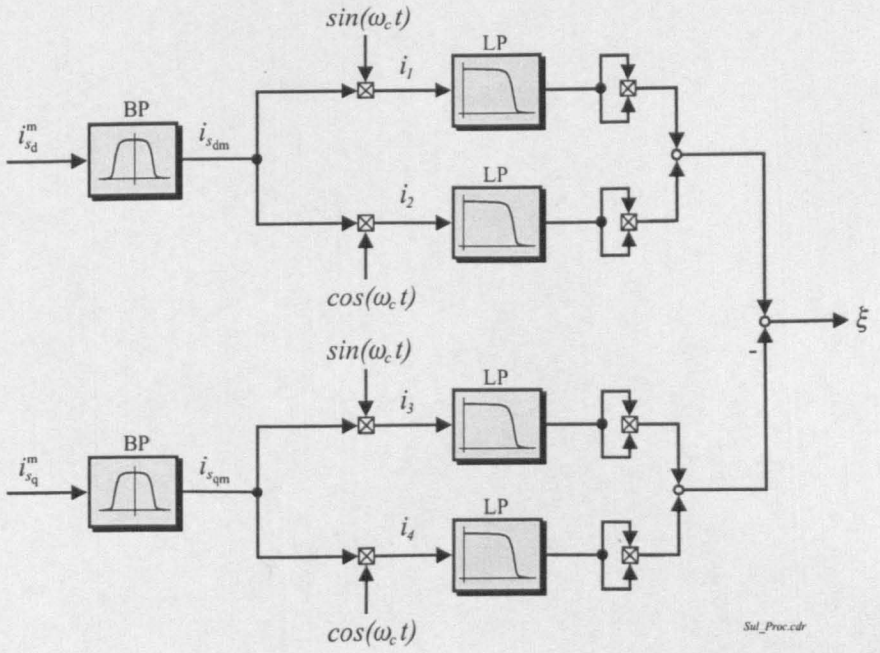

Figure 5.8: *Flux angle processor to extract saliency angle deviation for frame correction*

Bandpass filters are used to remove the unwanted excitation signals. The remaining *hf* currents $i_{s_{dm}}$ and $i_{s_{qm}}$ are then sent into the flux angle processor. The following transformation describes how the currents $\underline{i}^m_{s_{dq}}$ of the measurement frame are obtained from the stator currents in the *dq* frame.

$$
\begin{aligned}
[\underline{i}^m_{s_{dq}}] &= [e^{j\phi_m}][\underline{i}_{s_{dq}}] \\
\begin{bmatrix} i^m_{s_d} \\ i^m_{s_q} \end{bmatrix} &= \begin{bmatrix} \cos\phi_m & -\sin\phi_m \\ \sin\phi_m & \cos\phi_m \end{bmatrix} \begin{bmatrix} i_{s_d} \\ i_{s_q} \end{bmatrix}
\end{aligned}
$$

Note that the *hf* currents $\underline{i}_{s_{dqm}}$ are separated from the large fundamental currents using the bandpass filter BP in Fig. 5.8, with $\underline{i}_{s_{dqm}} = BP\{\underline{i}^m_{s_{dq}}\}$. This analysis first uses ϕ_m as a variable and it is shown later that the best choice is $\phi_m = -45°$. This means that the impedance on both measurement axes will ideally be the same as shown in Fig. 5.10. The flux angle processor therefore acts as a balancer for the *hf* impedances.

The voltage injection will be in the *dq* frame. The orientation of the frame is in fact initially unknown and will be determined by extracting the angle θ_e of the saturation saliency. This is shown in Fig. 5.9. For the analysis, the voltages will have to be transformed into the measurement frame with angle ϕ_m. The saturation saliency can

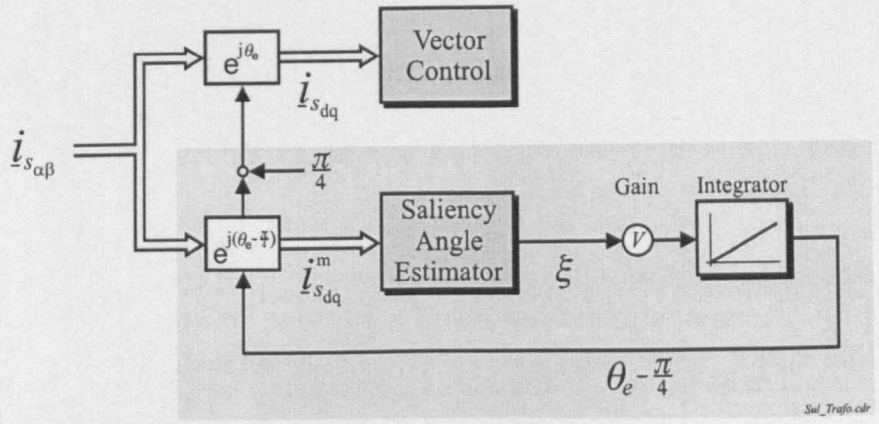

Figure 5.9: *Flux orientation using flux angle processor (saliency angle estimator) with integral control*

be described by a two-axis model (see Section 5.2.3) where the d-axis shall be aligned in the direction of the minimum saturation where $Z_d > Z_q$ as shown in Fig. 5.10. It will however depend on the injection frequency f_c, if the *hf* signal will pick up the maximum saturation in the d or q axis (see Section 5.2.3). The relation between *hf* voltages and currents in the measurement frame can be expressed as:

$$\begin{bmatrix} \cos\phi_m & -\sin\phi_m \\ \sin\phi_m & \cos\phi_m \end{bmatrix} \begin{bmatrix} v_{s_d} \\ v_{s_q} \end{bmatrix} = \begin{bmatrix} \cos\phi_m & -\sin\phi_m \\ \sin\phi_m & \cos\phi_m \end{bmatrix} \begin{bmatrix} Z_d & 0 \\ 0 & Z_q \end{bmatrix} \begin{bmatrix} \cos\phi_m & \sin\phi_m \\ -\sin\phi_m & \cos\phi_m \end{bmatrix} \begin{bmatrix} i_{s_{dm}} \\ i_{s_{qm}} \end{bmatrix}$$

$$\begin{bmatrix} v_{s_d}\cos\phi_m - v_{s_q}\sin\phi_m \\ v_{s_d}\sin\phi_m + v_{s_q}\cos\phi_m \end{bmatrix} = \begin{bmatrix} \overline{Z} + \Delta Z\cos(2\phi_m) & \Delta Z\sin(2\phi_m) \\ \Delta Z\sin(2\phi_m) & \overline{Z} - \Delta Z\cos(2\phi_m) \end{bmatrix} \begin{bmatrix} i_{s_{dm}} \\ i_{s_{qm}} \end{bmatrix} \tag{5.48}$$

where

$$\begin{aligned} \overline{Z} &= 0.5(Z_d + Z_q) \\ \Delta Z &= 0.5(Z_d - Z_q) \\ Det(Z) &= Z_d \cdot Z_q \end{aligned}$$

Matrix inversion gives the expression for the currents in the measurement axes:

$$\begin{bmatrix} i_{s_{dm}} \\ i_{s_{qm}} \end{bmatrix} = \frac{1}{Det(Z)} \begin{bmatrix} \overline{Z} - \Delta Z\cos(2\phi_m) & -\Delta Z\sin(2\phi_m) \\ -\Delta Z\sin(2\phi_m) & \overline{Z} + \Delta Z\cos(2\phi_m) \end{bmatrix} \begin{bmatrix} v_{s_d}\cos\phi_m - v_{s_q}\sin\phi_m \\ v_{s_d}\sin\phi_m + v_{s_q}\cos\phi_m \end{bmatrix}$$

For a pulsating injection in the d-axis only with $\underline{v}_c = \underline{v}_{s_{dq}}$ and amplitude V_c:

$$\underline{v}_c = V_c \begin{bmatrix} \cos(\omega_c t) \\ 0 \end{bmatrix}$$

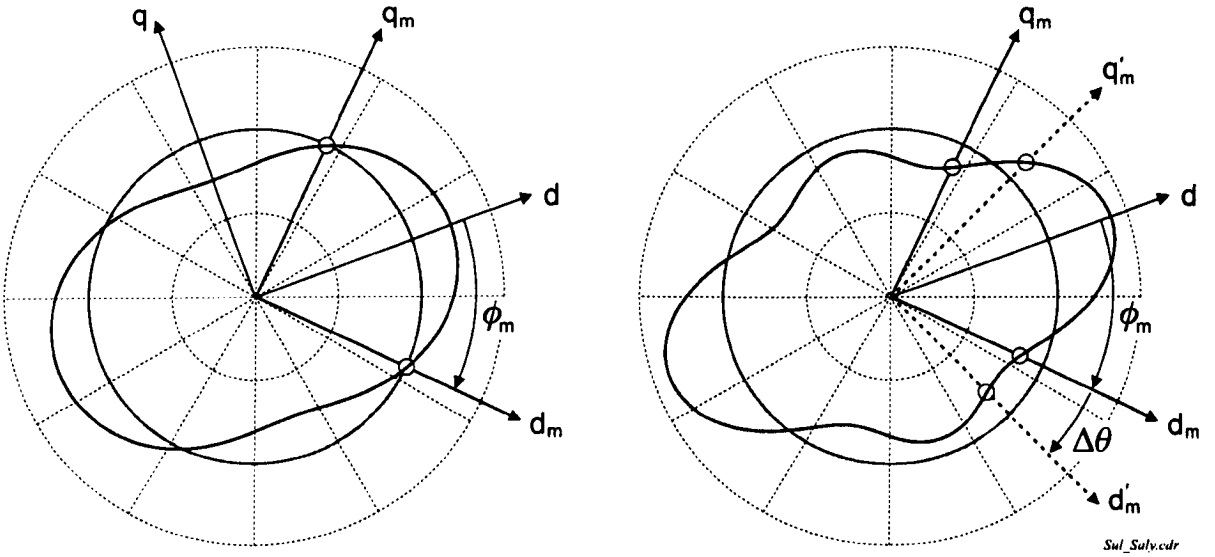

Figure 5.10: *Orientation of dq_m measurement frame with respect to dq-axis to resolve hf saliency impedance. Left: typical saturation saliency. Right: symmetric higher-order saturation saliency*

Rewriting the expressions for the currents in the measurement frame:

$$i_{s_{dm}} = \frac{\overline{Z}}{Det(Z)} \cdot V_c \cos(\omega_c t) \cos\phi_m - \frac{\Delta Z}{Det(Z)} \cdot V_c \cos(\omega_c t) \cos\phi_m = I \cos(\omega_c t) \cos\phi_m$$

$$i_{s_{qm}} = \frac{\overline{Z}}{Det(Z)} \cdot V_c \cos(\omega_c t) \sin\phi_m - \frac{\Delta Z}{Det(Z)} \cdot V_c \cos(\omega_c t) \sin\phi_m = I \cos(\omega_c t) \sin\phi_m$$

Multiplication with the *sinus* and *cosinus* of the carrier frequency gives four terms as shown in Fig. 5.8:

$$i_1 = i_{s_{dm}} \cdot \sin(\omega_c t) = 0.25 \cdot I\Big(\sin(2\omega_c t + \phi_m) + \sin(2\omega_c t - \phi_m)\Big)$$

$$i_2 = i_{s_{dm}} \cdot \cos(\omega_c t) = \frac{I}{2}\cos\phi_m + 0.25 \cdot I\Big(\cos(2\omega_c t + \phi_m) + \cos(2\omega_c t - \phi_m)\Big)$$

$$i_3 = i_{s_{qm}} \cdot \sin(\omega_c t) = 0.25 \cdot I\Big(\cos(2\omega_c t - \phi_m) - \cos(2\omega_c t + \phi_m)\Big)$$

$$i_4 = i_{s_{qm}} \cdot \cos(\omega_c t) = \frac{I}{2}\sin\phi_m + 0.25 \cdot I\Big(\sin(2\omega_c t + \phi_m) + \sin(2\omega_c t - \phi_m)\Big)$$

After the lowpass filters, i_1 and i_3 vanish and only the low frequency components of two branches remain. All terms containing the carrier components are transformed to $2f_c$ and these signals at twice the injection frequency will be rejected by the low-pass filters. The two remaining expressions (i_2 and i_4) are only a function of the

current amplitude and the angle offset ϕ_m. Of the two branches for each current component $i_{s_{dm}}$ and $i_{s_{qm}}$ shown in Fig. 5.8, only the signal of one branch remains after the filtering. With $i_{s_{dm}} = I\cos(\omega_c t)\cos\phi_m$, $i_1 = 0$ and $i_2 = 0.5 \cdot I\cos\phi_m$ after the lowpass. If there is a 90° phaseshift between the voltage injection and the *hf* currents due to the saliency or a delay in processing, the current on the d_m-axis will be $i_{s_{dm}} = I\sin(\omega_c t)\cos\phi_m$ (with a $\sin(\omega_c t)$ instead of the $\cos(\omega_c t)$ from before). This results in $i_1 = 0.5 \cdot I\cos\phi_m$ and $i_2 = 0$ after the lowpass filter. The result is still the same except that the branches are swapped. For any condition with a phase difference κ and $i_{s_{dm}} = I\cos(\omega_c t + \kappa)\cos\phi_m$, both branches will produce an output signal after the filters. Using the squaring and following addition shown in Fig.5.8 [131], the output error ξ will not be a function of the phase shift κ.

The amplitude I of the processed currents does not contain any useful information. This is why the phase information ϕ_m can be extracted directly using an *arcus tangens* or a PLL. A phase shift κ would reduce the absolute amplitude but the ratio in two of the four branches (e.g. i_2 and i_4) would remain the same. It only has to be ensured that the two of the four possible currents should be those with the larger amplitude. The output of an *arcus tangens* function would be directly the measurement angle ϕ_m. The method chosen by [131] to extract the phase information is a different one and shown below:

$$\begin{aligned} i_{2_{LP}}^2 &= \left[\frac{I}{2}\cos\phi_m\right]^2 = \frac{I^2}{8}\Big(1+\cos(2\phi_m)\Big) \\ i_{4_{LP}}^2 &= \left[\frac{I}{2}\cos\phi_m\right]^2 = \frac{I^2}{8}\Big(1-\cos(2\phi_m)\Big) \end{aligned}$$

$$i_{2_{LP}}^2 - i_{4_{LP}}^2 = \frac{I^2}{4}\cos(2\phi_m) = \xi \qquad (5.49)$$

Forming the difference of the two signals removes the constant term. The processor in Fig. 5.8 produces a term that depends on the angular difference between injection frame and measurement frame.
Equation (5.49) can be further simplified by substituting the measurement angle ϕ_m by a constant orientation angle of $-45°$ and an error term $\Delta\theta$. This results in:

$$\xi = \frac{I^2}{4}\sin(2\Delta\theta), \qquad \phi_m = -\pi/4 + \Delta\theta$$

The *cosinus* has been replaced by a *sinus* term which has the advantage to be linearized for small angle errors $\Delta\theta$ with a proportional factor k for

$$\xi \approx k \cdot \Delta\theta$$

This error term can be used to adjust the measurement frame via a feedback controller as shown in Fig. 5.9. The currents are originally measured in the stationary $\alpha\beta$ frame and then transformed into the measurement frame. If this measurement frame is not $-45°$ from the dq frame of the saturation saliency, the error ξ is not zero but $k \cdot \Delta\theta$. An alignment error will be amplified and integrated. This serves as orientation angle for the measurement frame and ideally is $\theta_e - \pi/4$. From the orientation of the measurement frame, the orientation of the dq frame can be derived by adding 45°. This orientation θ_e is the estimate of the direct axis needed for field orientation.

The difficulty of the tracking technique [20] described above is that it does not estimate the saliency position instantaneously. The structure shown in Fig. 5.9 is in fact that of a PLL. The dynamic properties of the PLL are described in Section 5.5.2. If the flux angle processor of Fig. 5.9 only comes with the loop filter V, higher speeds will cause a phase lag and possible distortion of the estimate. A solution can be the estimator proposed in [77]. Using the *arcus tangens* will directly produce a linear correction angle $\xi = \Delta\theta - 45°$ even if the misalignment of the measurement frame is large. The lowpass filters shown in Fig. 5.8 will also limit the dynamic response of the saliency angle estimator. The only solution is to select the frequency f_c of the carrier as high as possible so that the cutoff frequency of the lowpass filters can be also high.

If higher saliency harmonics are present (possibilities are shown in Chapter 3 of [69]), the tracking method can cope, providing that the saliency remains symmetric about the d-axis. This means that the amplitude of the hf currents $i_{s_{dm}}$ and $i_{s_{qm}}$ in the measurement frame is the same. This effect is shown on the right of Fig. 5.10. In addition to the $2f_e$ saliency harmonic, a $4f_e$ harmonic exists that has four periods per 360° electrical. Since this higher saliency harmonic is in phase to the main saliency harmonic, the resulting impedance in the measurement axis is the same. The additional saliency harmonic does not cause a problem for this condition. A potential problem can however be seen in the right plot of Fig. 5.10 in case of a misalignment of the measurement frame (denoted by d'_m and q'_m) when $\Delta\theta$ is not small. Decreasing $\Delta\theta$ (anti-clockwise rotation) will cause a reduction in saliency impedance on both measurement axis. An increase in $\Delta\theta$ will again change the saliency impedance in the same direction. The balancing controller will fail to orientate the measurement frame by $-45°$ from the dq frame. Also a higher saliency harmonic that is not in phase to the $2f_e$ harmonic will cause problems. If the harmonic distortion stems from discrete effects such as the clamping phenomenon (see Section 6.1.3), the estimate of the saliency position will be distorted as seen in the figures published in [92], showing experimental results.

5.4 Frequency Transformations for Demodulation

In the previous sections it has been shown that the saturation or rotor saliencies cause a modulation of the stator currents when using *hf* voltage injection. Voltage modulation is the case when using *hf* current injection. The latter is not commonly used for vector controlled induction machines due to the high bandwidth demand for the current controllers. The modulation containing the saliency position is an amplitude modulation (AM) that contains the large carrier signal. More specifically, it is a single sideband AM and because the signals are vectors, they contain an additional information about the direction of rotation. This allows the split of the modulated signal in the carrier that is a positive sequence harmonic and the saliency component that is a negative sequence harmonic.

In a typical AM system, the carrier has to be regenerated or estimated in the receiver from the information contained in the modulated signal. Since the carrier signal is generated by the digital processor, it is well known and can be used for the demodulation.

5.4.1 Homodyning

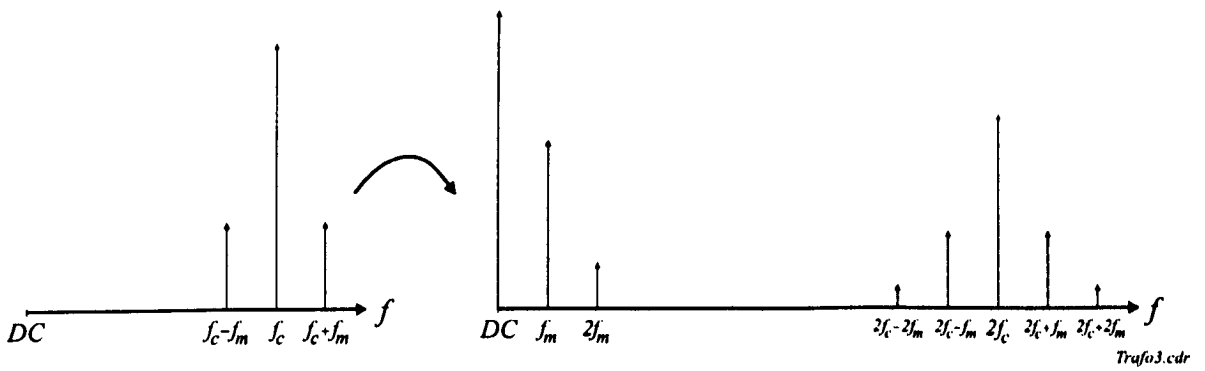

Figure 5.11: *Spectrum transformation using squaring or homodyning (scalar signals)*

Homodyning is by definition the demodulation of a signal by multiplication with a sinusoidal signal that is in phase and frequency synchronism with the incoming carrier frequency.

A very simple way to synchronously demodulate is to multiply the signal by itself. This is possible if the modulated signal contains the carrier. The result of the squaring is shown in Fig. 5.11. On the left, the original spectrum with a carrier at frequency f_c

and the upper and lower sideband at $f_c + f_m$ and $f_c - f_m$ respectively. On the right, the resultant spectrum is shown. When using the square-law for the $\underline{i}_{s_{\alpha\beta\_c}}$ vectorial signal, conditions are better than for the signal shown on the left of Fig. 5.11. Since $\underline{i}_{s_{\alpha\beta\_c}}$ only has one sideband, squaring will not produce the the $2f_m$ harmonic in the baseband. The two resulting signal components $i_{s_{\alpha\_c}}$ and $i_{s_{\beta\_c}}$ will however contain a large DC offset after lowpass filtering. Also they are not orthogonal but shifted by 180°. This phase shift can be used to eliminate the DC offset by subtracting the two signal components. The disadvantage is that only one scalar signal remains that contains the saliency position. A phase locked loop (PLL) can be used to extract the information contained in the argument. A better method using squaring is shown in Section 5.4.5.

5.4.2 Rectification

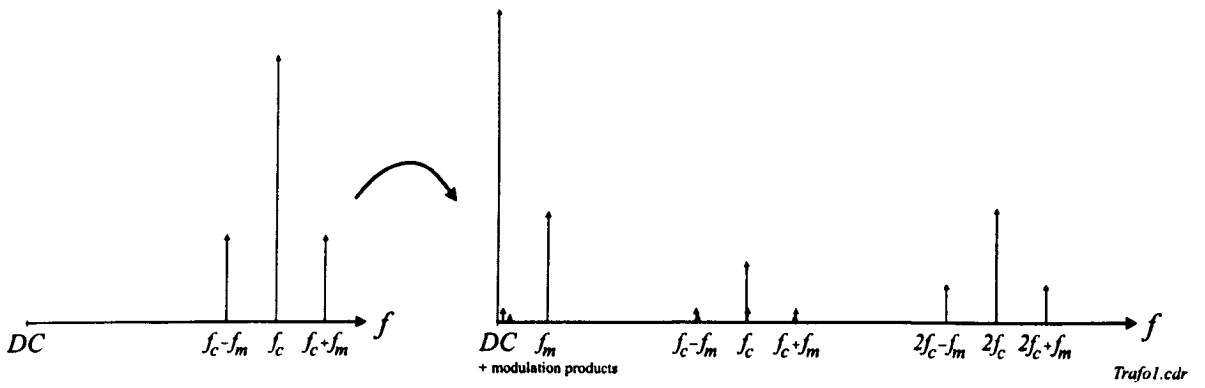

Figure 5.12: *Spectrum transformation using rectification (scalar)*

Rectification can easily be achieved mathematically by using the *ABS* function. In analogue circuitry, a simple diode is used that suppresses the negative part of the incoming signal. The signal obtained from this diode circuit differs slightly from that using the *ABS* function. To extract the information contained in the modulated signal, the rectified signal is then sent through a lowpass filter. This can be a capacitor and a resistor in parallel for the analogue circuit that are connected to the kathode of the diode. The capacitor is charged and discharged and the voltage across follows the carrier envelope that is the modulating signal if the *RC* time constant is chosen correctly. Rectification of a signal $\cos\omega_c t$ is mathematically equivalent to a multiplication by the Fourier series of a rectangular signal $s(\omega_c t)$ with the same period as $\cos\omega_c t$ [132]. With $\omega_c t = 2\pi f_c t$ and $T_c = 1/f_c$ one has

$$s(\omega_c t) = \begin{cases} 1 & : \text{ for } T_c/4 < t \leq T_c/4 \\ -1 & : \text{ for } T_c/4 < t \leq 3T_c/4 \end{cases} \tag{5.50}$$

The rectified signal $\cos(\omega_c t)$ can then be expressed as

$$\begin{aligned} |\cos\omega_c t| &= \cos\omega_c t \cdot s(\omega_c t) \\ &= \cos\omega_c t \cdot \frac{4}{\pi} \cdot \left[\cos\omega_c t - \frac{1}{3}\cos(3\omega_c t) + \frac{1}{5}\cos(5\omega_c t) - \ldots\right] \end{aligned}$$

Rectification is effectively a synchronous demodulation where the carrier is generated by the signal itself. The analogue implementation is commonly known as envelope detector for AM signals [132]. Fig. 5.12 shows the result of the rectification. The carrier, double-carrier components and higher spectral harmonics are filtered off so that a DC component and the baseband signal at frequency f_m remain. Unfortunately, small modulation products in the baseband region exist.

Rectification can be used to extract the saliency information from the extracted *hf* currents. The disadvantage is that a DC offset remains that has to be removed using a DC blocking filter. A filter will then introduce unacceptable phase shifts. Subtracting the two components of $|\underline{i}_{s_{\alpha\beta-c}}|$ after the lowpass filter also result in an offset-free signal. The basic problem is that small modulation products in the baseband remain that cause additional distortion. With spectral components around the carrier frequency in the demodulated signal, the cutoff frequency of the lowpass filter has to be lower than for the square-law demodulation.

5.4.3 Heterodynining

Heterodyning is the demodulation of a signal by multiplication with a different carrier signal. The basic equations for heterodyning are the following trigonometric relations:

$$\begin{aligned} \sin x \cdot \sin y &= 0.5 \cdot [\cos(x-y) - \cos(x+y)] \\ \cos x \cdot \cos y &= 0.5 \cdot [\cos(x-y) + \cos(x+y)] \\ \sin x \cdot \cos y &= 0.5 \cdot [\sin(x-y) + \sin(x+y)] \end{aligned}$$

If the argument of the signal is $x = 2\pi f_c t + 2\pi f_z t$ and the argument of the carrier $y = 2\pi f_c t$, the first term (e.g. $\cos(x-y)$) with the subtraction of the arguments performs a down-conversion. The harmonic will be at frequency f_z. The second term (e.g. $\cos(x+y)$) with the addition of the arguments performs an up-conversion, transforming the original spectrum by shifting on the frequency axis by f_c. The resulting harmonic will then be at frequency $2f_c + f_z$.

Fig. 5.13 shows on the right the resultant spectrum after multiplication with $\cos(2\pi f_c t)$. One part of the spectrum is around twice the carrier and the other spectral components can be found around DC. In this case, the arguments x and y are functions of the same carrier frequency and one gets the special case of a homodyne or synchronous demodulation. The higher harmonics around the double carrier frequency

can be filtered off easily. Only the DC offset and the modulating signal at frequency f_m remain.
Heterodyning for the demodulation and extraction of the saliency information is used in Sections 5.4.4 and 5.4.6.

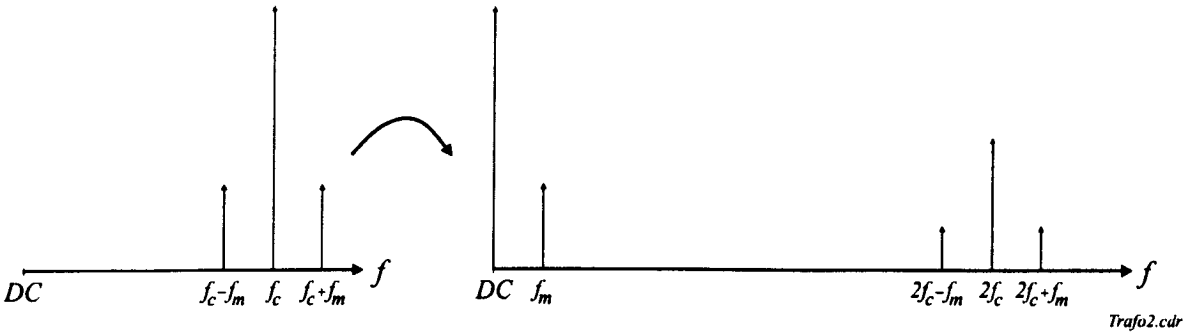

Figure 5.13: *Spectrum transformation using homodyne demodulation (scalar)*

5.4.4 Direct Homodyne Transformation

This transformation [96] makes use of the vectorial character of modulated signal. The idea is to separate the carrier from the negative sequence harmonics before filtering off the carrier. In theory, there is no difference if the signal or the filter is transformed [69] (see Section 5.4.7).
Here assuming a rotor saliency, the *hf* currents after the bandpass filter are:

$$i_{s_{\alpha\_c}} = I_1 \cos(\omega_c t + \phi_1) - I_2 \cos(2\theta_r - \omega_c t + \phi_2) \tag{5.51}$$

$$i_{s_{\beta\_c}} = I_1 \sin(\omega_c t + \phi_1) - I_2 \sin(2\theta_r - \omega_c t + \phi_2) \tag{5.52}$$

$$\underline{i}_{s_{\alpha\beta\_c}} = i_{s_\alpha} + j i_{s_\beta} = I_1 e^{j(\omega_c t + \phi_1)} - I_2 e^{j(2\theta_r - \omega_c t + \phi_2)} \tag{5.53}$$

Transforming $\underline{i}_{s_{\alpha\beta\_c}}$ to the negative sequence frame rotating at frequency $-f_c$ is achieved by multiplication with $e^{j\omega_c t}$. For the individual current components this is a homodyne transformation.

$$\underline{i}_{s_{\alpha\beta}} \cdot e^{j\omega_c t} = \left[i_{s_{\alpha\_c}} + j i_{s_{\beta\_c}}\right] \cdot \underbrace{\left[\cos(\omega_c t) + j \sin(\omega_c t)\right]}_{\text{transformation}} \tag{5.54}$$

$$\begin{aligned} \underline{i}_{s_{\alpha\beta\_c}} \cdot e^{j\omega_c t} = {} & i_{s_{\alpha\_c}} \cos(\omega_c t) - i_{s_{\beta\_c}} \sin(\omega_c t) \\ & + j \left[i_{s_{\alpha\_c}} \sin(\omega_c t) + i_{s_{\beta\_c}} \cos(\omega_c t)\right] \end{aligned} \tag{5.55}$$

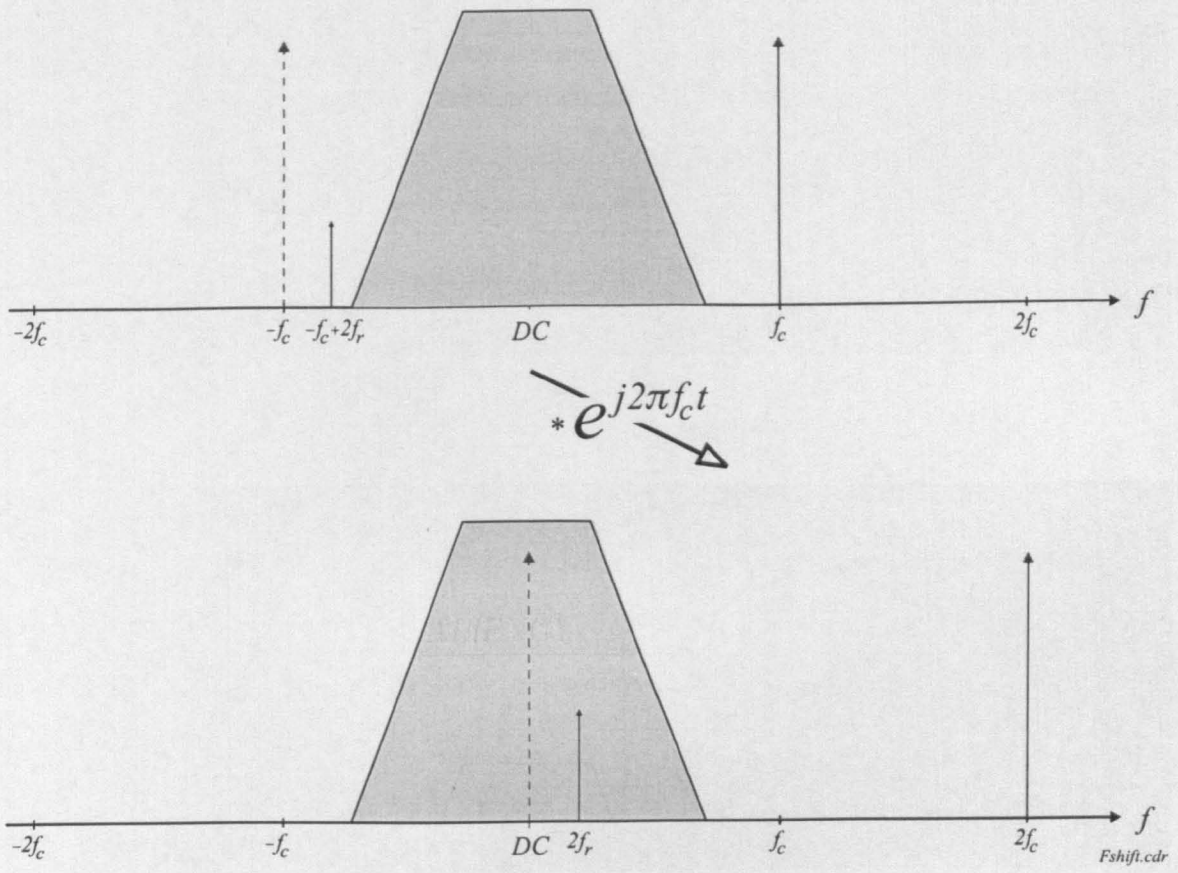

Figure 5.14: *Frequency shift of orthogonal signals. Upper: original spectrum. Lower: transformed spectrum where lowpass filter only removes carrier at* $2f_c$

$$
\begin{aligned}
\underline{i}_{s_{\alpha\beta\_c}} \cdot e^{j\omega_i t} \;=\; & I_1 \cos(\omega_c t + \phi_1) \cdot \cos(\omega_c t) \\
& -I_2 \cos(2\theta_r - \omega_c t + \phi_2) \cdot \cos(\omega_c t) \\
& -I_1 \sin(\omega_c t + \phi_1) \cdot \sin(\omega_c t) \\
& +I_2 \sin(2\theta_r - \omega_c t + \phi_2) \cdot \sin(\omega_c t) \\
& +j\,\{I_1 \cos(\omega_c t + \phi_1) \cdot \sin(\omega_c t) \\
& -I_2 \cos(2\theta_r - \omega_c t + \phi_2) \cdot \sin(\omega_c t) \\
& +I_1 \sin(\omega_c t + \phi_1) \cdot \cos(\omega_c t) \\
& -I_2 \sin(2\theta_r - \omega_c t + \phi_2) \cdot \cos(\omega_c t)\}
\end{aligned}
$$

$$
\begin{aligned}
\underline{i}_{s_{\alpha\beta\_c}} \cdot e^{j\omega_c t} \;=\; & \tfrac{I_1}{2}\left[\cos(\phi_1) + \cos(2\omega_c t + \phi_1)\right] \\
& -\tfrac{I_2}{2}\left[\cos(2\theta_r - 2\omega_c t + \phi_2) + \cos(2\theta_r + \phi_2)\right]
\end{aligned}
$$

$$
\begin{aligned}
&-\tfrac{I_1}{2}\left[\cos(\phi_1) - \cos(2\omega_c t + \phi_1)\right] \\
&+\tfrac{I_2}{2}\left[\cos(2\theta_r - 2\omega_c t + \phi_2) - \cos(2\theta_r + \phi_2)\right] \\
&+j\Big\{\tfrac{I_1}{2}\left[\sin(2\omega_c t + \phi_1) + \sin(-\phi_1)\right] \\
&\quad -\tfrac{I_2}{2}\left[\sin(2\theta_r + \phi_2) + \sin(2\omega_c t - 2\theta_r - \phi_2)\right] \\
&\quad +\tfrac{I_1}{2}\left[\sin(2\omega_c t + \phi_1) + \sin(\phi_1)\right] \\
&\quad -\tfrac{I_2}{2}\left[\sin(2\theta_r + \phi_2) + \sin(2\theta_r - 2\omega_c t + \phi_2)\right]\Big\}
\end{aligned}
\tag{5.56}
$$

$$
\begin{aligned}
\underline{i}_{s_{\alpha\beta\_c}} \cdot e^{j\omega_c t} &= -I_2\cos(2\theta_r + \phi_2) - jI_2\sin(2\theta_r + \phi_2) \\
&\quad + \underbrace{I_1\cos(2\omega_c t + \phi_1) + jI_1\sin(2\omega_c t + \phi_1)}_{\text{filter off}}
\end{aligned}
\tag{5.57}
$$

$$
\underline{i}_{s_{\alpha\beta\_c}} \cdot e^{j\omega_c t} = \underline{i}_{s_{dq\_c}}
$$

The resulting signal contains harmonics at $2f_c$ and at frequency $2f_r$. This means that the original signal with harmonics at f_c and $-f_c + 2f_r$ has been shifted on the frequency axis. Position signal and carrier now have a spectral separation $2f_c - 2f_r$ on the frequency axis instead of only $2f_r$ before. Note that the separation has been $2f_c - 2f_r$ also with the original signal $\underline{i}_{s_{\alpha\beta\_c}}$ but cannot be used since a filter does not consider the direction of rotation but only the absolute magnitude of the frequency that only differs by $2f_r$.

Fig. 5.14 visualizes the transformation in the frequency plane. The carrier is at frequency f_c and the harmonic containing the saliency information at $-f_c + 2f_r$. The dashed harmonic at $-f_c$ does not exist but is added to aid in understanding the transformation. In the amplitude spectrum, without using the phase information contained in the signals, the carrier and the saliency harmonic appear at f_c and $f_c - 2f_r$ respectively. As mentioned, they are just apart by $2f_r$, close enough that it might not be easily possible to separate them by filter as seen in the upper plot. The gray shaded areas indicate the area that is not filtered off by the lowpass filter. Note that the filter appears in the positive and negative frequency range. After the transformation, the carrier is shifted to $2f_c$ and is suppressed by the lowpass filter whereas the saliency harmonic is now close to DC. The frequency shift appears to an observer as if he has changed position and is now 'sitting' fixed to the negative sequence frame where the negative sequence harmonic $-f_c$ appears stationary.

5.4.5 Indirect Homodyne Transformation

In contrast to the direct homodyne transformation, there also is the possibility for an indirect homodyne transformation. This transformation does not require the knowl-

edge of the carrier frequency, but uses the carrier information contained in the signals itself. This is based on the square-law shown in Section 5.4.1. Here the transformation is not applied to scalar signals but vectors. The phase shift on the different frequency components can be used to cancel the DC or a possible harmonic at $2f_m$ as shown in Fig. 5.11.

With $\underline{i}_{s_{\alpha\beta\_c}}$ as specified in (5.53), the real part of $\underline{i}_{s_{dq\_c}}$ is obtained by the cross multiplication of both $\underline{i}_{s_{\alpha\beta\_c}}$ components:

$$\begin{aligned} \Re\{\underline{i}_{s_{dq\_c}}\} = i_{s_{d\_c}} &= \Re\{\underline{i}_{s_{\alpha\beta\_c}}\} \cdot \Im\{\underline{i}_{s_{\alpha\beta\_c}}\} \\ &= i_{s_{\alpha\_c}} \cdot i_{s_{\beta\_c}} \end{aligned} \tag{5.58}$$

$$\begin{aligned} \Im\{\underline{i}_{s_{dq\_c}}\} = i_{s_{q\_c}} &= (\Re\{\underline{i}_{s_{\alpha\beta\_c}}\}^2 - \Im\{\underline{i}_{s_{\alpha\beta\_c}}\}^2)/2 \\ &= (i^2_{s_{\alpha\_c}} - i^2_{s_{\beta\_c}})/2 \end{aligned} \tag{5.59}$$

The imaginary part of the transformed signal $\underline{i}_{s_{dq\_c}}$ is obtained by forming the mean difference of the two squared components of $\underline{i}_{s_{\alpha\beta\_c}}$. For the mathematical deduction similar to (5.56) one gets:

$$\begin{aligned} \underline{i}_{s_{dq\_c}} &= (i_{s_{\alpha\_c}} \cdot i_{s_{\beta\_c}}) + \frac{j}{2}\left(i^2_{s_{\alpha\_c}} - i^2_{s_{\beta\_c}}\right) \\ &= -I_1 I_2 \cdot \cos(2\theta_r + \phi_1 + \phi_2) - jI_1 I_2 \cdot \sin(2\theta_r + \phi_1 + \phi_2) \\ &= j(\underline{i}^{\star}_{s_{\alpha\beta\_c}})^2/(2i_{cp}) \end{aligned} \tag{5.60}$$

The result obtained is similar to (5.57). The main difference is that the amplitude of the carrier component I_1 scales the result. Extracting the saliency information via the *arcus tangens* function, this scaling factor cancels. For the PLL, the loop gain will be different to that using signals from the direct homodyne transformation. The difference in phase shift, compared to the direct homodyne transformation is not much of importance since this can be adjusted in the saliency estimator at start-up.

5.4.6 Phase Locked Loop Transformer

The phase detector of the phase-locked loop (PLL) [17, 24] is essentially a frequency shifter, similar to that shown in Section 5.4.

For two modulated signals after the bandpass filter to remove the fundamental currents:

$$\begin{aligned} i_{s_{\alpha\_c}} &= I_1 \cos(\omega_c t + \phi_1) - I_2 \cos(2\theta_r - \omega_c t + \phi_2) \\ i_{s_{\beta\_c}} &= I_1 \sin(\omega_c t + \phi_1) - I_2 \sin(2\theta_r - \omega_c t + \phi_2) \end{aligned} \tag{5.61}$$

The two perpendicular position signals are multiplied by a *sinus* and *cosinus* term containing the known carrier frequency and the estimated rotor position.

The signal error after the phase detector is

$$\begin{aligned}
\xi &= i_{s_{\alpha_c}} \cdot \sin(2\hat{\theta}_r - \omega_c t + \phi) - i_{s_{\beta_c}} \cdot \cos(2\hat{\theta}_r - \omega_c t + \phi) \\
&= I_1 \cos(\omega_c t + \phi_1) \cdot \sin(2\hat{\theta}_r - \omega_c t + \phi) \\
&\quad -I_2 \cos(2\theta_r - \omega_c t + \phi_2) \cdot \sin(2\hat{\theta}_r - \omega_i t + \phi) \\
&\quad -I_1 \sin(\omega_c t + \phi_1) \cdot \cos(2\hat{\theta}_r - \omega_c t + \phi) \\
&\quad +I_2 \sin(2\theta_r - \omega_c t + \phi_2) \cdot \cos(2\hat{\theta}_r - \omega_c t + \phi) \\
&= \tfrac{I_1}{2}\left[\sin(2\hat{\theta}_r + \phi_1 - \phi) + \sin(2\hat{\theta}_r - 2\omega_c t + \phi - \phi_1)\right] \\
&\quad -\tfrac{I_2}{2}\left[\sin(2(\theta_r + \hat{\theta}_r) - 2\omega_c t + \phi_2 + \phi) + \sin(2(\hat{\theta}_r - \theta_r) + \phi - \phi_2)\right] \\
&\quad -\tfrac{I_1}{2}\left[\sin(2\hat{\theta}_r + \phi_1 - \phi) - \sin(2\hat{\theta}_r + \phi - \phi_1 - 2\omega_c t)\right] \\
&\quad +\tfrac{I_2}{2}\left[\sin(2(\theta_r + \hat{\theta}_r) - 2\omega_c t + \phi_2 + \phi) - \sin(2(\hat{\theta}_r - \theta_r) + \phi - \phi_2)\right] \\
&= I_1 \sin(2\hat{\theta}_r - 2\omega_c t + \phi - \phi_1) - I_2 \sin(2(\hat{\theta}_r - \theta_r) + \phi - \phi_2) \qquad (5.62)
\end{aligned}$$

The signal contains harmonics at $-2f_c + f_r$ and at frequency f_r, similar to equation (5.57).
Clearly, from the results of Section 5.4, the position estimation error with $\phi = -2\hat{\theta}_r + \omega_c t$, instead of $\omega_c t$:

$$\xi = -\Im\left\{\underline{i}_{s_{\alpha\beta\_c}} \cdot e^{j\phi}\right\}, \quad \phi = -(2\hat{\theta}_r - \omega_c t)$$

For the PLL, the imaginary component of the transformation result is taken. Essentially, the PLL transforms the modulating envelope down to DC whereas the carrier is shifted to the frequency $2f_c$. This gives better spectral resolution to remove the carrier.
After lowpass filtering to remove the carrier:

$$\begin{aligned}
\xi &\approx -I_2 \sin(2(\hat{\theta}_r - \theta_r) + \phi - \phi_2) \\
&\approx -I_2 \cdot 2(\hat{\theta}_r - \theta_r) \qquad (5.63)
\end{aligned}$$

The final approximation and linearization are valid for small angle deviations. The resulting signal is an error input for the loop filter and is zero for a correct angle estimate.

5.4.7 Filter Transformation

The idea to transform a filter into a synchronous frame to suppress the carrier component is developed in [85]. This technique makes use of the vectorial characteristic of the harmonics that allows to distinguish them not only in their frequency or phase but also in the direction of rotation. Since the carrier component is a positive sequence harmonic it can be separated from the negative sequence harmonics that contain the saliency information. A transformation block first converts the signal frequency of interest to DC for filtering and a second inverse transformation back to its original frequency as shown in subplot *a)* of Fig. 5.15.

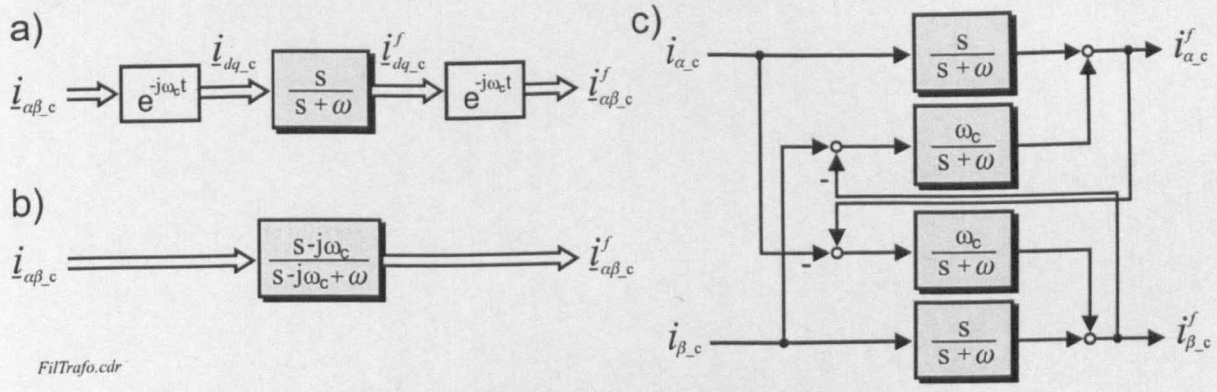

Figure 5.15: *Filter structure to eliminate positive sequence carrier harmonic. a) Transformation of signal. b) Transformation of filter using vectors. c) Transformation of filter using scalar signals*

Instead of transforming the signal, the filter can be transformed instead [85]. This results in a filter theory that extends that shown in e.g. [133]. It is common practice to specify filter characteristics only for normalized lowpass filters. These can easily be transformed to obtain any type of highpass, bandpass or bandstop filter with arbitrary centre, cutoff frequency or bandwidth. This is called *frequency scaling* [133] where s in the transfer function of the normalized lowpass filter gets substituted by e.g. $s \mapsto \frac{\omega}{s}$ where ω is the cutoff frequency of the desired highpass filter. Any filter transformation will however effect the positive and negative sequence harmonics equally. This is because the filter transformation shifts the filter symmetrically along the positive and negative frequency range.

A filter to separate positive and negative sequence harmonics will have to be shifted asymmetrically in the frequency domain. This can be achieved for example by mapping $s \mapsto (s - j\omega_c)$ where f_c is the frequency of the carrier. This will behave as if the filter is shifted by $+f_c$. The following example uses the original design of a highpass

filter $F_{HP}(s) = \frac{s}{s+\omega}$ to remove the carrier frequency at f_c.

$$\begin{aligned} \underline{i}^f_{dc\_c} \cdot (s+\omega) &= s \cdot \underline{i}_{dc\_c} \\ \left[\underline{i}^f_{\alpha\beta\_c} e^{-j\omega_c t}\right] \cdot (s+\omega) &= s \cdot \left[\underline{i}_{\alpha\beta\_c} e^{-j\omega_c t}\right] \\ \underline{i}^f_{\alpha\beta\_c} \cdot e^{-j\omega_c t} \cdot (s - j\omega_c + \omega) &= (s - j\omega_c) \cdot \underline{i}_{\alpha\beta\_c} \cdot e^{-j\omega_c t} \end{aligned} \tag{5.64}$$

where the derivative s or $\frac{d}{dt}$ has to be treated specifically [7]:

$$\begin{aligned} \frac{d}{dt}\left(\underline{i}_{dq\_c}\right) &= \frac{d}{dt}\left(\underline{i}_{\alpha\beta\_c} e^{-j\omega_c t}\right) \\ &= \left(\frac{d}{dt}(\underline{i}_{\alpha\beta\_c}) - j\omega_c \cdot \underline{i}_{\alpha\beta\_c}\right) \cdot e^{-j\omega_c t} \end{aligned}$$

It is obvious from (5.64) that the new stationary filter is $F_{HP_p}(s) = \frac{(s-j\omega_c)}{(s-j\omega_c)+\omega}$ that is shown in its vectorial form in subplot *(b)* of Fig. 5.15. In subplot *(c)* of Fig. 5.15, the scalar form is shown with the coupling terms. This filter has a very sharp bandstop characteristic that only eliminates the positive sequence harmonic at frequency f_c.
The same approach is possible to shift a lowpass filter $F_{LP}(s) = \frac{1}{s+\omega}$ from DC to $-f_c$. The mapping is $s \mapsto (s + j\omega_c)$, resulting in the stationary filter $F_{LP_n}(s) = \frac{1}{(s+j\omega_c)+\omega}$. This filter will also remove the carrier. The previous approach using the highpass filter however will be superior since the gain at f_c is zero and therefore will cancel the carrier completely and also will only cause a small phase shift for the negative sequence harmonics that therefore can be neglected.

Although the filter theory shown above is theoretically attractive, the practical implementation does not come without difficulties. The separate transformation of the signals and the filter in the synchronous frame (Fig. 5.15-*a*) is in general numerically more robust than the equivalent stationary filter (Fig. 5.15-*b*).
Using the highpass filter in the positive sequence domain $F_{HP_p}(s)$, eliminates the carrier. In practice, the carrier harmonic will not be the only positive sequence harmonic. These will not be suppressed sufficiently with this approach alone. A combination of the highpass filter on the f_c harmonic with a lowpass filter around the $-f_c$ harmonics is considered to be a good compromise for extracting the position component with minimum phase shift and a minimum of distorting harmonics. Obviously, this method cannot separate the position harmonic from the saliency harmonic.

5.5 Estimators for Obtaining the Saliency Angle

This section lists a number of techniques that allow to extract the saliency angle from the saliency-modulated currents or voltages. In principle, there is no difference if this is a rotor or saturation saliency. In practice however, the rotor saliencies are always accompanied by a saturation saliency. Also the modulation due to the saturation saliency might not only result in a single saturation harmonic. The saliency estimators presented here can only cope with a single (ideal) saliency harmonic. Additional harmonics in the spectrum will result in a distortion of the estimated saliency angle. Chapter 7 will show methods to decouple and suppress unwanted harmonics and improve the position estimation in real systems.

5.5.1 Instantaneous Phase Estimator

The currents or voltages containing the saliency angle information can be represented by a saliency signal vector. It might require some preprocessing (see Section 5.4) to obtain this vector. The carrier component has to be removed and the saliency harmonic has to be shifted to DC. The saliency signal vector can be derived from either a three-phase set or an orthogonal (d-q) set of signal components. For convenience, the saliency modulation is assumed to be contained in the stator currents. The saliency signal vector is then:

$$\begin{aligned} \underline{i}_{s_{dq\_c}} &= i_{s_{1\_c}} \cdot e^{j0} + i_{s_{2\_c}} \cdot e^{j2\pi/3} + i_{s_{3\_c}} \cdot e^{j4\pi/3} \\ &= i_{s_{d\_c}} + j i_{s_{q\_c}} \\ &= I\_c \cdot e^{j\theta_m} \end{aligned}$$

Using hf injection an orthogonal set of signals containing the saliency angle information is the result of the preprocessing:

$$\begin{aligned} i_{s_{d\_c}} &= I \sin(\theta_m) \\ i_{s_{q\_c}} &= I \cos(\theta_m) \end{aligned} \tag{5.65}$$

The argument θ_m shall be a function of the saliency given as $\theta_m = m \cdot \Theta$. Depending on the saliency, the mechanical angle Θ will be either a rotor or a flux angle. The number of saliency periods per mechanical revolution is specified by m. For a saturation saliency or an engineered rotor saliency usually $m = 4$ and for rotor slot harmonics, $m = N_r$ that is the total number of rotor slots.

For extracting the saliency angle, the orthogonal representation of (5.65) is most convenient:

$$\hat{\theta}_m = \arg(\underline{i}_{s_{dq\_c}}) = \arctan\left(\frac{i_{s_{d\_c}}}{i_{s_{q\_c}}}\right)$$

The phase estimator uses the *arcus tangens* function to extract the saliency angle. The phase extraction is instantaneous, so that $\hat{\theta}_m = \theta_m$ for the ideal signals of (5.65). No filter is required for the estimator itself. Since the preprocessing described in Section 5.4 requires a lowpass filter, the estimated position will however have an error that is proportional to speed. In contrast to the PLL of Section 5.5.2, the *arcus tangens* function requires no time for initialization and there is no dynamic tracking error.

Implementing the *arcus tangens* function can be either by using a Taylor series approximation or a lookup table. The Taylor series generally requires a high number of multiplications and is only suitable for modern digital signal processors. The lookup table implementation is preferable for fixed-point processors or processors with lower multiplication performance. Using trigonometric relations, the problems associated with the division by zero or the decrease in resolution when the argument tends towards infinity can easily be resolved (see e.g. [103]). Linear table interpolation provides a good compromise between high accuracy, small table size and low processing time. The approach using interpolation and trigonometric relations provides useful additional sub-period information about the two input signals $i_{s_{d\_c}}$ and $i_{s_{q\_c}}$. This information can be used to improve the robustness of the estimator, especially against cycle slipping.

A problem of the *arcus tangens* function is that it suffers from non-ideal saliency signals $i_{s_{d\_c}}$ and $i_{s_{q\_c}}$. An amplitude modulation of the same phase in both components cancels out by the division and does not cause an error on the estimated angle as long as the amplitude resolution does not get too small. DC offsets however, or differences in amplitude or higher harmonics, will result in a distortion of the extracted angle $\hat{\theta}_m$. For the most common case of additional harmonics, the harmonic suppression of Section 7.1 may be applied.

5.5.2 Phase Locked Loop and Heterodyning Estimator

A *phase locked loop* (PLL) consists of a phase detector $\Delta\Phi$, a loop filter $H(s)$ and a voltage controlled oscillator (VCO) that can be represented by an integrator as shown in Fig. 5.16. The output of the phase detector of an ordinary PLL produces an error term $\Delta\hat{\theta}$ that contains a low-frequency and a high-frequency component. Only the first component contains the phase difference between input and estimated phase that allows the tuning of the loop. The high-frequency component is filtered off by a lowpass filter contained in $H(s)$. This lowpass filter however creates problems with speed-reversals and at low speed since the high-frequency component moves to low frequencies and cannot be removed [134]. This component alters the principle of operation of the PLL and can cause instability (PLL out of lock) since the phase difference cannot be determined.

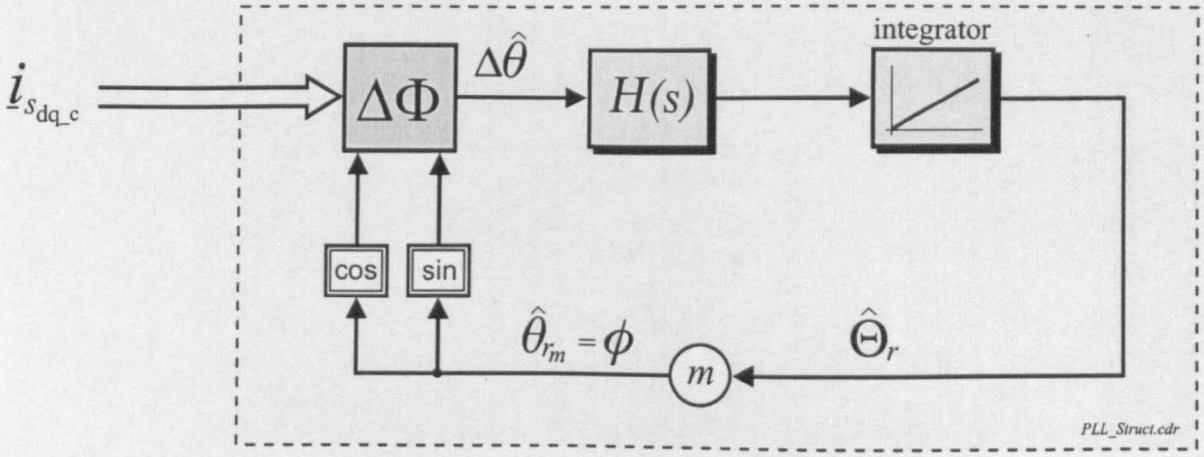

Figure 5.16: *Structure of vectorial phase locked loop*

This problem does not exist with a vectorial PLL that uses two orthogonal signal components that contain the phase information [77, 134]. Starting from the ideal signal in the negative sequence frame (see Section 5.4), the input to the PLL is

$$\begin{aligned} i_{s_{d\_c}} &= I \sin(\theta_{r_m}) \\ i_{s_{q\_c}} &= I \cos(\theta_{r_m}) \end{aligned}$$

where θ_{r_m} is the saliency angle. For a rotor saliency, $\theta_{r_m} = m \cdot \Theta_r$ where Θ_r is the mechanical rotor angle (see Section 2.2.3) and m is the number of saliency periods per mechanical revolution or the number of rotor slots. The phase detector $\Delta\Phi$ forms the crossproduct between input vector $\underline{i}_{s_{dq\_c}}$ and estimated vector:

$$\begin{aligned} \Delta\hat{\theta} &= i_{s_{d\_c}} \cdot \cos(\hat{\theta}_{r_m}) - i_{s_{q\_c}} \cdot \sin(\hat{\theta}_{r_m}) \\ &= I \cdot \sin(\theta_{r_m} - \hat{\theta}_{r_m}) \\ &\approx I \cdot (\theta_{r_m} - \hat{\theta}_{r_m}) \end{aligned} \tag{5.66}$$

The main difference between an ordinary scalar PLL and the vectorial PLL is, that in the latter no high-frequency component exists and no lowpass filter is needed. In contrast to the vectorial PLL phase detector in Section 5.4.6, the modulated signals are transformed externally by one of the techniques of Section 5.4. The lowpass filter in Section 5.4.6 is therefore applied outside the PLL.

For the simple case that the PLL is locked (the phase difference is smaller than $\pm 90°$) and tracking the incoming signal, the linearization of the phase error $\Delta\hat{\theta}$ in (5.66) is valid since $\hat{\theta}_{r_m}$ follows θ_{r_m} closely. The next stage in the PLL is a loop filter $H(s)$ that can be for example a gain V or a loop filter $(K_1 + \frac{K_2}{s})$. The additional gain m (see Fig. 5.16) can be included before the angle $\phi = \hat{\theta}_{r_m}$ is fed back into the phase

detector $\Delta\Phi$. The gain m in the loop ensures that the angle after the integrator will be an estimate of the mechanical rotor position Θ_r. The angle for the phase detector is the scaled angle $m \cdot \hat{\Theta}_r = \hat{\theta}_{r_m}$ that tracks the argument θ_{r_m} of the incoming signal but can be out of phase by multiples of 2π. This can result in a constant phase offset of $\frac{2\pi}{m} \cdot i$ for $\hat{\Theta}_r$, where i is an integer in $[0 \ldots m-1]$. This means only that the PLL cannot get absolute position information from an incremental signal. The phase offset will remain constant as long as the PLL is not out of lock.

- Type-1 Loop :
  For a type-1 PLL, the loop filter $H(s)$ is a gain V. Analyzing the PLL at discrete time steps $k \cdot T_a$ allows to determine the steady-state accuracy of the loop:

$$\text{a)} \quad \theta_{r_m} \stackrel{!}{=} \phi_k = \phi_{k-1} + T_a \cdot (V \cdot m \cdot \Delta\hat{\theta}) \equiv \hat{\theta}_{r_m} \tag{5.67}$$

$$\text{b)} \quad \Delta\theta_{r_m} = \underbrace{Ta \cdot (V \cdot m}_{c_V} \cdot \Delta\hat{\theta}) \tag{5.68}$$

  Comparing the left and right sides of (5.67), it becomes clear that the type-1 PLL correctly estimates the position for the case of a stationary machine where $\theta_{r_m} = const.$ When the phase error is zero $\Delta\hat{\theta} = I \cdot (\theta_{r_m} - \hat{\theta}_{r_m}) = 0$ the estimated angle is equal to the input angle $\hat{\theta}_{r_m} = \phi_k = \theta_{r_m}$.

  For the condition of constant speed where $\theta_{r_m} \neq const$, the phase error term is represented by $\Delta\theta_{r_m} = c_V \cdot \Delta\hat{\theta} = c_V \cdot I \cdot (\theta_{r_m} - \hat{\theta}_{r_m}) \neq 0$ from (5.68). A change in position θ_{r_m} will cause a phase error $\Delta\hat{\theta} \neq 0$ for the PLL. The larger the gain V, the smaller this phase error. This means that the type-1 PLL will not be able to track position accurately once the position is changing as the phase error supplies the control signal. The steady-state error for a frequency step is not zero.

- Type-2 Loop:
  To overcome the limitations of the type-1 loop, a PI controller can be used with $H(s) = (K_1 + \frac{K_2}{s})$. The analysis is done for discrete time steps where the controller is used in the discrete form $H(z) = (K_1 + K_2 \cdot \frac{zT_a}{z-1})$:

$$\text{a)} \quad \theta_{r_m} \stackrel{!}{=} \phi_k = \phi_{k-1} + T_a \cdot \left(K_1 + T_a \frac{K_2 \cdot z}{z-1}\right) \cdot (m \cdot \Delta\hat{\theta}) \equiv \hat{\theta}_{r_m} \tag{5.69}$$

$$\text{b)} \quad \Delta\theta_{r_m} = Ta \cdot (K_1 \cdot m \cdot \Delta\hat{\theta}) + \underbrace{T_a \cdot (K_2 \cdot m \cdot \Delta\hat{\theta}) \cdot \frac{z \cdot T_a}{z-1}}_{\nu_k} \tag{5.70}$$

$$\text{where} \quad \nu_k = \nu_{k-1} + T_a \cdot (T_a \cdot K_2 \cdot m \cdot \Delta\hat{\theta})$$

$$\text{c)} \quad \Delta^2\theta_{r_m} = T_a \cdot (T_a \cdot K_2 \cdot m \cdot \Delta\hat{\theta}) \tag{5.71}$$

For a constant position where $\Delta\theta_{r_m} = 0$, $\phi_k = \hat{\theta}_{r_m} = \theta_{r_m}$ and the error $\Delta\hat{\theta} = 0$ directly from (5.69). The steady-state error for a phase step is also zero.

The condition for constant speed where $\Delta\theta_{r_m} = const$ is shown in (5.70). The error $\Delta\hat{\theta} = I \cdot (\theta_{r_m} - \hat{\theta}_{r_m}) = 0$ when $\nu_k = \Delta\theta_{r_m}$. The additional integrator in the loop ensures that the estimated phase changes linearly even when the phase error is zero. The steady-state error for a frequency step is also zero.

For constant acceleration with $\Delta\theta_{r_m} \neq const$, an error $\Delta\hat{\theta} \neq 0$ will occur as is clear from (5.71).

The dynamics of the loop are determined by the factors K_1 and K_2. All other factors are lumped into the so-called loop gain ω_L that has the units of $[rad/s]$ [135]. Usually, the input signals are not normalized. Therefore the loop gain depends on the amplitude of the input signal. With the design parameters ω_N that is the natural frequency (approximately the loop bandwidth) and the damping factor D:

$$K_2 = \frac{\omega_N^2}{\omega_L}$$

$$K_1 = 2D\sqrt{\frac{K_2}{\omega_L}} = 2D\frac{\omega_N}{\omega_L}$$

The time for the PLL to lock to the incoming signal is approximately a function of the natural frequency with $T_{lock} = \frac{2}{\omega_N}$ [135]. The steady-state phase error due to acceleration is $\Delta\hat{\theta} = \ddot{\Theta}_r/K_2$. An increase in K_2 will reduce the phase error. Once the acceleration $\ddot{\Theta}_r$ is zero, the loop filter will bring the phase error back to zero. Since the phase error depends on the second derivative of the position ($\ddot{\Theta}_r$), a large acceleration can bring the loop close to the stability limit for large m.

- Heterodyning Estimator:
  The previous section has shown that a PI controller in the loop, cannot eliminate the error in the estimated phase during acceleration. Increasing the order of the loop filter $H(s)$ can be difficult since higher-order loops are only conditionally stable [135]. Jansen and Lorenz [77] propose a Luenberger style position and speed observer. This is a combination of PID controller and mechanical model that replace the loop filter $H(s)$ and VCO. The PLL now is of type 3 since it contains three integrators. With the knowledge of the drive inertia J, the estimated electrical torque T_{el} can be used as a feedforward term to improve the loop dynamics [136]. The feedforward will remove or reduce the acceleration error. The derivative term $K_3 \cdot s$ is not implemented directly in [77] but as a bypass of the $\frac{1}{Js}$ block in the form $\frac{K_3}{J}$. This avoids differentiation that can be a problem with noisy signals.

The difficulty of this implementation is firstly that the inertia has to be known and secondly that the load torque T_L is unknown. The load torque may change the resulting torque that is available for the actual acceleration of the machine. However, even a larger error or uncertainty in these two parameters will still reduce the acceleration error of the PLL. The loop controller determines the dynamic performance of the loop but has to be balanced with the need for filtering off noise or distortions.

Similar to the *arcus tangens* function, the PLL suffers from cycle slipping once the input signal vector contains additional large frequency components. Also a DC offset or amplitude differences distort the phase error. For the case of additional harmonics, the harmonic suppression of Section 7.1 may be used.

5.5.3 Consoli Estimator

In [81], the *hf* third harmonic stator voltage $v_{0_{hf}}$ of a star-connected induction machine is measured that contains the saliency angle information. In [93] it is the common mode current component $i_{0_{hf}}$ that is due to $v_{0_{hf}}$ and also contains the saliency angle:

$$i_{0_{hf}} = \sin(\theta_c - \theta_m + \phi_1) \tag{5.72}$$

In contrast to previous saliency estimators, only a scalar signal containing the saliency information is available. Also, this signal does not contain a carrier harmonic. The carrier frequency is however influencing the phase of $i_{0_{hf}}$ as well as the unknown saliency angle θ_m.

The standard method is to use a PLL. The phase detector multiplies the incoming signal $i_{0_{hf}}$ with $\cos(\theta_c - \hat{\theta}_m + \phi_2)$ that contains the known carrier frequency f_c and an estimate of the saliency position. After a lowpass filter, only a DC component remains that is zero, if $\hat{\theta}_m = \theta_m$. Otherwise, the output of the lowpass filter is a DC signal, that is proportional to the error between the real and estimated saliency position if the difference is small. This error is used as input for an integrator. The output of the integrator is usually scaled and is the estimated saliency position $\hat{\theta}_m$ that is then subtracted from θ_c to serve as input for a sine function. Feeding this into the phase detector closes the loop.

Trying to avoid delays and loop dynamics of the PLL in estimating the saliency angle, [81] uses a different approach. It can easily be shown that the saliency angle θ_m equals the angle of the *hf* injection signal plus a predictable offset for the following four conditions of $i_{0_{hf}}$:

Condition	$i_{0_{hf}}$	$\theta_c - \theta_m =$	$\theta_m =$
MAX (maximum)	$\max(i_{0_{hf}})$	$\pi/2$	$\theta_c - \pi/2$
DEC (zero crossing, decreasing)	$i_{0_{hf}} = 0$	π	$\theta_c - \pi$
MIN (minimum)	$\min(i_{0_{hf}})$	$3\pi/2$	$\theta_c - 3\pi/2$
INC (zero crossing, increasing)	$i_{0_{hf}} = 0$	$2\pi/0$	θ_c

Finding the two extremas and two zero crossings per period of the common mode current $i_{0_{hf}}$, the unknown θ_m can be determined from the known *hf* angle $\theta_c = \omega_c t$. Finding the extremas (MAX = maximum, MIN = minimum) and zero crossings (INC = $i_{0_{hf}}$ increasing, DEC = $i_{0_{hf}}$ decreasing) of $i_{0_{hf}}$ can be done by differentiating twice:

Condition	first derivative	second derivative
MAX	$\frac{di_{0_{hf}}}{dt} = 0$	$\frac{d^2 i_{0_{hf}}}{dt^2} < 0$
MIN	$\frac{di_{0_{hf}}}{dt} = 0$	$\frac{d^2 i_{0_{hf}}}{dt^2} > 0$
INC	$\frac{di_{0_{hf}}}{dt} > 0$	
DEC	$\frac{di_{0_{hf}}}{dt} < 0$	

In practice however, noise can be a problem for the derivatives. Also, the resolution of the detection is crucial for the resolution of the estimated saliency position. The angle used for the demodulation will be the same θ_c that is used to calculate the *hf* voltage injection. This angle can however have a phase shift compared to the angle θ_c of the sampled *hf* current $i_{0_{hf}}$. Clearly, the higher the sample rate the better the estimated saliency position. Noise however will reduce the accuracy obtained in a real system.

In [74], the *hf* current components from a PMSM are added to give

$$|I_{s_c}| = i^2_{s_{d\_c}} + i^2_{s_{q\_c}} \approx k \cdot \sin(\theta_c - \theta_r + \phi)^2 \tag{5.73}$$

This signal is similar to (5.72) of the induction machine. The same algorithm for estimating the saliency position is used. Here, an additional problem exists, because of the 180° position uncertainty.

If the amplitude of $i_{0_{hf}}$ or $|I_{s_c}|$ is known and constant, it might be tempting to use the *arcus sinus* function. This however is completely out of question for real systems. Phase and amplitude changes in (5.72) or (5.73) will cause large nonlinear errors in the extracted position.

5.5.4 Balancing Saliency Angle Estimator

This controller was already covered together with the saliency model in Section 5.3.2 and more detailed in Section 5.3.3. The structures used by Blaschke [79] and Sul [20] are essentially a PLL as shown for the *Sul*-approach in Fig. 5.9. The *Saliency Angle Estimator* serves here as the phase detector and includes the lowpass filters that remove the high-frequency $2\omega_c$ components. This lowpass filter limits the dynamics of the loop.

Assuming a phase change of the real measurement frame by $\Delta\theta$, the output of the phase detector is $\xi = k \cdot \Delta\theta$ that is then multiplied by the gain V of the loop filter. The integrator will increase the output until $\hat{\phi}_m = (\hat{\phi}_{m_{old}} + \Delta\theta) \stackrel{!}{=} \phi_m$. The dynamic is essentially that of the type-1 PLL of Section 5.5.2.

5.5.5 Sampling Estimator

A possible implementation of this discrete sampling technique that is used for signal demodulation is presented in [137]. The basis is the function $f(t)$ of (5.74), that can be a modulated voltage or current and contains two frequencies. The first frequency component is the known carrier ω_c and the second component can be the unknown rotor saliency $\frac{N_r}{ps}\omega_r$. The idea is to align the sampling with the first known frequency at multiples of $\Delta t = \frac{1}{f_c}$. This can be relatively simple since the carrier frequency is constant and can be selected an even fraction of the frequency of the current controllers or PWM generation.

$$
\begin{aligned}
f(t) &= \cos\left(\omega_c t - \frac{N_r}{ps} \cdot \omega_r t\right) && (5.74)\\
&= \cos\left(\omega_c(t_0 + n \cdot \Delta t) - \frac{N_r}{ps} \cdot \omega_r t\right)\\
&= \cos\left(2\pi(n_0 + n) \cdot \frac{f_c}{f_c} - \frac{N_r}{ps} \cdot \omega_r t\right)\\
&\cong \cos\left(\frac{N_r}{ps} \cdot \omega_r t - 2n_0\pi\right) = g(t) && (5.75)
\end{aligned}
$$

If $\omega_c \gg \frac{N_r}{ps}\omega_r$, the approximation of (5.75) is valid and the error is small. Only a phase offset $2n_0\pi$ distinguishes the real signal $f(t)$ from the demodulated signal $g(t)$. When rotor slot harmonics are used as the main saliency, the ratio f_c/f_{sal} will easily reach values smaller than 10 where $f_{sal} = N_r/ps \cdot f_r$ the frequency of the machine saliency. This condition assumes a maximum operable rotor frequency of $f_r = 5\text{Hz}$ for the sensorless drive. Above this, model-based techniques work reliably and can be utilized. The ratio f_c/f_{sal} can be increased for drives with a PWM frequency above

$10k$Hz and a carrier frequency of several kHz. For other rotor saliencies (resistance, inductance) or the saturation saliency, the ratio f_c/f_{sal} of carrier to saliency frequency will usually be above 50, where $f_{sal} = 2f_r$ or $f_{sal} = 2f_e$, typically.

Ishida, *et al.* [137] also suggest the sampling estimator to eliminate unwanted harmonics from the signal spectrum of $f(t)$. The idea is to select the sampling frequency also as a multiple n of the unwanted frequency f_x with $\Delta t = \frac{1}{f_c} = \frac{1}{n} \cdot \frac{1}{f_x}$. Two functions $g_-(t)$ and $g_+(t)$ are sampled that are 90° out of phase, i.e. $\Delta t/4$. The resulting signal without frequency f_x is the difference $g(t) = g_+ - g_-$.

The harmonic suppression by discrete sampling cannot easily be applied to removing unwanted saliencies. The frequencies f_r, f_e or their multiples are not constant during normal machine operation. The sampling frequency usually cannot easily be adopted fast enough to allow harmonic suppression during transient operation. The suppression also suffers from the difficulty of adapting the sampling frequency during operation near zero speed. It is very unlikely that the carrier frequency and unwanted saliency frequencies will be multiples. It therefore will be necessary to implement the sampling estimator in separate stages for each frequency suppression or demodulation.

5.5.6 Effect of Filters in Position Estimation

Any filter used for extracting the *hf* signal from the measured fundamental and any filter in the saliency estimator introduce a potential phase shift. The bandpass filter (filter 3 in Fig. 5.17) to extract the *hf* modulation from the fundamental currents is tuned for the carrier frequency f_c. Any signal at this frequency passes directly through the filter without a phase shift. If the machine is running at higher speeds, the position harmonic at $f_c \pm n \cdot f_r$ moves away from the center frequency and therefore is affected by a phase shift. If the width of the bandpass filter is wide enough, this phase shift can be kept small. The filter design is however a compromise. The useful position harmonic has to be extracted and other harmonics have to be reduced sufficiently. The wider the filter, the more noise couples into the extracted spectrum. Theoretically, a filter with adjustable center frequency, following the position harmonic would be ideal. There is however no independent and reliable signal other than the position harmonic that could be used to tune this filter. Practically, this might work for steady-state operation. Transients will however very likely cause a complete loss of signal if the filter cannot be adjusted fast enough.

A digitally implemented filter (lowpass filter 5 in Fig. 5.17) is normally used to remove the positive sequence harmonics [96]. This filter will have a similar impact on the phase shift of the position harmonic as the bandpass filter. Since the carrier harmonic is several times larger in amplitude than the position harmonic, the filter cutoff frequency cannot be too high if the carrier is to be suppressed sufficiently. A large remaining carrier harmonic will introduce a ripple on $\underline{i}_{s_{dq\_c}}$ that can cause

the estimator to become unstable. This lowpass filter will therefore determine the bandwidth of the sensorless system.
Using the ATAN function to resolve the flux or position angle, the estimate will be instantaneous. A PLL will in practice introduce another phase shift.

5.6 Summary of Implemented Method

The chapter has reviewed the different models of machine saliencies, shown their mathematical representation and commented on the physical background and origin. Different strategies for the saliency demodulation have been shown and possible saliency angle estimators have been compared. The problem of reliably estimating a saliency angle in the presence of additional or unwanted saliencies has not been addressed in this chapter. The saliency compensation will be the subject of Chapter 7.
For the work in the thesis, the techniques used for the estimation of the rotor position are shown in Fig. 5.17. High-frequency voltage injection is used that is superimposed onto the fundamental voltage demand, shown in the top of the structural diagram. A *hf* voltage injection for VSI is preferable over *hf* current injection (see Section 5.1.2). The bandpass filter 3 suppresses the large fundamental current components and obtains the modulated currents from the stator currents. This filter is realized in analogue to increase the signal resolution at the input of the A/D converter. The saliency compensation requires the fundamental currents $\underline{i}_s$ that are filtered using lowpass filters 1 and 2. A highpass filter that is tuned for the carrier in combination with a signal transformation (see Section 5.4.7) is particularly advantageous if the carrier frequency is low. The two lowpass filters are still recommended but can have a much higher cutoff frequency, resulting in an increased bandwidth for the compensation.
The demodulation of the saliency signals is done digitally and consists of the two transformers and filters 4 and 5. First, the signal $\underline{i}_{s_{\alpha\beta\_c}}$ is shifted into the positive-sequence frame where the carrier is suppressed using the highpass filter 4. The direct or indirect homodyne transformation can be used equally. The first method is preferred since it does not introduce a scaling by the amplitude of the carrier harmonic (see Sections 5.4.4 and 5.4.5). The filter transformation of Section 5.4.7 is not suggested since this method is numerically critical and can easily become unstable. Multiplication by $e^{-j2\omega_c t}$ then transforms the negative-sequence harmonics to DC. The lowpass filter 5 removes the remaining positive-sequence harmonics.
Earlier experiments did not make use of the carrier rejection filter 4. The *hf* currents $\underline{i}_{s_{\alpha\beta\_c}}$ of (5.19) were directly multiplied by $e^{j\omega_c t}$. This operation shifts the measurements onto the negative sequence axis (Sections 5.4.4 and 5.4.5) and $\underline{i}_{cp}$ is removed

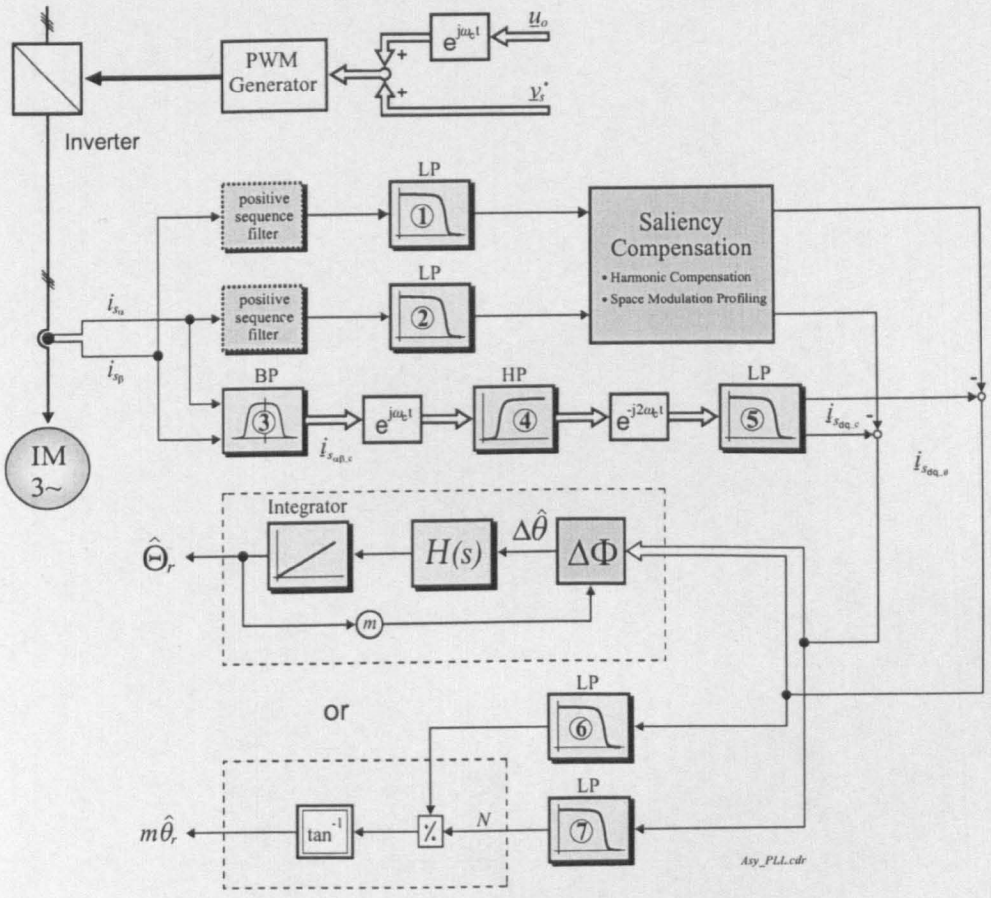

Figure 5.17: *Rotor position estimator with demodulator and saliency compensation*

by lowpass filter 5. The transformed *hf* currents are now given by:

$$\underline{i}_{s_{dq\_c}} = \sum_m \sum_k \underline{i}_{cn_{mk}} e^{j(h_{mk}\theta_m + \varphi_{mk})} \tag{5.76}$$

The output is the signal $\underline{i}_{s_{dq\_c}}$ that contains the low-frequency modulations of all machine saliencies. For this thesis, the primary saliency is that due to the engineered rotor or due to rotor slotting which is now at $h_{m1} f_r$ with $h_{21} = 28$ or $h_{31} = 2$ (see Sections 5.2.2 and 5.2.2 and rotors in Section 4.6.1). Adding the signal from the saliency compensator (see Chapter 7) will suppress the unwanted modulations. The remaining signal $\underline{i}_{s_{dq\_\theta}}$ then only consists of a component that contains the rotor angle information, that is sent to a *phase estimator*. This can be a PLL or the *arcus tangens* function to resolve the rotor position. The choice of the loop filter $H(s)$ of the PLL (Section 5.5.2) determines the dynamics of the rotor position estimation. Preferably the Type-2 loop or the Heterodyning Estimator are used to obtain best dynamic performance (see discussion in Section 5.5.2). The PLL was only used for the

machine with engineered rotor saliency. The preferred choice was the instantaneous phase estimator of Section 5.5.1. This is because the *arcus tangens* requires no time for initialization and is easier to set-up. The PLL also suffers from an acceleration error that requires additional signal estimation and complicates the loop design to reduce the error. This increased complexity is a disadvantage of the PLL when compared to the *arcus tangens* function. The *arcus tangens* might require the two additional lowpass filters 6 and 7 to smooth the $\underline{i}_{s_{dq\_\beta}}$ signal components before demodulation. These filters will introduce an additional phase shift and cause a speed-dependent position estimation error. These lowpass filters will however also have to be a part of the loop filter $H(s)$ of the PLL if the $\underline{i}_{s_{dq\_\beta}}$ signal is affected by distortion during transient operation (see Section 6.2). The PLL can be tuned with the multiplier m to directly output the rotor position estimate $\hat{\Theta}_r$ where m is equal to the number of saliency periods N_{sal}. The *arcus tangens* provides an estimate of $m \cdot \hat{\theta}_r$ that changes m times faster than the real rotor position. A differentiator with a range limiter and an integrator in combination with a *remainder*-function is required to rescale $m\hat{\theta}_r$ and to derive the estimate $\hat{\Theta}_r$ itself. The logic function is:

$$y(x) = rem\left(\frac{1}{m}\int rem\left(\frac{dx}{dt} + x_{\max}, \frac{x_{\max}}{2}\right) - z, y_{\max}\right) \tag{5.77}$$

where the output is $\hat{\Theta}_r = y \in [0 \ldots y_{\max}]$ with the slope of $1/m$ of the input signal $m\hat{\theta}_r = x \in [0 \ldots x_{\max}]$. For the rotor position, the limits are equal with $x_{\max} = y_{\max} = 2\pi$ and $z = x_{\max}/2$ for $dx/dt < 0$, else $z = 0$. This additional computation that is not required for the PLL appears to be a disadvantage for the *arcus tangens*. It is however for rotor #3 with $N_{sal} = N_r = 56$, where the *arcus tangens* requires the logic of (5.77) that the PLL fails easily. The reason is that during acceleration the phase error can exceed the stability margin of the phase detector which results in a cycle slipping and temporary loss of position. Since $m = 56$ is large, the stability margin is $0.25 \cdot 360°/m = 0.25 \cdot 6.43°$ compared to 4° phase error that can easily be reached during acceleration.

Reducing the phase error using a higher gain K_2 is not an option since the estimated signals contain noise and remains of suppressed saliency harmonics. Estimating the load torque to reduce the acceleration error with the *Heterodyning Estimator* is not that straightforward. The load can change instantaneously and the load torque can only be estimated reliably with the sensorless drive under field-orientation. The correct field-orientation however cannot be guaranteed with the PLL under dynamic conditions.

For the practical implementation, the *arcus tangens* has been found more robust and easier to implement with a predictable speed error. With the experimental drive under sensorless position control, operating at lower speeds and changing acceleration, the evaluation was in favour for the *arcus tangens* as saliency angle estimator. The

estimators of Sections 5.5.3, 5.5.4 and 5.5.5 were not considered suitable. For the *Consoli Estimator*, a very high sampling frequency is required that consumes a lot of processing power. The twofold differentiation of measured signals is not attractive due to unavoidable noise. For the *Balancing Estimator*, the implementation of the saliency compensation is more difficult. The loop dynamics are determined by a PLL which comes with a reduced robustness for high N_{sal}. The *Sampling Estimator* only provides a low resolution when detecting the extrema (min/max). The use of the inverse function $\cos^{-1}$ to extract the saliency angle can cause systematic errors.

Since the investigation started by testing the asymmetric rotor (rotor #1), a reduced structure of Fig. 5.17 was originally implemented. The results for rotor #1 (see Sections 8.1 and 8.1.2) did not use the $e^{j\omega_c t}$ transformer and highpass filter 4. Implementing this structure will improve the results since the injection frequency of 300Hz is relatively low.

The symmetric machine (rotor #3) applies an injection of 750Hz that allows for a better spectral separation of the modulation harmonics. The voltage injection is about 25V *rms* on the line voltages that can be considered a good compromise between a low distortion of the torque production and providing a sufficient *hf* excitation. The resulting *hf* ripple is 5.3A *rms* on the line currents. The amplification of the bandpass filter 3 is chosen so that 7.5A *peak* will equal 14250 increments after the A/D converter and currently only using 43% of the possible input range. This design does not provide the maximum resolution but leaves the possibility of increased *hf* injection if required. The position modulation due to rotor slotting is around 0.365A *rms* that is about 7.6% of the resulting carrier on the stator currents.

Chapter 6:

Additional Modulation

In the previous chapter, the modulation of the *hf* currents has been attributed to the various saliencies in the machine. These saliencies have in common that they can be conveniently described by a two-axis model. As many models can be combined as there are saliency harmonics present in the real machine. It is also important for the position estimation that the modulation due to these saliencies is a continuous effect. This means that the saliency remains constant as long as the operating conditions of the machine i.e. flux level, speed or load are not changed.

This chapter describes two causes for a discrete or temporary modulation of the *hf* currents that are not an inherent part of the machine. The two effects are the modulation due to the inverter deadtime and the modulation during dynamic machine operation. The latter only occurs when the machine is operated under transient conditions where the stator currents change quickly. Under steady-state and slow position, speed or torque transients, this modulation does not occur or can be neglected. The implication of this modulation on the performance of the position estimation and the sensorless control is shown experimentally in this chapter. A compensation function as described by Briz *et al.* [138] has not been implemented yet.

The focus of the research has been mainly on the modulation due to the inverter deadtime. This modulation has been suspected before [73] to cause a distortion of the *hf* currents or voltages and therefore to degrade the estimation of the saliency angle. This thesis however analyzes for the first time the inverter deadtime with its effect on the *hf* voltages and currents. As a result, a compensation strategy is developed in Section 7.2 to reduce the distortion due to the inverter modulation. It will be shown that the modulation due to inverter deadtime has many characteristics in common with the modulation due to the saturation saliency. This might be one

reason why the influence of the inverter non-linearities has been neglected so far in research using *hf* injection.

6.1 Modulation due to Inverter Deadtime

So far, the *hf* voltage injection is most popular in the research community to persistently excite the machine saliencies which gives an estimate of flux or rotor angle. This injection is on a VSI and in open-loop; the effective *hf* voltage that is applied to the machine terminals is not measured or used in a feedback system. Since the inverter is a non-linear amplifier, the actual voltage that is available at the machine terminals can differ from the requested voltage. This non-linearity has to be known to predict the distortion of the flux or rotor angle estimation. The analysis will begin with a review of the known distortion due to inverter deadtime for fundamental voltages and currents. From this background, the *hf* modulation due to the inverter will be developed. Different experiments were conducted to prove the existence and significance of the modulation due to the inverter deadtime.

6.1.1 Inverter Deadtime

Deadtime is inevitable in the PWM inverter to prevent the shoot-through phenomenon in an inverter leg when switching from one device to another. The turn-*off* usually takes longer than the turn-*on* in IGBTs, MOSFETs, BJTs or other power electronic switches. Deadtime is usually implemented in hardware by the manufacturer in the gate driver logic or can be integrated into silicon as part of the PWM generator of the microcontroller [14, 139]. The deadtime ensures that only one device in an inverter leg is on at a time. During the shoot-through delay or deadtime both devices are therefore disabled. The length of this time depends partially on the switching devices but also on the layout and design of the inverter itself. In commercial industrial environments with priority on the reliability of the inverter, a conservative setting is often used with deadtimes of 5 - 10μs for IGBT inverters in the range 5 to 50kW. During deadtime, the remaining current takes one of the two possible freewheeling paths through the diodes. This safety feature of the standard inverter is the cause for a voltage error. First, the voltage drop across the active switching device is less than through the anti-parallel diode when this gets active during freewheeling. Not the full DC-link voltage is available across the machine terminals but a reduced one. Under some conditions, the diode can also stop conducting (see Section 6.1.2) and the terminal voltage is determined by the other two phases and the load. The additional *on*-resistance of the devices can be obtained from the manufacturer's datasheets and included in the machine model [45]. The major problem however comes from the uncertain switchover between lower and upper freewheeling paths. During deadtime,

the current direction in the inverter leg and its magnitude (within limits) will determine at which instance within the shoot-through delay the commanded switching edge and therefore the terminal voltage will change.

For large currents, the situation is simple: If an active switch is already *reverse-biased* and the anti-parallel diode is conducting, the voltage will not change during the deadtime interval but at its *end* with the new switching device becoming active. If however a switch is *conducting*, the voltage changes at the *beginning* of the deadtime interval and the current then flows through the complementary diode. For large currents, a compensation can easily be implemented in silicon [139]. For small currents, the switching edge can occur anywhere within this deadtime interval [140]. In particular if the reference voltage is small, the relative error of the voltage can become be very large.

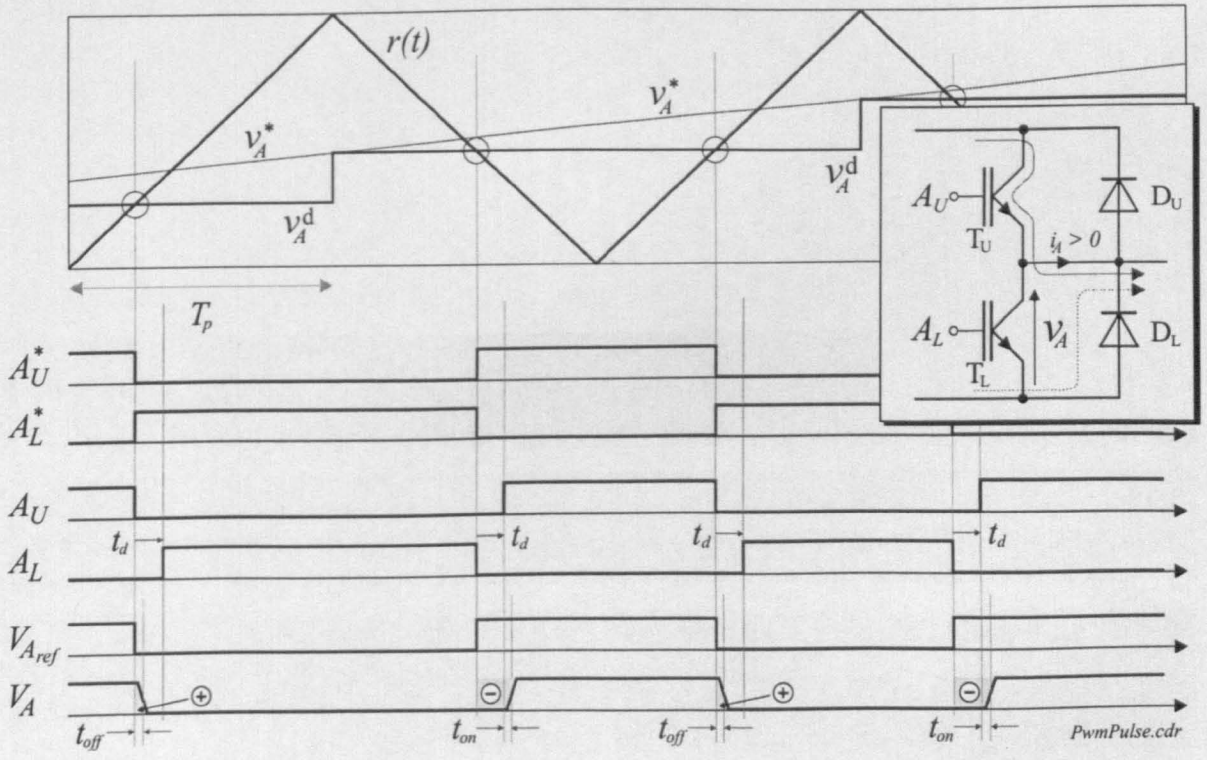

Figure 6.1: *Reference voltage v_A^* and actual phase voltage V_A due to deadtime and turn-on/off delays*

The operation of the PWM generator is visualized in Fig. 6.1. The reference voltage is v_A^* and $r(t)$ is a triangular ramp with the PWM period $2T_p$. For the pulse generation, v_A^* is sampled at a timer overflow $r(t) = r_{\max}$. This digital reference v_A^d is updated once per period $2T_p$. Comparing v_A^d with the ramp $r(t)$ determines the instance of the pulse edges. The pulses will have a theoretical symmetry around the timer

underflow where $r(t) = 0$. A_U^* and A_L^* are the ideal reference signals for the upper and lower switching device respectively. Due to deadtime, the *on*-switching edge will be delayed by t_d, resulting in the modified switching signals A_U and A_L. The actual voltage will depend on the direction of current through the inverter leg. Fig. 6.1 shows the resulting phase voltage V_A for a positive current i_A. When the upper device is switched *off*, the current maintains direction but flows through the lower diode and the voltage drops to zero. The voltage transition is delayed by the turn-*off* delay t_{off}. This delay increases the average voltage [141]. Due to deadtime, the turn-*on* process is delayed by t_d and t_{on}. These delays will reduce the average voltage. If the current is negative ($i_A < 0$), the switching edges of V_A will be aligned to the edges of A_L resulting in a net increase of the average voltage of V_A.

The typical method to reduce the voltage error due to deadtime is to implement a feedforward compensation voltage that is constant but depends on the sign of the actual current [142]. In [140] a diagram is shown with switching edge over the line current. Below a certain current threshold the switching edge can occur anywhere within a large section of the deadtime-interval. This large deadzone makes it difficult to implement a correct compensation. A small change in current results in a large voltage change.

The effect of using a feedforward voltage compensation is demonstrated in Fig. 6.2. After about 15sec the compensation is switched on (indicated by the step signal in the upper plot that changes from 0 to 15). The phase voltage v_A becomes much more sinusoidal with the compensation. The reference phase voltage v_A^* is here shown as a dotted line. It is interesting to see that there is still a significant distortion in v_A at the instance of the zero crossing of i_A. Further distortion is due to the zero-crossings of i_B and i_C. In the lower plot, the trace around zero shows the current error $\delta i_A = i_A^* - i_A$, that is the difference between reference and real line current. With the compensation switched on, the distortion reduces, however not significantly. Note that current controllers without prefilter were used here (see Section 3.3). The spikes during current crossing are very short and even could not be fully eliminated with faster current controllers.

6.1.2 Current Clamping

The inverter deadtime has a significant impact on the stator currents. This becomes very obvious when running the induction machine under V/f control. Fig. 6.3 shows the line currents for a speed of $n_r = 50$rpm. Subplot *a2)* shows the 3-phase currents under V/f control. A plateau is clearly visible in the three-phase currents during the zero-crossing. This phenomenon is called the *current clamping effect*. In the frequency spectrum of the line currents, the result is a large $5f_e$ and $7f_e$ harmonic component. The $\alpha\beta$ currents in subplot *a1)* also show the clamping as steps. Due to

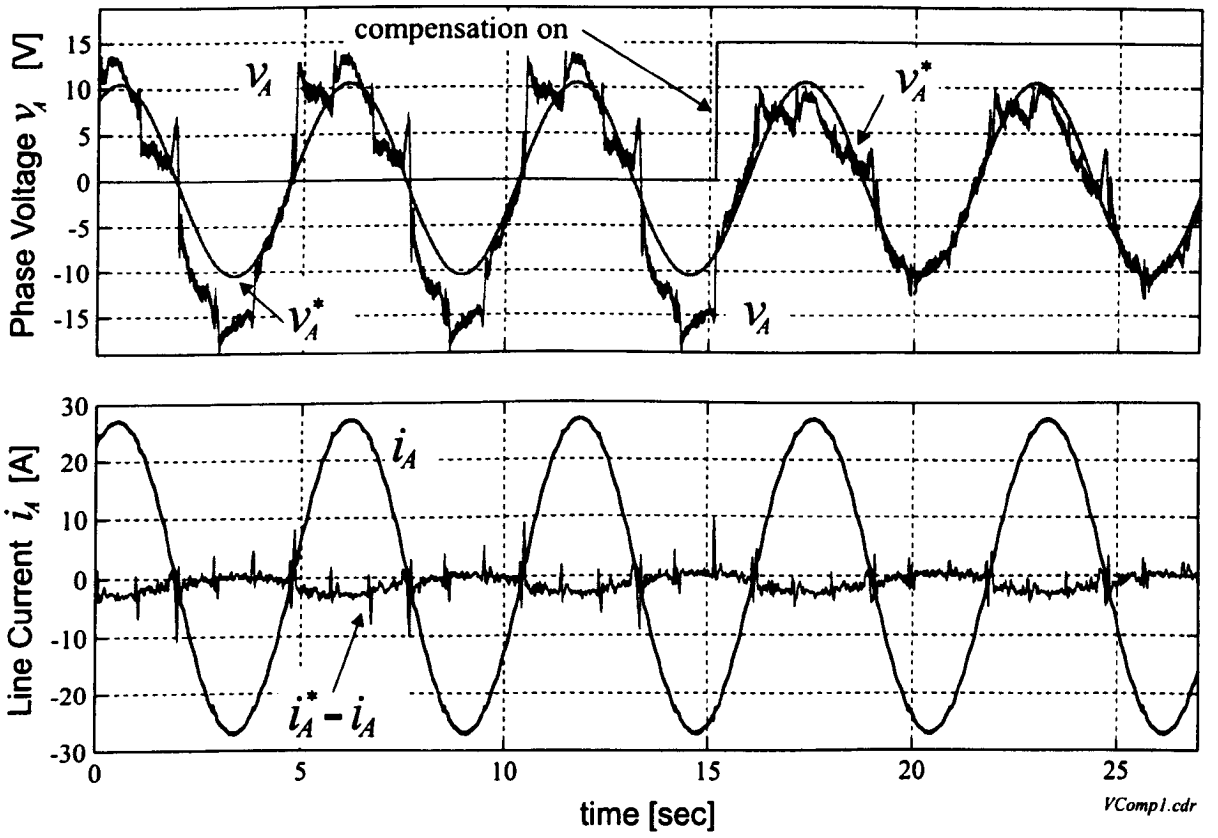

Figure 6.2: *Phase Voltage v_A, line current i_A and magnified current error Δi_A for field orientated drive at $n_r = 5rpm$ (1/6Hz) using feed-forward deadtime compensation*

the transformation to two-phase, the steps in the i_α current are actually not aligned to the zero-crossing. The clamping effect becomes more difficult to identify. The distortion of the line currents does not only occur during the zero-crossing but also when one of the other two currents is crossing through zero. This is because of the current balance ($\sum_{X=A,B,C} i_X = 0$). The current clamping causes oscillations in the torque and therefore also in the speed of the machine. The spectrum of the speed signal shows a large 3rd, 6th, 9th harmonic of the synchronous frequency f_e.

The 3-phase line currents for the drive under Vector Control are shown in subplot *b2)*. The current controllers ensure that the currents are sinusoidal. Zooming into the area of the currents crossing through zero, a small step can still be seen. Additionally, the currents will also be distorted when any of the other two line currents is around zero. Analyzing the i_{sq} current component, a large $6f_e$ harmonic due to the deadtime can be found. There is negligible distortion on the i_{sd} current. The clamping of i_{sq} causes unwanted torque ripple and a $6f_e$ harmonic in the speed. This distortion is however much smaller than for V/f control. Other harmonics can also be found in i_{sq}.

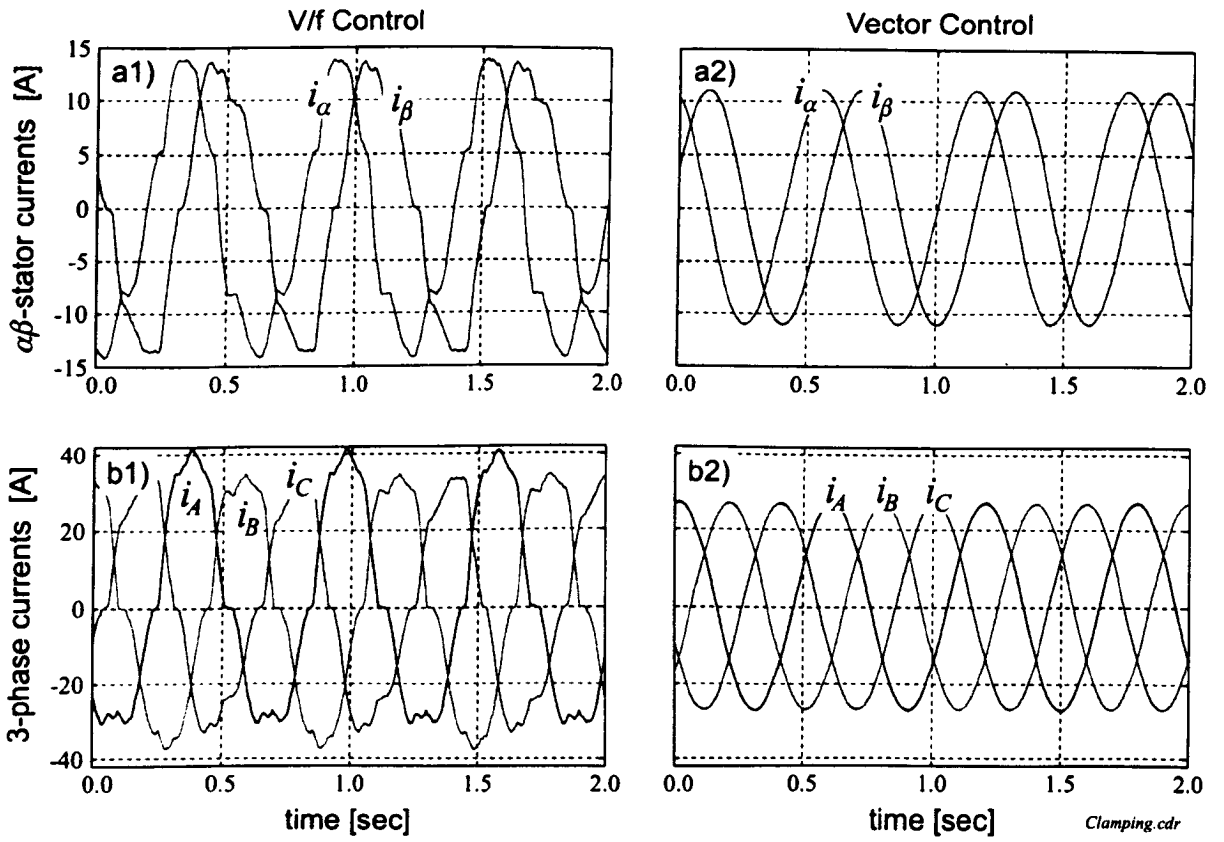

Figure 6.3: *Effect of inverter deadtime on stator currents for V/f (left) and Vector Control (right) for* $n_r = 50rpm$ *(5/3Hz)*

These are caused by DC offsets of the current transducers ($1f_e$ frequency ripple) and by current scaling errors of the current transducers or A/D converters ($2f_e$ frequency ripple) [114].

The reason for the current clamping is twofold. When the current through an inverter leg is small, the stray capacitors across the devices are not recharged immediately [142]. The voltage at point **A** in Fig. 6.1 builds up slowly. The average line-to-line voltage will then be much smaller than the demanded voltage. Another reduction of the voltage during deadtime is described in [143] for a **Y**-connected machine. If the current reaches zero during deadtime, the diodes will be reverse biased and the voltage at terminal **A** is only determined by the back-*emf* of the machine that is very small at low speed. Again, the voltage across the machine terminals can much smaller than the demanded voltage when the current through the inverter leg is low. The voltage error becomes more important the smaller the demanded voltage is. The controllers in a vector-controlled drive will therefore have to demand a much higher voltage to drive the currents through zero. The net effect is that the inverter gain is

reduced when a line current crosses through zero. When superimposing a *hf* voltage onto the stator voltages, the real voltages across the machine will be modulated by the changing gain of the inverter. Instead of a *hf* voltage of constant amplitude, the amplitude varies with the frequency of the current zero crossings which is the excitation frequency f_e.

For a three-phase load such as a machine, the inverter deadtime causes 6 ripples during one electrical period $T_e = 1/f_e$. This is because the three line currents will have two zero crossings each per period T_e.

The deadtime delay is about 12.0 - 12.7μsec for the 45kW inverter that is used in the research.

6.1.3 Inverter Clamping Modulation

The inverter effects discussed so far can be found in any induction machine drive. Inverter deadtime however can also cause a significant problem for the position estimator based on *hf* injected signals.

When injecting a *hf* voltage signal into the machine, this is done in an open-loop manner. The real signal applied to the machine is not fed back and compared to the reference injection. For small currents crossing through zero, the pulse-length uncertainty remains for a relative long time. It can easily exist for 100ms or more. During all this time, the actually injected voltage differs from the commanded injection voltage. The faster the current changes sign and crosses through zero, the shorter the voltage uncertainty and the smaller the unwanted modulation effect of the voltage injection. In fact, for the machine under Vector Control driving a high load, the harmonics due to the inverter modulation are smaller than under low or no load. The duration of the reduced gain becomes shorter.

Let g_x be the inverter gain for the *hf* phase voltage x with $g_x = v_x/v_x^*$, the ratio of actual *hf* voltage to *hf* reference voltage as shown in Fig. 6.4. During the time of zero or low current i_x, the gain g_x will be reduced. This means, the *hf* voltage gets modulated by the inverter gain g_x. This modulation will then also affect the *hf* currents that contain the information about the position saliency. It has been shown above that the clamping is a function of the excitation frequency f_e. This means that the inverter non-linearity due to deadtime causes a saliency similar to that due to saturation.

The dependency of the inverter gains g_A, g_B and g_C on the stator currents shown in Fig. 6.4 and determines the further characteristics of the inverter modulation harmonics in the *hf* current spectrum. During one electrical period of the stator current, the injection voltage gets modulated six times. This is because there are six zero crossings per electrical period in total, two crossings per line current. In the *hf* spectrum, the inverter modulation harmonic appears therefore at twice the stator

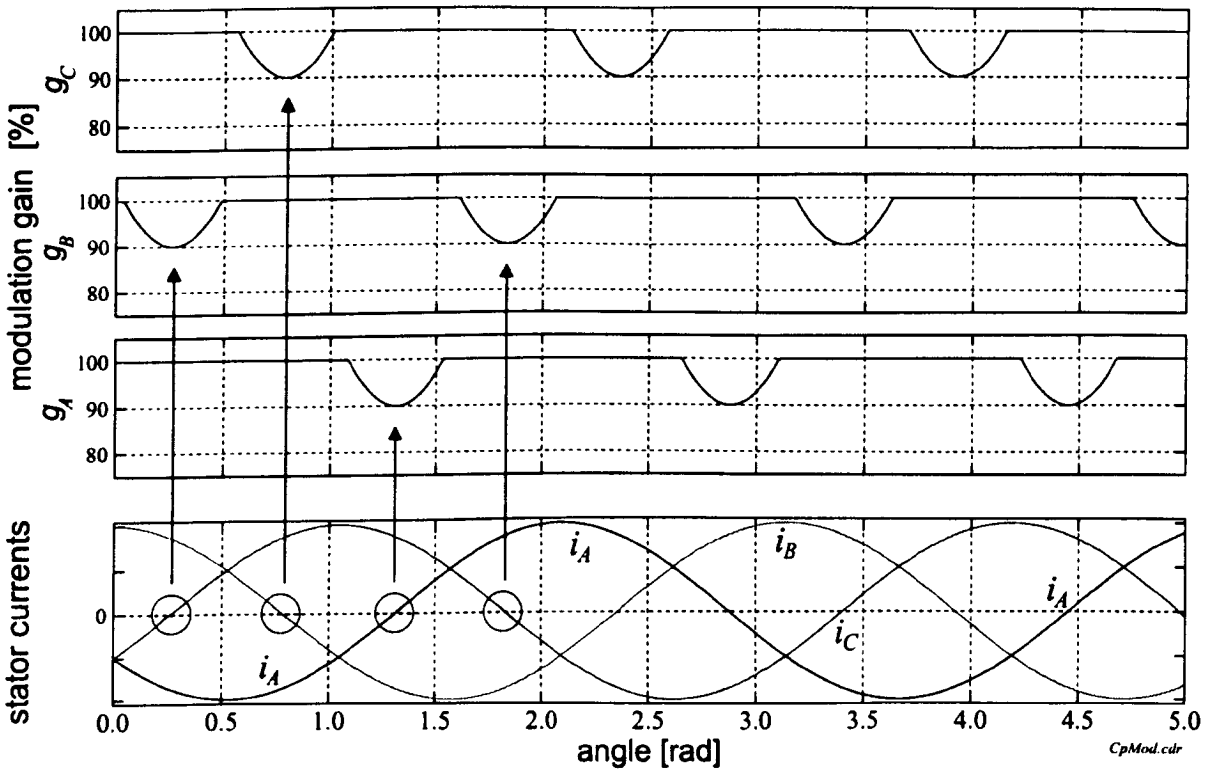

Figure 6.4: *Hf voltage modulation during current zero crossing*

current frequency f_e and its multiples. The fact that this harmonic can be found at $f_c - 2f_e$ makes it very difficult to distinguish from the saturation harmonic (see Section 5.2.3). In contrast to the saturation harmonic which increases with load, the inverter modulation harmonic will decrease. One very peculiar characteristic of the inverter modulation can be used to separate it from the saturation characteristic. When transforming the *hf* currents to DC, the higher multiples of the inverter modulation harmonic can be found in alternating order. This is, they will be at frequencies

$$f_{clamp} = \sum_{i=1}^{\infty}(-2)^i \cdot f_e \tag{6.1}$$

This interesting harmonic order has been mentioned in [125] where the *hf* harmonic spectrum of the machine without the rotor has been examined. The deadtime was not published in this paper. The cause of the alternating spectrum was concluded to stem from the number of stator windings.

The experimental spectrum of the *hf* negative sequence currents is shown in Fig. 6.5. The machine was operated under sensored Vector Control and full flux. Subplot *a)*

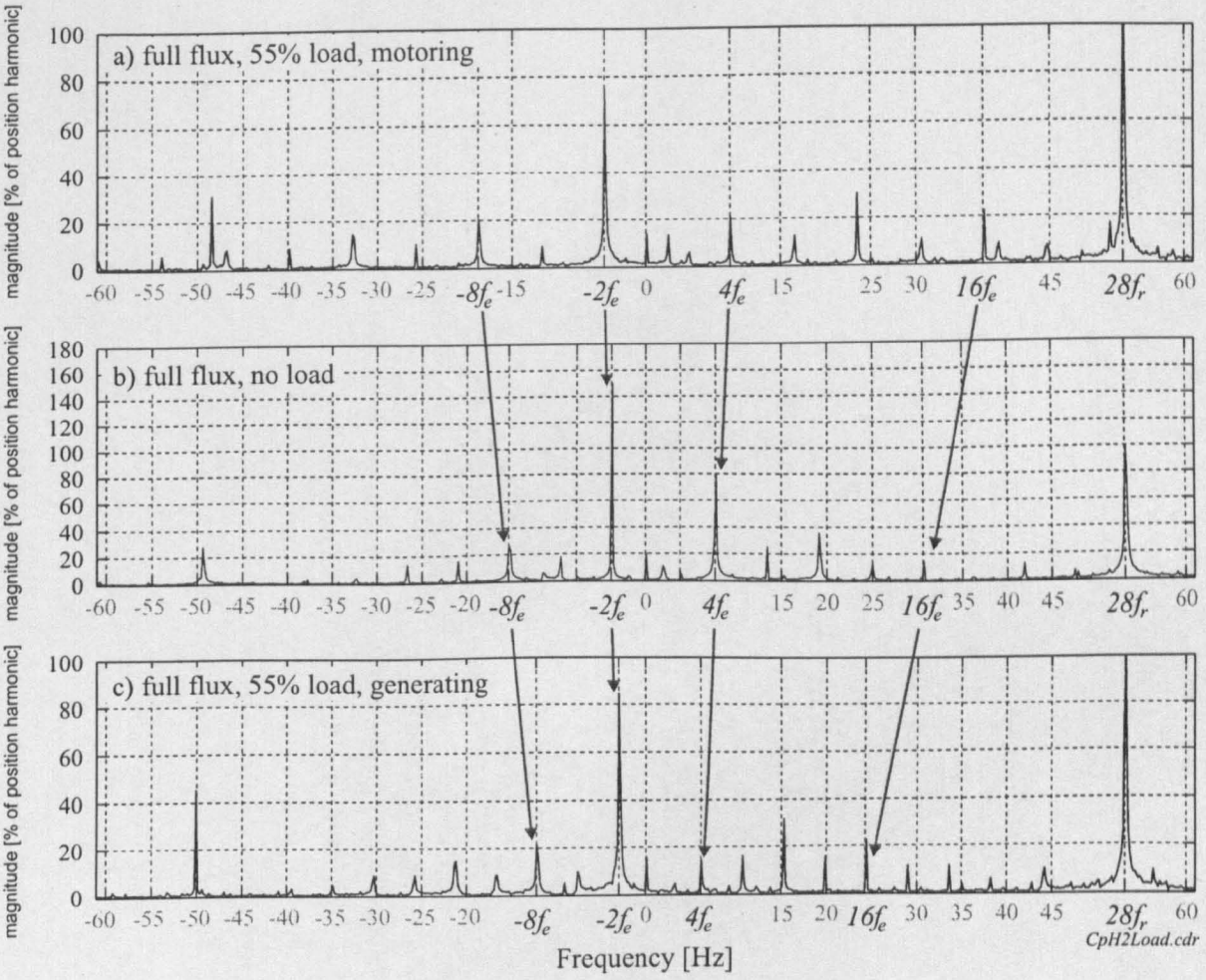

Figure 6.5: *Frequency spectrum of negative sequence harmonics*

shows the spectrum for the machine under 55% rated load and motoring conditions. The slip is about 0.46Hz and with a constant rotor speed of $n_r = 57$rpm, the synchronous frequency $f_e = 2.36$Hz. Subplot *b)* shows the spectrum for the same rotor speed under no-load. Here is $f_e \approx 1.91$Hz. Stiction in the system demands a small slip that is not zero but very small. The lower plot in Fig. 6.5 shows the conditions for 55% rated load and generating. The slip frequency is -0.62Hz and the speed is $n_r = 57$rpm.

The spectrum is shown with positive and negative frequencies. This has to be understood physically as harmonic vectors rotating in opposite directions [85]. Only the magnitude spectrum of one of the two perpendicular current components is shown but the phase information of the second component is included in Fig. 6.5. It can be seen that in practice, the amplitude of the higher inverter modulation harmonics for $i > 4$ is very small. Under loaded conditions, the $-8f_e$ and $16f_e$ harmonics increase.

To further examine the inverter modulation effect, a number of different tests were performed:

- fully fluxed machine with *hf* voltage injection under different load conditions
- operation without any fundamental current
- no fundamental current, emulated inverter modulation
- simulated inverter modulation

a) Injection of hf voltage into real machine (with fundamental):
The harmonic spectrum for different load conditions is shown in Fig. 6.5. Not only harmonics at multiples of f_e are visible. Saturation in the machine interacts with the clamping harmonics and the position harmonic at $28f_r$. Depending on the operating condition, this harmonic interaction changes. Under no-load, the clamping harmonics are clearly visible. For higher loads under motoring or generating, the *hf* clamping is reduced and the saturation increased.

b) Injection of unmodulated hf voltage into real machine (no fundamental):
The machine was operated without any fundamental current and only the voltage injection was applied. The machine was rotated by the load drive. As expected, only the rotor position harmonic due to the rotor saliency was picked up. Neither saturation, nor inverter modulation harmonics exist. An example is shown in Fig. 8.12, where the rotor is turned by hand. The signal after demodulation is only due to the rotor slotting saliency and the rotor position can be tracked easily. No distorting saliency exists and only noise is the cause for a small distortion.

c) Injection of modulated hf voltage into real machine (no fundamental):
The idea of this experiment is to *emulate* the nonlinearity of the inverter that is due to deadtime and caused by the currents. The fundamental is controlled to zero to prevent any *hf* signal modulation by the inverter. The reference *hf* voltages are altered, thus emulating the voltage modulation due to the inverter. The aim is to show that the clamping modulation is not due to a saliency in the machine but only due to the inverter nonlinearity. The conditions are the same as for test *b)*. Without fundamental currents, there is no clamping modulation as seen from the previous experiment and from Fig. 8.12. Only the injected *hf* voltage was artificially modulated. For the modulation, the following function was used:

$$g_x(t) = \begin{cases} \left(1.9 - |\sin(2\pi f_e t + p_x \cdot 2\pi/3)|\right) \cdot 100\% & : \quad g_x(t) < 100\% \\ 100\% & : \quad g_x(t) \geq 100\% \end{cases}$$

for the three phases $x = A, B, C$ and indices $p_A = 0$, $p_B = 1$ and $p_C = 2$ as shown in Fig. 6.4 and in Fig. 6.6. The approximation of the inverter gains comes from the non-linear effects described above. When the line current reduces to zero, the gain also reduces. With the increase in current, the gain increases also. For high currents, the inverter gain can be assumed to be constant. It is important to note that the inverter clamping modulation is a discrete effect and therefore is implemented by modulating the three *hf* voltages v_{A_c}, v_{B_c} and v_{C_c} as shown in the upper three plots of Fig. 6.4. One of the three resulting modulated *hf* voltages in shown in Fig. 6.6.

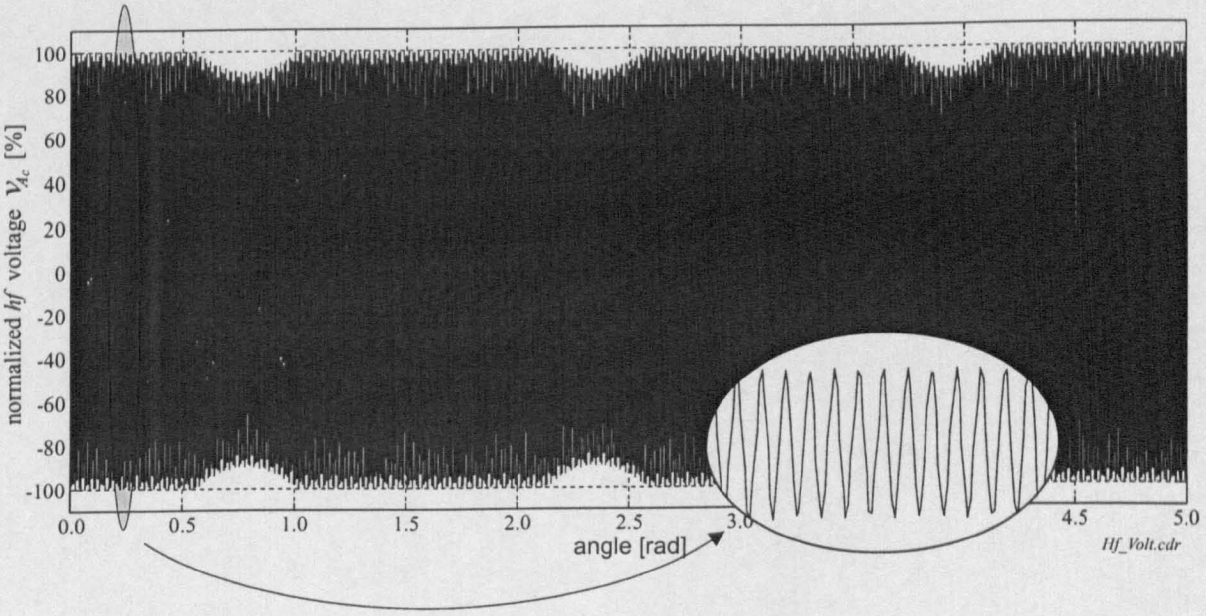

Figure 6.6: *Normalized and modulated hf voltage v_{A_c} (reference) for injection at $f_c = 750Hz$*

The synchronous frequency f_e is imposed as 7.5Hz with a period of $0.1\overline{3}$sec. The magnification shows the *hf* voltage that has a frequency of $f_c = 750$Hz. The deviation from the sinusoidal shape is because there are only 6.7 PWM updates per *hf* period. It is interesting to note that a similar modulation of the $\alpha\beta$ two-phase injection voltages will not result in the typical alternating spectrum but will be symmetrical with harmonics at $\pm 2^i \cdot f_e$. This is because the modulation is a discrete and non-linear effect that physically occurs in the three-phase system.

Fig. 6.7-*a* shows the spectrum of $i_{s_{d\_c}}$ for the rotor at zero speed. The *hf* stator currents (no fundamental) have been measured and demodulated as shown in Fig. 5.17. A compensation is not used. The spectrum of $i_{s_{d\_c}}$ contains the alternating harmonics as described by equation (6.1). In Fig. 6.7-*b*, the machine is driven by the DC load machine at $n_r = -57.6$rpm. The clamping harmonics do not change. Only the $28f_r$ harmonic moves away from zero.

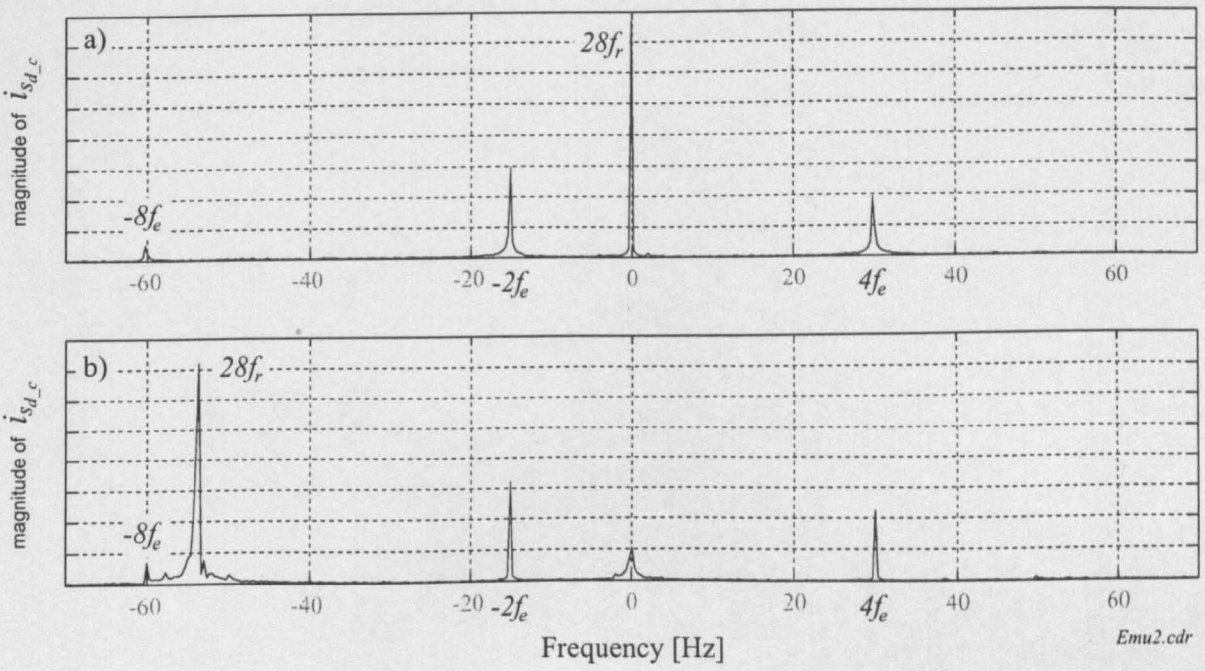

Figure 6.7: *Frequency spectrum from emulation with $f_c = 750Hz$. Upper: drive at zero speed. Lower: drive rotated at $n_r = -57.6rpm$ by the load machine*

The same alternating harmonic spectrum as that in Fig. 6.5 is shown in Fig. 6.7 as the result of the emulation test. The modulated *hf* voltage is clearly the cause for the *hf* current modulation harmonics.

d) Simulation of clamping using two-axis saliency model and modulated hf voltage modulation:
The real system is simulated by using a simple two-axis saliency model. A modulated *hf* voltage is fed into the model and the resulting *hf* currents are analyzed. Fig. 6.8 shows the spectrum of $i_{s_{d\_c}}$ for the rotor at speed $n_r = 57$rpm. The excitation frequency arbitrarily set to $f_e = 2.36$Hz for better comparison with Fig. 6.5-*a*. The result is that the slotting saliency is at $28f_r = 53.2$Hz and the $2f_e$ harmonic is at 4.72Hz. The voltages in the simulation have been modulated as shown in Fig. 6.4. The voltage modulation assumes a zero crossing in the fundamental currents every $1/(2f_e)$s, the period of the line current is 0.423s. The machine model only consists of the *hf* equivalent circuit as described in Section 5.2.2. The parameters of the saliency model are fixed during simulation and differ slightly from the real parameters. The magnitude information however is not too relevant. The interesting fact is that the harmonics show the alternating order as described by (6.1). Some smaller harmonics are contained in the frequency spectrum which can currently not be explained. Still,

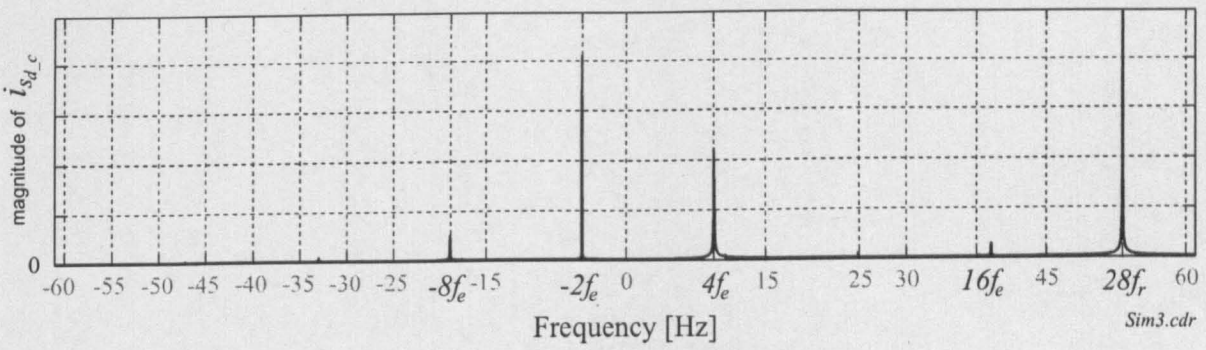

Figure 6.8: *Frequency spectrum of $i_{s_{d\_c}}$ from simulation including three-phase voltage modulation*

the simulation model using an *ideal* machine provides results that are consistent with that of the previous tests.

In order to reduce the clamping modulation, the *hf* voltages were measured and separated from the stator fundamental voltages. No correlation however could be found between the envelope of the *hf* voltages and the modulation of the *hf* currents. The measured *hf* voltages had been demodulated using different techniques of Section 5.4 and the positive and negative sequence harmonics had been analyzed separately. It is believed that the measurement path and the signal processing were not sufficiently designed for the instantaneous measurement of the *hf* voltages. An improvement here could allow the compensation of the clamping modulation in a closed loop system. Instead, the problem was tackled within the processor by applying an online compensation function (see Section 7.2).

6.1.4 Conclusion

It has been shown that the deadtime is the cause for an error in the voltage that is applied to the machine. The common solution is a compensation by adding or subtracting the deadtime from the reference voltage PWM timings, depending on the current direction. The difficulty of this approach is that the current direction has to be known precisely, including conditions with very low currents. It has been shown that the normal accuracy obtained from a current transducer is generally good enough to improve the fundamental voltage waveforms. This accuracy cannot be considered sufficient for improving the quality of the *hf* voltage that is applied to the machine. When the current crosses through zero, the voltage error changes very quickly from positive to negative or vice-versa. Tests by the author using a voltage compensation have not shown any significant improvement i.e. a reduced clamping modulation of the *hf* signals of the induction machine. The research is however ongoing [127] to prevent the *hf* voltage modulation.

Furthermore, it has been shown that the major distortion of the *hf* voltage appears during the zero-crossing of the line current on a Δ-connected machine. The voltages across the machine terminals differ significantly from the reference voltages when the line currents are small. The result is a delayed transition of the line currents through zero. The effect is visible as a plateau in the current and called *zero current clamping.* Also an injected *hf* voltage will be affected by the inverter deadtime. In contrast to the fundamental current, the stator current containing the *hf* modulation exhibits several zero crossings when the fundamental current is low. This will cause a voltage error with the consequence of a reduction of the *hf* inverter gain g_x in phase x. Practically, the *hf* voltage that is applied to the machine is modulated by the inverter gain g_x. If the current zero-crossing is faster, the *hf* voltage modulation will be shorter. This is the case when the machine is loaded and the line currents are larger (see Section 7.2.3).

This section has shown in simulation, emulation and in experiment, that the modulated three-phase *hf* voltages are the cause for a modulation that creates alternating negative sequence harmonics that are a function of the excitation frequency f_e.

The clamping effect is not only limited to large inverters with large deadtime. The same effect has been found on a small inverter (7.5kW) with a deadtime of 2.0μs and a control period of 100μs. It is therefore believed that the *hf* clamping modulation will apply to all types of AC machine drives using *hf* injection irrespective of their size and rating. Only if the primary saliency provides a significantly high modulation (see results for rotor #1), a compensation for the clamping modulation might not be necessary.
The periodic error of the estimated rotor position in [76] is attributed to an inductance with a non-sinusoidal distribution. The machine is an inverter-driven 18W salient-pole brushless DC motor with 8 poles. *Hf* current injection is used with $f_c = 200$Hz. A neuro-based fuzzy technique is applied to reduce the error in the estimated position. The estimation error shows characteristic similarities to that from the induction machines used in this research. During one electrical revolution, the position error consists of three sinusoidal deviations with equal period. Every third deviation has a larger magnitude. Closer analysis of the position error in Fig. 8.4 (rotor #1) reveals the same characteristic that is a result of the transformation of the 3-phase modulation into orthogonal coordinates. The mentioned error characteristic cannot be found in the plots showing the estimation error for the symmetrical machine (rotor #3) since the *SMP* (see Section 7.2) tackles and reduces the clamping modulation.

6.2 Modulation due to Transient Machine Operation

A modulation that only appears during the time of the transient operation of a machine drive is reported in [138]. This harmonic distortion affects drives that apply continuous *hf* signal injection to estimate the saliency. The reason is due to the bandpass filter that separates the *hf* spectrum from the fundamental machine signals. During the dynamic operation, the fundamental signals are not limited to low frequencies as under steady-state operation. Harmonic components of the fundamental currents or voltages can easily reach several *k*Hz at the instance of a torque change that can be due to a speed reversal or position change. These harmonic components couple through the bandpass filter in addition to the *hf* spectrum and cause an unwanted distortion. This distortion only last for a short time of generally less than 20*ms* after the transient in fundamental currents or voltages. Thus the name *transient modulation*. In this thesis only the transient modulation due to a fundamental current transient will be examined since the *hf* modulated stator currents contain all the saliency information.

Position change without hf injection:
The shape of the distorting transient *hf* waveform is a function of the fundamental current, the size of di/dt and the transfer function of the bandpass filter. Fig. 6.9 shows the resulting oscillations on the $\alpha\beta$ currents after bandpass filter 3 (see structure in Fig. 5.17) for a demanded stepwise position change by 100° under 70% rated load for the field-orientated drive without *hf* injection. The reason for no injection is to visualize the distortion that couples via the bandpass filter and that will add onto the *hf* signals $\underline{i}_{s_{\alpha\beta\_c}}$. The reference position is shown in the upper plot, the i_{sq} load current in the plot below. Clearly, a high di/dt is visible at time $t = 0.025$s. The load current then remains at the i_{sq}-limit and slowly decreases to its steady-state value. The third plot shows the resulting oscillations on $\underline{i}_{s_{\alpha\beta}}$ after the bandpass filter. Since there is no *hf* injection, the signal should ideally be zero. This condition is true for $i_{s_{\alpha\_c}}$ except for the short time of the i_{sq} transient. The peak *hf* current reaches 4.1A. The distortion on $i_{s_{\beta\_c}}$ is much less during the transient. The reason is that the transient is mostly aligned to the α direction in Fig. 6.9. In general however, the transient will be arbitrarily in the α and/or β direction. In the fourth plot, the dq current components are shown after the positive-sequence harmonics have been removed. This is directly before the lowpass filter 5 in Fig. 5.17. Due to the signal processing path with the transformations to remove the carrier, the transient distortion is equally distributed over both signals. The maximum distortion reaches a peak of 2.5A, that is about 5 times larger than the modulation due to rotor slotting.

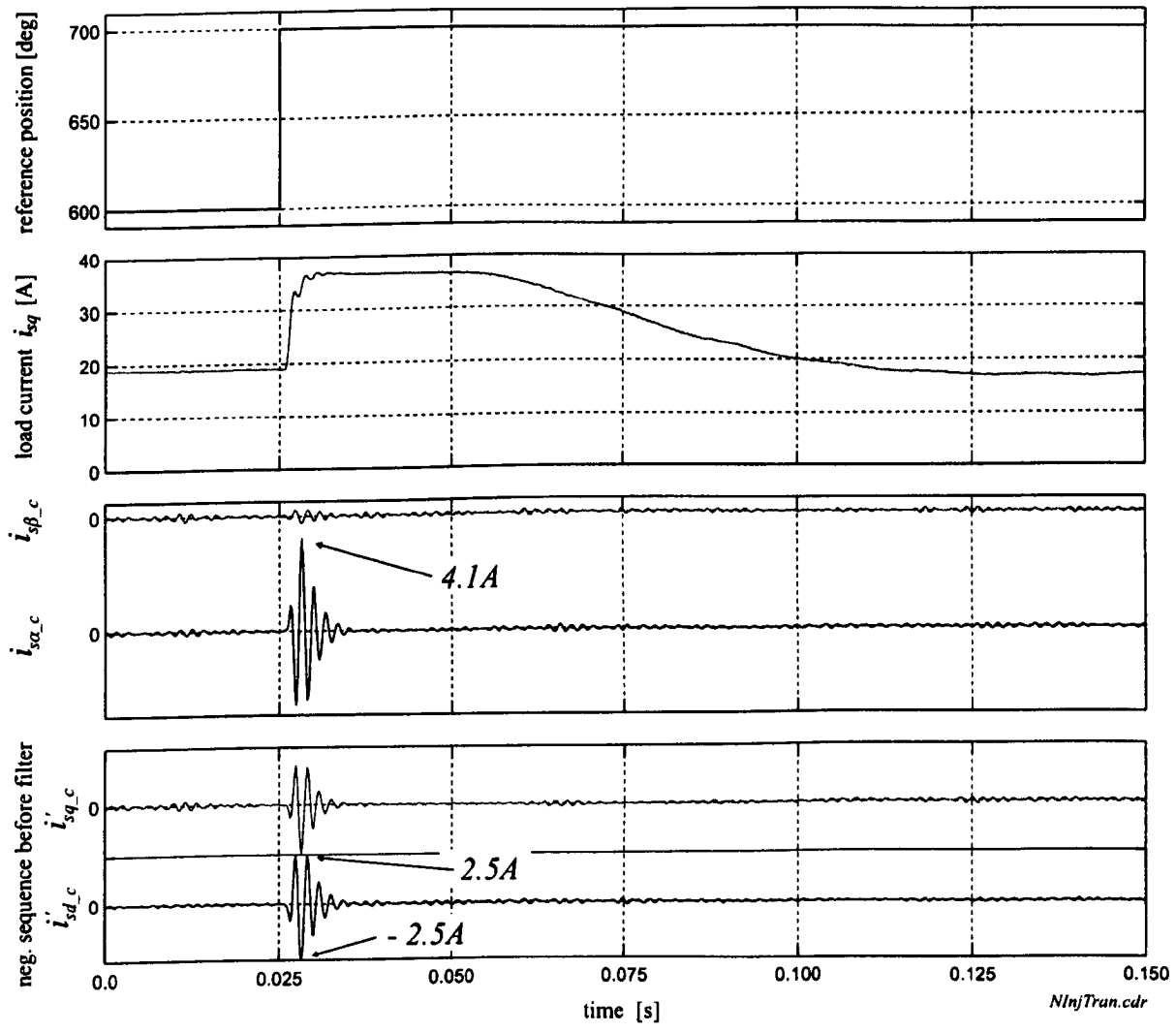

Figure 6.9: *Transient distortion during* 100° *position change (no hf injection)*

Position change with hf injection:
The same position change for the same load conditions as shown in Fig. 6.9 was performed in Fig. 6.10 but now with a *hf* voltage injection. The position reference is shown in the first plot. Below, the i_{sq} load current is printed. The *hf* current ripple is visible that is superimposed on the fundamental i_{sq}. The third plot shows the two *dq* signal components that contain the rotor position information. Again, the signals are taken before the lowpass filter 5 of the structure in Fig. 5.17. The transient spikes reach peak values of 2.5A and −3.2A on $i'_{s_{q\_c}}$ and $i'_{s_{d\_c}}$ respectively. Note that the machine with symmetric rotor was used here. The carrier has been removed but the signals are uncompensated. The modulation due to rotor slotting and saturation can be seen. Below, the measured rotor position and the estimated rotor position are

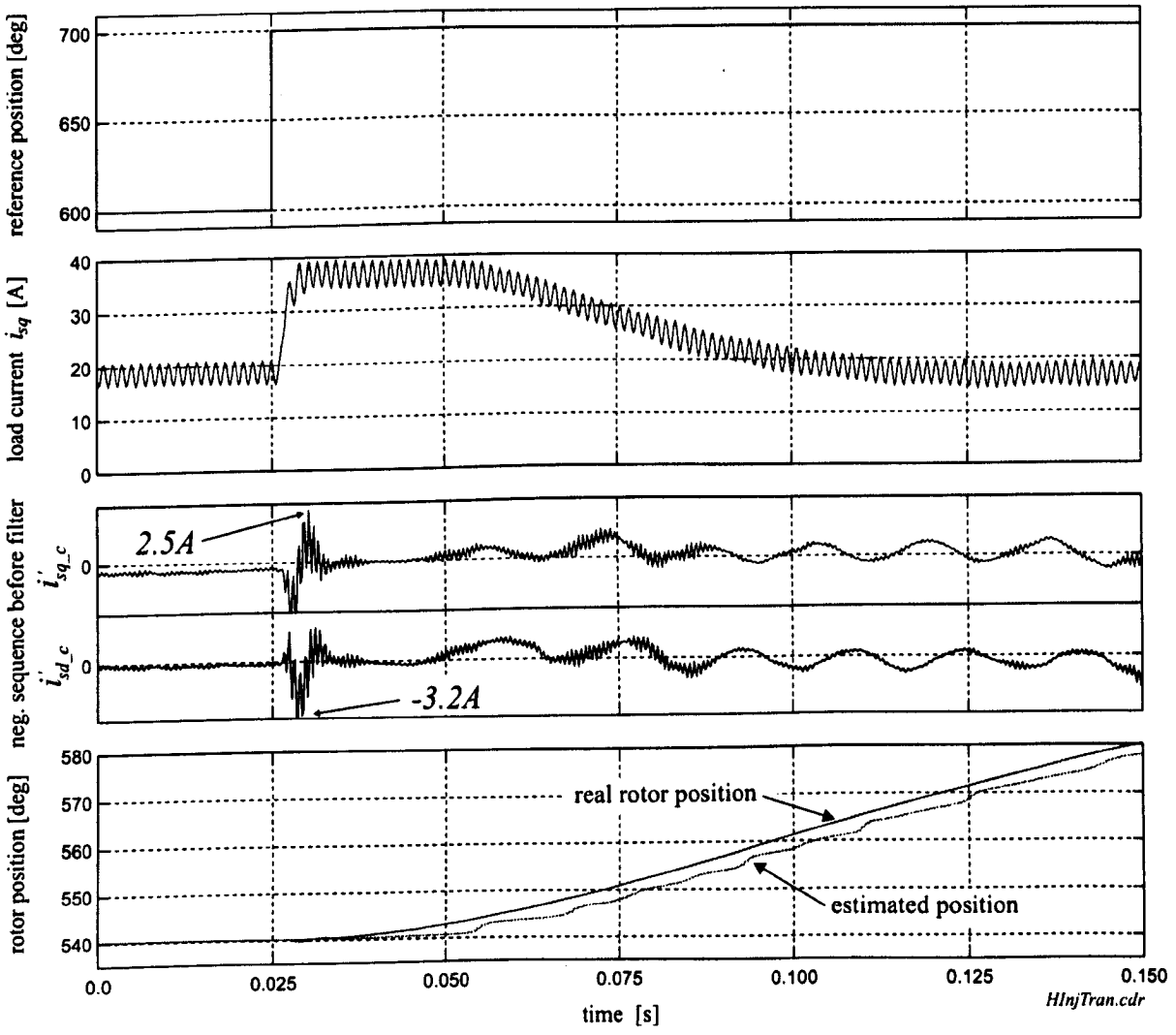

Figure 6.10: *Transient distortion during* 100° *position change*

shown. The latter is derived from the signals i'_{sd_c} and i'_{sq_c} from the plot above, using the structure in Fig. 5.17. The difference in the position is speed-dependent and due to the additional lowpass filters. Due to the low cutoff frequency, the transient modulation is suppressed sufficiently. In spite of the large amplitude of the transient distortion in relation to the rotor saliency modulation, the rotor position can be estimated reliably. Note that the difference between the reference and the measured rotor position is due to load. The position controller does not contain an integrator (see Section 3.6).

Position change with hf injection and transient error in position estimate:
Fig. 6.11 shows a similar operating condition to that of Fig. 6.10. The rotor position

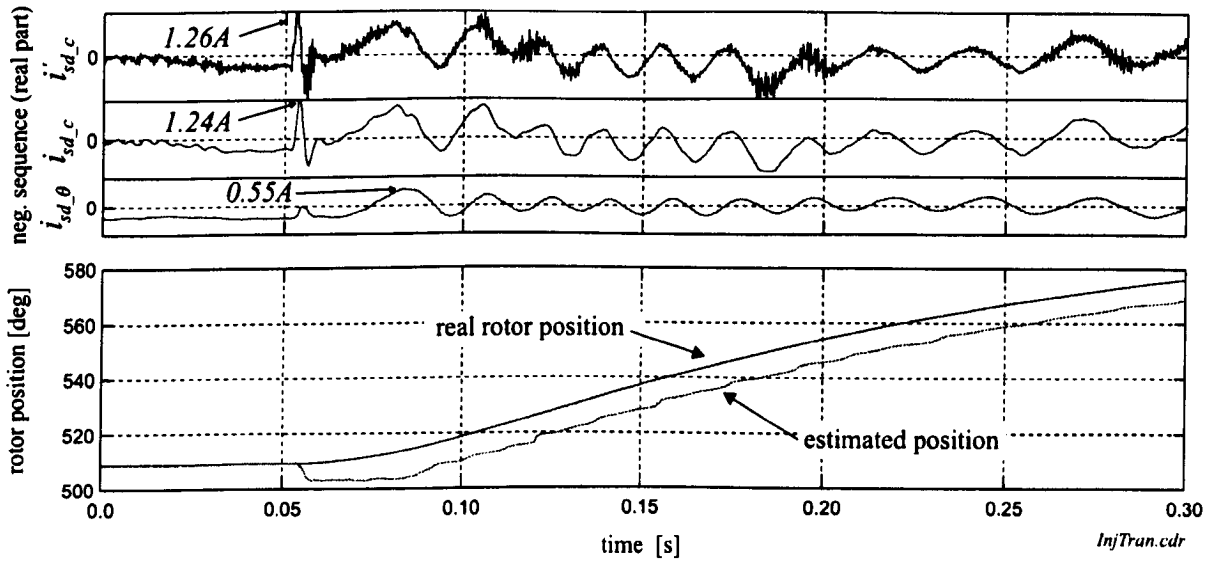

Figure 6.11: *Transient distortion during* 100° *position change with cycle slipping in estimated rotor position*

is changed by 100° and *hf* voltage injection is applied. The upper plot shows the real part of the negative-sequence current component. The transient distortion on $i'_{s_{d\_c}}$ is clearly visible. After lowpass filter 5 (in Fig. 5.17), the high-frequency distortion has been removed from $i_{s_{d\_c}}$. The unwanted modulations have been removed from $i_{s_{d\_\theta}}$. The remaining modulation is due to the rotor slotting. The transient spike is still visible whereas reduced in magnitude due to as low cutoff frequency of filters 6 and 7. The encoder position and the estimated rotor position are shown in the fourth plot of Fig. 6.11. The transient modulation is responsible for a temporary error in the position estimation, that is visible as a cycle slipping by $360°/N_r = 6.43°$ for $N_r = 56$ rotor slots. Once the transient modulation has died down, the position estimation proceeds without problems. Note that the final lowpass filters 6 and 7 shown in Fig. 5.17 ensure stability of the position estimator. An active compensation of the transient modulation as that in [138] would allow the increase in the cutoff frequency of these filters.

From Fig. 6.11 it is apparent that the duration of the transient distortion can be very short which poses a great demand on an active compensation scheme. The delay of an active compensation scheme by only a few milliseconds will cause the likely loss of the position estimate since the transient distortion is very large in magnitude. Experimental tests have verified that a slow position transient with a low di/dt will keep the transient distortion low. In all the experiments, the position reference was therefore sent via a ramp function.

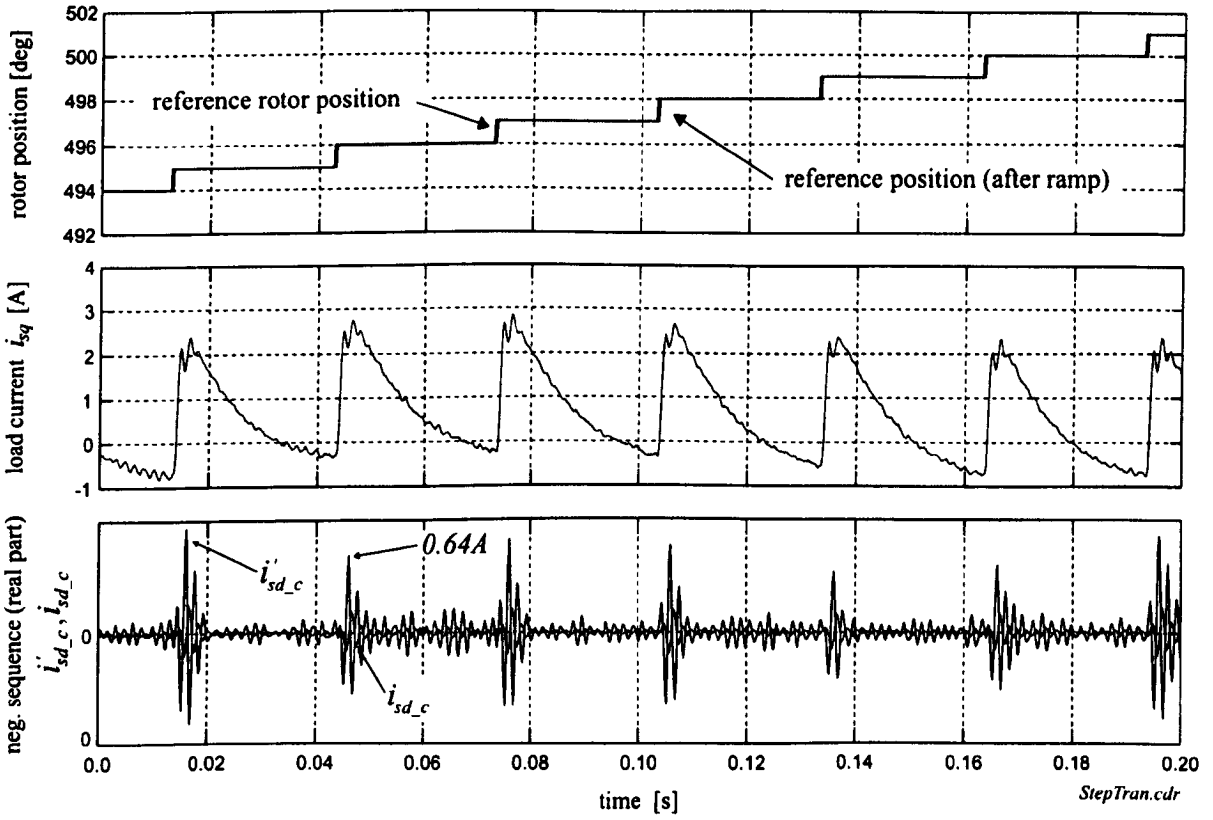

Figure 6.12: *Transient distortion during position step (no hf injection)*

Small position step without hf injection:
An interesting effect due to the transient modulation is shown in Fig. 6.12. The field-orientated drive is operated under sensored position control. The drive is unloaded and the reference position is supplied by a reference generator. Every $30ms$ the reference position is incremented by 1° mechanical as shown in the first plot of Fig. 6.13. This step demand is applied to the controller via a ramp function. The change-of-rate is set to $2500°/s$ that practically means that the ramp is transparent to the step demand. The resulting load current i_{sq} is shown in the plot below. The initial rate of change is very high although the change in magnitude is only about 3A. No *hf* voltage was injected. The transient distortion is visible in the plot below showing the real signal component of the negative sequence harmonics. The size of the distortion with around 0.64A is slightly larger than the magnitude of the position currents and only lasts for about $8ms$. The lowpass filter 5 in Fig. 5.17 helps to reduce the transient distortion significantly as can be seen by comparing $i'_{s_{d\_c}}$ and $i_{s_{d\_c}}$. An accurate prediction of the transient distortion could also reduce the phase-shift of the demodulation structure and position estimator since online compensation could be used instead of lowpass filtering.

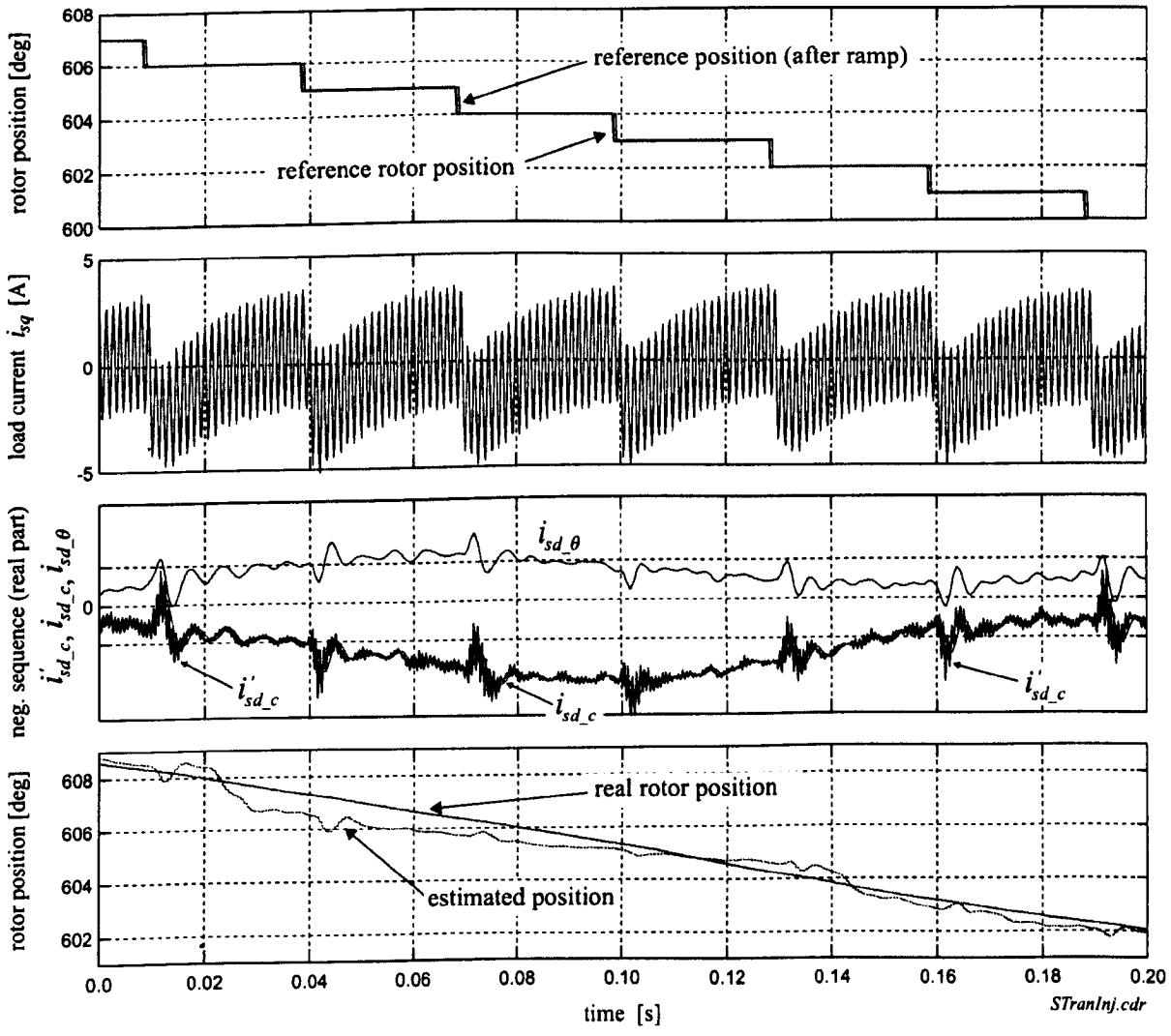

Figure 6.13: *Transient distortion during position steps showing error on position estimate (with hf injection)*

Small position step with hf injection:
The same conditions as those for Fig. 6.12 are valid for Fig. 6.13. Now, a *hf* voltage is injected at 750Hz. Another difference to Fig. 6.12 is that the reference position is *decreased* every 30*ms* by 1° mechanical as shown in the upper plot. The ramp function is practically disabled. Below, the load current i_{sq} with the resulting *hf* current ripple is printed. The reversed direction of rotation explains the difference in the shape of the load current. In the third plot of Fig. 6.13, the transient distortion is visible as short spikes of high magnitude. After the lowpass filter 5 the high-frequency ripples on $i_{s_{d\_c}}$ are reduced. Still, the oscillation due to the transient current change

is apparent. After compensation and lowpass filters 6 and 7, the saturation harmonic is removed but the transient modulation is still there. This distortion can also be seen on the fourth plot, showing the real and the estimated rotor position. The magnitude of the transient distortion is not large enough to cause a loss of rotor position in the estimator. It however is large enough to cause periodic position errors.

This section has visualized the degree of transient distortion that can be expected during operation of the $30kW$ induction machines. Transient modulation is currently the main limiting factor for the sensorless operation shown later in this thesis. The design of the lowpass filters in the present setup for the hf signal demodulation shown in Fig. 5.17 is dominated by the need to suppress the transient modulation. An active compensation as in [138] will allow an increase in the cutoff frequencies with improved dynamics under sensorless operation. Currently, the reference position is sent through a limited integrator that converts a step change into a position ramp to reduce the transient distortion.

Chapter 7:

Commissioning for Selective Saliency Signatures

In Chapters 5 and 6 it was shown that saliencies can be used to estimate the rotor angle or flux angle and that there will be more than one saliency present in a practical machine. Since it has not been possible until now to make use of more than one saliency, the other saliencies must be regarded as a distortion and have to be suppressed. Two suppression strategies have been developed that will be covered in this chapter. Both strategies allow the separation of a desired saliency from the negative-sequence spectrum in real-time. Since the various saliency harmonics are very close and since it is even possible that they overlay each other at the same frequency (see Section 5.2.4), filters including adaptive filters are not an option. The approach taken here is an online compensation that subtracts a known saliency function from the measured *hf* currents. The remaining signal is then only due to the wanted saliency and the saliency angle can be derived (see Fig. 5.17). This saliency function describes the unwanted saliencies and requires an offline commissioning process that provides the data for the compensation. The two strategies used are the *Harmonic Compensation* (HC) and the *Space-Modulation Profiling* (SMP), the latter conceived by the author. The *Harmonic Compensation* technique described here was developed by the author [50] although the principle is fundamentally similar to [95,126]. In [95], the aim was to use the commissioned data to correct the position of the saturation-induced saliency relative to the desired flux component (stator, rotor or airgap flux) needed for field-orientation, whereas here the aim was the opposite and to eliminate the saturation saliency.

7.1 Individual Harmonic Signature

As shown in Chapter 5, saliencies can be sufficiently approximated using a two-axis model. Transforming the saliency into its particular frame rotating with the angle θ_{C_k} where the saliency is stationary, the signature of the saliency can then be described by the parameters of the major and minor axes of an ellipse or in a polar form using magnitude and phase. The approach taken here is to experimentally determine the saliency parameters of the polar form in the stationary $\alpha\beta$ frame and to use this information for an online harmonic suppression.

7.1.1 Description

The *Harmonic Compensation* (HC) is a process where the individual harmonic signatures of the various saliencies are determined and it provides an analysis and 'fingerprint' of the saliencies in the machine [51] (see Fig. 5.2.4).
Since any harmonic can be fully described by its amplitude, frequency and phase, only a few parameters need to be known to suppress this harmonic later during the compensation. Practically, the parameter triplet (amplitude, frequency, phase) has to be known for every operating condition of the machine since the originating effects like saturation or current clamping also vary with the operating condition of the drive. If sensorless position control is only to be used at low speeds, the commissioning can be simplified by keeping the flux constant and only driving the machine through the possible load conditions. For each load condition, the machine has to be under steady-state while the parameters of each saliency harmonic are analyzed until they are reliably determined. *Harmonic Compensation* cannot distinguish the individual saliency signatures since it only works by determining the separate harmonics that are the net result of different saliencies (see Section 5.2.4). Currently it is therefore not possible to reliably work out the contribution of one saliency to the harmonic spectrum, for example if a saturation saliency consists of higher harmonics or if these are solely due to the current clamping distortion. *Harmonic Compensation* works well for sensorless control if only a few harmonics need to be suppressed and if the discrete modulations (see Chapter 6) are not dominant. Otherwise *Space-Modulation Profiling* might be better suited.

7.1.2 Commissioning and Auto-Commissioning

Commissioning can be performed 'by hand' or automatically with a structure such as that of Fig. 7.1. The aim of the *Harmonic Compensation* is to suppress the saturation harmonics by determining the compensating magnitude and phase functions f_1 and

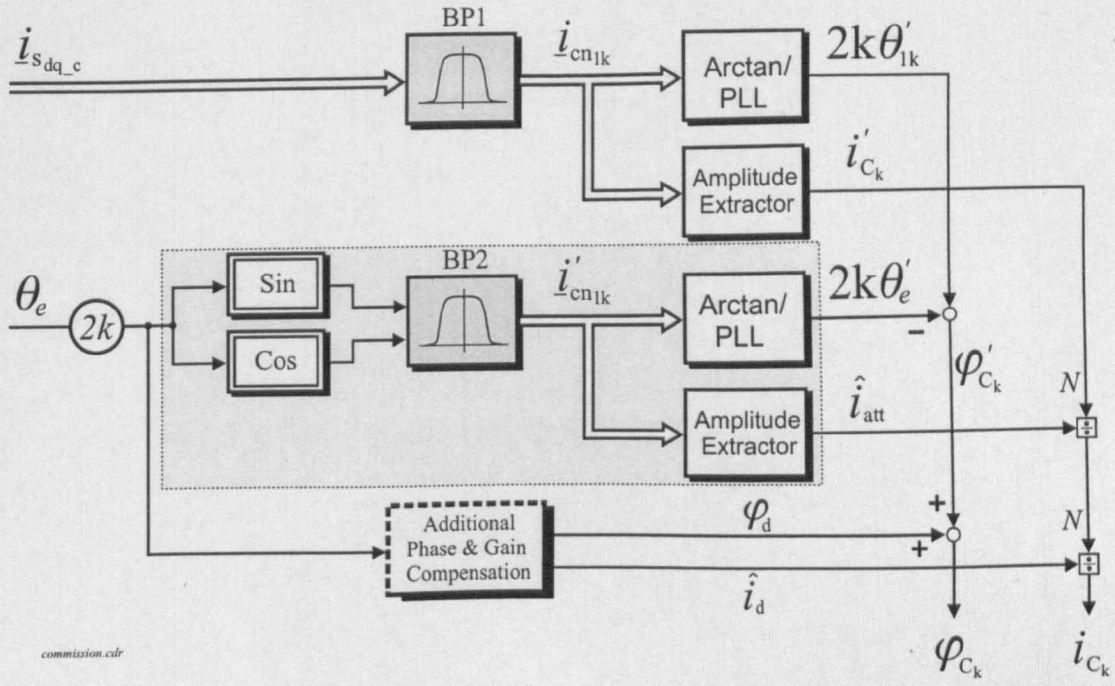

Figure 7.1: *Commissioning structure (N = numerator)*

f_2 in (7.1) and (7.2) below:

$$i_{C_k} = -i_{cn_{1k}} = f_{1_k}(\underline{i}_{s_{dq}}) \tag{7.1}$$

$$\varphi_{C_k} = \varphi_{1k} = f_{2_k}(\underline{i}_{s_{dq}}) \tag{7.2}$$

$$\theta_{C_k} = h_{1k} \cdot \theta_e + \varphi_{C_k} \tag{7.3}$$

The angle θ_e is any field orientation angle used for Vector Control; the rotor flux angle is used here. It also can be possible to use the stator current angle [125]. The saliencies targeted experimentally in this thesis were due to saturation and current clamping. If a rotor saliency is however to be suppressed, an estimate of the rotor position may be used. The functions f_{1_k} and f_{2_k} are assumed to be functions of i_{sd} which is proportional to steady-state flux level, and the load current i_{sq} representing the degree of slot saturation. Although it may be possible to determine f_{1_k} and f_{2_k} by finite element analysis, it is more convenient to determine them experimentally. If the commissioning procedure is performed 'by hand', the parameters of (7.1) to (7.3) are the unknowns in

$$i_{C_{k\_d}}(t) = i_{C_k} \cdot \sin(\theta_{C_k})$$

$$i_{C_{k\_q}}(t) = i_{C_k} \cdot \cos(\theta_{C_k})$$

The compensation harmonics $i_{C_{k\_d}}$ and $i_{C_{k\_q}}$ will be combined for each harmonic with the carrier-free negative sequence harmonics $\underline{i}_{s_{dq\_c}}$. The sign of $i_{C_{k\_q}}$ can be negative

if the direction of the negative-sequence harmonic is negative (see Section 5.2.4). The frequency should be known in this process and amplitude and phase will have to be varied until the specific saliency modulation is sufficiently suppressed. This procedure can take a long time if a spectrum analyzer is used for the visual feedback to evaluate the quality of the suppression.

A faster procedure is the self-commissioning that performs an offline saliency compensation. Here, the use of narrow band filters does not introduce dynamic constraints that would occur if used online for closed loop sensorless control. The structure of the commissioning is shown in Fig. 7.1 During normal motor operation, the compensation parameters i_{C_k} and θ_{C_k} are obtained from interpolating commissioned values from a look-up table and the compensator itself is operative as shown in Fig. 8.2.

Commissioning exploits the use of narrow band filters extracting the magnitude and phase of the required k^{th} harmonic of $\underline{i}_{cn_{1k}}$ from the currents $\underline{i}_{s_{dq\_c}}$ of (5.76). Initially, the inverse of the narrow band filter was used to compensate for unwanted additional phase shift and change in signal magnitude due to the filter. Also, when using tabulated correction parameters for the filter, this requires the accurate knowledge of the input signal frequency to select the proper inverse values. In practice the results obtained were inferior to those of the proposed improved scheme shown in Fig. 7.1 which is general for the k^{th} harmonic. If more than one harmonic needs to be suppressed, the structure of Fig. 7.1 is repeated for each value of k.

Commissioning proceeds as follows: the rotor is first locked and a succession of $\{i^*_{sd}, i^*_{sq}\}$ demand pairs fed to the drive operating under indirect field orientated control (IRFO). The rotor flux angle is multiplied by $2k$. The phase between $2k\theta_e$ and $\underline{i}_{cn_{1k}}$ would be altered due to filter *BP1*. Therefore $2k\theta_e$ is sent through an identical narrow band filter *BP2*. This angle cannot directly be fed into a filter as that filtering $\underline{i}_{s_{dq\_c}}$ to extract $\underline{i}_{cn_{1k}}$; the unit vectors $\sin(2k\theta_e)$ and $\cos(2k\theta_e)$ spanning the two-dimensional space however can. The filter centre frequency and bandwidth are set according to:

$$\omega_o = 2k\frac{i^*_{sq}}{T_r \cdot i^*_{sd}}, \qquad \omega_{BW} = \gamma \cdot \omega_o \tag{7.4}$$

where $0.1 < \gamma < 0.5$ in order to significantly attenuate the DC position harmonic or a neighbouring saturation harmonic; it should not be too low or the compensation parameters will take too long to settle after each demand pair. For low slip frequency, the settling time automatically will be high. The commissioning requires a total of four independent bandpass filters, two for $\underline{i}_{s_{dq\_c}}$ and one each for $\sin(2k\theta_e)$ and $\cos(2k\theta_e)$ for a particular range ω_{BW} of the input frequency. This can sum up to a relatively high number of filters, if ω_{BW} is small. Usually, hardware resources are limited so it is useful to optimize and reduce the amount of required memory registers by adapting the filter centre frequency and bandwidth with increasing input signal frequency. Currently, a set of filter parameters exists for each demand

pair, representing a particular frequency range. Simply exchanging the set of filter coefficients when $2k\theta_e$ enters a new frequency range has the disadvantage that the occurring oscillations have to settle down. A faster approach is to make use of a '*shadow filter*'. A second filter is set up for each of the four bandpass filters with the filter coefficients corresponding to the next demand pair; these filters settle down whilst the commissioned parameters are being derived for the current demand pair. At the next demand pair, one simply switches to the '*shadow filter*'. The first filter now can be adjusted for the next demand pair, without affecting the commissioning. In determining (7.4), the rotor time constant T_r does not have to be accurate, since the structure of Fig. 7.1 automatically supplies the attenuation factor $\hat{i}_{\text{att}}$ of the bandpass filter at the saturation harmonic frequency (the input to *BP2* is unity). The frequency $h_{1k}f_e$ of the saliency harmonic does not necessarily have to coincide with the filter centre frequency $\omega_\circ$. The attenuation factor is used to scale the amplitude i'_{C_k} which makes the commissioning independent of the specific bandpass filters used. Likewise the phase shifts of the two filters are cancelled by the subtraction $2k\theta'_{1k} - 2k\theta'_e = \varphi_{1k}$ which includes (7.3) to obtain the final compensation angle. The sole purpose of sending $2k\theta_e$ through the identical filter structure as that for $\underline{i}_{s_{dq\_c}}$ is to eliminate the unwanted effects (phase shift, amplification) of the bandpass filters. The amplitude extractor can be either a rectifier in combination with a lowpass filter or the euclidian length of the incoming vector can be determined from its polar representation. The angle is obtained by using one of the techniques of Section 5.5, the *arcus tangens* function is preferred.

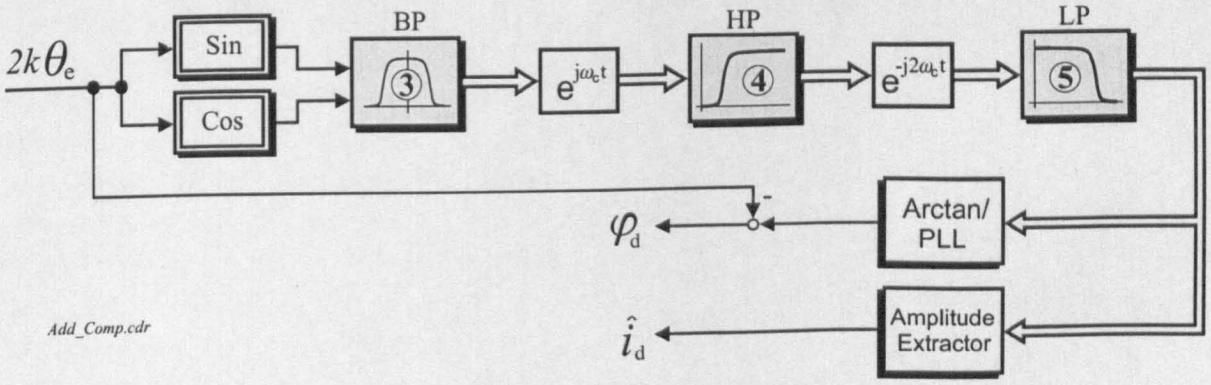

Figure 7.2: *Additional structure for phase and gain compensation*

Errors in the computation of (7.3) arise from two sources:
First, the actual angle φ_{1k} will have been shifted slightly by being passed through the pre-A/D analogue bandpass filter and also the filter that removes $\underline{i}_{cp}$ (see filters 3 to 5 in Fig. 5.17 or Fig. 7.2). In principle, this makes f_2 a function of ω_e. To overcome this, the two inputs to *BP2* may be passed through the identical phase-shifting filters, the

magnitude and angle compensation following the same principle as that of Fig. 7.1. If required, this additional phase compensation can more conveniently be placed in a separate structure in parallel as shown as a dashed box in Fig. 7.1. The additional phase and gain compensation is shown in detail in Fig. 7.2. The principle is the same as that of the compensation in Fig. 7.1.
Second, the angle $2k\theta_e$ from the vector control is subject to variations in T_r. It is therefore necessary to tune T_r during operation by one of a number of well known methods [9,10,16,29,31].

Commissioning for (7.1) and (7.3) can also be undertaken by driving the machine into a speed-controlled dynamometer with a shaft sensor. With this approach, commissioning can be undertaken at non-zero speed which may be more suitable for suppressing the saturation harmonic in the presence of rotor slotting saliencies. This is because, at speeds above zero, the position harmonic (due to rotor slotting) and the saturation harmonic are far apart and more easily separable. Finally, sensorless commissioning is also achievable by sensorless position control of the drive motor in which commissioned parameters are progressively derived and used in the commissioning process. It has to be ensured that the saturation interference harmonic is low at no load so that sensorless no-load position control can be obtained without compensation. The sensorless commissioning procedure runs as follows: Consider the demand pair $P(j) = (i^*_{sd_{rated}}, j\Delta I^*_a)$, $j = \pm 0, 1, 2, \ldots$ with the drive being controlled at ω_r (e.g. $\omega_r = 0$) and where I^*_a is the dynamometer torque current. Let $f_1(j)$, $f_2(j)$ be the compensation parameters corresponding to $P(j)$. Commissioning proceeds by successively incrementing j, and the parameters $f_1(j)$, $f_2(j)$ being commissioned with the previous values $f_1(j-1)$, $f_2(j-1)$ implemented in the harmonic compensator of Fig. 8.2. If the drive cannot be sensorless-position controlled on full flux, the field can first be weakened and the same procedure applied with incremental steps in Δi^*_{sd} with constant I^*_a (i.e. i^*_{sq}). In the case of engineered saliencies, it has been found that sensorless commissioning yields poor results because the parameters obtained are sensitive to rotor position jitter which is worse under sensorless position control. Note that any variation in f_2 with ω_e will be identified by the commissioning undertaken at non-zero ω_r; it is conjectured however, that these variations arise only from phase shifts in the filters as discussed above.

7.1.3 Commissioning Results for Asymmetric Machines

The computation of i_{C_1}, φ_{C_1} and θ_{C_1} takes place at the end of each 10s period and the values are fed to an array in the processor memory to be accessed by the compensator for normal drive operation. The compensation values for rotor #1 are shown in Fig. 7.4. Note that θ_{C_1} and φ_{C_1} are referred to the fixed $\alpha\beta$ and rotor flux frame

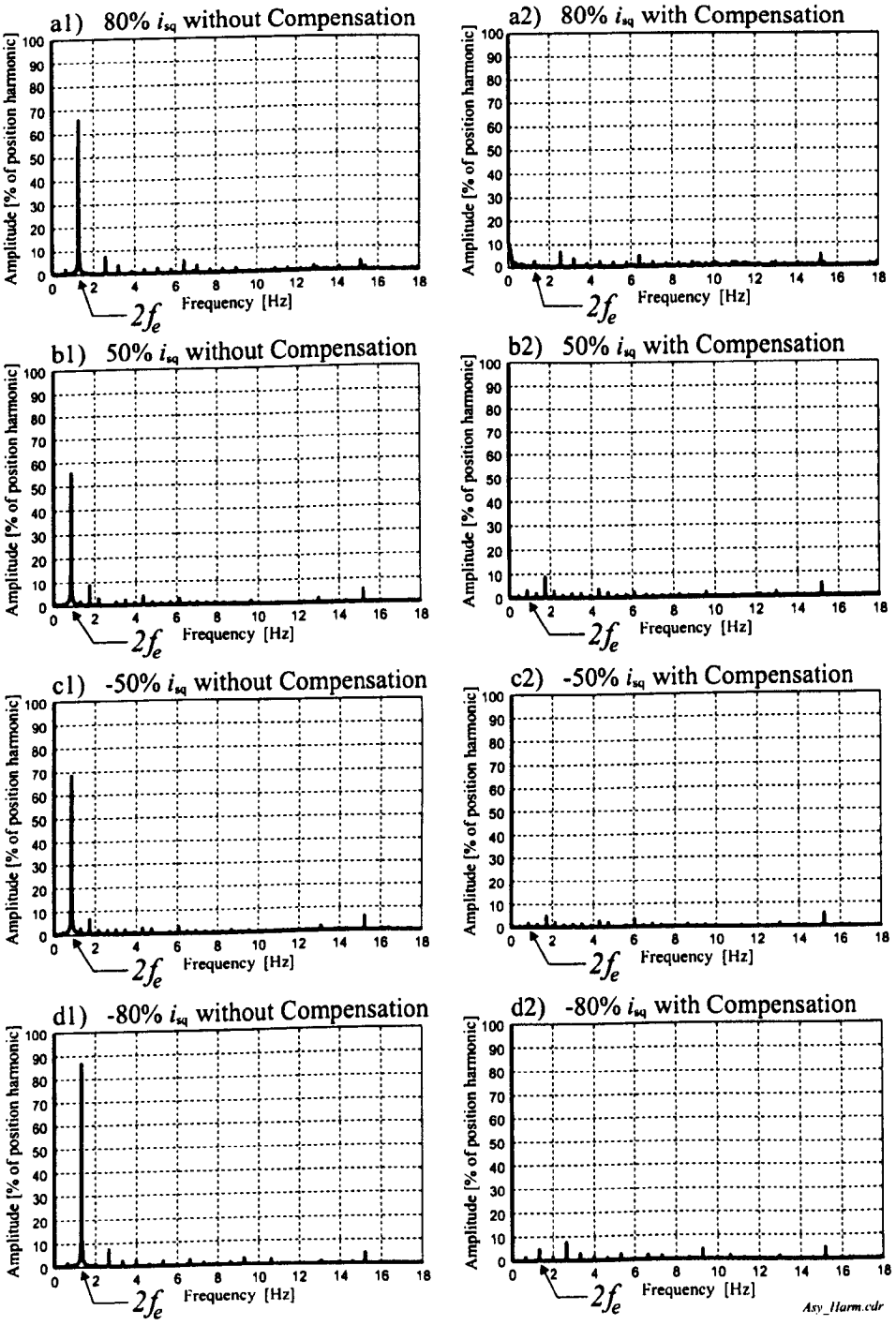

Figure 7.3: *Amplitude spectrum of $i_{s_{d\_c}}$ for motoring and generating mode and various load conditions at zero speed (locked rotor) and $f_c = 300Hz$. Left: without compensation. Right: with compensation*

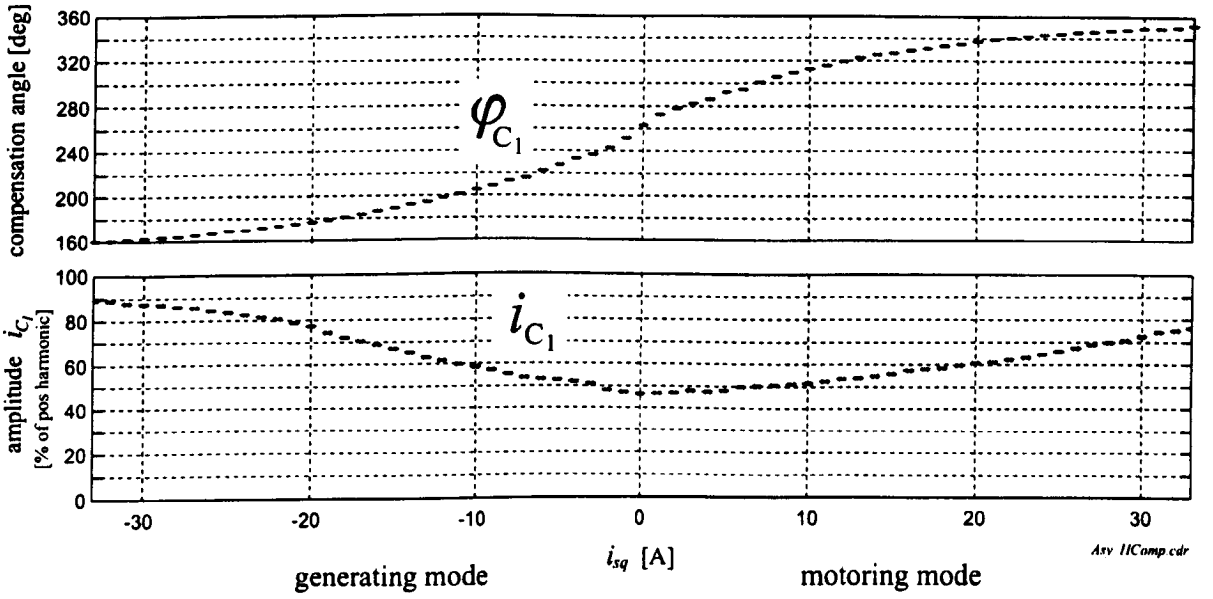

Figure 7.4: *Compensation amplitude i_{C_1} and compensation phase φ_{C_1} for rated flux ($i_{sd} = 14A$) as function of i_{sq} for rotor #1 ($f_c = 300Hz$)*

respectively; thus although it is θ_{C_1} that is used by the compensator, the φ_{C_1} results are more instructive.

The steady characteristic of the compensation parameters makes it possible to reduce the commissioning time by incrementing the load in larger steps and applying an interpolation to obtain a finer resolution.

The effectiveness of the compensation for rotor #1 using the commissioned values of Fig. 7.4 is illustrated in Fig. 7.3. The drive is held at zero speed by locking the rotor. The amplitude spectra of $i_{s_{d\_c}}$ are shown for four different loads, before and after compensation. The spectrum for no-load is not included because the saturation-induced saliency harmonics overlap at zero Hertz. Note that the harmonic sequence information contained in $i_{s_{q\_c}}$ is not used when calculating the amplitude spectra.

Fig. 7.5 shows the amplitude spectrum of $i_{s_{d\_c}}$ for 80% rated load when the sensored drive using rotor #1 is loaded by the dynamometer at n_r = 30rpm. Although the filters introduce an additional phase error of 5.7° at 30rpm, the suppression of the $2f_e$ saturation saliency is still seen to be effective.

The commissioning results for rotor #2 shown in Fig. 7.6 were slightly disappointing. The intention of the rotor design was to reduce the saturation saliency. This could not be achieved. The magnitude of the $2f_e$ saturation saliency is about that in Fig. 7.4 for rotor #1. In addition to the $2f_e$ harmonic, a large $4f_e$ saliency exists.

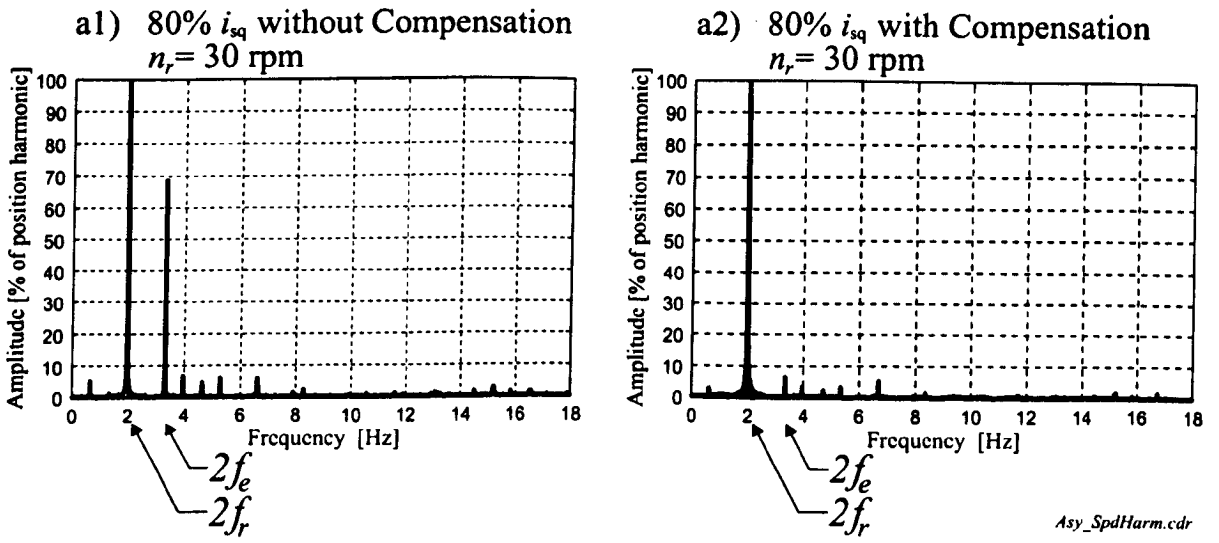

Figure 7.5: *Amplitude spectrum of $i_{s_{d\_c}}$ under sensored speed control at n_r = 30rpm showing the effectiveness of the compensation at higher speeds (f_c = 300Hz). Left: no compensation. Right: with compensation*

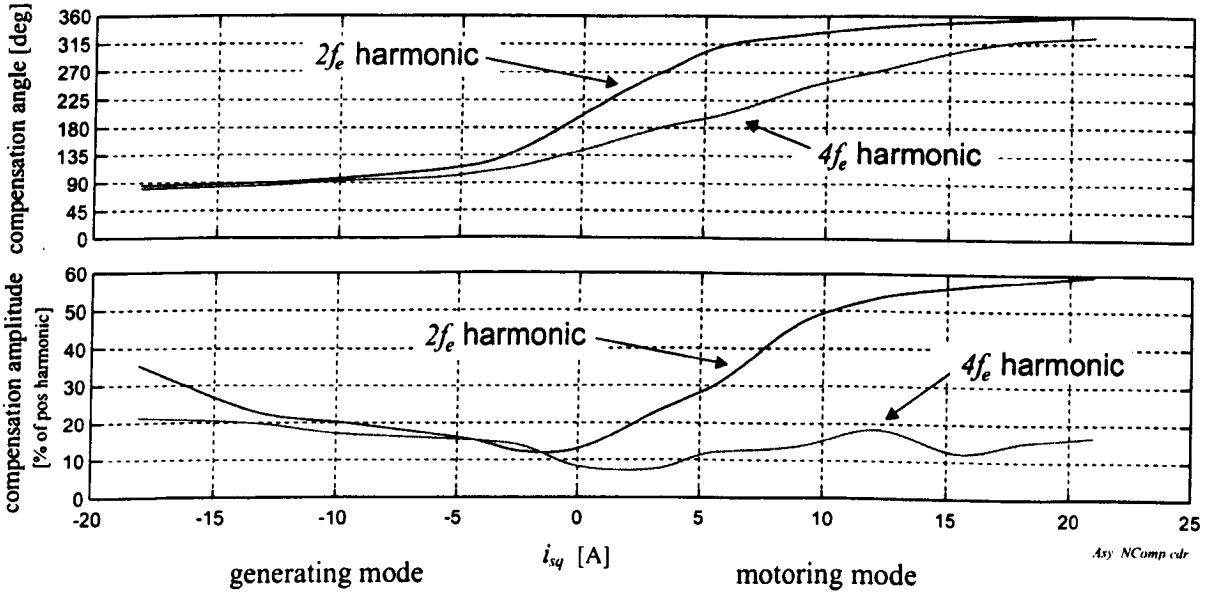

Figure 7.6: *Compensation parameters i_{C_k} and φ_{C_k} as function of i_{sq} for rotor #3 (f_c = 300Hz)*

The data of Fig. 7.6 however is only from a preliminary test. It is not known to which degree the modulation due to the inverter zero-current clamping caused an uncertainty in the determination of the parameters. Limited time prevented a more

thorough analysis. It is known that *Harmonic Compensation* does not cope very well with discrete modulation effects. The interest for sensorless control of machines without engineered saliencies shifted the focus of the research towards the work on rotor #3.

7.1.4 Commissioning Results for Symmetric Machine

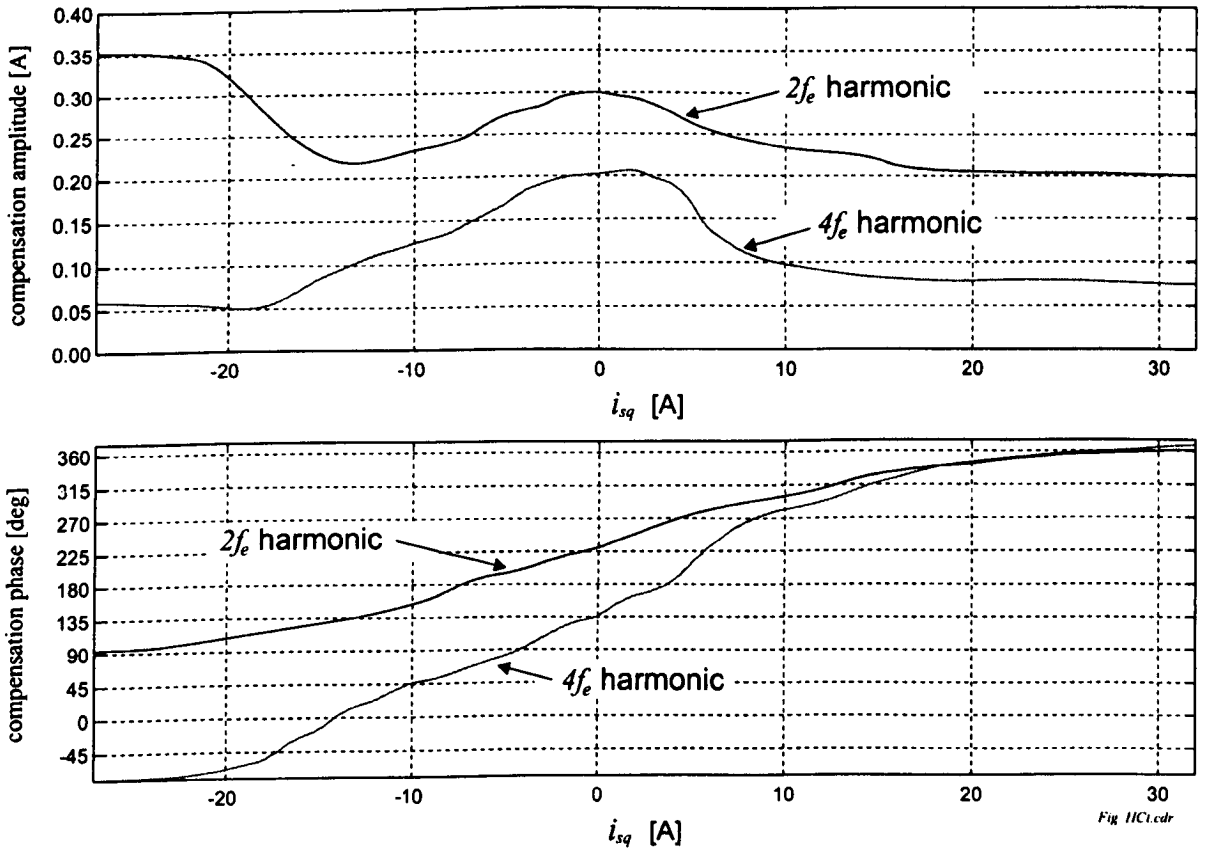

Figure 7.7: *Harmonic compensation parameters i_{C_k} and φ_{C_k} for $2f_e$ and $4f_e$ saturation harmonics and $i_{sd} = 14A$ for rotor #3 ($f_c = 300Hz$)*

The commissioning for rotor #3 uses the same structure for the *Harmonic Compensation* as shown in Fig. 7.1. The compensation parameters obtained for the symmetric machine are shown in Fig. 7.7. Two large harmonics have been identified that have to be suppressed. The figure shows the compensation amplitudes i_{C_k} and compensation angles φ_{C_k}. The compensation angle θ_{C_k} requires any angle θ_e for field orientation used for vector control. The rotor flux angle ρ is used here, so that $\theta_{C_k} = h_{1k} \cdot \rho + \varphi_{C_k}$. The *hf* voltages are injected in the $\alpha\beta$ frame at a frequency of $f_c = 300$Hz. The upper

plot shows the amplitudes for the $2f_e$ and $4f_e$ harmonics. The parameters have been determined for rated flux (i_{sd} = 14A) and different load conditions, represented by the load current i_{sq}. A local maximum exists for low or no-load conditions. This is the inverse of the case where the machine has an engineered rotor saliency [50] (Fig. 7.4); there an increase in load made the saturation harmonic increase. This difference is a result of the clamping modulation that is discrete and highly nonlinear. The $2f_e$ harmonic is a result of the superposition of saturation and clamping modulation. The latter modulation contributes more to the $2f_e$ harmonic at low loads since the clamping pulses are wider. The pulses get narrower for high load when the zero crossing of the line currents gets shorter. Since the *Harmonic Compensation* essentially av-

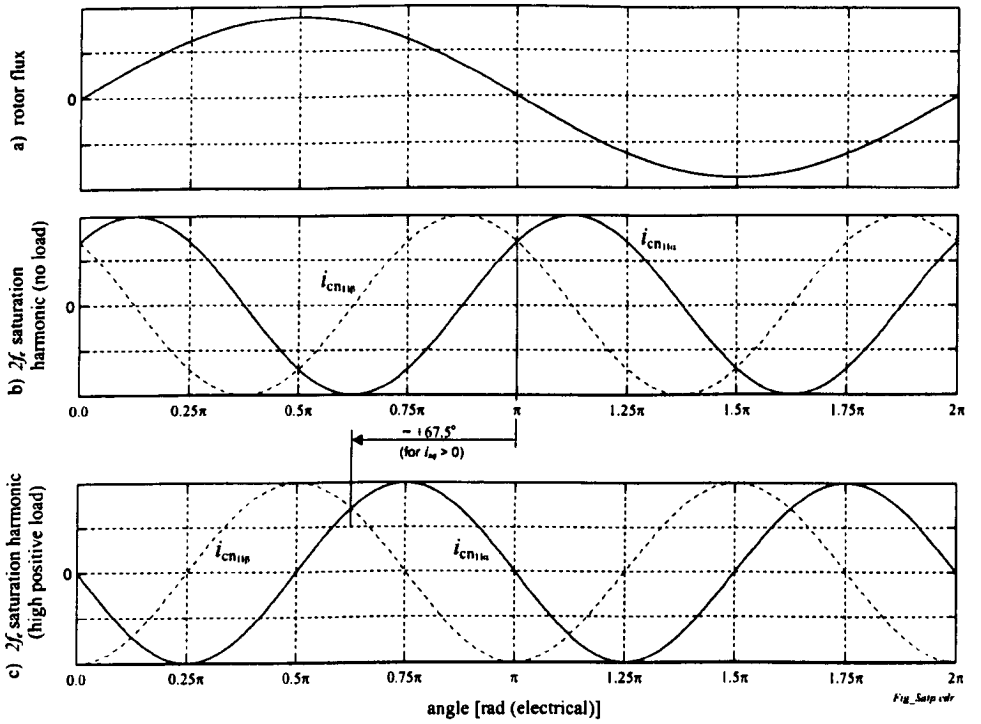

Figure 7.8: *Phase of $2f_e$ harmonic in respect to rotor flux vector*

erages the harmonic distribution over a long time, the wide clamping pulses cause an increase in the $2f_e$ harmonic. The compensation might therefore not always be optimal, since the technique cannot cope with time-discrete modulation effects.

The phase components of Fig. 7.7 have a very similar shape to those reported in [95]. For no-load conditions, the phase of the $2f_e$ harmonic is approximately 225°. This represents the situation shown in Fig. 7.8-*b*. Shown are the α and β component of the $2f_e$ saturation harmonic $\underline{i}_{cn_{11}}$ with $i_{cn_{11\alpha}} = -i_{C_2}\sin(2\omega_e t + \varphi_{C_2})$ and $i_{cn_{11\beta}} = i_{C_2}\cos(2\omega_e t + \varphi_{C_2})$. Note that the saturation harmonic has a phase shift of

180° from its compensating harmonic. The highest saturation does not occur at the points 0.5π or 1.5π where the amplitude of the rotor flux fundamental reaches its maximum (Fig. 7.8-*a*), but 90° electrical apart. The explanation for this characteristic of the $2f_e$ harmonic in the $\underline{i}_{s_{\alpha\beta\_c}}$ signal is given by the simplified model of Fig. 5.2 and in Section 5.2.3. The $\alpha\beta$ components of the $2f_e$ harmonic from Figs. 7.7 and 7.8 have the same phase relation to the rotor flux as that reported in [95,130]. Reference [95] displays the saliency position as $360° - \varphi_{C_2}$ and in [130] the maximum of the terminal impedance was shown to be aligned to the rotor flux angle. As the impedance is inverse proportional to the amplitude of the saturation harmonic ($Z_{inj} = V_{inj}/I_{inj}$), it will be the minimum amplitude of the saturation harmonic that is aligned to the maximum of the rotor flux. This is shown in Fig. 7.8-*b*.
As the load is increased for the motoring mode, φ_{C_2} becomes larger. The conditions for a value of 360° is shown in Fig. 7.8-*c*. The maximum of the $2f_e$ harmonic has moved by 67.5° electrical compared to Fig. 7.8-*b* and nearly coincides with the maximum amplitude of the flux vector. For generating conditions, φ_{C_2} decreases, the $i_{cn_{11\alpha}}$ and $i_{cn_{11\beta}}$ components shift to the right and the $2f_e$ saturation harmonic gets aligned to the maximum of the rotor flux wave again, therefore showing its maximum at the point of the minimum flux.
The phase of the $4f_e$ harmonic changes approximately with twice the rate of the $2f_e$ phase. This means that the magnetic saturation 'profile' maintains its phase relation for different loads. The profile will however change since the amplitude of the saliencies in Fig. 7.7 changes with load.

The effectiveness of the compensation for rotor #3 is demonstrated in Fig. 7.9. The amplitude spectrum for $i_{s_{d\_c}}$ is shown, not considering the harmonic sequence contained in $i_{s_{q\_c}}$. Subfigure 7.9-*a* is the spectrum for the machine running at $n_r = 8$rpm under 80% rated load. The 30kW drive is operated under sensored closed loop vector control. The amplitude of the position harmonic at $28f_r$ is taken as the reference and set to 100%. The two harmonics causing most unwanted distortion are at frequencies $2f_e$ and $4f_e$ in Fig. 7.9 and are marked. In Fig. 7.9-*b* the two harmonics are successfully suppressed online, using the harmonic compensation strategy. Figs. 7.9-*c* and 7.9-*d* show the drive for the same load but at standstill with $f_{sh} = 28f_r = 0$, the position harmonic at DC. From this figure it is obvious that it is not possible to real-time filter the saturation harmonics without introducing a large phase-shift. In Fig. 7.9-*d* the $2f_e$ and $4f_e$ harmonics have been significantly reduced using the *Harmonic Compensation.*

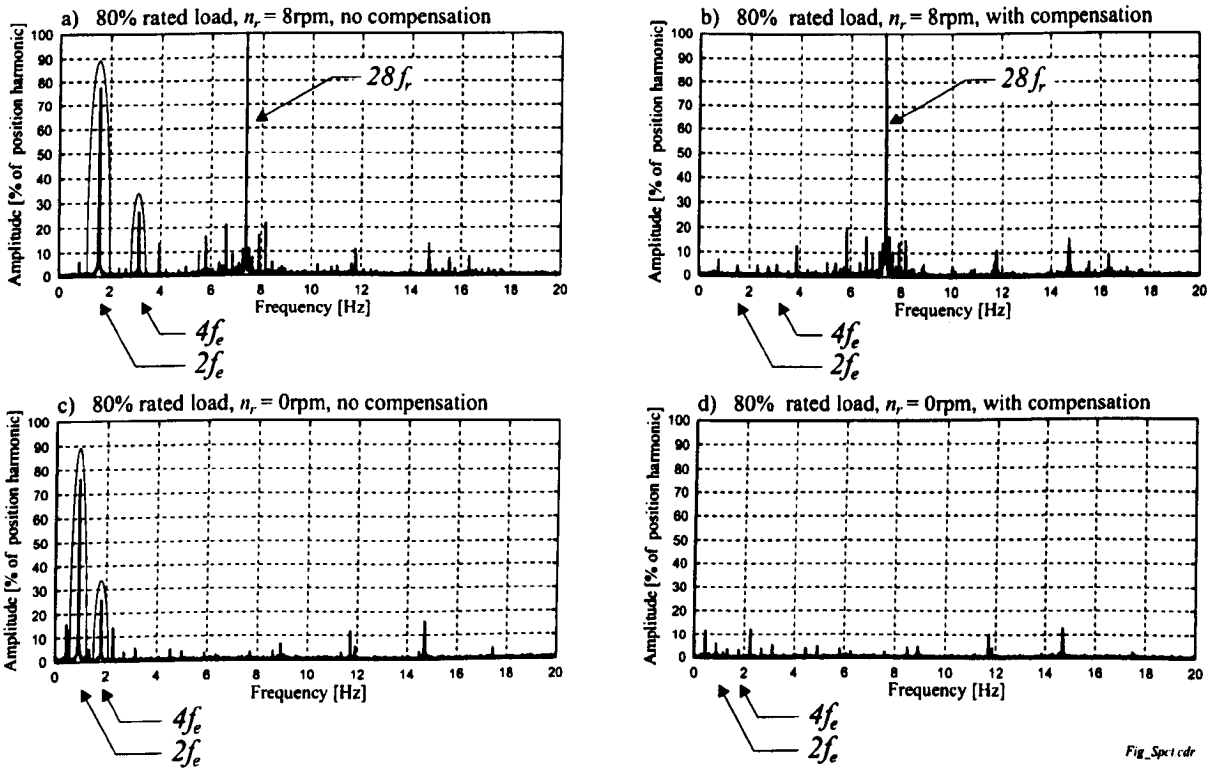

Figure 7.9: *Amplitude spectrum of $i_{s_{d\_c}}$ under sensored speed control at $n_r = 8rpm$ and zero speed, showing the effectiveness of the compensation ($f_c = 300Hz$). Left: no compensation. Right: with compensation*

7.2 Space-Modulation Profiling

Two different commissioning strategies were used on the symmetric machine. The *Harmonic Compensation* was adopted from the asymmetric machine for an injection frequency of $f_c = 300$Hz. Analysis of the *hf* modulation showed that the effect of clamping modulation was not sufficiently addressed. Therefore a second compensation technique termed *Space-Modulation Profiling* (SMP) was developed. The injection frequency was also increased to $f_c = 750$Hz, resulting in an improved suppression of the carrier harmonic.

7.2.1 Description

Space-Modulation Profiling (SMP) is a technique to record the spacial harmonic saliency profile in the time-domain. This can be an advantage over the *Harmonic Compensation* technique where the signature of all unwanted harmonics has to be determined individually. *Harmonic Compensation* has shown to be very suitable and to reliably suppress the saturation harmonics where the number of distorting harmonics is small. The previous section has however shown that this compensation technique is not too suitable to suppress the clamping modulation. This is because this inverter modulation is a discrete effect (Section 6.1.3) and the instantaneous suppression might therefore be poor. To overcome the difficulties, a new technique was developed called *Space Modulation Profiling* (SMP). The new *SMP* can cope better in this case since the full harmonic content for one operating condition of the drive can be described by one profile. This technique is therefore suitable for short discrete harmonic distortions such as that due to current clamping that would require a high number of harmonics to approximate the time-domain signal. A single saliency can also be described reliably, here however the *Harmonic Compensation* will have an advantage since it requires less memory to describe the harmonic.

Consider an envelope of the high frequency currents over an angle θ_e (this could be a flux angle or the stator current angle):

$$SMP_d(\theta_e) = \sum_{k=0}^{\infty} A_{d_k} \sin(k \cdot \theta_e + \varphi_{d_k}) \tag{7.5}$$

$$SMP_q(\theta_e) = \sum_{k=0}^{\infty} A_{q_k} \cos(k \cdot \theta_e + \varphi_{q_k}) \tag{7.6}$$

$$\underline{SMP}_{dq} = \underline{i}_{s_{dq\_c}} - \underline{i}_{s_{dq\_\beta}} \tag{7.7}$$

Let $\underline{SMP}_{dq}$ be the envelopes due to the unwanted modulation effects in the stationary α and β axes. The subscript $_{dq}$ denotes the transformation of the negative sequence

harmonics to DC. The function $\underline{SMP_{dq}}$ then describes the total modulation minus the rotor position modulation and can be represented as a series of sinusoids of amplitude A_k, phase φ_k and frequency $d(k\theta_e)/dt$. For a successful suppression in [50,51], only the compensation amplitude and phase had to be known. With the new *SMP*, the whole sum of sinusoidal terms is used. The profile is of course operation-point dependent. As with the *Harmonic Compensation*, a commissioning is required, running the machine in all operating conditions. Practically, the profile is determined only for operation under constant flux (i_{sd} = const) and for changing load (i_{sq}). Within the operating range that is determined by the bandwidth of the filters shown in Fig. 5.17, the profile is independent of speed.

7.2.2 Commissioning

Since the profile changes due to load and flux level, it has to be determined for every operating point and can result in a large number of data. Using the *SMP* can be a disadvantage when compared to the *Harmonic Compensation* that only required two parameters (i.e. amplitude and phase) per harmonic and operating point if the frequency is known. With the *SMP*, the harmonic profile over 360° electrical has to be stored for every operating point. In contrast to the *Harmonic Compensation*, *SMP* requires the complete profile over one electrical revolution. Practically, a suitable interpolation helps to reduce the required memory size. However, the commissioning time for *SMP* can be shorter than the time to acquire the harmonic compensation parameters. This is because the individual characteristics of all the harmonics do not have to be determined separately since the *SMP* profile contains all harmonics.

For the symmetric machine (rotor #3), the stator current angle $\angle \underline{i}_s$ was used instead of the rotor flux angle ρ. This results in an improvement in robustness for the compensation since the stator current vector can be determined easily and is not parameter dependent. The stator current angle is the natural choice since the clamping modulation is physically due to the stator current. In the experimental implementation, one data point was stored for every 1° in position and 1A difference in i_{sq}. In particular the fine resolution in space was necessary since the clamping distortion produces short spikes of high amplitude. A lower spacial resolution could easily result in an inferior suppression.

The structure in Fig. 7.10 shows the extraction and estimation of the rotor position from the stator currents $i_{s\alpha}$ and $i_{s\beta}$. The lower path removes the carrier and other positive sequence harmonics and transforms the negative sequence harmonics to DC. In the upper path, the angle of the stator current $\angle \underline{i}_s$ is derived from the $\alpha\beta$ stator currents. This angle, the load current i_{sq} and the flux level i_{sd} serve as selectors of the *SMP* table. Outputs are the compensation values SMP_d and SMP_q that are

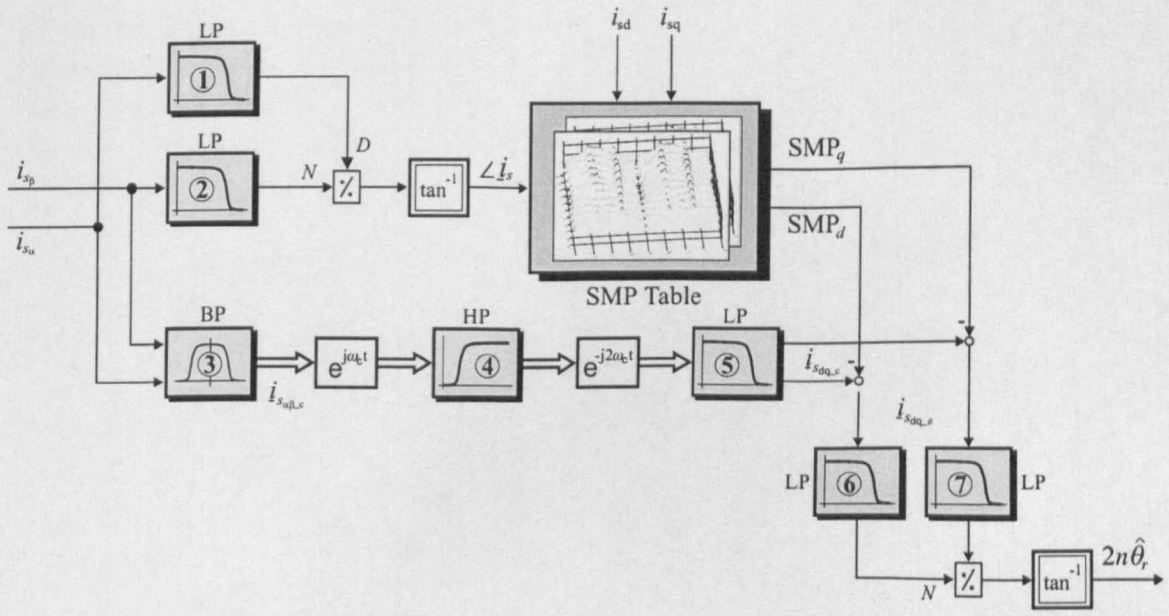

Figure 7.10: *Signal path for hf signal demodulation with SMP compensation (N = numerator)*

subtracted from the negative sequence harmonics $i_{s_{dq\_c}}$. The compensated position signals $\underline{i}_{s_{dq\_\theta}}$ are fed into an *arctan*-function to give an estimate of the rotor position Θ_r. The logic function (not shown in the figure) described by equation (5.77) is needed to convert the slotting angle $\theta_{r_{slot}} = 2n\hat{\theta}_r$ to the mechanical and electrical rotor angle. This is necessary since the slotting angle changes N_r times faster than the mechanical rotor angle Θ_r. Some filters are required in the signal path, numbered from 1 to 7. The lowpass filters 1 and 2 remove the *hf* currents from the fundamental. The bandpass 3 extracts the *hf* harmonics and suppresses the fundamental. The centre-frequency is equal to the carrier frequency f_c of the injection. First, the positive sequence harmonics are transformed to DC and suppressed by the highpass filter 4 with a cutoff frequency of a few Hertz, high enough to guarantee a short settling time. Then the negative sequence harmonics are transformed to DC. A lowpass filter 5 removes remaining positive sequence harmonics. The cutoff frequency was set to $0.4 \cdot f_c$. Ideally, the highpass 4 should be sufficient to remove the positive sequence harmonics from the spectrum which is certainly true for the large carrier component. Practically, there can be more positive sequence harmonics in the spectrum next to the carrier. These additional harmonics are not well suppressed by only using the filter 4. The lowpass filter 5 suppresses these higher harmonics at $2f_c$ and also removes noise that is spread across the whole frequency spectrum. The two lowpass filters 6 and 7 can generally have a high cutoff frequency and are first order filters of the type $1/(T_f s + 1)$. The filter design depends on the quality of the *SMP*. If the clamping

spikes are narrow and high, a small misalignment of the compensation can cause large spikes remaining in the $\underline{i}_{s_{dq\_\theta}}$ signals that will result in possible cycle slipping. The term *cycle slipping* expresses the loss of position by one slot pitch, that is $360°/N_r$. For the *SMP* with 1° angular resolution, the filter coefficient $T_f = 1.5 \ldots 5ms$ in the experiments.

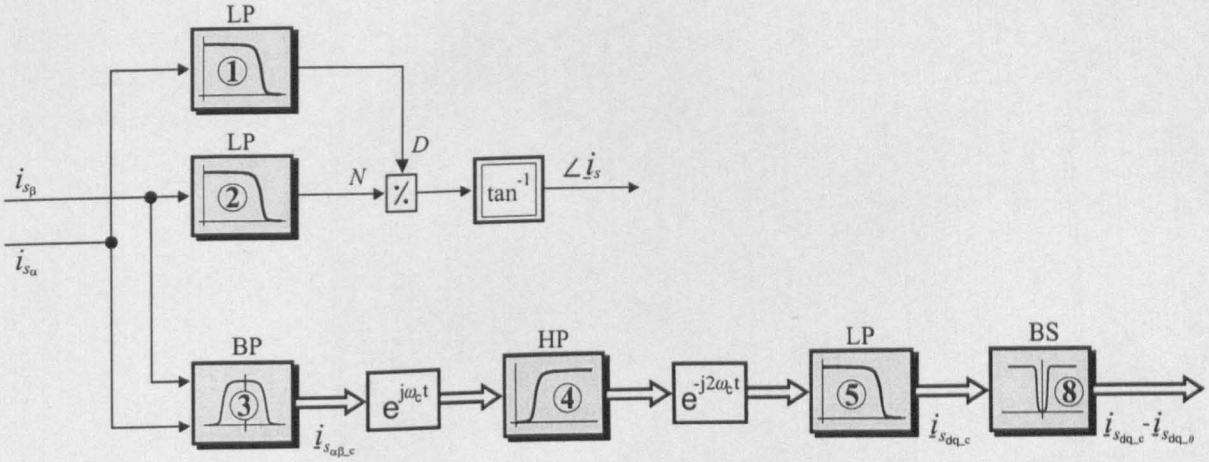

Figure 7.11: *Signal path for commisioning of SMP*

Ideally, the commissioning is obtained from the sensored drive. To separate the rotor slot modulation, the drive is operated at a higher speed. The chosen speed was $n_r = 35$rpm that ensured optimal spectral separation. The load was increased in steps by about 5% of rated torque. The stator current vector angle $\angle\underline{i}_s$ and the position currents i_{d_c} and i_{q_c} were obtained as shown in Fig. 7.11. Additionally, the load current i_{sq} was sampled, once that the drive was under steady-state for a particular load. The flux level was kept constant. Therefore i_{sd} did not need to be sampled. The four parameters were stored for every operating condition and for a number of revolutions. The commissioning is then performed off-line and makes use of the bandstop filter 8 that is tuned to remove the rotor slot harmonics $\underline{i}_{s_{dq\_\theta}}$ from $\underline{i}_{s_{dq\_c}}$. The signal difference ideally only contains the unwanted modulation and noise, that is SMP_{dq}. The mean and optimal *SMP* is then determined that is stored in the compensation table shown in Fig. 7.10.

The filter 8 is an anti-causal implementation with zero-phase delay. This works for FIR filters that have a linear phase [144, 145]. The phase can be expressed as a delay by a fixed number of samples in a discrete implementation. The signal is filtered twice with the same filter $H(z)$ by processing the input data in both the forward and reverse directions. After each filter, the output $y(z)$ is time-reversed which is $y(z^{-1})$. This signal then serves as the input $x(z)$ for the next filter stage. A time-reversal means practically that the data has to be stored as a batch. When running the data

back through the filter, the data is read in inverse order from the last sample down to the first. This process allows to remove the rotor slotting modulation $\underline{i}_{s_{dq\_\theta}}$ without affecting the phase of the spectral components of the remaining signal.

7.2.3 Commissioning Results for Symmetric Machine

This section shows the commissioning results for the symmetric machine (rotor #3). *SMP* has not been applied to the asymmetric machine since the clamping distortion has been found to be smaller in relation to the position harmonics $\underline{i}_{s_{sq\theta}}$. Fig. 7.12

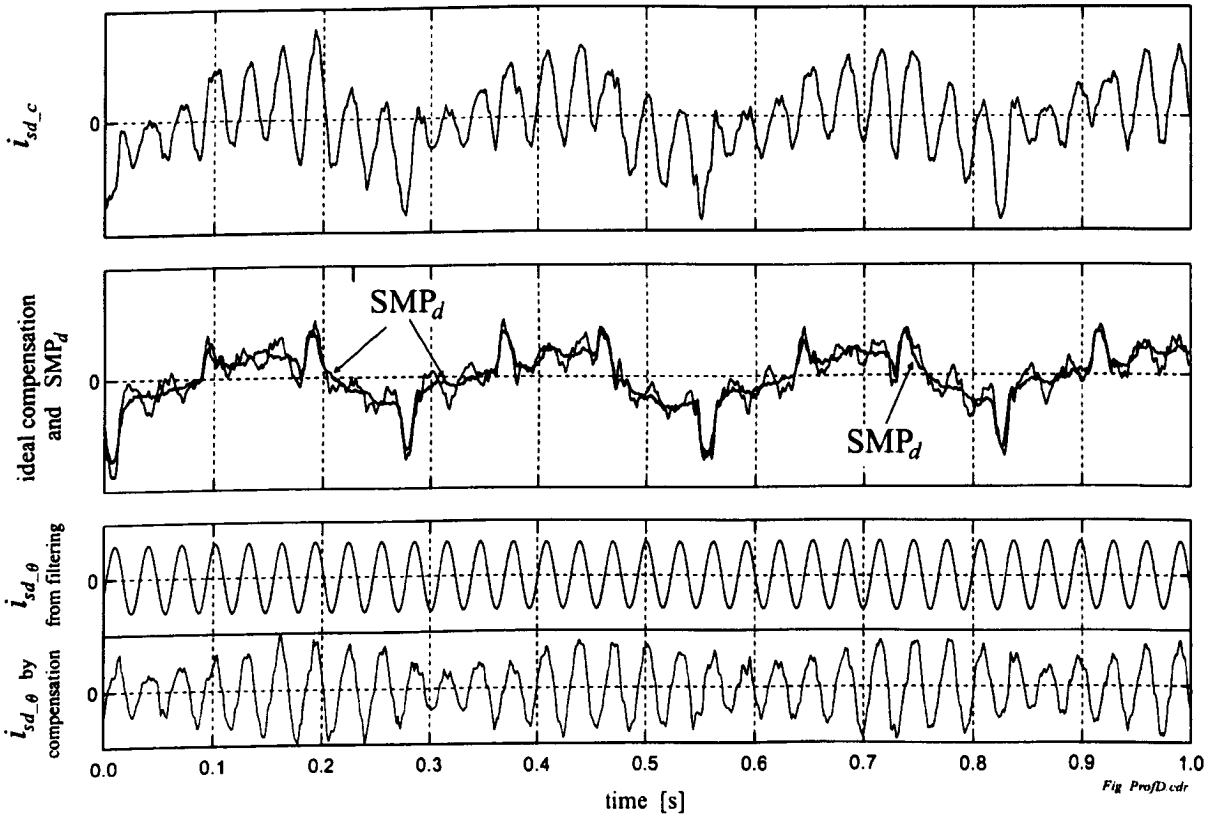

Figure 7.12: *Determining the SMP_d for one operating condition (90% rated load)*

shows the *space-modulation profiling* (SMP) for the real component $i_{s_{d\_c}}$ of the negative sequence spectrum. The machine is field oriented using IRFO and controlled to maintain a speed of n_r = 35rpm. The load is 90% of rated. The removal of the *hf* carrier and transformation of the negative sequence harmonics to DC results in the waveform shown in the upper plot. Clearly, the ripples due to the rotor slotting can be seen. There are 32.67 ripple periods per second. Also the modulation due to saturation and the clamping spikes can be seen. The second plot shows the ideal com-

pensation and the resulting *SMP*. The ideal compensation is determined by filtering the rotor slotting modulation from $i_{s_{d\_c}}$. The anti-causal bandstop filter is used here that is tuned for the slotting frequency $28f_r$. Subtracting the ideal compensation from $i_{s_{d\_c}}$ of the first plot, results in the ideal $i_{s_{d\_\theta}}$ waveform in the upper third plot of Fig. 7.12. In practice, this ideal compensation is not available in sensorless control since anti-causal filtering is an off-line operation. The *SMP* is derived by forming the average over a number of periods from the ideal compensation. The result is SMP_d and shown in the second plot. Applying the compensation to $i_{s_{d\_c}}$ by subtracting SMP_d results in $i_{s_{d\_\theta}}$ in the lower third plot. This signal is obtained via a fast online process and is suitable for use in sensorless control. Clearly, the rotor slotting modulation has been extracted from the negative sequence harmonic spectrum without filtering. However, one unwanted modulation remains. This can be seen as a $2f_e$ amplitude modulation of $i_{s_{d\_\theta}}$. The cause is the harmonic at $-28f_r + 2f_e$ that contributes mainly to the difference between ideal compensation and the SMP_d in the second plot. The *SMP* cannot compensate for this saturation harmonic since it is speed-dependent.

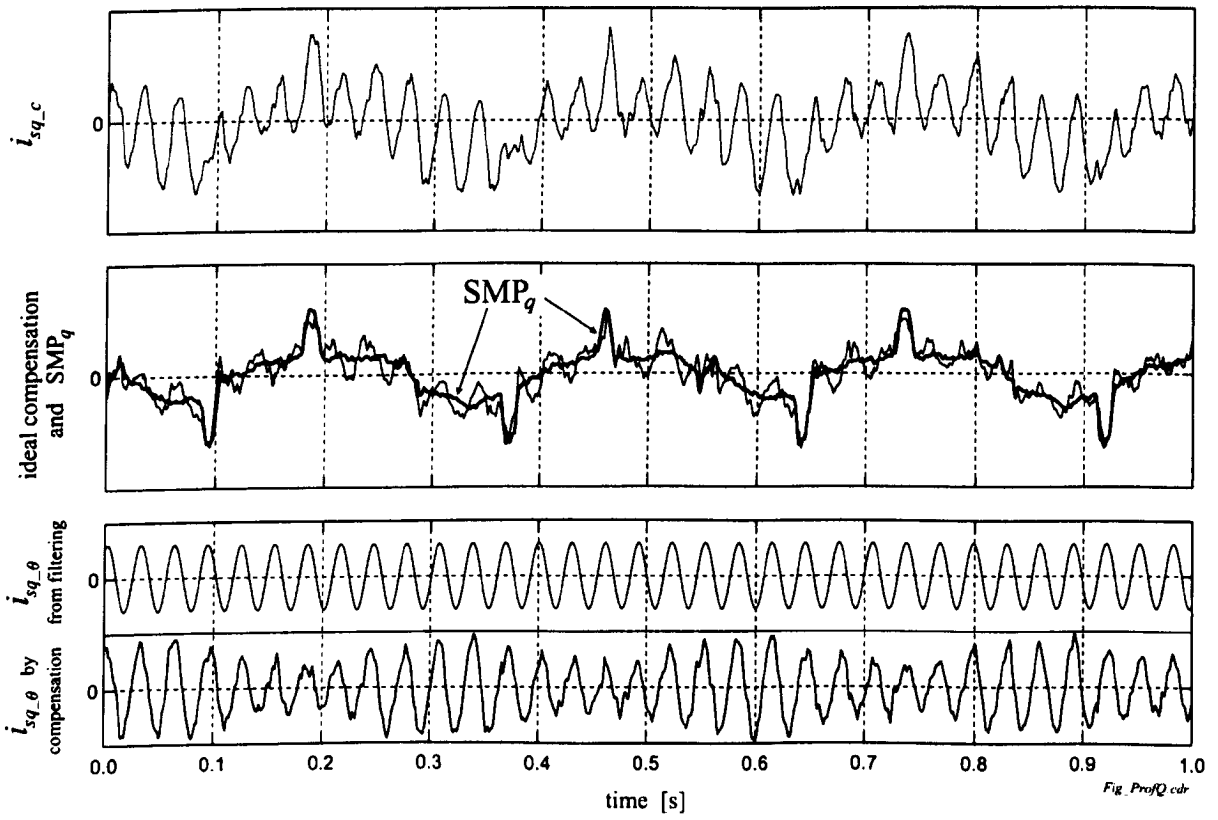

Figure 7.13: *Determining the SMP_q for one operating condition (90% rated load)*

Fig. 7.13 shows the commissioning results for the same data as in Fig. 7.12 but for the imaginary or $i_{s_{q\_c}}$ signal. The negative sequence harmonics are shown in the upper plot. The second plot of Fig. 7.13 compares the ideal compensation and SMP_q. The latter is used for online compensation. Again, the difference is mainly due to the unwanted harmonic at $-28f_r+2f_e$. The waveforms show the saturation and clamping spikes. The third plot shows the ideal $i_{s_{q\_\theta}}$ waveform on top that is obtained by filtering and the practical $i_{s_{q\_\theta}}$ signal. The latter is determined by subtracting SMP_q from $i_{s_{q\_c}}$. The envelope is not constant as for the ideal $i_{s_{q\_\theta}}$ waveform above. This modulation has a frequency of $2f_e$. Comparing the $i_{s_{d\_\theta}}$ and $i_{s_{q\_\theta}}$ signals from using SMP, it can be seen that the $2f_e$ modulation causes the envelope of the d signal to be at a minimum when the envelope of the q signal is at a maximum. The signal remaining after the SMP compensation is the rotor position and $2f_e$ modulation:

$$i_{s_{d\_\theta}} = I_1 \cos(28\omega_r t) - I_2 \cos(2\omega_e t - 28\omega_r t) \quad (7.8)$$

$$i_{s_{q\_\theta}} = I_1 \sin(28\omega_r t) - I_2 \sin(2\omega_e t - 28\omega_r t) \quad (7.9)$$

where $I_1 > I_2$. Compensation for this $2f_e$ modulation has not been included. A suppression of this harmonic using the *Harmonic Compensation* is not possible since the modulation is not additive but influences the scaling. A possible compensation would be

$$i_{d\_scale} = 1 + c_{dq} \cdot \sin(2\omega_c t + \phi_{dq}) \quad (7.10)$$

$$i_{q\_scale} = 1 - c_{dq} \cdot \sin(2\omega_c t + \phi_{dq}) \quad (7.11)$$

where c_{dq} is a gain and ϕ_{dq} a phase that have to be determined for every operating condition. The compensation works by multiplication of (7.8) and (7.9) with (7.10) and (7.11) respectively. Neglecting the $-28f_r + 2f_e$ modulation is not much of a problem for the rotor position tracking and sensorless control. The effect is an error that changes with frequency f_e. The resulting position error is relatively small and is typically smaller than $\pm 0.3°$ mechanical. The $-28f_r + 2f_e$ modulation however can cause problems since it causes a reduction of the position signal amplitude. A mismatch in the SMP compensation during a clamping spike will increase the chance for a cycle slipping when the position amplitude is reduced.

Fig. 7.14 shows on the top row (subplots *a* and *b*) the two waveforms of $\underline{i}_{s_{dq\_c}}$ after the position modulation has been removed by the bandstop filter. These signals are $i_{s_{d\_c}} - i_{s_{d\_\theta}}$ and $i_{s_{q\_c}} - i_{s_{q\_\theta}}$. Several periods have been recorded and are displayed in a polar plot over the angle of the stator current vector $\angle \underline{i}_s$ while the load is constant and at 90% rated. The speed is controlled to be constant and 35rpm. Still, the speed varies practically by up to ± 0.5rpm. Noise and the $-28f_r + 2f_e$ harmonic are responsible for the wide band around the optimal SMP similar to that in an *eye diagram*. Note that the signal amplitude increases in the radial direction and

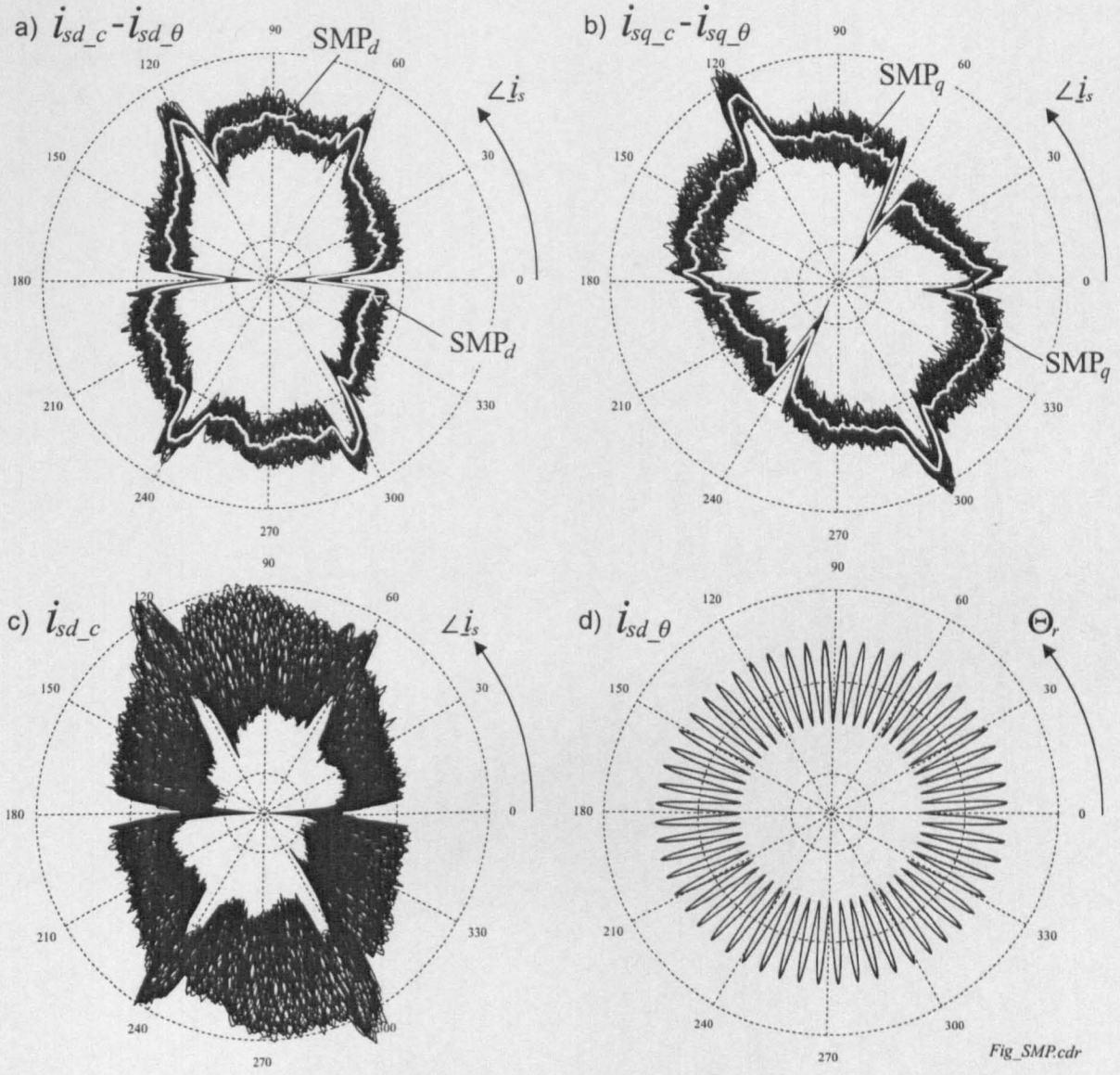

Figure 7.14: *Determining the SMP for one operating condition (90% rated load). Top row: SMP over the stator current angle. Bottom row left: real component of negative sequence. Bottom row right: rotor slotting modulation contained in* $i_{s_{d\_c}}$

the zero line is indicated by a dashed circle. Signal processing is used to find the mean path that is SMP_d and SMP_q, indicated by the white line in plots *a* and *b* of Fig. 7.14. Care is taken that an optimal path is also found for the short clamping spikes. Subplot *c* in the lower row of Fig. 7.14 shows the $i_{s_{d\_c}}$ signal over $\angle \underline{i}_s$ before the position modulation is removed. The circular band is much wider as in the plots of the upper row. This is because the rotor position modulation is not aligned to the angle $\angle \underline{i}_s$. The extracted position modulation $i_{s_{d\_\theta}}$ contained in $i_{s_{d\_c}}$ (subplot *c*) after

the bandpass filter is shown in Fig. 7.14-*d*. The signal is plotted over the measured encoder position Θ_r. There are 56 periods per mechanical revolution. The quality of $i_{s_{d\_\theta}}$ in Fig. 7.14-*d* is very good with a minimum of noise or jitter which is due to the optimal conditions during commissioning (constant speed and use of an anti-causal filter).

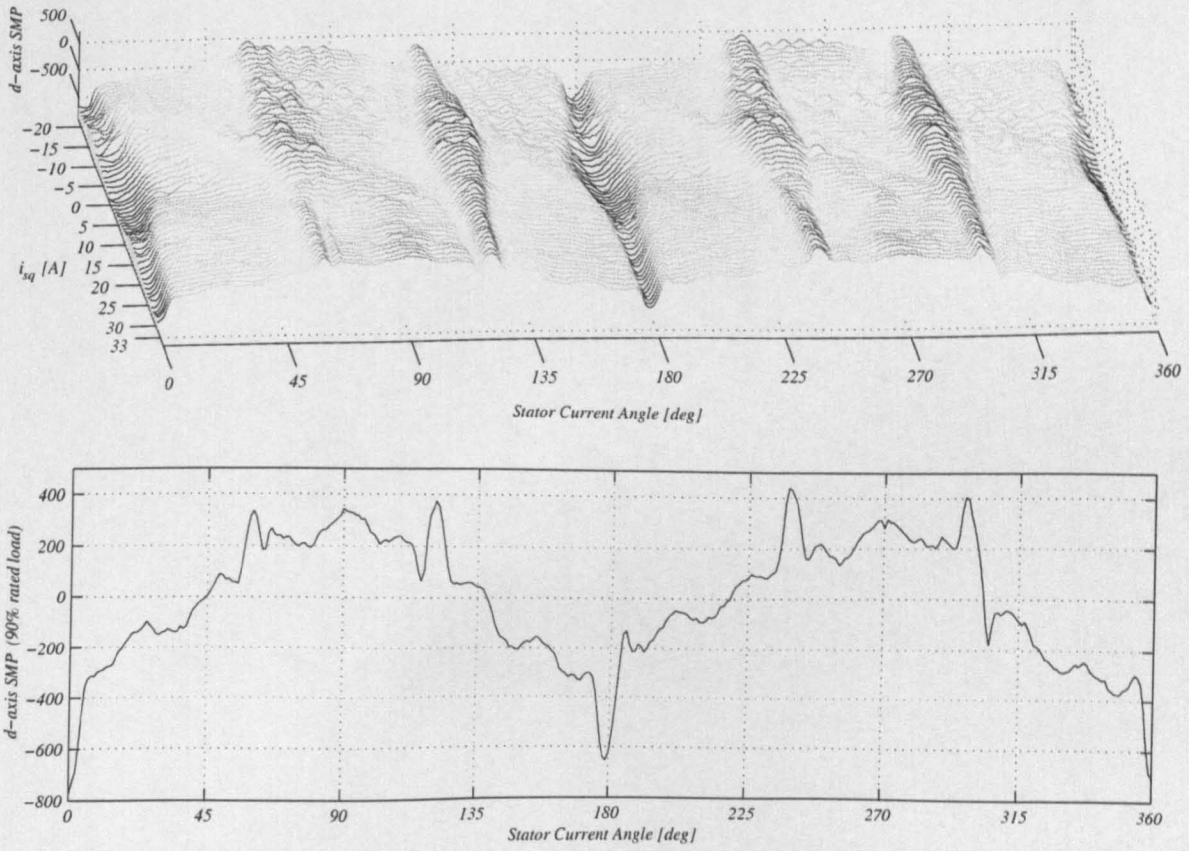

Figure 7.15: *Top: compensation table of the d-SMP over the angle of the stator current vector* $\underline{i}_s$. *Bottom: slice through d-compensation table for* 90% *rated load*

The full SMP_d table as used in sensorless control of the symmetric machine is shown in the upper plot of Fig. 7.15. Selectors are the load current i_{sq} and the stator current angle $\angle \underline{i}_s$. The main visible characteristic are the six narrow strips. Four of them are ridges and two are troughs. They are due to the current clamping modulation since the three fundamental currents have a total of six zero crossings per electrical revolution. If a fundamental zero-crossing results in a ridge or in a trough depends on the demodulation process for the negative-sequence harmonics and on the initial three-phase to orthogonal transformation. This is because the clamping effect is inherently a three-phase phenomenon (see Section 6.1.3). The SMP_q table in Fig. 7.16 shows a different distribution of ridges and troughs. Also, two of the ridges

are higher than any in the SMP_d table and two ridges are relatively flat and difficult to see. This distribution is again a result of the signal transformations. Another interesting effect is that the width of the strips changes. For low values of i_{sq}, the ridges and troughs are relatively wide and for high load, i_{sq}, they get narrower. The lower plot in Fig. 7.15 shows a single slice from the 3-dimensional table for 90% rated load. This view visualizes better how narrow and high the spikes are. The reason is that at low load, the fundamental currents remain longer in the zero-crossing region than under high load where the line currents are much higher and the di/dt is also high. Visible as well, but dominated by the clamping effect is the $2f_e$ saturation saliency. Two ridges can be seen that start at 90° and 270° respectively for high

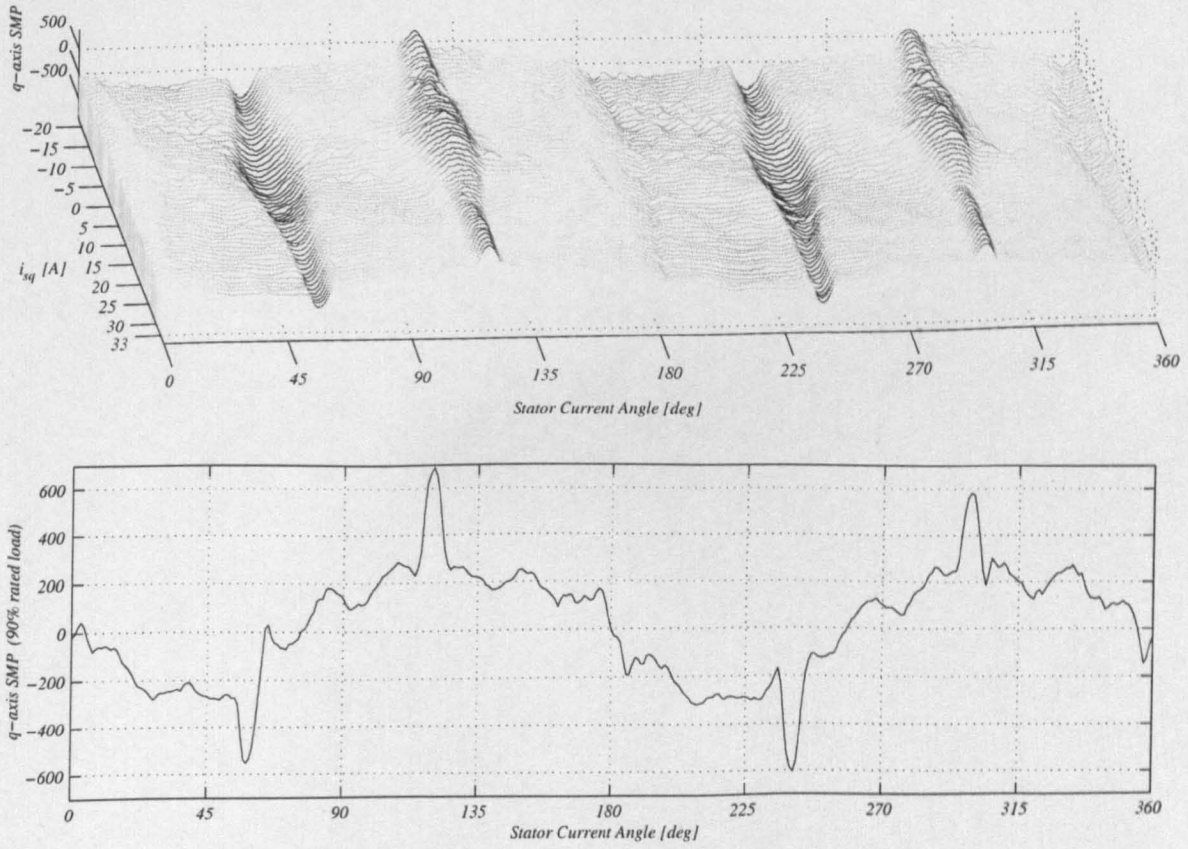

Figure 7.16: *Top: compensation table of the q-SMP over the angle of the stator current vector $\underline{i}_s$. Bottom: slice of q-axis compensation table for 90% rated load*

loads and move to smaller angles in an S-shape for smaller and negative values of i_{sq}. The saliency harmonic can be better seen in the lower plot of Fig. 7.15 where it is responsible for the main sinusoidal shape with maxima at 90° and 270° and minima at 180° and 360°. The *SMP* in Fig. 7.16 is similar to that of Fig. 7.15. The narrow strips due to the zero clamping are in the same locations as those in the SMP_d

table, only the direction and size is different as described before. The reason that the clamping spikes can be found for the same angular position of the stator current angle $\angle \underline{i}_s$ for the d and q profiles is that the clamping effect is inherently 3-phase. The angular position of the saturation saliency however differs from that in Fig. 7.15. The maxima and minima of the sinusoidal shape can be found at angles that are 45° higher. This angular shift is because the real and imaginary components of the $2f_e$ saturation saliency modulation are a quarter of a $2f_e$-period out of phase which is 45° electrical. The course of the saturation saliency for different load conditions is more difficult to see in Fig. 7.16 than in Fig. 7.15 but it also has that of an S-shape.
The processor-internal representation of the *SMP* data is in increments. A value of 500 increments is equivalent to a peak line current of 0.64A.

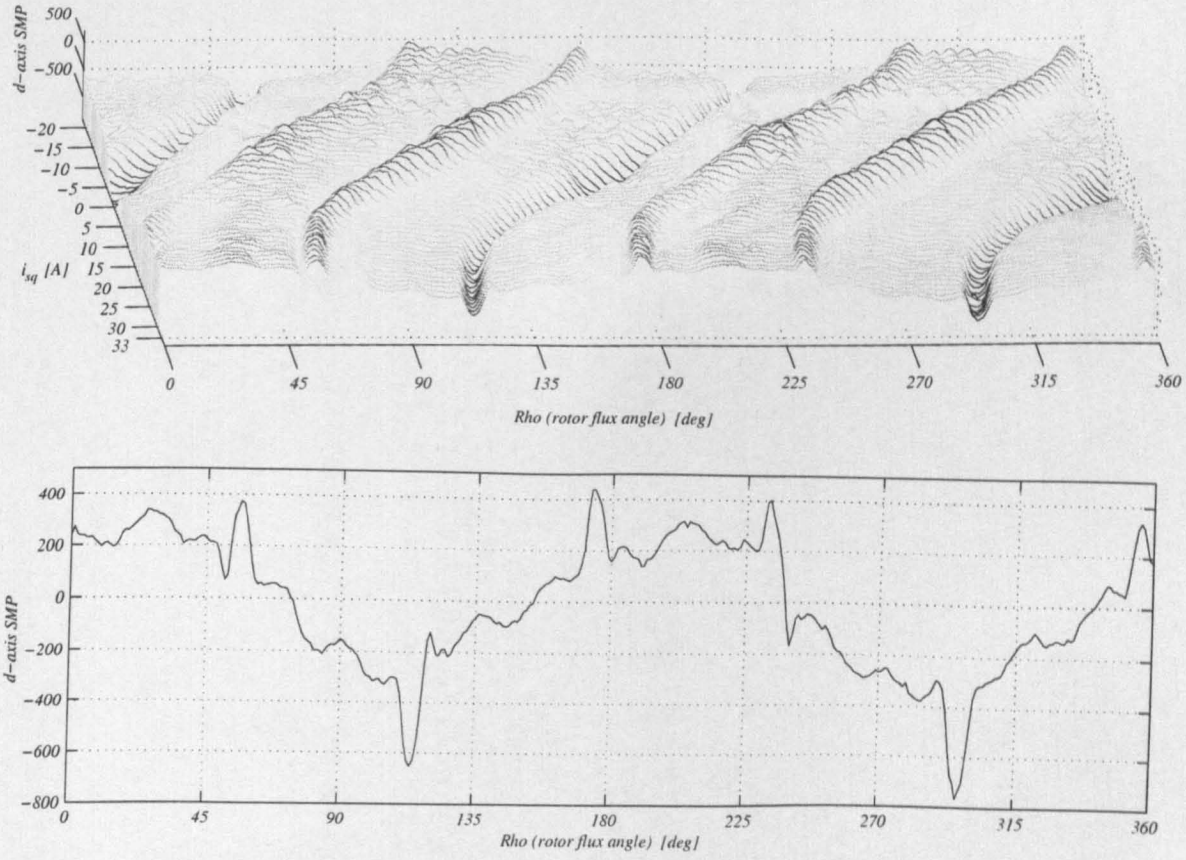

Figure 7.17: *Compensation table of d-SMP over rotor flux angle* ρ

For the commissioning, the rotor flux angle ρ was recorded in addition to the angle of the stator current vector $\angle \underline{i}_s$. Fig. 7.17 shows the SMP_d from Fig. 7.15 printed over the rotor flux angle. Now it is the strips (ridges and troughs) due to the current clamping that change over load in an S-shape. The extrema of the $2f_e$ saturation

saliency are mostly in a straight line and only shift by a few degrees with load. The reason why the clamping modulation now changes with load is that the profile in Fig. 7.17 is a function of the load angle δ [7]. For the load angle:

$$\delta = \angle \underline{i}_s - \rho \tag{7.12}$$

$$= \arctan(i_{sq}/i_{sd}) \tag{7.13}$$

Relations (7.12) and (7.13) are visualized in Fig. 7.18. If the machine is unloaded and $i_{sq} = 0$, all of the stator current contributes to flux the machine and $i_{sd} = \underline{i}_s$. Obviously, the load angle $\delta = 0$ and $\rho = \angle \underline{i}_s$. Comparing Figs. 7.15 and 7.17 for this condition, the profiles are identical. When the load increases, i_{sq} increases and also the load angle δ. The clamping modulation printed over ρ (Fig. 7.17) then shifts to the left towards smaller angles. This behaviour can be explained from (7.12) where $\rho < \angle \underline{i}_s$ for $\delta > 0$. The S-shape is due to (7.13) and is that of the *arctan* function. With a rated d current of $i_{sd} = 14A$, the load angle $\delta \approx 65.7°$ for high positive load and $i_{sq} = 31$A.

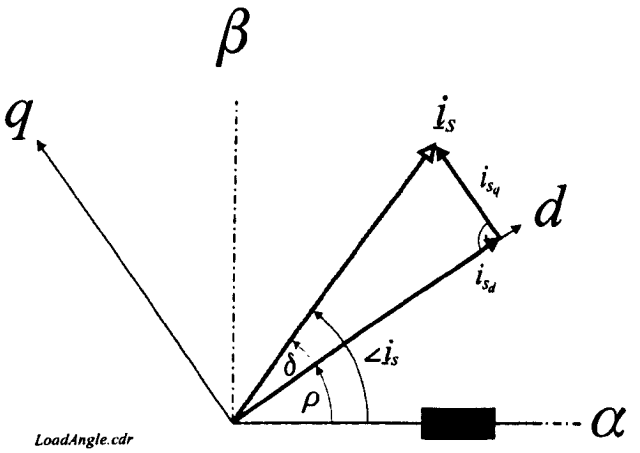

Figure 7.18: *Load angle δ under field orientation*

Unfortunately, relation (7.12) with the knowledge of δ and $\angle \underline{i}_s$ cannot be used to ensure that the drive is correctly field-orientated. The reason is that the load angle with (7.13) is a result of field-orientation under commissioning. The flux axis d could be placed arbitrarily without violating (7.12).

An interesting comparison is that between the parameters of the *Harmonic Compensation* of Section 7.1.4 for the symmetric machine (rotor #3) with that of the *SMP* of Fig. 7.17. Both compensation functions are a function of the rotor flux angle

ρ. One factor that makes a comparison difficult is that he injection frequency f_c was 300Hz for the *Harmonic Compensation* and 750Hz for the *SMP*. However, with $\mathrm{HC}_d = i_{C_2} \cdot \sin(2\pi \cdot 2f_e t + \varphi_{C_2})$, where i_{C_2} and φ_{C_2} are taken from Fig. 7.7, the shape of the SMP_d in Fig. 7.17 can be approximated sufficiently. The same can be done with $\mathrm{HC}_q = -i_{C_2} \cdot \cos(2\pi \cdot 2f_e t + \varphi_{C_2})$ to describe the SMP_q. The compensation parameters from Fig. 7.7 are a compromise in compensating the clamping modulation and the saturation saliency.

Chapter 8:

Results for Position Tracking and Sensorless Position Control

This chapter shows the experimental tracking and sensorless control results for the asymmetric and symmetric machines. Rotor position tracking requires the drive to be operated under field-orientation. For sensorless position control, the estimated rotor position is used to provide a feedback for the position controller and to derive the angle for field orientation. The encoder is only used for monitoring to provide a reference for evaluating the quality of the sensorless drive. The demodulation and rotor position estimation is that of Fig. 5.17. For the asymmetric machine (rotor #1), *Harmonic compensation* is used to suppress unwanted saliency harmonics. The symmetric machine (rotor #3) applies *Space-Modulation Profiling*. A compensation to minimize the distortion due to transient machine operation (Section 6.2) has not been used. The position reference is sent via a rate-of-change limiter to reduce the transient distortion.

8.1 Asymmetric Machine

The structure of the sensorless drive is shown in Fig. 8.1. The stator currents are measured. The *hf* current modulation is separated from the fundamental currents for estimating the rotor position. The stator voltages are not used for the operation at low speeds and standstill. The position controller is that of Section 3.6 and does not contain an integrator. The reference position Θ_r^* is passed via a ramp. The estimated rotor position $\hat{\Theta}_r$ serves as the negative input for the position controller. The output of the controller is the load current reference i_{sq}^* that is limited to $\pm$36A (125% of rated i_{sq}). The inner loops consist of fast current controllers for i_{sd} and i_{sq}, discussed in Section 3.3. The angle for field orientation $\hat{\theta}_e$ is derived from the estimated (electrical) rotor position $\hat{\theta}_r$ and the slip angle θ_{sl} as shown by the structure

in the shaded area. The slip angle is the integral over the ratio i_{sq}^*/i_{sq}^*, divided by the rotor time constant T_r (current model in Section 2.2.4). Fig. 8.2 shows the structure

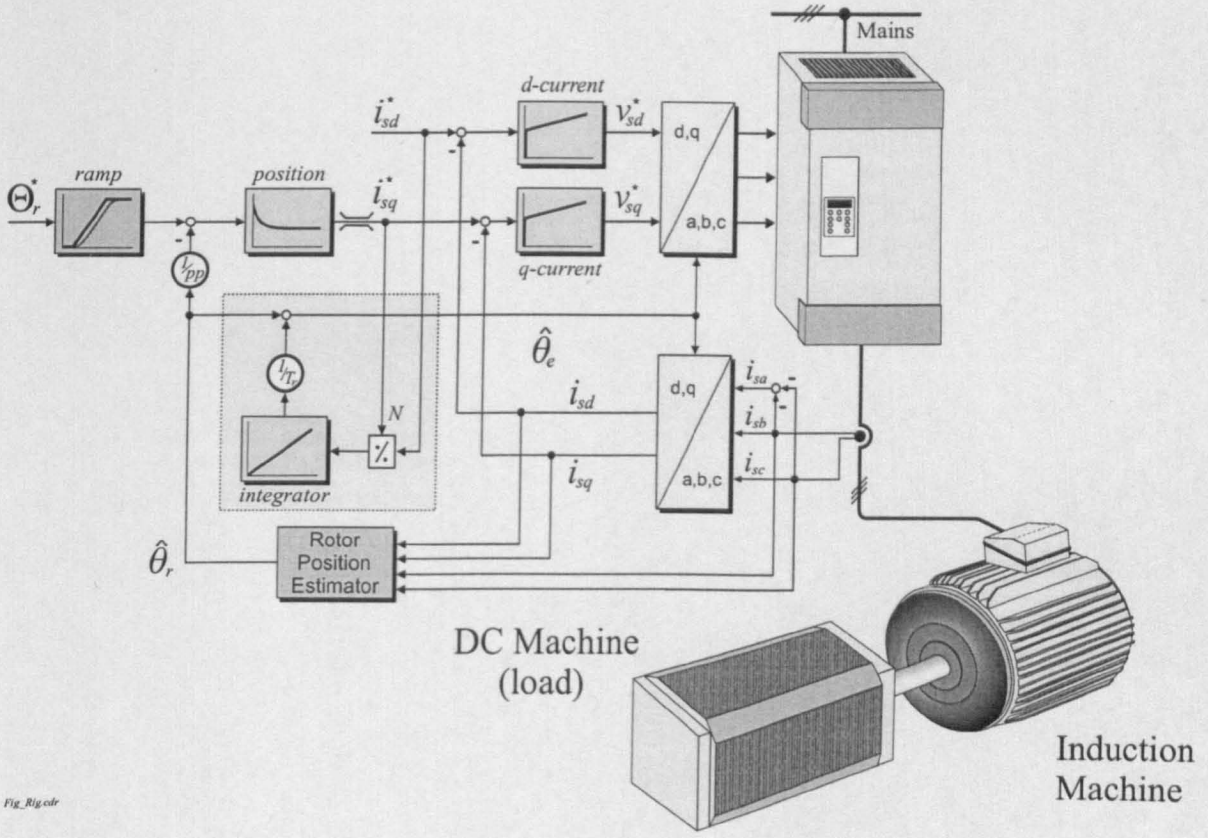

Figure 8.1: *Structure for sensorless position control (pp: number of pole pairs, T_r: rotor time constant)*

of the estimator that is a reduced version of that in Fig. 5.17. The highpass filter 4 in the positive sequence frame is not used here. Implementing this filter will improve the dynamic properties of the rotor position estimator since the cutoff frequency of the lowpass filter can be chosen higher. For most of the experiments, the lowpass filter 5 was a second order Butterworth with a cutoff frequency of 49.5Hz. Some experiments used a reduced cutoff frequency of 25Hz (see Appendix C.2). A low voltage *hf* signal $\underline{u}_o e^{-j\omega_c t}$ is added to the voltage demand (in stator $\alpha\beta$ coordinates) producing a stator flux linkage vector rotating at ω_c in addition to the normal flux vectors rotating at ω_e. The machine saliencies set up a complex series of *hf* impedance variations which result in corresponding *hf* modulations in the stator currents. The saliency due to the engineered rotor (Sections 4.6.1 and 4.6.1) is used to estimate the (mechanical) rotor position angle Θ_r. From (5.13) the factor h_{m1} of Fig. 8.2 is $h_{31} = 2$ for the

estimation of the electrical rotor position θ_r since there are two sinusoidal periods of the engineered pitch saliency per 360° electrical.

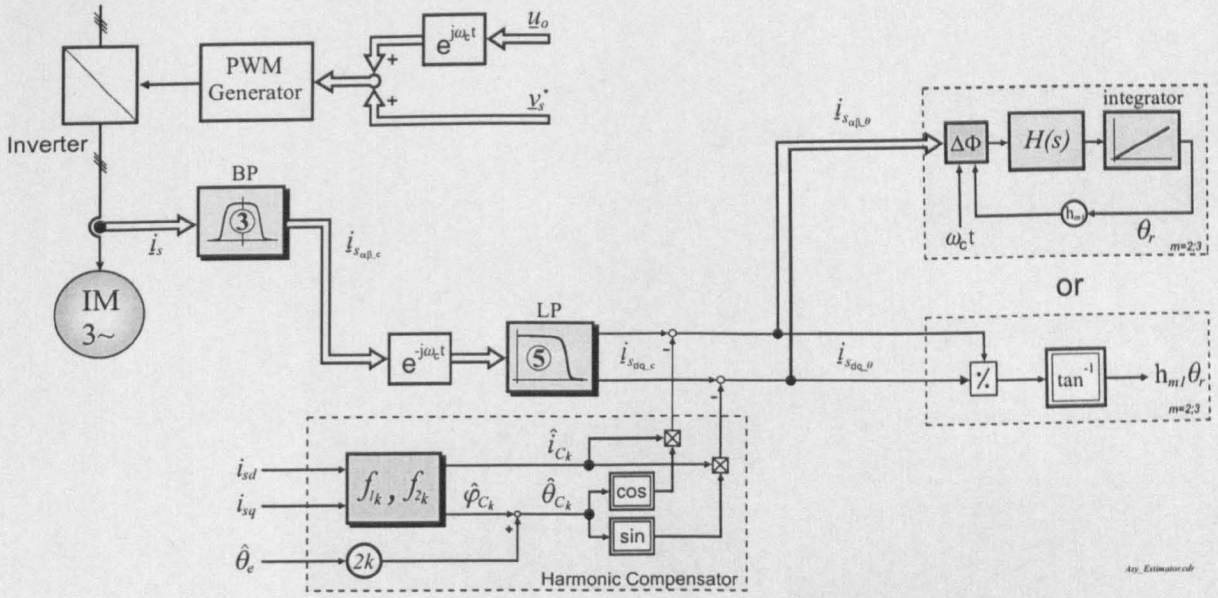

Figure 8.2: *Rotor position estimator with saturation compensation for rotor #1*

The main distorting saliency harmonic is at $2f_e$ and due to saturation. The close harmonic proximity of the position harmonic at $2f_r$ and the saturation harmonic means that it is probably impossible to suppress them by online filtering. This filter would introduce unacceptable phase shifts that will not allow the estimated position to be used as a feedback signal for sensorless control. The solution applied here is to use a superposition scheme to cancel the harmonics online. *Harmonic Compensation* is implemented by the structure in Fig. 8.2 for $k = 1$. The compensation parameters of Fig. 7.4 are used. Note that $\hat{\theta}_e$ is that of Fig. 8.1.

8.1.1 Rotor Position Tracking

In order to illustrate the effectiveness of the commissioned harmonic compensation parameters, the behaviour of the position estimator is first investigated under sensored speed control for $i^*_{s_q}$ 80% rated (the dynamometer of the *TRANSPUTER rig* was rated only at 25kW) and the induction machine fully fluxed. The result is shown in Fig. 8.3 and demonstrates that both the harmonic compensation and position tracking is effective under high load and speeds away from zero. The figure shows the real and estimated (mechanical) rotor position. The speed is initially $n_r = 100$rpm and then at $t = 3$s changed to $n_r = -100$rpm. The position offset between real and estimated

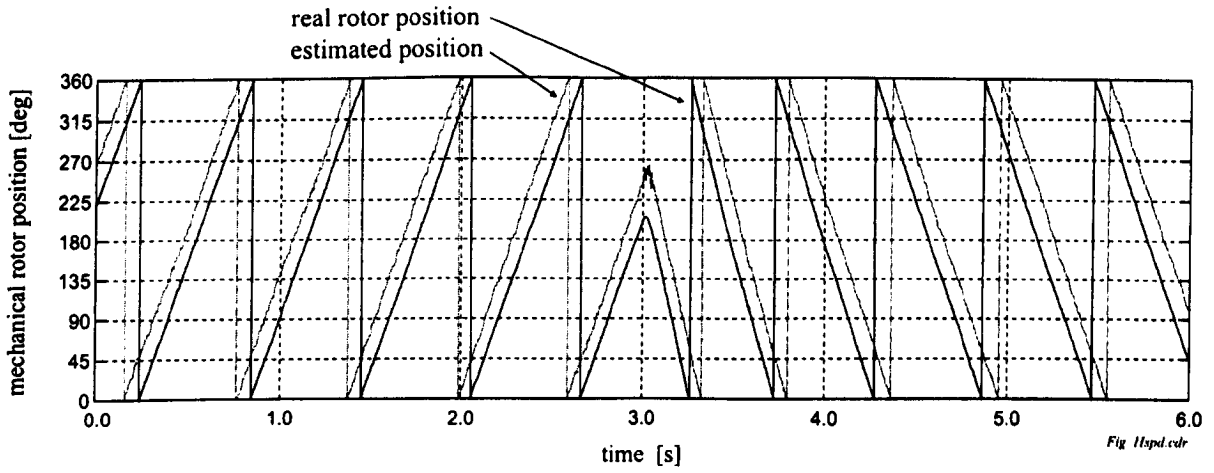

Figure 8.3: Rotor position tracking for higher speeds under high load (80% rated load)

position is random at startup but constant when the estimator is running. With the engineered rotor saliency with four sinusoidal variations per revolution ($N_{sal} = 4$), the absolute position could be determined within $360°/N_{sal}$ mechanical. It is however the *TRANSPUTER rig* that only uses the incremental rotor position of the encoder because it does not make use of the zero-marker.

The upper speed for reliable position estimation is limited by the phase errors in the analogue bandpass filter and the positive sequence rejection filters. Operation at $n_r = 120$rpm (4Hz electrical) introduces a phase error for $\hat{\Theta}_r$ of 2.6° due to the bandpass filter 3 and 3.25° due to the second-order lowpass filter 5 with $f_{cut} = 49.5$Hz. The accumulated phaseshift will cause a deviation from field-orientation so that the maximum speed the sensorless drive can be operated at, will have to be below 200rpm. For higher speed, the *hf* injection will be turned off for efficiency and stability reasons and a standard model-based observer can be used. Above 3 to 5Hz there is a sufficient magnitude of voltage available for the reliable operation of model-based observers. If the improved carrier suppression is used (see filter 4 in Fig. 5.17), the cutoff frequency of the lowpass filter (filter 5 in Fig. 5.17) can be increased and operation towards higher speeds becomes possible with the drive using rotor #1.

In [131], the transition from the *hf* injection method to an adaptive observer is shown at 5Hz for a linear induction motor with locked rotor. The authors in [146] use a *hf* current injection at $f_c = 200$Hz that is injected for operation in the speed range from -125 to 125rpm (4.2Hz) of a 3.75kW, 60Hz synchronous reluctance motor (SynRM). The transition between the estimation methods occurs between ± 80 and ± 90rpm.

In [18, 87] a sensorless speed-controlled and a torque-controlled induction machine

drive are presented that use the voltage model of Section 2.2.4 with an INFORM correction to operate from standstill to high speed.

The combined operation of *hf* injection method and model-based observer for the seamless transition from low-speed to high-speed for a position-controlled *sensorless induction machine* has not been published yet.

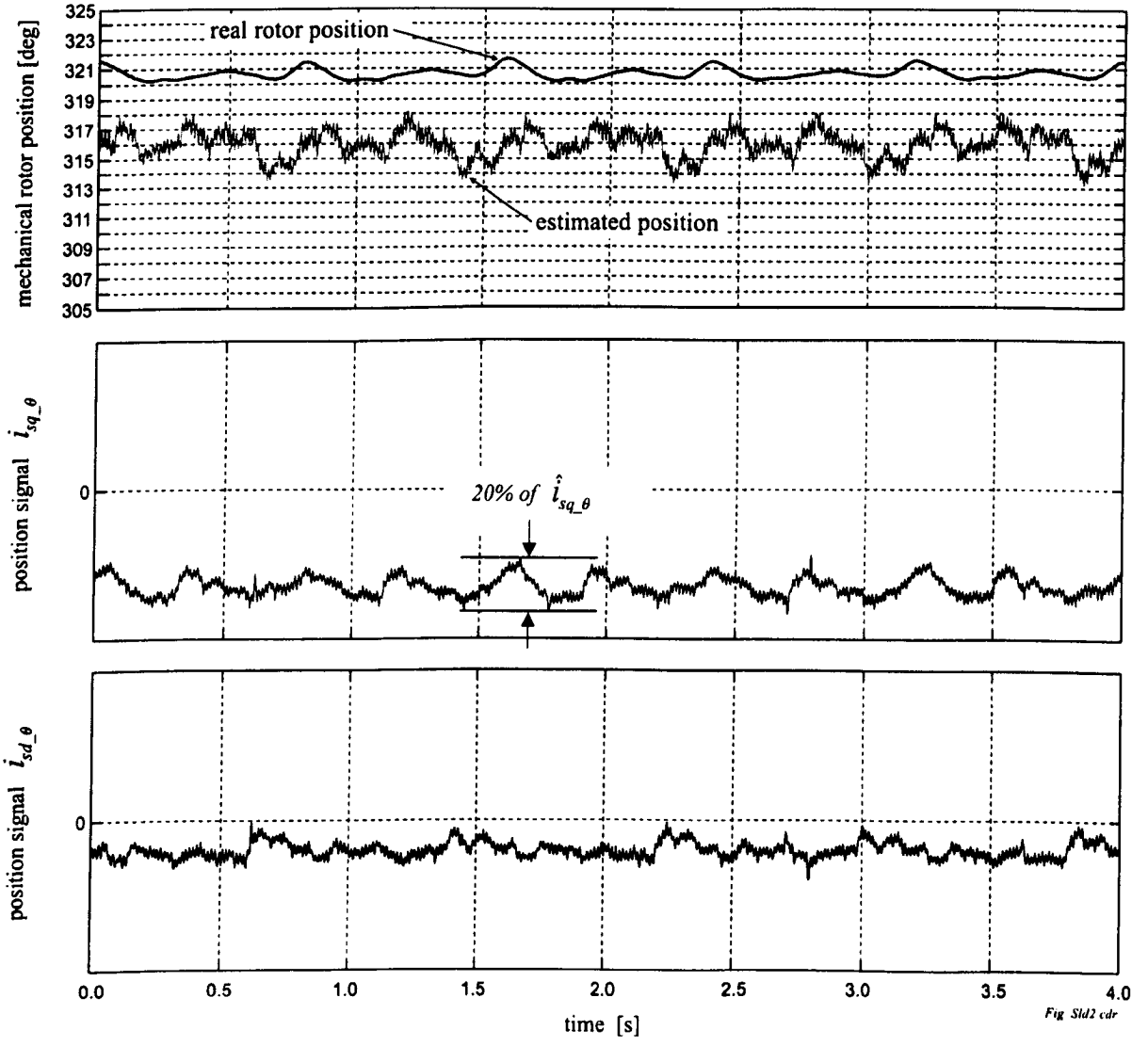

Figure 8.4: *Rotor Position tracking for position holding under 80% rated load. Top: real and estimated (mechanical) rotor position. Centre and Bottom: position currents* $i_{s_{q\_\theta}}$ *and* $i_{s_{d\_\theta}}$

With the commissioned compensation on $\underline{i}_{s_{dq\_c}}$ for the $k = 1$ saturation harmonic, the position estimate can be seen in Fig. 8.4. The drive is position controlled using an en-

coder as feedback and the lead controller of Section 3.6 that is also used for sensorless position control. For 80% rated load, the real rotor position can be maintained within $\pm 0.8°$ mechanical. Note that the offset between estimate and real position is purely for illustrative purposes; the position control being incremental in nature. The position estimate oscillates by about 1° to 2° mechanical; this is equivalent to a 300–700 line shaft encoder. However the oscillation frequency is low and is therefore amplified when the estimate is used as the feedback signal for position control. The oscillation also limits the position control dynamics and is felt to derive from interference from the $k > 1$ saturation harmonics. These harmonics will be mainly due to the inverter deadtime, causing a zero-clamping modulation. This causes small variations in the compensated $\underline{i}_{s_{dq\_\theta}}$ currents. From peak to peak, the variation can reach up to 20% of the peak of the position signals. The resulting error on the estimated (mechanical) rotor position will however only be affected by $1/N_{sal} = 1/4^{th}$ of the error on the position that is derived directly from $\underline{i}_{s_{dq\_\theta}}$.

In Fig. 8.5, the drive is operated under sensored Vector Control for different operating conditions. The mechanical rotor position from the encoder and the estimated position are printed in the upper plot. Below, the load current i_{sq} is shown. The bottom plot shows the position signals $\underline{i}_{s_{dq\_\theta}}$ after compensation. With $N_{sal} = 4$, there are four sinusoidal periods of the position signals per mechanical revolution.

In the horizontal axis, the operating conditions are changed over time, showing permutations of low speed, no speed, no load and half rated load operation. The figure demonstrates that rotor position tracking is possible using *Harmonic Compensation*. The compensation works online for changing operation conditions without the need for adaptation or adjustment. The error in the position estimation is within about $\pm 2°$ mechanical, also when the operating condition is changed. The phase error due to the filters (bandpass filter 3 and lowpass filter 5 in Fig. 5.17) is not a problem since the speed is low. During the load change (condition *c)* to *d)*) the maximum speed reaches 40rpm which causes a short additional position error of 2°. Note that the load reference for the dynamometer is set 'by hand' which explains the differences in the load change that can be seen from di_{sq}/dt. The distortion shown in Fig. 8.4 is also visible in the lower plot of Fig. 8.5, especially when the machine is held at standstill. The distortion is mainly the result of a clamping modulation (Section 6.1.3) and inaccuracies in the compensation.

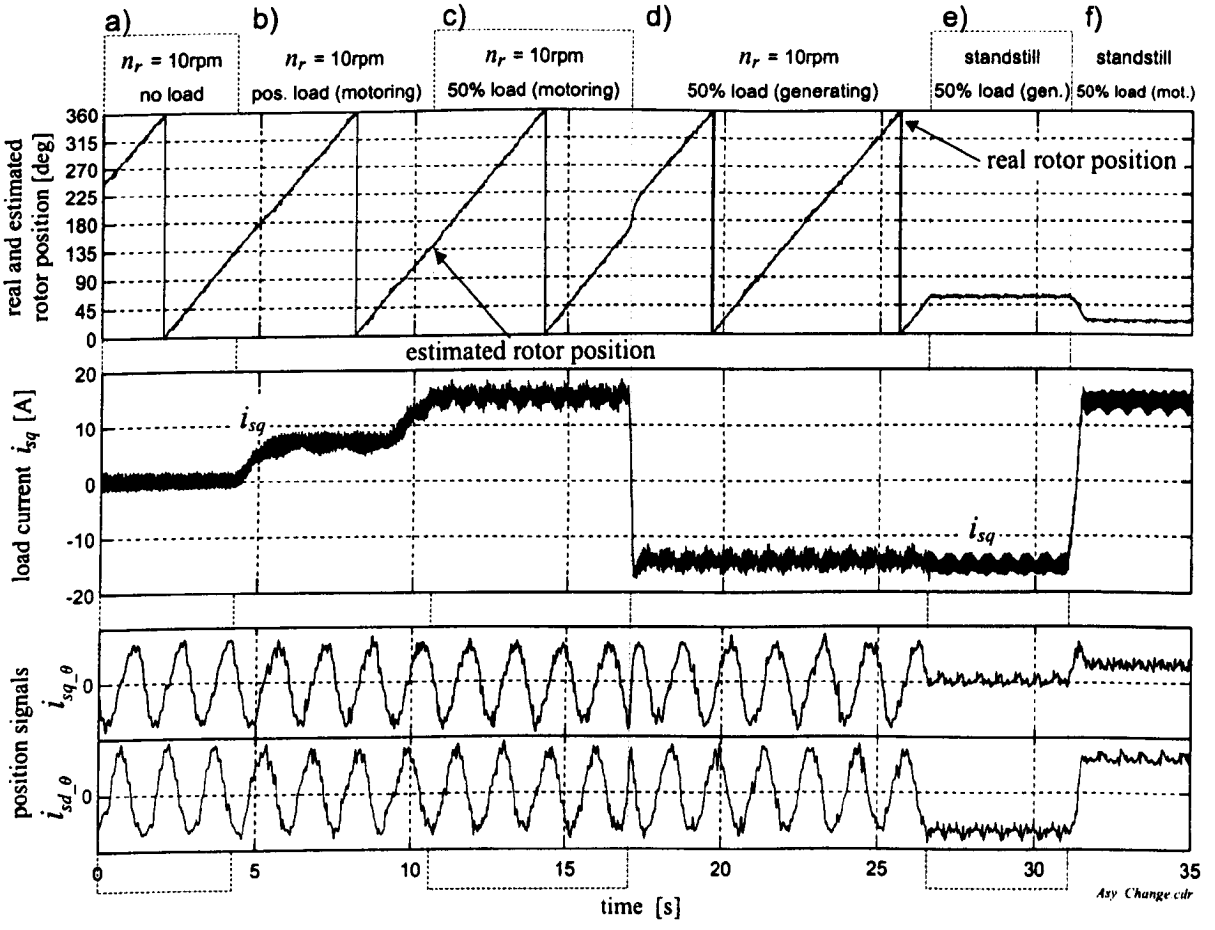

Figure 8.5: *Rotor Position tracking for changing operation conditions. Top: real and estimated (mechanical) rotor position. Centre: load current i_{sq}. Bottom: position currents $i_{s_{q\_\theta}}$ and $i_{s_{d\_\theta}}$*

8.1.2 Closed Loop Sensorless Position Control

Closing the loop by disabling the encoder feedback and using the estimated rotor position instead, the structure for sensorless position control is that of Fig. 8.1.

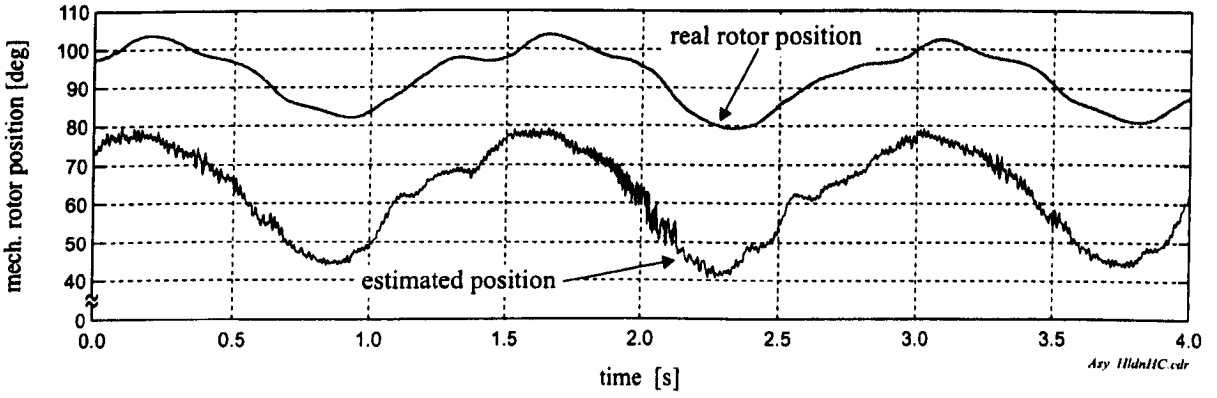

Figure 8.6: *Sensorless position holding without compensation*

In [24], true sensorless position control has been demonstrated with a good transient response for no-load and reduced flux. This section demonstrates results for sensorless position control under full flux and operating conditions up to full load. Some of the earlier results only allow a maximum of 80% rated load due to the limitation of the DC drive of the *TRANSPUTER rig*. The asymmetric machine was later operated on the new *DSP rig* where 100% loading became possible.

Position holding under load without and with compensation:
Under loaded conditions, the interference from the saturation harmonics is severe and position control and any zero speed operation would not be possible without the *Harmonic Compensation*. This fact is emphasised when comparing Figs. 8.6 and 8.7. These show the position accuracy for the uncompensated and compensated case respectively. Fig. 8.6 shows uncompensated sensorless position holding for a load of 45% rated. Shaft oscillations of up to 25° occur. Above 45% rated load, control is lost completely. Fig. 8.7 shows the compensated case under 80% load. Position holding is maintained with an accuracy of about ±1.4° mechanical. The estimated position is actually worse than in the tracking results of Section 8.1.1. The reason for the ripples is the distortion due to the clamping modulation (Section 6.1.3). The extra harmonics on the position signals $i_{s_{dq}\_\theta}$ are not suppressed by the online compensation. Another reason for the ripples is the reduced quality of the compensation under sensorless field-orientated operation. The compensation requires the correct load current i_{sq} to address the compensation parameters. The field angle θ_e is needed to calculate the saliency angle. If the drive is not correctly in field-orientation, the quality of the compensation decreases. Proof that a detuned sensorless drive can still operate reliably is

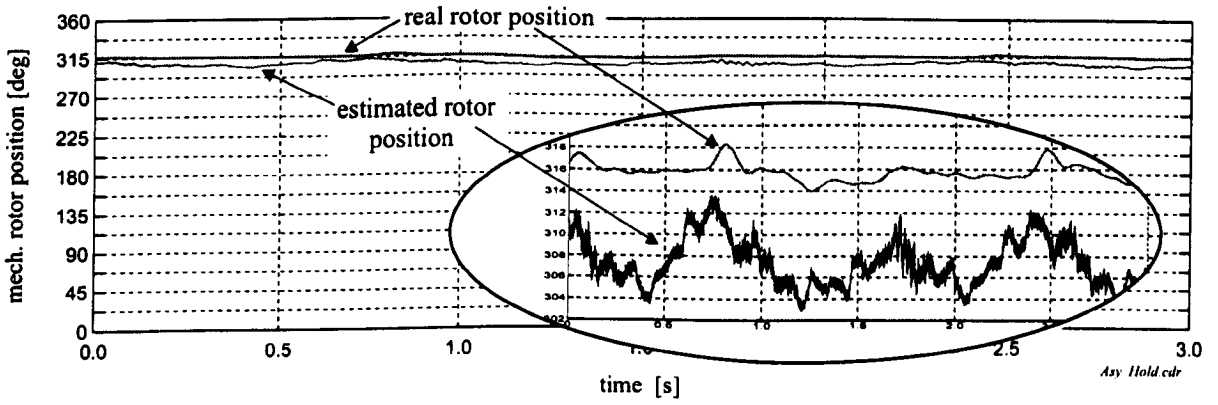

Figure 8.7: *Sensorless position holding under 80% rated load*

given in some of the following figures showing fast position changes. During transient operation, the quality of the position estimate decreases, causing a misalignment of θ_e.

Comparison of sensored and sensorless drive for position transient under no-load: The comparison is shown in Fig. 3.8 of Section 3.6. The position is changed by 900° or 2.5 revolutions under no-load. Results for the sensorless drive using *Harmonic Compensation* are shown in the central row. The controller settings and input reference were the same for the sensored and sensorless drive. *Hf* voltage injection is only used for the sensorless drive, causing a visible band of *hf* currents on i_{sq}. The ramp was set for a rate-of-change of $1000°/s$ and the ramp-filter had a time constant $T_f = 95ms$. The parameters for the lead controller differed slightly from the settings listed in Section 3.6 with $z_p = 0.48$ and the gain $k_p = 420$. Since the distortion due to the clamping modulation and saturation is less severe, the increased gain resulted in a slightly improved dynamic response with 2.5 revolutions in 2 seconds.

Comparison of position transient under load for sensored and sensorless drive: Fig. 8.8 shows the comparison between position sensorless and position sensored operation for a position step demand 360° mechanical with a constant load torque of 80% rated and the motor fully fluxed. The corresponding torque currents i_{sq} and field currents i_{sd} are also shown. The same controller parameters were used for the sensored and sensorless drive and the same reference position Θ_r^* and ramp function were used. The position change was limited to 900° and the ramp filter was set with a filter constant of $T_f = 40ms$. For comparison, *hf* voltage was injected for the sensorless and sensored control, even that the sensored drive does not require a *hf* signal. The sensorless position response is close to that of the sensored case, albeit with increase in i_{s_q} perturbation. The figure shows operation using rotor #1 near the dynamic maximum that could be achieved without using a transient compensation [138] (Sec-

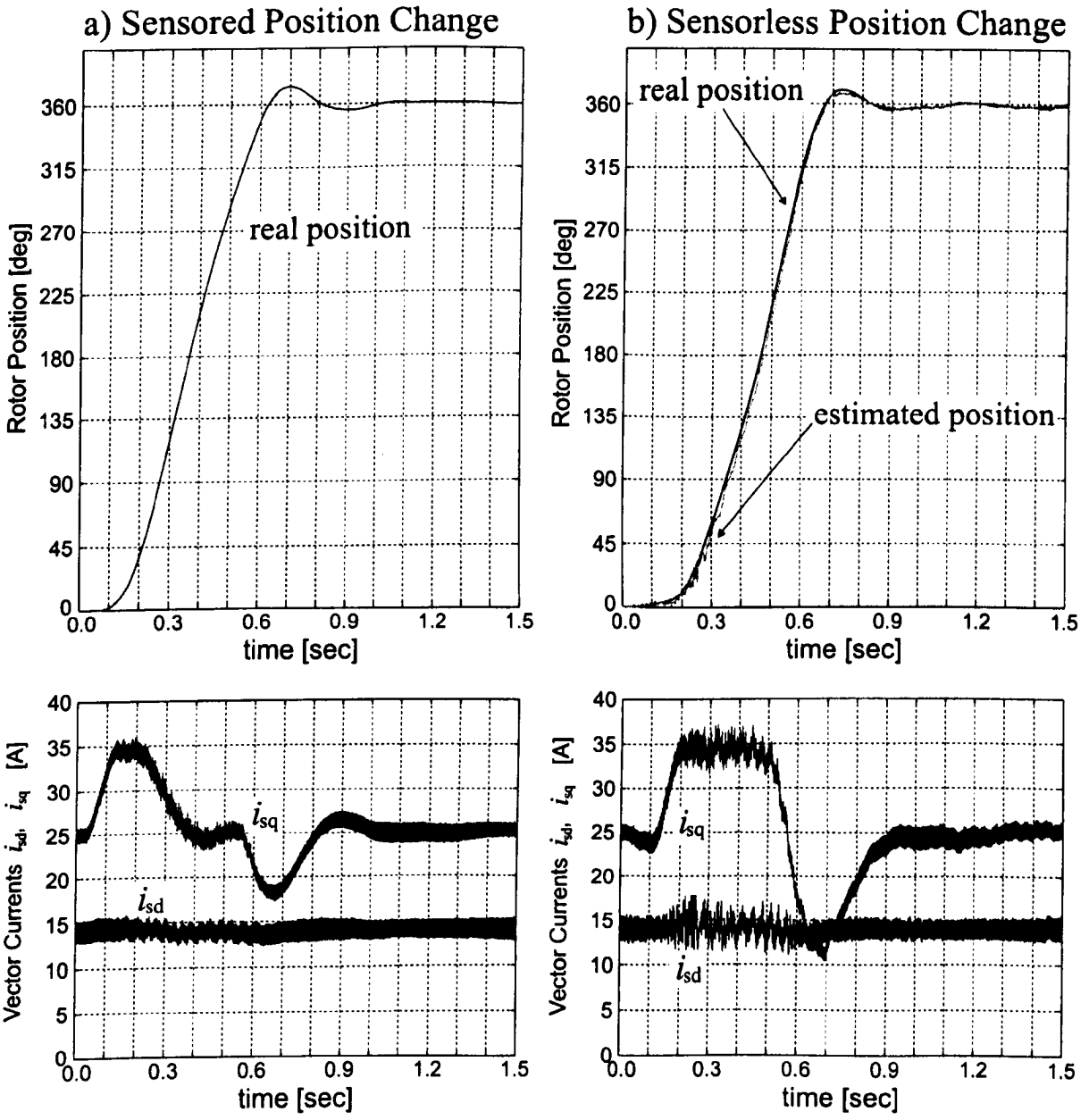

Figure 8.8: *Comparing sensored and sensorless drives for* 360° *position change under* 80% *load for the same reference signal. Left: sensored drive. Right: sensorless drive*

tion 6.2) and without the improved carrier rejection filtering [85]. Comparing the currents in the lower row of Fig. 8.8, the measured i_{sq} for the sensorless drive remains longer at the current limit of 36A and shows a larger undershoot than i_{sq} of the sensored drive. This is a clear indicator for detuning. The sensorless drive is not fully in field orientation during the time of the transient. This detuning is due to the *transient*

modulation (Section 6.2) and the phase shift in $\hat{\Theta}_r$ introduced by the bandpass and lowpass filters when the rotor is at a higher speed during the transient. Stability is however maintained in the sensorless drive and the field-orientation is regained once the demanded position is reached and the drive is in steady-state again. If the ramp is set for a lower rate-of-change, the transient response of the sensorless drive under field-orientation will be closer to that of the sensored drive.

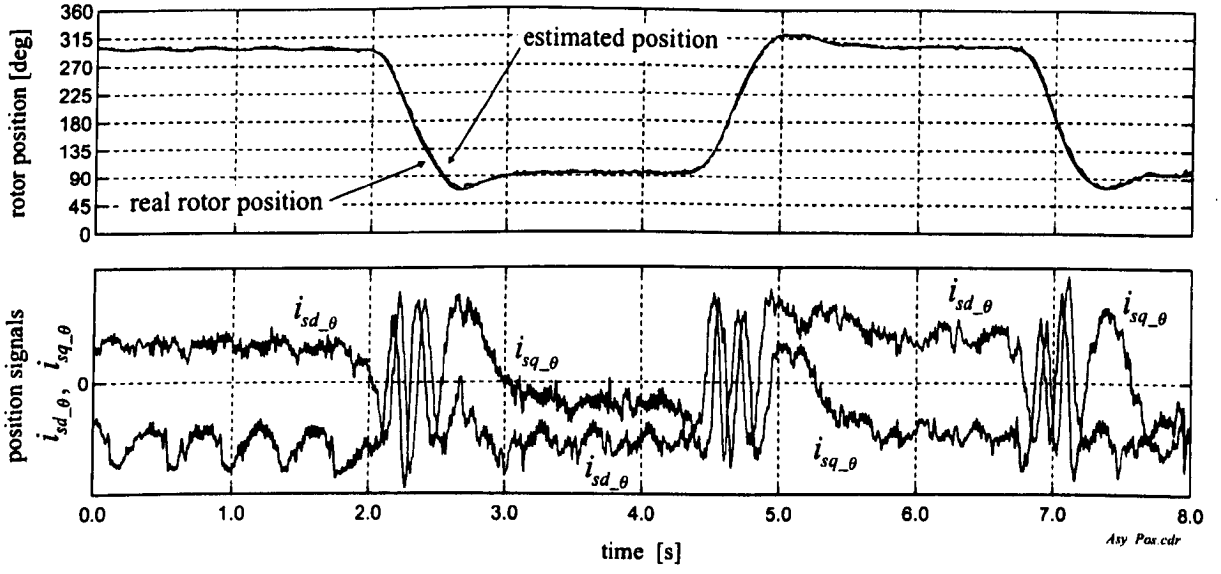

Figure 8.9: *Sensorless* 200° *position change under* 100% *load. Top: real and estimated (mechanical) rotor position. Bottom: position signals* $\underline{i}_{s_{dq\_\theta}}$

Position transient under load for sensorless drive:
Fig. 8.9 shows the sensorless operation for a sequence of position step changes of 200° mechanical with a maximum possible load torque of 100% rated and the motor fully fluxed. The figure demonstrates repeatability of the sensorless position control for constant load and fast position transients. The rotor reaches peak speeds of ±95rpm during the transient, causing a temporary estimation error of about 7°. The accuracy of the position estimate is generally within ±1.5° with short spikes reaching up to ±3.5°. The position signals to derive the estimated rotor position are shown. In steady-state the remaining distortion can be seen clearly. Ideally, the position signals $\underline{i}_{s_{dq\_\theta}}$ should be constant, the DC values representing the position. During the position transient, the position signals change rapidly where the period of the sinusoids is an indicator for the rotor speed.

Sequence of fast position changes under load:
Fig. 8.10-*a* shows a repeated sequence of position changes of 500° for the machine under 30% load. The figure demonstrates fast position changes where the rotor tem-

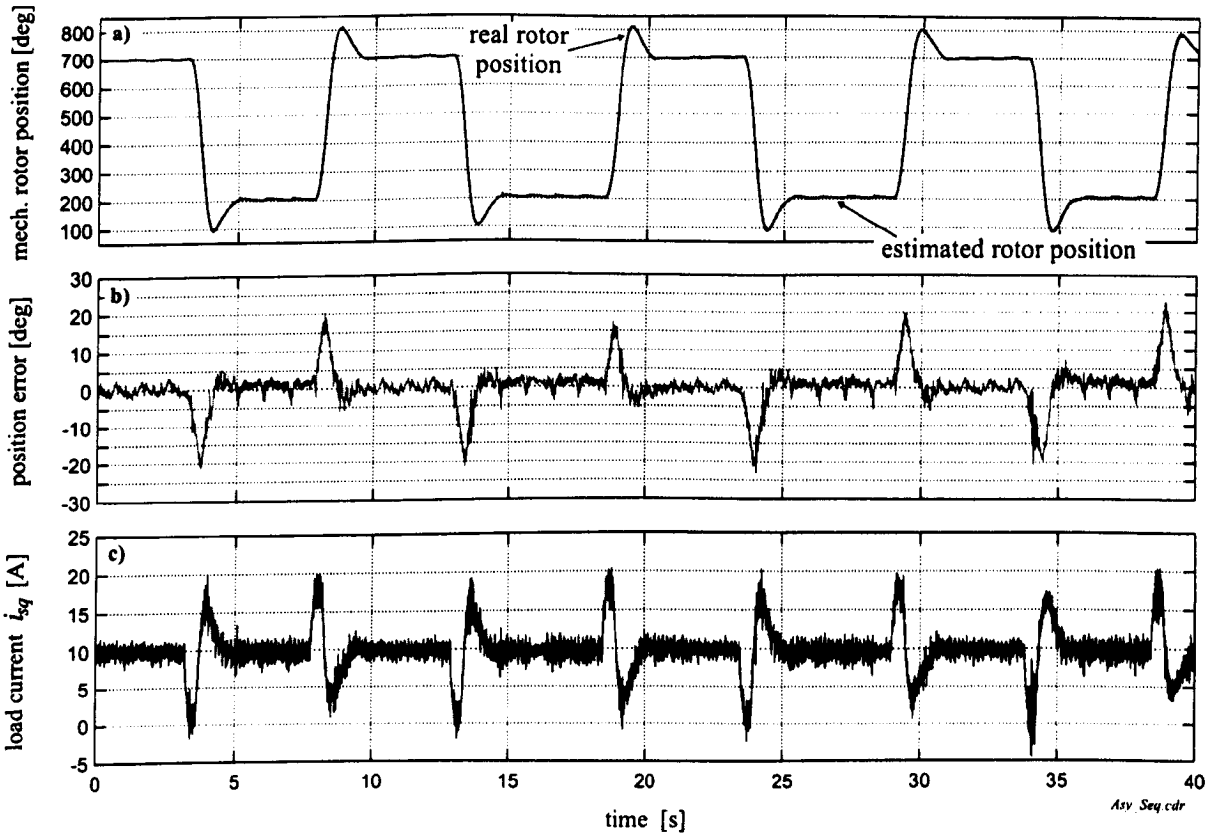

Figure 8.10: *Sequence of sensorless position changes for 30% rated load. Top: real and estimated (mechanical) rotor position. Centre: mechanical position error. Bottom: load current* i_{sq}

porarily reaches 200rpm (6.5Hz). The lowpass filter 5 of Fig. 5.17 is a second order Butterworth with 25Hz cutoff frequency. During the transients, the error between real and estimated rotor position can reach up to 20° mechanical. This error decreases linearly with speed and disappears at zero speed. To illustrate the difference between real and estimated rotor position, the position error is plotted in Fig. 8.10-*b*. In Fig. 8.10-*c*, the torque producing current i_{sq} is plotted, showing that field orientation is maintained during steady-state. The detuning for transient conditions is severe. However, the drive remains controllable.

Sequence of load changes:
Fig. 8.11 shows the compensated sensorless position response to a load impact of 100% rated. The dynamometer is switched on and off to generate a sequence of load impacts for the sensorless drive. There is no integrator in the position controller, so that the shaft does not return to its pre-impact position when the load is changed.

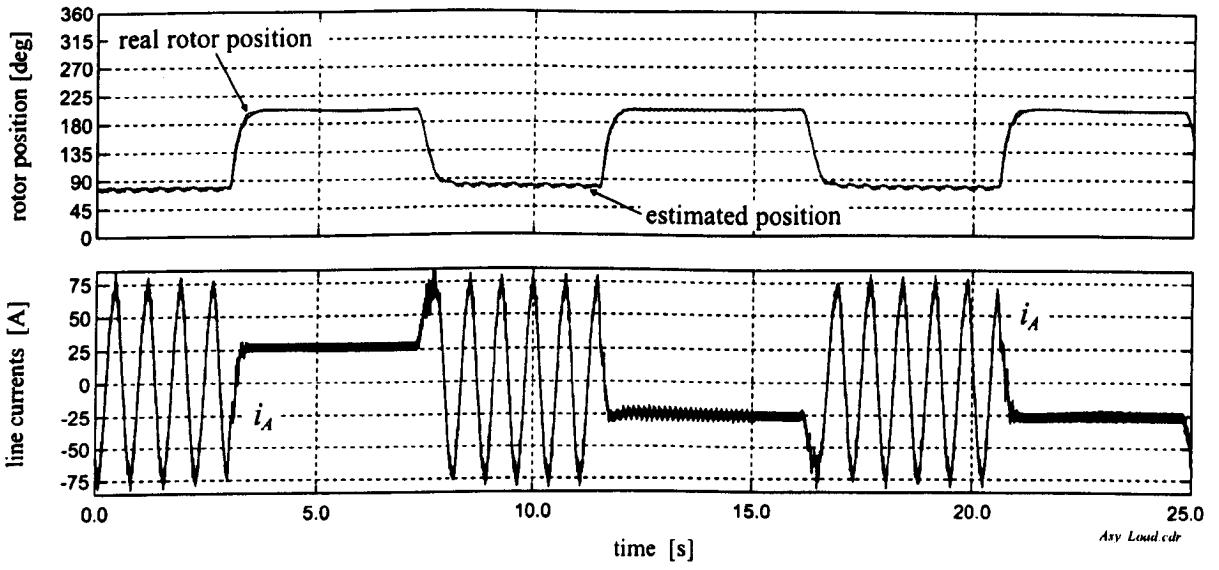

Figure 8.11: *Sensorless position holding during no-load and 100% load impact. Top: real and estimated (mechanical) rotor position. Bottom: stator line current*

When the load is removed, the rotor moves back to its initial no-load position. The lower plot shows one of the stator currents. Under no-load, the excitation frequency is zero and the line current is at DC. Other experiments, performed with changing loads did not show the similarity of the DC current levels under no-load as in Fig. 8.11 since the reference torque for the dynamometer was set 'by hand'. When the high load is applied, the amplitude, phase and frequency of the current changes instantaneously. The machine operates at rated slip and rated current. A slightly reduced quality of the position estimation can be seen in the upper plot of Fig. 8.11. During no-load, the rotor position is constant. Under load, small ripples in the real and estimated rotor position indicate the earlier mentioned distortions.

Choice of filters for position estimation in sensorless drive:
The lowpass filter 5 of Fig. 5.17 has been mentioned a few times in this section and directly linked to the dynamic performance of the sensorless drive. A number of tests, changing the cutoff frequency of this filter, were performed on the sensorless drive. The idea was to experimentally evaluate the limits introduced by selecting a lower cutoff frequency. A lower cutoff frequency will assist the compensation is smoothing any remaining distortion on the position signals $\underline{i}_{s_{dq\_\theta}}$.

The position was commanded to change by 600° for the sensorless drive. A cutoff frequency of 25Hz was chosen first, then 10Hz. For the first setting, the unloaded

drive worked reliably and a load condition of 40% rated also worked reliably. For the 10Hz cutoff frequency, the unloaded drive also performed the demanded position change. Loading the drive however, the position estimate was lost. Only a change of 100° could be performed without instability. Obviously, the higher the bandwidth of the position estimation, the better the sensorless drive will perform. The only drawback is that errors in the compensation will increase torque ripples and cause small position oscillations.

Another critical choice is that of the filter for the i_{sq}-selector to address the correct compensation parameters. Only the fundamental component of the measured load current is suitable for selecting the *Harmonic Compensation* parameters. High-frequency ripples due to the injection and noise have to be reduced. Best results were obtained by choosing a filter time constant of $T_f = 5ms$.

Implementing the technique of Section 5.4.7 allows the increase of the bandwidth of the demodulator and position estimator. A positive-sequence filter can aid in removing *hf* ripples from the fundamental currents to improve the selection of *Harmonic Compensation* parameters. Section 7.2.2 shows that the choice of the stator current angle instead of the flux angle as input for the harmonic compensator can additionally improve the sensorless drive.

8.2 Symmetric Machine

The rotor position estimation for the symmetric machine using rotor #3 relies on the natural rotor saliency due to rotor slot harmonics (RSH). Rotor slot harmonics exist practically in all induction machines (see Appendix B) but rotor #3 was chosen with $N_r = 56$ rotor slots to give a particularly high magnitude of the slot harmonics [120]. The *hf* position modulation is about $6-7\%$ of the magnitude of the carrier harmonic. Testing other machines in the laboratory, it was discovered that an 11kW induction machine that was a standard machine, off-the-shelf and ordered from the manufacturer via a catalogue, had a slightly better magnitude ratio of position modulation to carrier harmonic. This discovery was even more astonishing since the machine is a skewed, closed slot machine. This example supports the view that the slotting effect is still not completely predictable and is applicable to a wider range of machine design than was initially thought.

The structure for the field-orientated sensorless drive is that of Fig. 8.1. The rotor position is estimated using the structure of Fig. 5.17. Unwanted saliencies are suppressed using *Harmonic Compensation* or *SMP*. The *Harmonic Compensation* allowed the estimation of the rotor position angle while the machine was controlled under field-orientation. Sensorless position control using the *Harmonic Compensation* was only possible for reduced flux and full flux under no-load. Better and more robust results were achieved using *SMP* that allowed the operation of the sensorless drive under full flux and high load.

8.2.1 Rotor Position Tracking

Two compensation techniques were used for the tracking of the rotor position. The *Harmonic Compensation* was implemented using the compensation parameters of Section 7.1.4. The structure for the online suppression of the $2f_e$ and $4f_e$ saliency harmonics is that of Fig. 8.2 for $k = 1$ and $k = 2$. This means that there are two *Harmonic Compensators* implemented. The position estimator is designed for the rotor slotting saliency with $m = 2$, $k = 1$, $N_r = 56$ and $pp = 2$ (Section 5.2.4), tracking the $28\theta_r$ harmonic. Preferred choice for the estimator to resolve the rotor position angle is the *arcus tangens* function or *instantaneous phase estimator* of Section 5.5.1 (see discussion in Section 5.6). The logic function of (5.77) is used to derive the mechanical rotor position angle Θ_r from the rotor slotting angle which requires the scaling by $N_r = 56$ rotor slots.

Position tracking for machine without fundamental excitation:
The idea of this experiment is to demonstrate that the estimation of the rotor position of a machine with a rotor slotting saliency is straightforward if no fundamental

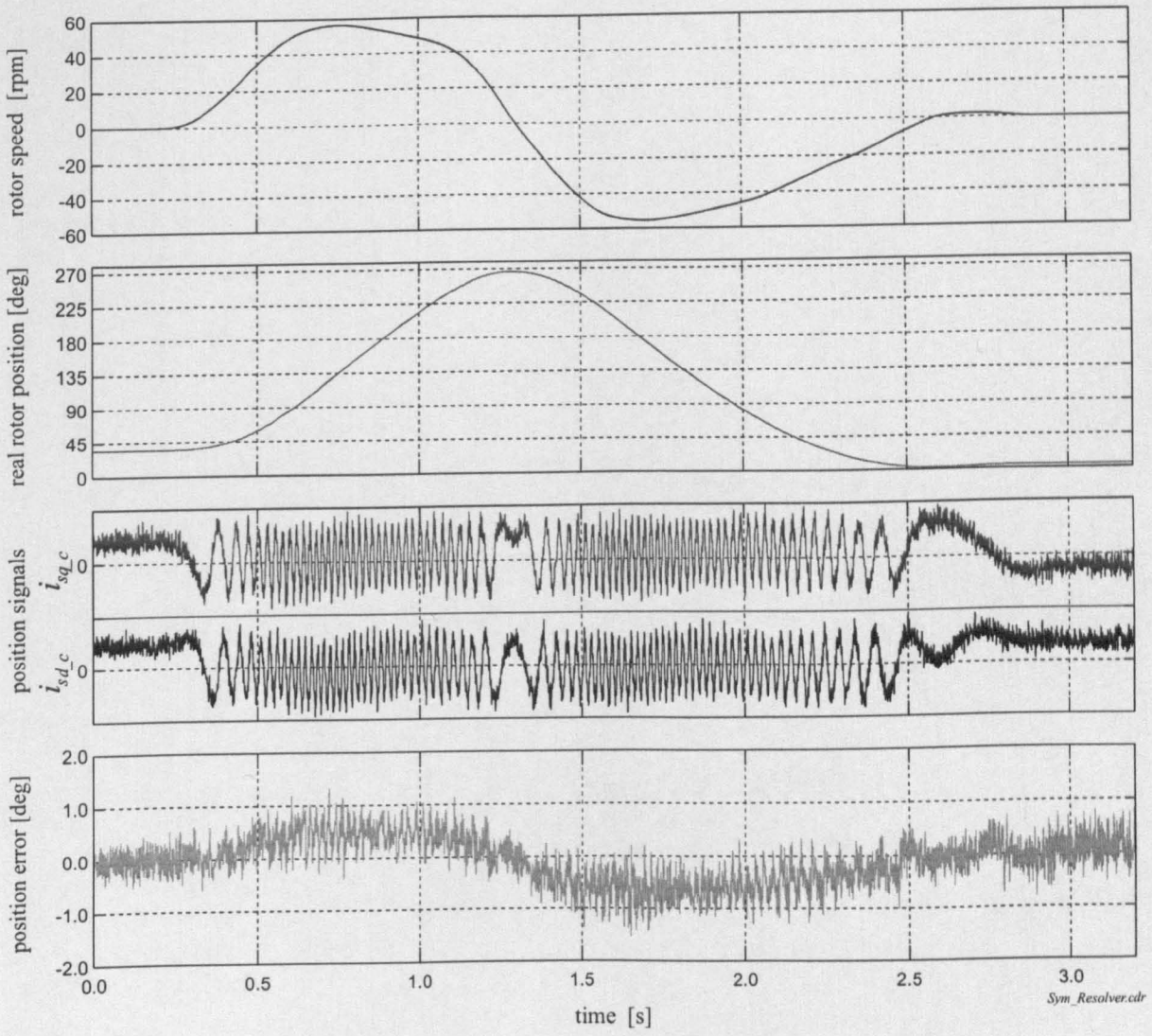

Figure 8.12: *Rotor position tracking for machine without fundamental and current controllers disabled. The rotor is turned manually*

excitation is present in the machine. No additional saliencies are present and no compensation is required.

Fig. 8.12 shows the tracking of the rotor position for the machine where only *hf* injection is applied. The injection frequency is $f_c = 750\text{Hz}$. The amplitude of the injection is 13V peak on the line-to-line voltages, resulting in a line current of 1.9A peak. The output of the current controllers are set to zero so that the machine is not fluxed, nor a fundamental current exists. The rotor is turned manually. The maximum speed n_r shown in the upper plot is approximately 60rpm in both directions and measured by the encoder. The (mechanical) rotor position Θ_r from the encoder is shown in the second plot of Fig. 8.12. The change in position is about $3/4^{th}$ of

a revolution before moved back beyond its initial position. The third plot displays the real and imaginary parts of the extracted current modulation $\underline{i}_{s_{dq\_c}}$. The signals are affected by noise but the modulation is only due to the rotor slotting effect. The number of sinusoidal periods in $\underline{i}_{s_{dq\_c}}$ corresponds to the rotor position Θ_r. The position signals $i_{s_{d\_\theta}} = i_{s_{d\_c}}$ and $i_{s_{q\_\theta}} = i_{s_{q\_c}}$ can directly be used and sent through an *arcus tangens* function to extract the rotor position information. The position error is shown in the bottom plot. This error is the difference between real and estimated rotor position. Since the estimation is incremental, the estimated position was aligned to the encoder position at start-up.

One part of the error is due to the bandpass filter (number 3 in Fig. 5.17) to extract the position modulated signals from the stator currents and the filters 3 and 5 to suppress the carrier. This error changes linearly with speed and at 60rpm the error is 0.6°. The remaining error is due to noise. The error due to speed can easily be predicted when the filter transfer function is known (see Appendix C.2). Without fundamental excitation, the machine is practically a resolver with N_r poles. The rotor position can be estimated easily and theoretically also for fast transients because there is no modulation due to transient operation without fundamental excitation. Practical tests have however shown that a transient distortion exists even without fundamental currents. The reason for this is not clear yet.

Rotor Position Tracking using *Harmonic Compensation*

Since no machine is operated without flux and rarely without load, the optimal conditions for estimating the rotor position as in Fig. 8.12 do not apply in practice. For a practical machine, the rotor slotting saliency will be accompanied by additional saliencies that will have to be suppressed using one of the methods of Section 7.

Position tracking for fully fluxed and loaded machine for different speeds:
The quality of the tracking is now investigated for a machine under full flux and operating over a range of load. For this tracking a compensation technique is now necessary and *Harmonic Compensation* is applied here. The injection is $f_c = 300$Hz which is also the centre frequency of the analogue bandpass filter. The bandwidth of this filter is 155Hz.

With increased speed, the harmonics of the rotor slotting saliency move quickly away from the carrier frequency, leaving the bandwidth window of the analogue bandpass filter 3. Since the frequency of the rotor slotting saliency harmonic is N_r/pp times higher than the electrical rotor frequency f_r, the bandwidth is reached at relatively low speeds. The speed range had to be limited. A practical speed range was $n_r \in [-60 \ldots +60]$rpm since the position signals $\underline{i}_{s_{dq\_c}}$ will not be too much attenuated by the bandpass filter. The higher the speed, the more the position signals will

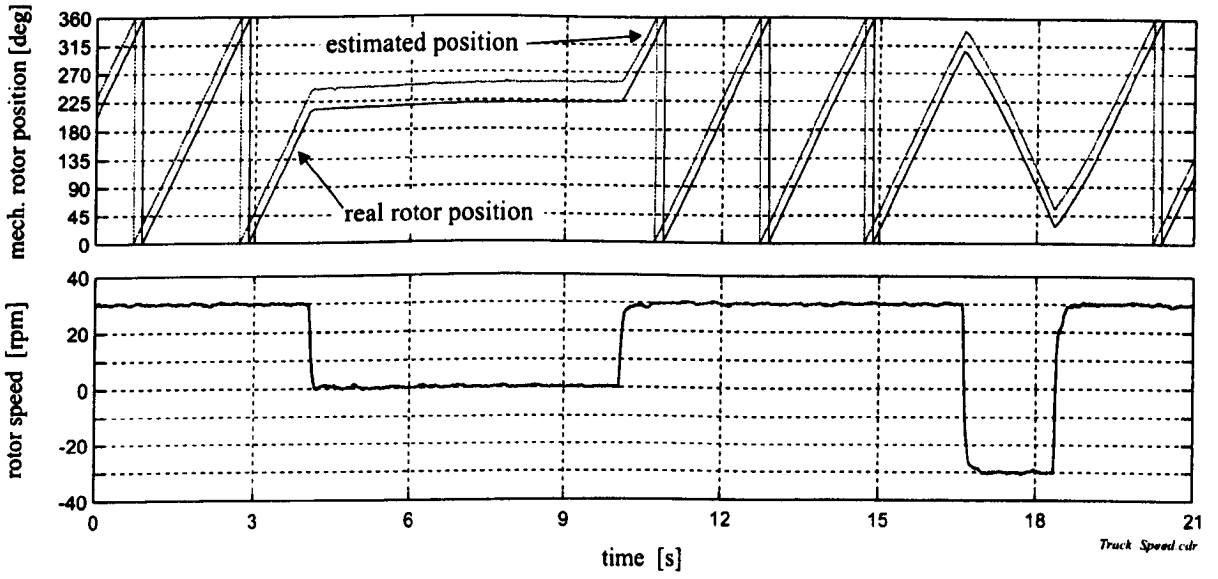

Figure 8.13: *Rotor position tracking for 90% rated load and different speeds, including near standstill*

be reduced in magnitude whereas the amplitude parameters i_{C_k} of the *Harmonic Compensation* will remain unchanged. The difference in magnitude will cause an over-compensation and the position estimation will eventually fail. It could be possible to use a gain adaptation for i_{C_k} to extend the allowable speed range. The solution chosen however is to select a higher injection frequency as will be shown later. Then the analogue bandpass filter with a wider filter characteristic can be used, higher speeds are possible and switching harmonics and the fundamental currents will still be sufficiently removed.

The machine is controlled under sensored *indirect rotor flux orientation* (IRFO) and a speed reference applied as shown in the bottom of Fig. 8.13. The load is 90% rated. The upper plot in Fig. 8.13 shows the real and estimated (mechanical) rotor position. The initial difference is arbitrary since the position estimation is incremental.

The drive is controlled for a speed change from $n_r = +30$rpm to zero speed and back to +30rpm before reversing the speed to -30rpm and back to $n_r = +30$rpm according to the speed profile is shown in Fig. 8.13. The figure demonstrates that position tracking is possible for dynamically changing conditions using *Harmonic Compensation*. Although the compensation parameters of Fig. 7.7 were obtained under steady-state conditions (see Section 7.1.4), the distorting harmonics of Fig. 7.9 can also be suppressed under transient conditions.

Position tracking for fully fluxed machine during load changes:

Fig. 8.14 demonstrates that harmonic compensation can be applied to changing satu-

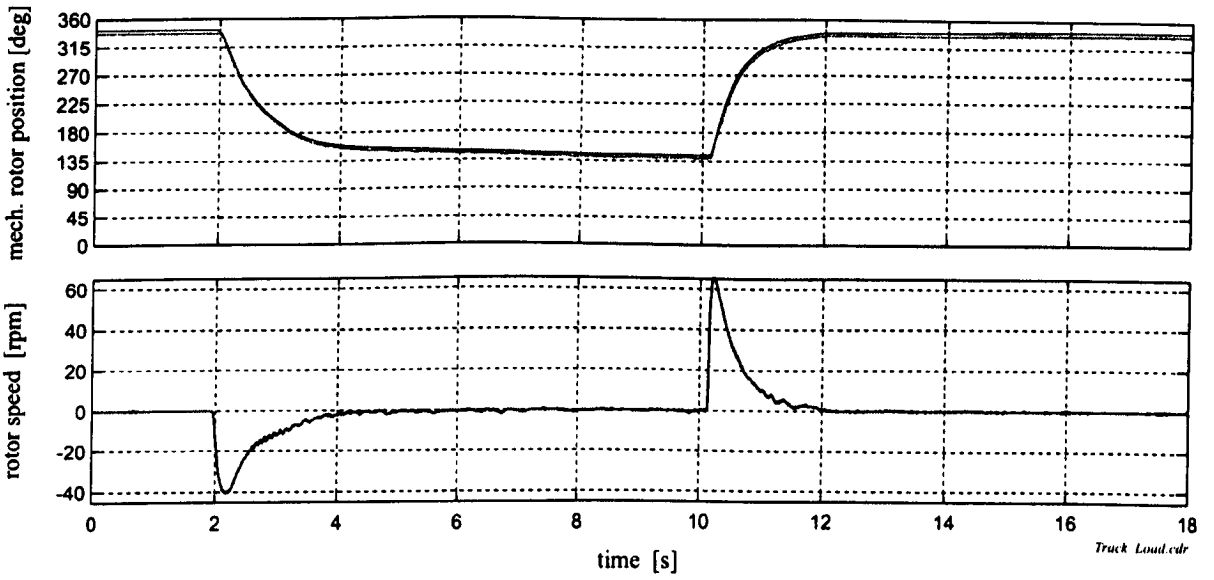

Figure 8.14: *Position tracking at standstill for load change from zero to 90% rated load*

ration conditions due to load changes. The drive is controlled to maintain a speed of n_r = 0rpm when the load is changed. Originally, the load is zero, then changes to 90% rated for about 8 seconds before it is removed again. The resulting speed from the encoder is shown in the lower graph.
As stated earlier, reliable compensation could only be achieved for lower speeds. The controller therefore had to be modified so that a maximum rotor speed of n_r = 60rpm would not be exceeded significantly.

Position tracking for drive under high load during fast position change:
Real and estimated rotor position are shown in Fig. 8.15 whilst the drive is under sensored position control. The drive is controlled for a 360° position change under 80% rated load. The reference position was sent via a ramp to ensure that the maximum allowable speed of $n_r \approx$ 60rpm was not exceeded. Under these conditions, position tracking is shown to be successful. The plot in the centre shows the vector currents i_{sd} and i_{sq} during this position change and the bottom plot shows the position currents $\underline{i}_{s_{dq\_c}}$ after compensation.

Position tracking for drive under high load for crawling speeds:
Fig. 8.16-*a* demonstrates the compensation of harmonics for the machine at a crawling speed of +5rpm under 80% rated load. A speed reversal is applied at t = 1.75sec. The position error cannot directly be seen in this graph, thus it is extracted and magnified in subplot 8.16-*b* and is mostly within ±0.5° mechanical. With the speed

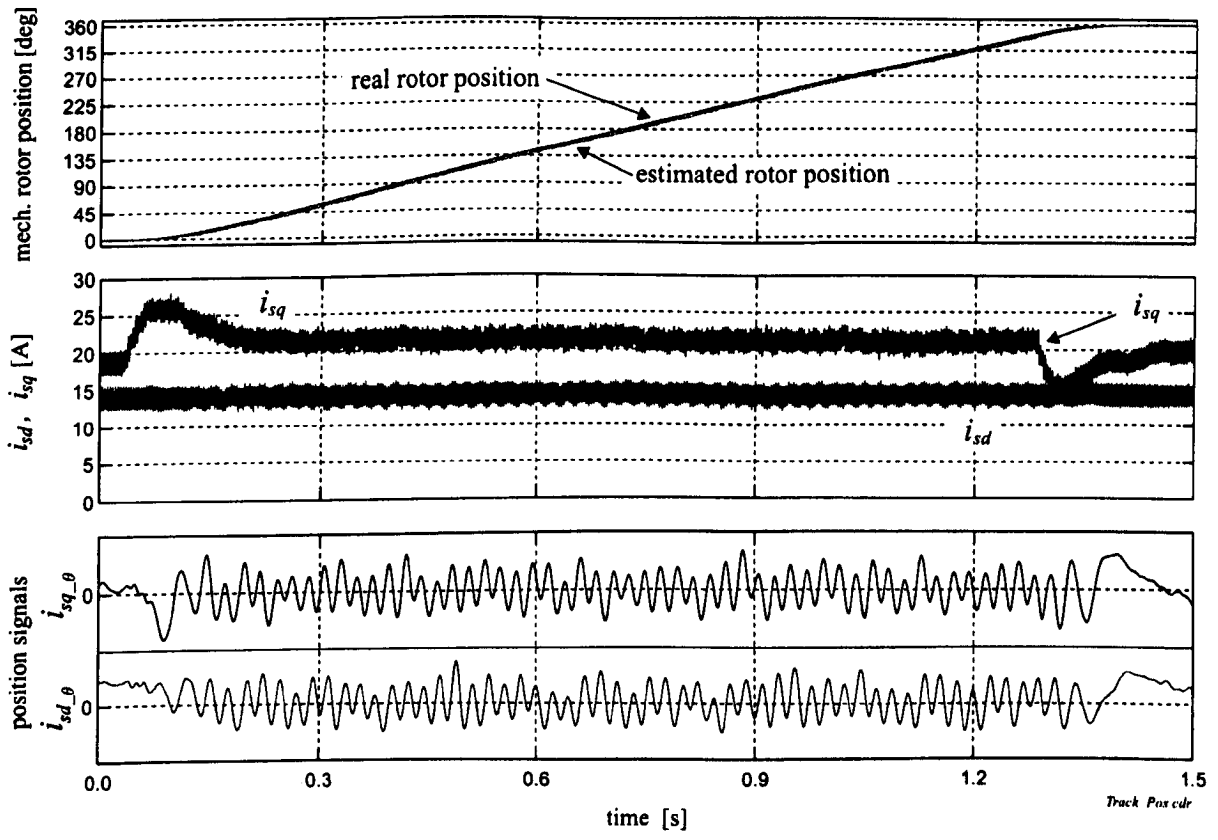

Figure 8.15: *Tracking of rotor position for* 360° *position change under* 80% *rated load (drive under sensored position controlled). Top: real and estimated (mechanical) rotor position. Centre: load and flux currents. Bottom: position signals* $\underline{i}_{s_{dq\_\theta}}$

change, an additional offset error of about 0.5° becomes apparent. This is due to the phase shift introduced by bandpass filter 3 and lowpass filter 5 shown in Fig. 5.17 as discussed above. Note that the rotor position estimator is incremental in nature. The angle difference between real and estimated position has been removed at startup with the machine at standstill.

The position currents $\underline{i}_{s_{dq\_c}}$ and $\underline{i}_{s_{dq\_\theta}}$ (the latter is after the harmonic compensation) are shown in subplot 8.16-*c* and *d* respectively. In 8.16-*c* the distorting effect of saturation can be seen in the time domain. Some cycles are lifted up or below the zero line, which causes errors in the position estimation. The effect of missing signal periods is visible as cycle-slipping in $\hat{\theta}_r$ (see Section 8.2.2). After the speed reversal from t = 3sec onwards, the distortion due to the low-frequency $2f_e$ harmonic can be seen. Before the speed reversal, the beat frequency is higher due to the different direction of the rotor.

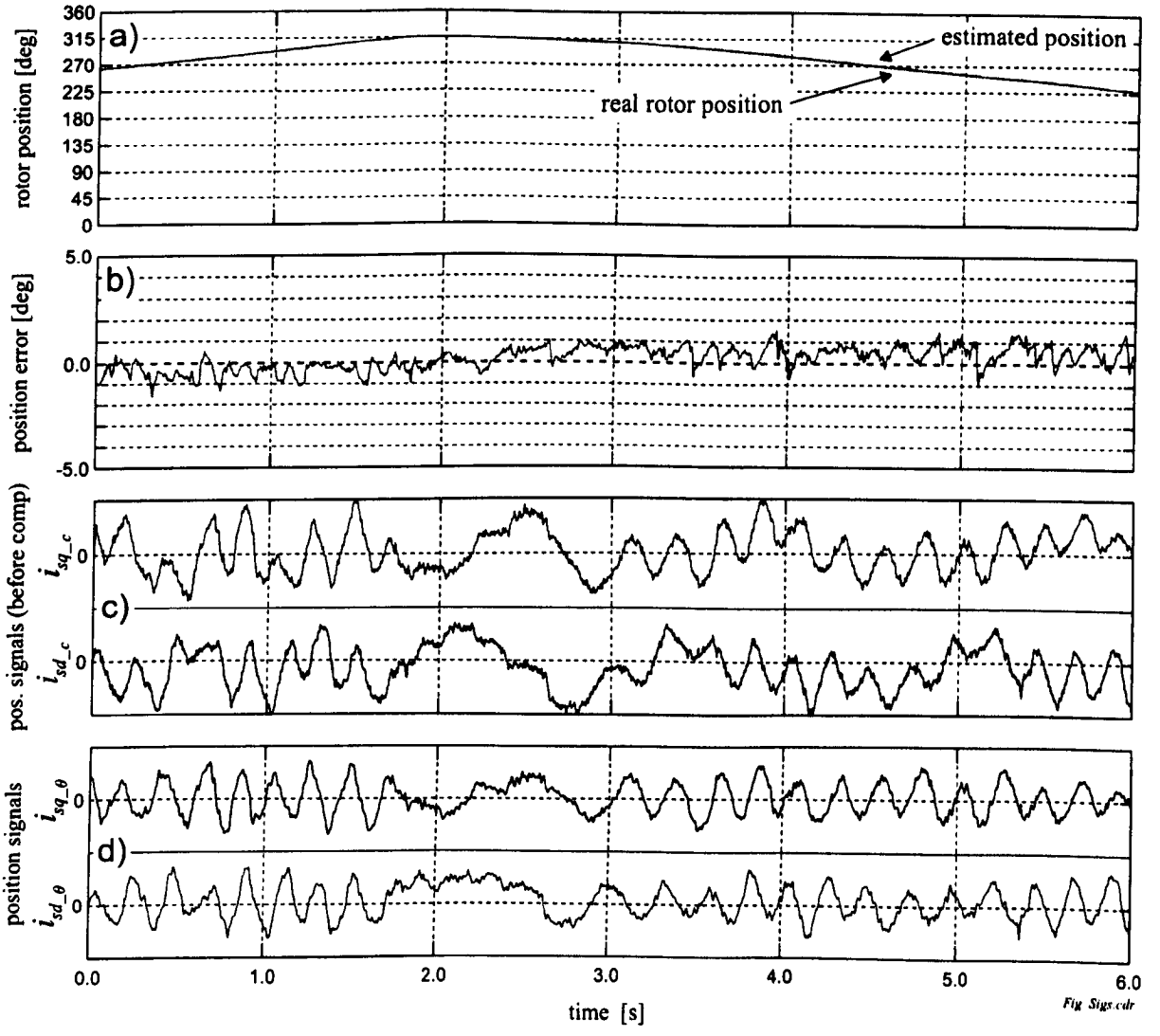

Figure 8.16: *Position tracking for low speed and speed reversal under 80% rated load*

With applied compensation in *(d)*, reliable position estimation is possible. However, the compensated is not perfect and some remaining distortion is visible. This is because only the two major saliency harmonics are tackled (see Section 7.1.4). Some remains of the carrier harmonic f_c can also be seen as high frequency ripples on the signals. A higher injection frequency combined with the carrier rejection filtering of Fig. 5.17 would reduce this distortion.

Rotor Position Tracking using *SMP*

To overcome the limitations in speed, a higher injection frequency was chosen with $f_c = 750$Hz. The analogue bandpass filter 3 has a centre frequency of f_c and the bandwidth is 440Hz. The stator current angle $\angle \underline{i}_s$ is now used for the online commissioning instead of the rotor flux angle of the previous section.

Position tracking for high speed using SMP:
The performance for tracking of the rotor position for a higher speed of $n_r = 150$rpm is illustrated by Fig. 8.17 using *SMP*. The machine is at 60% rated flux. Initially no load is applied and the load current i_{sq} is zero. The rotor flux angle ρ and the angle of the stator current vector are equal. When the load of 23% rated is applied, i_{sq} increases and the difference between ρ and the angle of the stator current vector is clearly visible. This difference is the load angle δ. The position tracking works very well for the high speed and for the load change as can be seen from the third subplot of Fig. 8.17. The magnification of the real and imaginary components of the compensated position signal $\underline{i}_{s_{sq\_c}}$ in the second plot of Fig. 8.17 shows that the distortion on the remaining slot modulation is small.

Position tracking for high and changing speed for fully fluxed machine:
In Fig. 8.18 the rotor position tracking is demonstrated for the fully fluxed machine under 72% of rated load and high speed. The drive is running under sensored IRFO while the speed is increased from 150rpm to 165rpm which can be seen from the upper plot. No scheme is implemented to compensate for the *transient modulation*. This is why only a small change in the speed can be applied. Larger steps will generally cause a short deterioration in the position estimation. This can lead to a loss of a few cycles during the transient process. The encoder position and the estimated rotor position are shown in the second plot. The estimated rotor position has been aligned to the real position at zero speed. The estimation error is shown in the third plot. The offset of $\approx 3°$ mechanical at 150rpm is due to bandpass filter 3 and lowpass filters 4 and 5. The remaining estimation error has a deviation of less than $\pm 0.5°$ mechanical. The lower plot shows the load current i_{sq} during the speed change.

Position tracking for high speed and load change:
Fig. 8.19 shows the rotor position tracking for high speed operation during a load change. The drive is operated under sensored IRFO at $n_r = 100$rpm. A load is applied and switched off again. Initially, the loading is zero, then increased to full load and decreased to zero as visible in the bottom plot of Fig. 8.19 that shows the load current i_{sq}. The first plot shows the measured encoder speed. The speed drops for about 0.5s when the load is switched on and is then controlled to maintain the demanded speed of 100rpm. Removing the load results in a short overshoot in the

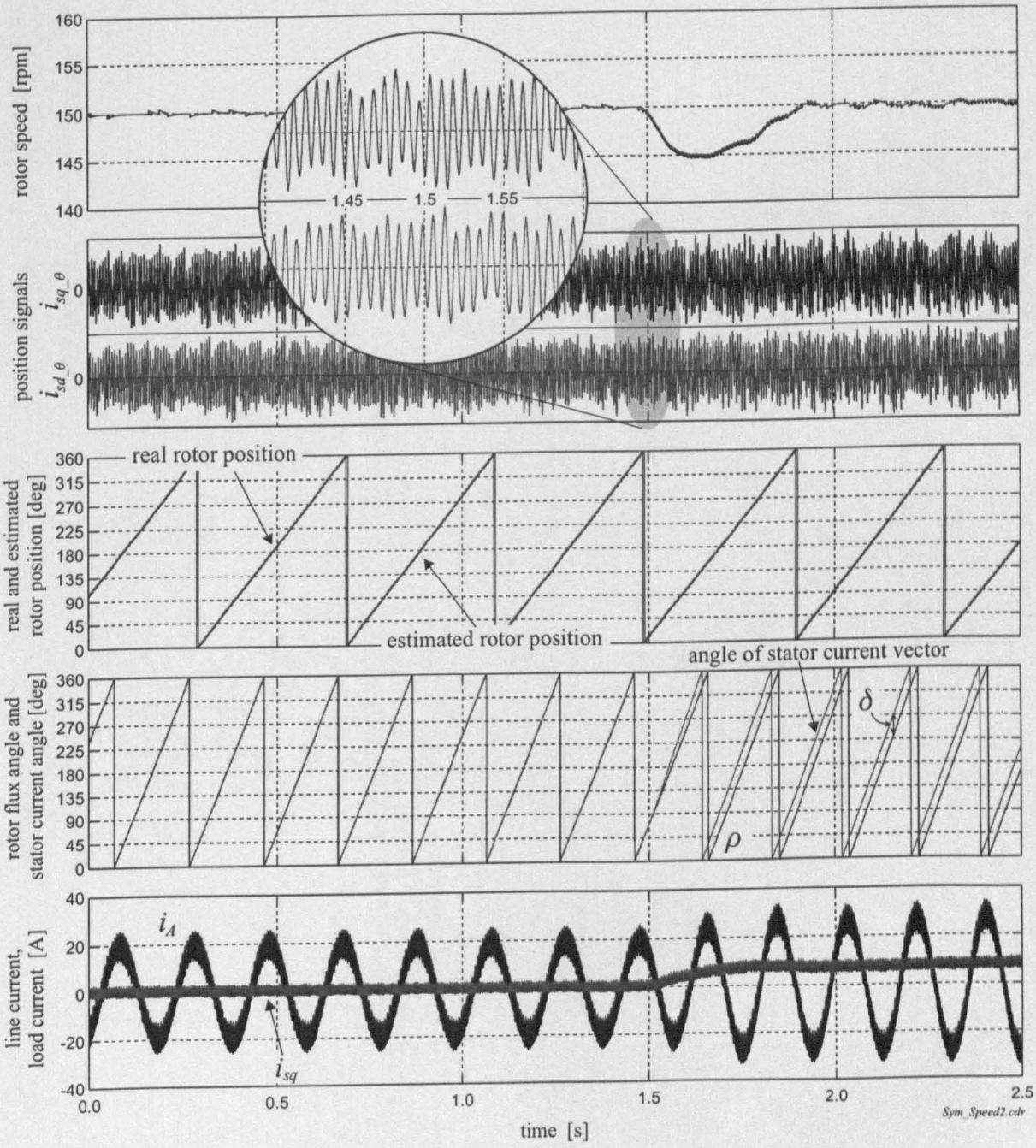

Figure 8.17: *Rotor position tracking for high speed while a load change of* 23% *rated load is applied (using SMP)*

speed that reaches 155rpm. Real and estimated rotor position can be seen in the second plot. The latter has been aligned to the encoder position at start-up. The estimated position follows the encoder position well. The estimation error is shown in

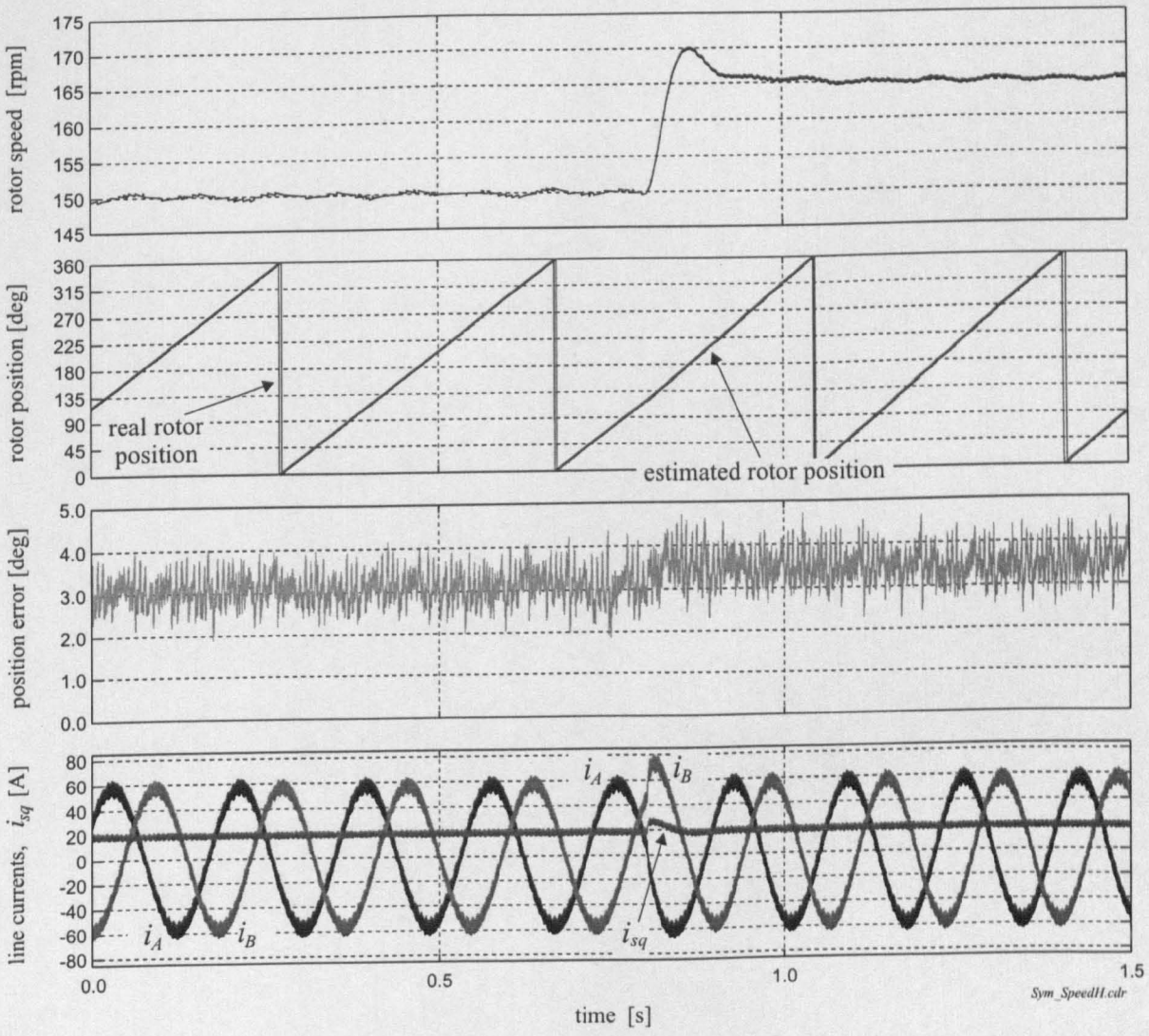

Figure 8.18: *Rotor position tracking for loaded machine at high and changing speed and fully fluxed machine*

the plot below. The speed-dependent error is $\approx 1.9°$ at 100rpm. This error increases as the speed increases during the speed-overshoot. The remaining estimation error has a deviation of less than $\pm 0.5°$ mechanical.

8.2.2 Cycle Slipping in Rotor Position Estimation

This section covers the reliability of sensorless position estimation and control. Since Vector Control requires the information of the rotor position for low-speed operation and standstill, an error in the position estimation is as severe as if an encoder fails.

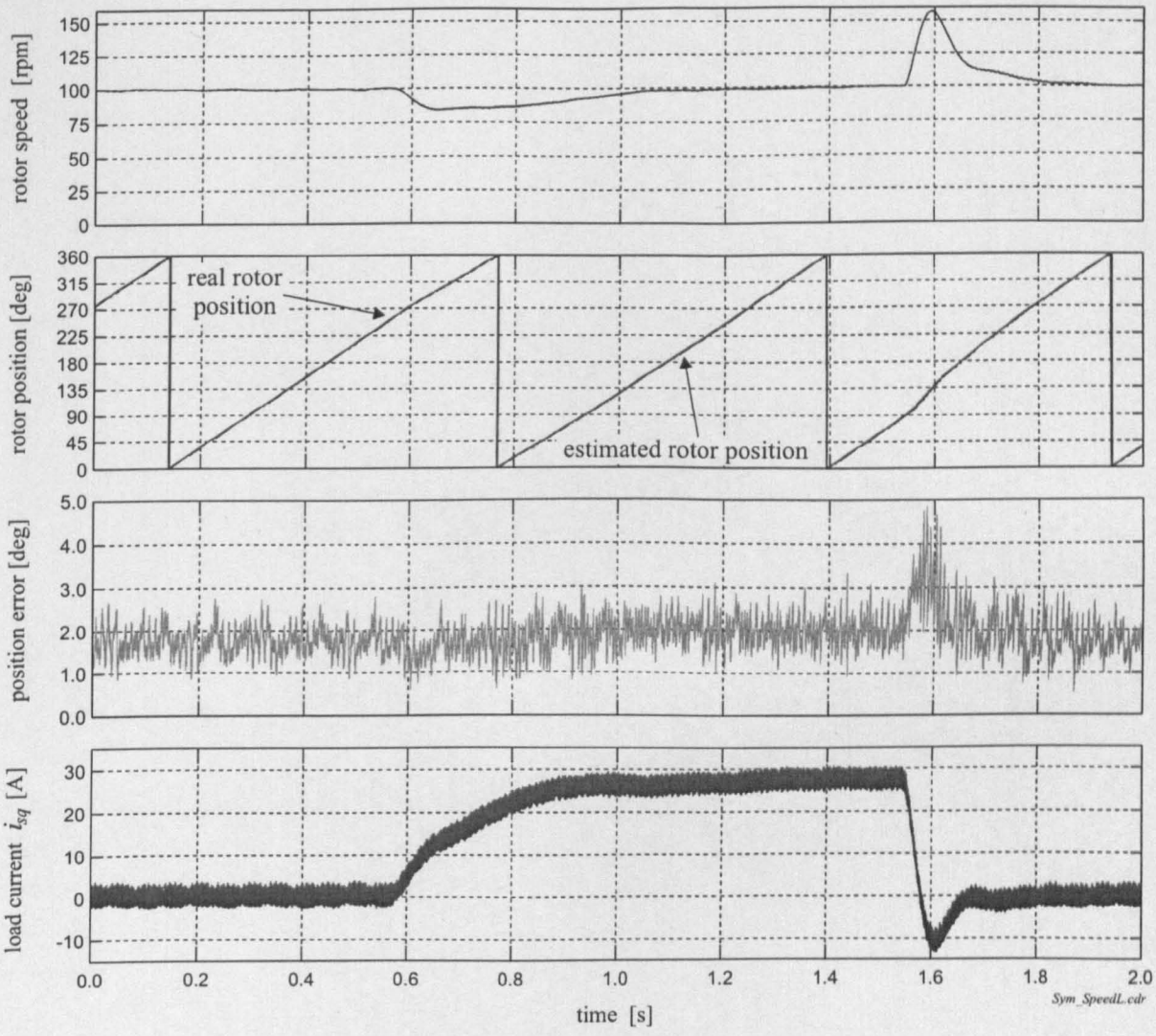

Figure 8.19: *Rotor position tracking for loaded machine at high and changing speed and fully fluxed machine*

This however does not imply that the drive automatically becomes unstable.

Position tracking under no-load:
Fig. 8.20 shows the effect of a compensation error while the rotor position is estimated. *Harmonic Compensation* is used and the machine is under IRFO and controlled using an encoder. A short distortion exceeds the commissioned compensation value and a cycle is missed. The result is the slipping of a cycle by $6.43° = 360°/N_r$. The same condition under sensorless control very likely causes the loss of orientation. This is because the *Harmonic Compensation* as applied, requires the flux angle for the correct compensation. The flux angle however gets distorted during a cycle slipping.

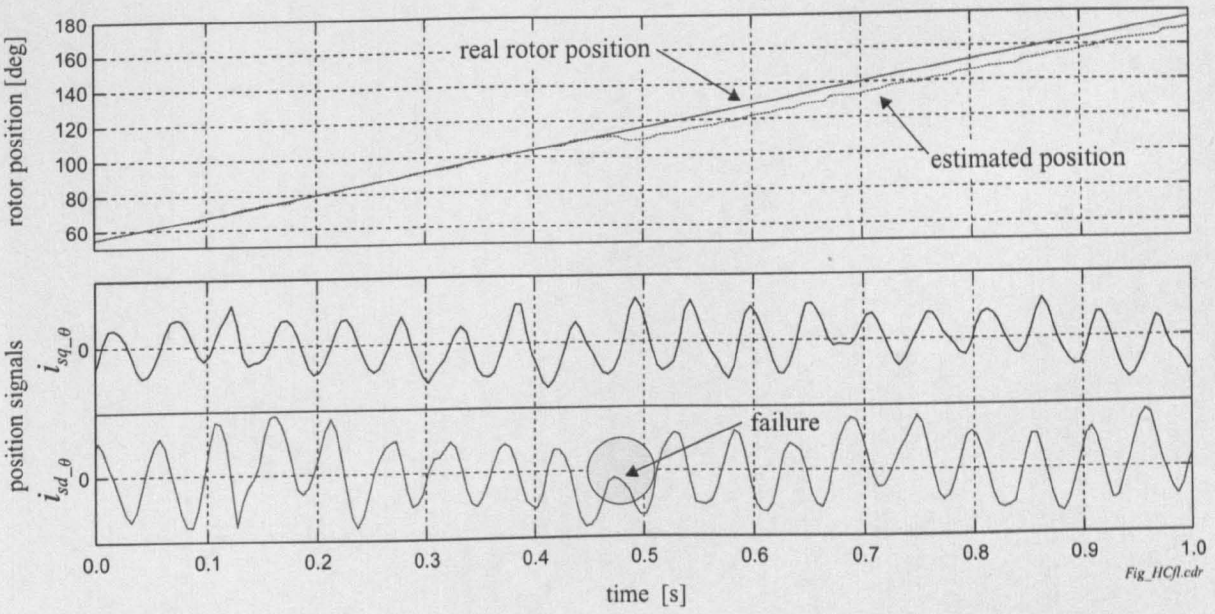

Figure 8.20: *Cycle slipping for harmonic compensation under sensored control and no load*

Sensorless position control under high load:
Fig. 8.21 shows the effect of a cycle slipping under sensorless position control using *SMP*. A short spike causes the $i_{s_{d\_\theta}}$ component to change the quadrant and the direction of the estimated rotor position is reversed for a short time. This effect cannot directly be seen on the measured position due to the inertia of the rotor. The rotor is controlled reliably, however now with an offset of $360°/N_r$ between estimated and real position. The temporary loss of position has a direct effect on the line currents. A spike can be seen on the currents in the lower plot of Fig. 8.21. The use of the angle of the stator current vector $\angle \underline{i}_s$ is responsible for the improved robustness of the sensorless drive. Comparing *Harmonic Compensation* with the *SMP*, the latter is currently the better method. The result in Fig. 8.21 is for the sensorless drive and high load whereas Fig. 8.20 is for no-load and during position tracking. The sensorless drive using the *Harmonic Compensation* became unstable when cycle slipping occurred.

It has not been investigated so far how to improve the robustness of the sensorless drive and how to reliably detect cycle slipping. Cycle slipping can be the result of *transient modulation*, modulation due to inverter zero-clamping or insufficient compensation. One possibility might be the analysis of the quadrants of the *arcus tangens* function during the position estimation. This technique allows the detection,

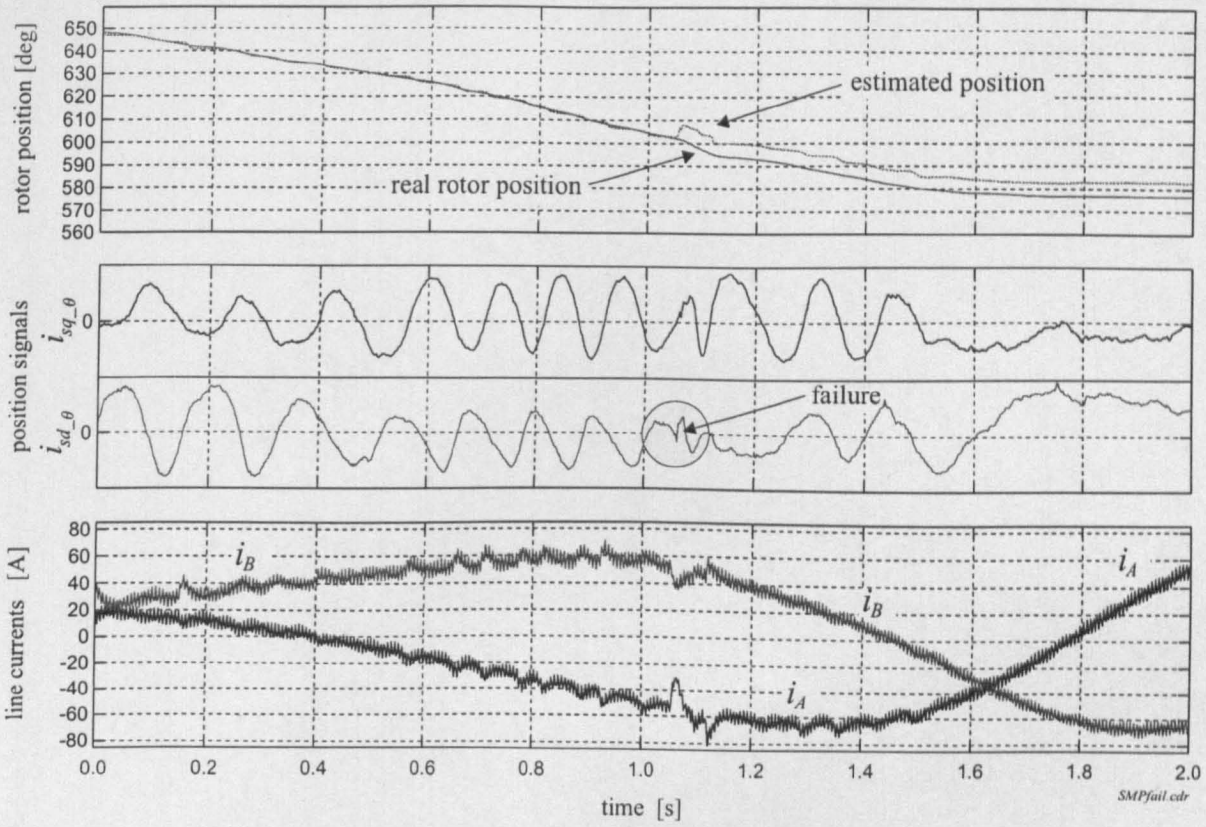

Figure 8.21: *Cycle slipping for sensorless control using SMP for drive under high load*

if a quadrant has been missed out. The technique has not yet been implemented and verified in the experiment. The general difficulty of detecting estimation errors is that a short position distortion can also be due to a change of the load by the dynamometer. In an industrial system, the load is difficult to predict.

8.2.3 Closed Loop Sensorless Position Control

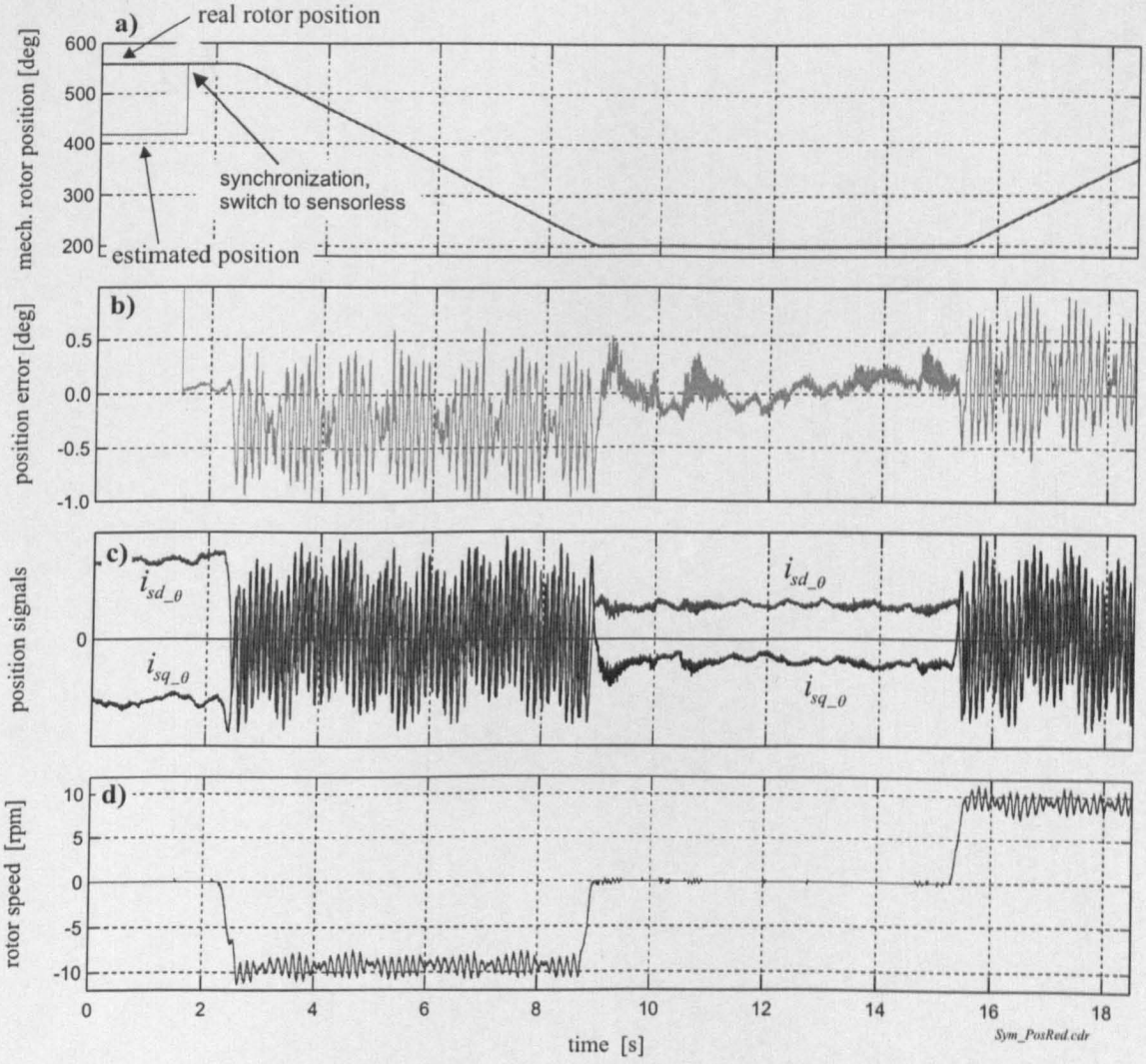

Figure 8.22: *Encoderless position control for induction machine for reduced flux level*

This section shows the experimental results for the closed loop and sensorless position control of the symmetric machine (rotor #3). The structure of the sensorless drive is that of Fig. 8.1. The sampling of the *hf* currents was running every 200μs. The demodulation was performed at the same rate. Compensation and the estimation of the rotor position was performed every 600μs. Also the current model and the position controller were updated and executed at this rate. An initial result is shown

for sensorless position control that using *Harmonic Compensation.* The other results use *SMP.*

Sensorless position control using Harmonic Compensation:
In Fig. 8.22 the 30kW induction machine is operated under encoderless IRFO. The drive is controlled for slow changes in the rotor position for the machine at no load and 60° rated flux. *Harmonic Compensation* is applied to reduce the distortion that is on the rotor slotting saliency harmonic. Fig. 8.22-a shows the real and estimated rotor position. While at standstill, the drive is switched to sensorless operation by synchronizing the estimated position with the real position. Then the real position is merely used as a reference for evaluating the quality of the sensorless operation. The estimated rotor position serves as feedback for the position controller and to calculate the angle for field orientation. The position is changed by one revolution. Subplot *(d)* shows the speed from the encoder during the position changes which is −10rpm or +10rpm for decreasing or increasing position respectively. The drive is not speed-controlled, the position controller follows a slowly changing ramp with 58°/s. The position error is less than ±1° and shows the typical speed-dependency. The position signals in subplot 8.22-c have $N_r = 56$ sinusoidal periods since the position is changed by exactly one revolution. When the position is constant, the position signals $\underline{i}_{s_{dq\_\vartheta}}$ are at DC.

Sensorless position control using SMP:
Initial results for the 30kW induction machine under encoderless IRFO using *SMP* are shown in Fig. 8.23. The drive is controlled for a 360° position change (mechanical) under no load and full flux. The ramp is set for 85°/s. The negative sequence harmonics are extracted using the additional Lowpass filter 5 of Fig. 5.17 with f_{cut} = 100Hz suppresses the carrier and positive sequence harmonics. Filter 4 was initially not used. The α and β stator currents are sent through lowpass filters 1 and 2 with f_{cut} = 100Hz to derive the stator current angle. The compensated position signals $i_{s_{d\_\vartheta}}$ and $i_{s_{q\_\vartheta}}$ are smoothed by a first order lag (filters 6 and 7) with $T_f = 8ms$.
From the *SMP* compensation data in Figs. 7.15 and 7.16 it can be seen that for full flux a large saturation saliency exists even at no-load. The distortion due to *inverter zero-clamping* is also severe. The relation of saturation and clamping modulation to the magnitude of the position signals $\underline{i}_{s_{dq\_\vartheta}}$ due to the rotor slotting is given by comparing subplots 8.23-c and d. The mean amplitude of the position signals is here defined as 100%. From Fig. 8.23-d, the magnitude of the required *SMP* compensation can reach up to twice the magnitude of the position signals. In Fig. 8.22 the compensation applying *Harmonic Compensation* was easier since the machine was not fully fluxed which reduces saturation and the current clamping effect.
Fig. 8.23-a shows the real and estimated rotor position. The drive is initially sen-

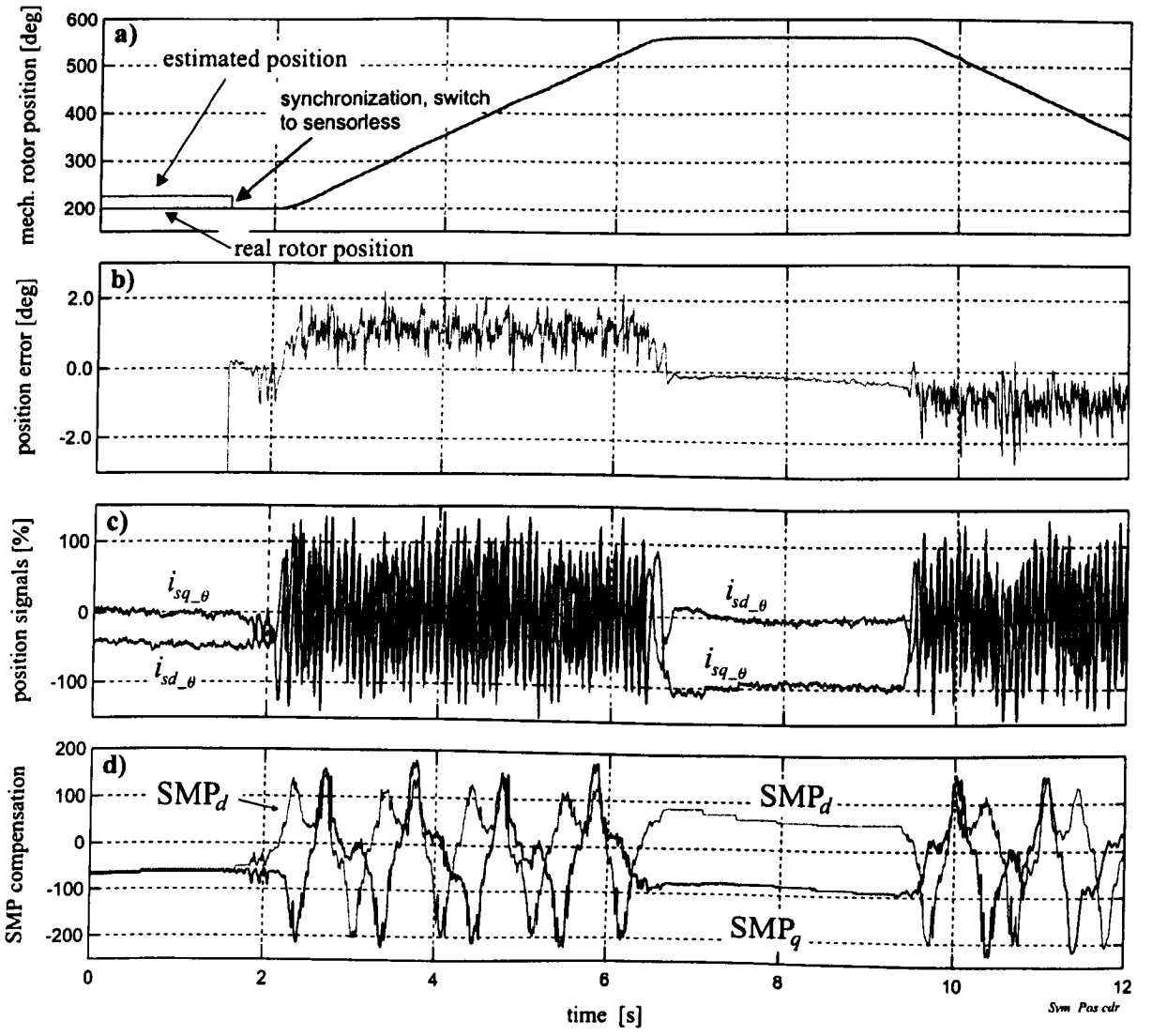

Figure 8.23: *Encoderless position control for fully fluxed machine over a* 360° *position change*

sored, using the position information from the encoder. Then the estimated rotor position is aligned to the real position and the drive is switched over to encoderless operation. Alignment is a simple software procedure. An extended register is used in the microprocessor to hold the value of the rotor position estimate. Since the position estimation works incrementally (see differentiation in equation (5.77)), the difference between two position samples is computed and added to the position register. By aligning, the value of the position register is loaded once with the value of the encoder position. A state variable is used to prevent continuous reloading of the position register. The advantage of the alignment or position synchronization is

that the switch-over to sensorless position control is smooth and does not cause any position transients. Position alignment is however not mandatory and the drive can of course be started directly in encoderless mode. The position alignment also allows the determination of the position error that is shown in subplot 8.23-*b*. The position accuracy is mostly within ±1.5° mechanical. Fig. 8.23-*c* shows the modulation envelopes $\underline{i}_{s_{dq\_\theta}}$ that are used to derive the rotor position.

Results for sensorless operation are only shown for low dynamics. This is because a fast position transient causes a high $\frac{di_{sq}}{dt}$ that will result in a *transient modulation.* This modulation has currently not been compensated for. It usually lasts for only a few milliseconds (typically less than $10ms$) but can cause a complete loss of the estimated position.

With the structure of the estimator as used for the results in Fig. 8.23, the maximum speed at that could be reliably operated was around 25rpm to 30rpm only. The problem could be diagnosed to be in the insufficient quality of the original *SMP* commissioning. A better strategy for data averaging and the introduction of the anti-causal filter (number 6 in Fig. 7.11) were major improvements. In addition, the filters shown in the demodulator and estimator of Fig. 5.17 were tuned for higher bandwidth. Care was taken that the delays in parallel filter paths as that for demodulation and for addressing the compensation tables was similar. The negative sequence harmonics are extracted using the additional highpass filter 4 with f_{cut} = 15Hz to remove the carrier component. Lowpass filter 5 with f_{cut} = 300Hz suppresses the remaining positive sequence harmonics.
The α and β stator currents are sent through lowpass filters 1 and 2 with f_{cut} = 100Hz to derive the stator current angle. The index to address the tabulated *SMP* data online was derived from i_{sq} via a lowpass filter of 100Hz cutoff frequency. Finally, the compensated position signals $i_{s_{d\_\theta}}$ and $i_{s_{q\_\theta}}$ are smoothed by a first order lag (filters 6 and 7) with $T_f = 3.5ms$. These two lowpass filters became necessary under sensorless operation to minimize errors due to short misalignments in the compensation that easily result in cycle slipping (see Section 8.2.2).

Sensorless position control for a sequence of position changes:
Fig. 8.24 shows a slow position change of 85° mechanical while a constant load of 90% rated is applied. The reference is a periodic increasing and decreasing ramp with a short plateau of zero speed. The reference position is smoothed by a lowpass filter with time constant $T_f = 60ms$ that accounts for the slightly blurred shape of the estimated and real position in the upper plot. At the instance t = 2.2s the drive is switched to sensorless. This does not significantly affect the operation of the drive. The ripples on the line currents have increased for sensorless control as visible in

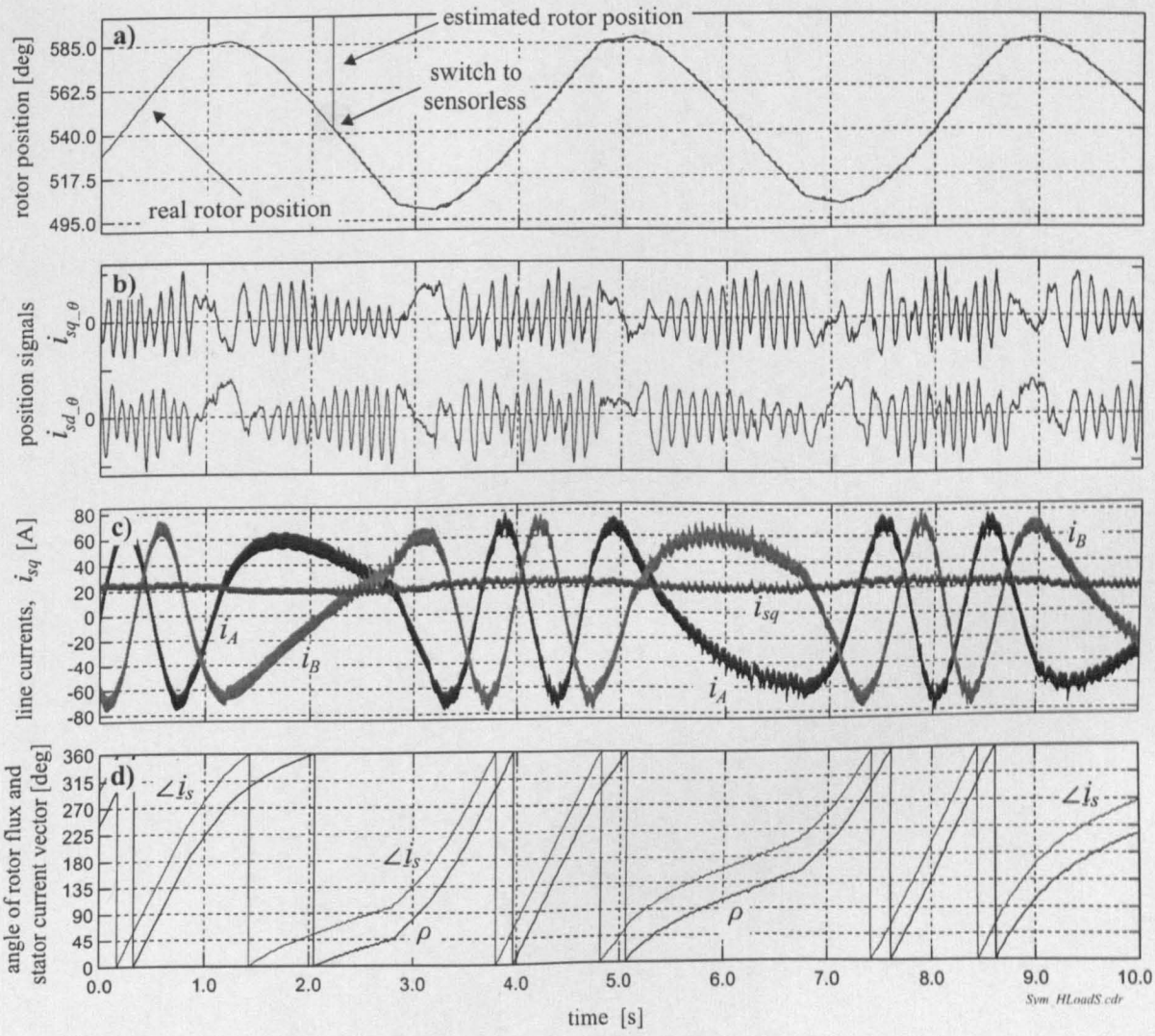

Figure 8.24: *Sensorless control for slow position transient under* 90% *rated load*

subplot *(c)*. The difference between real and the estimated rotor position is very small.

Fig. 8.24-*b* shows the two compensated position signals $\underline{i}_{s_{dq\_\theta}}$ that are sent to the position estimator to derive the rotor position. The 85° mechanical position change can be found in the number of slot ripples. There are about 13.3 periods since one revolution causes $N_r = 56$ slot periods. An unwanted modulation of the signal amplitude is visible on the real and imaginary part of $\underline{i}_{s_{dq\_\theta}}$ that is different for motoring and generating. This modulation is mainly caused by the harmonic at $\frac{N_r}{pp} \cdot f_r - 2f_e$ that currently is not included in the compensation. This modulation accounts for most of the distortion of the estimated rotor position.

The position error is the cause of the ripples on the line currents i_A and i_B in subplot *(c)*. The load current i_{sq} is also shown in this subplot and is mostly constant at a high level. The drive is operating in motoring mode when the position is increased and generating when the rotor position is decreased. The frequency of the line currents reflects this change in $f_e = f_r + f_{sl}$. During motoring, f_r and f_{sl} are positive and f_e is the sum of the two. In generating mode, f_r is negative and f_e is low. The slip frequency is relatively constant. The excitation f_e is between 0.16Hz during generation and 1.0Hz for the motoring mode.
The field angle ρ and the angle of the stator current vector $\underline{i}_s$ are shown in subplot *(d)* of Fig. 8.24. The angular difference is the load angle δ that is $\delta = \arctan(i_{sq}/i_{sd})$.

Sensorless position control for a sequence of position changes during load change:
Fig. 8.25 shows the sensorless drive during a sequence of position changes while the load is increased. The initial load is about 65% of rated load, the final load is 95% of rated. The reference torque of the dynamometer was changed slowly 'by hand'. The combined effect of load and position change can be seen on the line currents i_A and i_B in Fig. 8.25-*c* and the load current i_{sq} in subplot *(d)*. While the drive is changing position, the position feedback is switched from the encoder to the estimated rotor position. The estimated position gets aligned by software to the real position at this instance. The lead controller is not capable of maintaining the initial position for a load change. The shape of the position is tilted from the shape of Θ_r in Fig. 8.24. The compensated signals that provide the position estimate are shown in Fig. 8.25-*b*.

Sensorless position control for a load change:
Fig. 8.26 shows the encoderless drive controlled to maintain a given rotor position. The machine is fully fluxed. The load is increased manually from zero to full load and back to zero load. Since the position controller is not integral, it cannot maintain the position during the load change as could be seen similarly in Fig. 8.25. For a fixed load however the rotor position will be constant as can be seen in the centre of Fig. 8.26-*a* around $t = 15$s where the load is at rated value. The rotor position in the upper plot does not change linearly or smoothly because the load is set and changed manually via a potentiometer. Real and estimated position however match very well. Subplot *(b)* shows the imaginary position component $i_{s_{q\_c}}$ before compensation. The *SMP* is shown in the same plot. The result of the compensation can be seen in subplot *(c)* showing $i_{s_{d\_\beta}}$ and $i_{s_{q\_\beta}}$. During operation at full load a ripple component is visible on both compensated position signals. This slow ripple has the frequency $2f_e$ and is due to a small mismatch in the compensation of the saturation modulation. Fig. 8.26-*d* shows the line currents i_A and i_B and the load current i_{sq}. Starting from no-load where the line currents are at DC, the frequency and amplitude increases with increased load.

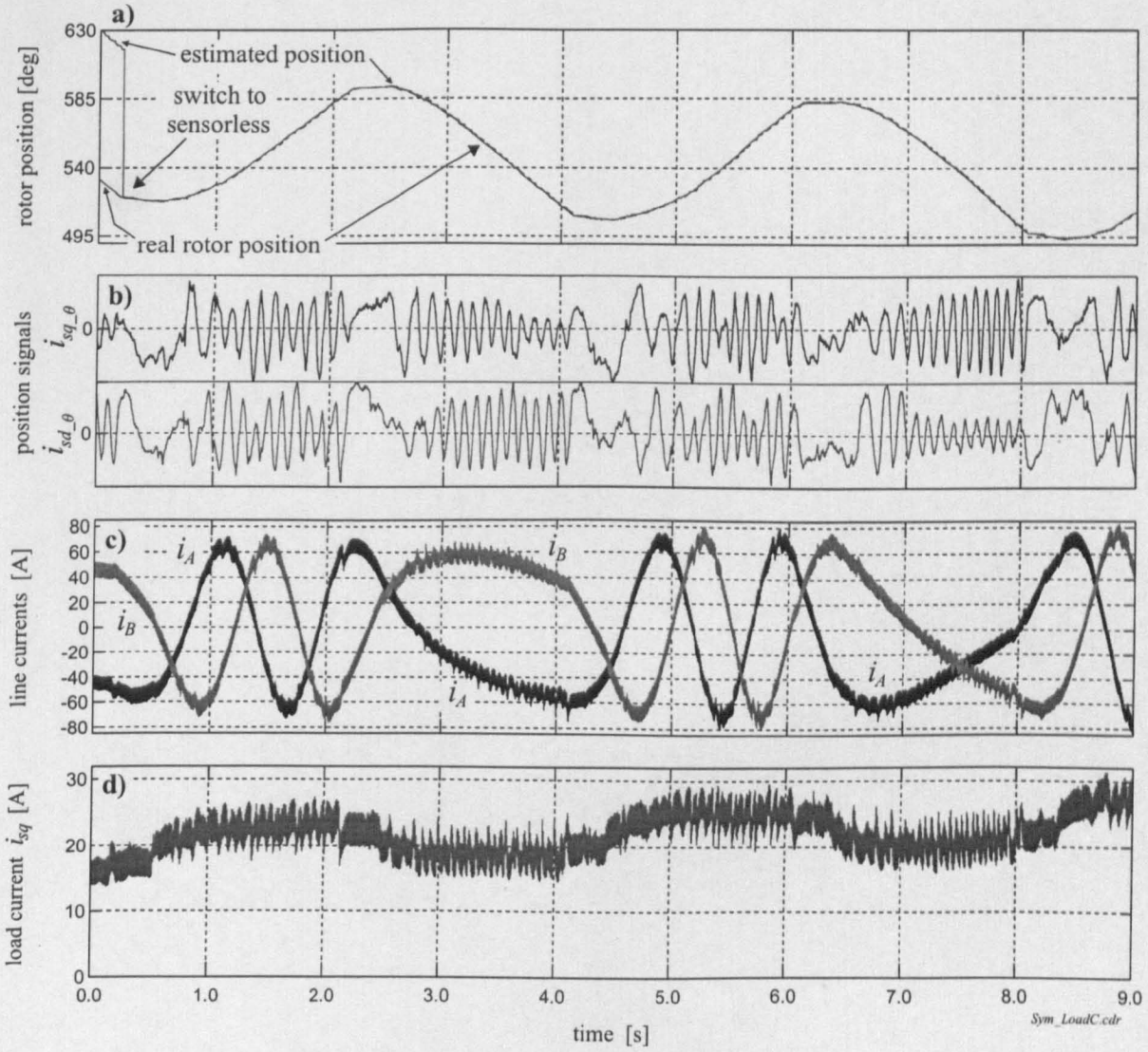

Figure 8.25: *Encoderless position control for fully fluxed machine under high and increasing load*

Sensorless position control performing fast transient:
A faster position transient of the sensorless drive is shown in Fig. 8.27. The machine is fully fluxed and the load is constant and 80% of rated load. The commanded position change of 180° takes 0.75 seconds. The maximum rate of change of the ramp is 300° per second that is 50rpm. The speed profile obtained from the encoder is shown in the third plot. The upper plot shows the rotor position in mechanical degrees. The real rotor position follows the reference position very closely. The difference

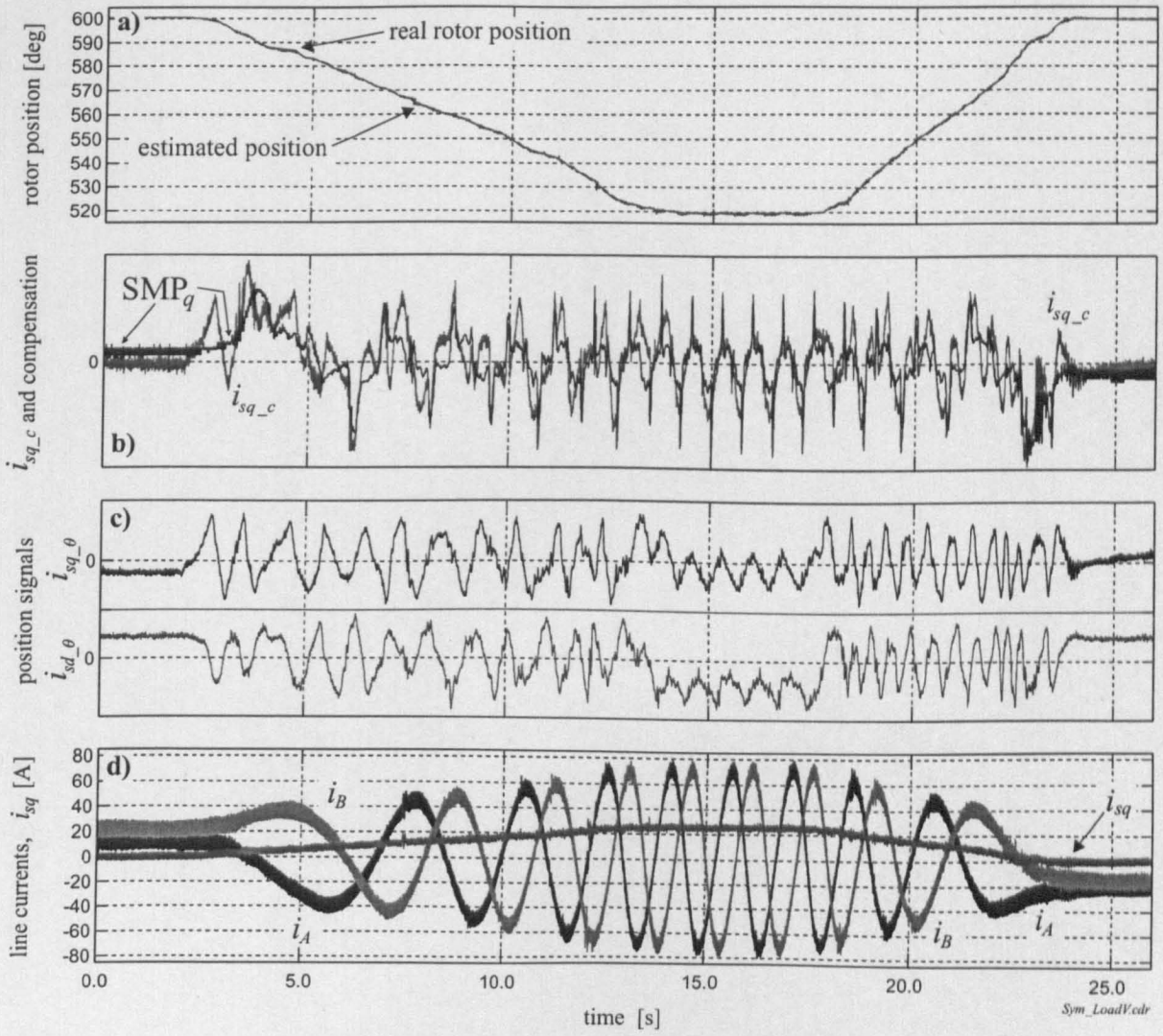

Figure 8.26: *Encoderless position control for fully fluxed machine under changing load*

between real and estimated position is very small and can hardly be seen in the figure. The position signals $i_{s_{d\_\theta}}$ and $i_{s_{q\_\theta}}$ that are obtained after compensation are shown in Fig. 8.27-*b*. They are used to derive the position estimate of subplot *(a)*. In steady-state, the position signals are ideally DC values and constant. In reality, the rotor is moving slightly which can be seen in the small sinusoidal variation in $i_{s_{d\_\theta}}$ and $i_{s_{q\_\theta}}$. The reason is an imperfect compensation and small torque ripples due to the load. Short spikes are the result of the imperfect compensation and cause a position estimation error and can also cause a distortion of the currents as seen in Fig. 8.27-*d*. The two measured line currents i_A and i_B are shown and the load

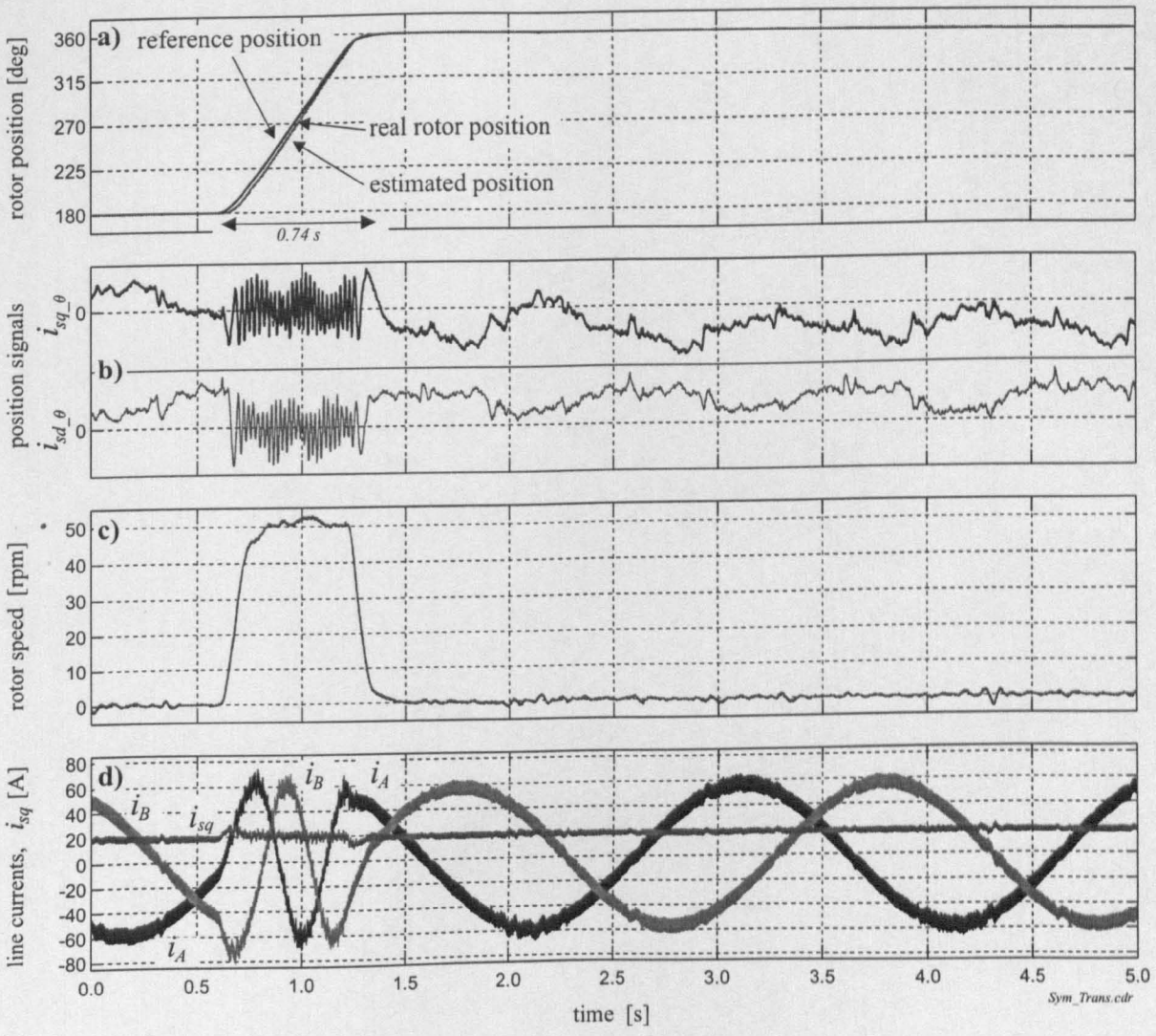

Figure 8.27: *Sensorless control of fast position transient*

current i_{sq}. For the position change at $t = 0.6$s, the frequency and amplitude of the line currents changes instantaneously. After the position transient, the line currents are back to the initial amplitude and frequency. The *hf* currents due to the *hf* voltage injection can be seen as a band around the fundamental currents in subplot *(d)*. The short distortions from the sinusoidal shape on the line currents is due to errors in the position estimation. This distortion is largest when one of the line currents is crossing through zero. Since the currents are balanced, a distortion can also be seen on the other two currents when these have an amplitude of ±86.6%. An improvement in the *SMP* compensation would reduce this distortion.

This current is magnified in the upper plot of Fig. 8.28. During steady-state operation, the load current is a DC value with the superimposed *hf* currents of 750Hz. Due

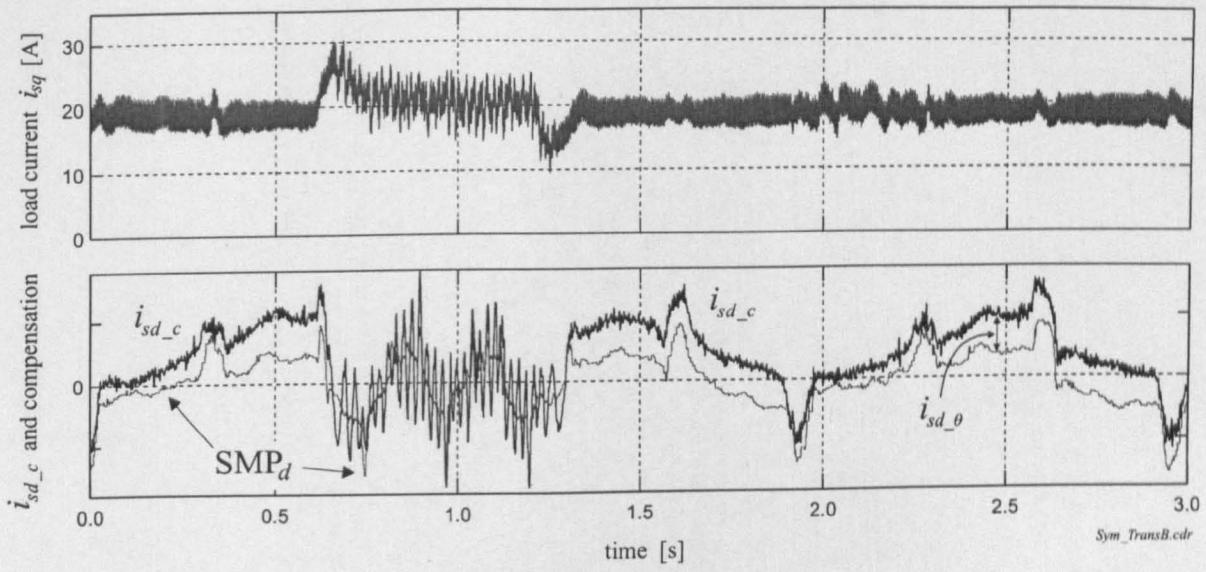

Figure 8.28: *Sensorless control of fast position transient showing i_{sq} and the compensation using SMP (additional signals for transient of Fig. 8.27)*

to the *d-q* transformation, the frequency of the *hf* current ripple will be altered by f_e. This frequency however is small compared to the injection frequency of f_c. The increase in i_{sq} is due to the acceleration of the machine and the negative dip slows the machine when the demanded position is reached. The lower plot of Fig. 8.28 shows $i_{s_{d\_c}}$, that is one of the two position signals before compensation. The compensation profile SMP_d is shown that is used in real-time to remove the saturation and clamping modulation. The difference of $i_{s_{d\_c}}$ and SMP_d is the compensated signal $i_{s_{d\_\theta}}$ that is shown in Fig. 8.27. During standstill, the clamping distortion can last in the range of up to $100ms$. During the position transient however, the distortion causes spikes of $10ms$ and less. It can clearly be seen in the lower plot of Fig. 8.28 that the *SMP* is well aligned to suppress this distortion.

The transient shown in Fig. 8.27 currently represents the upper range for forward speeds. It is expected that a compensation of the distortion due to *transient modulation* will further improve the dynamics. The maximum negative speed is lower than 50rpm. The reason for that has not been sufficiently examined. It is possible that the saturation harmonic at $-28f_r + 2f_e$ might have to be compensated in this case.

Sensorless position control performing sequence of transients:
Another position transient of the sensorless drive is shown in Fig. 8.29. The position change is 300° mechanical and larger than in Fig. 8.27. The machine is fully fluxed and the stationary load is 90% of rated load. The upper plot (subplot *(a)*) shows

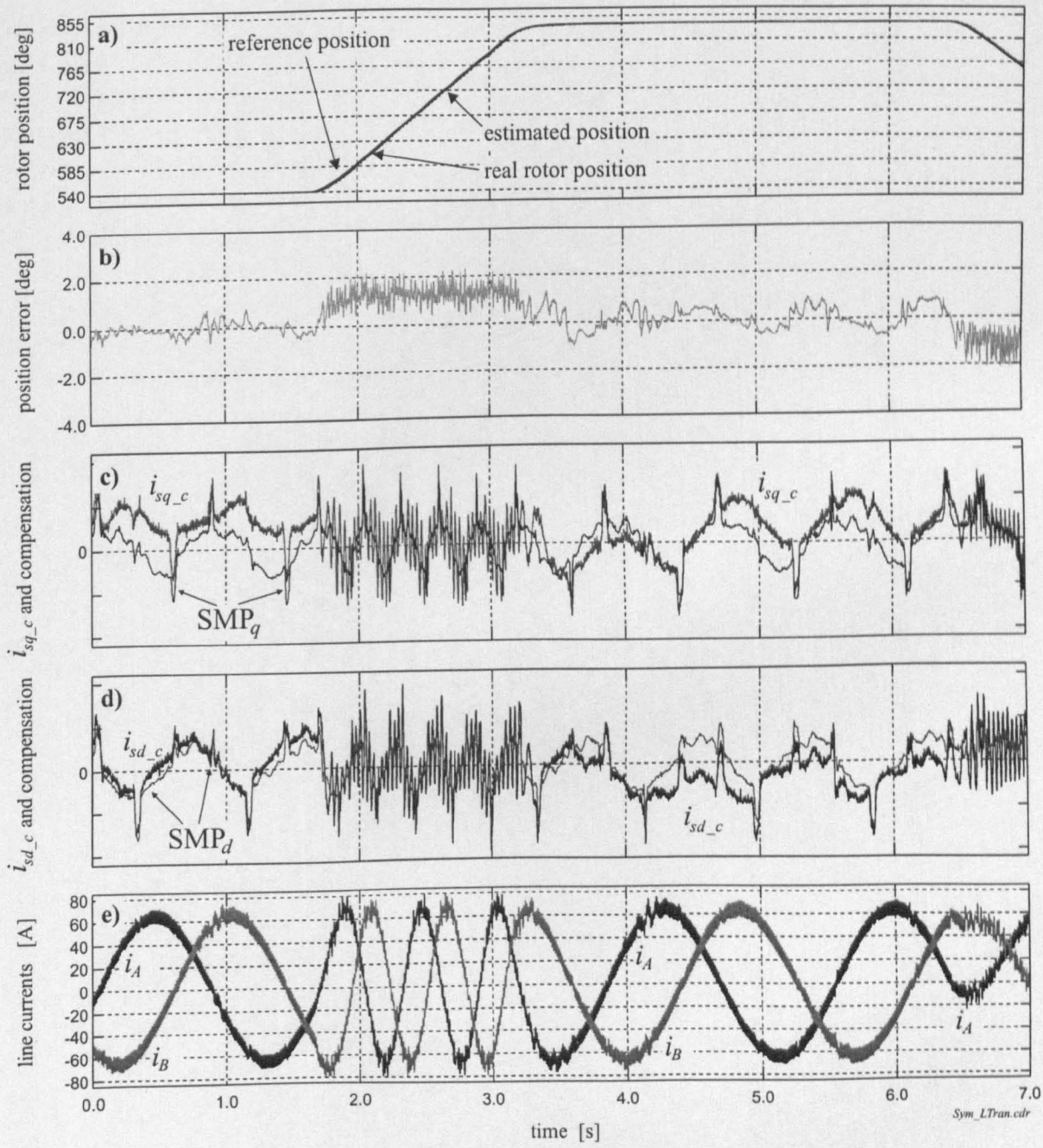

Figure 8.29: *Sensorless control of fast position transient showing rotor position, position error position signals and respective space-modulation profiles and line currents*

the demanded reference position, estimated and real rotor position. The difference between real and estimated rotor position is shown in subplot *(b)*. The mean error during sensorless operation is less than $\pm 0.9°$. For higher speeds, the filters introduce

an additional error that is currently about 2.6° mechanical per 100rpm. Fig. 8.29-*c* and Fig. 8.29-*d* show the position signals $\underline{i}_{s_{dq\_c}}$ and the respective *space-modulation profiling* that is used in real-time to remove the interfering modulation and to extract the rotor position information. There are 6 clamping spikes per electrical revolution or one period of the line currents that are shown in subplot *(e)*. Clearly, the clamping spikes are larger than the modulation signal from the rotor slots. Without *SMP* and suppression, the position estimator would fail at the first instance of a current crossing. The pre-commissioned *SMP* table ensures reliable and sensorless operation. The suppression algorithm manages transient and steady-state operation and allows field-orientated control of an induction machine. Amplitude and frequency of the line currents are controlled dynamically as demonstrated in Fig. 8.29-*e*.

Chapter 9:

Conclusion

This thesis deals with the estimation of rotor saliencies for use in sensorless position-controlled induction machine drives.

Rotor saliencies can be due to the natural slotting effect of the rotor or can be engineered (asymmetric rotor). They cause a position-dependent modulation in currents or voltages that is independent of the machine parameters and even exists at standstill. High-frequency voltage injection is used in this research to separate the modulated currents from the large fundamental.

The objective was to exploit the use of rotor saliencies to enhance the operation of vector controlled induction machine drives at low speeds and standstill without the need for an encoder.

This thesis has shown that additional harmonics due to saturation in the machine, modulations due to the nonlinearity of the inverter and transient machine operation interfere with the rotor saliency harmonics and cause a severe distortion of the signals supplying the position estimation. This distortion prevents the useful application of rotor saliencies in machine control in particular when the machine is loaded.

The main aim was to make sensorless position control possible under all loads. For the asymmetric machine this has been achieved. For the symmetric machine, initial results for the machine under full flux and under different loads and speeds are presented. These results demonstrate for the first time that sensorless position control of induction machines is feasible.

Two compensation strategies have been developed for the effective online compensation of the interfering saliency harmonics. *Harmonic Compensation* requires an offline commissioning to analyze the characteristic of each saliency harmonic which one wishes to eliminate. The data is then stored in a lookup table for the use in an online compensation to suppress the respective saliency harmonic. The commissioning accounts for the change of the saliency harmonics in magnitude, phase and frequency with the operation condition.

A structure for auto-commissioning has been developed to simplify the acquisition of the saliency parameters.

This research has also shown that the inverter can cause a significant distortion of the *hf* signals due to *hf* modulation during fundamental current zero-crossing. This *hf* phenomenon has not been addressed before in literature. A theoretical and practical analysis of this problem is given in this thesis. A second commissioning strategy termed *Space-Modulation Profiling* has been developed to cope better with the zero-current clamping modulation.

Space-Modulation Profiling determines the difference between the rotor saliency and the remaining *hf* modulation profile in the time-domain. This information can be stored for every operation condition in a lookup table to be used online for harmonic suppression. This strategy allows the tracking of the rotor position and sensorless position control.

The research has also contributed in analyzing and assessing different saliency models, position estimators and demodulation techniques. The result is an improved signal processing for the demodulation and estimation of the rotor position.

The *Space-Modulation Profiling* is an open-loop feedforward compensation. This structure is not optimal when system parameters of the drive change, such as controller bandwidth or injection frequency. A feedback system would be more attractive in practice to reduce the zero-current clamping modulation of the *hf* currents. A possible choice of the feedback signal are the *hf* stator voltages that could be measured and compared to the known reference voltages. The difficulty is the correct and instantaneous measurement of the voltage pulses. This might be the reason why it has not been possible yet to correlate the *hf* voltage modulation with clamping phenomenon.

During the work with the symmetric rotor the distortion during dynamic operation was identified as the primary limiting factor for higher performance of the sensorless

drive. A solution might be the use of a compensation such as that in [138].

A further point that will have to be addressed in future research is how to improve the robustness of the sensorless drive. For the asymmetric drive, good compensation was achieved when the compensation was aligned to the rotor flux vector. Alignment with different vectors such as the stator current vector should be investigated to determine if the stability of the compensation can be improved. The rotor flux angle might not be the best choice under dynamic operation since it is parameter dependent. If the compensation fails, the rotor position estimate will not be correct and the drive might lose orientation. Research into this field can be instructive.
Possibilities for this field of investigation might be the analysis of position estimation under V/f control and maybe the inclusion of estimating the saturation saliency in parallel to estimating the position saliency. The latter might be possible for rotors with two accentuated harmonics only, i.e. the position harmonic and only one saturation harmonic. A more sophisticated estimator will be required to estimate rotor speed and saturation angle simultaneously.

An outstanding question is the optimal design for engineered rotor saliencies. More attractive are symmetric rotors where the rotor slotting saliency can be used for estimating the rotor position. A more thorough examination on a wider range of machines is required to identify more accurately the required slotting geometry of machines for sensorless position control using the rotor slotting effect.

A main issue is the improvement of the structure of the position controller. The current lead controller does not maintain position when the load is changed. The solution would be an outer PI position controller and an inner speed loop. The cascaded structure overcomes the difficulty of the controller design with two integrator poles from the mechanical plant. Deriving a speed estimate from the estimated rotor position is however not a trivial problem if the dynamic performance is not to be sacrificed. The speed estimate will be very noisy and requires filtering. A solution could be to include a model of the mechanical plant where the output is adjusted by the estimated position. The possible disadvantage is that the estimated speed from this observer is likely to be also noisy and the structure is not too attractive since the mechanical parameters and the load torque have to be known.

A topic not addressed in this thesis is how to estimate the absolute position in an induction machine. Possible solutions include the addition of a built-in and known distortion into the rotor, e.g. a once per revolution notch in the slot bridge or wider/narrow slot channel.

One application of using saliencies in sensored drives could be the tuning of field orientation via the saliency angle. This can be difficult under transients due to the limited dynamics of the *hf* signal processing and the current problems due to the *transient modulation.* It should however work under low dynamic conditions given the knowledge of the 'saliency profile' for the specific machine.

A topic not examined in this thesis is the combination of model-based sensorless control with saliency control during the low-speed operation. A possible solution is to combine the rotor saliency estimator with an adaptive observer for high-speed operation via a PI-controllers (MRAS). The speed range of rotor #1 with the engineered rotor saliency of ±150rpm or possibly ±200rpm is regarded as sufficient for a reliable transition. Rotor #3 still requires improvements to double the operational speed range.

An interesting task would be the implementation of the *Harmonic Compensation* and *Space-Modulation Profiling* for other saliency estimators such as that by Schrödl [18] or by Sul [20].

Interesting for sensorless position control of induction machines is the saliency modulation due to an anisotropy in the rotor. To exploit this saliency, the laminations need to be aligned during manufacturing. The anisotropy has the potential to be used on any rotor. It is however not known if the magnitude of the saliency will be sufficient and if the resolution of the estimated position will be high enough for reliable machine operation.

Publications:

This research has resulted in two conference papers [50,83] and one journal publication [51] with two more publications pending [147,148].

Bibliography

[1] Charles A. Ruch, "George Westinghouse – Engineer and Doer," *IEEE Transactions on Industry Applications*, vol. 20, no. 6, pp. 1395 – 1402, Nov./Dec. 1984.

[2] G. R. Slemon, "Electrical Machines for Variable-Frequency Drives," *in Proc. of the IEEE*, vol. 82, no. 8, pp. 1123 – 1139, Aug. 1994.

[3] A. T. de Almeida and P. Fonseca, "Characterisation of EU Motor Use," in *Energy Efficiency Improvements in Electric Motors and Drives*, P. Bertoldi, A. T. de Almeida, and H. Falkner, Eds., pp. 143 – 167. Springer-Verlag, Heidelberg, Germany, ISBN: 3-540-67489-6, 2000.

[4] T. Sawa and K. Hamada, "Introduction to the Permanent Magnet Motor Market," in *Energy Efficiency Improvements in Electric Motors and Drives*, P. Bertoldi, A. T. de Almeida, and H. Falkner, Eds., pp. 81 – 94. Springer-Verlag, Heidelberg, Germany, ISBN: 3-540-67489-6, 2000.

[5] Bimal K. Bose, Ed., *Power Electronics and Variable Frequency Drives*, IEEE Press, Piscataway, NJ, USA, ISBN: 0-7803-1084-5, 1997.

[6] F. Blaschke, "The Principle of Field Orientation as Applied to the New Transvektor Closed-Loop Control System for Rotating-Field Machines," *Siemens Review 39*, , no. 5, pp. 217 – 220, 1972.

[7] W. Leonhard, *Control of Electrical Drives*, 2. Auflage. Springer-Verlag, Berlin Heidelberg, Germany, ISBN: 3-540-59380-2, 1986.

[8] K. Hasse, *Zur Dynamik drehzahlgeregelter Antriebe mit stromrichtergespeisten Asynchron-Kurzschlußläufermaschinen*, Ph.D. thesis, TH Darmstadt, Darmstadt, Germany, 1969.

[9] H. Schierling, "Self-Commissioning – A Novel Feature of Modern Inverter-Fed Induction Motors," in *Proc. PEVD Conf.*, London, UK, 1988, pp. 287 – 290.

[10] G. Heinemann, *Selbsteinstellende, feldorientierte Regelung für einen asynchronen Drehstromantrieb*, Ph.D. thesis, TU Braunschweig, Braunschweig, Germany, Aug. 1992.

[11] H. Kubota and K. Matsuse, "Speed Sensorless Field-Oriented control of Induction Motor with Rotor Resistance Adaptation," *IEEE Transactions on Industry Applications*, vol. 30, no. 5, pp. 1219 - 1224, September/October 1994.

[12] J. Bier and C. Kellerhoff, "Qual der Wahl - der 'richtige' DSP," *Elektronik*, vol. 10, pp. 94 - 107, 1996.

[13] H. Le-Huy, "Microprocessors and Digital ICs for Motion Control," *in Proc. of the IEEE*, vol. 82, no. 8, pp. 1140 - 1163, Aug. 1994.

[14] TMS320C24x DSP Controllers: Reference Set, "Volume 2: Peripheral Library and Specific Devices, Literature Number: SPRU161A," Tech. Rep., Texas Instruments, Houston, Texas, USA, Mar. 1997.

[15] J. Holtz, "Methods for Speed Sensorless Control of AC Drives," in *Sensorless Control of AC Motor Drives*, K. Rajashekara, Ed., pp. 21 - 29. IEEE Press, Piscataway, 1996.

[16] R. Blasco-Giménez, G. M. Asher, and M. Sumner, "Rotor Time Constant Identification in Sensorless Vector Control Drives Using Rotor Slot Harmonics," in *Proc. EPE Conf.*, Sevilla, Spain, 1995, pp. 1083 - 1088.

[17] P. L. Jansen and R. D. Lorenz, "Transducerless Position and Velocity Estimation in Induction and Salient AC Machines," in *Conf. Rec. IEEE-IAS Annual Meeting, no. 29*, 1994, pp. 488 - 495.

[18] M. Schrödl, *Sensorless Control of A.C. Machines*, Fortschr.-Ber., VDI Reihe 21, Nr. 117. VDI-Verlag GmbH, Düsseldorf, 1992.

[19] P. L. Jansen and R. D. Lorenz, "Transducerless Field Orientation Concepts Employing Saturation-Induced Saliencies in Induction Machines," in *Conf. Rec. IEEE-IAS Annual Meeting, no. 30*, Orlando, USA, Oct. 1995, vol. 1, pp. 174 - 181.

[20] S.-K. Sul and J.-I. Ha, "Sensorless Field Orientation Control of an Induction Machine by High Frequency Signal Injection," in *Conf. Rec. IEEE-IAS Annual Meeting, no. 32*, New Orleans, USA, Oct. 1997, vol. 1, pp. 426 - 432.

[21] J. Holtz and J. Jiang, *Verfahren und Vorrichtung zur geberlosen Rotorlagemessung bei Asynchronmaschinen mit Kurzschlussläufer*, Patent EP 0 860 939 A1. European Patent Office, Munich/Den Haag, 1997.

[22] J. Cilia, *Sensorless Speed and Position Control of Induction Motor Drives*, Ph.D. thesis, Department of Electrical & Electronic Engineering, University of Nottingham, England, Oct. 1997.

[23] P. L. Jansen and R. D. Lorenz, *Method and Apparatus for Transducerless Position and Velocity Estimation in Drives for AC Machines*, Patent 5,585,709. U.S. Patent Office, USA, Dec. 1996.

[24] J. Cilia, G. M. Asher, K. J. Bradley, and M. Sumner, "Sensorless Position Detection for Vector-Controlled Induction Motor Drives using an Asymmetric Outer-Section Cage," *IEEE Transactions on Industry Applications*, vol. 33, no. 5, pp. 1162 -1169, Sept./Oct. 1997.

[25] C. Spiteri Staines, *Sensorless Position Estimation in Asymmetric Induction Machines*, Ph.D. thesis, Department of Electrical & Electronic Engineering, University of Nottingham, England, Nov. 1998.

[26] Frost & Sullivan International Marketing Consulting, "AC Technology Anticipated to Boost Sales in Variable Speed Drives Market," *Press Release*, p. on WEB page, (http://207.88.20.210/verity/press/industrial/pr328917.htm).

[27] Dr. Detlev Stupperich, "Fortschritte bei Servo-Reglern," *Konstruktion & Entwicklung: Sonderteil Antriebstechnik*, , no. 4, pp. on WEB page, (http://www.baumueller.com/PressePublikationen.htm#Fortschritte).

[28] A. Hughes, "Visualizing Vector Control in Cage Motors," in *Advances in Induction Motor Control*, IEE Seminar. IEE Power Division, London, UK, 23rd May 2000.

[29] M. Sumner, G. M. Asher, and R. Pena, "The Experimental Investigation of Rotor Time Constant Identification for Vector Controlled Induction Motor Drives during Transient Operating Conditions," in *Proc. EPE Conf.*, Brighton, UK, 1993, pp. 51 - 56.

[30] J. A. Campbell, M. Sumner, and M. Curtis, "An Improved sensorless Vector Controlled Induction Motor Employing Artificial Neural Networks for Stator Resistance Estimation," in *Proc. EPE Conf.*, Lausanne, Switzerland, Sept. 1999, vol. on CD-ROM.

[31] A. M. Khambadkone and J. Holtz, "Vector-Controlled Induction Motor Drive with a Self-Commissioning Scheme," *IEEE Transactions on Industrial Electronics*, vol. 38, no. 5, pp. 322 - 327, Oct. 1991.

[32] P. K. Kovács and I. Rácz, *Transiente Vorgänge in Wechselstrommaschinen*, Verlag der Ungarischen Akademie der Wissenschaften, Akadémiai Kiadó, 1959.

[33] I. Rácz, "Dynamic Behaviour of Inverter Controlled Motors," in *IFAC Conference*, London, UK, June 1966, pp. 20 – 25.

[34] P. K. Kovács, *Transient Phenomena in Electric Machines*, Studies in Electrical and Electronic Engineering 9. Elsevier Science Publishers B.V., Amsterdam, Netherlands, ISBN: 0-444-99663-X, 1984.

[35] I. Takahashi and T. Noguchi, "A New Quick-Response and High-Efficiency Control Strategy of an Induction Motor," *IEEE Transactions on Industry Applications*, vol. 22, no. 5, pp. 820 – 827, Sept./Oct. 1986.

[36] D. Lemp, *Realisierung eines asynchronen Antriebs mit direkter Fluß- und Drehmomentregelung*, Ph.D. thesis, Fachbereich 17 – Elektrische Energietechnik –, Technische Universität Darmstadt, Germany, Dec. 1997.

[37] M. Depenbrock, "Direkte Selbsregelung (DSR) für hochdynamische Drehfeldantriebe mit Stromrichterspeisung," *etz-Archiv, Band 7, Heft 7*, pp. 211 – 218, 1985.

[38] J.-K. Seok and S.-K. Sul, "Pseudorotor-Flux-Oriented Control of an Induction Machine for Deep-Bar-Effect Compensation," *IEEE Transactions on Industry Applications*, vol. 34, no. 3, pp. 429 – 434, May/June 1998.

[39] E. Kiel, *Anwendungsspezifische Schaltkreise in der Drehstrom-Antriebstechnik*, Ph.D. thesis, Technische Universität Braunschweig, Braunschweig, Germany, 1994.

[40] R. Blasco-Giménez, *High Performance Sensorless Vector Control of Induction Motor Drives*, Ph.D. thesis, Department of Electrical & Electronic Engineering, University of Nottingham, England, Dec. 1995.

[41] K. D. Hurst, H. G. Habetler, G. Griva, and F. Profumo, "Zero-Speed Tacholess IM Torque Control: Simply a Matter of Stator Voltage Integration," *IEEE Transactions on Industry Applications*, vol. 34, no. 4, pp. 790 – 795, July/Aug. 1998.

[42] R. Wu and G. R. Slemon, "A Permanent Magnet Motor Drive Without a Shaft Sensor," *IEEE Transactions on Industry Applications*, vol. 27, no. 5, pp. 1005 – 1011, Sept./Oct. 1991.

[43] M. Niemelä, *Position Sensorless Electrically Excited Synchronous Motor Drive for Industrial Use Based on Direct Flux Linkage and Torque Control*, Ph.D. thesis, Lappeenranta University of Technology, Lappeenranta, Finland, ISBN: 951-764-314-4, Mar. 1999.

[44] N. Hur, K. Nam, and S. Won, "A Two-Degree-of-Freedom Current Control Scheme for Deadtime Compensation," *IEEE Transactions on Industrial Electronics*, vol. 47, no. 3, pp. 557 - 564, June 2000.

[45] J.-W. Choi and S.-K. Sul, "Inverter Output Voltage Synthesis using Novel Dead Time Compensation," *IEEE Transactions on Power Electronics*, vol. 11, no. 2, pp. 221 - 227, Mar. 1996.

[46] H. Reinold, *Optimierung dreiphasiger Pulsdauermodulationsverfahren*, ABISEA Band 15. Mainz Publishing, Aachen, ISBN: 3-86073-235-8, 1996.

[47] H. W. Van der Broek, H.-C. Skudelny, and G. V. Stanke, "Analysis and Realization of a Pulsewidth Modulator Based on Voltage Space Vectors," *IEEE Transactions on Industry Applications*, vol. 24, no. 1, pp. 124 - 150, Jan./Feb. 1988.

[48] N. Teske, "Space Vector Modulation - A Description," Tech. Rep., Department of Electrical & Electronic Engineering, University of Nottingham, UK, Nov. 2000.

[49] K. Rajashekara, A. Kawamura, and K. Matsuse, Eds., *Sensorless Control of AC Motor Drives: Speed and Position Sensorless Operation*, IEEE Press, Piscataway, USA, ISBN: 0-201-52747-2, 1996.

[50] N. Teske, G. M. Asher, K. J. Bradley, and M. Sumner, "Sensorless Position Control of Induction Machines using Rotor Saliencies under Load Conditions," in *Proc. EPE Conf.*, Lausanne, Switzerland, Sept. 1999, vol. on CD-ROM.

[51] N. Teske, G. M. Asher, M. Sumner, and K. J. Bradley, "Suppression of Saturation Saliency Effects for the Sensorless Position Control of Induction Motor Drives under Loaded Conditions," *IEEE Transactions on Industrial Electronics*, vol. 47, no. 5, pp. 1142 - 1150, Oct. 2000.

[52] G. M. Asher, "Chapter 8: Sensorless Control of Induction Motor Drives, MSc Course handout," Tech. Rep., Department of Electrical & Electronic Engineering, University of Nottingham, UK, 2001.

[53] J.-S. Lee, T. Takeshita, and N. Matsui, "Stator-Flux-Oriented Sensorless Induction Motor Drive for Optimum Low-Speed Performance," *IEEE Transactions on Industry Applications*, vol. 33, no. 5, pp. 1170 - 1176, Sept./Oct. 1997.

[54] C. Schauder, "Adaptive Speed Identification for Vector Control of Induction without Rotational Transducers," *IEEE Transactions on Industry Applications*, vol. 28, no. 5, pp. 1054 - 1061, Sept./Oct. 1992.

[55] P. L. Jansen, R. D. Lorenz, and D. W. Novotny, "Observer-Based Direct Field Orientation - Analysis and Comparison of Alternative Methods," *IEEE Transactions on Industry Applications*, vol. 30, no. 4, pp. 945 - 953, 1994.

[56] T. Ohtani, N. Takada, and K. Tanaka, "Vector Control of Induction Motor without Shaft Encoder," *IEEE Transactions on Industry Applications*, vol. 28, no. 1, pp. 157 - 164, Jan./Feb. 1992.

[57] H. Kubota and K. Matsuse, "New Adaptive Flux Observer of Induction Motor for Wide Speed Range Motor Drives," in *Proc. IEEE IECON'90*, Nov. 1990, vol. 2, pp. 921 - 926.

[58] Siemens Documentation, "MICROMASTER, MICROMASTER Vector, MIDIMASTER Vector, COMBIMASTER: Variable Frequency Inverters for AC Motors up to 90 kW, Catalogue DA 64 -1998/99," Tech. Rep., Drives and Standard Products Group, Variable-Speed Drives Division, Siemens plc., Erlangen, Germany, Apr. 1999.

[59] R. Blasco-Giménez, J. Cilia, G. M. Asher, and K. J. Bradley, "Field Weakening at High and Low Speed for Sensorless Vector Controlled Induction Motor Drives," in *Proc. PEVD Conf.*, London, UK, Sept. 1996, vol. 4, pp. 258 - 261.

[60] M. Depenbrock, Ch. Foerth, and S. Koch, "Speed Sensorless Control of Induction Motors at Very Low Stator Frequencies," in *Proc. EPE Conf.*, Lausanne, Switzerland, Sept. 1999, vol. on CD-ROM.

[61] G. M. Asher K. Ohyama and M. Sumner, "Comparison of the Practical Performance and Operating Limits of Sensorless Induction Motor Drive using a Closed loop Flux Observer and a Full Order Flux Observer," in *Proc. EPE Conf.*, Lausanne, Switzerland, Sept. 1999, vol. on CD-ROM.

[62] J. Jiang and J. Holtz, "High Dynamic Speed Sensorless AC Drive with On-Line Parameter Tuning and Steady State Accuracy," *IEEE Transactions on Industrial Electronics*, vol. 44, no. 2, pp. 240 - 246, Mar./Apr. 1997.

[63] G. Turl, M. Sumner, and G. M. Asher, "Use of Adaptive Notch Filtering for Accurate Speed Holding in a Sensorless Induction Motor Drive," in *Proc. PEVD Conf.*, London, UK, Sept. 2000, pp. 268 - 273.

[64] A. Ferrah, K. J. Bradley, and G. M. Asher, "Application of the FFT to the Speed Measurement of Inverter fed Induction Mototrs," in *Conf. Rec. IEEE Instrumentation and Measurement Technology*, May 1992, pp. 647 - 652.

[65] A. Ferrah, K. J. Bradley, P. J. Hogben, M. S. Woolfson, and G. M. Asher, "A Transputer-Based Speed Identifier for Induction Motor Drives using Real-Time Adaptive Filtering," in *Conf. Rec. IEEE-IAS Annual Meeting, no. 31*, San Diego, USA, Oct. 1996, vol. 1, pp. 394 - 400.

[66] M. Schrödl and R. S. Wieser, "EMF-Based Rotor Flux Detection in Induction Motors using Virtual Short Circuits," *IEEE Transactions on Industry Applications*, vol. 34, no. 1, pp. 142 - 147, Jan./Feb. 1998.

[67] D. S. Zinger, F. Profumo, T. A. Lipo, and D. W. Novotny, "A Direct Field-Oriented Controller for Induction Motor Drives Using Tapped Stator Windings," *IEEE Transactions on Power Electronics*, vol. 5, no. 4, pp. 446 - 453, Dec. 1990.

[68] L. Kreindler, J. C. Moreira, A. Testa, and T. A. Lipo, "Direct Field Orientation Controller Using the Stator Phase Voltage Third Harmonic," *IEEE Transactions on Industry Applications*, vol. 30, no. 2, pp. 441 - 447, 1994.

[69] M. W. Degner, *Flux, Position, And Velocity Estimation In AC Machines using Carrier Signal Injection*, Ph.D. thesis, Department of Mechanical Engineering, University of Wisconsin - Madison, Madison, USA, 1998.

[70] M. Schrödl, "Detection of the Rotor Position of a Permanent Magnet Synchronous Machine at Standstill," in *Conf. Rec. ICEM*, Pisa, Italy, 1988, pp. 195 - 197.

[71] S. Ogasawara and H. Akagi, "Implementation and Position Control Performance of a Position-Sensorless IPM Motor Drive System Based on Magnetic Saliency," in *Conf. Rec. IEEE-IAS Annual Meeting, no. 32*, New Orleans, USA, Oct. 1997, pp. 464 - 470.

[72] M. J. Corley and R. D. Lorenz, "Rotor Position and Velocity Estimation for a Salient-Pole Permanent Magnet Synchronous Machine at Standstill and High Speeds," *IEEE Transactions on Industry Applications*, vol. 34, no. 4, pp. 784 - 789, July/Aug. 1998.

[73] P. L. Jansen, M. J. Corley, and R. D. Lorenz, "Flux, Position, and Velocity Estimation in AC Machines at Zero and Low Speed via Tracking of High Frequency Saliencies," *EPE Journal*, vol. 9, no. 1 - 2, pp. 45 - 50, Nov. 1999.

[74] A. Consoli, G. Scarcella, and A. Testa, "Sensorless Control of PM Synchronous Motors at Zero Speed," in *Conf. Rec. IEEE-IAS Annual Meeting, no. 34*, Phoenix, USA, Oct. 1999, pp. 1033 - 1040.

[75] M. Mamo, J. Oyama, T. Abe, T. Higuchi, and E. Yamada, "Carrier Frequency Method of IPM Motor Rotor Position Determination," in *Proc. EPE Conf.*, Lausanne, Switzerland, Sept. 1999, vol. on CD-ROM.

[76] N. Kasa and H. Watanabe, "A Mechanical Sensorless Control System for Salient-Pole Brushless DC Motor with Autocalibration of Estimated Position Angles," *IEEE Transactions on Industrial Electronics*, vol. 47, no. 2, pp. 389 - 395, Apr. 2000.

[77] P. L. Jansen and R. D. Lorenz, "Transducerless Position and Velocity Estimation in Induction and Salient AC Machines," *IEEE Transactions on Industry Applications*, vol. 31, no. 2, pp. 240 - 247, Mar./Apr. 1995.

[78] J.-H. Jang, J.-I. Ha, and S.-K. Sul, "Vector Control of Surface Mounted Permanent Magnet Motor without any Rotational Transducer," in *Conf. Rec. IEEE-APEC Annual Meeting, no. 16*, Mar. 2001, vol. 2, pp. 845 - 849.

[79] F. Blaschke, J. van der Burgt, and A. Vandenput, "Sensorless Direct Field Orientation at Zero Flux Frequency," in *Conf. Rec. IEEE-IAS Annual Meeting, no. 31*, San Diego, USA, Oct. 1996, vol. 1, pp. 189 - 196.

[80] Seung-Ki Sul and Jung-Ik Ha, *Sensorless Field Orientation Control Method of an Induction Machine by High Frequency Signal Injection*, Patent 5,886,498. U.S. Patent Office, USA, Mar. 1999.

[81] A. Consoli, G. Scarcella, and A. Testa, "A New Zero-Frequency Flux-Position Detection Approach for Direct-Field-Oriented-Control Drives," *IEEE Transactions on Industry Applications*, vol. 36, no. 3, pp. 797 - 804, May/June 1999.

[82] M. W. Degner and R. D. Lorenz, "Position Estimation in Induction Machines Utilizing Rotor Bar Slot Harmonics and Carrier-Frequency Signal Injection," *IEEE Transactions on Industry Applications*, vol. 36, no. 3, pp. 736 - 742, May/June 2000.

[83] N. Teske, G. M. Asher, K. J. Bradley, and M. Sumner, "Sensorless Position Estimation for symmetric Cage Induction Motor under Loaded Conditions," in *Conf. Rec. IEEE-IAS Annual Meeting, no. 35*, Roma, Italy, Oct. 2000, vol. 3, pp. 1835 - 1841.

[84] M. Schrödl, "Operation of the Permanent Magnet Synchronous Machine without a Mechanical Sensor," in *Proc. PEVD Conf.*, London, UK, 1990, pp. 51 – 56.

[85] M. W. Degner and R. D. Lorenz, "Using Multiple Saliencies for the Estimation of Flux, Position, and Velocity in AC Machines," *IEEE Transactions on Industry Applications*, vol. 34, no. 5, pp. 1097 – 1104, Sept./Oct. 1998.

[86] M. Schrödl, "Sensorless Control of AC Machines at Low Speed and Standstill Based on the 'INFORM' Method," in *Conf. Rec. IEEE-IAS Annual Meeting, no. 31*, San Diego, USA, Oct. 1996, pp. 270 – 277.

[87] M. Schrödl, D. Hennerbichler, and T. M. Wolbank, "Induction Motor Drive For Electric Vehicles without Speed- and Position Sensors," in *Proc. EPE Conf.*, Brighton, UK, Sept. 1993, pp. 271 – 275.

[88] T. M. Wolbank and B. Haidvogl, "Influence of Different Inverter Control and Test Pulse Generation Schemes on Sensorless Control of AC Machines," in *Proc. PEVD Conf.*, London, UK, Sept. 2000, pp. 280 – 285.

[89] S. Ogasawara and H. Akagi, "An Approach to Real-Time Position Estimation at Zero and Low Speed for a PM Motor Based on Saliency," *IEEE Transactions on Industry Applications*, vol. 34, no. 1, pp. 163 – 168, Jan./Feb. 1998.

[90] S. Ogasawara and H. Akagi, "Rotor Position Estimation Based on Magnetic Saliency of an IPM Motor – Realization of a Wide-speed Range from Zero to the Rated Speed," in *Conf. Rec. IEEE-IAS Annual Meeting, no. 33*, St. Louis, USA, Oct. 1998, vol. 1, pp. 460 – 466.

[91] L. A. S. Ribeiro, M. W. Degner, F. Briz, and R. D. Lorenz, "Comparison of Carrier Signal Voltage and Current Injection for the Estimation of Flux Angle or Rotor Position," in *Conf. Rec. IEEE-IAS Annual Meeting, no. 33*, St. Louis, USA, Oct. 1998, vol. 1, pp. 452 – 459.

[92] J.-I. Ha, S.-K. Sul, K. Ide, I. Murokita, and K. Sawamura, "Physical Understanding of High Frequency Injection Method to Sensorless Drives of an Induction Machine," in *Conf. Rec. IEEE-IAS Annual Meeting, no. 35*, Roma, Italy, Oct. 2000, vol. 3, pp. 1802 – 1808.

[93] A. Consoli, G. Scarcella, G. Tutino, and A. Testa, "Sensorless Field Oriented Control Using Common Mode Currents," in *Conf. Rec. IEEE-IAS Annual Meeting, no. 35*, Roma, Italy, Oct. 2000, vol. 3, pp. 1866 – 1873.

[94] P. L. Jansen and R. D. Lorenz, "Transducerless Field Orientation Concepts Employing Saturation-Induced Saliencies in Induction Machines," *IEEE Transactions on Industry Applications*, vol. 32, no. 6, pp. 1380 - 1393, Nov./Dec. 1996.

[95] M. L. Aime, M. W. Degner, R. D. Lorenz, and N. Tice, "The Effects of Saturation on Flux Angle Estimation for Sensorless, Direct Field Oriented Control of Induction Machines," in *Proc. EPE 99 Conf.*, Lausanne, Switzerland, Sept. 1999, vol. on CD-ROM.

[96] M. W. Degner and R. D. Lorenz, "Using Multiple Saliencies for the Estimation of Flux, Position, and Velocity in AC Machines," in *Conf. Rec. IEEE-IAS Annual Meeting, no. 32*, New Orleans, USA, Oct. 1997, pp. 760 - 767.

[97] C. Spiteri Staines, G. M. Asher, M. Sumner, and K. J. Bradley, "A Periodic Burst Injection Method for Deriving Rotor Position in Saturated Cage-Salient Induction Motors without a Shaft Encoder," *IEEE Transactions on Industry Applications*, vol. 35, no. 4, pp. 851 - 858, July/August 1999.

[98] J. Holtz, J. Jiang, and H. Pan, "Identification of Rotor Position and Speed of Standard Induction Motors at Low speed including Zero Stator Frequency," in *Conf. Rec. IEEE IECON'97*, Nov. 1997, vol. 2, pp. 971 - 976.

[99] J. Jiang, "Drehgeberlose feldorientierte Regelung für Asynchronmaschinen bei Ständerfrequenz Null," Berichte aus der Elektrotechnik, zugl.: Wuppertal, Univ.-GH, Diss., 1999. Shaker Verlag, Aachen, ISBN: 3-8265-7534-2, 2000.

[100] J. Holtz, "Sensorless Position Control of Induction Motors - An Emerging Technology," *IEEE Transactions on Industrial Electronics*, vol. 45, no. 6, pp. 840 - 852, Dec. 1998.

[101] H. Klaassen, *Selbsteinstellende, feldorientierte Regelung einer Asynchronmaschine und geberlose Drehzahlregelung*, Ph.D. thesis, Fakultät für Maschinenbau und Elektrotechnik der Technischen Universität Carolo-Wilhelmina zu Braunschweig, Braunschweig, Germany, Dec. 1998.

[102] Gene F. Franklin, J. David Powell, and A. Emami-Naeini, *Feedback control of dynamic systems*, 3rd edition. Addison-Wesley Publishing Company, Inc., Reading, Massachussetts, USA, ISBN: 0-201-52747-2, June 1995.

[103] N. Teske, "Programmierung und Inbetriebnahme einer Motorregelung mit einem digitalen Signalprozessor," Diplomarbeit, Technische Universität Braunschweig, Braunschweig, Germany, May 1997.

[104] W. Leonhard, *Digitale Signalverarbeitung in der Meß- und Regelungstechnik*, Teubner Studienbücher: Elektrotechnik, 2. Auflage. B. G. Teubner, Stuttgart, Germany, ISBN: 3-519-16120-6, 1989.

[105] DPC/C40 TMS320C40 PC Board, "User Guide and Technical Reference, version 1.0," Tech. Rep., Loughborough sound Images Ltd., Loughborough, United Kingdom, Jan. 1993.

[106] N. Teske, "Summary of C40 Tools - A Description," Tech. Rep., Department of Electrical & Electronic Engineering, University of Nottingham, UK, Apr. 2000.

[107] N. Teske, "Hardware Connections for the Inverter and Converter - A Description," Tech. Rep., Department of Electrical & Electronic Engineering, University of Nottingham, UK, Mar. 2000.

[108] N. Teske, "Model for the Communication between the TMS320C40 and a PC - A Description," Tech. Rep., Department of Electrical & Electronic Engineering, University of Nottingham, UK, Mar. 2000.

[109] F. Blaabjerg and J. K. Pedersen, "A New Low-Cost, Fully Fault-Protected PWM-VSI Inverter with True Phase-Current Information," *IEEE Transactions on Power Electronics*, vol. 12, no. 1, pp. 187 – 197, Jan. 1997.

[110] Texas Instruments Application Report, "Three phase current measurements using a single line resistor on the TMS320F240, Literature Number: BPRA077," Tech. Rep., Texas Instruments Europe, Houston, Texas, USA, May 1998.

[111] R. B. Sepe and J. H. Lang, "Implementation of Discrete-Time Field-Oriented Current Control," *IEEE Transactions on Industry Applications*, vol. 30, no. 3, pp. 723 – 727, May/June 1994.

[112] S.-H. Song, J.-W. Choi, and S.-K. Sul, "Current Measurement of Digital Field Oriented Control," in *Conf. Rec. IEEE-IAS Annual Meeting, no. 31*, San Diego, USA, Oct. 1996, vol. 1, pp. 334 – 338.

[113] S.-H. Song, J.-W. Choi, and S.-K. Sul, "Current Measurements in Digitally Controlled AC Drives," *IEEE Industry Applications Magazine*, vol. 6, no. 4, pp. 51 – 62, July/August 2000.

[114] D.-W. Chung and S.-K. Sul, "Analysis and Compensation of Current Measurement Error in Vector-Controlled AC Motor Drives," *IEEE Transactions on Industry Applications*, vol. 34, no. 2, pp. 340 – 345, March/April 1998.

[115] W. Schumacher, P. Rojek, and H.-H Letas, "Hochauflösende Lage- und Drehzahlerfassung optischer Geber für schnelle Stellantriebe," *Elektronik*, vol. 10, pp. 65, May 1985.

[116] Texas Instruments Application Report, "TMS320F240 DSP-Solution for High-Resolution Position with Sin/Cos-Encoders, Literature Number: SPRA496," Tech. Rep., Martin Staebler, Texas Instruments Europe, Houston, Texas, USA, Dec. 1998.

[117] P. L. Alger, *Induction Machines - Their Behavior and Uses*, 2nd edition. Gordon & Breach Science Publishers Inc., New York, USA, ISBN: 0-201-52747-2, 1970.

[118] R. W. A. A. De Doncker, "Field-Oriented Controllers with Rotor Deep Bar Compensation Circuits," *IEEE Transactions on Industry Applications*, vol. 28, no. 5, pp. 1062 - 1071, Sept./Oct. 1992.

[119] R. C. Healey, S. Williamson, and A. C. Smith, "Improved Cage Rotor Models for Vector Controlled Induction Motors," *IEEE Transactions on Industry Applications*, vol. 31, no. 4, pp. 812 - 822, July/August 1995.

[120] A. Ferrah, K. J. Bradley, P. J. Hogben-Laing, M. S. Woolfson, G. M. Asher, M. Sumner, J. Cilia, and J. Shuli, "A Speed Identifier for Induction Motor Drives Using Real-Time Adaptive Digital Filtering," *IEEE Transactions on Industry Applications*, vol. 34, no. 1, pp. 156 - 162, Jan./Feb. 1998.

[121] H. Guldemir and K. J. Bradley, "The Effect of Rotor Design on Rotor Slot Harmonics in Induction Machines," in *Electric Power Components and Systems*. Taylor & Francis Group, London, to be published in 2001.

[122] Jinsheng Jiang, *Drehgeberlose feldorientierte Regelung für Asynchronmaschinen bei Ständerfrequenz Null*, Ph.D. thesis, Universität-Gesamthochschule Wuppertal, Wuppertal, Germany, June 1999.

[123] S. Williamson and R. G. Cann, "A comparison of PWM Switching Strategies on the Basis of Drive System Efficiency," *IEEE Transactions on Industry Applications*, vol. 20, no. 6, pp. 1460 - 1472, Nov./Dec. 1984.

[124] M. G. Say, *Alternating Current Machines*, 4th edition. Pitman Publishing Limited, 39 Parker Street, London, WC2B 5PB, England, ISBN: 0-273-36197-X, 1978.

[125] F. Briz, M. W. Degner, A. Diez, and R. D. Lorenz, "Measuring, Modeling and Decoupling of Saturation-Induced Saliencies in Carrier Signal Injection-Based

Sensorless AC Drives," in *Conf. Rec. IEEE-IAS Annual Meeting, no. 35*, Roma, Italy, Oct. 2000, vol. 3, pp. 1842 - 1849.

[126] M. L. Aime, M. W. Degner, and R. D. Lorenz, "Saturation Measurements in AC Machines Using Carrier Signal Injection," in *Conf. Rec. IEEE-IAS Annual Meeting, no. 33*, St. Louis, USA, Oct. 1998, pp. 159 - 166.

[127] C. Silva, "Internal Report - Modelling of Saturation in PMSM," Tech. Rep., Department of Electrical & Electronic Engineering, University of Nottingham, UK, Apr. 2001.

[128] K. Ide, I. Murokita, M. Sawamura, M. Ohto, Y. Nose, J.-I. Ha, and S.-K. Sul, "Finite Element Analysis of Sensorless Induction Machine by High frequency Voltage Injection," in *Conf. Rec. IPEC*, Tokyo, Japan, 2000, pp. 1842 - 1847.

[129] J. E. Brown, P. K. Kovács, and P. Vas, "A Method of Including the Effects of Main Flux Path Saturation in the Generalized Equations of AC Machines," *IEEE Transactions on Power Apparatus and Systems*, vol. 102, no. 1, pp. 96 - 103, Jan. 1983.

[130] Seung-Ki Sul and Jung-Ik Ha, "Sensorless Field-Orientation Control of an Induction Machine by High-Frequency Signal Injection," *IEEE Transactions on Industry Applications*, vol. 35, no. 1, pp. 45 - 51, Jan./Feb. 1999.

[131] H. M. Ryu, J.-I. Ha, and S.-K. Sul, "A New Sensorless Thrust Control of Linear Induction Motor," in *Conf. Rec. IEEE-IAS Annual Meeting, no. 35*, Roma, Italy, Oct. 2000, vol. 3, pp. 1655 - 1661.

[132] Bhagwandas P. Lathi, Ed., *Modern Digital and Analog Communication Systems*, Series in Electrical Engineering, 2nd Edition. The Dryden Press, Saunders College Publishing, USA, ISBN: 0-03-027933-X, 1983.

[133] H. Y-F. Lam, *Analog and Digital filters: Design and Realization*, Prentice-Hall series in electrical and computer engineering. Prentice-Hall, Englewood Cliffs, New Jersey, USA, ISBN: 0-13-032755-7, 1979.

[134] T. Emura and L. Wang, "A High-Resolution Interpolator for Incremental Encoders Based on the Quadrature PLL Method," *IEEE Transactions on Industrial Electronics*, vol. 47, no. 1, pp. 84 - 90, Feb. 2000.

[135] F. Harris, "A Tutorial: Phase Locked Loops in DSP based Modems," Tech. Rep., San Diego State University, San Diego, California, USA, 2000.

[136] R. D. Lorenz and K. W. Van Patten, "High-Resolution Velocity Estimation for All-Digital, AC Servo Drives," *IEEE Transactions on Industry Applications*, vol. 27, no. 4, pp. 701 - 705, July/Aug. 1991.

[137] M. Ishida and K. Iwata, "A New Slip Frequency Detector of an Induction Motor Utilizing Rotor Slot Harmonics," *IEEE Transactions on Industry Applications*, vol. 20, no. 3, pp. 575 - 582, May/June 1984.

[138] F. Briz, A. Diez, and M. W. Degner, "Dynamic Operation of Carrier-Signal-Injection-Based Sensorless Direct Field-Oriented AC Drives," *IEEE Transactions on Industry Applications*, vol. 36, no. 5, pp. 1360 - 1368, Sept./Oct. 2000.

[139] DSP56F801/803/805/807 Users's Manual, "Chapter 11: Deadtime Generators," Tech. Rep., Motorola, USA, June 2000.

[140] D. Butt, *An Investigation of Harmonic Correction Techniques using Active Filtering*, Ph.D. thesis, Department of Electrical & Electronic Engineering, University of Nottingham, England, Aug. 1999.

[141] A. R. Muñoz and T. A. Lipo, "On-Line Dead-Time Compensation Technique for Open-Loop PWM-VSI Drives," *IEEE Transactions on Power Electronics*, vol. 14, no. 4, pp. 683 - 689, July 1999.

[142] R. B. Sepe and J. H. Lang, "Inverter Nonlinearities and Discrete-Time Vector Current Control," *IEEE Transactions on Industry Applications*, vol. 30, no. 1, pp. 62 - 70, Jan./Feb. 1994.

[143] J.-W. Choi and S.-K. Sul, "A New Compensation Strategy Reducing Voltage/Current Distortion in PWM VSI Systems Operating with Low Output Voltages," *IEEE Transactions on Industrial Electronics*, vol. 31, no. 5, pp. 1001 - 1008, Sept./Oct. 1995.

[144] A. V. Oppenheim, R. W. Schafer, and J. R. Buck, *Discrete-Time Signal Processing*, Signal Processing Series, 2nd edition. Prentice-Hall, Inc., New Jersey, USA, ISBN: 0-13-754920-2, 1999.

[145] Signal Processing Toolbox, "User's guide, version 4.2, release 2," Tech. Rep., The MathWorks Inc., 24 Prime Park Way, Natick, MA 01760-1500, USA, Jan. 1999.

[146] Jung-Ik Ha, Seog-Joo Kang, and Seung-Ki Sul, "Position-Controlled Synchronous Reluctance Motor Without Rotational Transducer," *IEEE Transactions on Industry Applications*, vol. 35, no. 6, pp. 1393 - 1398, Nov./Dec. 1999.

[147] N. Teske, G. M. Asher, M. Sumner, and K. J. Bradley, "Encoderless Position Control of Induction Machines," in *Proc. EPE Conf.*, Graz, Austria, Aug. 2001, vol. on CD-ROM.

[148] N. Teske, G. M. Asher, K. J. Bradley, and M. Sumner, "Analysis and Suppression of Inverter Clamping Saliency in Sensorless Position Controlled Induction Machine Drives," in *Conf. Rec. IEEE-IAS Annual Meeting, no. 36*, Chicago, USA, Sept./Oct. 2001.

[149] A. Ferrah, P. J. Hogben-Laing, K. J. Bradley, G. M. Asher, and M. S. Woolfson, "The Effect of Rotor Design on Sensorless Speed Estimation Using Rotor Slot Harmonics Identified by Adaptive Digital Filtering Using the Maximum Likelihood Approach," in *Conf. Rec. IEEE-IAS Annual Meeting, no. 32*, New Orleans, USA, Oct. 1997, pp. 128 - 135.

[150] R. Blasco-Giménez, G. M. Asher, M. Sumner, and K. J. Bradley, "Performance of FFT-Rotor Slot Harmonic Speed Detector for Sensorless Induction Motor Drives," *in Proc.-Electr. Power Appl.*, vol. 143, no. 3, pp. 258 - 268, May 1996.

[151] Kaye & Laby, *Tables of Physical and chemical Constants*, 16^{th} Edition. Longman, USA, 1995.

[152] N. Teske, "The F240 PWM Generator and Position Encoder - A Description," Tech. Rep., Department of Electrical & Electronic Engineering, University of Nottingham, UK, Apr. 2000.

[153] Matthias Bienert, "Development of Hardware for High Dynamic Control of Induction Machines, using a DSP," Diplomarbeit, Department of Electrical and Electronic Engineering, University of Nottingham, Sept. 1998.

Appendix A:

Vector Control Theory

A.1 Signal Transformations

A.1.1 Star-Delta Conversion

Working with a phase-equivalent circuit, it can be important to consider and keep phase relations between voltages and currents through the transformations consistent. Large machines (usually > 5kW) are connected in delta (Δ). The measured line-to-line voltages are then equal to the phase voltage of the equivalent circuit. The measured line currents however have to be explicitly converted to phase currents. The situation is the inverse for a star (Y) connected machine. In general, it does not matter, if the star-equivalent circuit is used and the machine in reality is connected in delta. Important is, that voltages and currents are matched.

For a given set of balanced sinusoidal phase-to-neutral voltages with the *rms* amplitude $U_s = 240\text{V}$ and the frequency $\omega_e = 2\pi f_e$:

$$\begin{aligned} v_A(t) &= \sqrt{2}U_s \cos(\omega_e t + \alpha) \\ v_B(t) &= \sqrt{2}U_s \cos(\omega_e t + \alpha - 2\pi/3) \\ v_C(t) &= \sqrt{2}U_s \cos(\omega_e t + \alpha - 4\pi/3) \end{aligned} \tag{A.1}$$

The angle α is an arbitrary offset at time $t = 0$. The resulting line-to-line voltages can easily be computed as:

$$\begin{aligned} v_{AB} &= v_A - v_B = \sqrt{3} \cdot \sqrt{2}U_s \cos(\omega_e t + 30° + \alpha) \\ v_{BC} &= v_B - v_C \\ v_{CA} &= v_C - v_A \end{aligned} \tag{A.2}$$

The inverse conversion, back from line-to-line voltages to line-to-neutral voltages is:

$$\begin{aligned} v_A &= (v_{AB} - v_{CA})/3 \\ v_B &= (v_{BC} - v_{AB})/3 \\ v_C &= (v_{CA} - v_{BC})/3 \end{aligned} \tag{A.3}$$

Comparing line-to-line voltage v_{AB} with the line-to-neutral voltage v_A, two differences can be seen:

- $|v_{AB}| = \sqrt{3}|v_A|$ — The maximum amplitude of the line-to-line voltage is by $\sqrt{3}$ larger than that of the line-to-neutral voltage
- $\angle v_{AB} = \angle v_A + 30°$ — The line-to-line voltage v_{AB} is leading by 30°.

In many implementations for machine control, only the first fact is considered by deriving v_{AB} from simply scaling v_A. The phase shift however is often not considered. This can be a problem when using the voltage model (see Section 2.2.4) that is based on voltages and currents.

The situation for the currents is similar to that of the voltages. In the practical implementation chosen for this thesis where the machine was connected in Δ, the machine model was also derived in Δ. Therefore the measured line-to-line voltages can directly be used, but the measured line currents need to be transformed into phase currents:

$$\begin{aligned} i_{AB} &= (i_A - i_B)/3 \\ i_{BC} &= (i_B - i_C)/3 \\ i_{CA} &= (i_C - i_A)/3 \end{aligned} \tag{A.4}$$

Similar, the *rms* value of a phase current i_{AB} is lower than the *rms* value of the line current i_A and lagging it by 30°:

$$I_{AB_{rms}} = I_{A_{rms}}/\sqrt{3} \tag{A.5}$$

$$\angle i_{AB} = \angle i_A - 30° \qquad i_A \text{ is leading!} \tag{A.6}$$

The inverse conversion from phase to line currents is useful when comparing reference currents with real line currents. These reference currents will be transformed according to:

$$\begin{aligned} i_A &= i_{AB} - i_{CA} \\ i_B &= i_{BC} - i_{AB} \\ i_C &= i_{CA} - i_{BC} \end{aligned} \tag{A.7}$$

A.1.2 Orthogonal Transform

In a balanced system, 3-phase signals can be converted to an equivalent orthogonal set of signals. The orientation of this orthogonal systems is arbitrary as well as the scaling, as long as the reverse transformation matrix multiplied with the transformation matrix itself results in the unity matrix.

The preferred scaling used in this work is the so-called *RMS transformation*. This means that the new α-axis is aligned to the phase axis AB. Additionally, the α-signal value is scaled to be of the amplitude of the *rms* phase signal. This gives the advantage of interpreting signals as 'real' physical and that physically measurable output quantities like the torque can directly be determined from using the *rms*-transformed currents or voltages. Signals can easily be compared with the common single-phase equivalent circuit in steady-state.

The input transformation for currents and voltages:

$$i_\alpha = i_{AB}/\sqrt{2} \tag{A.8}$$

$$i_\beta = \frac{\sqrt{3}}{2} \cdot \frac{2}{3}(i_{BC}/\sqrt{2} - i_{CA}/\sqrt{2}) = (i_{BC} - i_{CA})/\sqrt{6} \tag{A.9}$$

$$v_\alpha = v_{AB}/\sqrt{2} \tag{A.10}$$

$$v_\beta = (v_{BC} - v_{CA})/\sqrt{6} \tag{A.11}$$

In (A.9), relation (2.5) is used, assuming a balanced 3-phase system. The inverse transformation is shown for the voltages only. This will be necessary, when calculating the PWM switching signals from the 3-phase voltages:

$$v_{AB} = \sqrt{2}v_\alpha \tag{A.12}$$

$$v_{BC} = (\sqrt{6}v_{s\beta} - \sqrt{2}v_{s\alpha})/2 = (\sqrt{3}v_{s\beta} - v_{s\alpha})/\sqrt{2} \tag{A.13}$$

$$v_{CA} = -(v_{AB} + v_{BC}) \tag{A.14}$$

For the current space-phasor in (2.6):

$$\underline{I}_s = \sqrt{i_\alpha^2 + i_\beta^2} \cdot e^{j \tan^{-1}(i_\beta/i_\alpha)} \tag{A.15}$$

A.1.3 Coordinate Transform

Before the use of cheap microprocessors, control of induction machines had to make use of the measurable stator signals and was therefore restricted to the stationary stator frame. Transforming the stator quantities into a rotating frame however can result in significant simplification in the machines equations due to disappearing coupling

terms. Well known is the rotor frame used for field-oriented Vector Control [6]. This frame is aligned to the rotor flux at angle ρ and rotating with the angular frequency ω_e.

Multiplying a space phasor $\underline{i}_{s_{\alpha\beta}} = (i_{s\alpha} + j i_{s\beta})$ by $e^{-j\rho}$ will cause a rotation in the mathematical negative direction (clockwise rotation):

$$\begin{aligned} \underline{i}_{s_{dq}} &= \underline{i}_{s_{\alpha\beta}} e^{-j\rho} \\ (i_{s_d} + j i_{s_q}) &= (i_{s_\alpha} + j i_{s_\beta})(\cos(\rho) - j \sin(\rho)) \end{aligned}$$

In the stationary frame, voltage, current and flux linkage space vectors are time varying variables. Direct control over these variables is very difficult. Therefore it is common practice to transform these variables into another reference frame which rotates synchronously with the flux vector. This can be the stator, rotor or air-gap flux. During steady-state operation, the resulting space phasors are then simple DC variables in the rotating frame.

A.2 Scalar Control

Scalar control of the induction machine is not very suitable to perform dynamic operation. It is however very robust, easy to setup and only requires knowledge of basic machine parameters that can usually be found on the name-plate of the machine. Scalar control is used in this work to set up Vector Control.

A.2.1 Open Loop Voltage/Frequency Control

Voltage/frequency control is also known as V/f control. The control strategy is derived from the steady state equivalent circuit of the induction machine. The idea is to keep the magnetic flux more or less constant by changing the magnitude of the stator voltage linearly with the synchronous frequency.

This assumes that the amplitude of the stator voltage V_s is close to that of the voltage V_m across the magnetizing branch. This is true for higher speeds where the voltage drop across the stator resistance R_s can be neglected. For lower speeds the stator voltage is increased by adding a voltage boost that accounts for this voltage drop across R_s. The electrical torque can be calculated from the single phase equivalent circuit:

$$\begin{aligned} T_{el} &= 3 \cdot \frac{sR_r V_m^2}{\omega_e [R_r^2 + (s\omega_e L_r)^2]} \\ &\approx 3 \cdot \frac{sR_r V_s^2}{\omega_e R_r^2} \\ &\approx k \cdot \left(\frac{V_s}{\omega_e}\right)^2 \cdot \omega_{sl} \end{aligned} \tag{A.16}$$

If the ratio V_s/ω_e is kept constant, the torque is only a function of slip. The machine is then operated in the linear region of the steady state torque-speed characteristic.

This open loop control is very cheap and simple to implement and does not require any voltage or current measurements or an encoder feedback. A simple voltage measurement and at least one current transducer are nevertheless integrated into most commercial inverters for reasons of drive protection. V/f control provides a simple way to adjust speed and avoids the high inrush currents when operating induction machines directly from the mains.

Disadvantage is that it only works well for quasi-stationary operation. The dynamic quality is bad. This makes it only suitable for applications without stringent requirements for speed regulation. With the use of a speed ramp, the steady-state conditions can be approximated and torque oscillations are reduced. Open-loop V/f control does not provide speed control or speed-holding during load changes.

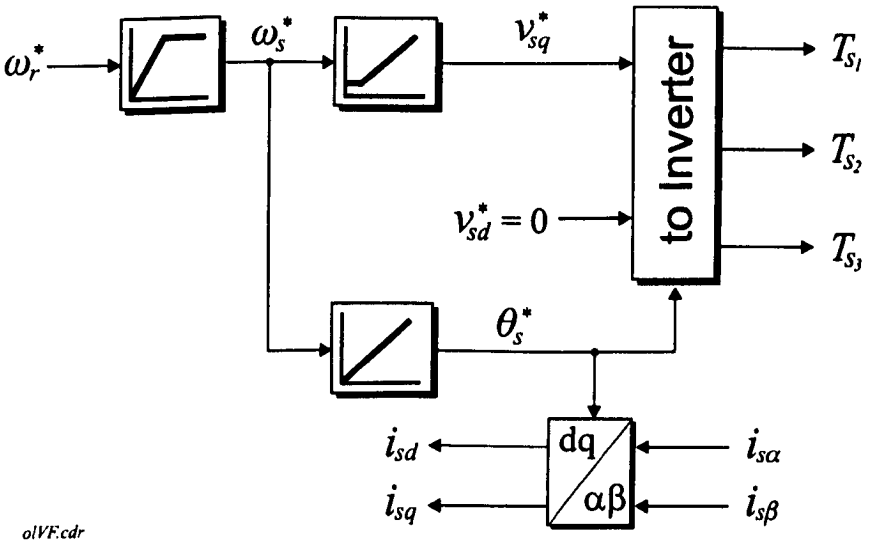

Figure A.1: *Structure of open loop V/f Control*

A possible implementation for open loop V/f control is shown in Fig. A.1. The speed reference is sent via a ramp first. The output is integrated and provides the synchronous angle θ_s for the voltage output transformation. The reference voltage v_{sq}^* is derived from ω_e according to $V_s/\omega_e = const$, including the voltage boost. Under steady state conditions, the stator currents can be transformed with the synchronous angle to give an approximation of the vector currents i_{sd} and i_{sq}. This structure allows to set up vector control easily, because the signs of all signals can be checked easily. Under no load, i_{sd} should be positive and i_{sq} will be at a low positive value.

A.2.2 V/f Feedback Control

Adding a speed encoder allows to control the speed of the drive and to maintain a given speed for changing loads. Again, quasi-stationary conditions have to be ensured. The most common type of closed loop V/f control is slip frequency control. A controller is used to add a load dependent compensation that is proportional to the slip. The same structure from Fig. A.1 can be used. Now, the difference between the demanded speed and the encoder speed is sent into the PI controller that provides the ω_{sl}^* term. Now, $\omega_e^* = \omega_{sl}^* + \omega_r^*$ where the demanded angular velocity of the rotor is taken after the ramp.

Closed loop V/f control is very suitable when setting up vector control. The voltage equations (2.17) can be checked under steady state conditions:

$$v_{sd} = R_s \cdot i_{sd} - \omega_e \cdot \sigma L_s i_{sq}$$

$$v_{sq} = R_s \cdot i_{sq} + \omega_e \cdot L_s i_{sd} \tag{A.17}$$

The voltage drop due to R_s is usually small. The term with σL_s can also be neglected. The correct sign of currents, voltages and encoder signal can be verified as well as the stator inductance. This test is very useful when designing the feedforward compensation for the current controllers under vector control (see Section 3.3).

A.3 Space Vector Modulation

The two conditions for obtaining an optimal PWM (see Section 2.2.6) can be fulfilled in general when for a given (analog) $\underline{v}_s$ only the two adjacent discrete voltage vectors are used. For the mean voltage vector, when minimizing the switching frequency, a switching sequence has to be arranged so that a change of the discrete voltage vector only results in switching one inverter leg. This is possible by forming the desired analog voltage vector by vector addition of only the two adjacent voltage vectors that clamp the sector of the hexagon in which $\underline{v}_s$ lies.
This is shown in the left graphic in Fig. A.2. The switching times determine the mean value of the voltages and therefore their vectorial length. If not the maximum amplitude of $\underline{v}_s$ is needed, which is indicated by the circle in Fig. 2.8 (Section 2.2.6), additional zero states have to be introduced. Zero states are achieved by using the zero vectors $\underline{u}_{s_0}$ and $\underline{u}_{s_7}$. Depending on the chronological order of these zero states, a modulation with two or three switches results.

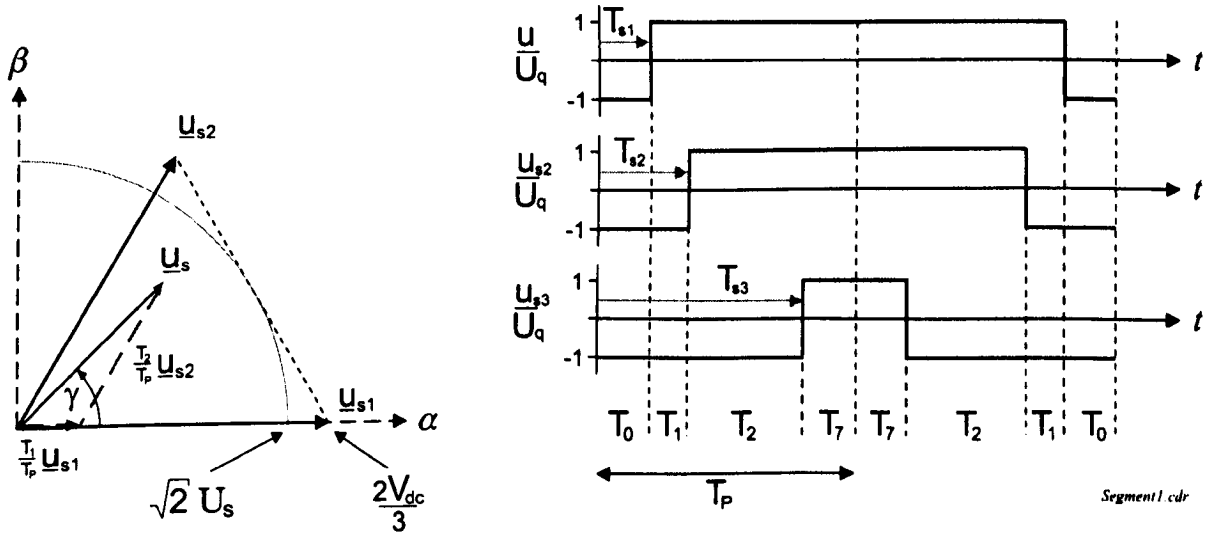

Figure A.2: *Calculation of switching times for the first sector of the inverter hexagon*

A description is carried out according to Fig. A.2. For the approximation of the voltage vector $\underline{v}_s$ with three switches, the sequence starts with the zero vector $\underline{u}_{s_0}$, then switches to $\underline{u}_{s_1}$ and goes via $\underline{u}_{s_2}$ to the zero vector $\underline{u}_{s_7}$. For reasons of symmetry, the sequence back to $\underline{u}_{s_0}$ is carried out vice versa. For the modulation with two switches, only two of the three inverter legs are switched: Starting with $\underline{u}_{s_0}$ via $\underline{u}_{s_1}$ to $\underline{u}_{s_2}$ and back with $\underline{u}_{s_1}$ to $\underline{u}_{s_0}$.

A.3.1 Switching Times in Polar Coordinates

The calculation of switching times depends on the coordinate system in which $\underline{v}_s(t)$ is described. For the voltage vector in polar coordinates (described by amplitude and angle), the calculation for the first sector is:

$$\int_0^{T_p} \underline{v}_s(t)dt = \sum_{k=1}^{2} T_k \underline{u}_{s_k} \tag{A.18}$$

where $1/T_p = f_p$ is the pulse or switching frequency of the inverter. Basis of the shown relation is the demand for equality of voltage-time areas (VTA). With the vectors $\underline{u}_{s_1}$ and $\underline{u}_{s_2}$ from $\underline{u}_{s_k} = \frac{2}{3}V_{dc}e^{j(k-1)60°}$ for $k = 1 \ldots 6$ (see (2.44) Section 2.2.6)

$$\begin{aligned} \underline{u}_{s_1} &= \frac{2V_{dc}}{3} \\ \underline{u}_{s_2} &= \frac{2V_{dc}}{3}e^{j60°} = \frac{2V_{dc}}{3}(\cos 60° + j \sin 60°) \end{aligned}$$

and the vector $\underline{v}_s$ from $\underline{v}_s(t) = \frac{3}{2}\sqrt{2}\underline{V}_s e^{j\omega_e t}$ (see (2.43) in Section 2.2.6) with $U_s = m \cdot V_s$

$$\underline{v}_s = m \cdot V_s e^{j\gamma}$$

equation (A.18) can be rewritten so as to determine T_1 and T_2:

$$m \cdot T_p\sqrt{2}V_S\,(\cos\gamma + j\sin\gamma) = T_1\frac{2V_{dc}}{3} + T_2\frac{2V_{dc}}{3}\,(\cos 60° + j\sin 60°) \tag{A.19}$$

The switching time T_2 can directly be calculated from the imaginary parts:

$$T_2 = T_p\frac{m \cdot \sqrt{3}\sqrt{2}V_S}{V_{dc}}\sin\gamma \tag{A.20}$$

and for T_1 which follows from (A.19) and (A.20):

$$\begin{aligned} T_1 &= T_p\frac{3}{2}\frac{m \cdot \sqrt{2}V_S}{V_{dc}}\cos\gamma - T_p\frac{3}{2}\frac{m \cdot \sqrt{2}V_S}{V_{dc}}\frac{\cos 60°}{\sin 60°}\sin\gamma \\ &= T_p\frac{m \cdot \sqrt{3}\sqrt{2}V_S}{V_{dc}}\sin(60° - \gamma) \end{aligned} \tag{A.21}$$

For the modulation with three switches, the zero state is symmetrically split into $\underline{u}_{s_0}$ and $\underline{u}_{s_7}$ (Fig. A.2):

$$T_0 = T_7 = 0.5(T_p - T_2 - T_1) \tag{A.22}$$

Note that $|m \cdot V_S| \leq 240V_{rms}$, where $m \in [0 \ldots 1]$ is the modulation index and the DC link voltage $V_{dc} = \sqrt{3}\sqrt{2} \cdot V_S$.
Equations (A.20), (A.21) and (A.22) are valid for all sectors, however with different subscripts, according to the describing discrete voltage vectors. The switching times for the first sector are

$$T_{s1} = T_0 \tag{A.23}$$
$$T_{s2} = T_0 + T_1 \tag{A.24}$$
$$T_{s3} = T_0 + T_1 + T_2 \tag{A.25}$$

The absolute amplitude of the phase voltage $\underline{v}_s$ can reach a maximum of $V_{dc} \cdot \cos 30° = \sqrt{3}V_{dc}/2$. This is equal to the effect, that $\underline{v}_s$ cannot leave the hexagon in Fig. 2.8 and has to remain within the circle. Furthermore $\sqrt{2}V_S = \hat{V}_S = \frac{V_{dc}}{\sqrt{3}}$, the peak value of the line-to-line voltage cannot exceed the DC link voltage V_{dc}.

Practical Space Vector Calculation

Implementation in a practical system requires a few additional steps to that described in the previous section. For a delta connected machine, a phase shift of 30° has to be introduced to take the phase shift from phase (= line-to-line) voltages to phase-to-neutral voltages into account. This means that the 30° have to be subtracted from the vector angle ϕ.
For the *delta* or *mesh* connection, the voltage output transformations are

$$\begin{aligned} v_\alpha &= m \cdot \sqrt{3}V_S \cos\phi \\ v_\beta &= m \cdot \sqrt{3}V_S \sin\phi \end{aligned} \tag{A.26}$$

$$\begin{aligned} v_{AB} &= \sqrt{2} \cdot v_\alpha \\ v_{BC} &= (\sqrt{3} \cdot v_\beta - v_\alpha)/\sqrt{2} \\ v_{CA} &= -(v_{AB} + v_{BC}) \end{aligned}$$

$$\begin{aligned} v_A &= (v_{AB} - v_{CA})/3 \\ v_B &= (v_{BC} - v_{AB})/3 \\ v_C &= (v_{CA} - v_{BC})/3 \end{aligned}$$

the resulting vector is

$$\underline{v}_s(t) = \frac{3}{2}\sqrt{2} \cdot (v_\alpha + jv_\beta)/\sqrt{3} = v_A + v_B e^{j2\pi/3} + v_C e^{j4\pi/3} \tag{A.27}$$

In case of a delta connected machine, the following equations hold:

$$\begin{aligned}
\vartheta &= \phi - 30° \\
\gamma &= \mathrm{rem}(\vartheta, 60°) \\
m_x &= m \cdot \frac{\sqrt{3}\sqrt{2}V_s}{V_{dc}} = \sqrt{2} \cdot \sqrt{v_\alpha^2 + v_\beta^2}\Big/V_{dc} \\
T_1 &= m_x \cdot T_p \sin(60° - \gamma) \\
T_2 &= m_x \cdot T_p \sin(\gamma) \\
T_0 &= (T_p - T_2 - T_1)/2
\end{aligned}$$

$2T_p$ is the PWM period and for $\phi = \arctan(v_\alpha/v_\beta)$. The peak of the $\alpha\beta$ voltages are scaled to represent the **rms** phase voltage. This is 415V for the Δ connected machine. This is a result of the scaling in (A.10) with $v_\alpha = V_{AB}/\sqrt{2}$ and (A.11) with $v_\beta = (v_{BC} - v_{CA})/\sqrt{6}$ (see Section A.1).

In Fig. A.3, the distribution of switching times for every sector is shown. It is obvious, that the two vectors limiting a particular sector will make up the longest time ($T_0 + T_1 + T_2$) and the shortest time (T_0). The latter is for the inverted vector (for *sector 0* this will be `-c`), the first is for the positive vector (here: `a`). The remaining vector is made up of an alternating calculation from either ($T_0 + T_1$) or ($T_0 + T_2$).

For every sector, the PWM timings have to be calculated separately. There is a difference, for the *low-to-high* and the *high-to-low* switching time calculation, if the PWM counter only makes use of a count-up **or** a count-down mode. For a triangular PWM counter shape, only one set of calculation relations is needed.

a) low-to-high switching times:

sector	T_{s1}	T_{s2}	T_{s3}
0	$T_0 + T_1 + T_2$	$T_0 + T_2$	T_0
1	$T_0 + T_1$	$T_0 + T_1 + T_2$	T_0
2	T_0	$T_0 + T_1 + T_2$	$T_0 + T_2$
3	T_0	$T_0 + T_1$	$T_0 + T_1 + T_2$
4	$T_0 + T_2$	T_0	$T_0 + T_1 + T_2$
5	$T_0 + T_1 + T_2$	T_0	$T_0 + T_1$

b) high-to-low switching times:

sector	T_{s1}	T_{s2}	T_{s3}
0	T_0	$T_0 + T_1$	$T_0 + T_1 + T_2$
1	$T_0 + T_2$	T_0	$T_0 + T_1 + T_2$
2	$T_0 + T_1 + T_2$	T_0	$T_0 + T_1$
3	$T_0 + T_1 + T_2$	$T_0 + T_2$	T_0
4	$T_0 + T_1$	$T_0 + T_1 + T_2$	T_0
5	T_0	$T_0 + T_1 + T_2$	$T_0 + T_2$

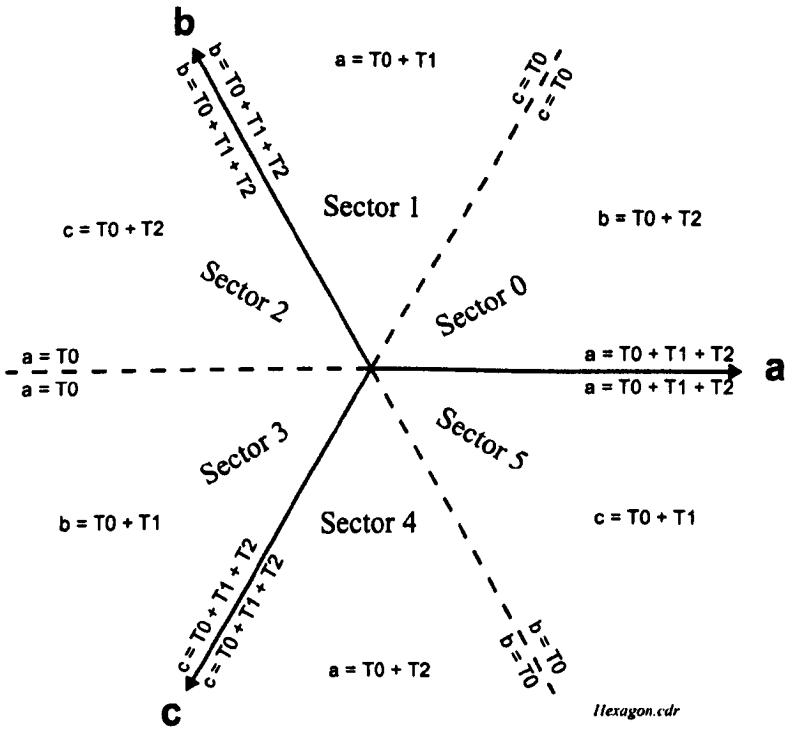

Figure A.3: *Inverter hexagon with switching time calculation*

See document [48] for more details about the practical implementation of Space Vector Modulation.

A.3.2 Switching Times in Three-Phase Coordinates

If phase voltages are directly available, the switching times can be derived directly by means of calculating a mean value. The calculation then is much easier than the polar approach in the previous section. The results are exactly the same. According to Fig. A.2, the phase voltages can only have the two discrete values U_q and $-U_q$ (quantization in amplitude). U_q is equivalent to high-level, when the upper switch is closed (device conducting) and the lower switch is open (the relation between U_q and V_{dc} can be seen in Fig. 2.7, Section 2.2.6). The low-level state $-U_q$ results from the inverse switching state. The mean value of a phase voltage $\overline{U}_n$ in a switching interval T_p is determined by the ratio of high-level to low-level at a load terminal connection. From this results:

$$\overline{U}_n = \frac{1}{T_p}\left(-U_q T_n + U_q(T_p - T_n)\right), \qquad V_{dc} = 2U_q$$

$$= -\frac{U_q T_n}{T_p} - \frac{U_q T_n}{T_p} + U_q$$

$$= V_{dc}\left(\frac{1}{2} - \frac{T_n}{T_p}\right) \qquad \text{for} \quad n = s1, s2, s3$$

By rearranging, the switching times per phase follow

$$T_n = \left(\frac{1}{2} - \frac{\overline{U}_n}{V_{dc}}\right) T_p \tag{A.28}$$

For T_{s1}, T_{s2}, T_{s3} with: $0 \leq T_n \leq T_p$. Introducing a third harmonic voltage component, added to the desired mean voltage $\overline{U}_n$, will result in the same Space Vector Modulation as shown in the polar approach.

The Third Harmonic

Displaying the maximum possible modulating phase voltages as vectors, displaced in space by 120°, results in case (b) in Fig. A.4.
The real axis is in the vertical of the graphic, limited by the voltages of the rectifier. The instantaneous values of the phase voltages can be determined by projection of the space vector on the real axis. The dotted line marks the virtual zero of the inverter. The imaginary axis is in the horizontal. For better understanding of the chronological development, three states are shown on the horizontal axis and the shape of the zero displacement is shown in addition. This shape is also displayed in Fig. A.5.
In pictures b_1) and b_3) it can be seen, that the limits of the rectifier are not used efficiently. However, an enlargement of the vectors is not possible, because the level of the DC link voltage must not be exceeded. This is equivalent to T_n not larger than T_p in equation (A.28). The peak value of the maximum phase voltage results in U_q. A possibility for optimization exists when shifting the centre of the voltage star out of the virtual zero line. Depending on the position of the voltage vector, the offset has to be positive or negative (see a_1, a_3, c_1 and c_3).
The maximum length of the vectors is shown in case a_2) and c_2). The higher efficiency comparing to b_2) can be seen clearly and is about 15%.
For the modulation with two switches, the third harmonic shifts the vector threepod from the virtual origin by a value, that the longest projection on the real axis would exceed the DC link limit. Therefore $\underline{u}_{s_1}$ runs from c_1) to c_2) with its tip along the limit U_q. In c_2) both $\underline{u}_{s_1}$ and $\underline{u}_{s_2}$ are tight, then $\underline{u}_{s_2}$ runs along the negative limit $-U_q$.

- For calculating the third harmonic with two switches, U_{max}, the maximum positive phase voltage, and U_{min}, the minimum phase voltage, have to be determined. For picture c_1 is $U_{max} = \mathrm{Re}\{\underline{u}_{s_1}\}$ and $U_{min} = \mathrm{Re}\{\underline{u}_{s_2}\}$.
  The third harmonic can be calculated for $U_{max} > |U_{min}|$ by

$$U_{harm3} = U_q - U_{max} \tag{A.29}$$

otherwise

$$U_{harm3} = -U_q - U_{min} \tag{A.30}$$

- For the modulation with three switches the third harmonic provides a centering of the vector threepod between the rectifier limits. The mentioned condition, that the distance on the real axis between vector tips and DC link limit for upper and lower bounds have to be equal, leads to the calculation of the third harmonic:

$$|U_q - (U_{max} + U_{harm3})| \stackrel{!}{=} |-U_q - (U_{min} + U_{harm3})| \tag{A.31}$$

rearranging of (A.31) for U_{harm3} gives

$$U_{harm3} = -\frac{U_{max} + U_{min}}{2}$$

Independent, if using a modulation with two or three switches, the switching times including the third harmonic are (based on A.28):

$$T_n = \left(\frac{1}{2} - \frac{\overline{U}_n + U_{harm3}}{V_{dc}}\right) T_p \tag{A.32}$$

The phase voltages can now be increased without the switch-on time exceeding the length of the switching interval T_p.

The presented method, based on voltages in the three-phase coordinate system have the advantage that the sector in the hexagon does not have to be known as in equations (A.23) to (A.25).

The characteristics of the third harmonic (bias) and envelope of the phase voltages for two and three switches can be seen in Fig. A.5. This explains the name for the third harmonic, because its frequency is three times that of the fundamental. For the modulation with three switches (dotted), a triangular shape results. The third harmonic for two switches (dashed) is sinusoidal. The envelope of the phase voltage is determined by the real part of the voltage vector in Fig. A.4. Note that the third harmonic has no influence on the line-to-line voltages, as it cancels when subtracting the phase voltages.

In [48] it is shown that the space vector modulation in polar coordinates (Section A.3.1) and the technique using the 3rd harmonic (Section A.3.2) are mathematically the same.

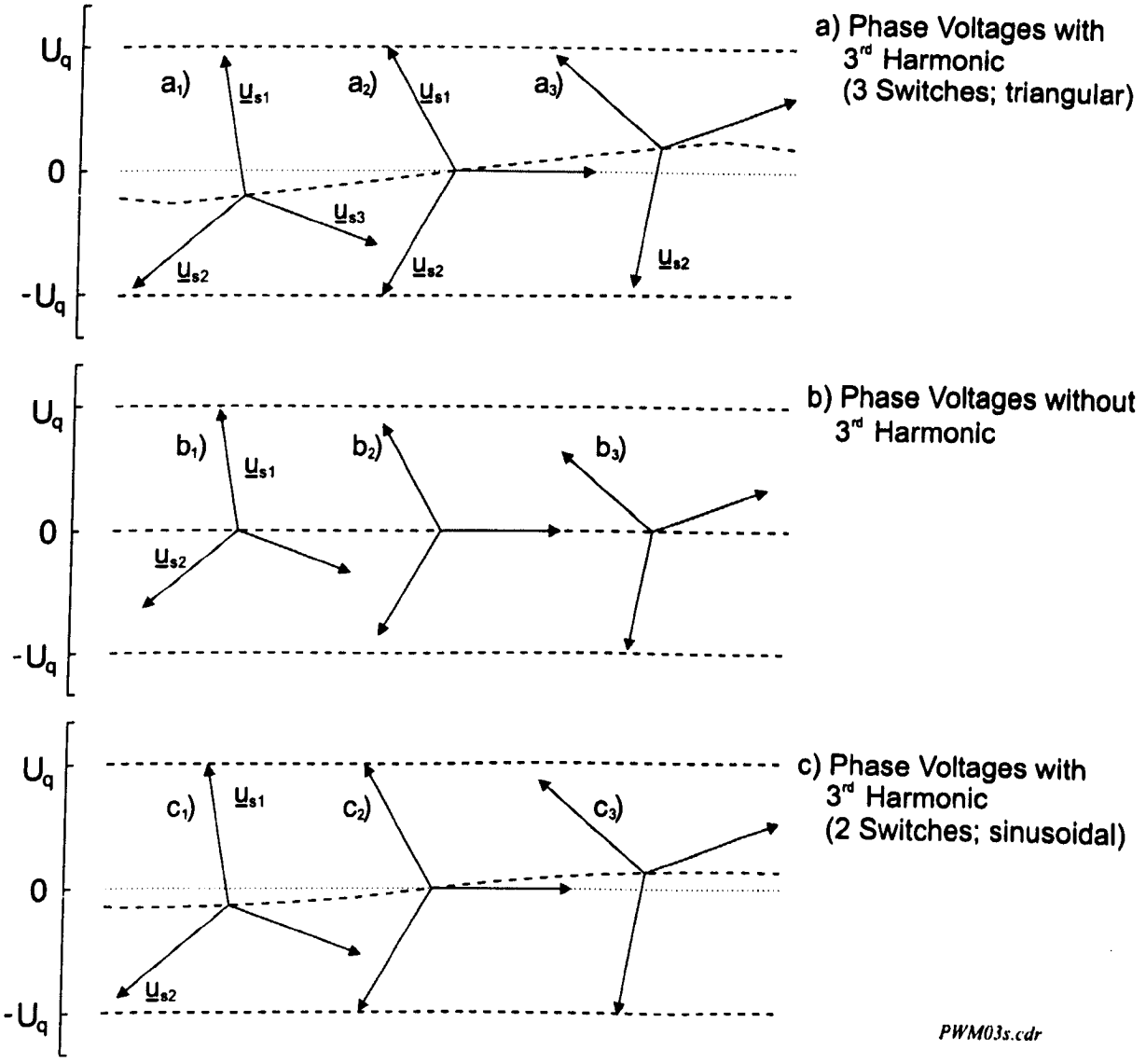

Figure A.4: *Three phase vector in the complex plane*

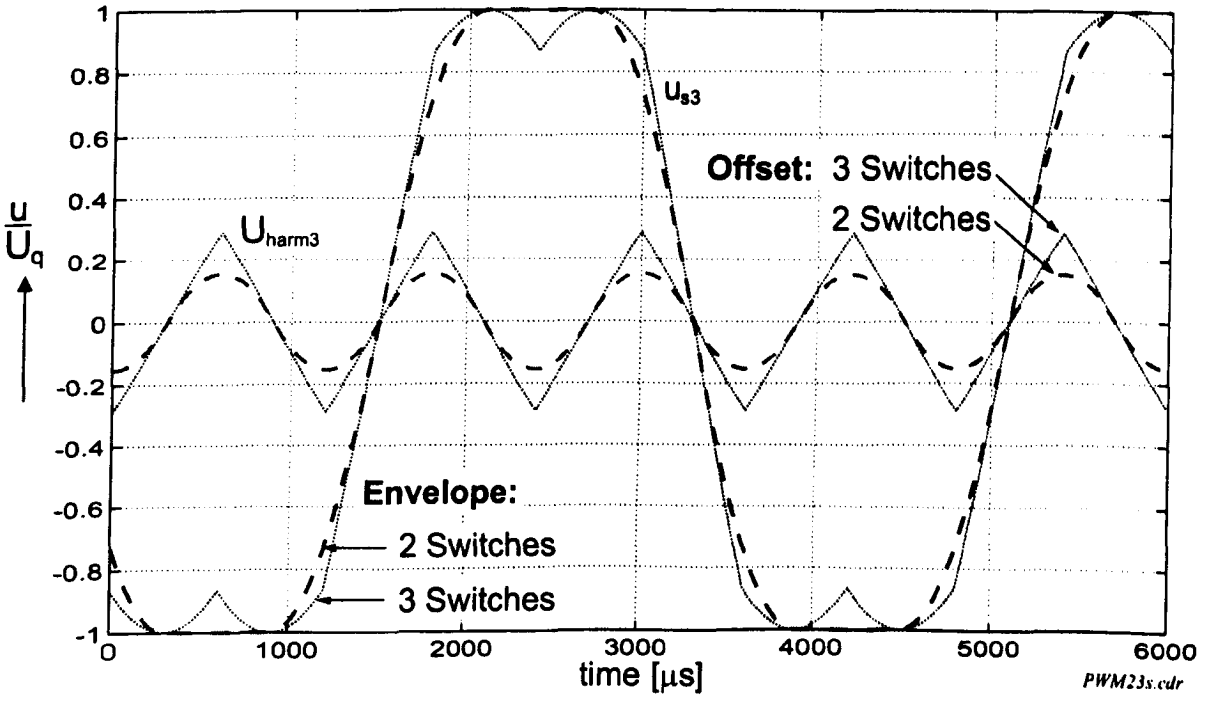

Figure A.5: *Phase Voltages and 3rd Harmonic for PWM with 2 and 3 Switches*

Appendix B:

Rotor Slot Harmonics

Rotor slot harmonics RSH) are not necessarily a wanted effect in the induction machine. An ideal machine would not have any RSH and they are not included in the linear model of the machine. Practically however, they exist in all induction machines. A short introduction to RSH is given and a summary of factors that determine if a machine has rotor slot harmonics that can be exploited for the use of speed or position estimation.

B.1 Fundamental Rotor Slot Harmonics

The slots in the rotor of an induction machine produce a regular variation of the radial air-gap permeance that interacts with the fundamental magnetizing component of the air-gap MMF. Assuming a sinusoidally distributed air-gap MMF at frequency f_e, the fundamental air-gap flux density will be modulated by the passing rotor slots. This modulation produces two harmonic components at frequencies

$$f_{sh} = \pm f_e + \frac{N_r}{pp} \cdot f_r \tag{B.1}$$

where the rotor frequency is f_r and N_r/pp is the number of rotor slots per pole pair. The flux harmonics will then cause corresponding current harmonics in the stator windings at the same frequency. For real machines, the rotor slots will not only interact with the fundamental component of the air-gap flux distribution but will also interact with time and space harmonics due to saturation, eccentricity, stator slotting, spacial asymmetries and non-sinusoidal supply. For a loaded machine where rotor currents flow, the rotor-slot MMF will increase the magnitude of the resulting

rotor slot harmonics.

The existence of rotor slot harmonics depends on a number of factors [121, 149].

a.) An even number of rotor bars per pole pair N_r/pp results in an odd harmonic pole number pp_{sh}. This fact is shown in the central row of Table B.1 with $pp_{sh} = N_r/pp \pm 1$.

b.) Any slot harmonic pole number pp_{sh} that is a multiple of 3 will produce zero sequence conditions for the slot harmonic voltages under ideal conditions. Hence no slot harmonic currents should exist. Second order effects may cause harmonics of small amplitude.

c.) for ideal conditions, machines where N_r/pp is odd or a fractional number, produce no rotor slot harmonics. Third order effects may produce small harmonics.

d.) Static permeance terms that stem from stator slotting or static eccentricity only alter the pole number but not the frequency of a slot harmonic MMF.

e.) Dynamic eccentricity will change the slot harmonic frequency.

f.) Skewing of the rotor will reduce the amplitude of the rotor slot harmonic.

g.) The magnitude of the rotor slot harmonic is in proportion to $1/N_r^2$. An increase in the number of rotor slots will reduce the current through each bar when comparing for the same load condition [121].

h.) The type of rotor bar determines the amplitude change under no-load and full-load condition. Semi-closed rotor slots will only cause a small reduction for less load. Tunnel slot rotors will cause a substantial reduction in the amplitude for less load.

The type of stator used can be important as well. If the number of stator slots N_s is equal to N_r, high cogging torques are the result [121]. Also a difference between N_s and N_r of the number of poles $2pp$ should be avoided.

Table B.1 shows the possible harmonic pole numbers for machines with N_r rotor slots, N_s stator slots and $ps = 2pp$ poles. The harmonic pole number pp_{sh} is the number of poles shown as a harmonic multiple of the pp pole pairs. Note that the factor 2 appears with the slot numbers since there are two poles (or extrema) of the permeance wave per slot. The structure builds up from the left to the right in form of a tree. The rotor slot permeance with $2N_r$ poles interacts with the stator slot permeance,

Source:	Rotor Slot Permeance	Stator Slot Permeance	Static Eccentricity	Fundamental *mmf*	Harmonic Pole No. pp_{sh}
Poles:	$2N_r$	$\pm 2N_s$	$\pm pp$	$\pm ps$	$\frac{1}{ps}$
	$2N_r$	$2N_r - 2N_s$	$2N_r - 2N_s - pp$	$2N_r - 2N_s - 3pp$	$(N_r - N_s)/pp - 1.5$
				$2N_r - 2N_s + pp$	$(N_r - N_s)/pp + 0.5$
			$2N_r - 2N_s$	$2N_r - 2N_s - 2pp$	$(N_r - N_s)/pp - 1$
				$2N_r - 2N_s + 2pp$	$(N_r - N_s)/pp + 1$
			$2N_r - 2N_s + pp$	$2N_r - 2N_s - pp$	$(N_r - N_s)/pp - 0.5$
				$2N_r - 2N_s + 3pp$	$(N_r - N_s)/pp + 1.5$
		$2N_r$	$2N_r - pp$	$2N_r - 3pp$	$N_r/pp - 1.5$
				$2N_r + pp$	$N_r/pp + 0.5$
			$2N_r$	$2N_r - 2pp$	$N_r/pp - 1$
				$2N_r + 2pp$	$N_r/pp + 1$
			$2N_r + pp$	$2N_r - pp$	$N_r/pp - 0.5$
				$2N_r + 3pp$	$N_r/pp + 1.5$
		$2N_r + 2N_s$	$2N_r + 2N_s - pp$	$2N_r + 2N_s - 3pp$	$(N_r + N_s)/pp - 1.5$
				$2N_r + 2N_s + pp$	$(N_r + N_s)/pp + 0.5$
			$2N_r + 2N_s$	$2N_r + 2N_s - 2pp$	$(N_r + N_s)/pp - 1$
				$2N_r + 2N_s + 2pp$	$(N_r + N_s)/pp + 1$
			$2N_r + 2N_s + pp$	$2N_r + 2N_s - pp$	$(N_r + N_s)/pp - 0.5$
				$2N_r + 2N_s + 3pp$	$(N_r + N_s)/pp + 1.5$

Table B.1: Deriving the slot harmonic pole number including stator slotting and eccentricity [149]

resulting in the three terms $2N_r$, $2N_r + 2N_s$ and $2N_r - 2N_s$. Note that the two central rows lead to the well-known harmonic pole numbers $N_r/pp \pm 1$. These will be 28 and 30 for a machine with $N_r = 56$ and $pp = 2$, or 19 and 21 for $N_r = 40$ and $pp = 2$ pole pairs. The principle pole number will be a multiple of 3.

Table B.1 lists the possible interactions of stator and rotor with the resulting space harmonics. The table only gives a key to derive the possible harmonics. No information about the amplitude of the individual harmonics can be deduced since this requires more sophisticated tools like mesh analysis of FEM. Also, the table does not provide a tool to derive the frequency of a RSH but it shows the components contributing to the RSH. Of the possible interactions in the machine described by the parameters in the rightmost column (*Harmonic Pole No.*) of the table, not all will exist. The criteria are given in the enumeration above and in [121, 149].

Applying the analysis from Table B.1 for the symmetric rotor with $N_r = 56$, $N_s = 48$ and $pp = 2$ ($ps = 4$), the harmonic pole numbers of Table B.2 are derived. From

Source:	Rotor Slot Permeance	Stator Slot Permeance	Static Eccentricity	Fundamental *mmf*	Harmonic Pole No. pp_{sh}
Poles:	$2N_r = 112$	$\pm 2N_s = \pm 96$	$\pm pp = \pm 2$	$\pm ps = \pm 4$	$\frac{1}{ps} = \frac{1}{4}$
	112	16	14	10	2.5
				18	4.5
			16	12	3
				20	**5**
			18	14	3.5
				22	5.5
		112	110	104	**26**
				114	28.5
			112	108	27
				116	**29**
			114	110	27.5
				118	29.5
		208	206	202	50.5
				210	52.5
			208	204	51
				212	**53**
			210	206	51.5
				214	53.5

Table B.2: Deriving the slot harmonic pole number for $N_r = 56$, $N_s = 48$ and $pp = 2$

Table B.2 it can be seen that after cancelling the fractional and even harmonic pole numbers (*c.*) and those that are a multiple of three (*b.*), only the following interactions remain: 5, 29 and 53. According to (*g.*), the harmonic pole number with $pp_{sh} = 5$ has the major contribution to the RSH.

B.2 Rotor Slotting Modulation due to *hf* Injection

The overview so far has been mainly on the use of RSH for sensorless speed-controlled drives. However, the given criteria are also valid when using *hf* signal injection to realize sensorless position-controlled drives. The rotor slots cause a modulation of the *hf* signal [82, 83] that can be extracted from the line currents and used to estimate the rotor position. In [99] the rotor slots change the zero voltage in a Y-connected machine for transient injection.

If *hf* voltage injection is applied, the modulation harmonic containing the position information can be found close to the injected frequency f_c in the frequency spectrum of the stator currents with

$$f_{sh_c} = \pm f_c + \frac{N_r}{pp} \cdot f_r \tag{B.2}$$

where f_r is the rotor frequency. The total number of rotor slots in the machine is N_r and $pp = ps/2$ is the number of pole pairs. The position harmonic can easily be

separated from the carrier (see Section 5.4).

The relations (B.2) and (B.1) are practically equal if $f_c = f_e$. The analysis of Table B.1 is equally valid for a fundamental in the machine as well as for *hf* signals. In the latter, the magnitude of the possible harmonic contributions will obviously differ from those resulting from only a fundamental flux in the machine.

A popular choice to obtain rotor slot harmonics in a machine are $N_r = 28$ rotor slots and two pole pairs ($pp = 2$) for small machines [82, 99, 150] and $N_r = 56$ with $pp = 2$ [83,99] for larger machines (7.5kW, 30kW). Other common choices are $N_r = 20$ where $pp = 2$ [62] (7.5kW machine) and $N_r = 40$ with $pp = 2$ [64] (37kW machine). In [149] a 30kW, 4-pole induction machine was analyzed using a number of different rotors. Good results due to sufficient amplitude of the RSH could be obtained with $N_r = 40$ (skewed rotor) and $N_r = 56$ (unskewed). For $N_r = 56$ and skewed, the RSH was smaller but tracking was possible. Operation for $N_r = 57$ (skewed) was difficult and only possible above a certain load. Finally, the rotor with $N_r = 58$ and skewed hardly had any useable RSHs. In [121], a 30kW machine with $N_s = 48$ stator slots and four different rotors was examined. A sufficient RSH signal for speed detection was obtained with all rotors. Three rotors had the same number of slots with $N_r = 56$, two without skew and one skewed. One of the unskewed rotors was semi-closed, the other two had closed rotor slots. The fourth rotor was a $N_r = 40$ skewed rotor with closed rotor slots.

Appendix C:

Parameters

C.1 Machine Parameters

C.1.1 Manufacturer's Data

Manufacturer's data for the 30kW induction machine (parameters for typical direct on line operation):

frame:	W-DF200LNX
output	30kW
poles	4
phases	3
rated speed	1465 rpm
rated full load torque	195Nm
rated full load current I_N (at 415V)	53A
pull out/ breakdown torque	507Nm
rated frequency	50Hz
full load efficiency	93.2%
full load power factor	0.86
efficiency at 1/4 load	87.0%
power factor at 1/4 load	0.52
direct on-line starting current ratio	7.5
starting current	405A
Rotor inertia	0.31Nms^2
insulation class	F
duty cycle	S1 (continuously rated)
enclosure	IP55
construction	cast iron

C.1.2 Symmetric Rotor

A load test was performed under V/f control under rated conditions. The drive was accelerated to n_r = 1500rpm under no-load. Then the DC machine was switched on, applying 100% rated load. The speed of the induction machine dropped down to 1477rpm. The line current had an rms value of 53A.

- The phaseshift between current and voltage can be determined from the sampled signals. The filter in the voltage channel introduces a phaseshift of 11.2° at 50Hz that has to considered. The corrected phaseshift is then 17.188° + 11.2° = 28.388°. The phaseshift gives a **power factor** of $\cos\varphi = 0.88$.

- The current necessary to flux the machine is $\mathbf{i_{sd}}$ = 13.8A for rated speed and full load. The **load current** $\mathbf{i_{sq}}$ was at 28A. Note that $\sqrt{i_{sd}^2 + i_{sq}^2} \cdot \sqrt{3} = \sqrt{13.8^2 + 28^2} \cdot \sqrt{3}\text{A} = 54.0\text{A}$ which is the rated current.

- From the slip calculation for rated synchronous speed and full load, $\omega_{sl} = 2\pi 50 \frac{1500-1477}{1500} = 4.817\text{rad/s}$. The IRFO model sets $\omega_{sl} = \frac{i_{sq}}{T_r \cdot i_{sd}}$. Setting both sides equal, results in a **rotor time constant** of $T_r = L_r/R_r = 0.415\text{s}$ for rated conditions. The rotor time constant was confirmed by performing speed-reversal tests. With the calculated T_r, the reversal time was at a minimum.

- The **input power** is:

$$P_{\text{in}3\sim} = 3 \cdot \Re\{\underline{u}_s(\underline{i}_s)^*\} \tag{C.1}$$

$$= 3 \cdot \Re\{\underbrace{u_{sd}i_{sd} + u_{sq}i_{sq}}_{P} - \underbrace{ju_{sd}i_{sq} + ju_{sq}i_{sd}}_{Q}\}$$

$$= 3 \cdot (u_{sd}i_{sd} + u_{sq}i_{sq}) \tag{C.2}$$

- The **output power** can be derived from the single phase (dynamic) equivalent circuit in stator coordinates:

$$\underline{u}_s = R_s\underline{i}_s + \frac{d\underline{\psi}_s}{dt} = R_s\underline{i}_s + \sigma_s L_o \frac{\underline{i}_s}{dt} + \frac{d}{dt}(L_o\underline{i}_s + L_o\underline{i}_r) \tag{C.3}$$

$$0 = R_r\underline{i}_r + \sigma_r L_o \frac{\underline{i}_r}{dt} + \frac{d}{dt}(L_o\underline{i}_s + L_o\underline{i}_r) - j\omega_r\underline{\psi}_r \tag{C.4}$$

All signals are viewed in respect to the stator frame and a linear model is assumed. From the speed-*emf* term $j\omega_r\underline{\psi}_r$ multiplied with the conjugate complex

of the phase rotor current, the (mechanical) output power is found:

$$P_{\text{out}_{3\sim}} = 3 \cdot j\omega_r \underline{\psi}_r \cdot \underline{i}_r^* \quad \text{(C.5)}$$
$$= 3 \cdot j\omega_r (L_r \underline{i}_r + L_o \underline{i}_s) \cdot \underline{i}_r^* \quad \text{(C.6)}$$

Where ω_r is the rotor angular velocity and the factor 3 is required to get the three phase output power from the single phase equivalent circuit.

- With the **torque** $T_{3\sim} = \frac{P_{\text{out}_{3\sim}}}{\Omega_r}$ and the electrical rotor speed $\omega_r = pp \cdot \Omega_r$ where pp is the number of pole pairs and $\omega_{r_{max}} = 2 \cdot 1500 \text{ rpm}/60 = 50\text{Hz}$. Then, the output torque is:

$$\begin{aligned} T_{3\sim} &= 3\,pp \cdot j(L_o \underline{i}_s + L_r \underline{i}_r) \cdot \underline{i}_r^* \\ &= 3\,pp \cdot \Im\{(L_o \underline{i}_s + L_r \underline{i}_r) \cdot \underline{i}_r^*\} \\ &= \boxed{3\,pp \cdot L_o \cdot \Im\{\underline{i}_s \cdot \underline{i}_r^*\}} \end{aligned} \quad \text{(C.7)}$$

As it is difficult to measure the rotor currents on a squirrel cage induction motor, the rotor currents are replaced by the magnetizing current $\underline{i}_{mR}$ with

$$L_o \underline{i}_{mR} \stackrel{!}{=} \underline{\psi}_r = L_r \underline{i}_r + L_o \underline{i}_s \quad \text{(C.8)}$$

If the magnetizing current is aligned to the flux axis (= d-axis), the imaginary part is zero:

$$\Re\{\underline{i}_{mR}\} = i_{mR} \quad \text{(if aligned to flux axis)} \quad \text{(C.9)}$$
$$\Im\{\underline{i}_{mR}\} = 0 \quad \text{(if aligned to flux axis)} \quad \text{(C.10)}$$

Using the substitution in *(C.8)*, *eq. (C.7)* is modified to:

$$T_{3\sim} = 3\,pp \cdot L_o \cdot \Im\{\underline{i}_s \cdot \left(\frac{L_o \underline{i}_{mR} - L_o \underline{i}_s}{L_r}\right)^*\} \quad \text{(C.11)}$$

Working now in the flux oriented dq frame, the torque equation simplifies:

$$T_{3\sim} = 3\,pp \cdot \frac{L_o^2}{L_r} i_{mR} \cdot \Im\{i_{sd} + j i_{sq}\} = \boxed{3\,pp \cdot \frac{L_o^2}{L_r} i_{mR} \cdot i_{sq}} \quad \text{(C.12)}$$

With $i_{mR} = 14\text{A}$, $i_{sq} = 28\text{A}$, $pp = 2$, $L_o = 82.5m\text{H}$ and $L_r = 83.5m\text{H}$:

$$T_{3\sim_{\text{max}}} = 3 \cdot 2 \cdot \frac{(82.5m\text{H})^2}{83.5m\text{H}} \cdot 14\text{A} \cdot 28\text{A} = 192\text{Nm}$$

also from the steady-state equivalent circuit of the induction machine:

$$T_{3\sim} = 3\,pp \cdot L_o \cdot I_s^2 \cdot \Im\{\frac{j\omega_e L_o}{R_r/s - j\omega_e L_r}\}$$

The current I_s is the rms value of the single phase circuit, thus the phase current $I_p = I_{LL}/\sqrt{3} = 53\text{A}/\sqrt{3} = 30.6\text{A}$ for rated conditions. Inserting rated values, the electrical torque is

$$T_{3\sim_{\max}} = 3 \cdot 2 \cdot 82.5m\text{H} \cdot \left(\frac{53\text{A}}{\sqrt{3}}\right)^2 \cdot \Im\left\{\frac{j2\pi 50 \cdot 82.5m\text{H}}{\frac{0.2\Omega}{0.0153} - j2\pi 50 \cdot 83.5m\text{H}}\right\} = 184\text{Nm}$$

- A crude estimation of the **magnetizing inductance** can be obtained by evaluation of the steady-state single phase equivalent circuit used for V/f control. First, the stator resistance and the voltage drop across the stator inductance are neglected. Then, the magnetizing voltage is equal to the phase voltage that is the line-to-line voltage for the Δ-connected machine. The current through the magnetizing inductance will be close to the i_{sd} value, the imaginary component of the stator current to flux the machine.

$$\begin{aligned} \Im\{\underline{I}_p\} &\approx \frac{V_p}{\omega_e L_o} \\ \rightarrow L_o &\approx \frac{V_p}{2\pi f_e \cdot I_{p_{\text{imag}}}} \\ &\approx \frac{415\text{V}}{2\pi 50\text{Hz} \cdot 14\text{A}} \\ &\approx 94m\text{H} \end{aligned} \qquad \text{(C.13)}$$

- The **inertia** of the drive system can be determined in different ways.

  1. By Geometry [7]:
     For the induction machine with the rotor length $l \approx 0.225\text{m}$, the radius $r = 0.108905\text{m}$, the material density $\rho \approx 7.0 \ldots 7.9\text{g/cm}^3$ [151], the mass M and the volume V.

$$J_{IM} = \int_0^M r^2 dM$$

     where the unknown mass M can be determined via the volume V:

$$dM = \rho \cdot dV = \rho \cdot 2\pi\, r\, l \cdot dr$$

$$\begin{aligned} J_{IM} &= \frac{\pi}{2} \cdot \rho \cdot l \cdot r^4 \\ &\approx \frac{\pi}{2} \cdot \frac{7 \cdot 10^{-3}\text{kg}}{0.01^3\text{m}^3} \cdot 0.23 \cdot 0.1089^4 \\ &\approx 0.355\text{Nms}^2 \end{aligned}$$

2. From Manufacturer's data:

J_{IM}	=	0.31Nms^2	for the induction machine
J_{dc}	=	0.27Nms^2	for the DC drive
J_{couple}	=	0.036Nms^2	for the coupling
$J = \sum J_i$	=	0.616Nms^2	total inertia

3. From Speed reversal test:
   The mechanical equation can be simplified in the point $n_r = 0\text{rpm}$:

$$(J\dot{\omega} + b_F\omega)\Big|_{\omega=0} = T_{el}\Big|_{\omega=0}$$

The speed dependent term cancels and only the speed change has to be determined. The electrical torque produced by the machine should ideally be constant. The torque-producing current in Fig. C.1 is $i_{sq} = 33.05\text{A}$ during the speed reversal which is 1.18 times larger than the nominal value of $i_{sq_n} = 28\text{A}$. Therefore $T_{el} = 1.18 \cdot 195\text{Nm}$. For determining the speed slope in the origin, the two symmetric points for $\pm 900\text{rpm}$ ($\pm 30\text{s}^{-1}$) are chosen, so that $t_1 = 0.0417\text{s}$, $n_1 = -900\text{rpm}$, $t_2 = 0.54165\text{s}$ and $n_2 = +900\text{rpm}$.

$$\begin{aligned} J\dot{\omega}\Big|_{\omega=0} &= J \cdot \frac{\Delta\omega}{\Delta t}\Big|_{\omega=0} = 1.18 \cdot 195\text{Nm} \\ &= J \cdot 2\pi \frac{(30 - (-30))\,1/\text{s}}{t_2 - t_1} \end{aligned}$$

The resulting total inertia of the drive is $J = 0.61\text{Nms}^2$.

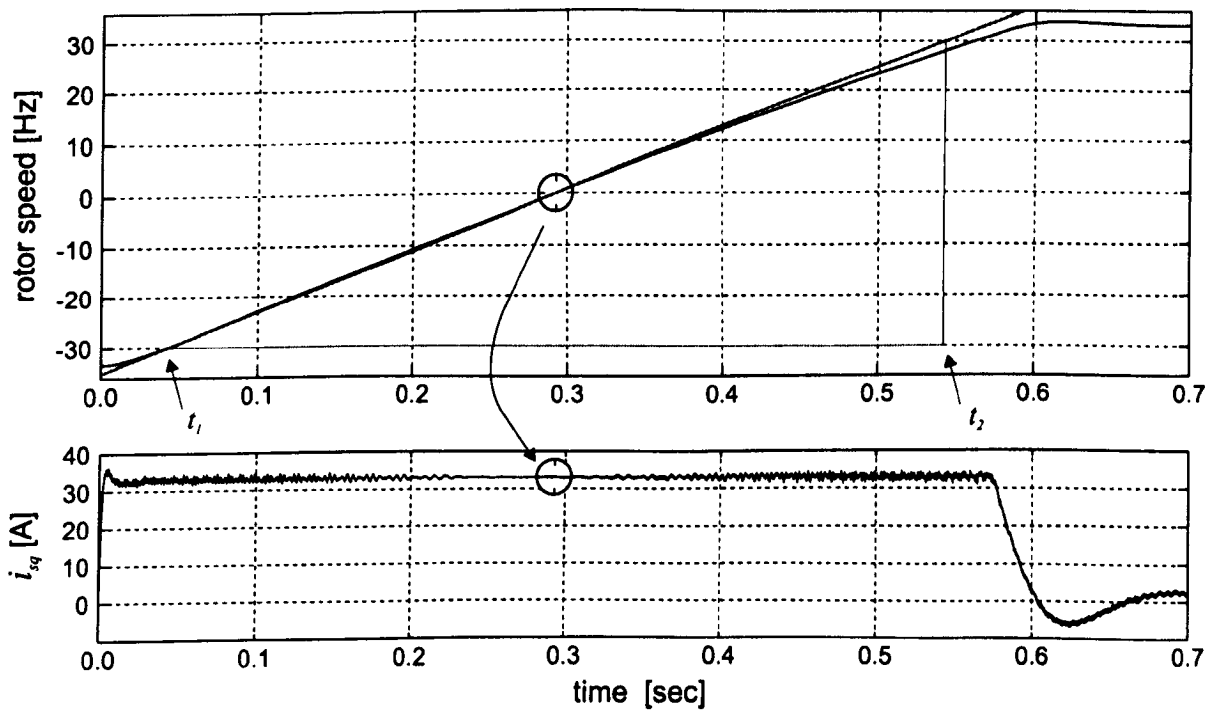

Figure C.1: Speed reversal from −1000rpm to +1000rpm under no load to determine the drive inertia

C.2 Filters

This section briefly describes the analogue and digital filters that are used in the rig. These filters can be for the measurement of the fundamental voltages or to separate and demodulate the *hf* current modulation.

C.2.1 Voltage Filter

For the measurement of the line-to-line voltages at the output of the voltage transducers, a first order lowpass filter is used. The cutoff frequency is 340Hz as determined experimentally.

C.2.2 Analogue Bandpass Filter

Two channels analogue bandpass filters are needed to separate the *hf* currents from the fundamental line currents.

$$G(s) = \frac{K \cdot s^4}{(s+p_1)(s+p_1^*)(s+p_2)(s+p_2^*)(s+p_3)(s+p_3^*)(s+p_4)(s+p_4^*)}$$

with p_i^* the conjugate complex of p_i

- Analogue pre-A/D bandpass filters for 300Hz centre frequency (rotor #1 and rotor #3):

$$\begin{array}{lllllllll} p_1 & = & 805.2 & + & j1960.1, & p_1^* & = & 805.2 & - & j1960.1 \\ p_2 & = & 1955.9 & + & j815.4, & p_2^* & = & 1955.9 & - & j815.4 \\ p_3 & = & 559.9 & + & j1363.0, & p_3^* & = & 559.9 & - & j1363.0 \\ p_4 & = & 1360.1 & + & j815.4, & p_4^* & = & 1360.1 & - & j815.4 \\ K & = & 1.35e14 & & & & & & & \end{array}$$

- Analogue pre-A/D bandpass filters for 750Hz centre frequency (rotor #3):

$$\begin{array}{lllllllll} p_1 & = & 2255.5 & + & j5490.2, & p_1^* & = & 2255.5 & - & j5490.2 \\ p_2 & = & 5478.4 & + & j2283.9, & p_2^* & = & 5478.4 & - & j2283.9 \\ p_3 & = & 1395.9 & + & j3397.9, & p_3^* & = & 1395.9 & - & j3397.9 \\ p_4 & = & 3390.6 & + & j1413.6, & p_4^* & = & 3390.6 & - & j1413.6 \\ K & = & 8.29e15 & & & & & & & \end{array}$$

C.2.3 Digital Lowpass Filters

For the demodulation of the *hf* current harmonics, a number of lowpass filter are digitally implemented on the processor.

$$G(z) = \frac{c_5 z^2 + c_4 z + c_3}{c_2 z^2 + c_1 z + c_0}$$

- Positive sequence elimination filter (second order Butterworth, $f_{cut} = 49.5$Hz, rotor #1):

$$\begin{aligned} c_5 &= 0.000168 \\ c_4 &= 0.000336 \\ c_3 &= 0.000168 \\ c_2 &= 1.00 \\ c_1 &= -1.97 \\ c_0 &= 0.96 \\ T_s &= 84.0\mu s \quad \text{(sampling period)} \end{aligned}$$

- Positive sequence rejection filter (second order Butterworth, $f_{cut} = 25$Hz, rotor #1):

$$\begin{aligned} c_5 &= 0.000241 \\ c_4 &= 0.000482 \\ c_3 &= 0.000241 \\ c_2 &= 1.00 \\ c_1 &= -1.9555 \\ c_0 &= 0.9565 \\ T_s &= 200.0\mu s \quad \text{(sampling period)} \end{aligned}$$

- Positive sequence elimination filter (second order Butterworth, $f_{cut} = 300$Hz, rotor #3):

$$\begin{aligned} c_5 &= 0.02786 \\ c_4 &= 0.05571 \\ c_3 &= 0.02786 \\ c_2 &= 1.00 \\ c_1 &= -1.475 \\ c_0 &= 0.5869 \\ T_s &= 200.0\mu s \quad \text{(sampling period)} \end{aligned}$$

- Lowpass filter for stator current angle (second order Butterworth, $f_{cut} = 100$Hz, rotor #3):

$$\begin{aligned} c_5 &= 0.027859 \\ c_4 &= 0.055719 \\ c_3 &= 0.027859 \\ c_2 &= 1.00 \\ c_1 &= -1.4754 \\ c_0 &= 0.5869 \\ T_s &= 200.0\mu\text{s} \quad \text{(sampling period)} \end{aligned}$$

A first order lowpass filter is used to smooth i_{sq} when addressing the table for *Harmonic Compensation*

$$G(z) = \frac{c_2}{c_1 z + c_0}$$

- Table index filter (first order, $f_{cut} = 20$Hz, $T_f = 8ms$, rotor #1):

$$\begin{aligned} c_2 &= 0.02469 &&= (1 - e^{-T_s/T_f}) \\ c_1 &= 1.00 \\ c_0 &= -0.97531 &&= e^{-T_s/T_f} \\ T_s &= 200.0\mu\text{s} && \text{(sampling period)} \end{aligned}$$

- Lowpass filters for smoothing *SMP* data (first order, $f_{cut} = 31.8$Hz, $T_f = 5ms$, rotor #3):

$$\begin{aligned} c_2 &= 0.03921 &&= (1 - e^{-T_s/T_f}) \\ c_1 &= 1.00 \\ c_0 &= -0.96079 &&= e^{-T_s/T_f} \\ T_s &= 200.0\mu\text{s} && \text{(sampling period)} \end{aligned}$$

C.2.4 Highpass Filters

For the demodulation of the *hf* current harmonics, a highpass filter is digitally implemented on the processor to improve the carrier harmonic rejection.

$$G(z) = \frac{c_5 z^2 + c_4 z + c_3}{c_2 z^2 + c_1 z + c_0}$$

- Positive sequence elimination filter (second order Butterworth, $f_{cut} = 15\text{Hz}$, rotor #3):

$$
\begin{aligned}
c_5 &= 0.98676 \\
c_4 &= -1.97352 \\
c_3 &= 0.98676 \\
c_2 &= 1.00 \\
c_1 &= -1.9733 \\
c_0 &= 0.9736 \\
T_s &= 200.0\mu\text{s} \quad \text{(sampling period)}
\end{aligned}
$$

Appendix D:

Schematics

This chapter is dedicated to the description of the interface circuits and external boards that are needed for machine control and sensorless position estimation. The schematics are given and a brief description for each of the boards to simplify understanding. Most boards were derived from earlier designs. The experience was the basis for completely new designs providing more flexibility, more security and more accuracy.

D.1 PWM and Encoder Board

This board serves two purposes. Firstly, the PWM signals are generated and sent via the interface board to the inverter and secondly, the encoder is connected to determine position and speed of the induction machine. The hardware is simplified by using the integrated peripherals of the TMS320F240 digital signal processor. This DSP is connected to the LSI motherboard with the C40 via a Dual-Port RAM (DPRAM). The C40 sends the PWM voltages or switching times to the F240 by writing into the DPRAM.
If PWM voltages are sent, these are the *d-q* reference voltages. Addition of *hf* voltage injection and the output transformations and calculation of switching times is done in software on the F240. The calculated timings are written into the F240 compare registers. The PWM outputs are on pins 3, 5 and 7 of the primary header of the evaluation board and can be accessed via connector `Con1`. The three PWM signals are also sent to LEDs at the front of the board to allow a quick visual check if the PWM is working. The deadtime generator of the F240 is not used. This is built into the IGBT driver boards of the *Eurotherm* 584SV inverter. For secure signal transmission from the board to the inverter, a differential transmission is used. The `DS26LS31` driver

chip converts the TTL levels to differential signals according to standard RS-422. Additional to the three PWM pulses, a reset signal is sent to the inverter where it is combined with the reset signal of the inverter (see page 306). A small disadvantage is that no reset feedback from the inverter to the F240 exists. The F240 is therefore not informed if the inverter detects a reset condition and continues to generate the PWM signals. It will have to be manually restarted together with the C40 after clearing the trip condition. The trip conditions of the F240 board are caused by a low on $\overline{\texttt{PWMOFF}}$ that is the input for $\overline{\texttt{PDPINT}}$, the pin to start the power-down and protection interrupt of the F240. This line can be pulled low by the C40 and sets the PWM pins instantaneously into high impedance state. The F240 can also set a trip by pulling pin $\overline{\texttt{XF}}$ low. This pin is low on reset and startup to ensure the inverter is in trip mode and no spurious signals get through. Both trip signals are passed to the external reset box shown in Fig. D.7 that allows the user to manually cause a trip to disable the inverter.

The output of *IC1a* is a combination of the trip condition coming from the F240 board on pin 2 and the condition of the trip switch U1. If the switch is open, pin 1 is tied high and the output of the OR-gate *IC1a* is high, indicating a trip. If the switch is closed, the output of the OR-gate will be only low if also the F240 trip signal is low. A low will then indicate that no trip exists. In case a trip has occurred or the circuit in the reset box is currently powered up, *IC1b* latches a trip state. The closed switch U2 will hold input pin 5 at high level if output pin 6 is also high. Opening the switch U2 is the only way to clear a trip from pin 6 if no trip exists on pin 4 any more (at low level). The capacitor will be discharged via the resistor and input 5 goes low and output pin 6 as a result. This will prevent the capacitor from being charged again. The transistor T1 decouples the control signal from powering the status LED. This will indicate a trip condition and therefore a high level for `ResetOut` shining in red colour. The reset line $\overline{\texttt{RS}}$ of the evaluation board is connected to the $\overline{\texttt{RESET}}$ line coming from the C40 motherboard. The F240 will be kept in reset until the C40 is running. The diode in the path is necessary for decoupling, to prevent feedback. If the F240 is used alone e.g. in debug mode, the LSI motherboard must not be in reset.

The F240 board also provides the trigger impulse for the ADC boards (see Section D.6). This allows to align and synchronize the signal conversion with the PWM pulses. The cutoff frequency of the filters in the current paths can be much higher. This allows for a higher bandwidth of the current controllers in Vector Control. The ADC boards are triggered by the signal `ADCTRIG` that is obtained by XORing the signals of pins 11 and 12 from the primary header. The two auxiliary PWM signals are required to generate the ADC trigger impulse that has to be longer than $40ns$ and shorter than $6\mu s$ to guarantee a correct A/D conversion. The trigger signal is combined with the `NoTrig` line from the C40 before it is inverted. A rising edge on

ADCTRIG therefore starts a conversion. The **NoTrig** line allows the C40 to prevent a conversion.

To simplify code development, a basic evaluation board of the F240 DSP was purchased. This provides easy access to the 132 pins of the F240 via four headers. The F240 evaluation board comes with a monitor program burnt into the FLASH for programming code and for debugging. The evaluation board has to be connected to the PC via a serial cable for this purpose. Next to debugging and programming, the F240 can also be run user code. Then the monitor program is disabled by connecting pins 16 and 34 of header P14 on the evaluation board. An external switch is connected to the two pins. This setting ensures that the user code is loaded when the F240 boots up and that the secondary (user) interrupt vector table is used. When the processor is powered up, the position of the switch determines which of the three modes is used. If pin $\overline{\text{BIO}}$ is grounded, the monitor is disabled and the primary vector table is mapped to the secondary table at address **FE00h** in program RAM that allows to run the user code. For $\overline{\text{BIO}}$ at high level, the user code can be loaded into the FLASH behind the resident monitor program.
The programming software is also part of the evaluation package. Once the FLASH is programmed, the processor has to be reset to start the user code that now remains in the on-chip memory. In debug-mode, the debugging software can be used to step through code that is in RAM. This can be on-chip RAM or external RAM. Code in the FLASH cannot be tested. The debug software provides access to all registers of the F240, the program code and data memory that can also be changed on-the-fly. Step-over and trace-into are possible or the processor can be operated in two different free-run modes.

Two different types of encoders can be connected to the F240 board. The direction of the connected encoder is analyzed in the F240 and output via the **EncDir** pin that connects to a bicolour LED. The red LED indicates positive direction. For negative direction, the green LED in on. Connector **Con5** interfaces to a standard quadrature-pulse encoder. The connector is for a **BEC 735** encoder with 3000 pulses per revolution and marker impulse. The transmission of the two position signals and the zero marker is differentially. The signals **CHA+**, **CHA-** and **CHB+**, **CHB-** and the lines of the zero pulse **CHZ+**, **CHZ-** are sent via the **DS26LS32** receiver chip. Output are the TTL signals **Aout**, **Bout** and **Cout**. The digital switch **74x157** has to be in '**port B**' position (**SW2** is up in position 1) to send the **BEC 735** encoder signals to the F240 pins 17, 18 and 19 of the primary header. The first two pins are configured as **QEP1** and **QEP2**. In this mode, the encoder pulses are the inputs for the integrated quadrature-unit QEP that clocks the position counter register of the F240. Pin 19 can be used to reset this counter register with the zero marker. This feature is currently unused but

can provide an absolute position information within one mechanical revolution. Note that the rotor has to be turned up to 360° to align the counter register value with the real position. The initial register value might not represent the initial position so that one zero marker pulse is needed.
With SW2 in position 2 (that is 'port A' for the digital switch 74x137), a SinCoder can be used. This encoder is attached to connector Con6 and requires the two QEP pins and two ADCs of the F240. A SinCoder by *Stegmann* is used. This sends two analogue sine waves that are a quarter of a period out of phase with 1024 periods per mechanical revolution. Digitizing these signals provides the position and direction in the same way as a normal digital encoder. Using the full analogue information using ADCs allows to interpolate the position information. The position information can be resolved much finer. This can be particularly important for the speed calculation at low speeds. The SinCoder can be controlled via the DATA+ and DATA- lines. Manufacturer settings and parameters can be read out. Also the resolution can be changed. Initially, the 360° absolute position is needed when starting the drive. The SinCoder is configured to provide one sinewave per revolution similar to a resolver. The two position values converted by the two ADCs can be sent through an arctan function to give a crude absolute position. Note that the single period per mechanical revolution removes the position ambiguity. Then, the SinCoder is configured to provide 1024 sine periods per revolution. The encoder works incrementally with high resolution. A zero marker pulse finally corrects initial differences in determining the absolute position. The analogue position signals are sent via the differential pins REFSIN, SIN and REFCOS, COS of connector Con6. The first stage is a differential amplifier to convert the differential signals to analogue unipolar signals. The second stage adds an offset of 2.5V, that is half the supply voltage. The analogue signals are also scaled to suit the input range of the integrated AD converters of the F240. A lowpass filter follows and connects the signal to either pin 1 or 2 of the secondary header. The stage in parallel is a comparator or Schmitt-trigger that digitizes the sinewaves. This serves as input for the quadrature-unit of the F240. The supply and range of the internal ADCs can be also adjusted. This is done via the potentiometers on pins 7 and 8 of the secondary header. A differential driver/receiver device SN75176A is used for communication with the SinCoder. The receive line can be connected to the RXD pin to receive data or to the QEPZero line when the communication is finished and to analyze the zero marker pulse. An additional +8V voltage generator is needed for the SinCoder. The voltage is derived from the +15V rail and buffered by tantal and ceramic capacitors.

The DPRAM has a size of 2048 x 16bit and is mapped into the external program and data space for the F240 as indicated by the darker sections in Fig. D.1. Half of the DPRAM can be addressed via the data addresses 0x8000 - 0x83FF. The memory is

mirrored and therefore can be accessed across the whole data space up to 0xFFFF. The 1k of data memory is subdivided into 4 pages. This stems from the addressing technique required from the C40 side. Only the lower address lines A0 to A6 were used to access boards via the DSPLINK bus. In contrast to the C40, the F240 can access the DPRAM linearly. For the 1k WORDs of program memory, the mapping into the F240 program space is similar to that of the data memory. The mapping follows directly after the internal flash memory (0x0 - 0x3FFF) from 0x4000 to 0x43FF. The mapping is mirrored contiguously in 1k sections up to address 0xFDFF. Addresses 0xFE00 - 0xFEFF cover the internal RAM. The DPRAM is divided into *pages* 0 to 3. The F240 memory map in Fig. D.1 also shows the internal data RAM and program space (FLASH and RAM). For the program space, it would appear more logical to use the space 0xFA00 - 0xFDFF which is directly followed by the internal RAM. Note however that the secondary vector table has to start from 0xFD00. For the data space, the partitioning into 256 WORDs is in accordance to the limitation of the F240 for direct addressing.

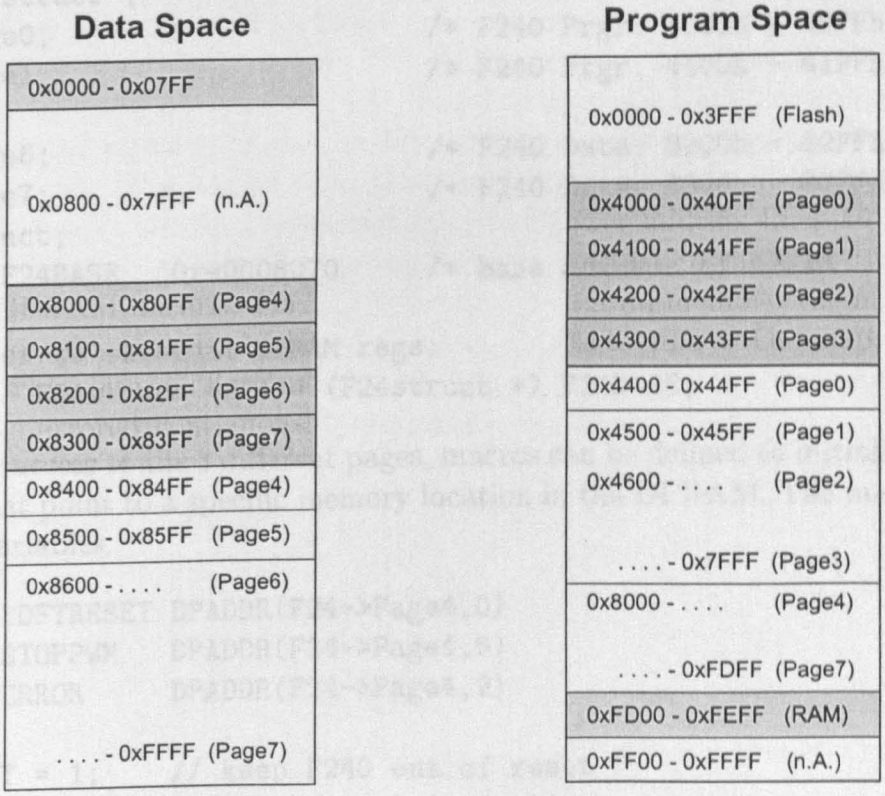

Figure D.1: *F240 Memory Map, (n.A. = not available)*

For the C40, the address bits A6 - A3 of the DSPLINK bus are used to select one out of 16 possible peripheral boards of the rack. They are accessible via the C40

address space 0x90008000 to 0x9000807F. For every board, the address bits A2 - A0 are used to write/read a maximum of 8 individual registers. As this is not enough for addressing the DPRAM, the remaining (upper) DSPLINK address bits A14 - A7 are used. Note that address line A15 is not connected on the C40 motherboard and some new versions also lack address line A14. Lines A14 to A7 are mapped to the DPRAM address lines AR7 to AR0 respectively. This covers a range of $2^8 = 256_d$ = 0xFF which makes a page. Using the C40 address lines A2 to A0 and connecting them to AR10 to AR8 respectively, a total of 8 *pages* can be addressed.

For the address remapping from the C40, a simple macro can be used. This simplifies the access when writing in a high-level language like *C*. The two parameters of the macro are x, that is a pointer to a page and y, the address within a page that can be within [0...255].

```
#define DPADDR(x,y) *(&(x) + ((y) << 7))

typedef struct {                    /* 256 locations per page} */
 int Page0;                         /* F240 Prgr: 4000h - 40FFh*/
 int Page1;                         /* F240 Prgr: 4100h - 41FFh*/
       :
 int Page6;                         /* F240 Data: 8200h - 82FFh*/
 int Page7;                         /* F240 Data: 8300h - 83FFh*/
} F24struct;
#define F24BASE   0x90008070        /* base address of DPRAM   */

// pointer to external DPRAM regs:
volatile  F24struct *F24 = (F24struct *) F24BASE;
```

To simplify access to the 8 different pages, macros can be defined to initialize constant pointers that point to a specific memory location in the DPRAM. The macros can be used like variables.

```
#define SOFTRESET DPADDR(F24->Page4,0)
#define STOPPWM   DPADDR(F24->Page4,6)
#define ERROR     DPADDR(F24->Page4,9)

SOFTRESET = 1;     // keep F240 out of reset
```

Pages 0 - 3 are mapped into the F240 program space, *pages* 4 - 7 are in the F240 data space. The C40 page mapping that uses lines A0 to A2 is shown in the following table. If not all of the DPRAM memory is needed, some address combinations could be used to set modes of other devices on the board. This is currently not implemented.

A2	*A1*	*A0*	
0	0	0	Page0
0	0	1	Page1
0	1	0	Page2
0	1	1	Page3
1	0	0	Page4
1	0	1	Page5
1	1	0	Page6
1	1	1	Page7

F240		C40
8000h	$\Longleftrightarrow$	90008074h
8001h	$\Longleftrightarrow$	900080F4h
8002h	$\Longleftrightarrow$	90008174h
8003h	$\Longleftrightarrow$	900081F4h
8004h	$\Longleftrightarrow$	90008274h
8005h	$\Longleftrightarrow$	900082F4h
8006h	$\Longleftrightarrow$	90008374h
8007h	$\Longleftrightarrow$	900083F4h
8008h	$\Longleftrightarrow$	90008474h
⋮		⋮

An example for the data memory mapping of *page4* is given in the left table. The F240 addressing is linear, for the C40 the addresses are located in steps of *80h* from the base address *90008070h* + *page4* = *90008074h*.

On the F240 side, the lines $\overline{\texttt{DS}}$ and $\overline{\texttt{PS}}$ are used to select and enable the DPRAM when external memory is to be accessed. The $\overline{\texttt{WE}}$ line of the F240 is connected to the R/$\overline{\texttt{W}}$ line of the left control interface of the DPRAM to control if the F240 writes to or reads from the external memory. A low on the W/R line is additionally necessary to enable the drivers of the DPRAM so that data can be read into the F240. The DPRAM signals that data is stored or provided for the F240 with its $\overline{\texttt{BUSY}}$ line. Connecting this to the READY pin of the F240 allows a flexible handshaking that replaces a fixed wait-state policy.

For more information about the configuration of the F240 registers and details about the communication between C40 and F240 can be found in [152]. This document also specifies the initialization for the C40 and specific settings.

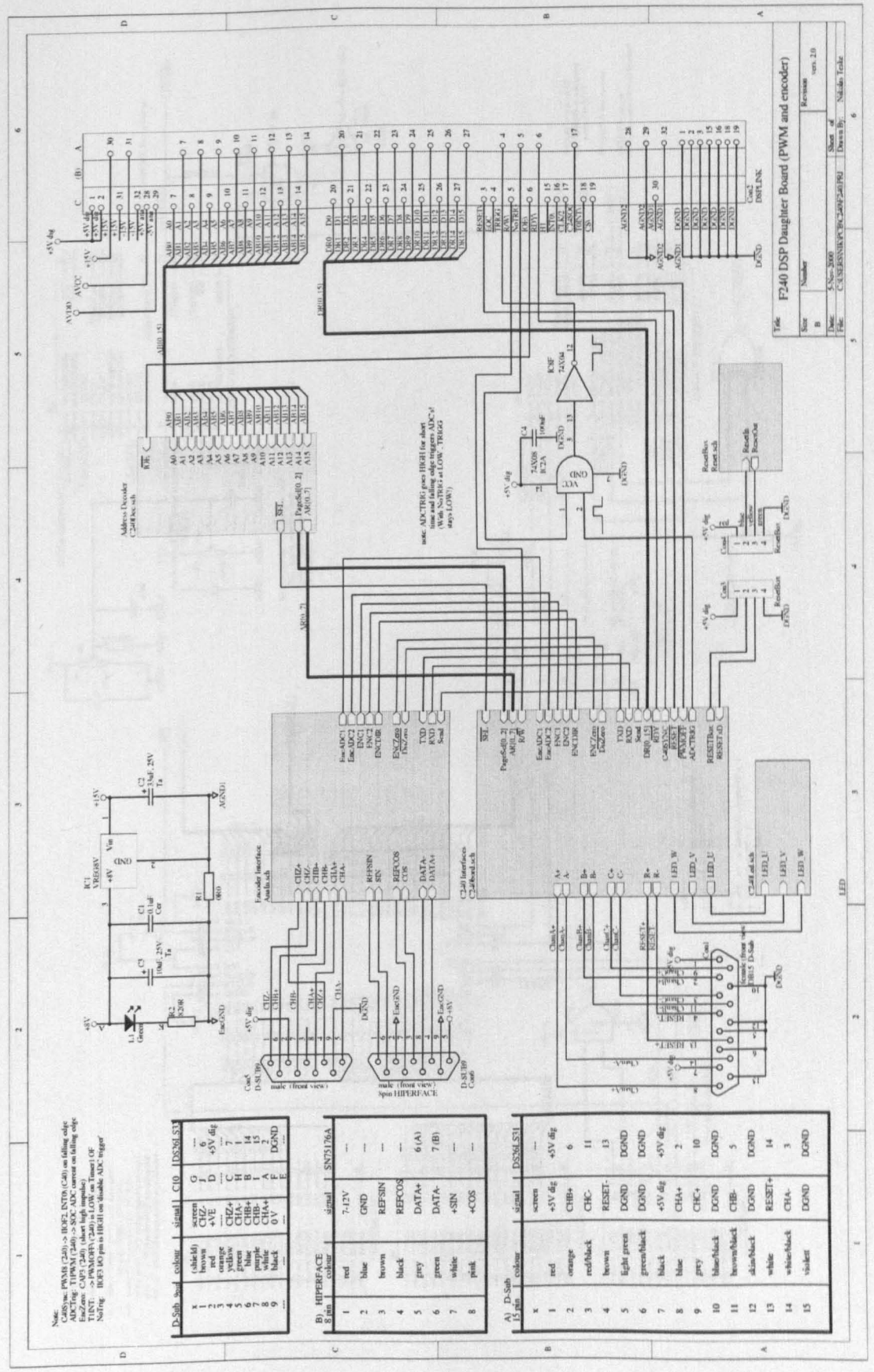

Figure D.2: *Schematic of PWM and Encoder Board*

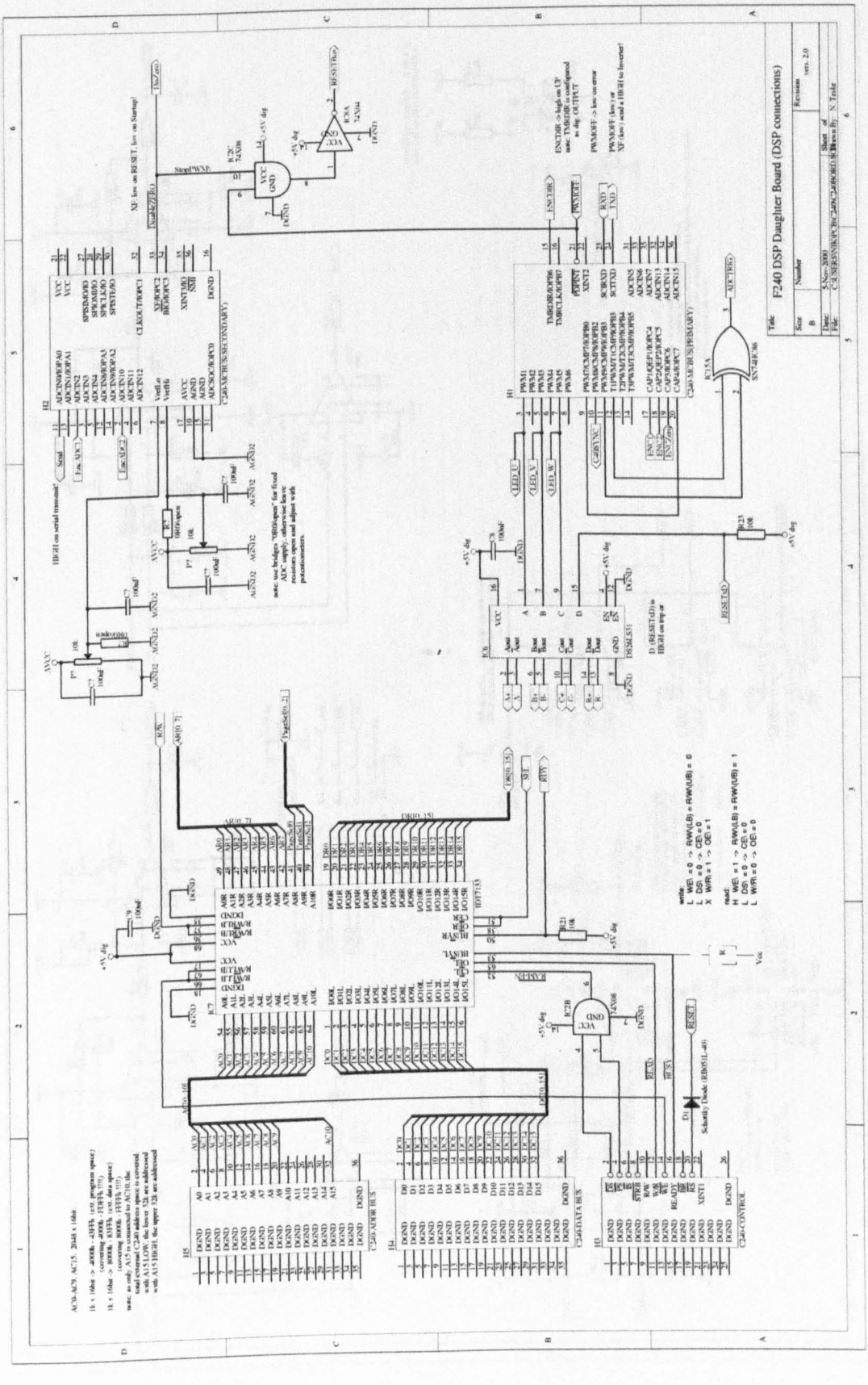

Figure D.3: *Schematic of Connections for F240 Board*

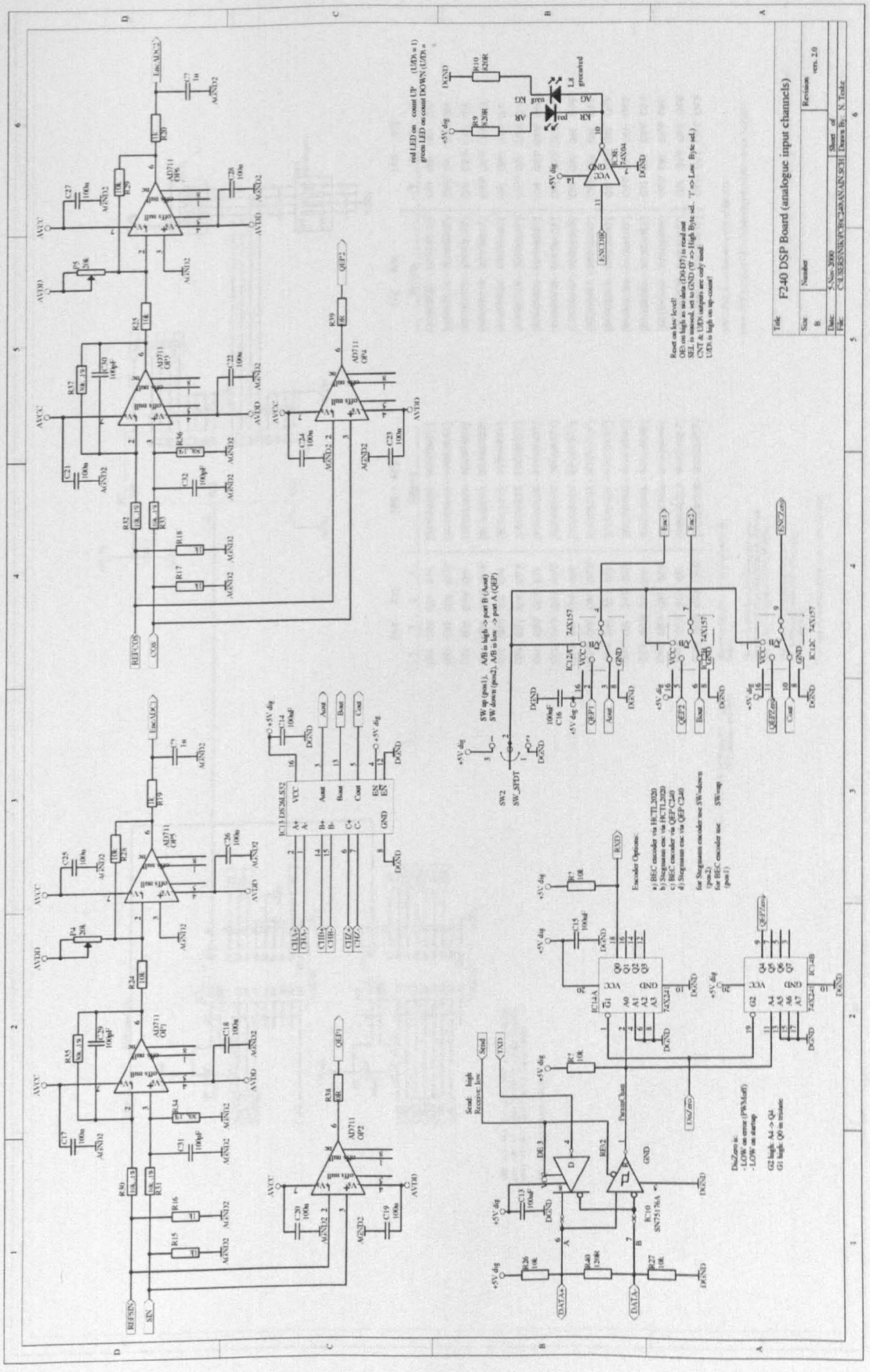

Figure D.4: *Schematic of Analogue Inputs for F240 Board*

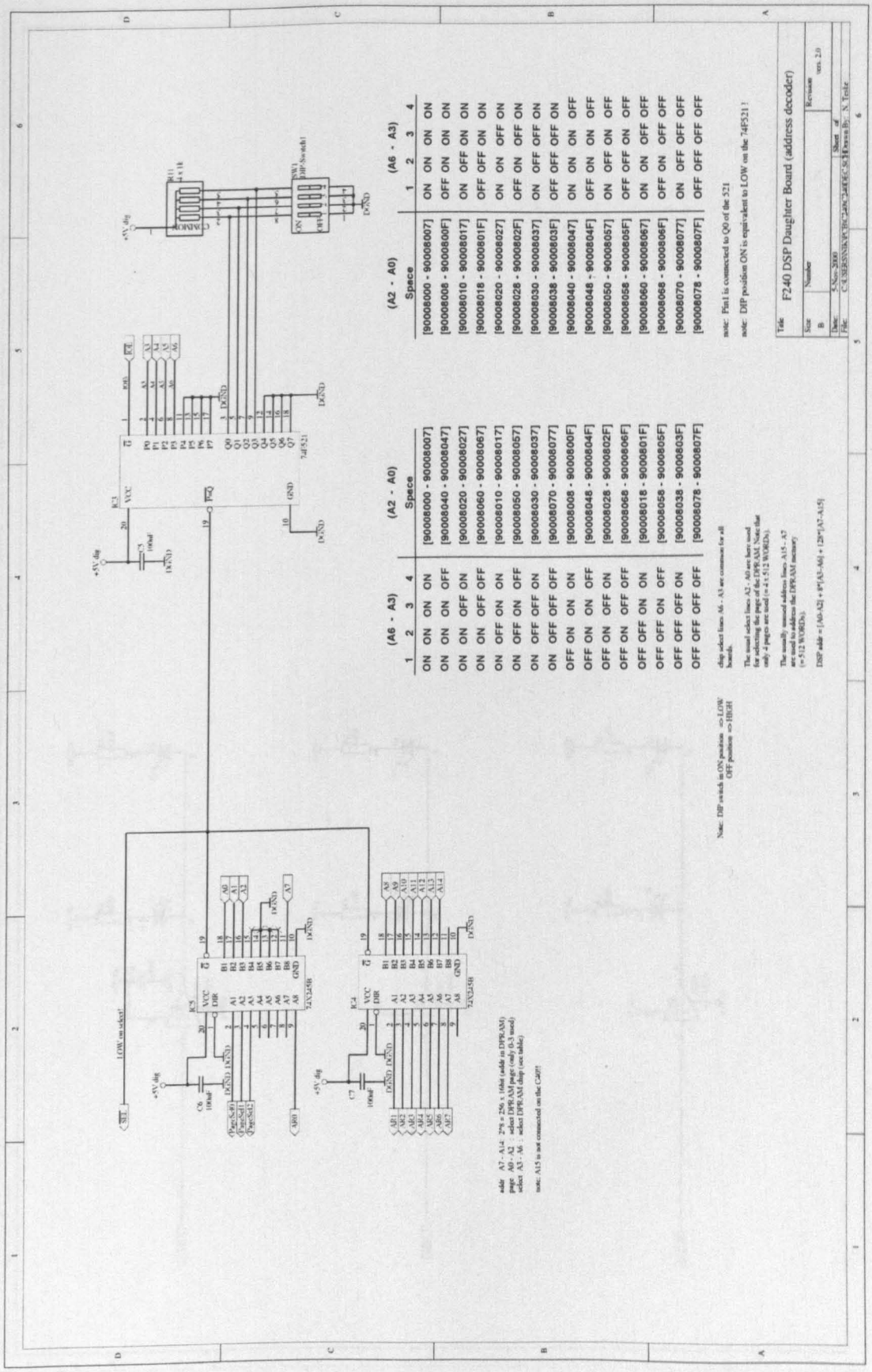

Figure D.5: *Schematic of Decoder for F240 Board*

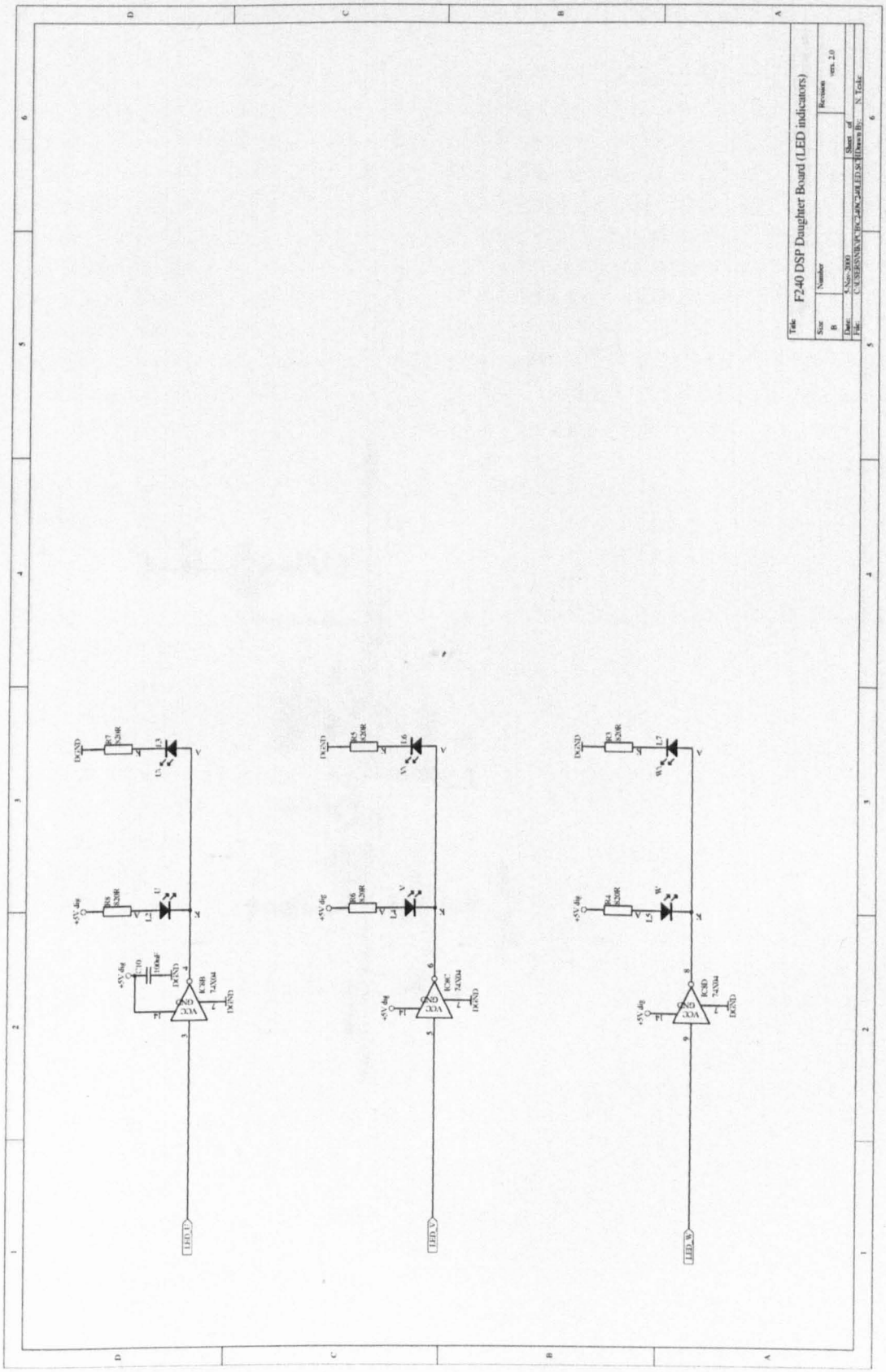

Figure D.6: *Schematic of LED feedback for F240 Board*

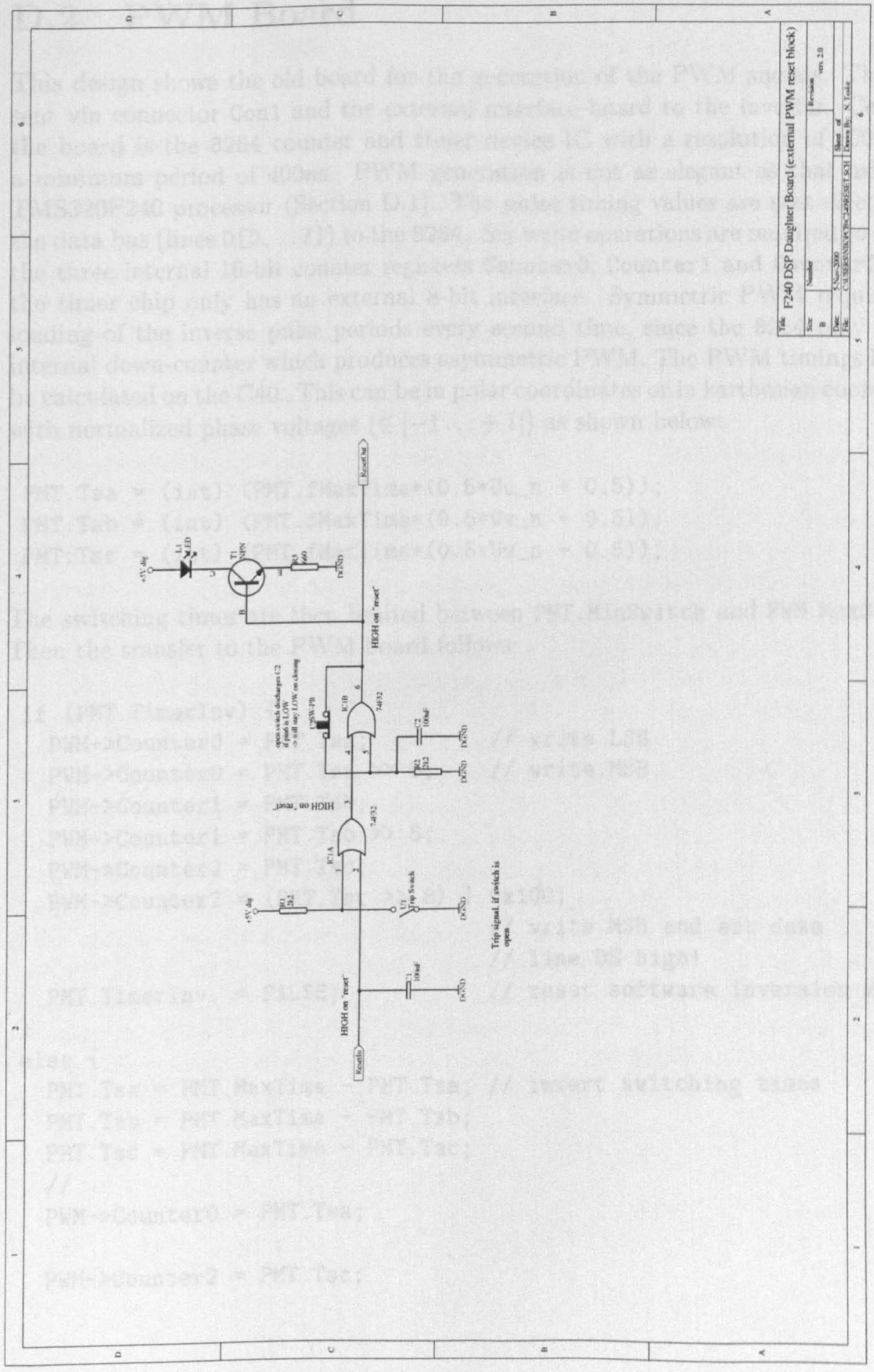

Figure D.7: *Schematic of external Reset Box*

D.2 PWM Board

This design shows the old board for the generation of the PWM signals. These are sent via connector Con1 and the external interface board to the inverter. Centre of the board is the 8254 counter and timer device IC with a resolution of 200*ns* and a minimum period of 400*ns*. PWM generation is not as elegant as that using the TMS320F240 processor (Section D.1). The pulse timing values are sent directly via the data bus (lines D[0...7]) to the 8254. Six write operations are required to update the three internal 16-bit counter registers Counter0, Counter1 and Counter2, since the timer chip only has an external 8-bit interface. Symmetric PWM requires the loading of the inverse pulse periods every second time, since the 8254 only has an internal down-counter which produces asymmetric PWM. The PWM timings have to be calculated on the C40. This can be in polar coordinates or in karthesian coordinates with normalized phase voltages ($\in [-1 \ldots +1]$) as shown below:

```
PMT.Tsa = (int) (PMT.fMaxTime*(0.5*Uu_n + 0.5));
PMT.Tsb = (int) (PMT.fMaxTime*(0.5*Uv_n + 0.5));
PMT.Tsc = (int) (PMT.fMaxTime*(0.5*Uw_n + 0.5));
```

The switching times are then limited between PMT.MinSwitch and PWM.MaxSwitch. Then the transfer to the PWM board follows:

```
if (PMT.TimerInv) {
  PWM->Counter0 = PMT.Tsa;          // write LSB
  PWM->Counter0 = PMT.Tsa >> 8;     // write MSB
  PWM->Counter1 = PMT.Tsb;
  PWM->Counter1 = PMT.Tsb >> 8;
  PWM->Counter2 = PMT.Tsc;
  PWM->Counter2 = (PMT.Tsc >> 8) | 0x100;
                                    // write MSB and set data
                                    // line D8 high!
  PMT.TimerInv  = FALSE;            // reset software inversion flag
}
else {
  PMT.Tsa = PMT.MaxTime - PMT.Tsa; // invert switching times
  PMT.Tsb = PMT.MaxTime - PMT.Tsb;
  PMT.Tsc = PMT.MaxTime - PMT.Tsc;
  //
  PWM->Counter0 = PMT.Tsa;
   :                 :
  PWM->Counter2 = PMT.Tsc;
```

```
  PWM->Counter2 = PMT.Tsc >> 8;
  PMT.TimerInv  = TRUE;              // set the software inversion flag
}
```

If the flag `PMT.TimerInv` is set, data line `D8` is set that sets the D-latch `IC13A`. Every second interval, this latch is reset. The `8254` buffers the written timer values in shadow-registers. According to the initial configuration, the internal timer-compare registers are reloaded from these buffers at the instance that the timer period is over and is restarted. The initialization words are:

```
// for all 3 counters:      RW1,RW0  = [11];  (LSB first)
//                          M2,M1,M0 = [001]; (Mode1)
PWM->Control = 0x32;     // SC1,SC2  = [00];  (select Counter0)
PWM->Control = 0x72;     // SC1,SC2  = [00];  (select Counter1)
PWM->Control = 0xB2;     // SC1,SC2  = [00];  (select Counter2)
```

The control registers are only written once during the initialization of the drive. The board design also allows the individual timer update with the line `TRIGG` that is connected to the gate inputs of the `8254`. A simple write to `PWM->Trigger` will sent a pulse via the `TRIGG` line.

The three PWM signals are provided via connector `Con1` and are also sent to LEDs at the front of the board to allow a quick visual check if the PWM is working. Deadtime is not generated since this is built into the IGBT driver boards of the *Eurotherm* 584SV inverter. For secure signal transmission from the board to the inverter, a differential transmission is used. The `DS26LS31` driver chip converts the TTL levels to differential signals according to standard RS-422. Additional to the three PWM pulses, a reset signal is sent to the inverter where it is combined with the reset signal of the inverter (see page 306). A small disadvantage is that no reset feedback from the inverter to the PWM board exists. The PWM generator is therefore not informed if the inverter detects a reset condition and continues to generate the PWM signals. The PWM will have to be manually restarted together with the C40 control code after clearing the trip condition. A basic protection on the PWM board is provided by using the `MAX6301` watchdog. This device checks the $+5V$ voltage rail and basic PWM timing. If the software does not trigger the `8254` within $900\mu s$, the connection to the inverter is disabled. More details can be found in [153].

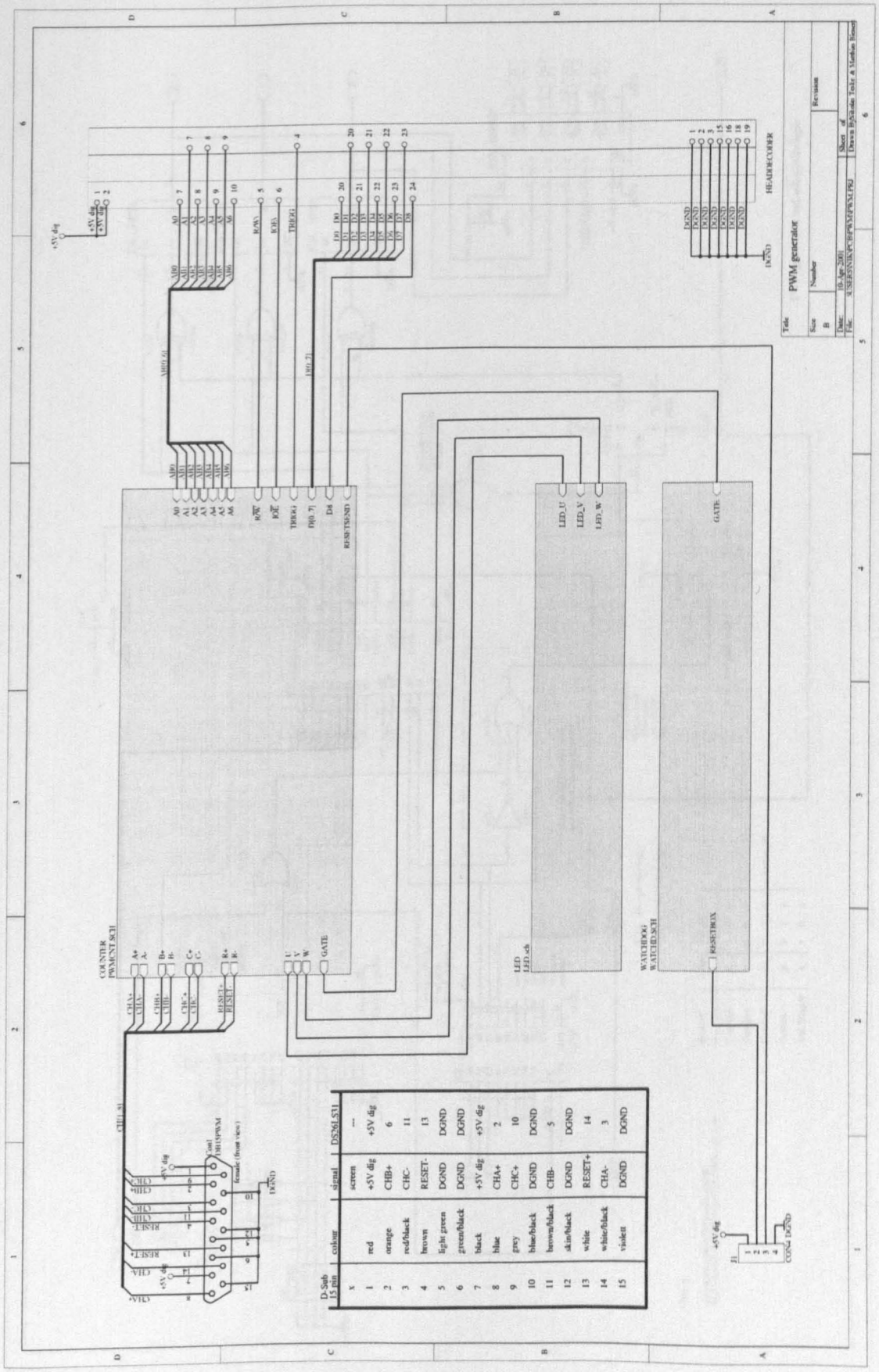

Figure D.8: *Schematic of PWM Board*

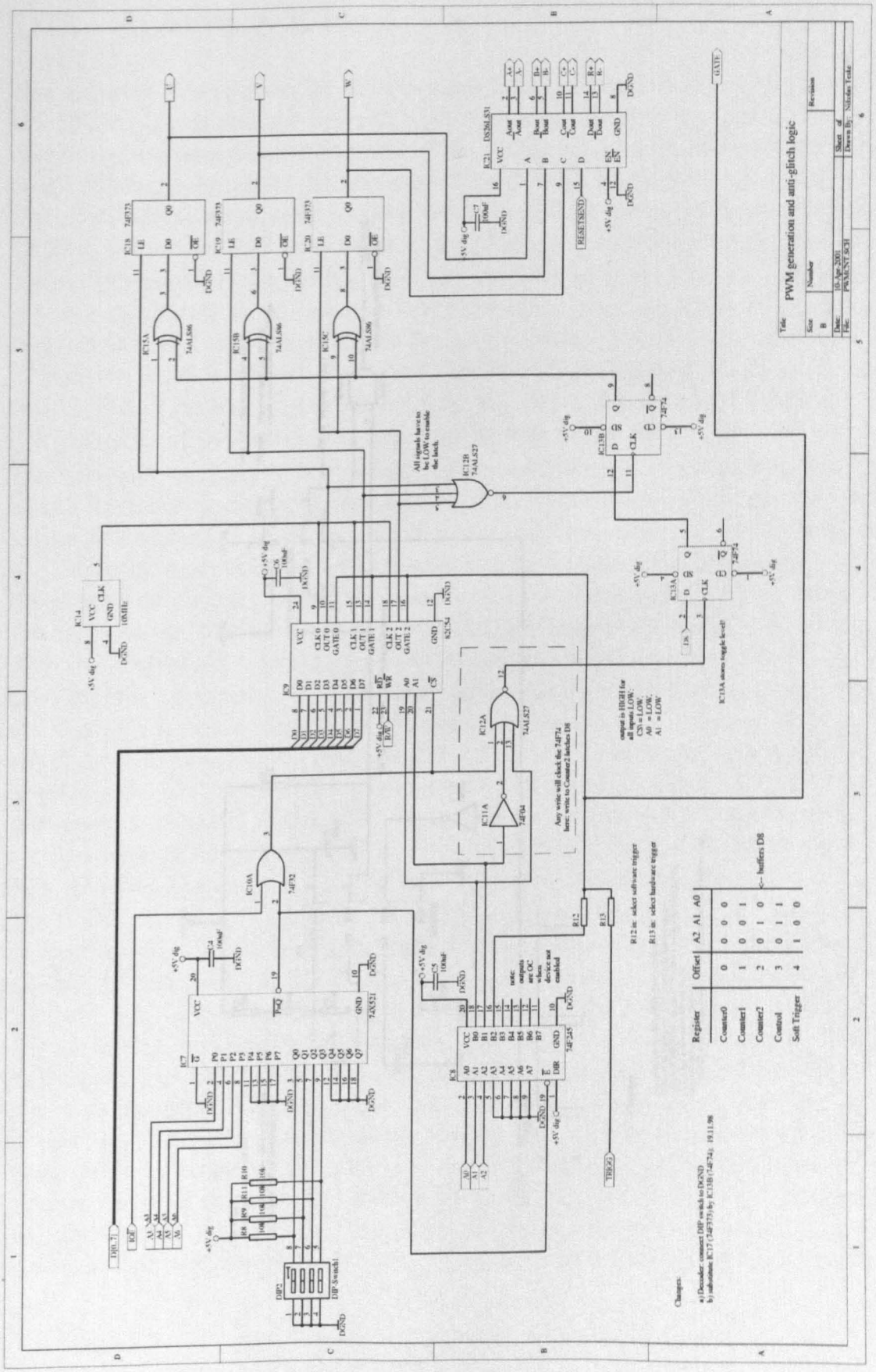

Figure D.9: *Schematic of PWM counter board with anti-glitch logic*

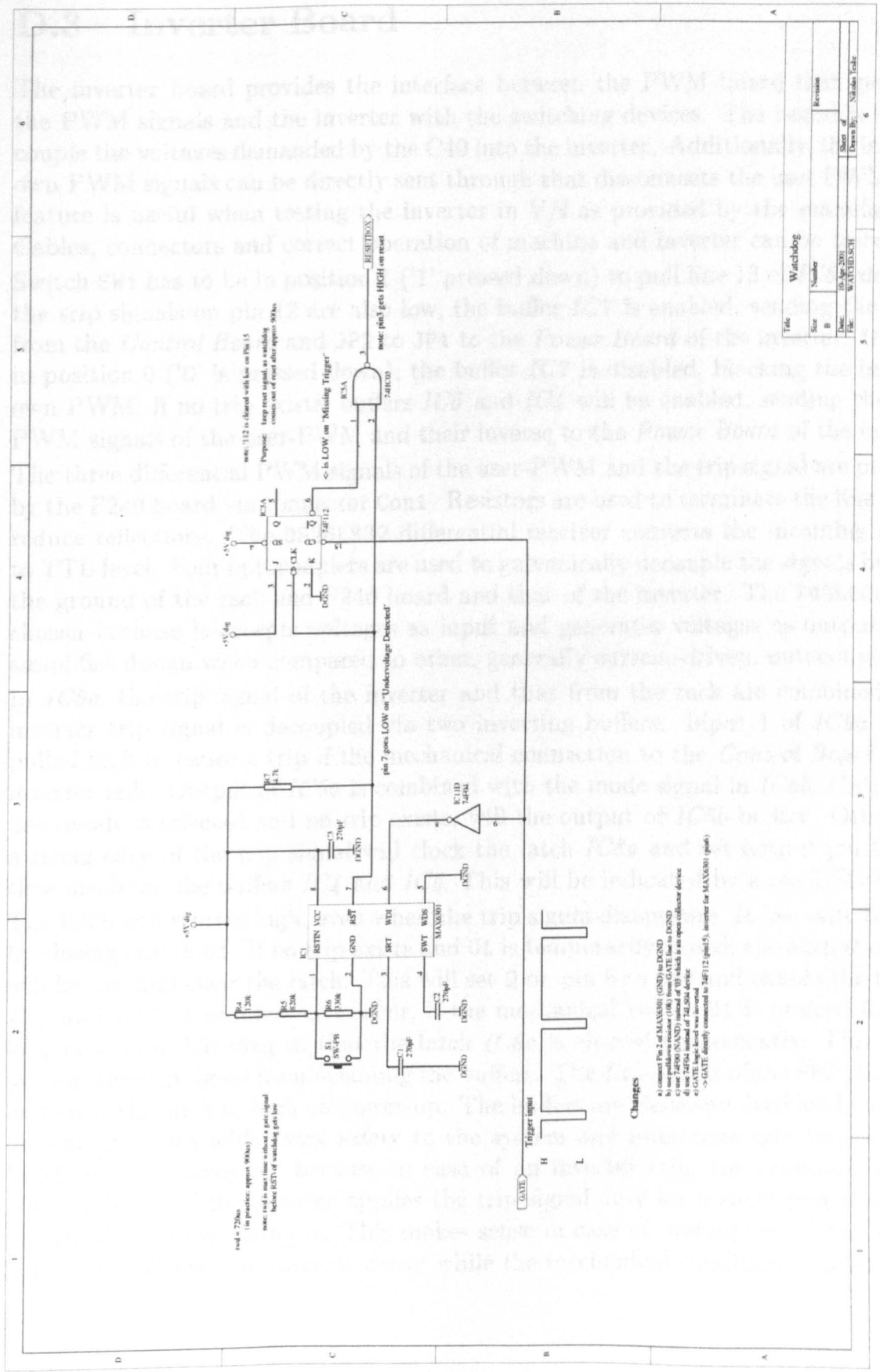

Figure D.10: *Schematic of watchdog protection circuit*

D.3 Inverter Board

The inverter board provides the interface between the PWM board that generates the PWM signals and the inverter with the switching devices. The board is used to couple the voltages demanded by the C40 into the inverter. Additionally, the inverter-own PWM signals can be directly sent through that disconnects the user PWM. This feature is useful when testing the inverter in V/f as provided by the manufacturer. Cables, connectors and correct operation of machine and inverter can be tested.

Switch SW1 has to be in position 1 ('I' pressed down) to pull line 13 of *IC5d* down. If the trip signals on pin 12 are also low, the buffer *IC7* is enabled, sending the PWM from the *Control Board* and JP2 to JP1 to the *Power Board* of the inverter. If SW1 is in position 0 ('0' is pressed down), the buffer *IC7* is disabled, blocking the inverter-own PWM. If no trip exists, buffers *IC6* and *IC4* will be enabled, sending the three PWM signals of the user-PWM and their inverse to the *Power Board* of the inverter.

The three differential PWM signals of the user-PWM and the trip signal are provided by the F240 board via connector Con1. Resistors are used to terminate the line and to reduce reflections. The DS26LS32 differential receiver converts the incoming signals to TTL level. Four optocouplers are used to galvanically decouple the signals between the ground of the rack and F240 board and that of the inverter. The 740L6000 was chosen because it accepts voltages as input and generates voltages as output. This simplifies design when compared to other, generally current-driven, optocouplers.

In *IC5a*, the trip signal of the inverter and that from the rack are combined. The inverter trip signal is decoupled via two inverting buffers. Input 1 of *IC9a* is also pulled high to cause a trip if the mechanical connection to the *Control Board* of the inverter fails. Output of *IC5a* is combined with the mode signal in *IC5b*. Only if the user-mode is selected and no trip exists, will the output of *IC5b* be low. Otherwise, a rising edge of the trip signal will clock the latch *IC8a* and set output pin 6 high, thus disabling the buffers *IC4* and *IC6*. This will be indicated by a red LED L1.

The latch will remain high, even when the trip signal disappears. It can only be reset by closing switch U1. If no trip exists and U1 is temporarily closed, the output of *IC5c* will be low and clear the latch. This will set Q on pin 6 to low and enable the buffers *IC4* and *IC6*. A problem can occur, if the mechanical switch U1 is pressed for very long or is even blocking so that the latch *IC8a* is cleared permanently. This would prevent the trip signal from disabling the buffers. The *RC*-circuit of the $\overline{\text{PRE}}$ pin of the latch sets the latch to high on power-up. The buffers are therefore disabled by default on startup. This adds extra safety to the system and minimizes user intervention. Latch *IC8a* is necessary because in case of an inverter trip, the processor on the *Control Board* of the inverter applies the trip signal only for a short period of time ($\approx 10ms$) before releasing it. This makes sense in case of overcurrent. The inverter is switched off and the currents decay while the mechanical conditions (speed, load)

still remain. Then no fault exists and the inverter can be operated in V/f again, or attempt to do so. This strategy increases the reliability of the inverter in industrial environments. As there is no trip feedback to the F240, a trip will cause the F240 to demand higher voltages to compensate for the current error in Vector Control. If the inverter switches on again, the high voltage demand can easily cause a short-circuit condition that damages the power devices. This is why a trip will keep the buffers *IC4* and *IC6* blocked. Only manual reset of the machine control and a manual clear on button U1 can restart the control and enable the buffers.

Fig. D.13 shows the simplified logic and interface between the *Control Board* and the *Power Board* of the 584SV inverter. Care has to be taken with other versions of this model as they might differ. For the 40kW inverter in use, the PWM signals coming from the 80C196 processor do not include deadtime. For example, signal U is the inverse of signal X. The deadtime is generated on the *Power Board* and the device driver modules. This is why the F240 only sends three PWM signals that are sent through a non-inverting buffer **74x244** and an inverting buffer **74x240**. Other versions might require deadtime generation.

Fig. D.14 shows the simplified structure of the power electronics and the terminals on the *Power Board*. Varistors are used at the inputs L1, L2 and L3, then the discrete diode bridge follows. The capacitor bank is charged via a resistor. This will be short-circuited later. The IGBTs are arranged vertically as shown. The anti-parallel diode is integrated in the package. Currents are measured using two LEM modules in phases U and W.

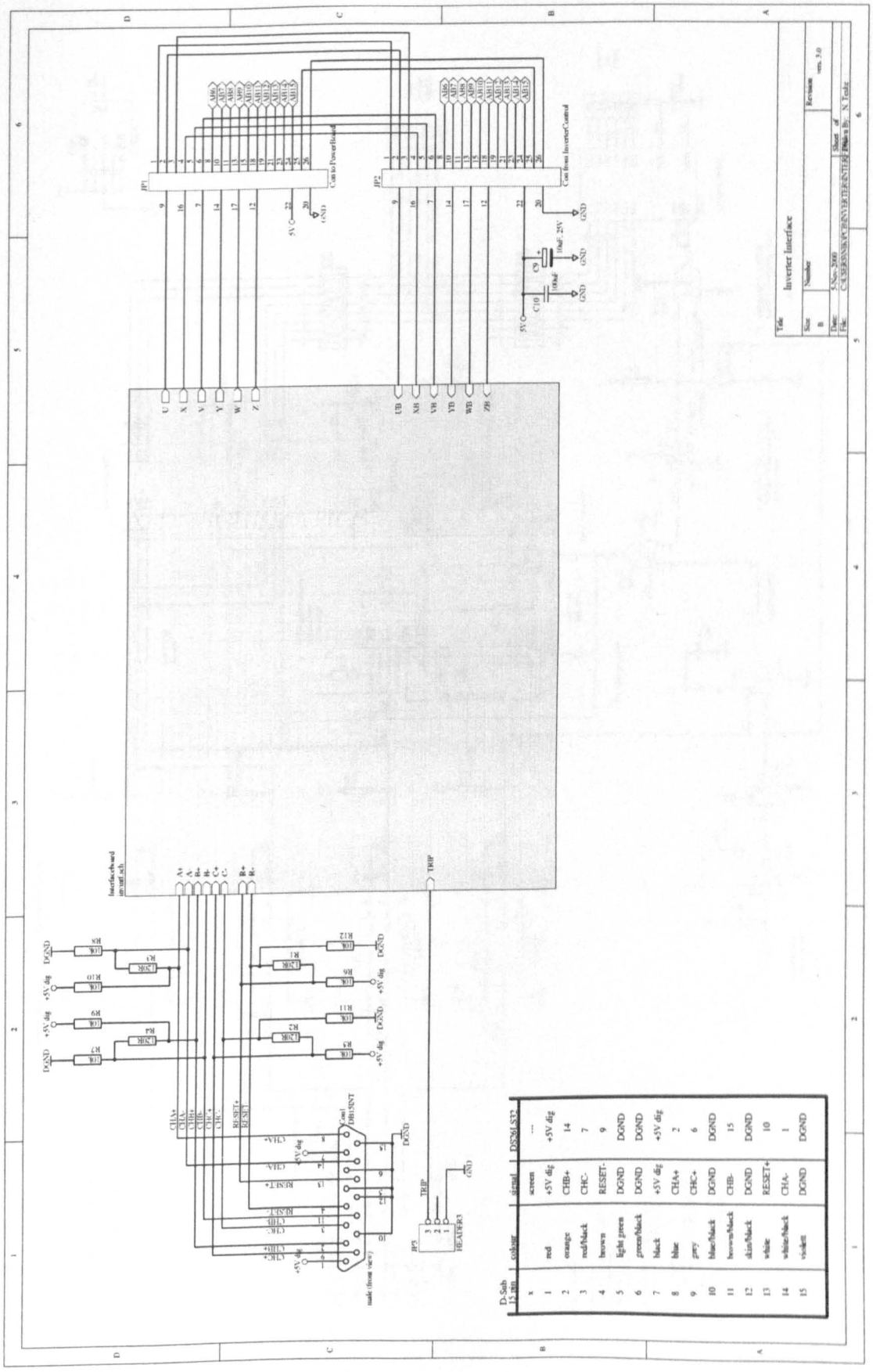

Figure D.11: *Schematic of Inverter Interface Board*

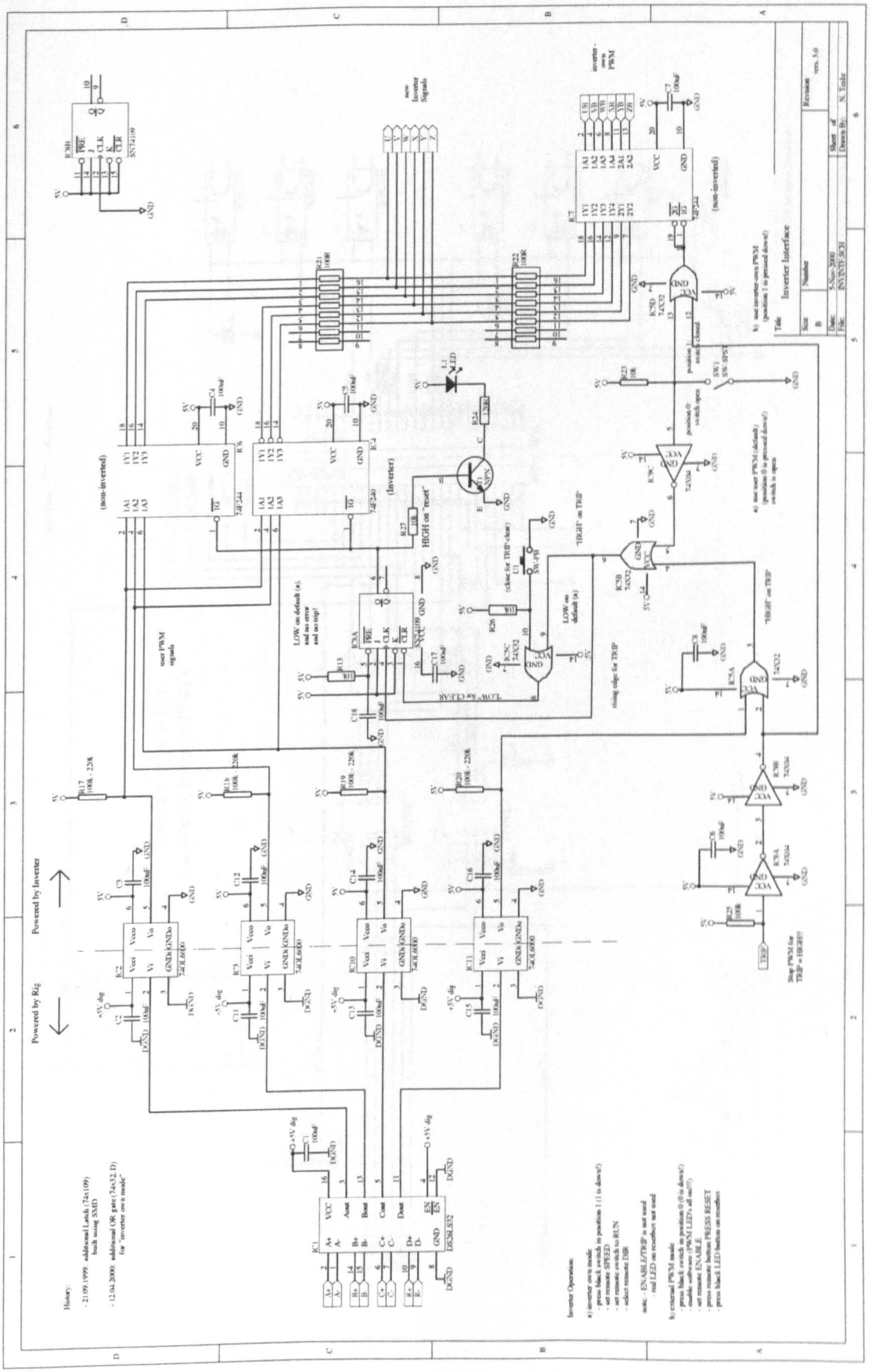

Figure D.12: *Schematic of Inverter Interface Logic*

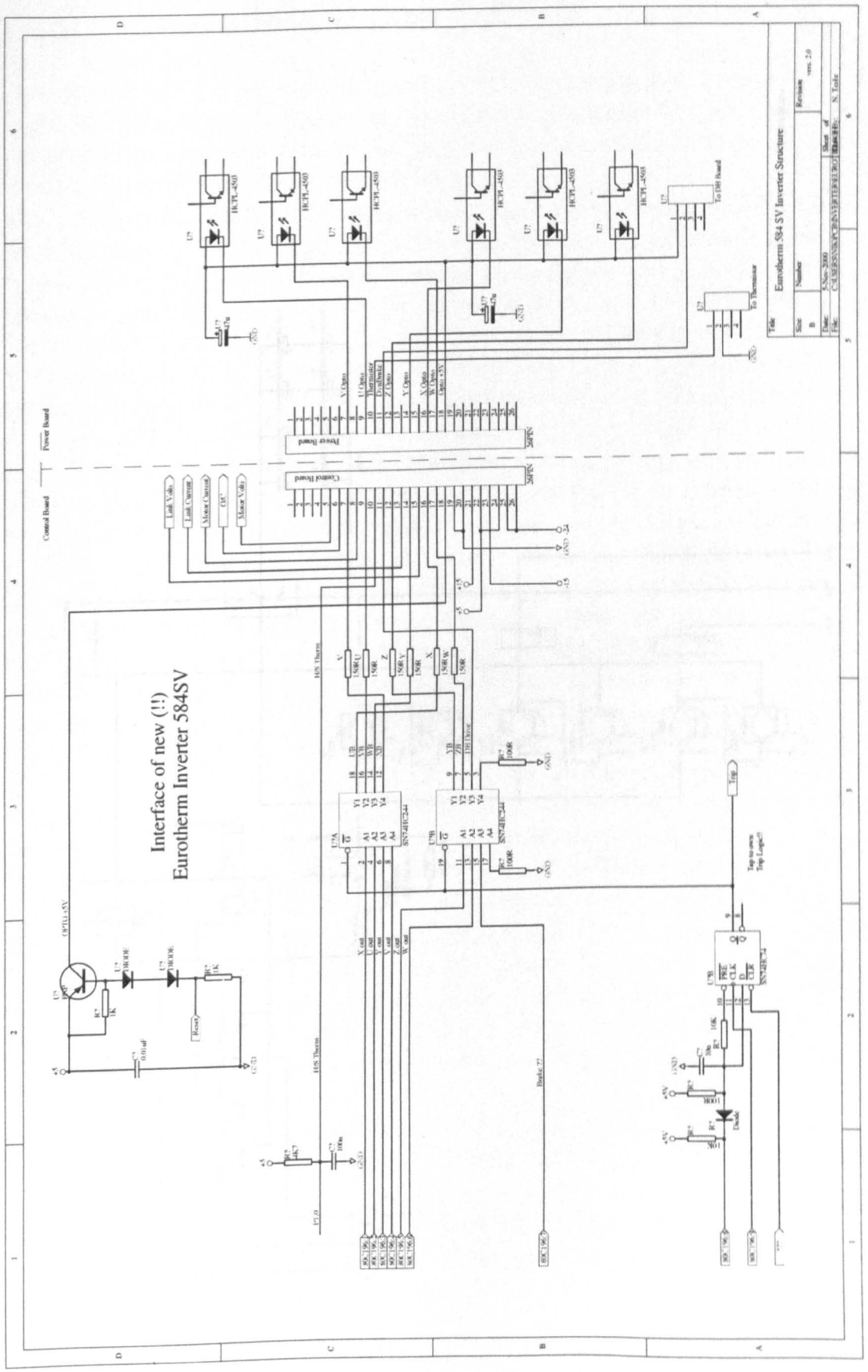

Figure D.13: *Simplified Schematic of Inverter Control Board*

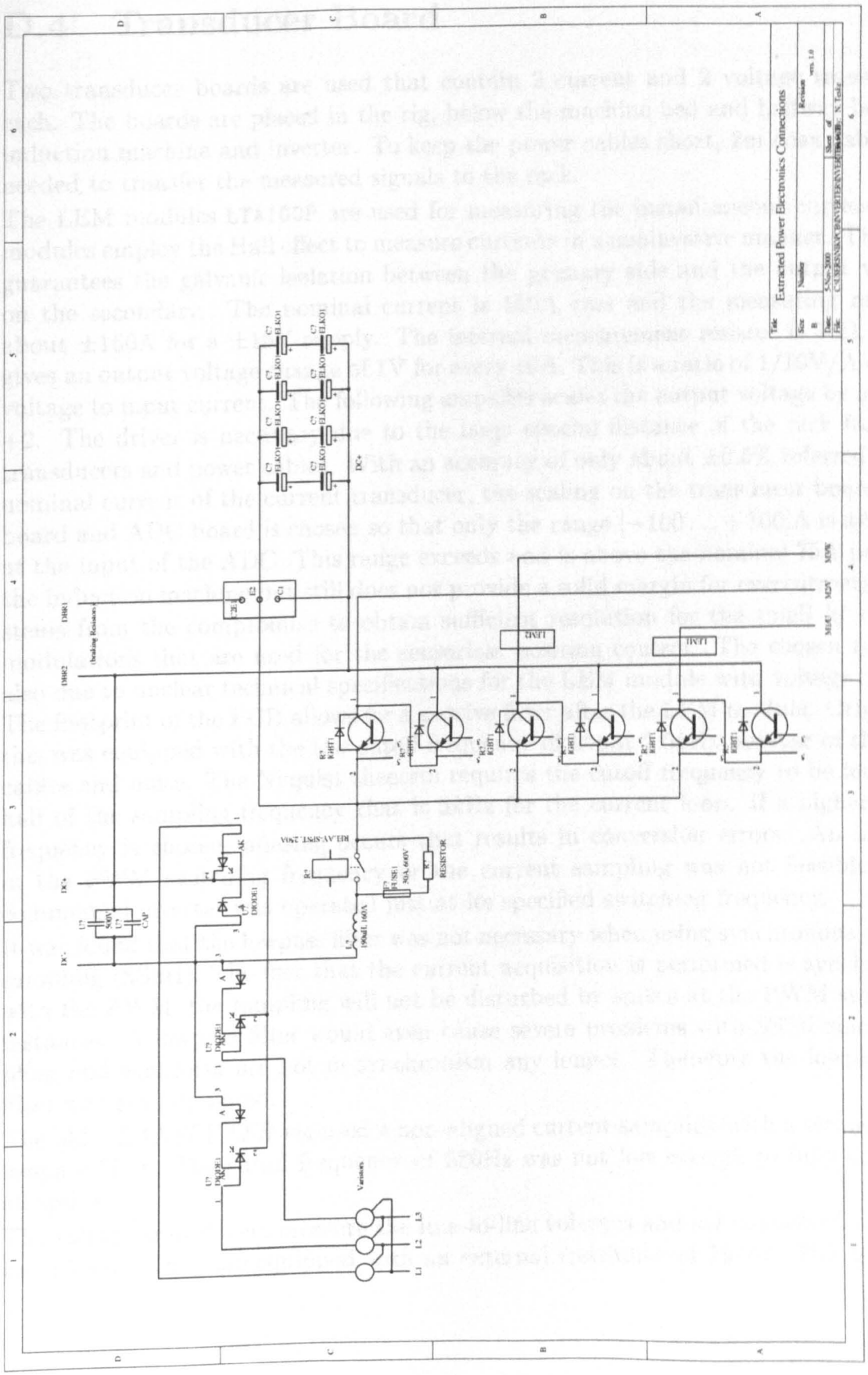

Figure D.14: *Simplified Schematic of Inverter Power Board*

D.4 Transducer Board

Two transducer boards are used that contain 2 current and 2 voltage transducers each. The boards are placed in the rig, below the machine bed and halfway between induction machine and inverter. To keep the power cables short, 2m coax cables are needed to transfer the measured signals to the rack.

The LEM modules LTA100P are used for measuring the instantaneous current. The modules employ the Hall effect to measure currents in a noninvasive manner. This also guarantees the galvanic isolation between the primary side and the output voltage on the secondary. The nominal current is 100A *rms* and the measuring range is about ±160A for a ±15V supply. The internal measurement resistor is 50Ω, which gives an output voltage change of 1V for every 10A. This is a ratio of 1/10V/A output voltage to input current. The following amplifier scales the output voltage by a factor +2. The driver is necessary due to the large spacial distance of the rack from the transducers and power cables. With an accuracy of only about ±0.5% referred to the nominal current of the current transducer, the scaling on the transducer board, gain board and ADC board is chosen so that only the range $[-100 \ldots +100]$A is available at the input of the ADC. This range exceeds and is above the nominal 75A peak for the induction machine but still does not provide a solid margin for overcurrents. This stems from the compromise to obtain sufficient resolution for the small *hf* current modulations that are used for the sensorless position control. The chosen range is also due to unclear technical specifications for the LEM module with voltage output. The footprint of the PCB allows for a passive filter after the LEM module. Originally, this was equipped with the low cutoff frequency of about 2.5kHz because of the long cables and noise. The Nyquist theorem requires the cutoff frequency to be less than half of the sampling frequency that is 5kHz for the current loop. If a higher cutoff frequency is chosen, aliasing occurs that results in conversion errors. An increase in the PWM switching frequency or the current sampling was not feasible. The commercial inverter was operated just at its specified switching frequency.

It was found that the lowpass filter was not necessary when using synchronous current sampling (SSSH). The fact that the current acquisition is performed is synchronism with the PWM, the sampling will not be disturbed by spikes at the PWM switching instances. A lowpass filter would even cause severe problems with SSSH since sampling and waveform are not in synchronism any longer. Therefore the lowpass *RC* filter was not populated.

The old *TRANSPUTER rig* used a non-aligned current sampling with a second order lowpass filter. The cutoff frequency of 680Hz was not low enough to fully suppress all spikes.

The voltage transducers measure the line-to-line voltages and are connected between two phases. They are equipped with an external resistance of 76.9Ω. This gives an

output voltage of 10V for approximately 650V input voltage. The gain is specified by $R_x/5000$ that is $0.01538 = 1/65.0195$ with the given resistor. The cutoff frequency is chosen by the capacitor in parallel to the resistor and is $f_{cut} = \frac{1}{2\pi R_x \cdot C_x} \approx 5k\text{Hz}$ for the $390p\text{F}$ capacitor. An OpAmp is connected as a voltage follower for decoupling and to stabilize the signal for transmission to the gain or ADC board.

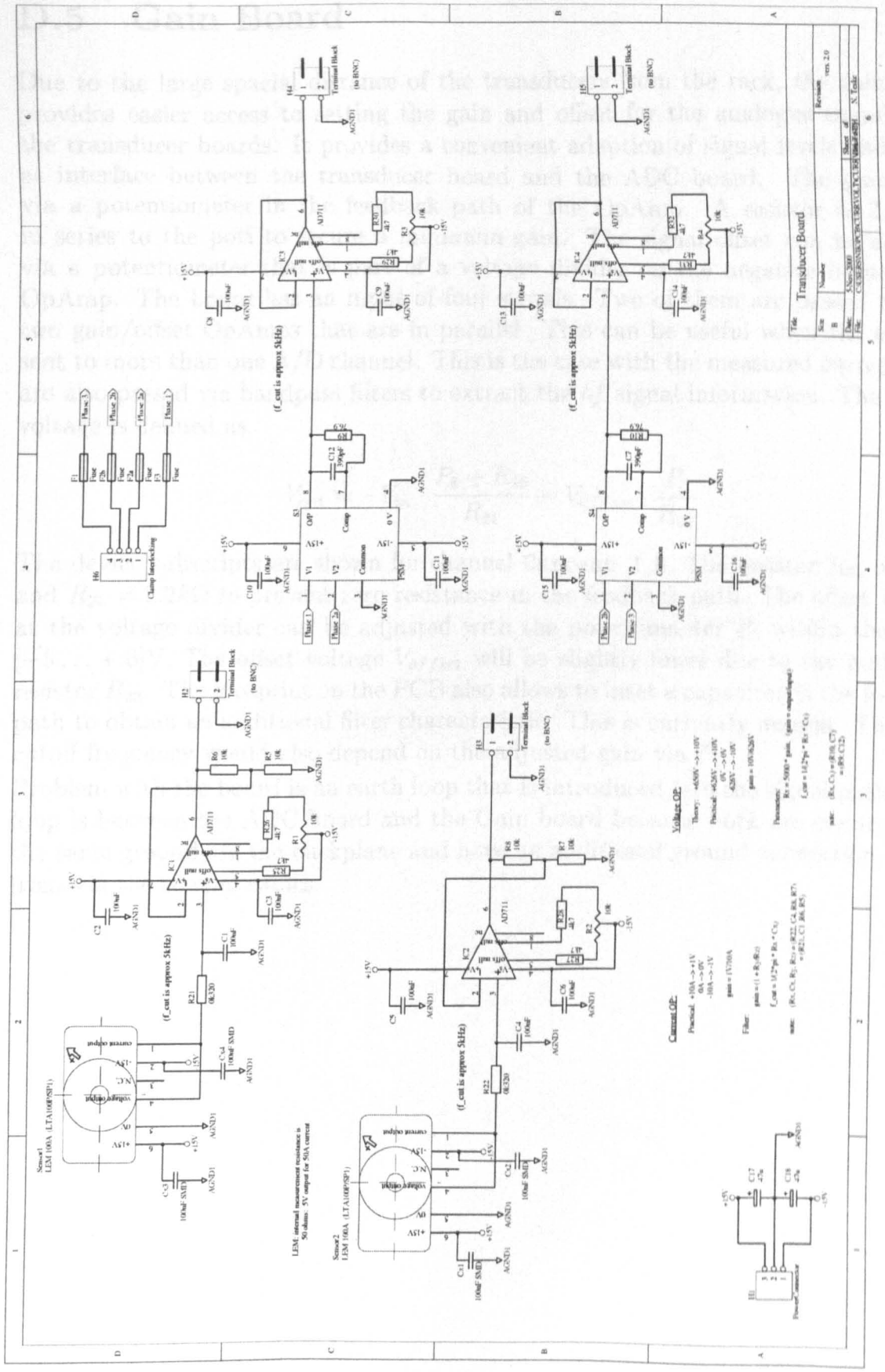

Figure D.15: *Schematic of Transducer Board*

D.5 Gain Board

Due to the large spacial distance of the transducers from the rack, the gain board provides easier access to setting the gain and offset for the analogue signals from the transducer boards. It provides a convenient adaption of signal levels and serves as interface between the transducer board and the ADC board. The gain is set via a potentiometer in the feedback path of the OpAmp. A resistor of $2.2k\Omega$ is in series to the poti to secure a minimum gain. The signal offset can be adjusted via a potentiometer that is part of a voltage divider on the negative input of the OpAmp. The board has an input of four signals. Two of them are passed through two gain/offset OpAmps that are in parallel. This can be useful when the signal is sent to more than one A/D channel. This is the case with the measured currents that are also passed via bandpass filters to extract the *hf* signal information. The output voltage is defined as

$$V_{out} = -V_{in} \cdot \frac{P_6 + R_{26}}{R_{21}} - V_{offset} \cdot \frac{P_5}{R_{21}}$$

The device subscripts are shown for channel `Current I_B`. The resistor $R_{21} = 10k\Omega$ and $R_{26} = 2.2k\Omega$ to prevent zero resistance in the feedback path. The offset voltage at the voltage divider can be adjusted with the potentiometer P_5 within the range $[-5 \ldots +5]$V. The offset voltage V_{offset} will be slightly lower due to the additional resistor R_{23}. The footprint on the PCB also allows to inset a capacitor in the feedback path to obtain an additional filter characteristic. This is currently unused. The filter cutoff frequency would also depend on the adjusted gain via P_6.

Problem with the board is an earth loop that is introduced into the signal path. This loop is between the ADC board and the Gain board because both are connected to the same ground via the backplane and have an additional ground connection on the front via the coaxial cables.

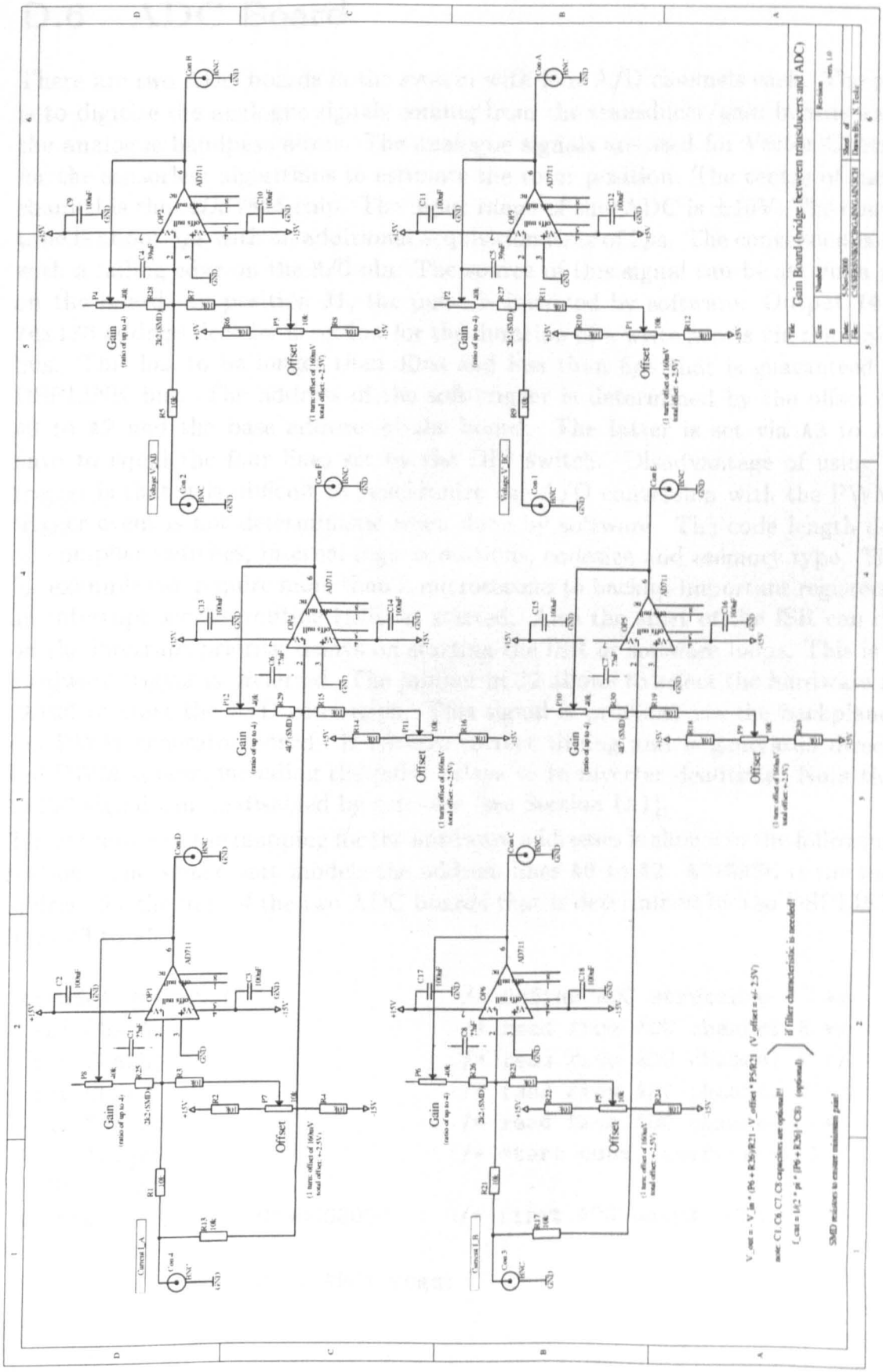

Figure D.16: *Schematic of Gain Board (input to ADCs)*

D.6 ADC Board

There are two ADC boards in the system with four A/D channels each. The purpose is to digitize the analogue signals coming from the transducer/gain boards and from the analogue bandpass filters. The analogue signals are used for Vector Control and for the sensorless algorithms to estimate the rotor position. The centre of each A/D channel is the *ADS7805* chip. The input range of this ADC is $\pm$10V. The conversion time is about 8μs with an additional acquisition time of 2μs. The conversion is started with a falling edge on the R/$\overline{C}$ pin. The source of this signal can be set via a jumper on the board. In position J1, the pulse is initiated by software. Output Y4 of the 74x138 address decoder is set low for the duration of a write access via the DSPLINK bus. This has to be longer than 40ns and less than 6μs that is guaranteed by the DSPLINK bus. The address of the soft-trigger is determined by the offset of lines A0 to A2 and the base address of the board. The latter is set via A3 to A6 that have to equal the four lines set by the DIP switch. Disadvantage of using a soft-trigger is that it is difficult to synchronize the A/D conversion with the PWM. The trigger event is not deterministic when done by software. The code length depends on compiler switches, internal logic conditions, codesize and memory type. The C40 for example can require more than a microsecond to backup important registers when an interrupt service routine (ISR) is started. Also the start of the ISR can depend on the interrupt priority, delays on starting the ISR or software loops. This is why a hardware trigger is preferred. The jumper in J2 allows to select the hardware trigger TRIGG to start the A/D conversion. This signal is provided via the backplane from the PWM generator board. It ensures correct timing and is generated directly by the PWM timers, including the pulse delays to to inverter deadtime. Note that the TRIGG signal can be disabled by software (see Section D.1).

The structure of the mapping for the hardware addresses is shown in the following code section. The *struct* part models the address lines A0 to A2. AD1BASE is the memory address for the first of the two ADC boards that is determined by the DSPLINK and lines A3 to A6.

```
typedef struct {                    /* define ADC structure    */
 int ChanA;                         /* read from ADC channel A */
 int ChanB;                         /* read from ADC channel B */
 int ChanC;                         /* read from ADC channel C */
 int ChanD;                         /* read from ADC channel D */
 int Trigger;                       /* start conv. (soft-trigg)*/
} ADCstruct;
#define AD1BASE   0x90008000        /* first ADC board: ChanA  */

// pointer to external ADC1 regs:
```

```
volatile  ADCstruct *AD1 = (ADCstruct *) AD1BASE;
```

Input to each of the four converters on the board is a differential amplifier. Other possibilities for configuring the OpAmp AD711 are shown in Fig. D.19. The differential amplifier is preferred to break earth loops. These loops cannot be avoided when sending signals across different boards that are all connected to the same backplane and thus share the same ground. The differential amplifier provides a high resistance path for common mode signals and a low resistive path for differential mode signals. The output voltage of the differential amplifier with v_3 the potential between pin 6 of the OpAmp AD711 and analogue ground AGND2 is

$$v_3 = -\frac{R_{12}}{R_{11}} \cdot (v_1 - v_2) + \frac{R_{11}R_{14} - R_{13}R_{12}}{R_{11}(R_{13} + R_{14})} \cdot v_2$$

It is clear that for equal ratios $\frac{R_{11}}{R_{12}} = \frac{R_{13}}{R_{14}}$, the impact of voltage v_2 on v_3 becomes zero. This is important as the output voltage will then only be a function of the voltage between the two input pins AnaIn and $\overline{\text{AnaIn}}$. The voltage v_2 between $\overline{\text{AnaIn}}$ and AGND2, that can be non-zero for the input voltage $v_x = v_1 - v_2$ from another board, has no impact on the output voltage v_3. The earth loop is also broken by the high-value resistances R_{13} and R_{14} in the ground path. Care has to be taken that the resistance ratio fits. Resistors with a tolerance of a maximum of 1% were chosen therefore. All resistances were the same to provide symmetrical and balanced signal paths. The gain is -1 for the input signal $v_x = v_1 - v_2$.
Using bridges, a filtering inverter, an inverting amplifier, a unity gain inverter or a noninverting amplifier can be realized with the same footprint on the PCB.

Once the conversion is finished, the ADS7805 sets the $\overline{\text{BUSY}}$ line to high. This rising edge clocks the output buffers, two 74x574, that latch the digital 16 bit word that is provided at the data pins of the ADS7805. The timing of the data transfer ensures that no digital switching noise occurs during a conversion that could degrade the converter performance. The buffers keep this conversion result until a new word is latched from the ADC. The C40 can read the data via the data bus of the DSPLINK interface. The individual channels are addressed by the A0 and A1 address lines and the address decoder 74x138. The $\overline{\text{CS}}$ signal is tied low permanently to reduce the number of control lines. Also BUSY is tied low because full 16 bit reading is used.
The data is provided by the ADS7805 in the 16 bit binary 2^s complement. This requires a conversion when working with a 32 bit processor. The ADC is scaled so that -10V is represented by 8000_h and $+10$V is about $7FFF_h$. The MSB therefore determines the sign. A shift operation on the C40 is the fastest solution to convert to singed 32 bit. Care has to be taken when the analogue input range of the ADS7805 is exceeded. Overvoltage protection is guaranteed within ± 25 volts. The digital

representation may switch from $7FFF_h$ to 8000_h, resulting in a sign change when the range is exceeded. This can crash the current controllers in Vector Control. The software code to read from an AD channel is shown below. Care has to be taken that the data is read at least $10\mu s$ after the conversion has been started. This can easily be timed within the control ISR when this is synchronized to the PWM.

```
#define TOSIGNEDFLOAT(x) ((double) (((x) << 16) >> 16))

// read ADC1 value (channel A):
AdSig.AD1A = AD1->ChanA;
I_B = AdSig.ScaleI_B * TOSIGNEDFLOAT(AdSig.AD1A + AdSig_OffsetCh0);
```

Each channel is trimmed in hardware. A pre-trimming is done, using the two potentiometers P1 and P2. The latter is used to adjust the gain, P1 is for removing the offset. The resistors suggested for the ADS7805 should be 1% metal film resistors. For the practical board, resistors were hand-selected to obtain the required accuracy. An individual trimming for each channel is achieved by using the gain board (see Section D.5). This allows more flexible adjustment to the individual voltage or current signal that is being measured. A final adjustment is shown in the software code above. The offset for each channel is determined during startup. The mean value over a measurement period of at least a few seconds is taken when the input signal should be zero. This offset is stored for each individual channel and subtracted during signal measurements when the machine is controlled. The scaling factor `AdSig.ScaleI_B` (here for channel A) is determined only once when using the signal calibrator when the rig is set up. This term does hardly change and is therefore stored in a table as a constant.

Due to noise on the board, coupling via the cables and due to tolerances in resistors and the transducers, the resolution is not reach true 16 bit. In average two and sometimes up to three bits are lost. Shorter cables would improve the resolution. The long cables however are necessary if the current versatility, flexibility and convenience shall be maintained. Similar for the gain board. This would remove the earth loop. Disadvantage without this board would be a more complex calibration procedure.

A second source to the Burr-Brown ADS7805 is the AnalogDevices AD976 that has the same pinout and similar characteristics. The AD976A is an improved version with half the conversion time. Another alternative is the LinerTechnologies LTC1605 that comes with a reduced input range and lower power consumption. The Burr-Brown ADS7815 is also an improved version with 2.5 times the throughput rate. This chip however is only available in a 28-lead SOIC package and the reduced input range of ± 2.5 volts.

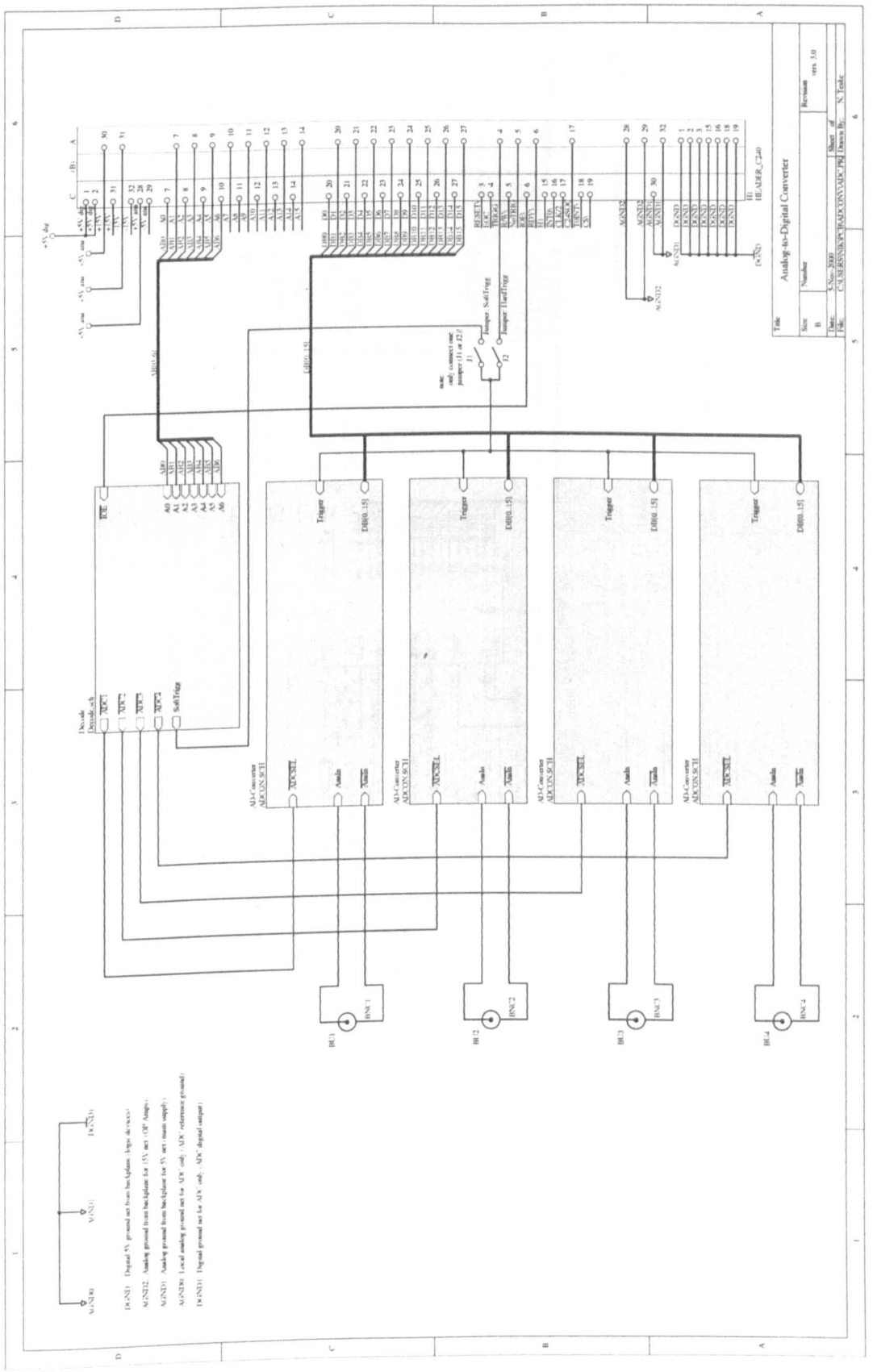

Figure D.17: *Schematic of ADC Board*

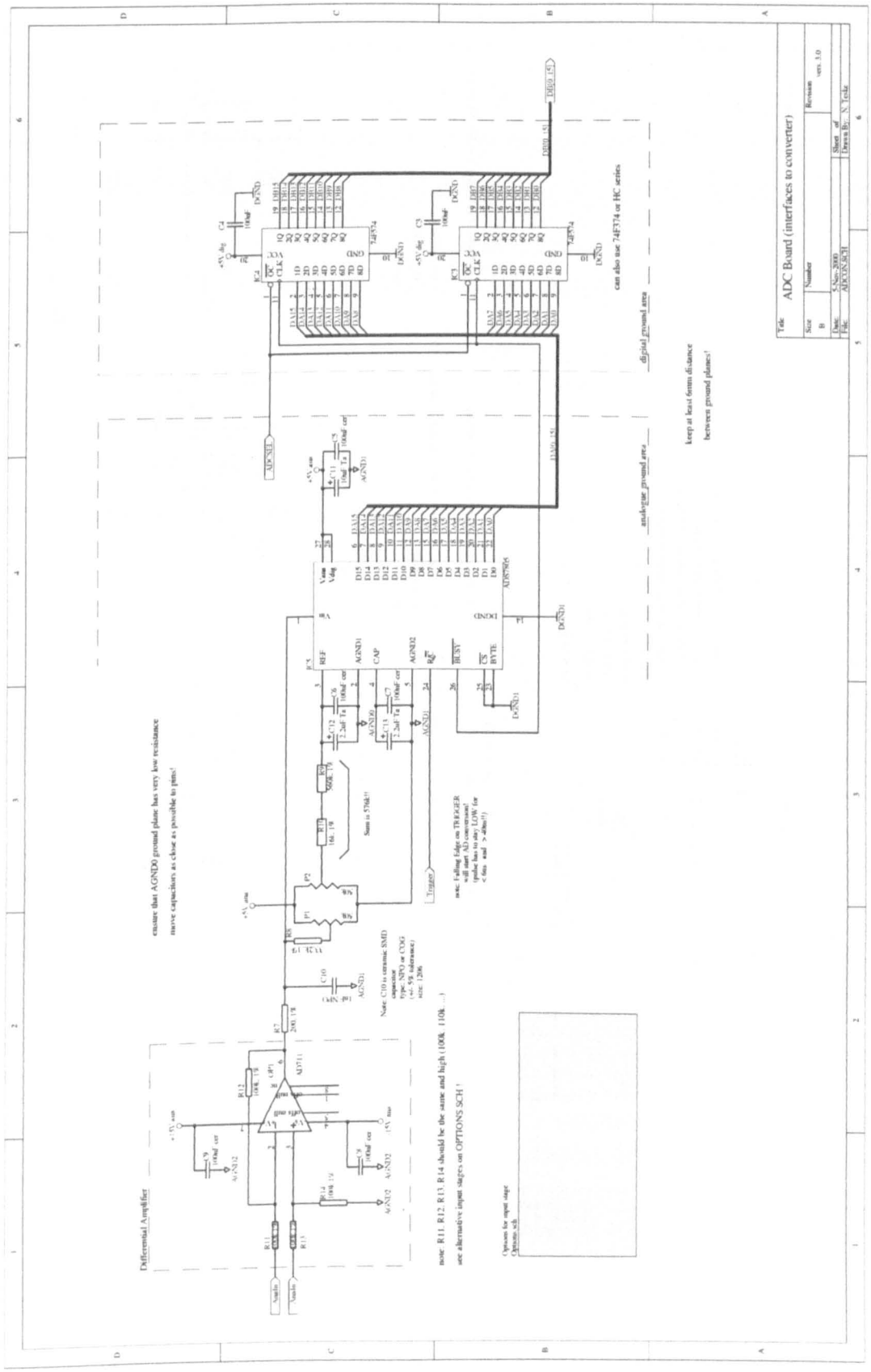

Figure D.18: *Schematic of ADC Channel connections*

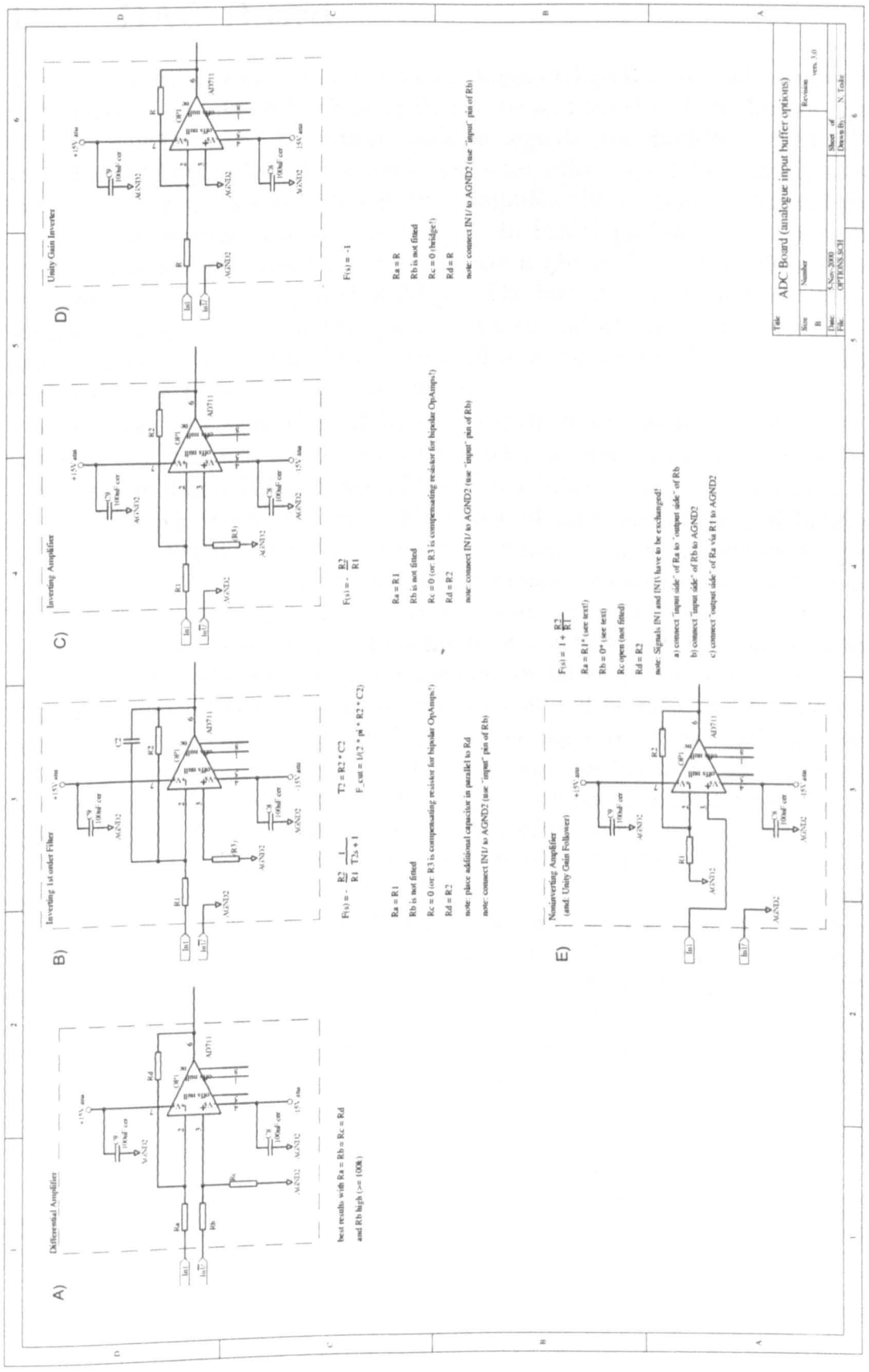

Figure D.19: *Schematic of optional analogue inputs for ADC Board*

D.7 DAC Board

The DAC board provides interfaces for the input of digital levels and outputs of digital and analogue signals. A bank of LEDs can be addressed and the binary position of switches can be read. To output analogue signals, the AD7835 is used. This is a four channel DAC with 14 bit resolution where the digital data word is loaded in parallel. The high degree of integration simplifies the amount of external glue logic and discrete devices. The chip is in a 44 pin PLCC package. The conversion and settling time for the output of a new voltage is about $T_c = 10\mu s$. This is fast when compared to the control period of $200\mu s$. The high output resolution simplifies the scaling of integer data. The two control lines A0 and A1 are used to select one of the four channels. Control line A2 can be used to select all DAC channels. This is not used here, why A2 is connected to ground.

The DAC can be activated on $\overline{CS}$ by selecting the board address via A3 to A6 and A2 has to be low. Lines A0 and A1 are used to select a channel where the new data word is written to. Lines $\overline{IOE}$ and R/$\overline{W}$ of the C40 DSPLINK bus are also used. Writing is in 16-bit mode in parallel, where the upper 14 data lines of the DSPLINK bus are used. The pin $\overline{BYSHF}$ is connected to high potential because the byte shift input is not required. Data written to the AD7835 is firstly stored in internal buffers. Depending on $\overline{LDAC}$, the data can be immediately updated and converter to analogue or can be kept in the channel buffer and updated synchronously with all other channels. A hardware switch is used on the board to select the update mode. If switch S1 is in position 77, $\overline{LDAC}$ is grounded. Data written to any channel will be latched immediately to the internal DAC and converted to analogue, appearing about T_c seconds later as voltage on the external pin. With switch S1 not in position 77, a specific update pulse is used for the synchronous update. This trigger requires A2 high to select line Y6 of the address decoder 74x138. The minimum width of the low pulse on $\overline{LDAC}$ of $40ns$ is the same as for $\overline{CS}$ and $\overline{WR}$. If required, the DAC chip can be reset manually via the switch PB1 or by the reset line from the C40 motherboard. Each channel of the AD7835 is followed by an CA3140 OpAmp. These buffers allow a higher loading of the output lines and thus protect the DAC chip. The OpAmps have a passive lowpass filter at the input and are configured as non-inverting amplifiers with a gain of 2. The time constant of the passive filter is set to $T_f = R \cdot C = 680\Omega \cdot 4.7nF \approx 3.2\mu s$ to smooth glitches. These can occur in form of voltage spikes when the converter changes state and depend on the input of the converter. The typical length is about $0.5\mu s$ with an amplitude of up to 0.5 volts.

In software, the *struct* construction is used to model the address range of A0 to A2 that is hardwired on the board. The base address DACBASE is determined by the DIP switch on the board. The easiest way to access the individual functions provided by the AD7835 in software is to use pointers. A pointer DAC is initialized of the type

DACstruct that points to the external address DACBASE:

```
typedef struct {                    /* define DAC structure    */
  int ChanA;                        /* write to DAC channel A  */
  int ChanB;                        /* write to DAC channel B  */
  int ChanC;                        /* write to DAC channel C  */
  int ChanD;                        /* write to DAC channel D  */
  int dummy0;                       /* positon unused for DAC  */
  int dummy1;                       /* address unused for DAC  */
  int Trigger;                      /* sync update of DAC      */
} DACstruct;
#define DACBASE   0x90008048        /* base address for DAC    */

// pointer to external DAC regs:
volatile  DACstruct *DAC = (DACstruct *) DACBASE;
```

The digital part of the AD7835 is powered by the digital $+5V$ supply. The analogue stage is powered by the $-15V$ and $+15V$ analogue supply. The DAC chip is used in unipolar mode. The AD587 voltage reference is used to provide the positive $+10V$ reference voltage. The negative reference pins of the AD7835 are connected to the analogue ground. Thus, the output voltage range of the AD7835 is $[0 \ldots +10]$ volts and $[0 \ldots +10]$ volts after the OpAmps. The digital value 0_b represents 0V and $11\,1111\,1111\,1111_b$ is equivalent to +10V at the output.

To adjust signed data, the offset of half the output range is added that is multiplied by 4 because of the alignment of the available 14 bit to the MSB of the 16 bit data bus. This digital offset is $32768_d = 1000\,0000\,0000\,0000_b$ or +5 volts at the output of the OpAmp.

Following code is used to write to channel A and trigger all channels to update the output voltage. For every channel, the variable can be selected dynamically. The address of the output variable for channel A is held in DacAAddr. The value at this address is converted to a float and written into the temporary variable DacVar. Offset, scaling and output mode can then be chosen. In signed mode, the offset of 32768_d is added to the scaled variable before it is converted to integer and written via the DSPLINK bus to the AD7835. For the trigger, a dummy value is written to the decoder to address Y6.

```
#define DACFSIGNED(x)     (x) + 32768.0

// write to channel A (or 1):
if (DacAMode > 0) {
  DacVar = *(double *)DacAAddr;
```

```
  if (DacAMode < 2)
    // DacAMode = 1 (unsigned):
    DAC->ChanA = (int) (DacVar*DacAScale + DacAOffs);
  else
    // DacAMode = 2 (signed):
    DAC->ChanA = (int) DACFSIGNED(DacVar*DacAScale + DacAOffs);
}

// synchronous DAC update:
DAC->Trigger = 0x0;
```

Further digital I/O functions are integrated on the board. A digital 8 bit word can be output to an LED bank. Output Y5 of the address decoder is used to access the buffer chip 74x273. This chip contains buffers so that the data word is available at the outputs until a new input is latched. The current driving capability is high enough to power the eight LEDs via a $1k$ resistor bank. The base address is the same as for the DACs but with the address offset of 5 for pin Y5. A structure is not required. This is why the pointer LEDaddr is of type *int*. A set of switching conditions for the LEDs can be defined. These have to be written to a temporary variable LedWrite first before they can be output to the board.

```
#define LEDOFF    0x0             /* switch off all LEDs     */
#define LEDRUN    0x40            /* switch on left gr. LED  */
#define LEDSTOP   0x80            /* switch on red left LED  */
#define LEDBASE  (DACBASE + 0x5) /* LED write @ 0x9000804D  */

volatile  int    *LEDaddr  = (int *)   LEDBASE;
LedWrite       = LEDSTOP;          // indicate control disabled
*LEDaddr       = LedWrite;         // write to LEDs
```

A similar feature is realized by reading from the switch block DIP 2. This can be useful when configuring the control software on the fly. Predefined modes can be set by the DIP-switches. The inputs of the 74x245 buffer are pulled up. If the DIP switch is open, the voltage is high, for a closed switch, the level is low. Line Y4 enables the buffer chip. The software structure is similar to that for the LEDs:

```
#define DIPBASE  (DACBASE + 0x4) /* read DIP @ 0x9000804C   */

volatile  int    *DIPaddr  = (int *)   DIPBASE;
```

For the digital I/O, two 74x245 buffers are used. A slide switch S2 is used to determine the direction of the data flow. In in position, the buffers only allow data from the B

to A bus. This is reading of data into the C40. For the **out** position, the C40 can only write digital data via the buffers. Reading data results in undefined values. In W/R position, the direction of the data flow is determined by the $\overline{W}$/R signal and thus by software. Out of 16 bits, the upper 13 bits can be sent via the buffers to the header J1. The lower three pins of J1 are connected to Ground, Power and the $\overline{W}$/R signal.

```
#define PIOBASE  (DACBASE + 0x7) /* port I/O  @ 0x9000804F  */

volatile  int    *PIOaddr  = (int *)   PIOBASE;
OutWrite       = 0x0550;          // set pins 11,9,7,5
*PIOaddr       = OutWrite;        // send 0000010101010[xxx]b
```

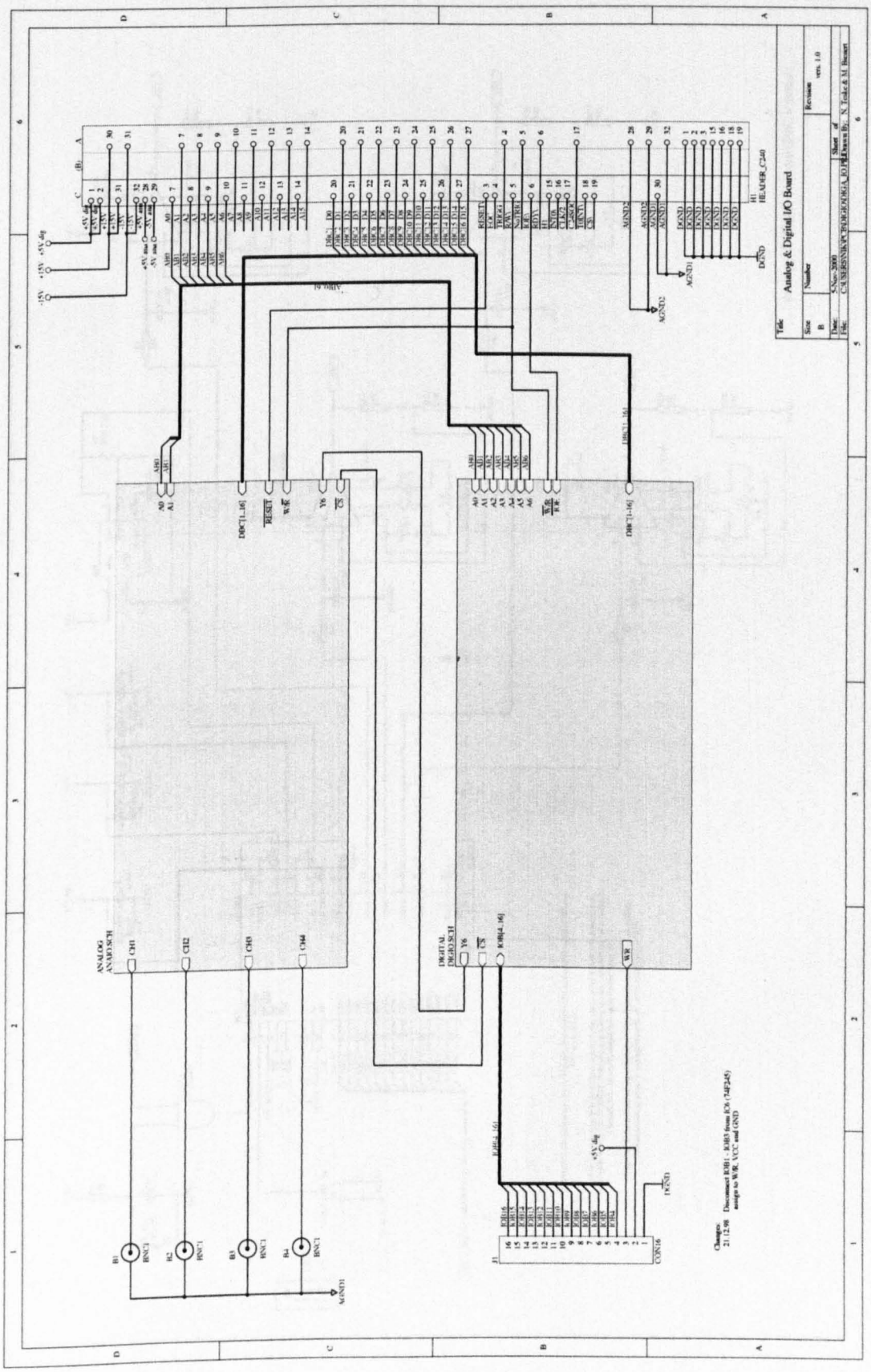

Figure D.20: *Schematic of Digital and analogue output Board*

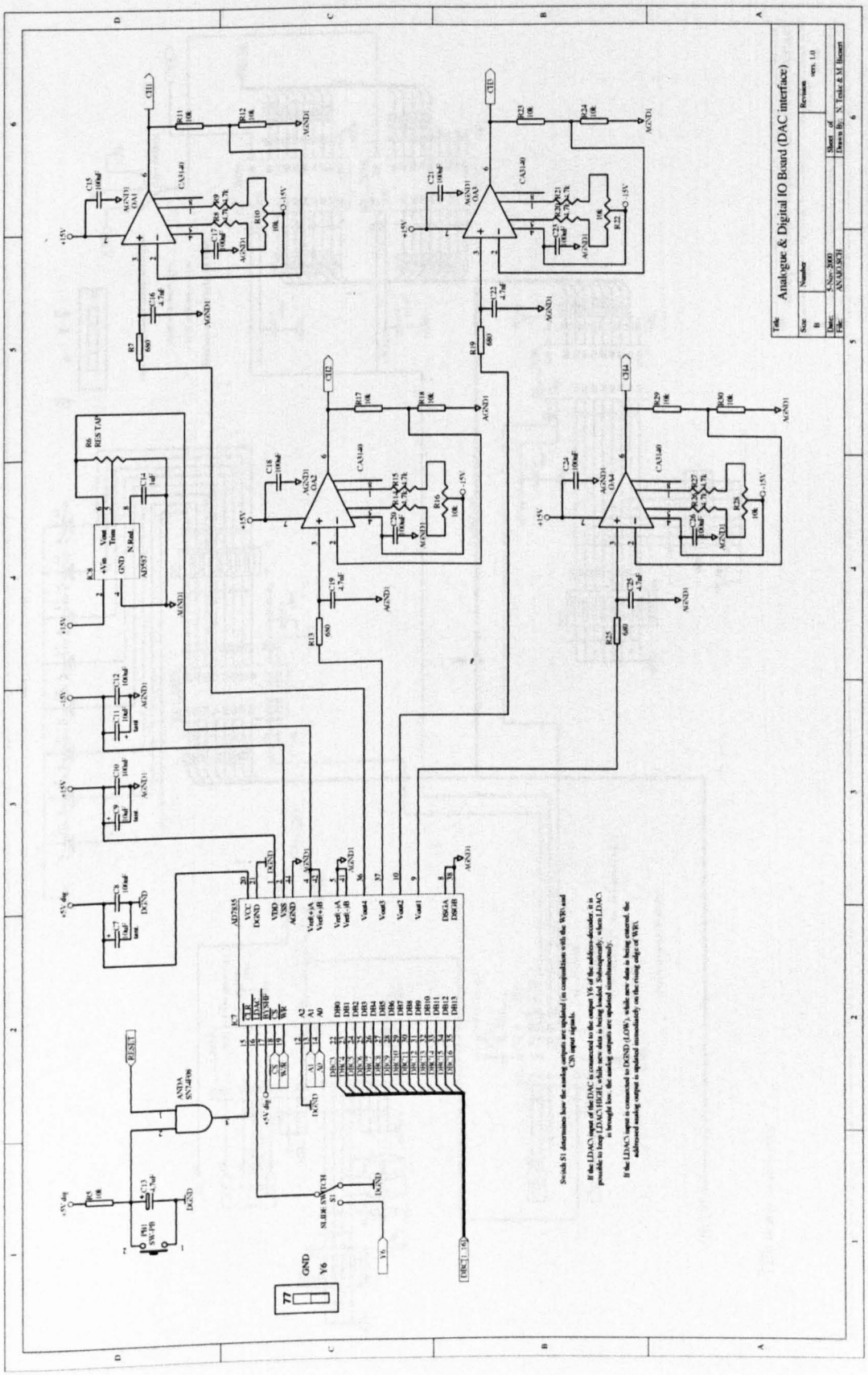

Figure D.21: *Schematic of DAC connections (analogue outputs)*

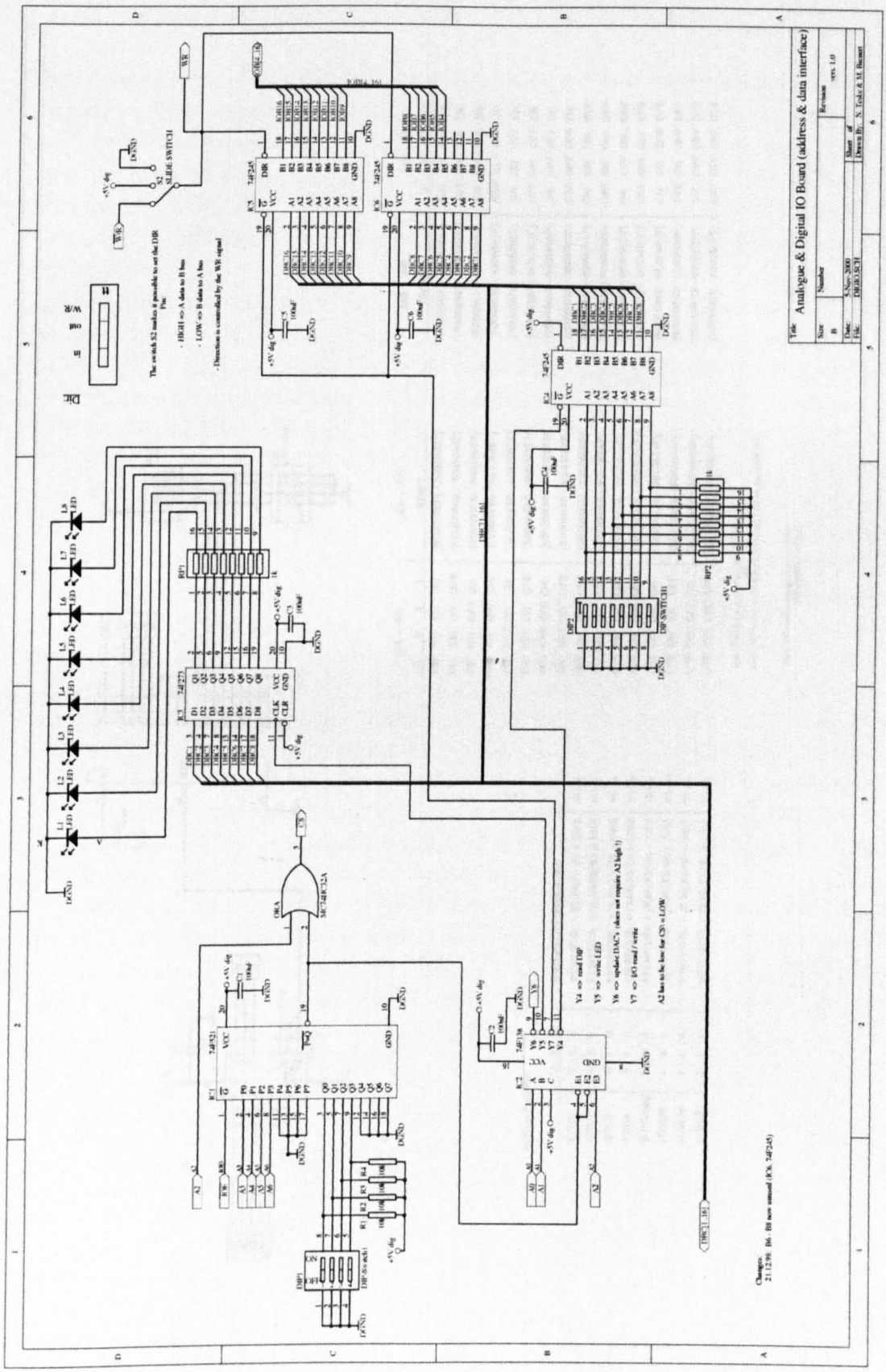

Figure D.22: *Schematic of digital outputs on DAC Board*

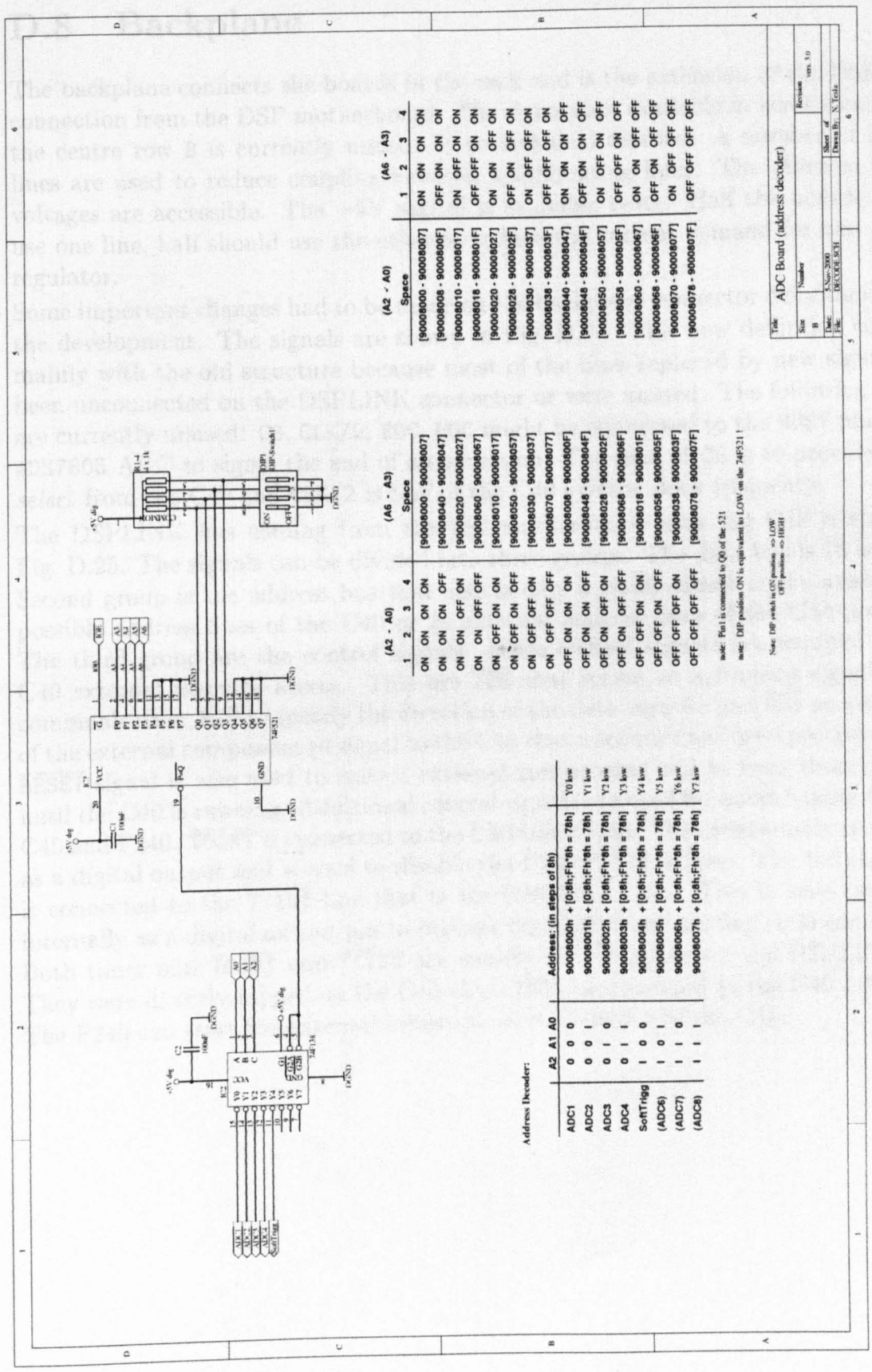

Figure D.23: *Schematic of DAC Address Decoder Board*

D.8 Backplane

The backplane connects the boards in the rack and is the extension of the DSPLINK connection from the DSP motherboard. The signals are available in three rows where the centre row B is currently unused to to technical reasons. A number of ground lines are used to reduce coupling between neighbouring lines. The different supply voltages are accessible. The +5V digital is available twice. Half the boards should use one line, half should use the other to reduce the current demand for one voltage regulator.

Some important changes had to be made on the backplane connector definition during the development. The signals are shown in Fig. D.24. This new definition complies mainly with the old structure because most of the lines replaced by new signals had been unconnected on the DSPLINK connector or were unused. The following signals are currently unused: CS, CLK/2, EOC. EOC might be connected to the BUSY pin on the ADS7805 ADC to signal the end of a conversion. The idea of CS is to provide a *chip select* from the C40 and CLK/2 is half of the C40 system clock frequency.

The DSPLINK bus coming from the LSI motherboard with the C40 is shown in Fig. D.25. The signals can be divided into three groups. The data bus is 16 bit wide. Second group is the address bus that also is only a small subset of the available 32 possible address lines of the C40 or 24 external address lines of the C44 processor. The third group are the control signals. Basic control signals are required for the C40 external memory access. This are $\overline{\text{IOE}}$ that serves as a framing signal of the communication, R/$\overline{\text{W}}$ to specify the direction of the data transfer and $\overline{\text{RDY}}$ as a feedback of the external component to signal to the C40 that a transfer has been processed. The $\overline{\text{RESET}}$ signal is also used to restart external components and to keep them disabled until the C40 is running. Additional control signals are used for handshaking between C40 and F240. $\overline{\text{TOINT}}$ is connected to the C40 timer0 pin. This is internally configured as a digital output and is used to disable the F240 PWM output. The NoTrig signal is connected to the $\overline{\text{T1INT}}$ line that is the C40 timer1 pin. This is here configured internally as a digital output pin to prevent the F240 from starting A/D conversions. Both timer pins $\overline{\text{TOINT}}$ and $\overline{\text{T1INT}}$ are usually not available via the DSPLINK bus. They were directly tapped on the C40 chip. $\overline{\text{INT0}}$ is connected to the C40 IIOF2 pin. The F240 can start the external interrupt service routine of the C40.

Busplane: male connector

	C	B	A	
1	+5V dig		DGND	1
2	+5V dig		DGND	2
3	$\overline{\text{RESET}}$		DGND	3
4	EOC		TRIGG	4
5	R/$\overline{\text{W}}$		$\overline{\text{NoTRIG}}$	5
6	$\overline{\text{IOE}}$		$\overline{\text{RDY}}$	6
7	A0		A1	7
8	A2		A3	8
9	A4		A5	9
10	A6		A7	10
11	A8		A9	11
12	A10		A11	12
13	A12		A13	13
14	A14		A15	14
15	H1		DGND	15
16	$\overline{\text{INT0}}$		DGND	16
17	CLK/2		F24SOC	17
18	$\overline{\text{T0INT}}$		DGND	18
19	$\overline{\text{CS}}$		DGND	19
20	D0		D1	20
21	D2		D3	21
22	D4		D5	22
23	D6		D7	23
24	D8		D9	24
25	D10		D11	25
26	D12		D13	26
27	D14		D15	27
28	+5V ana		AGND2	28
29	-5V ana		AGND2	29
30	AGND1		+15V	30
31	+15V		-15V	31
32	-15V		AGND1	32
	C	B	A	

inner (upper) row

middle row

outer (lower) row

$\overline{\text{RESET}}$ from C40 motherboard, reset all peripherals

EOC (unused),
ADC's signal end of conversion

TRIGG ADC - SOC (started by F240)
note: > 40ns, < 6µs!!

NoTRIG C40 prevents F240 starting ADC conversion while C40 reads ADC's.
-> C40 TIMER1 I/O pin, high act

$\overline{\text{RDY}}$ DPRAM access from C40 finished

R/$\overline{\text{W}}$ read/ write from C40

$\overline{\text{IOE}}$ C40 performs external memory access via DSPLINK when low

$\overline{\text{INT0}}$ C40 sync by F240, starts C40 control period (connected to the C40 IIOF2 pin!)

$\overline{\text{T0INT}}$ C40 Timer0 overflow (to stop F240 PWM!)
-> C40 TIMER0 I/O pin

F24SOC (unused), extra trigger

CLK/2 (unused), C40 CPU speed

$\overline{\text{CS}}$ (unused), chip select

note: TRIGG was formerly sent by C40
NoTrig signal replaces STRB\
INT0\ replaces (unused) H3 clock
T0INT\ replaces (unused) TCLK

BPLANE3.cdr
26.06.1999

Figure D.24: *New Bus Plane Layout*

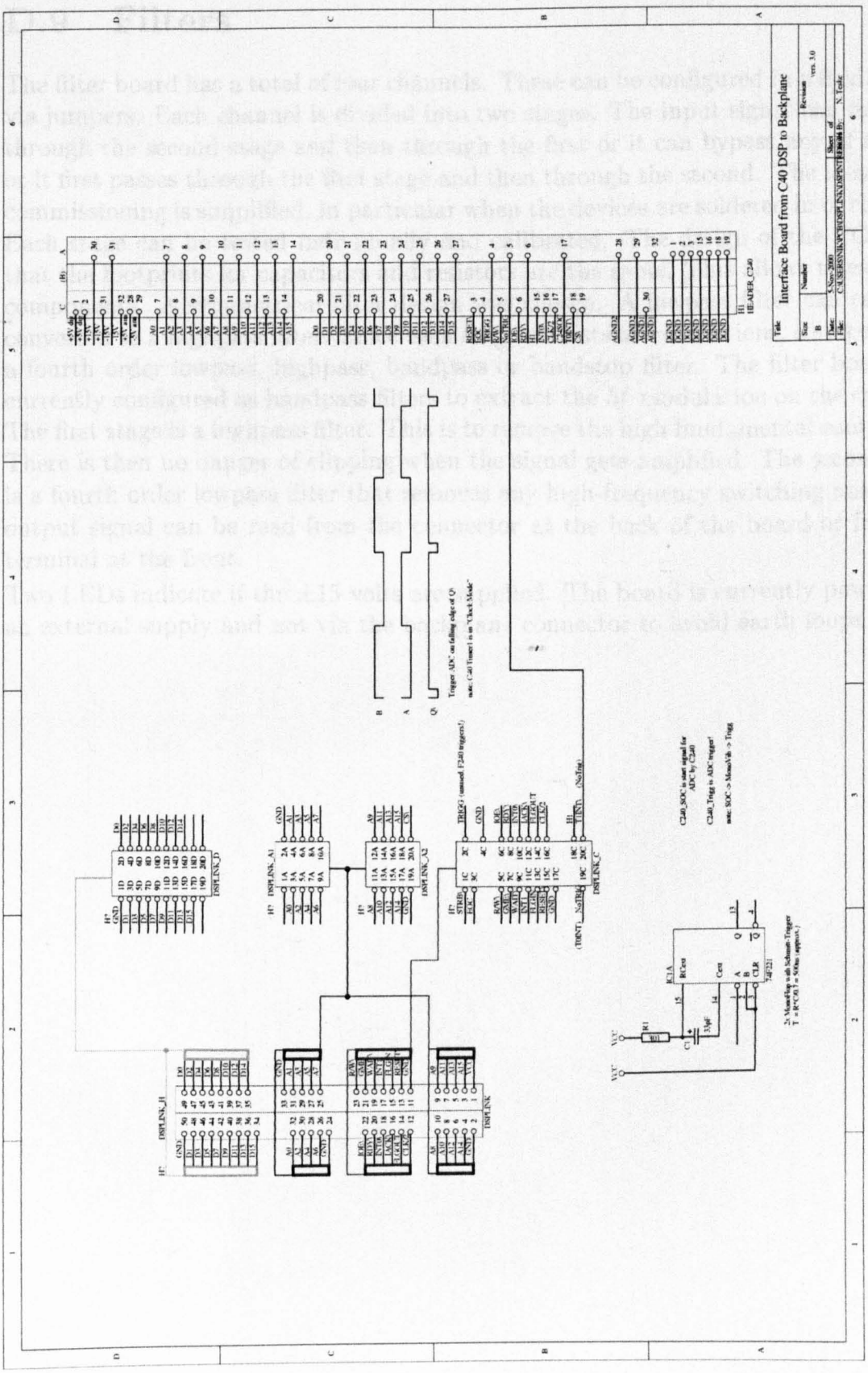

Figure D.25: *Schematic of Backplane connections to DSP Motherboard*

D.9 Filters

The filter board has a total of four channels. These can be configured in a flexible way via jumpers. Each channel is divided into two stages. The input signal can first pass through the second stage and then through the first or it can bypass any of the two or it first passes through the first stage and then through the second. The idea is that commissioning is simplified, In particular when the devices are soldered in or changed. Each stage can be tested individually and calibrated. The design of the PCB is so that the footprints for capacitors and resistors are the same. This allows to exchange components. A symmetrical filter design was chosen. A lowpass filter can easily be converted to a highpass filter. Since each stage consists of two sections, a stage can be a fourth order lowpass, highpass, bandpass or bandstop filter. The filter boards are currently configured as bandpass filters to extract the *hf* modulation on the currents. The first stage is a highpass filter. This is to remove the high fundamental component. There is then no danger of clipping when the signal gets amplified. The second stage is a fourth order lowpass filter that removes any high-frequency switching noise. The output signal can be read from the connector at the back of the board or from the terminal at the front.

Two LEDs indicate if the ± 15 volts are supplied. The board is currently powered by an external supply and not via the backplane connector to avoid earth loops.

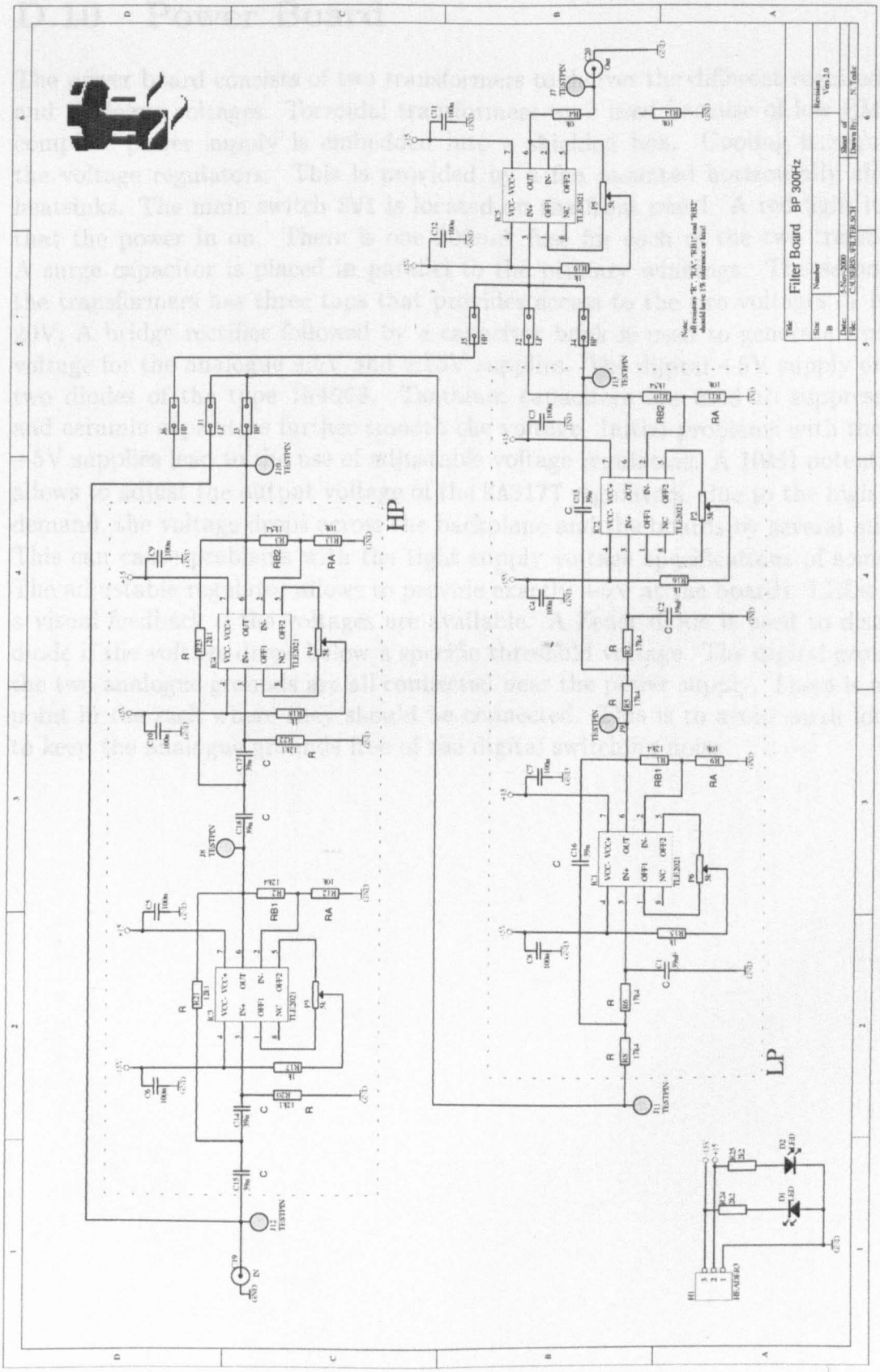

Figure D.26: *Schematic of 300Hz analogue bandpass filter (1 channel out of 4)*

D.10 Power Board

The power board consists of two transformers to deliver the different required digital and analogue voltages. Torroidal transformers were used because of low EMC. The complete power supply is embedded into a shielded box. Cooling is required by the voltage regulators. This is provided by a fan mounted horizontally above the heatsinks. The main switch `SW1` is located on the front panel. A red light indicates that the power in on. There is one $200mA$ fuse for each of the two transformers. A surge capacitor is placed in parallel to the primary windings. The secondary of the transformers has three taps that provides access to the two voltages of 10V and 20V. A bridge rectifier followed by a capacitor bank is used to generate smooth dc voltage for the analogue $\pm$5V and $\pm$15V supplies. The digital +5V supply only uses two diodes of the type `1N4003`. Tantalum capacitors are used to suppress spikes and ceramic capacitors further smooth the voltage. Initial problems with the digital +5V supplies lead to the use of adjustable voltage regulators. A $10k\Omega$ potentiometer allows to adjust the output voltage of the `KA317T` regulators. due to the high current demand, the voltage drops across the backplane and the boards by several millivolts. This can cause problems with the tight supply voltage specifications of some chips. The adjustable regulator allows to provide exactly +5V at the boards. LEDs provide a visual feedback if the voltages are available. A Zener diode is used to disable the diode if the voltage drops below a specific threshold voltage. The digital ground and the two analogue grounds are all connected near the power supply. There is no other point in the rack where they should be connected. This is to avoid earth loops and to keep the analogue grounds free of the digital switching noise.

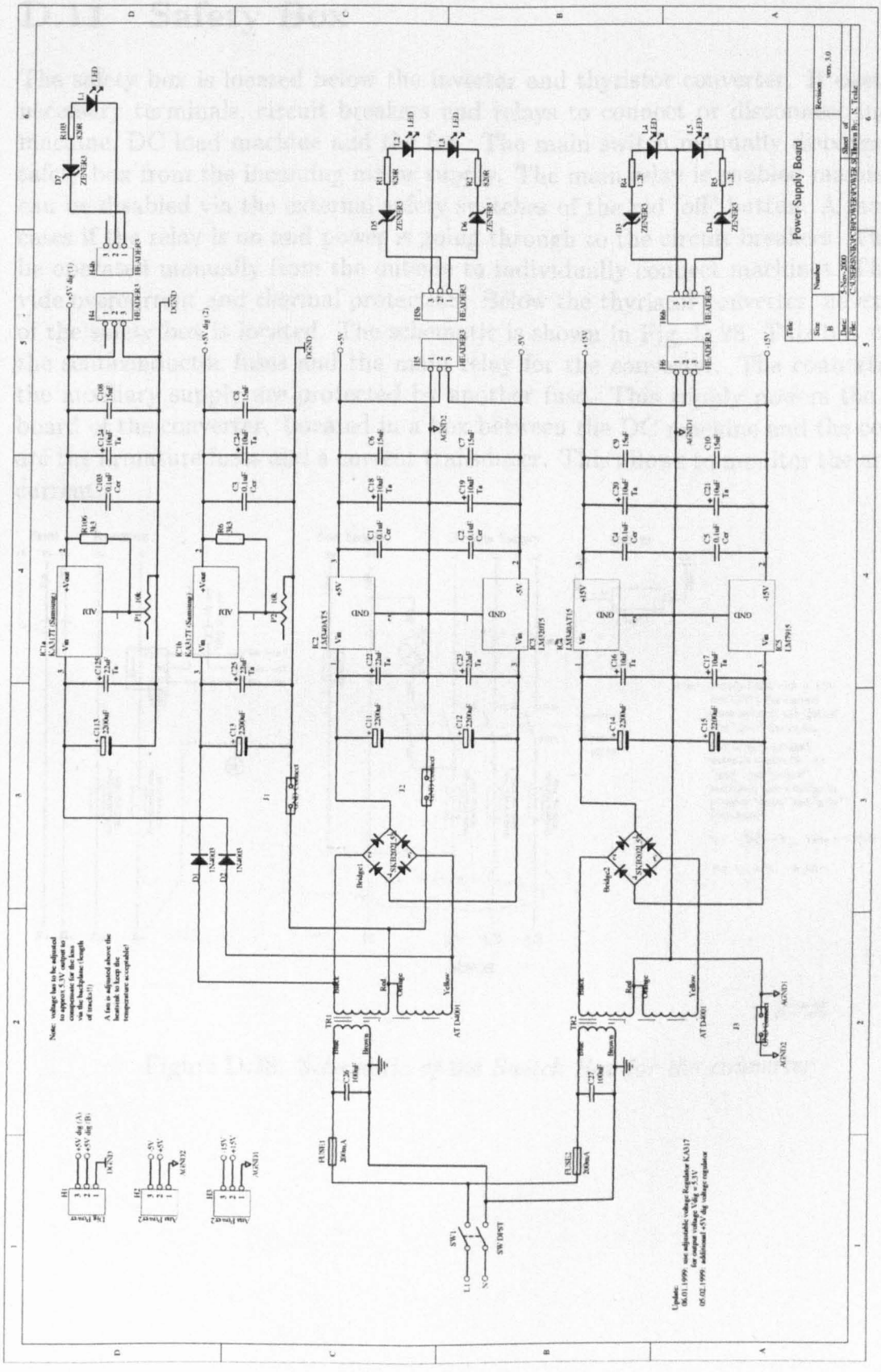

Figure D.27: *Schematic of Power Board*

D.11 Safety Box

The safety box is located below the inverter and thyristor converter. It contains all necessary terminals, circuit breakers and relays to connect or disconnect induction machine, DC load machine and the fan. The main switch manually disconnects the safety box from the incoming mains supply. The main relay is enabled manually and can be disabled via the external safety switches of the red 'off' button. A lamp indicates if the relay is on and power is going through to the circuit breakers. These can be operated manually from the outside to individually connect machines. They provide overcurrent and thermal protection. Below the thyristor converter, an extension of the safety box is located. The schematic is shown in Fig. D.28. This box contains the semiconductor fuses and the main relay for the converter. The connections for the auxiliary supply are protected by another fuse. This supply powers the control board of the converter. Located in a box between the DC machine and the converter are the armature fuses and a current transducer. This allows to monitor the armature current.

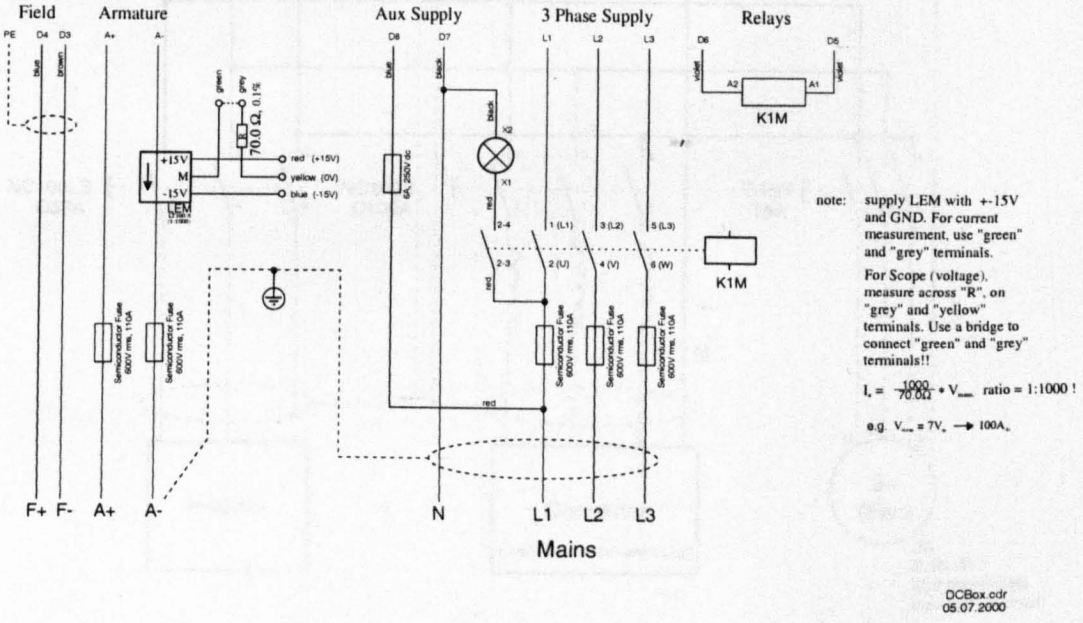

Figure D.28: *Schematic of the Switch Box for the converter*

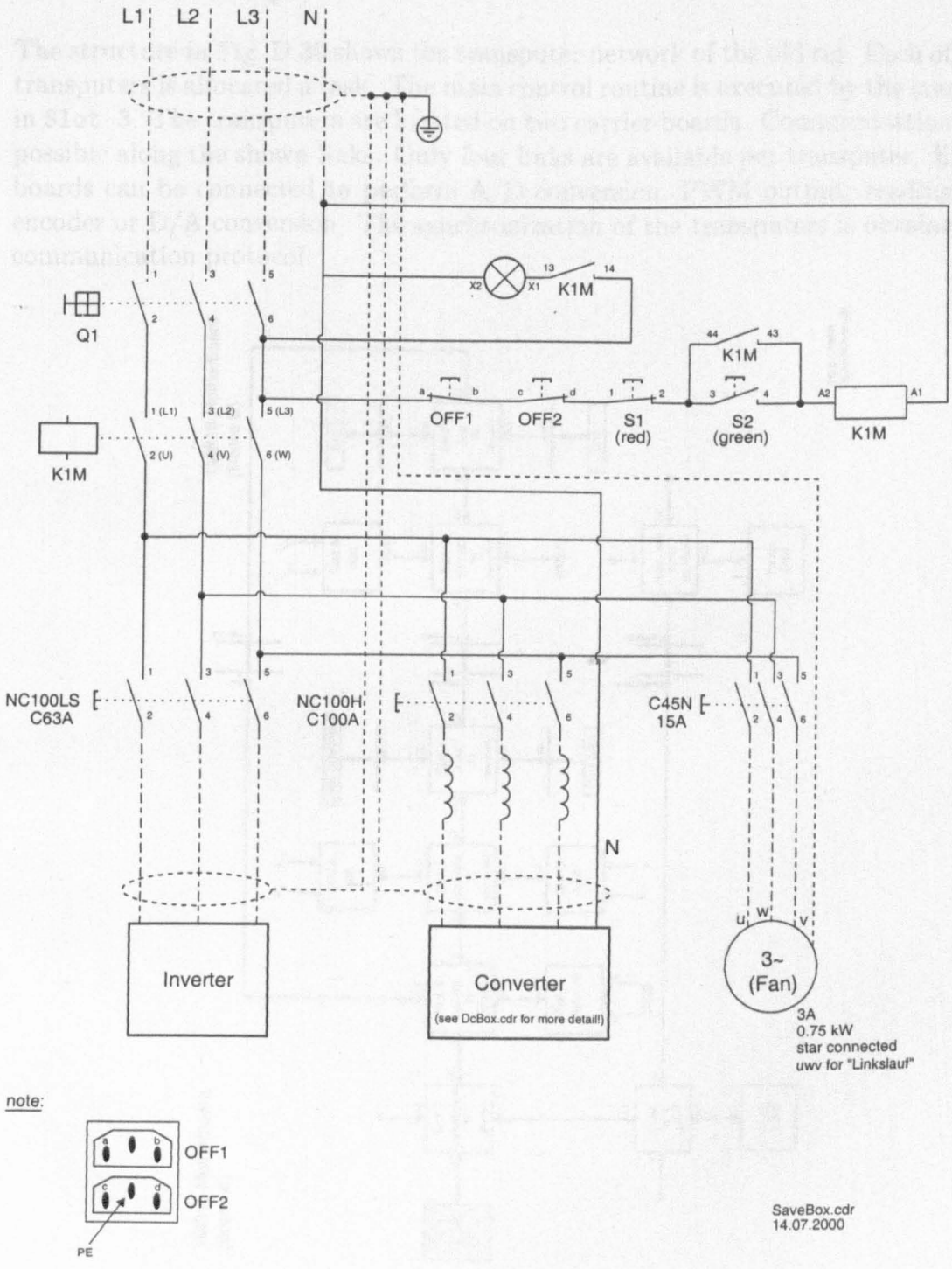

Figure D.29: *Schematic of the Safety Box*

D.12 Transputer Structure

The structure in Fig. D.30 shows the transputer network of the old rig. Each of the six transputers is allocated a task. The main control routine is executed by the transputer in `Slot 3`. The transputers are located on two carrier boards. Communication is only possible along the shown links. Only four links are available per transputer. External boards can be connected to perform A/D conversion, PWM output, reading of the encoder or D/A conversion. The synchronization of the transputers is obtained via a communication protocol.

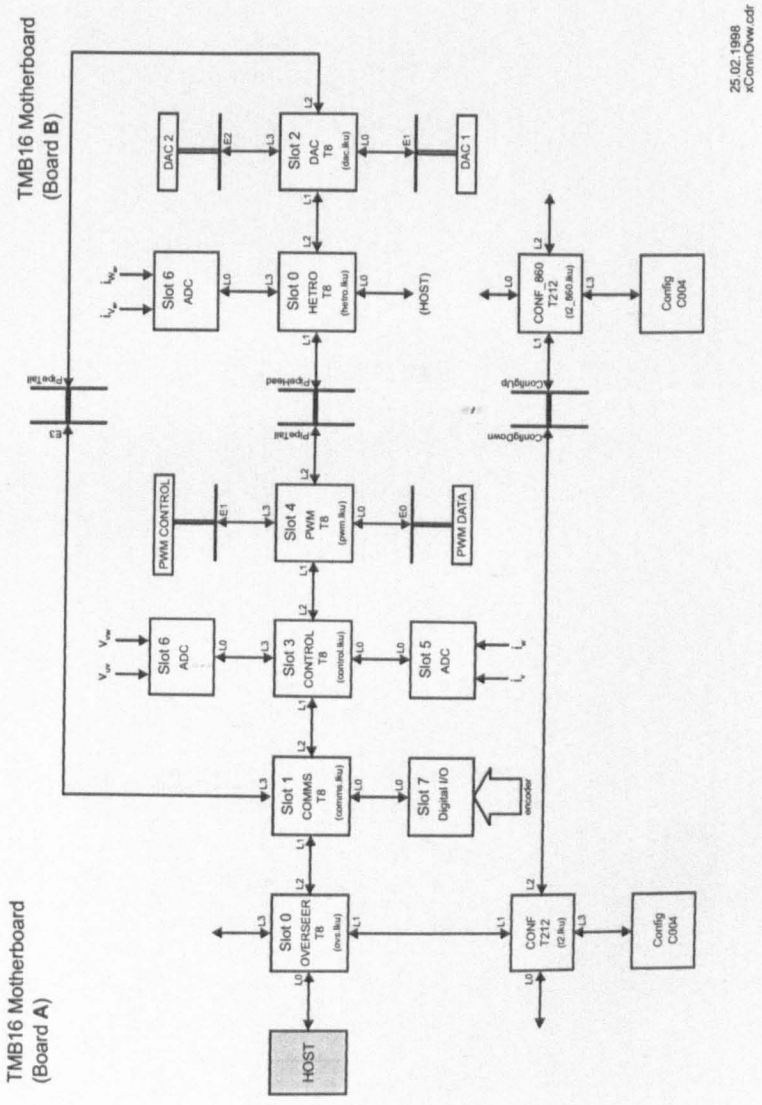

Figure D.30: *Structure of the transputer network with interfaces*